Functionalised Metal-Organic Frameworks

Rixson, Daniel

Award date:
2020

Awarding institution:
University of Bath

Functionalised Metal-Organic Frameworks

Daniel Rixson

A thesis submitted for the degree of Doctor of Philosophy

University of Bath

Department of Chemistry

Supervisors: Professor Andrew Burrows and Dr Mary Mahon

May 2020

This thesis is dedicated to Ruth Lunt

“The flower that blooms in adversity is the most rare and beautiful of all.”

Abstract

The research in this thesis builds upon the field of metal-organic frameworks (MOFs) and is concerned with two research themes. The first involves the investigation of novel MOFs constructed using newly designed and synthesised semi-rigid organic ligands. The second looks at the application of functionalised MOFs in the uptake and release of guest pheromones and semiochemicals, with a view to enhancing the performance of lure traps for pest species.

Chapter 1 introduces the research space of MOFs, outlining definitions and terminology associated with this class of crystalline coordination polymer. Framework building blocks are discussed along with the concept of reticular synthesis. The key properties of MOFs are emphasised and some of the characteristic structural features highlighted. Examples pertaining to the most commonly studied applications for MOFs including gas adsorption, catalysis, sensing and drug delivery are also detailed.

Chapter 2 presents the design and synthesis of the new organic molecule 5-((carboxymethyl)amino)isophthalic acid (H_3cmai). This species was targeted for study due to its semi-rigid nature, variety of coordination sites on anions derived from this and unexplored research space in the MOF area. H_3cmai was reacted with cadmium(II) salts, leading to the formation of six different frameworks. Zinc(II), copper(II) and cobalt(II) salts were also reacted with H_3cmai, resulting in the formation of a further four new MOFs. The cadmium MOFs showed extensive variety in dimensionality, ligand coordination modes, thermal behaviour and internal void sizes. The frameworks based on the first-row d-block metals showed less structural variation, with the cobalt, copper and one of the zinc MOFs being isostructural. The copper-based material was found to be photocatalytically active for the decomposition of the environmentally persistent dye Rhodamine B. Common themes identified within the 10 MOFs were the chelating bidentate binding mode of the flexible arm intrinsic to the cmai-based linker and the presence of water ligands. Notably, only the cadmium-based MOFs formed 3-D frameworks.

Chapter 3 focuses on the synthesis of cmai-containing frameworks that also contained neutral N-donor ligands. These were targeted as a way of increasing framework dimensionality in an effort to produce networks with larger cavities. Five new compounds were obtained with cadmium(II) centres and four new compounds were synthesised containing zinc(II) centres. As with the compounds in **Chapter 2**, the MOFs formed were diverse in structure and properties. A higher proportion of the synthesised materials were three-dimensional networks, suggesting the addition of the N-donor ligands had the intended effect. Two charged frameworks were

observed, one containing a balancing nitrate ion whilst the other contained a second charge balancing framework, a very rare structural feature.

Chapter 4 introduces another new linker, 2,2'-((1,4-phenylenebis(methylene))bis(azanediyl))-diterephthalate (tpat). This linker contains a semi-rigid tethering *p*-xylene group, connecting two terephthalate units together. The combination of this linker with zinc(II) led to the synthesis of two novel cross-linked frameworks. The MOFs share their base topology with previously reported structures, the difference being the presence of the tethering group spanning the pores. The location of the tethering group was postulated using geometric considerations as it could not be viewed in the single-crystal data. The presence of the cross-linking tether was shown to increase guest retention within the framework. The synthesis of mixed-linker MOFs, varying the amount of cross-linking within the framework, was shown to provide a route to control the extent of the guest entrapment.

Chapter 5 describes the use of MOFs as hosts for guest semiochemicals for application in lure-based traps for pest species. Three different semiochemicals were targeted for study, 3-octanone, isoamyl acetate and 1-hexanol. Out of a range of investigated MOF systems IRMOFs, $[Zn_4O(bdc\text{-}X)_3]$ (bdc = 2-X-1,4-benzenedicarboxylate, X = H, NH_2, NHPr and OPr), were shown to be most promising hosts due to high semiochemical uptake in combination with their propensity to allow functionalisation of the dicarboxylate linker. Careful selection of the linker functionalisation was shown to enhance uptake of the semiochemicals. The release of the semiochemicals was also tracked and the linker functionalisation was again highlighted as a method of controlling the system's behaviour. The three different semiochemicals studied all interacted with the frameworks differently, giving unique release profiles, leading to the conclusion that optimisation of a semiochemical-MOF system must be carried out on a case by case basis.

Acknowledgements

Firstly, I would like to thank both of my supervisors for their continuous and unwavering support for the duration of my PhD. Andy, the importance of the ability to drop in and discuss anything and everything cannot be understated. Thank you, Mary, for the hours and hours invested into my crystallography knowledge, I really appreciate it and it has become my favourite area of study.

Thanks goes to all past and present members of the Burrows research group, including project students, for making my time in the lab and office enjoyable. Special thanks go to Sébastien Rochat, Joe Paul-Taylor and Güneş Günay Sezar whom I have had the pleasure of sharing in their expertise and ideas on various aspects our projects.

At this point I would also like to thank and acknowledge Güneş Günay Sezar for collaboration on the synthesis of compounds **15** and **19** as well as for the catalytic studies performed on compounds **7**, **8** and **9**. I would also like to thank my project student Kate George for work pertaining to compound **18**.

I would like to thank my parents for their support throughout all parts of my education, allowing me to make it this far. Finally thank you to Ruth, having you with me has made this experience one that I have truly loved. You have pushed me to succeed and grow in both in my academic career and personally.

Abbreviations

ASU	Asymmetric Unit
atc	1,3,5,7-adamantanetetracarboxylate
bdc	1,4-benzenedicarboxylate
bdc-NH_2	2-amino-1,4-benzenedicarboxylate
bdc-NHBu	2-aminobutyl-1,4-benzenedicarboxylate
bdc-NHPr	2-aminopropyl-1,4-benzenedicarboxylate
bdc-NHOct	2-octylamino-1,4-benzenedicarboxylate
bdc-OPr	2-propoxy-1,4-benzenedicarboxylate
bpdc	Biphenyl-4,4'-dicarboxylate
BET	Brunauer-Emmett-Teller
bipy	4,4'-bipyridine
bpe	1,2-bis(4-pyridyl)ethylene
btb	1,3,5-benzenetribenzoate
btc	1,3,5-benzenetricarboxylate
dabco	1,4-diazabicyclo[2.2.2]octane
cadi	5,5'-(carbonylbis(azanediyl))diisophthalate
cboi	5-((4-carboxybenzyl)oxy)isophthalate
cdc	9H-carbazolyl-3,6-dicarboxylate
cmai	5-((carboxylatomethyl)amino)isophthalate
CSD	Cambridge Structural Database
DEF	*N,N*-Diethylformamide
Hdfp	Deferiprone
DMF	*N,N*-Dimethylformamide
dobdc	2,5-dioxido-1,4-benzenedicarboxylate
FTIR	Fourier transform infrared
γ-CD	γ-cyclodextrin
hex	1-hexanol
HKUST	Hong Kong University of Science and Technology

iaa	Isoamyl acetate
Im	Imidazolate
IRMOF	Isoreticular metal-organic framework
mbdc-NH_2	5-amino-1,3-benzenedicarboxylate
1-MCP	1-methylcyclopropene
Meim	2-methylimidazolate
mhp	4-methyl-3-heptanone
MIL	Materials Institute Lavoisier
MOF	Metal-organic framework
NMR	Nuclear magnetic resonance
NU	Northwestern University
oct	3-octanone
PBS	Phosphate buffered saline
Phen	1,10-phenanthroline
PSM	Post-synthetic modification
PTFE	Polytetrafluoroethylene
PXRD	Powder X-ray diffraction
RhB	Rhodamine B
SBU	Secondary building unit
tbta	4,4’-(1,4-(trans-2-butene)diyl)bis(1,2,4-triazole)
TGA	Thermogravimetric analysis
tpat	2,2'-((1,4-phenylenebis(methylene))bis(azanediyl))diterephthalate
tpt	2,4,6-tri(4-pyridinyl)-1,3,5-triazine
UiO	University of Oslo
ZIF	Zeolitic imidazolate framework

Table of Contents

Chapter 1 - Introduction

1.1 What is a Metal-Organic Framework?

Metal-organic frameworks (MOFs) are a class of crystalline polymer formed from the well-established principles of coordination chemistry. MOFs are most well known for their porosity and high surface areas, ranging from 800 – 8000 $m^2 g^{-1}$, exceeding that of other porous materials such as activated carbons and zeolites. They are highly tuneable; the topology and dimensions of the network formed can be altered by changing the metal-containing node or organic linkers. In general, they possess good thermal and chemical stability, and have been investigated for use in an array of fields, the majority of which utilise their porosity and large internal surface areas. These include gas storage, separations, catalysis, sensing and drug delivery.[1-5]

MOFs are polymeric networks composed of metal containing nodes connected by organic ligands. The framework DMOF-1 is constructed from zinc dimer nodes, connected by 1,4-benzenedicarboxylate (bdc) and 1,4-diazabicyclo[2.2.2]octane (dabco) ligands. The structures of these three components are shown in **Figure 1.1**.[6]

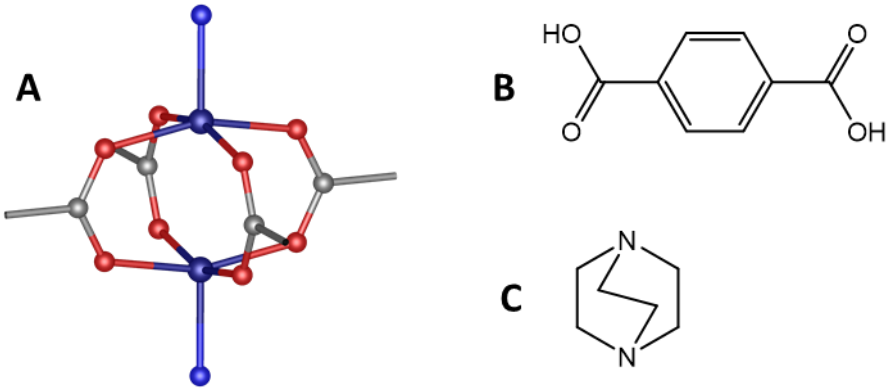

Figure 1.1. A – Zinc dimer node, **B** – 1,4-benzenedicarboxylate (bdc) and **C** – 1,4-diazabicyclo[2.2.2]octane (dabco).

DMOF-1 has the formula $[Zn_2(bdc)_2(dabco)]$ which comprises of 2-D square networks, formed from zinc dimers and bdc ligands, connected by pillaring dabco ligands to give a 3-D network. The zinc dimer is supported by the interaction of four bridging carboxylate groups originating from the bdc ligands. The ligands sit at 90° to each other, which in combination with their linear configuration leads to the formation of a 2-D square network as shown in **Figure 1.2**.

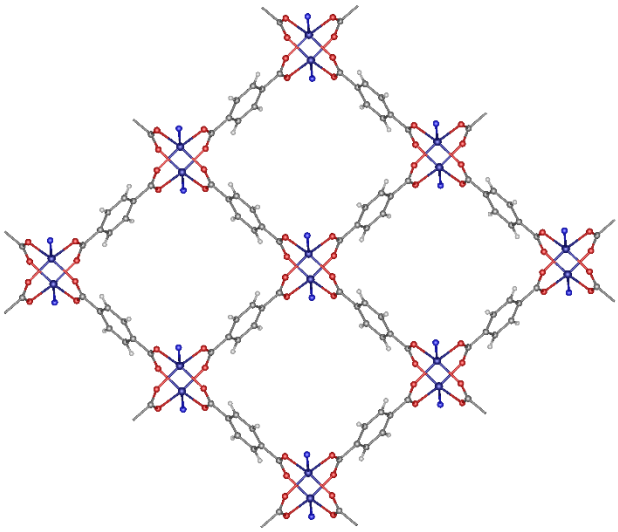

Figure 1.2. 2-D square network in DMOF-1 which sit in parallel to the *ab* plane.

The axial sites in the zinc dimers are occupied by dabco ligands which serve to join adjacent square network sheets into the overall 3-D structure, this is shown from two different angles in **Figure 1.3 A** and **B**. The CH_2 groups of the dabco molecules are disordered. As can be seen in **Figure 1.3 A,** DMOF-1 contains channels running in between the layers, these lie parallel to both the *a* and *b* axes.

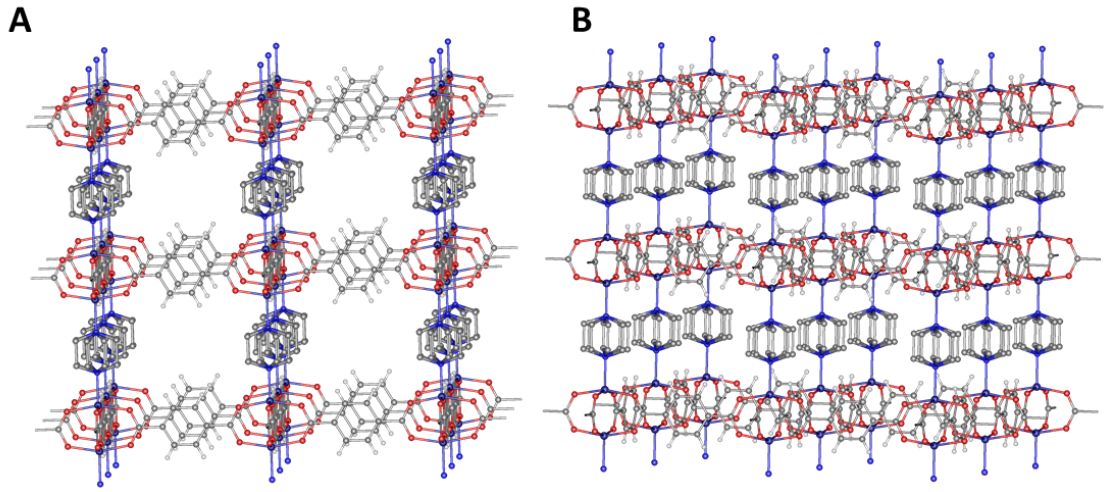

Figure 1.3. The structure of DMOF-1 shown from two different angles.

Channels also run in the direction of the *c*-axis, these run in the square-shaped gaps in the 2-D network formed by the zinc dimers and bdc linkers and are shown in **Figure 1.4**. These channels in the structure are the origin of the MOFs porosity and surface area. DMOF-1 has a BET surface area of 1450 $m^2\ g^{-1}$ and has been investigated for applications in hydrogen gas storage, CO_2 separation and catalysis.[6-8]

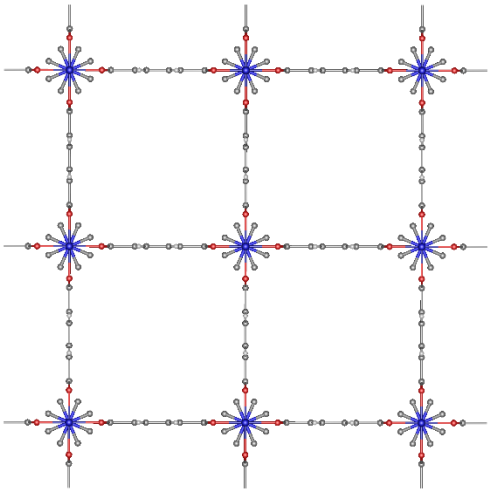

Figure 1.4. The structure of DMOF-1 as viewed down the *c*-axis.

1.1.1 Terminology: Coordination Polymers, Coordination Networks and Metal-Organic Frameworks

Since Yaghi *et al.* coined the term 'metal-organic framework' in a 1995 paper there have been different and sometimes conflicting definitions surrounding coordination polymers and MOFs, which revolve around chemical composition, crystallinity, dimensionality, porosity and robustness.[9-11]

In 2013 IUPAC released guidelines outlining definitions and descriptions for compounds falling into these classes and read as follows:[12]

Coordination Polymer – "A coordination compound with repeating coordination entities extending in 1, 2, or 3 dimensions."

Coordination Network – "A coordination compound extending, through repeating coordination entities, in 1 dimension, but with crosslinks between two or more individual chains, loops or spiro-links, or a coordination compound extending through repeating coordination entities in 2 or 3 dimensions."

Metal-Organic Framework – "A metal-organic framework, abbreviated to MOF, is a coordination network with organic ligands containing potential voids."

From these definitions it can be established that coordination networks are a sub-set of the overarching group of coordination polymers and that MOFs are a sub-set of coordination

networks, bring them under the umbrella of coordination polymers. These can be represented in a Venn diagram as shown in **Figure 1.5**.

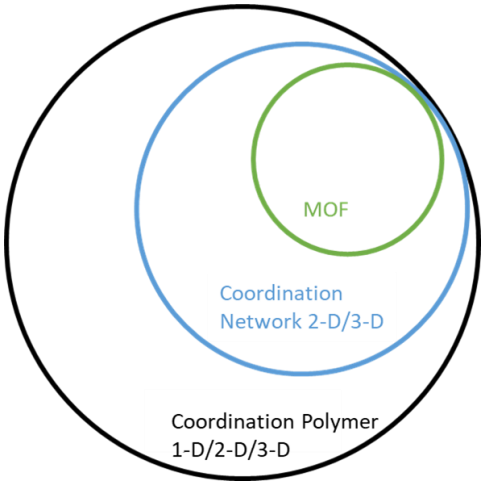

Figure 1.5. Venn diagram showing the relationship between MOFs, coordination networks and coordination polymers.

The IUPAC definition for a MOF states that the framework must contain potential voids. This describes a framework which, if the guest solvent molecules were removed, would contain pores and thus has the potential for porosity. It has been argued that porosity is not an absolute property and is dependent on both the nature of the guest and the framework, so there is some ambiguity in the IUPAC definition. It does not preclude the possibility of having non-crystalline MOFs, and there are examples of non-crystalline porous materials constructed from metal nodes and organic ligands. It can be argued however, that a well ordered structure is an essential parameter in the formation and identity of a framework and therefore crystallinity is an important factor. Despite IUPAC's suggestions, the definition of what exactly constitutes a MOF is still evolving and debated, with its use in the literature varying from group to group.[9, 13]

1.1.2 MOF Composition

Metal-organic frameworks consist of two component parts. These are the nodes of the framework, which are made up of metal centres or aggregates of metal centres. These nodes are bridged by organic moieties referred to as linkers. The combination of these components can form one-, two- or three-dimensional networks. The two and three dimensional networks, relevant for MOFs, are depicted schematically in **Figure 1.6**.

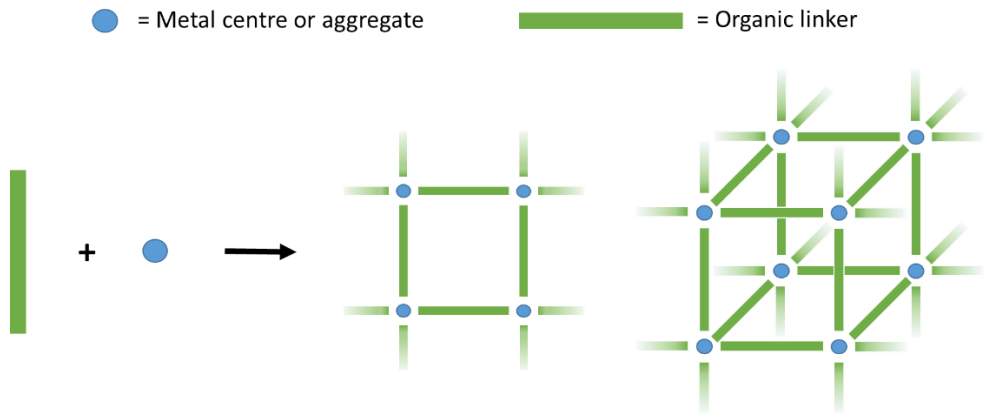

Figure 1.6. The components used in the formation of a 2-D and 3-D MOF.

The nodes in a MOF are formed from single metal centres or, more commonly, aggregates of two or more metal ions along with other species. The aggregates are held together by supporting interactions from the organic linkers and are known as secondary building units (SBUs). The formation of SBUs has several important ramifications for MOFs. In general, the number of interactions associated with the SBU is far larger than the number of interactions that would be associated with a corresponding single metal ion and its coordination sphere. This imparts a significant increase in stability due to the larger number of bonds that must be broken in order to disassemble the MOF relative to a single metal ion. The SBU can also possess geometry different to that of the metal centres it contains. This is to say, that through the use of SBUs, the nodes of a MOF can be of a much wider variety of geometries and sizes.[14, 15]

A specific example of a SBU common in MOF chemistry is $[Zn_4O(CO_2)_6]$, the structure of which is presented in **Figure 1.7**. The SBU contains four tetrahedral zinc centres arranged in a tetrahedron around a central oxygen anion. Each of the 6 edges of the tetrahedron formed by the zinc atoms is bridged by a carboxylate group originating from an organic linker, to give an overall octahedral geometry for the SBU, in contrast to the tetrahedral geometry of the individual zinc ions. It can also be seen that the SBU has a total of 16 Zn-O bonds, far more than the 6 that might be expected of a lone octahedral zinc centre.

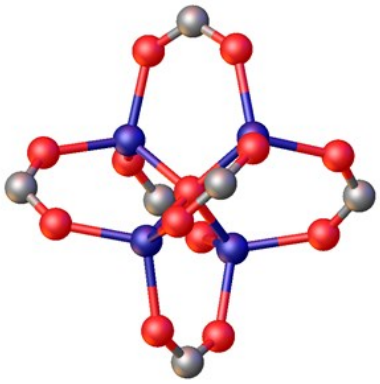

Figure 1.7. The structure of the SBU $[Zn_4O(CO_2)_6]$. (Navy Blue = zinc, red = oxygen, grey = carbon)

A huge number of SBUs of varying size, geometry and composition have been reported, some examples are presented in **Figure 1.8**. The identity of the metal, organic linker and reaction conditions all contribute to which SBU is likely to form during a synthesis and as such careful control of these parameters can allow for targeted synthesis of frameworks containing a specific SBU.

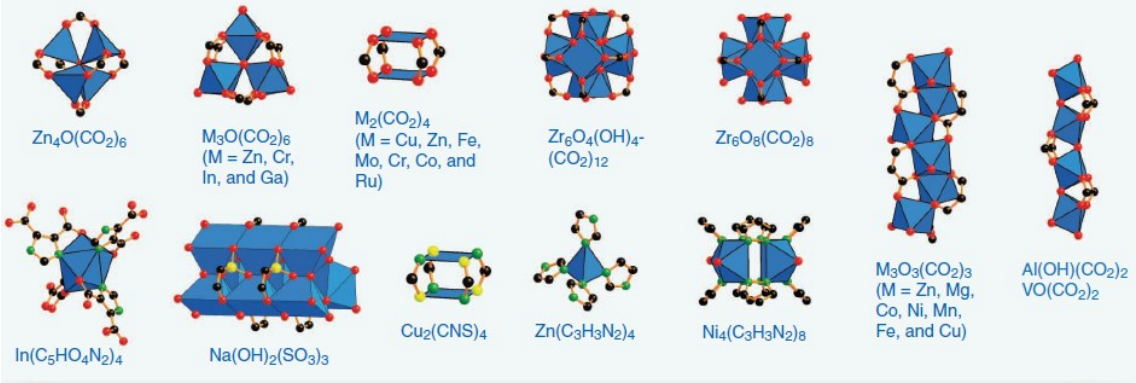

Figure 1.8. Examples of SBUs used in the formation of MOFs. The polyhedra represent the metal centres and their coordination geometry. (Blue = metal, red = oxygen, black = carbon, green = nitrogen, yellow = sulphur).[1]

The second constituent component of a MOF is the organic linker. These are organic moieties that contain two or more possible points of coordination and bridge between the nodes to form the overall network. The coordination is most commonly through oxygen and nitrogen containing functional groups. Where oxygen is concerned the linkers are usually polycarboxylates and ligating linkers based on nitrogen are usually polypyridine based or imidazolates.

The organic linkers play an equally important role in the overall topology of the MOF as the SBUs. Not only does the ligating group influence which SBU forms during the synthesis but the geometry and size of the organic linker also dictates the topology of the network formed. Some

examples of organic linker precursors and neutral linkers with different ligating groups, sizes and geometries are presented in **Figure 1.9**.

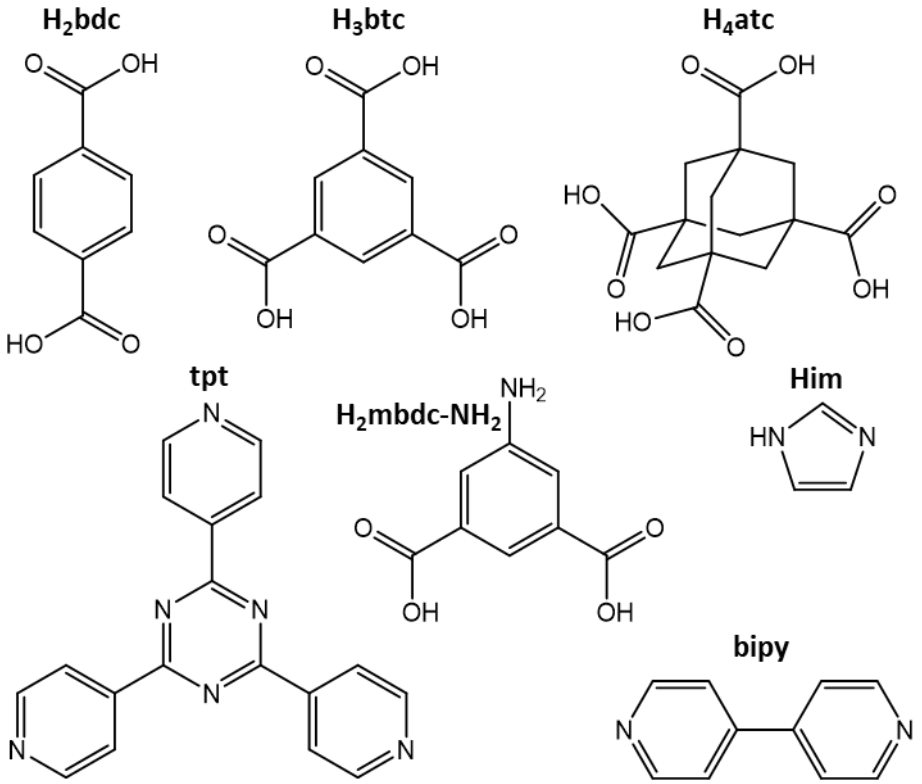

Figure 1.9. A range of organic linkers and precursors. (H_2bdc – 1,4-benzene dicarboxylic acid, H_3btc – 1,3,5-benzenetricarboxylic acid, H_4atc - 1,3,5,7-adamantanetetracarboxylic acid, H_2mbdc-NH_2 – 5-amino-1,3-benzenedicarboxylic acid, Him – imidazole, tpt - 2,4,6-tri(4-pyridinyl)-1,3,5-triazine, bipy – 4,4'-bipyridine).

1.1.3 Reticular Chemistry and Isoreticular Series

MOFs have well described building blocks in the form of SBUs and organic linkers which allow chemists to draw on reticular chemistry principles. This is the process of assembling discrete building units into predetermined ordered structures, in this case, MOFs. This facilitates the design of frameworks by drawing on SBU and linker libraries, the MOF can then be synthesised in the lab. Reticular synthesis is a powerful tool for allowing specific properties of a material to be targeted with specific applications in mind.[16-18]

Reticular chemistry can be exploited in the formation of isoreticular series of MOFs. These are families of frameworks that share the same overall topology. The members of these series can be synthesised by varying either the functionality or the length of the organic linker. The resulting framework must retain its connectivity, this leads to MOFs with different pore sizes,

shapes and functionalities. Isoreticular series can also be formed by changing the identity of the metal ion present in the SBU, while maintaining the topology of both the SBU and the framework.

An example of an isoreticular series is the IRMOFs. The 'IR' stands for isoreticular, the family of zinc(II) MOFs were first reported by Yaghi *et al.* and have the generic formula $[Zn_4O(L)_3]$ (L = linear dicarboxylate).[19] The SBU contains a tetrahedral arrangement of zinc(II) centres with an oxygen ion at its centre, supported by 6 carboxylate groups from the organic linkers, as shown in **Figure 1.7**. A total of 16 structures were reported in the original paper, with other examples reported since.

The most simple example is that of IRMOF-1 (also known as MOF-5) which contains bdc as a linker and has the formula $[Zn_4O(bdc)_3]$.[20] The associated cubic structure can be seen in **Figure 1.10 A**. The large number of linear dicarboxylates available allows for synthesis of isoreticular MOFs with a wide range of pore sizes, surface areas and pore functionalities. One example, shown in **Figure 1.10 B,** is that of IRMOF-8 which contains the linker 2,6-naphthalenedicarboxylate. This linker is longer than bdc so the distance between the nodes in the cubic network is increased, leading to a larger internal void space and a larger surface area. This same principle can also be used to introduce additional functionality into the pores of a framework by using linkers that fulfil the same structural role and bear the desired functional group.

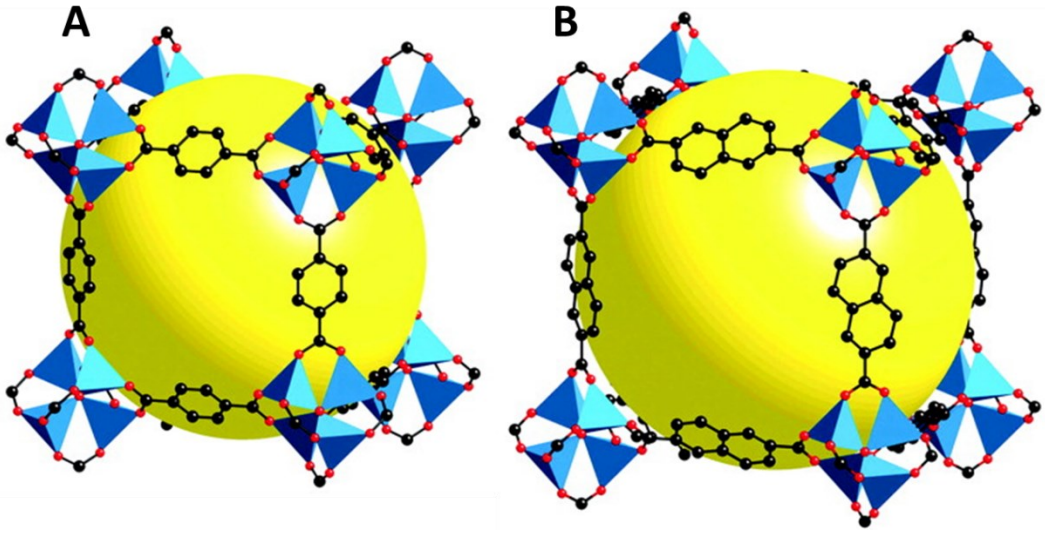

Figure 1.10. The structures of **A** MOF-5 (IRMOF-1) and **B** IRMOF-8. The yellow spheres give an indication of comparative void space.[21]

In the isostructural MIL-100 series the metal centres can be varied while retaining the overall topology of the framework. The first member of the series, MIL-100(Cr) with the formula

$[Cr_3(O)(X)(H_2O)_2(btc)_2]\cdot nH_2O$ (X = OH or F), was originally synthesised in the hydrothermal reaction of chromium metal in an aqueous solution of HF and 1,3,5-benzenetricarboxylic acid (H_3btc). The structure of MIL-100 is shown in **Figure 1.11**. The SBU is made up of a trimer of chromium(III) centres surrounding a μ_3-O anion. The chromium cations are bridged by six carboxylate groups from the btc linkers and also have an axial bond to a water ligand or charge balancing counter ion (X). Four of these units, linked by four btc linkers, form a supertetrahedron. These extend by sharing corners generating the overall MIL-100 framework. The structure contains three different pore sizes, a micropore at the centre of the supertetrahedron and two mesopores with diameters of 25 Å and 29 Å.[22]

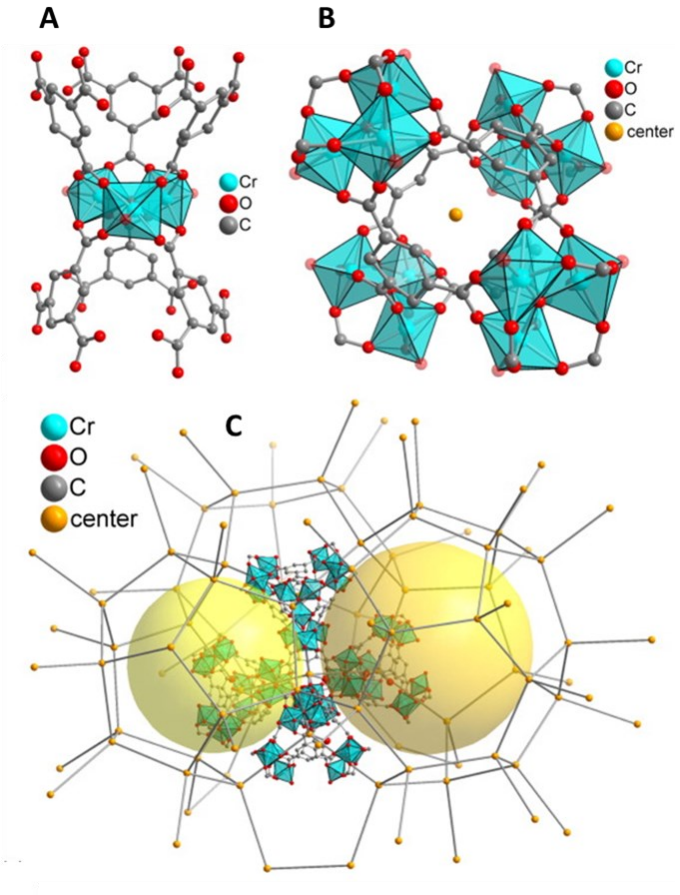

Figure 1.11. A – The secondary building unit of MIL-100(Cr), **B** – supertetrahedron with centre marker, **C** - overall structure of MIL-100 showing the small and large cage formed by the corner sharing supertetrahedra. Part of the structure is shown with just the centre marker of the supertetrahedra for clarity.[23]

MIL-100 analogues can be synthesised using a number of other metal(III) ions, such as iron, aluminium, scandium and vanadium.[24-27] All these structures have the same network topology as described above. Despite having the same overall structure, the differing metal centres offer unique advantages as well as fine-tuning properties in certain applications. For example, MIL-

100(Fe) is an attractive material as it is non-toxic, has unique redox chemistry and is environmentally sustainable. The non-toxic nature of this material has been exploited and the framework investigated for use in the delivery of the drug asprin.[28, 29]

1.1.4 Post-synthetic modification of MOFs

Post-synthetic modification (PSM) is the use of chemistry to alter a pre-formed framework, the MOF is transformed into a new MOF in a crystal-to-crystal transformation. PSM is an attractive strategy allowing for the formation of MOFs that would be otherwise unobtainable via direct synthesis. Reactive functional groups or groups that could coordinate to metal sites are challenging to incorporate into MOFs via direct synthesis; the groups are either intolerant to the synthetic conditions or interfere with the SBU formation, leading to a different topology. PSM allows access to MOFs with different chemical and physical properties to those of the as-synthesised MOF, such as surface area, porosity, guest interaction strength and stability. It's therefore possible to utilise PSM to fine-tune properties towards a desired application.[30, 31]

There are different transformations that can be carried out on a MOF during PSM. An example of covalent post-synthetic modification of the organic linker in a MOF was reported by Burrows *et al.*[32] In this work, IRMOF-3, a member of the IRMOF family discussed in **Section 1.1.3** with the formula [Zn_4O(2-amino-1,4-benzenedicarboxylate)$_3$], was reacted with diketene forming a β-amidoketone functionalised MOF, the reaction scheme for its formation can be seen in **Figure 1.12**. 82% conversion was achieved with retention of the framework topology. The β-amidoketone group is a well-known metal chelating group which was introduced to investigate potential applications in catalysis.[32]

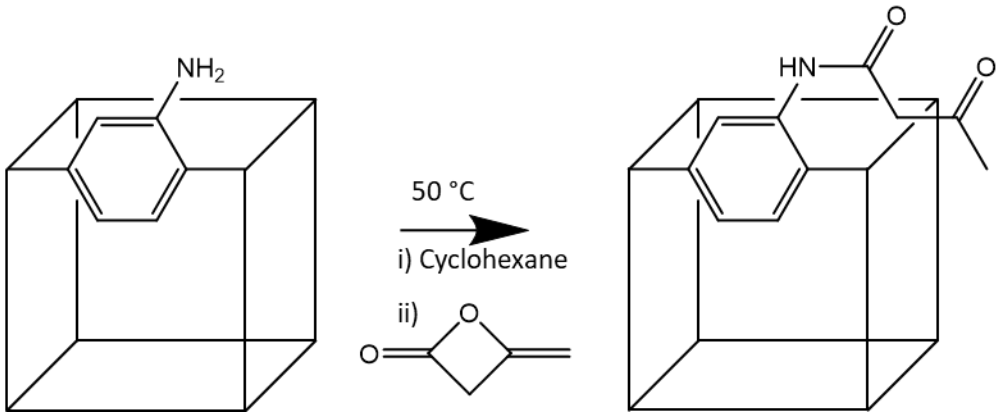

Figure 1.12. The post-synthetic modification of IRMOF-3 to form the β-amidoketone functionalised IRMOF.[32]

A second method of modifying a framework is classified as inorganic PSM, this involves transforming the SBU in the MOF. The two ways of doing this are by a ligand exchange reaction or by a metal ion exchange reaction. An example of the later was reported by Mandal *et al.* The reaction of barium(II) in the presence of 1,3,5-benzenetribenzoic acid (H_3btb) resulted in the formation of the MOF [Ba(btb)(H_2O)][$NH_2(CH_3)_2$]. The barium centres in this material were post-synthetically exchanged with terbium(III) ions. This is a particularly interesting PSM example as the original anionic barium(II) MOF contained a charge balancing dimethylammonium ion, on exchange with terbium(III) this counterion was lost, giving the neutral MOF [Tb(btb)(H_2O)]. The structure of the organic linker and the terbium modified framework are shown in **Figure 1.13**.

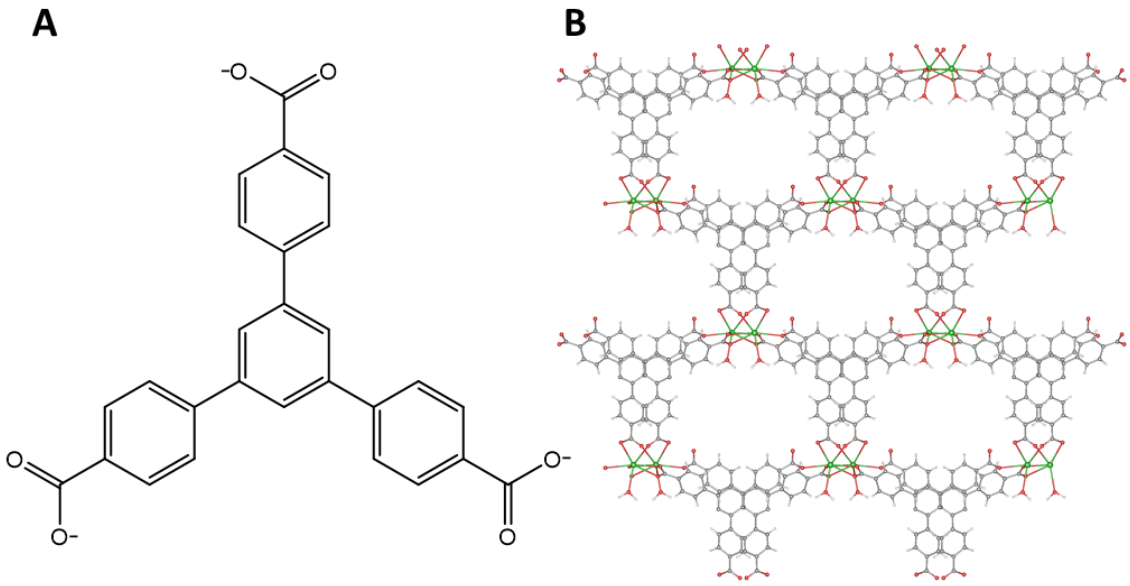

Figure 1.13. A – The structure of H_3btb. **B** – The structure of [Tb(btb)(H_2O)] viewed down the *a*-axis.

The topology of the barium framework is the same as the terbium one with channels running through the structure in the direction of the *a*-axis. The terbium MOF exhibited enhanced photoluminescence and was shown to be a selective sensor for phosphate ions in aqueous solutions. By exchange of the metal centre and introduction of photoluminescence behaviour the as-synthesised barium MOF has been transformed to a terbium MOF which can be used in phosphate sensing.[33]

1.2 Properties of Metal-Organic Frameworks

1.2.1 Accessing Porosity: Activation

One of the key properties of MOFs that make them attractive materials for a wide variety of applications is their high surface area, a property intrinsically linked to their porosity. When a MOF is synthesised, the pores of the framework usually contain guest solvent molecules. In order to access permanent porosity within the framework, the guests must be removed in a process called activation.[34, 35]

The simplest way to evacuate the pores of a framework is by conventional heating in combination with a vacuum, in an analogous manner to strategies used for zeolites. This method has found limited utility in MOF activation because, as the guest solvent passes through the liquid-gas phase boundary, there are significant strains placed on the framework by surface tension and capillary forces. These forces are often sufficient to break coordination bonds thus causing the framework to collapse.[34]

A technique employed to alleviate these forces is known as solvent exchange. This introduces an extra step in the activation process in which the synthesis solvent, commonly a high boiling point, high polarity solvent such as DMF, is exchanged for one with a low boiling point and lower polarity, for example $CHCl_3$ or MeOH. Lower boiling point, less polar solvents have weaker intermolecular forces and so the surface tension and capillary forces are reduced, such that their removal can be achieved at lower temperatures. Although widely employed, this technique is not successful in all cases and it can lead to surface areas lower than those predicted from the single-crystal structure suggesting that the framework has been partially damaged.[35-37]

A further development of this process involves utilising supercritical CO_2. Typically, under high pressure, liquid CO_2 is exchanged with the synthesis solvent. The system is then brought above the supercritical temperature for CO_2 resulting in a supercritical CO_2 loaded framework. Finally, the equipment is vented while keeping the temperature high, moving the supercritical CO_2 into the gas phase, avoiding the forces involved in a liquid to gas phase transition. This method has been widely implemented in the activation of more delicate MOFs and has the added benefit of being relatively low cost and scalable.[35]

Another method of activation is benzene freeze drying. The MOF is subjected to a solvent exchange step in which the synthesis solvent is exchanged for benzene. The benzene loaded MOF is then submerged in liquid benzene. The sample is the subjected to freeze-thaw cycles between 0 °C and room temperature. On the final freeze cycle a vacuum is introduced to move

the pressure below benzene's triple point. As the sample is warmed, the benzene sublimes going straight from the solid phase to the gas phase. As with supercritical CO_2 exchange, the liquid to gas phase transition is avoided, eliminating the potentially destructive capillary and surface tension forces.[34]

The principles employed in the different activation methods are presented in **Figure 1.14**, highlighting how supercritical CO_2 exchange and benzene freeze drying avoid the liquid-gas phase transition.[34]

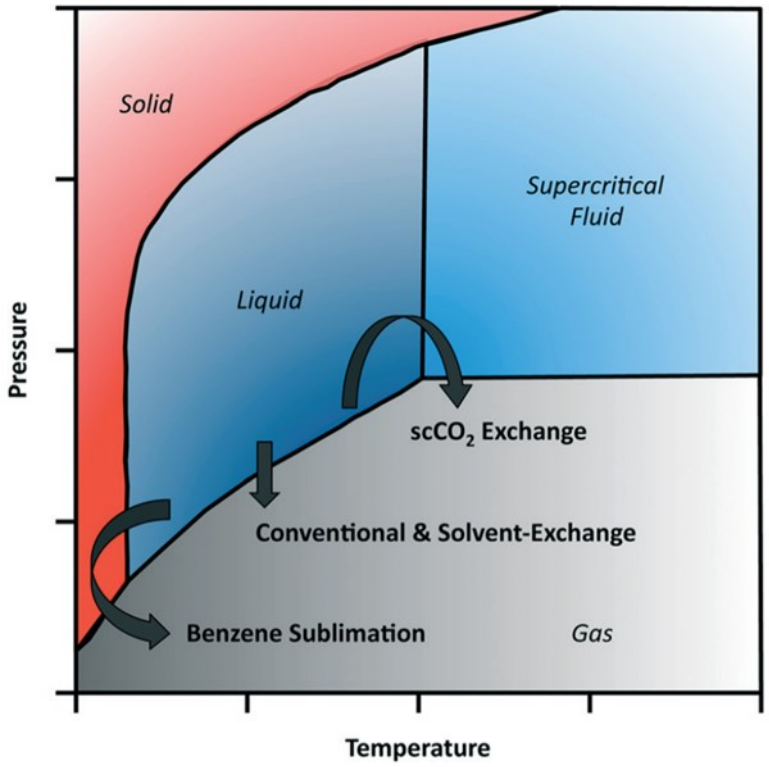

Figure 1.14. The phase transitions employed in different MOF activation techniques.[34]

1.2.2 Interpenetration

Empty space is thermodynamically unfavourable, this is the reason that framework cavities tend to be filled with solvent when synthesised and require activation. Another way in which the thermodynamic drive to reduce void space can be satisfied is the growing of a second network inside the void spaces of the first, giving two frameworks that are not chemically bonded but cannot be separated without breaking bonds, analogous to catenation. This phenomenon is known as interpenetration and is depicted in **Figure 1.15**.

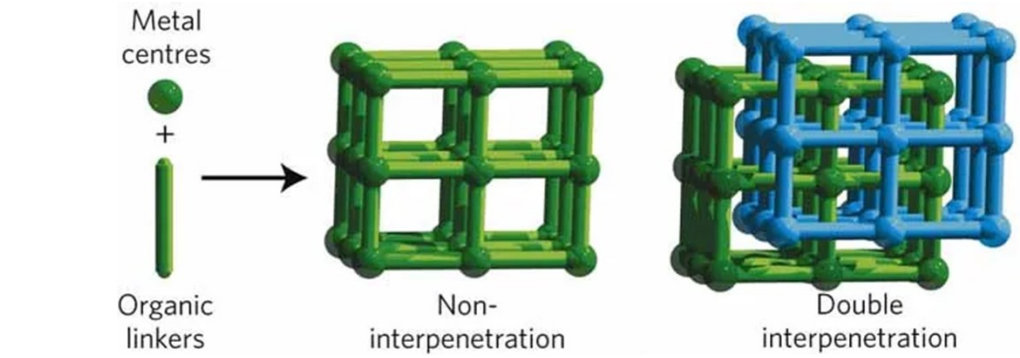

Figure 1.15. A schematic representation of an interpenetrated MOF.[38]

Interpenetration can occur more than once, depending on the available pore space, leading to three-fold, four-fold, or higher interpenetrations. Interpenetration is usually perceived as a negative attribute as the presence of the second framework reduces the size of the pores and therefore the surface area. However, for some applications such as separations or gas storage, pores of specific dimensions are required, and interpenetration can provide a route to access these.

An example of an interpenetrated framework is IRMOF-9, one of the members of the isoreticular series with a formula of $[Zn_4O(L)_3]$. In IRMOF-9 the linker is biphenyl-4,4'-dicarboxylate (bpdc) and this combines with the $[Zn_4O(CO_2)_6]$ SBU, shown in **Figure 1.7**, to create a cubic framework. The longer biphenyl linker means that the distance between nodes is greater than in IRMOF-1 and IRMOF-8 (**Figure 1.10**), allowing for the formation of an interpenetrating second framework within the pores of the first. The two interpenetrating frameworks are shown highlighted in green and orange in **Figure 1.16**. The non-interpenetrated analogue of the framework, IRMOF-10, has also been obtained by careful choice of synthetic conditions.[21]

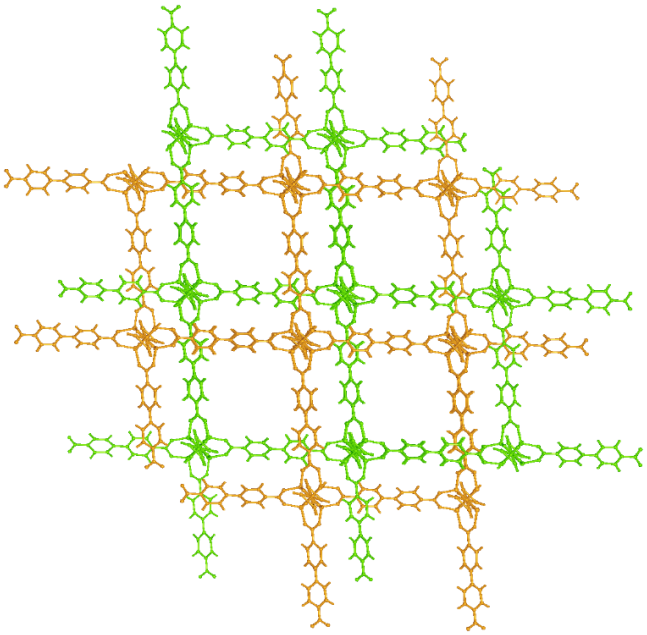

Figure 1.16. The interpenetrated structure of IRMOF-9 with the two discrete frameworks shown in green and orange.

The advantages and disadvantages of interpenetration are highlighted in the CO_2 adsorption capacity of IRMOF-9 when compared with that of IRMOF-10. It was shown that at low pressures, between 0-12 bar, interpenetrated IRMOF-9 had a higher capacity for CO_2 than the non-interpenetrated IRMOF-10. This is due to the higher binding strength of CO_2 in IRMOF-9 because of the favourable pore sizes. Above 12 bar the trend is reversed and non-interpenetrated IRMOF-10 has the higher CO_2 capacity. The larger surface area and voids in IRMOF-10 allow for more CO_2 to be included in the MOF.[39]

1.2.3 Flexibility in Metal-Organic Frameworks

Due to their crystalline nature and geometrically constrained building blocks, MOFs are often thought of as being rigid structures. This is not necessarily the case, with many applications relying on the fact MOFs contain some inherent flexibility. In extreme cases this can lead to a change in overall structure, forming a subgroup of MOFs known as 'flexible' or 'breathing' MOFs. Breathing refers to an alteration in structure upon exposure to an external stimulus, for example, heat, light or pressure.

The archetypal example of a breathing MOF is that of MIL-53(Cr), for which the formula of the activated framework is [Cr(OH)(bdc)]. The structure is composed of octahedral Cr(III) centres, which are formed into a 1-D chain SBU in combination with bridging hydroxide ions and bridging

carboxylate groups. The 1-D SBUs are linked to 4 adjacent SBUs creating the 3-D structure with rhomboidal shaped channels running in one direction parallel to the SBU chains.[40]

The as-synthesised MOF, MIL-53as, contains disordered H_2bdc molecules in the pores and is shown in **Figure 1.17 A**. After heating to temperatures above 300 °C, an activated phase, MIL-53ht, is observed, shown in **Figure 1.17 B.** A third phase, MIL-53lt, is obtained on cooling in air of the high temperature form to ambient temperature where the structure adsorbs a water molecule into the pores. MIL-53ht and MIL-53lt can be readily interchanged by heating and cooling, in air, between room temperature and 200 °C.[40]

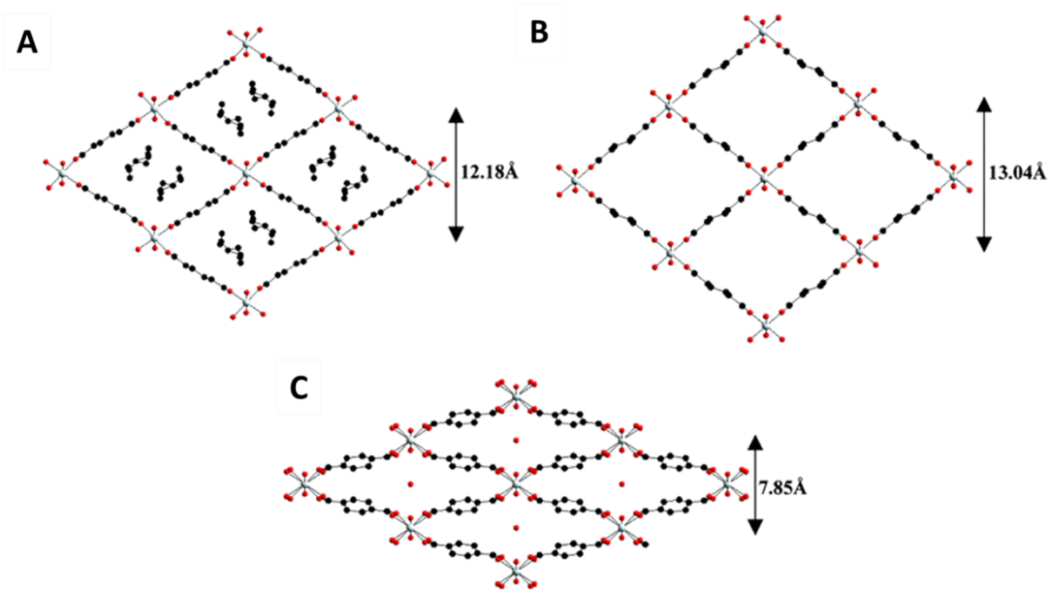

Figure 1.17. The breathing of MIL-53(Cr) with Cr – Cr distances. **A –** MIL-53as (as synthesised), **B** – MIL-53ht (high temperature) and **C** – MIL-53lt (low temperature). (Grey = chromium, red = oxygen and black = carbon) [40]

The as-synthesised and high-temperature forms, **Figure 1.17. A** and **B** respectively, represent an open pore phase of the material. Upon cooling and the uptake of water the framework contracts, **Figure 1.17 C**, diminishing the size of the pores. The breathing effect in this case is triggered by heating, causing guest removal, and subsequent guest (water) adsorption. The same framework has also been shown to undergo similar transformations when exposed to other guests such as short chain hydrocarbons.[41]

1.3 Synthesis of Metal-Organic Frameworks

A wide range of procedures have been reported in the literature for synthesising MOFs. All MOF syntheses require a source of the metal ion and the organic linker that make up the constituent parts of the framework. Generally, the source of choice for the metal is a metal salt and the source of the linker is its neutral form (e.g. carboxylic acid or pyridine). In the majority of cases, these are combined with a solvent to form the reaction mixture. A summary of synthetic techniques is presented in **Figure 1.18**.[3, 42, 43]

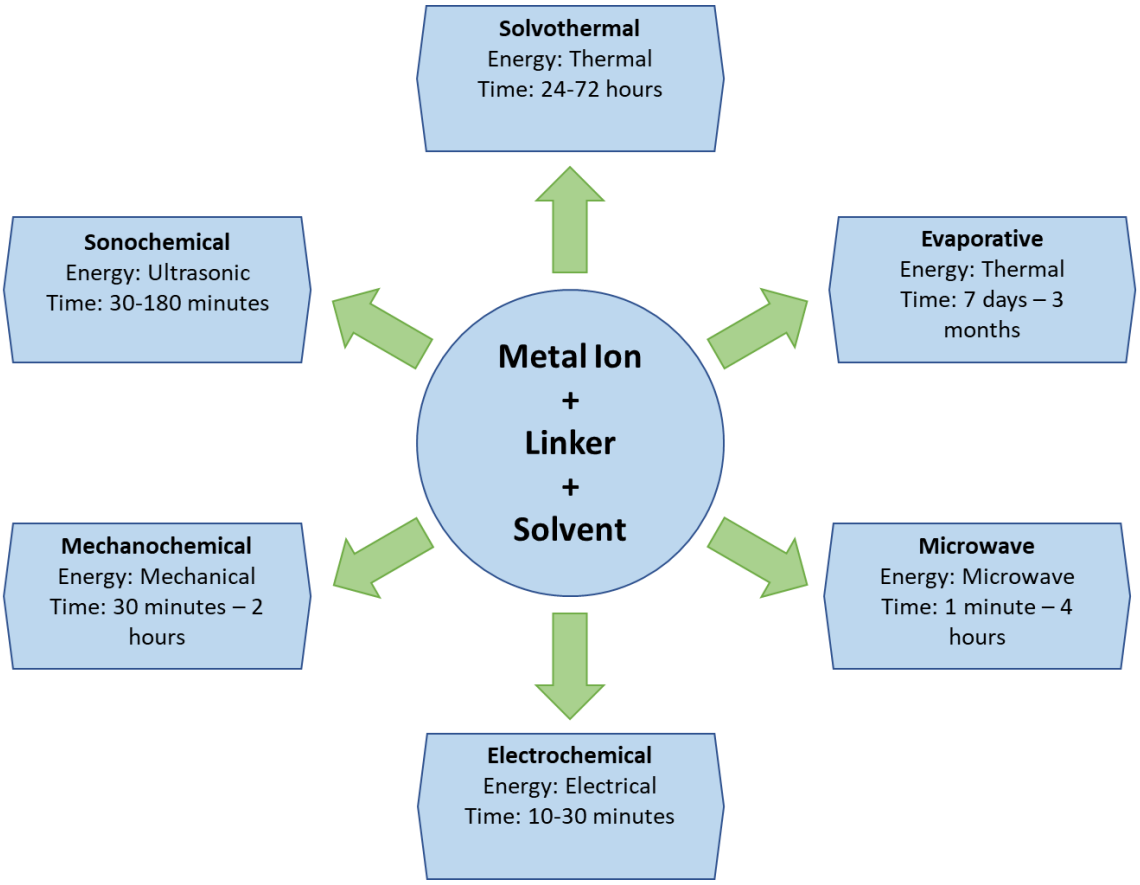

Figure 1.18. A summary of MOF synthetic techniques.[3]

1.3.1 Evaporative Crystallisation

Evaporative crystallisation is the simplest method for synthesising MOFs. A mixture of a metal salt, the linker precursor and solvent are combined to form the reaction solution. The solvent is then evaporated, usually at room temperature, concentrating the reactants until crystallisation occurs. The lack of an external energy source, in combination with high boiling point solvents such as water and DMF, mean that reaction times can be very long, ranging from days to months.

The benefit of a long reaction time and slow crystal growth is that formation of large single-crystals is maximized which is important for single-crystal X-ray diffraction analysis of new MOFs. This allows detailed structural characterisation of a material, thus is an important facet to consider in the synthesis of novel frameworks.[3]

1.3.2 Solvothermal and Hydrothermal Synthesis

Solvothermal synthesis is the most common method used in the synthesis of MOFs. The synthesis involves the heating of a mixture of the metal salt, linker precursor and a solvent to temperatures exceeding the boiling point of that solvent in a sealed vessel. This creates autogenous pressure and, as such, is usually carried out in an autoclave. Examples of some typical reactors are shown in **Figure 1.19**, these are Parr acid digestion bombs and utilise a PTFE insert in order to resist corrosion. The high temperatures and pressures reached in this type of reaction allow for formation of phases that are otherwise unobtainable. The copper MOF HKUST-1, $[Cu_3(btc)_2(H_2O)_3]$, is synthesised using this methodology. $Cu(NO_3)_2{\cdot}3H_2O$ and H_3btc are dissolved in a 1:1 mixture of EtOH:water in a Teflon-lined autoclave, the sealed vessel is heated at 180 °C for 12 hours, yielding the turquoise crystalline product.[3, 44, 45]

Figure 1.19. Parr acid digestion bombs.[46]

Variations of the solvothermal approach exist, for example, when the solvent in question is water, the process is known as a hydrothermal synthesis and is particularly attractive due to the more sustainable nature of using water as a solvent. This approach was utilised in the synthesis of both MIL-100(Cr), **Figure 1.11**, and MIL-53(Cr), **Figure 1.17**.[22, 40] Another variation is to carry out the reaction at temperatures lower than the boiling point of the solvent. This variation has

the benefit of being less energetically demanding and does not require the use of an autoclave, instead sealed glass vials or jars can be used. The ability to track the progress of a reaction visually allows for better optimisation of reaction times. Of course, the change in synthetic environment means that the same product is not always obtained. This lower temperature synthesis was exploited in the formation of IRMOF-8, **Figure 1.10**. $Zn(NO_3)_2{\cdot}6H_2O$ and 2,6-napthalenedicarboxylic acid were dissolved in a scintillation vial using DMF. The reaction was placed in an oven at 85 °C for 36 hours, in which time the pale yellow crystalline product formed.[44, 47]

1.3.3 Microwave-Assisted Synthesis

Microwave-assisted synthesis is similar to solvothermal methods but uses microwave radiation as the source of energy for heating rather than conventional thermal energy. Microwave radiation interacts with mobile electric charges, such as those that exist in polar solvents so solvent choice is an important factor. One advantage of this method is high efficiency, both in terms of energy and time, with reaction times being in the order of minutes not days. Other benefits are a greater degree of control of particle size distribution and morphology. The crystals produced are very small as they have been formed quickly and this can be advantageous in the synthesis of nanoparticle sized MOF crystals but precludes the use of single-crystal X-ray diffraction as a characterisation method for novel MOFs.[44, 48]

1.3.4 Electrochemical Synthesis

Electrochemical synthesis is different to other synthetic methods in that it involves generation of the metal ions from the bulk, which acts as an anode in an electrochemical cell. The linker precursor is dissolved in an electrolyte and the MOF product is formed when current is passed through the cell. The main advantages of this method are short synthesis times, facile synthesis of nanoparticles, morphological control and scalability. The latter is particularly relevant when considering industrial applicability of materials. MIL-100(Al), which is isostructural to MIL-100(Cr) (**Figure 1.11**), can be synthesised by electrochemical routes. H_3btc was dissolved in an electrolyte made up of 3:1 mixture of ethanol and water. Aluminium electrodes placed 3 cm apart were placed in the electrolyte and the system heated the 60 °C. The product was formed when a current was applied across the cell.[36, 44, 49]

1.3.5 Mechanochemical Synthesis

Mechanochemistry is the process of performing a chemical reaction by introducing energy to the system via mechanical means. This is an attractive method of MOF synthesis as it requires little or no solvent, does not require external heating and has short reaction times. A common method of conducting mechanochemical synthesis is using a ball mill. This involves placing the reactants in a jar with stainless steel ball bearings. The jar is sealed and then moved in a circular motion by the mill, causing the bearings to move around at high speed. This imparts mechanical force on the reactants, giving energy to drive the chemical reaction. A ball mill jar is shown in **Figure 1.20**. Due to the nature of the synthesis the crystals produced are small and not suitable for single-crystal X-ray characterisation, making analysis of new phases challenging.[50, 51]

Figure 1.20. Nylon jar from a ball mill.[52]

1.3.6 Sonochemical Synthesis

Sonochemical synthesis relies on the use of ultrasonic radiation (20 kHz – 10 MHz) to supply energy to the reaction. The energy is delivered via a cavitation process in which bubbles in the liquid are formed, grow and then collapse in very short time frames creating hotspots of very high temperature and pressure, promoting chemical reactions. These conditions lead to short reaction times and small crystal sizes. MOF-5 (**Figure 1.10**) has been made using sonochemical synthesis. $Zn(NO_3)_2 \cdot 6H_2O$ and H_2bdc were dissolved in 1-methyl-pyrrolidinone and then exposed to sonic radiation at 20 kHz and 100 W for 30 mins, forming colourless MOF-5 crystals.[3, 53]

1.3.7 Continuous Methods

The vast majority of reported MOF syntheses rely on solvothermal or related methodologies. The quantity of material produced is limited by the size of reactor and in many cases the

synthesis does not scale well. This is a problem when considering MOFs for use at an industrial scale. One solution to this is to move from batch synthesis and crystallisation to a continuous platform. Several of the aforementioned synthetic methods have been adapted into continuous platforms.

An example of a continuous flow synthesis of MIL-53(Al) was reported by Bayliss *et al.* In this work 500 g of MOF was produced over a 4 hour period. In typical gram scale batch reactions, the same material takes three days to synthesise and would be carried out in multiple vessels.[54] The material was synthesised by pumping three separate solutions: preheated water, aqueous Na_2bdc, and aqueous $Al(NO_3)_3$ through a cross piece and into a reactor at high pressures and temperatures, analogous to solvothermal conditions. The material produced was shown to be highly crystalline and have higher BET surface areas than MIL-53(Al) synthesised in batch. The drawback of this setup is the challenge of keeping the flow reactor tubing under high temperature and pressure.[55]

Microwave radiation can be integrated into a flow set up very similar to that described above. This alleviates the need for thermal heating and lowers the pressure demands on the set up. Of course, the necessary safety precautions when using microwave radiation must be observed. A microwave assisted flow synthesis was carried out by Laybourn *et al.* to make MIL-53(Al). In this experiment 63 mg of the MOF was produced in just 4.3 seconds.[56] They subsequently combined a microwave flow set up with a continuous flow oscillatory baffled reactor. This comprises of a tube containing regularly spaced bottlenecks through which the reaction mixture is pumped in an oscillating manner, creating eddies which facilitate enhanced mixing. Combined with the microwave radiation, the reactor was able to synthesise HKUST-1, $[Cu_3(btc)_3(H_2O)_3]$, at a rate of 97.42 g h^{-1}, claimed to be the highest rate of production of the MOF by the authors at the time of publication.[57]

Extrusion is an example of a synthetic procedure derived from mechanochemistry that has also been used to produce MOFs in a continuous process. The use of a twin-screw extruder was reported by Crawford *et al.* in the synthesis of HKUST-1 and ZIF-8, [Zn(2-methylimidazolate)$_2$]. The extruder can be seen in **Figure 1.21** and works by feeding the reactants into a feed port where is enters a barrel containing two interlocking screw-like rods that rotate, moving the material along the length of the reactor whilst grinding. The product is forced out of an exit port where it is collected.[58]

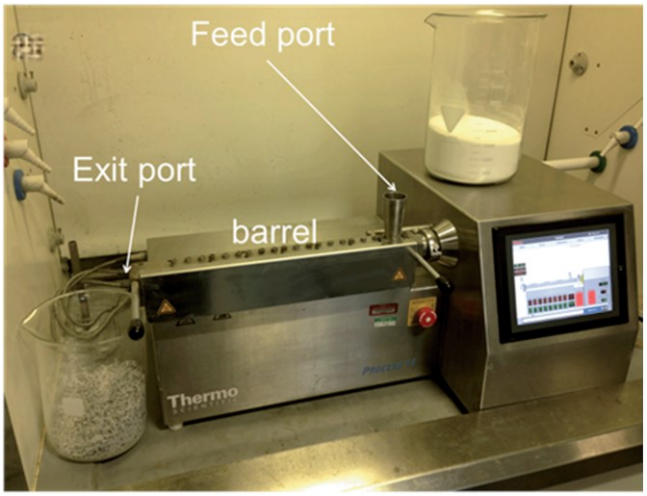

Figure 1.21. A twin-screw extruder.[58]

This mechanochemical technology was the basis in the formation of a spin-out company, MOF Technologies, which manufactures MOFs for commercial use and currently produces 14 different MOFs at scales from 25 grams up to tonnes.[59]

1.4 Characterisation of Metal-Organic Frameworks

1.4.1 X-ray Crystallography

The crystalline nature of MOFs lends them to being characterised using diffraction techniques and this is routinely carried out, in-house, using X-rays. Powder X-ray diffraction (PXRD) can be used to assign the identity of an unknown crystalline solid to that of a reported structure by matching the collected pattern with one previously collected or reported in the literature. Crystal structures are deposited in the Cambridge Structural Database (CSD) in the form of a CIF file, which can be used to simulate the PXRD pattern for the material. PXRD is a bulk analysis technique and gives information on the phase purity of the bulk material as well as the particle size and crystallinity. If high quality data are obtained unit cell parameters can be determined by indexing the reflections. A model can be proposed for the crystal structure of the material and, using Rietveld refinement, refined against the diffraction data. This requires very good quality data, usually obtained from a synchrotron source.[60]

Single-crystal X-ray diffraction allows for the determination of the unit cell, space group and atom locations within that unit cell. This is a very important technique in the characterisation of novel materials. It gives unparalleled structural detail, such as composition, topology, bond distances and angles. The use of this technique relies on the acquisition of a single-crystal of suitable size and quality from the synthesis, which can be a limiting factor in a novel materials characterisation.[61]

1.4.2 Spectroscopy

Spectroscopic techniques are useful for characterising a wide range of materials and investigating their properties. Nuclear magnetic resonance (NMR) spectroscopy probes the nuclei of the target element and gives information on its environment. In MOF chemistry solid-state NMR spectroscopy can provide information on structure and host-guest interactions. Solution-phase NMR spectroscopy requires the breakdown of the insoluble MOF (in a process known as digestion) into its component parts. The digestion solution can then be interrogated giving information on composition, for example, the linker ratios in a mixed ligand MOF or information about guest molecules.[62]

IR spectroscopy probes individual bond stretching and bending vibrations within the structure. This can give information on the nature of the bonding in the framework, including the bonding associated with any guests that may be within the pores.[63]

1.4.3 Thermogravimetric Analysis

Thermogravimetric analysis (TGA) is used to measure the change in mass of a sample when it is exposed to a constant heating rate. Mass losses at lower temperatures tend to give information about the solvent present in a material, such as the quantity and how strongly associated it may be with the framework. The technique can also be used to ascertain the temperature to which a material needs to be heated in order to activate it. At higher temperatures mass losses indicate the breakdown of the MOF and the organic components, giving an upper limit for the thermal stability of the material. The residue can also be analysed and is usually made up of oxides if the experiment is carried out in air.[64]

1.4.4 Gas Adsorption Isotherms

An adsorption isotherm refers to the measurement of the amount of gas adsorbed on the material as a function of pressure at a constant temperature. There are six main types of adsorption isotherm which are presented in **Figure 1.22**. The shape of the isotherm gives information about the nature of the adsorbate material. Type I and II are the isotherms typically associated with MOFs.[65, 66]

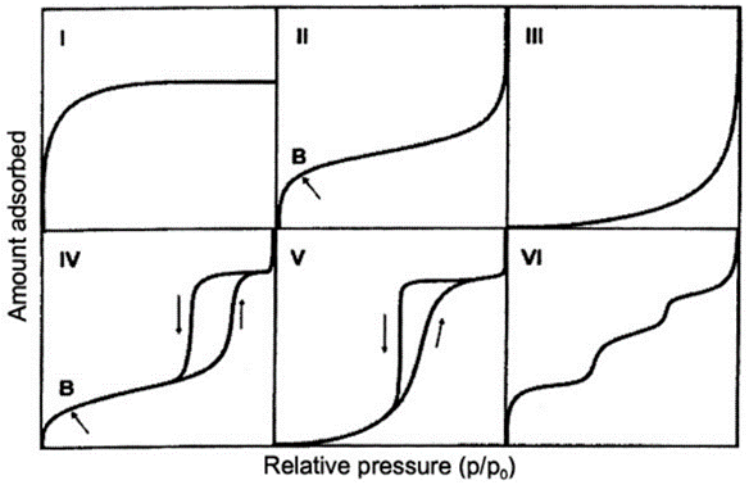

Figure 1.22. Six types of gas adsorption isotherm.[66]

Type I isotherms represent monolayer formation on a surface or can indicate micropore filling. This can be described using **Equation 1** for the Langmuir adsorption isotherm. It describes how the fractional coverage of a monolayer varies with pressure. k_a and k_d are the rate constants for adsorption and desorption respectively.[66, 67]

$$\theta = \frac{N_a}{N} = \frac{KP}{1+KP} \quad \left(K = \frac{k_a}{k_d}\right)$$

Equation 1. The Langmuir isotherm.

Extension of Langmuir theory to include the possibility of multi-layer formation gives rise to Brunauer-Emmett-Teller (BET) isotherm, type II from **Figure 1.22**, and is described by **Equation 2**. V_a and V_m are the total volume of gas adsorbed and volume of monolayer adsorbed gas respectively. P_0 is the saturation pressure of the adsorptive gas while C is the BET parameter. The isotherm can be used to obtain the monolayer volume, and therefore, a surface area.[66, 67]

$$\frac{P}{V_a(P_0 - P)} = \frac{1}{V_m C} + \frac{C-1}{V_m C}\left(\frac{P}{P_0}\right)$$

Equation 2. BET adsorption isotherm.

Surface area is a property routinely quoted for MOFs and can be determined through the use of the appropriate isotherm to work out the monolayer coverage. The adsorptive gas of choice is usually nitrogen although sometimes argon is used. MOF surface areas typically range from 800 – 8000 $m^2\ g^{-1}$, although MOFs with higher values have been reported. Other information about the material can also be calculated from adsorption isotherms such as the pore size distribution, adsorption capacities and binding energies. These are important properties to recognise for gases of study in applications such as gas storage and separation.[65-67]

1.5 Applications of Metal-Organic Frameworks

The porous nature of MOFs combined with their robust structure, diverse functionality and high surface areas have led to their application in a wide variety of fields. Some of the most reported applications pertain to gas adsorption, catalysis, sensing and drug delivery.

1.5.1 Gas Adsorption: Storage, Capture and Separation

The ability of porous materials to adsorb large quantities of gas has led to the application of MOFs in the fields of gas storage, capture and separation. The large surface areas and pore volumes associated with MOFs allow them to adsorb more gas than conventional porous materials such as activated carbons and zeolites.

Gas storage is of interest in the energy materials sector where there is a drive towards the use of more sustainable and cleaner fuels such as methane or hydrogen. These gases have a high gravimetric energy density, 1 kg of hydrogen contains almost three times as much energy as 1 kg of petrol. However, the volumetric energy density of hydrogen is just 0.03% of petrol under ambient conditions. In order to improve the volumetric energy density for hydrogen, cryogenic temperatures and high pressure are required, these are expensive and are accompanied by safety concerns. The use of adsorbents, such as MOFs, in storage tanks can densify the gas, alleviating the need for such high pressures and low temperatures. This not only makes the technology safer but also more economically viable.[1, 68]

An example of a MOF exhibiting one of the highest reported hydrogen adsorption capacities is NU-100 reported by Snurr and Hupp *et al.*[69] The MOF has the formula $[Cu_3(L)(H_2O)_3]$, H_6L = 5,5',5''-(((benzene-1,3,5-triyltris(ethyne-2,1-diyl))tris(benzene-4,1-diyl))tris(ethyne-2,1-diyl))tri-isophthalic acid, the structure of H_6L shown in **Figure 1.23 A**. The SBU is a copper paddlewheel with water molecules occupying the axial position as seen in **Figure 1.23 B**. The SBU propagates to form cuboctahedra, seen in **Figure 1.23 C,** which are linked by the bulk of the ligand forming the overall architecture shown in **Figure 1.23 D.** This framework contains three different cage sizes within the structure, with cages having approximate diameters of 13.4 Å, 15.4 Å and 27.4 Å respectively.

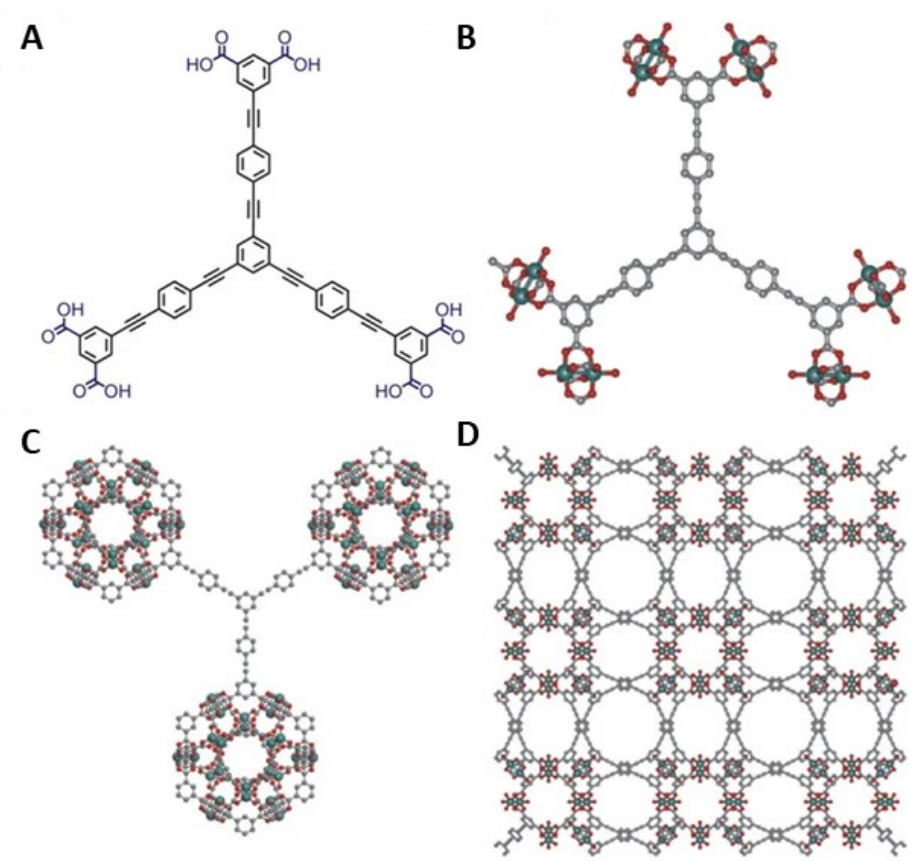

Figure 1.23. A – The structure of H_6L, **B** – The copper paddlewheel SBU in NU-100, **C** – The linking of adjacent cages in NU-100 by L, **D** – The pores in the crystal structure of NU-100. (Green = copper, red = oxygen, grey = carbon).[69]

The activated framework was accessed by employing solvent removal via freeze drying, other methods were unsuccessful. NU-100 has an experimental BET surface area of 6143 $m^2 g^{-1}$, which is very high even for a MOF. The total H_2 uptake at 70 bar and 77 K was calculated to be 164 mg g^{-1}, which exceeds the target value of 81 mg g^{-1} set by the US Department of Energy for on board H_2 storage, albeit at liquid nitrogen temperatures.[69]

MOFs have been widely explored as materials of interest for the cleaning of waste gases from a variety of different sources, such as car exhausts and power plant flue gas. Gas capture is the separation of a target gas from other components in a complex mixture. An example of where a MOF has been used in the adsorption of CO_2 was reported by Barea, Navarro *et al.* The MOF HKUST-1, which has the formula $[Cu_3(btc)_2]$, was post-synthetically modified with a number of amine containing ligands which are known to interact favourably with CO_2. The most successful of these utilised 3-picolylamine, which coordinated via the pyridyl nitrogen, giving the framework HKUST-1@3pico, $[Cu_3(btc)_2(3\text{-picolylamine})_3]$. The identity of the linkers and framework structure are shown in **Figure 1.24**.

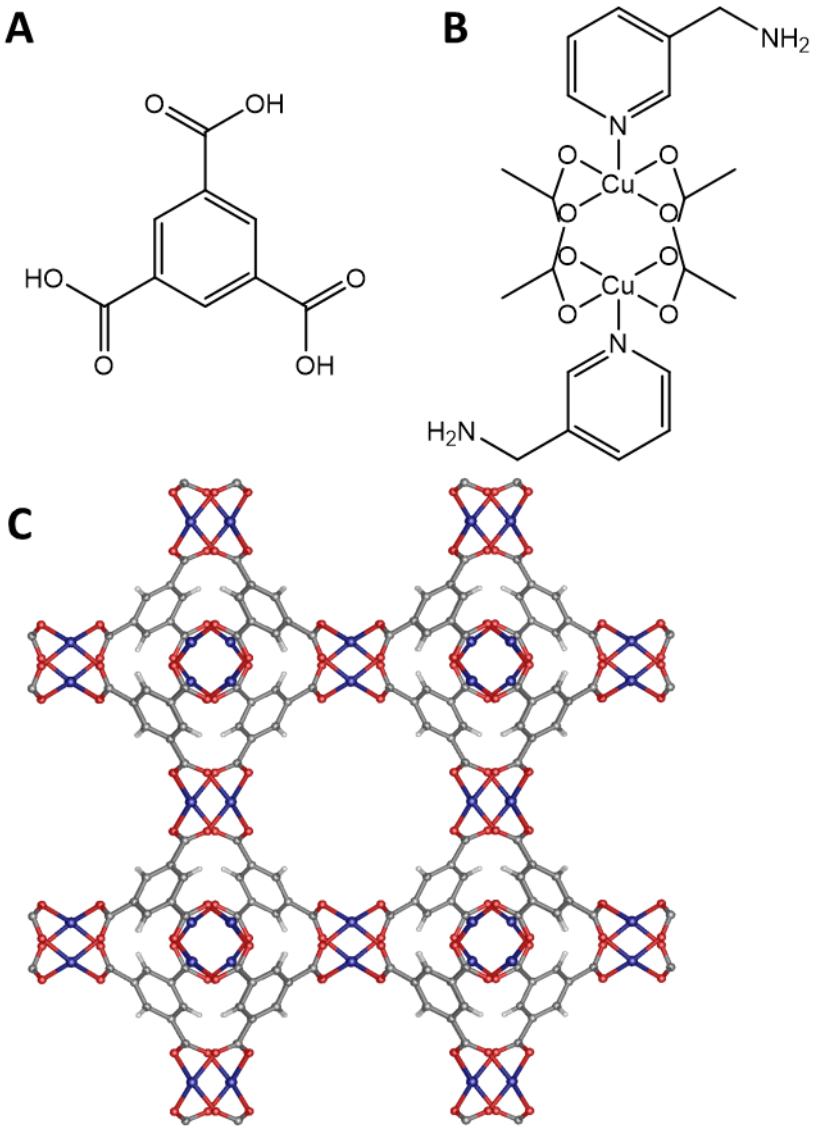

Figure 1.24. A – 1,3,5-benzenetricarboxylic acid (H_3btc), **B** – SBU with 3-picolylamine ligands, **C** – the structure of HKUST-1.

As can be seen in **Figure 1.24 B**, the amine containing ligand occupies the axial coordination sites in the copper paddlewheel SBU. The introduction of the amine functionality into the MOF pores improves the CO_2 interaction strength. This was highlighted in the CO_2 adsorption isotherm in which an increased binding strength was observed in HKUST-1@3pico over pristine HKUST-1 with heats of adsorption of 28.2 kJ mol^{-1} and 21.2 kJ mol^{-1} respectively. This was further corroborated by N_2/CO_2 breakthrough studies.[70]

Separations using MOFs, such as in the case of CO_2 capture from flue gas, rely on having a strong selectivity for one component of the mixture over the others. This selectivity can originate from a chemical interaction, like that between CO_2 and amines exploited in HKUST-1@3pico, or it can originate from size exclusion, using the framework like a sieve. This latter property has been

exploited in the separation of propene from propane along with a number of other short chain hydrocarbons using ZIF-8. Separations of small hydrocarbons is one of the most energetically intensive procedures in the processing of crude oil and, thus, is a process step that would benefit from improvement.[71, 72] ZIF is an abbreviation for zeolitic imidazolate framework, ZIF-8 has the formula [Zn(2-methylimdazolate)$_2$]. The term zeolitic is appropriated from zeolites due to the topological similarities the family of frameworks share with the aluminosilicates. The linker precursor 2-methylimidizole (HMeim) and the structure of ZIF-8 are shown in **Figure 1.25**. The zinc centres are tetrahedral in geometry and combine with the imidazolate linkers to form a three dimensional network forming a structure analogous to zeolite SOD.[73]

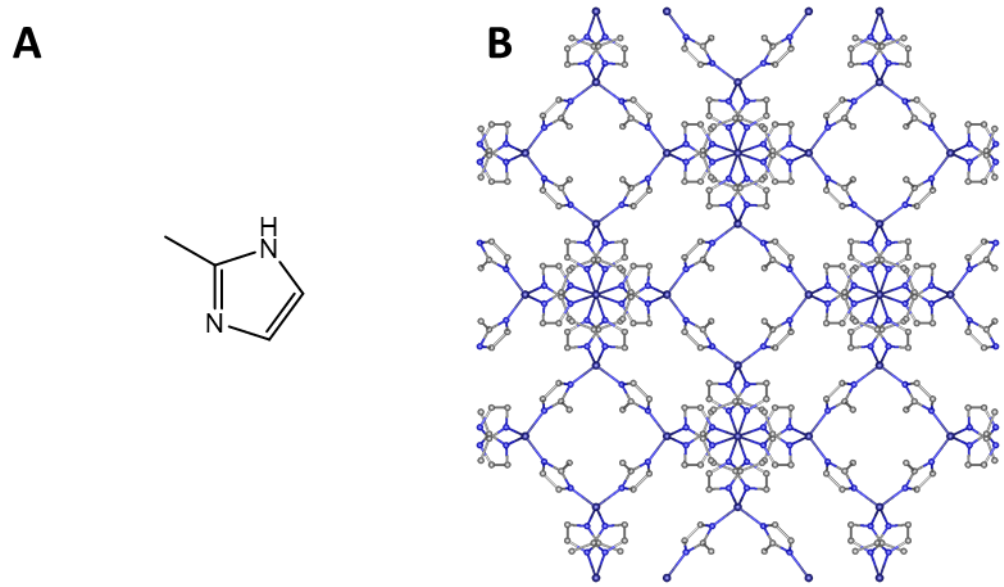

Figure 1.25. A – 2-methylimidazole (HMeim), **B** – The structure of ZIF-8, as viewed down the *c*-axis (hydrogens removed for clarity).

It was shown that membranes fabricated using ZIF-8 would be suitable candidates for the separation of propane from propene and iso-butane from iso-butene with calculated selectivities of 130 and 180 respectively. When compared to industrially relevant zeolites for the separation of propane from propene, ZIF-8 membranes have a lower selectivity (130 vs. >4000) but a far faster diffusion rate, thus making for a more efficient process.[72]

1.5.2 Catalysis

Early on in their inception the use of MOFs as heterogeneous catalysts was proposed based on their parallels to zeolites which are well known industrially important catalysts.[74, 75] The catalytic properties of zeolites originate from their porosity, relatively high surface areas and regular pore sizes. While MOFs share these properties there are some key differences between the two materials. Zeolites, being purely inorganic, are more robust than MOFs and therefore can

withstand harsher reaction conditions. This suggests MOFs may find more use in the synthesis of fine chemicals, requiring more moderate conditions. MOFs exceed zeolites in diversity as the former are far more structurally varied and can be fine-tuned. This allows greater control over the catalyst's function and allows optimisation of its performance. The presence of catalytically active metal sites and the potential for the inclusion of organocatalysts as part of the structure further enhances the opportunity to improve catalytic activity.[76-78]

A range of MOFs including MOF-5, ZIF-8, HKUST-1, MIL-101(Cr), as well as two zirconium based MOFs UiO-66 and UiO-66-NH_2, have been investigated as catalysts for the cycloaddition of CO_2 to styrene epoxide using a high pressure batch reactor, the reaction scheme is shown in **Figure 1.26**.[79]

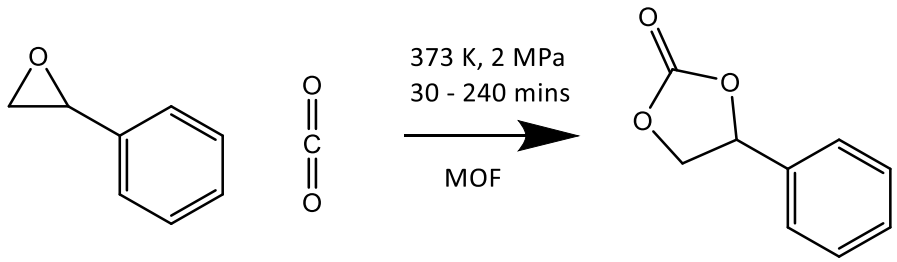

Figure 1.26. The reaction of styrene epoxide with CO_2 catalysed by a MOF.

UiO-66 is a zirconium-based framework that, along with its derivatives, has received a huge amount of interest for a large range of applications in the MOF community since discovery in 2008. The framework formula is $[Zr_6O_4(OH)_4(bdc)_6]$ and it is composed of 12-connected $[Zr_6O_4(OH)_4(CO_2)_{12}]$ SBU nodes coordinated by bdc linkers. The SBU contains six zirconium(IV) centres in an octahedral arrangement, with each face of octahedron capped by either an μ_3-O or μ_3-OH anion as shown in **Figure 1.27 A**. Each of the twelve edges of the octahedral cluster are bridged by a carboxylate group from the bdc linkers which can be seen in **Figure 1.27 B.** The MOF extends into three dimensions forming a framework analogous to a CCP structure which is depicted in **Figure 1.27 C** and **D**. The framework contains two different pore sizes, has a Langmuir surface area of 1187 $m^2\ g^{-1}$ and has a particularly high thermal decomposition temperature of 540 °C. The isoreticular framework containing bdc-NH_2 as the linker is known as UiO-66-NH_2 has the formula $[Zr_6O_4(OH)_4(bdc\text{-}NH_2)_6]$.[80, 81]

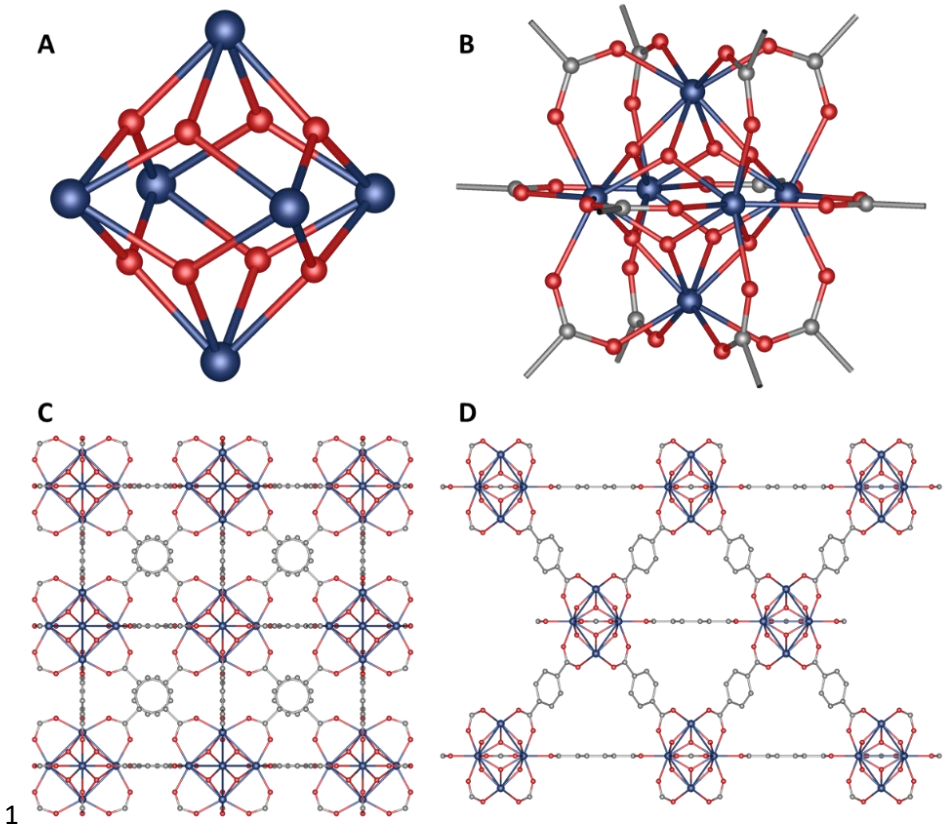

1

Figure 1.27. A – $[Zr_6O_4(OH)_4]$ cluster. **B** - $[Zr_6O_4(OH)_4(CO_2)_{12}]$ SBU. **C** – Structure of UiO-66 as viewed down the *a*-axis. **D** – Structure of UiO-66 as viewed in the 110 direction.

The aim of this catalytic study was to ascertain how the availability of Lewis acid sites or Lewis base sites in the different frameworks contributed to the catalytic activity. UiO-66, UiO-66-NH_2, HKUST-1 and MIL-101 are all known to have the potential for Lewis acid open metal sites. UiO-66-NH_2 and ZIF-8 are known to contain Lewis base sites while MOF-5 contains neither.

The results showed that UiO-66-NH_2 had the highest catalytic activity with 95% conversion in 4 hours and >99% selectivity for the 4-phenyl-1,3-dioxolan-2-one product. It was found that the best performing MOFs had both Lewis acid and Lewis base character. MOF-5, with neither acid or base functionality showed almost no activity at all.[79]

Linkers can be designed to function as organocatalysts within the framework pores. The MOF NU-601 is constructed from zinc(II) centres, bipy linkers and urea-containing 5,5'-(carbonylbis(azanediyl))diisophthalate (cadi), shown in **Figure 1.28 A**, and has the formula $[Zn_2(cadi)(bipy)_2]\cdot 7DMF$. Zinc dimers formed in combination with the interactions of the cadi linkers form 2-D sheets as seen in **Figure 1.28 B**. The 2-D sheets are linked by pillaring bipy ligands, giving the overall 3-D network shown in **Figure 1.28 C**. The structure contains channels in all three axial directions which is where the guest DMF is located.[82]

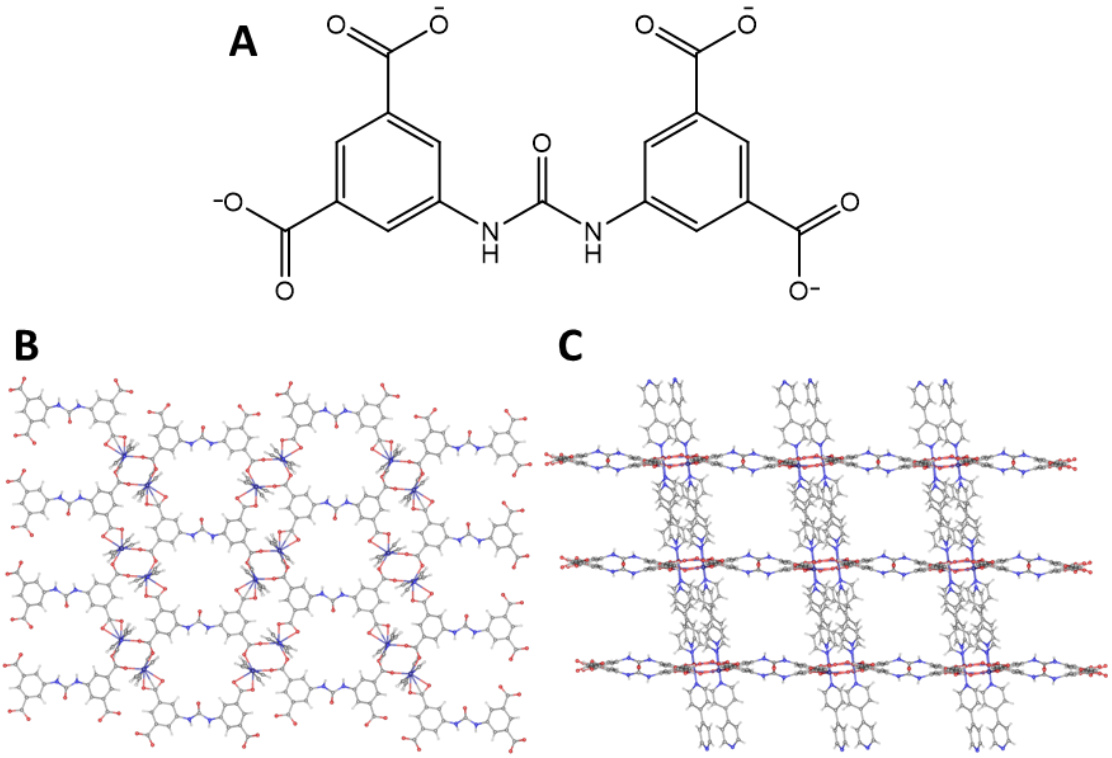

Figure 1.28. NU-601. **A** – 5,5'-(carbonylbis(azanediyl))diisophthalate (cadi) linker. **B** – The 2-D sheets formed by zinc(II) centres and cadi. **C** – Bipy linkers pillar between 2-D sheets. (Guest DMF removed for clarity).

NU-601 was constructed with the urea containing ligand to function as a hydrogen bond donating catalyst, which can generally catalyse a wide variety of reactions such as Friedel-Crafts or Diels-Alder reactions. This class of catalysts often undergo self-quenching by dimerisation or oligomerisation, this problem is circumvented due to the rigid nature of the MOF, keeping the linkers away from each other. In order to assess the catalytic activity of NU-601, a Friedel-Crafts reaction between N-methylpyrrole and (E)-1-nitroprop-1-ene was interrogated, the reaction scheme is shown in **Figure 1.29**. NU-601 was shown to have a higher activity than the control organocatalysts diphenylurea, achieving a 90% conversion after 18 hours vs. 65% conversion for diphenylurea. It also benefits from being a heterogeneous catalyst, making product recovery more simple.[82]

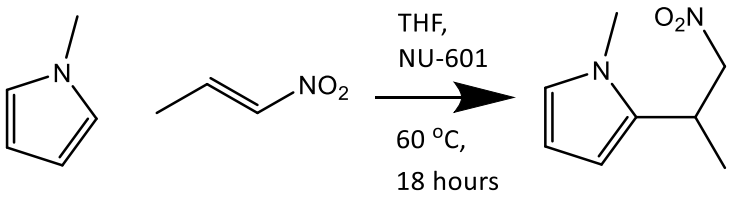

Figure 1.29. The reaction of N-methylpyrrole with (E)-1-nitroprop-1-ene.

1.5.3 Sensing

MOFs have received considerable attention in the field of sensing. This most commonly exploits compounds with luminescent properties and their interaction with an analyte. In particular, the presence of a target guest analyte causes a change in the luminescence of the system. A prerequisite for this type of sensing is that the MOF must exhibit photoluminescent behaviour, either by virtue of the metal centres or the organic ligands. MOFs have been used to sense a variety of analytes including metal ions, explosives and biomolecules. They have also been used as sensors for physical properties such as temperature, humidity and pH.[83, 84]

An example of a luminescent MOF being used for explosive detection was reported by Du *et al.*[85] The MOF reported was synthesised from $Zn(NO_3)_2 \cdot 6H_2O$, bipy and 9H-carbazolyl-3,6-dicarboxylic acid (H_2cdc), which can be seen in **Figure 1.30**. The MOF formula is $[Zn_3(cdc)_2(bipy)(OH)_2] \cdot 3H_2O$, with a SBU comprising of agglomerates containing nine zinc centres in combination with twelve carboxylate groups and six μ_3-hydroxide ions. The overall 3-D structure is hexagonal and can be seen in **Figure 1.30 C.**

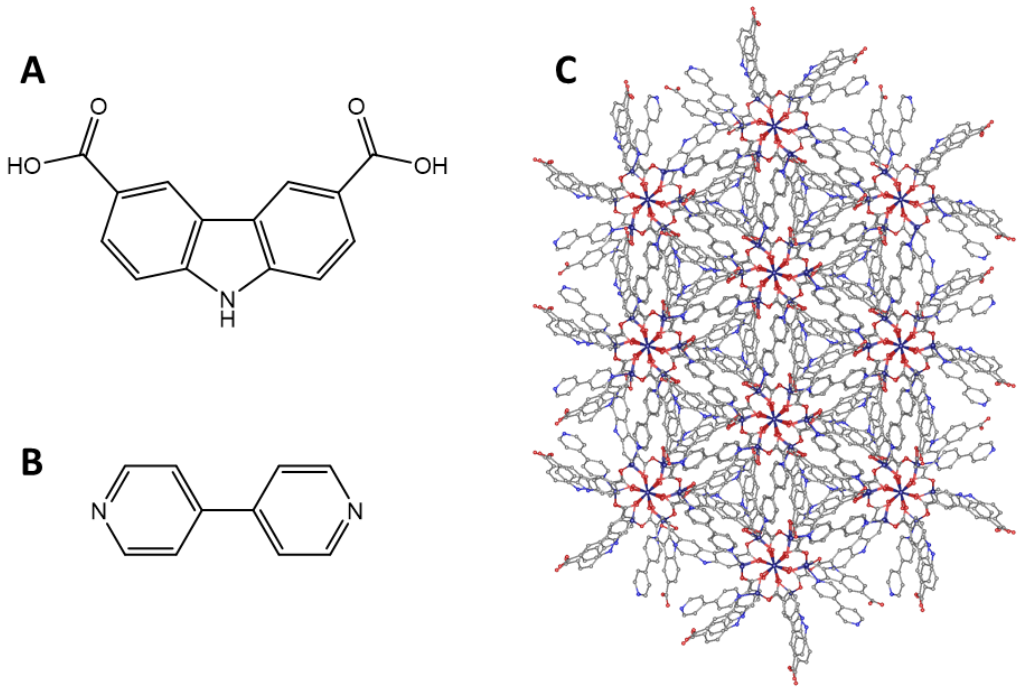

Figure 1.30. A – The structure of 9H-carbazolyl-3,6-dicarboxylic acid, **B** – bipy and **C** – the MOF $[Zn_3(cdc)_2(bipy)(OH)_2] \cdot 3H_2O$.

Solid state fluorescence measurements showed that H_2cbc and the MOF were both luminescent. The MOF was dispersed in several different solvents and it was shown that the fluorescence was completely quenched in nitrobenzene. This prompted the study of the sensitivity of the MOF to other nitroaromatic compounds relevant to explosive detection. The results of this investigation

are presented in **Figure 1.31**. It can be seen that all investigated nitrobenzene compounds can be detected at very low concentrations using the MOF.

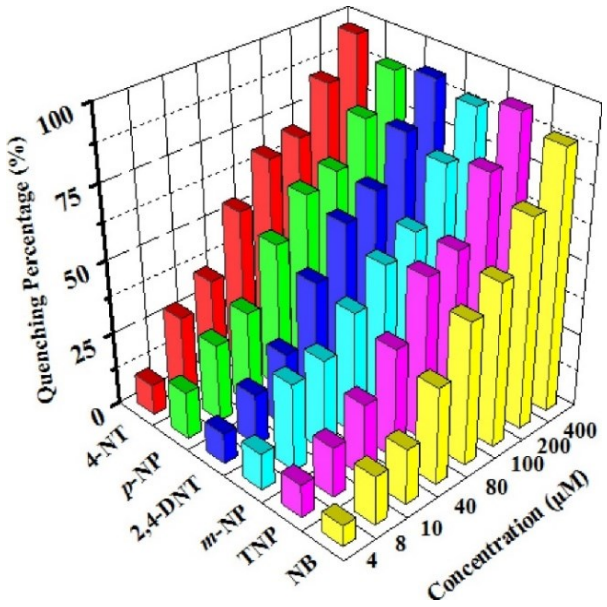

Figure 1.31. A graphical representation of the luminescent sensitivity of $[Zn_3(cdc)_2(bipy)(OH)_2]\cdot 3H_2O$ to nitroaromatic compounds. (4-NT = 4-nitrotoluene, *p*-NP = *p*-nitrophenol , 2,4-DNT = 2,4-dinitrotoluene, *m*-NP = *m*-nitrophenol, TNP = trinitrophenol , NB = nitrobenzene).[85]

$[Zn_3(cdc)_2(bipy)(OH)_2]\cdot 3H_2O$ proved to be a versatile MOF. It was also used in experiments to sense various aqueous metal ions and exhibited a large quenching phenomenon in the presence of Fe^{3+}, this can be seen in the chart in **Figure 1.32**. The sensitivity of this system was demonstrated by detection down to 4 μM concentration of Fe^{3+}.

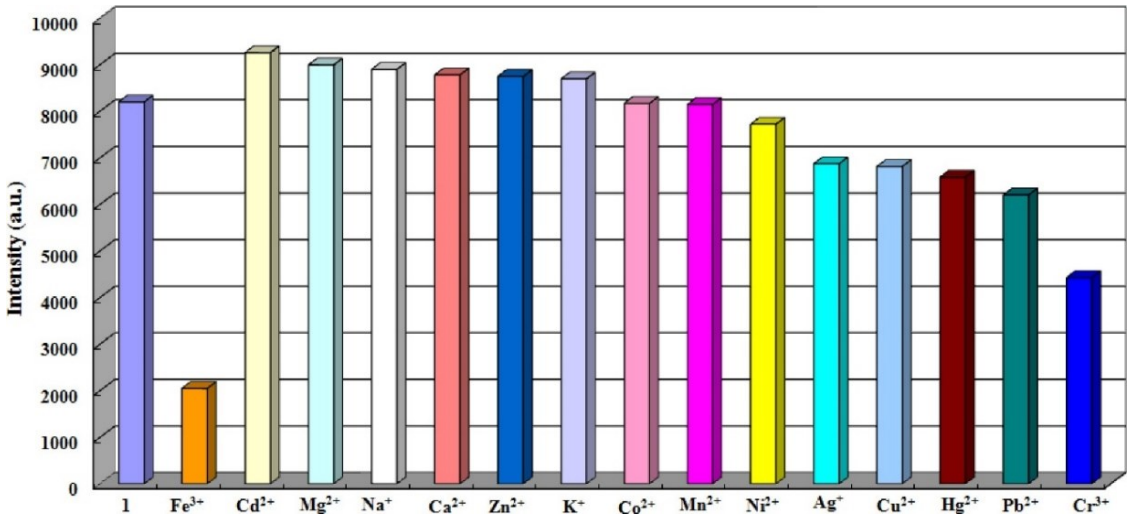

Figure 1.32. The fluorescence intensity of $[Zn_3(cdc)_2(bipy)(OH)_2]\cdot 3H_2O$ in aqueous solution with various metal ions present.[85]

1.5.4 Drug Delivery

MOFs have the potential for application in the medicinal field as drug delivery systems. Their high surface areas and porosity allow for high loadings of drug molecules. The wide array of known structures give rise to a versatile range of properties, which can be further fine-tuned using PSM. The coordination bonds that bind the organic and metal components together are weak enough that MOFs do not persist in the body and show good biodegradability. The selection of organic linkers and metal centres must be carried out in a rigorous and conscientious manner, so that the MOF and its degradation products are not harmful to the end user patient.[86]

There are several ways that MOFs can be utilised as drug delivery systems. The first of these is that the target drug is encapsulated inside the pores of the framework, a method utilised in work by Horcajada *et al.* Ibuprofen, the structure of which is shown in **Figure 1.33**, was loaded into flexible MIL-53(Cr) and the isoreticular MIL-53(Fe). The loading resulted in a material with a 0.22(1) molar ratio of ibuprofen to MIL-53 and was independent of the metal centre present in the framework, which is important as chromium is known to be toxic so the iron system would be preferable in biomedical applications.[87]

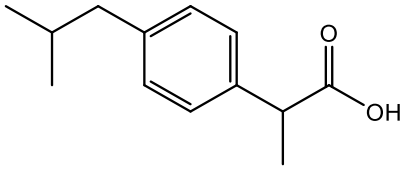

Figure 1.33. The structure of Ibuprofen.

Modelling of PXRD data has allowed for interrogation of the crystal structure of the ibuprofen loaded material, MIL-53-Ibu, in which the pores sizes were found to be between the high temperature open pore form, MIL-53-ht, and the low temperature closed pore form, MIL-53-lt. The three states can be seen in **Figure 1.34**. The data was of sufficient quality to observe ordered ibuprofen within the pores of MIL-53-Ibu.[87]

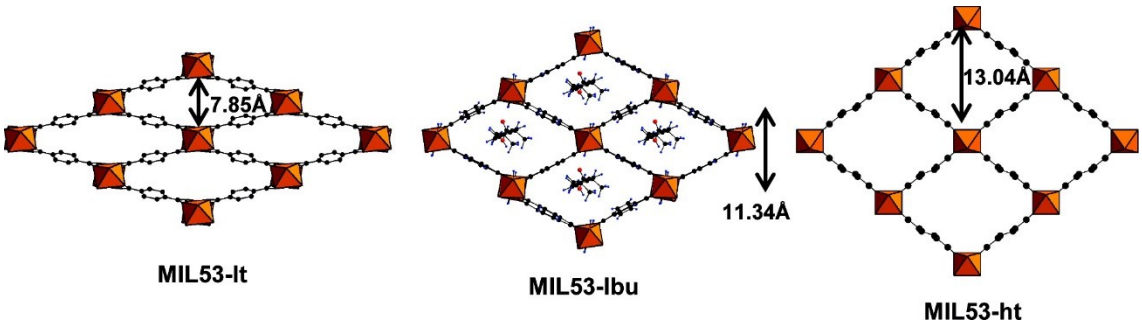

Figure 1.34. The structure of MIL-53 in the low temperature form, loaded with ibuprofen and high temperature form.[87]

Zirconium MOFs are a popular choice of materials for drug delivery due to their low toxicity and high stability in aqueous environments. The amine decorated analogue of UiO-66, UiO-66-NH_2, can be made using 2-amino-1,4-benzenedicarboxylic acid (H_2bdc-NH_2) in the synthesis rather than H_2bdc, resulting in an isoreticular structure, $[Zr_6O_4(OH)_4(bdc\text{-}NH_2)_6]$. This MOF was utilised in the uptake and release of 5-fluorouracil, a drug used in the treatment of a number of different cancers, the structure is shown in **Figure 1.35**.[88]

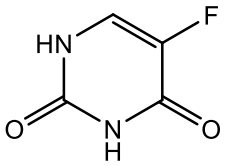

Figure 1.35. 5-fluorouracil.

27 wt.% of 5-fluorouracil was loaded into activated UiO-66-NH_2. The release of the drug was studied in a phosphate buffered saline (PBS) solution (pH = 7.4) at 37 °C, mimicking the human body. The release process was tracked using UV/Vis spectroscopy, the results of which are shown in **Figure 1.36**. It can be seen that the drug was released more quickly in the first 8 hours and then slowed to a plateau in the following 16 hours, with approximately 75% of the loaded drug being released in the 24 hour period.[88]

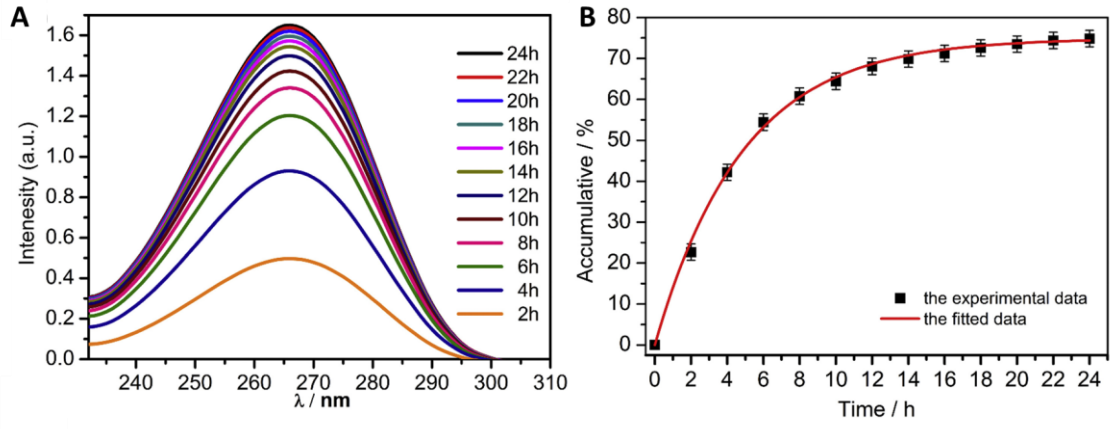

Figure 1.36. 5-fluorouracil release from UiO-66-NH_2, **A** – UV/Vis spectra. **B** – Drug release profile.[88]

Another strategy for the inclusion of drug molecules into MOFs is to incorporate the drug into the framework, either as a linker or by post-synthetically binding the drug to the MOF. An example of the former has been reported by Burrows *et al.* A series of zinc-based MOFs were synthesised utilising bdc derivatives and the drug molecule deferiprone (Hdfp) as linkers. Deferiprone, the structure of which is shown in **Figure 1.37**, is used for the treatment of hemosiderosis, a condition caused by too much iron in the body. The drug chelates to iron

allowing it to be excreted, however, current administration leaves 85% of the drug inactive as it is metabolised before it can carry out its function, thus, an improved delivery mechanism is required.[89]

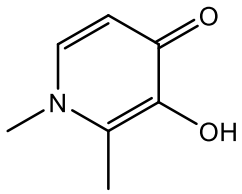

Figure 1.37. Deferiprone.

In the majority of the MOFs formed deferiprone binds to zinc centres via the ketone and deprotonated alcohol group. In combination with the interactions from bdc 1-D chain SBUs are formed. The structure of the chain SBU in $[Zn_3(bdc)_2(dfp)_2]\cdot 2H_2O$ is shown in **Figure 1.38 A** and the 3D network formed when these chains are linked by bdc moieties in **Figure 1.38 B.**[89]

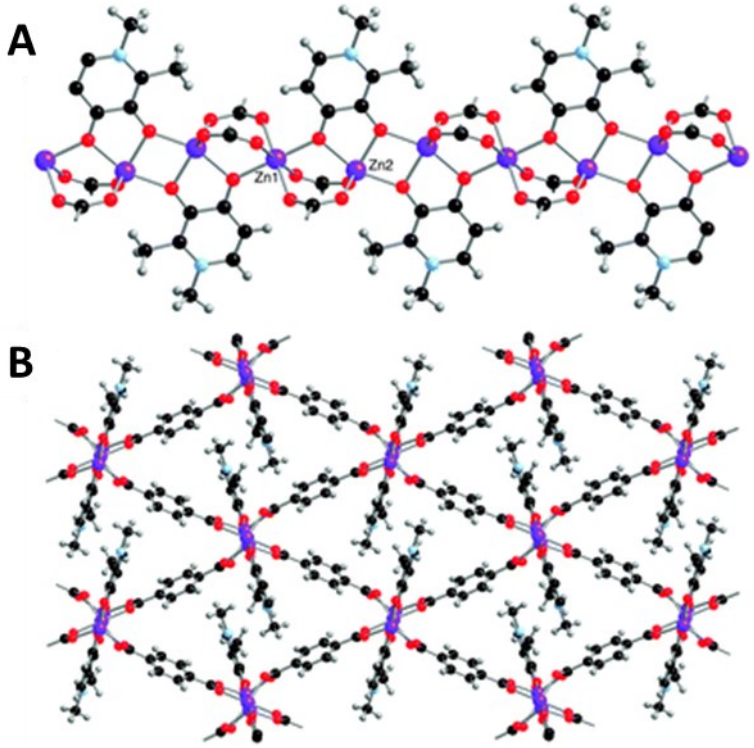

Figure 1.38. $[Zn_3(bdc)_2(dfp)_2]\cdot 2H_2O$. **A** – 1-D chain SBU. **B** – 3-D structure. (Purple = zinc, red = oxygen, black = carbon, grey = hydrogen).[89]

The release of the drug is reliant on the breakdown of the framework. The immediate release of deferiprone was effected on the treatment of the MOF with PBS, HCl-PBS (pH = 5.5), 1N HCl or a saturated citric acid solution. A more controlled release was observed in a 1:1 mixture of ethanoic acid and methanol.[89]

1.6 Aims

This project contains two research strands that concern functionalised metal-organic frameworks. The first of these aims is to investigate the synthesis and characterisation of novel MOF structures, constructed using new semi-rigid linkers. The linkers will be designed by using existing linker precursors bearing additional groups containing inherent flexibility. The products of these reactions will then be used in the synthesis of new MOFs. The frameworks formed will be fully characterised using X-ray diffraction, spectroscopies and thermal analysis methods. The structural trends and material properties will be discussed, revealing the merits of this method of MOF design as well as the specific linkers investigated. The implication of the identity of the metal centres used to construct the MOF will also be investigated, probing the impact of the relative size of 3d and 4d d-block metals. MOFs will be synthesised using N-donor pillaring ligands in combination with the semi-rigid linkers, allowing analysis of the pillaring ligands effect on the dimensionality and porosity of the frameworks formed.

The results of this work are presented in **Chapters 2**, **3** and **4**.

The second research theme will aim to investigate how functionalisation of MOFs can impact host-guest interaction. MOFs will be used as hosts for guest pheromones and semiochemicals with a view to improving the efficiency and lifetime of lure traps for pest insect species. In this study the factors that control the uptake and release properties of the MOF-pheromone systems will be investigated, specifically, the framework identity, functionalisation, loading method and semiochemical.

This work is discussed in **Chapter 5**.

Chapter 2 - Synthesis of Functionalised Metal-Organic Frameworks Using 5-((carboxymethyl)amino)isophthalic acid

2.1 Introduction

The library of reported metal-organic frameworks has rapidly increased in size over the past two decades. The continuing search for novel frameworks that could fill vacancies, or improve performance, in applications within the MOF field has driven research towards a variety of different synthetic strategies. These include post-synthetic modification,[30] the use of isoreticular chemistry,[90] varying synthetic conditions such as temperature, solvent system and reaction time,[91, 92] and the use of organic chemistry to synthesise novel organic molecules to be used as linkers.

The targeting of organic moieties that have not previously been used as linkers in the synthesis of MOFs is an effective strategy in the synthesis of novel frameworks. The selection of the target organic molecule can be informed by linkers previously used in MOF synthetic chemistry. Polycarboxylates are the most widely used type of linker in MOF chemistry due to their ideal binding strength, allowing for reversible bond formation with metal centres whilst being strong enough to form robust frameworks. The anionic charge also negates the need for charge balancing counter ions in the framework pores.

Rigid, usually aromatic, polycarboxylates are routinely used in the synthesis of MOFs because the rigid aromatic ring(s) provide(s) a geometric constraint on the linker. This enables the use of reticular chemistry as the linker has definitive angles and distances between its bonding functionalities that can be exploited. A good example of this is the IRMOF series described in **Section 1.1.3** Rigid linkers also facilitate the maintenance of porosity upon activation by preventing rearrangement into a more compact configuration that would minimise void space. The geometric constraint imposed by rigid linkers means that there are relatively few conformations they can adopt and, as such, the range of possible structures that can be produced is diminished.

Flexible linkers are less frequently employed, as their flexibility makes predicting the structure of the framework difficult. The frameworks produced can be difficult to activate as the linkers can change conformation on removal of the solvent to reduce void space, often giving dense non-porous structures.[93] However, the flexibility of the framework makes them highly responsive to guest molecules. This feature was demonstrated by Rosseinsky *et al.* who utilised

a polypeptide linker Gly–Gly–L-His (H_2ggh) in combination with zinc(II) centres to synthesise the MOF Znggh-1, with the formula [Zn(ggh)]·DMF·3H_2O, the structure of which is shown in **Figure 2.1**. Nine different framework conformations were identified, with the adopted structure dependent on the identity of the guest solvent present. The changes in framework structure were characterised by three different linker torsions.[94]

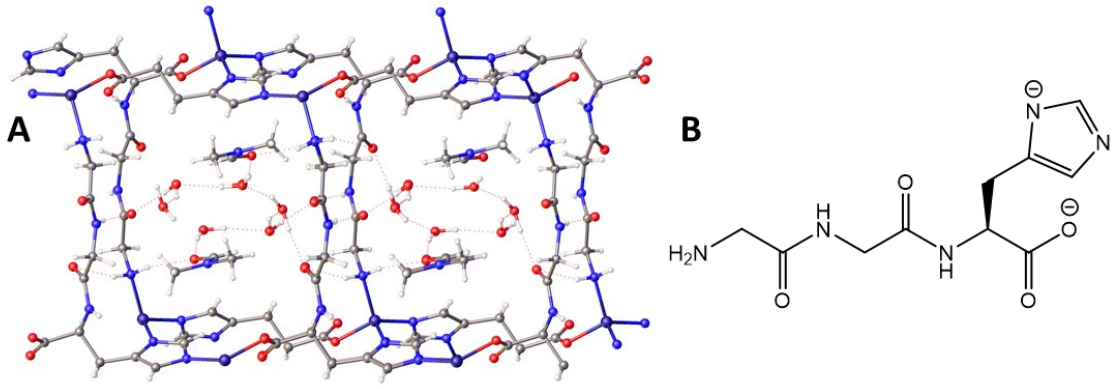

Figure 2.1. A The structure of ZnGGH-1 and **B** the structure of the linker ggh.

Semi-rigid linkers contain a rigid portion, usually based around a phenyl ring, together with some degree of flexibility. The use of these ligands aims to exploit the advantages of both rigid and flexible linkers, producing frameworks that give a structural response to external stimuli but still retain porosity on activation.

An example where a semi-rigid linker has been employed was reported by Murdock *et al.* The linker 4,4'-(1,4-(trans-2-butene)diyl)bis(1,2,4-triazole) (tbta), shown in **Figure 2.2 A**, was employed with copper(II) centres to synthesise the MOF $[Cu_2(tbta)_2(SO_4)(Br)_2]\cdot xH_2O$. This MOF was found to exhibit breathing behaviour based on the water content, switching between the two forms shown in **Figure 2.2 B** and **C**. The flexibility in the linker allows for the framework to contract upon the loss of guest water solvent and be regenerated on the addition of water. This flexibility in the linker stems from the presence of CH_2 groups between the triazoles and the central alkene double bond. Half of the linkers change conformation from one structure to the other. The portion of the linker highlighted in green shows where the conformation change occurs, the portion in red highlights where no conformation change is observed.[95]

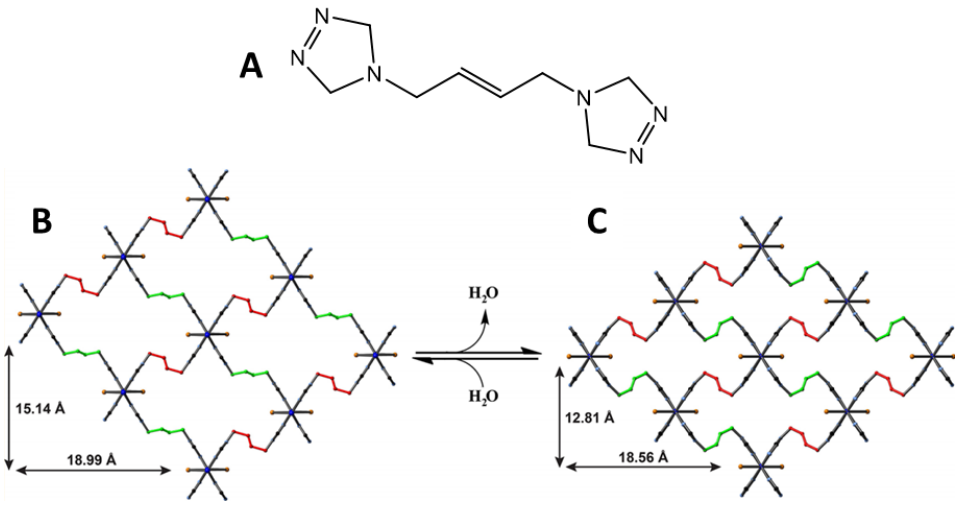

Figure 2.2. A The linker 4,4'-(1,4-(trans-2-butene)diyl)bis(1,2,4-triazole) (tbta), **B** The hydrated structure of $[Cu_2(tbta)_2(SO_4)(Br)_2]\cdot xH_2O$ and **C** the partially dehydrated structure $[Cu_2(tbta)_2(SO_4)(Br)_2]\cdot 4H_2O$.[95]

A semi-rigid tricarboxylate linker, 5-((4-carboxybenzyl)oxy)isophthalate (cboi) has been employed in combination with cadmium(II) centres in the synthesis of the 3-D MOF $[Cd_3(cboi)_2(\mu_2\text{-}H_2O)_2]\cdot 3H_2O$. The structure of the linker precursor is shown in **Figure 2.3**, the flexibility originates from the CH_2 group highlighted in red.[96]

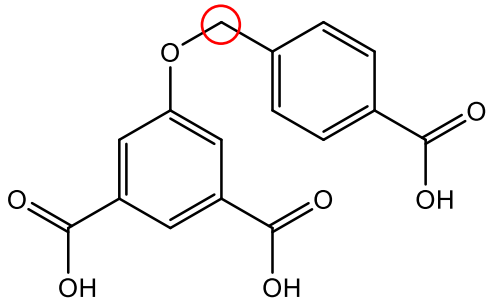

Figure 2.3. The structure of linker precursor H_3cboi.

The framework itself is composed of 1-D chain SBUs, running in the direction of the *c*-axis, that are formed in combination with the carboxylates from the linker and bridging μ_2-H_2O ligands. The isophthalate portion of the linker serves to join adjacent 1-D chains SBUs into a sheet while the benzoate portion serves to pillar between adjacent sheets, giving the 3-D network. **Figure 2.4** shows the structure of $[Cd_3(cboi)_2(\mu_2\text{-}H_2O)_2]\cdot 3H_2O$ as viewed down the *c*-axis. A 1-D chain SBU is circled in green running parallel to the *c*-axis, a 2-D sheet is highlighted in blue, and a channel is circled in purple, these run though the structure parallel to the 1-D SBUs. The channels contain guest water molecules forming an extensive hydrogen bonded network.

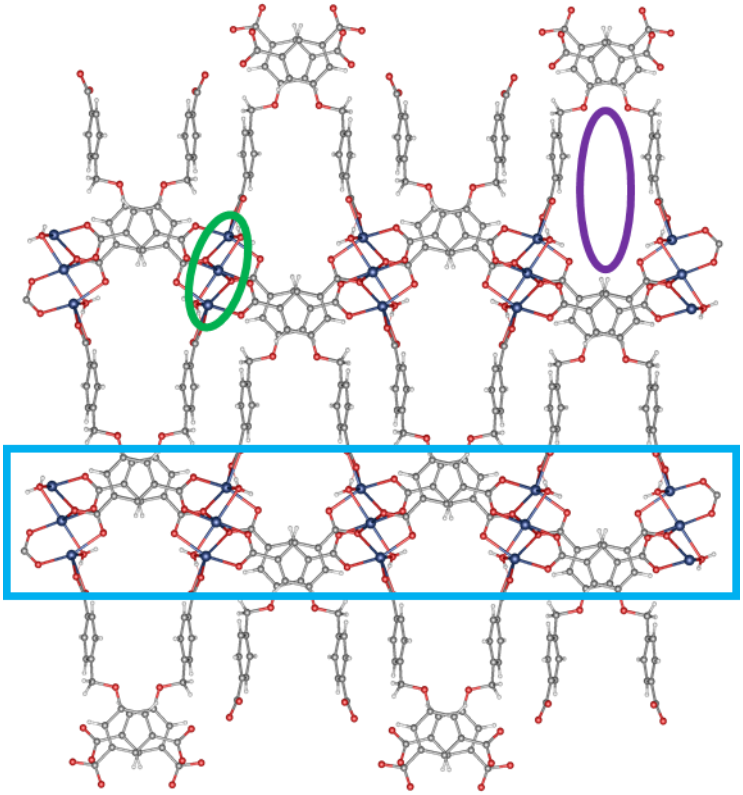

Figure 2.4. The structure of $[Cd_3(cboi)_2(\mu_2\text{-}H_2O)_2]\cdot 3H_2O$ viewed down the *c*-axis. A chain SBU is highlighted in green, a 2-D sheet in blue and a channel in purple. (Guest water removed for clarity).

The framework was found to exhibit a strong blue photoluminescent emission at 466 nm upon excitation at 381 nm. The acid of the linker, H_3cmoi, did not exhibit any emission in the range 380 - 600 nm so the photoluminescence of the MOF was ascribed to ligand-to-metal charge transfer.[96]

In this project the semi-rigid linker precursor targeted was 5-((carboxymethyl)amino)isophthalic acid (H_3cmai), the structure of which is shown in **Figure 2.5**. The resultant trianionic linker was anticipated to combine the properties of the rigid isophthalate backbone with the more flexible secondary amine appended acetate group. The novel linker represents an unexplored research space and as such was expected to yield interesting frameworks. In particular the presence of the secondary amine is anticipated to yield interesting structural trends due to its affinity to coordinate to metal centres, act as a hydrogen bond acceptor and as a hydrogen bond donor.

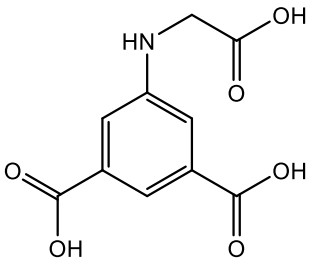

Figure 2.5. 5-((carboxymethyl)amino)isophthalic acid (H_3cmai).

H_3cmai was synthesised in good yield from a newly developed procedure involving an imine condensation between 5-aminoisophthalic acid and glyoxylic acid, followed by a reduction to an amine using sodium cyanoborohydride. The reaction scheme for the preparation of H_3cmai is shown in **Figure 2.6**.

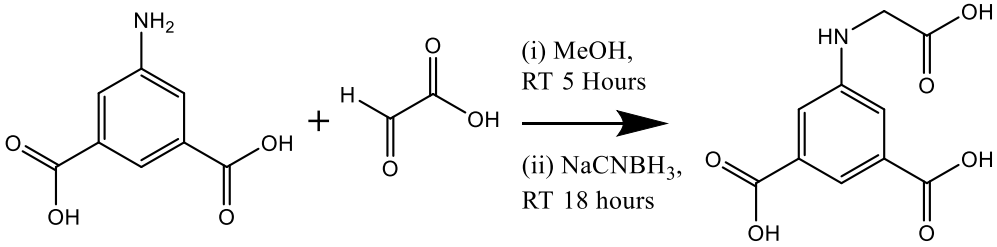

Figure 2.6. Reaction scheme for the synthesis of H_3cmai.

In a typical experiment, 5-aminoisophthalic acid was dissolved in MeOH and then to this solution was added glyoxalic acid monohydrate. The reaction mixture was stirred at room temperature for 5 hours forming the intermediate imine which was not isolated. This was reduced by adding $NaCNBH_3$ and stirring at room temperature overnight. The product precipitated as an off-white powder, this was collected by vacuum filtration and dried in an oven for 6 hours, giving a percentage yield of 71%. The identity of the product was confirmed via ^{1}H-NMR, shown in **Figure 2.7**, (500 MHz, DMSO-d_6); δ (ppm) 7.68 (1H, s), 7.23 (2H, s), 3.56 (2H, s) and ^{13}C{^{1}H}-NMR, shown in **Figure 2.8**, (125.7 MHz, DMSO-d_6); δ (ppm) 173.1, 168.8, 148.7, 134.3, 118.4, 116.3, 46.7.

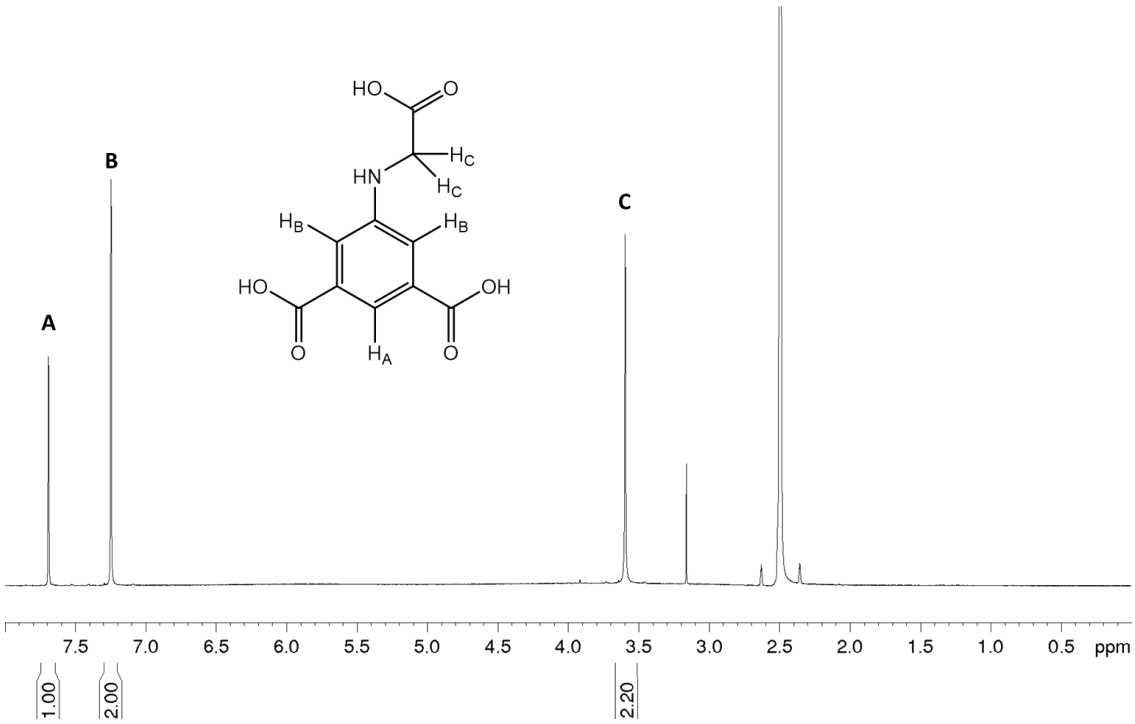

Figure 2.7. ^{1}H-NMR spectrum of H_3cmai.

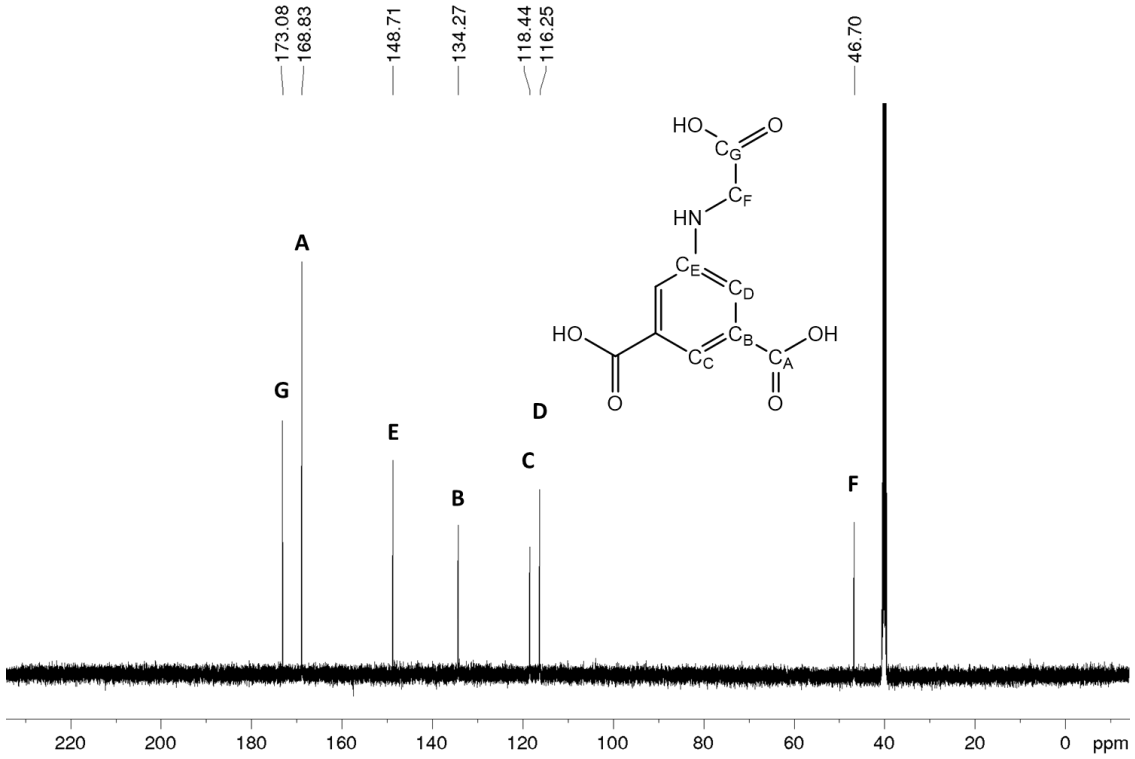

Figure 2.8. ^{13}C{^{1}H}-NMR spectrum of H_3cmai.

2.2 Results and Discussion: Reactions of H_3cmai and Cadmium(II) Salts

Cadmium(II) based coordination polymers and MOFs are well known and have been exploited for applications in optical devices, sensing, catalysis and molecular metal wires. The d^{10} metal centre has no electronic preference for any coordination geometry so adopts a wide variety of coordination modes, allowing for the synthesis of diverse and interesting structures.[97-103]

2.2.1 Synthesis and characterisation of $[Cd_2(Hcmai)_2(H_2O)_2]\cdot H_2O$ (**1**)

Compound **1** was synthesised from the reaction of $Cd(NO_3)_2\cdot 6H_2O$ with H_3cmai at 90 °C for 3 days. The brown intergrown tablet crystals were collected via vacuum filtration and a crystal of suitable quality was selected for a single-crystal X-ray diffraction experiment.

Compound **1** crystallises in the monoclinic space group *I*2/*a***,** with an asymmetric unit consisting of two cadmium centres, two Hcmai linkers, two water ligands and one guest water molecule. The asymmetric unit and the coordination sphere of the cadmium centres are shown in **Figure 2.9**.

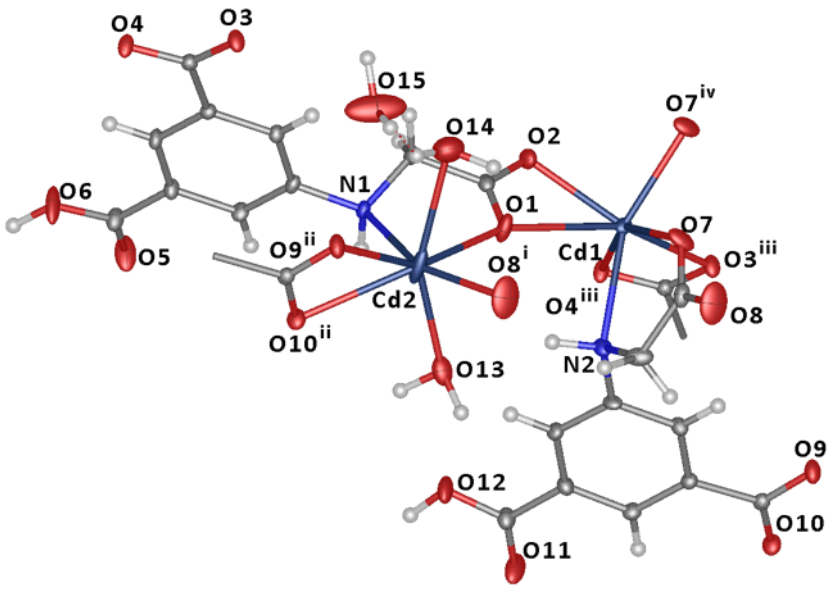

Figure 2.9. The asymmetric unit and cadmium coordination spheres in compound **1**. Atoms with labels containing superscripts are related to those in the asymmetric unit by the following symmetry operations: i, 1 – *x*; 1 –*y*, 1 – *z*; ii, + *x*, – 1 + *y*, + *z*; iii, + *x*, 1 + *y*, + *z*; iv, 3/2 – *x*, + *y*, 1 – *z*. (Atomic displacement parameters (ADPs) are plotted at 50% probability).

Cd1 is 7-coordinate and is bound to four different Hcmai linkers. Two of these bind through κ^2 bidentate carboxylate groups based on O1 and O2, and O3 and O4. The third linker also

coordinates in κ^2 bidentate manner but though N2 and O7 which can be seen in **Figure 2.9**. The fourth Hcmai linker coordinates through O7 and is part of a μ_2 bridging mode to a second Cd1 centre. The bridging mode of O7 between two Cd1 centres leads to the formation of a dimer motif as shown in **Figure 2.10**. These dimers in combination with Cd2 centres and the interactions from Hcmai linkers form 1-D chain SBUs in the structure, running in the direction of the *a*-axis.

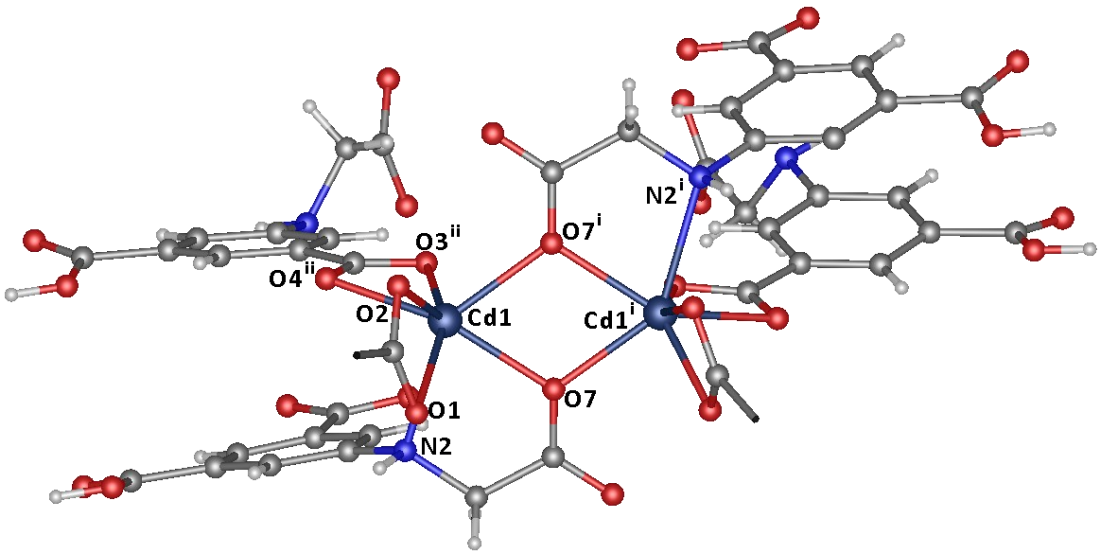

Figure 2.10. Cd1 dimer in compound **1** formed by virtue of μ_2 O7. (i, 3/2 – *x*, + *y*, 1 – *z*).

Cd2 is also 7-coordinate and is bound to three Hcmai linkers and two water molecules. The linkers all bond to Cd2 in different modes with one ligating in a κ^2 bidentate manner via the carboxylate based on O9 and O10, another in a κ^1 mode via O8 and the third in a κ^2 bidentate manner via N1 and O1. In the gross structure, Cd2 centres along with Cd1 dimers and the interactions from the linkers form a 1-D chain SBU. Each chain is linked to two adjacent SBU chains forming a 2-D sheet, which can be seen in **Figure 2.11**. The sheets contain channels that run parallel to the *a*-axis, in which the guest water, O15, resides. The water acts as a hydrogen bond donor to both O9 and O3 and as an acceptor for H14B from the water ligand based on O14. The structure also possesses a number of hydrogen bonds that are formed between adjacent planes, which stack to form the gross structure. One of these inter-plane hydrogen bonds is formed from the donation of the carboxylic acid hydrogen H6 and accepted by O4, the formation of this hydrogen bond may contribute to the fact that this carboxylic acid remains protonated while the other two on the linker are deprotonated.

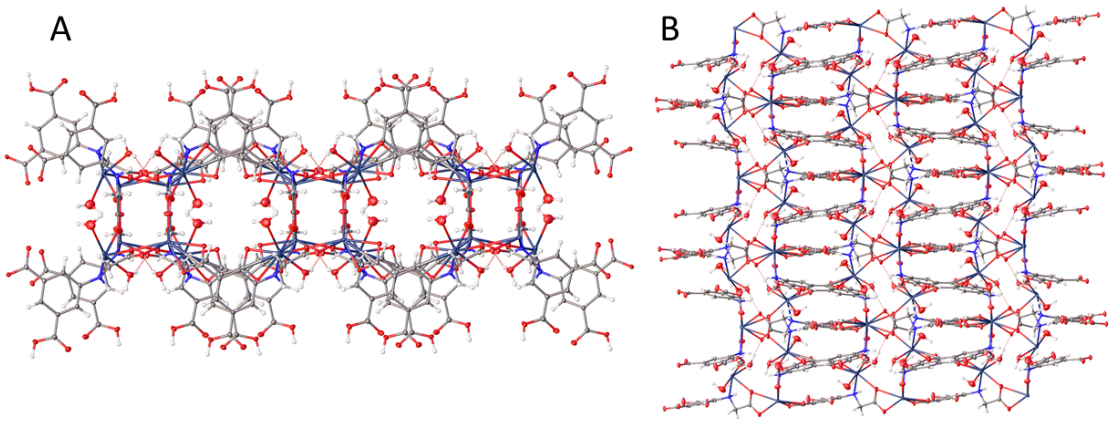

Figure 2.11. The 2-D sheets in compound **1** view looking down the (**A**) *a*-axis and (**B**) *b*-axis. Guest water has been removed for clarity.

Compound **1** was confirmed as the major constituent in the bulk material using powder X-ray diffraction which showed a good agreement between the pattern simulated from the single-crystal data and the experimental pattern, this comparison can be seen in **Figure 2.12**.

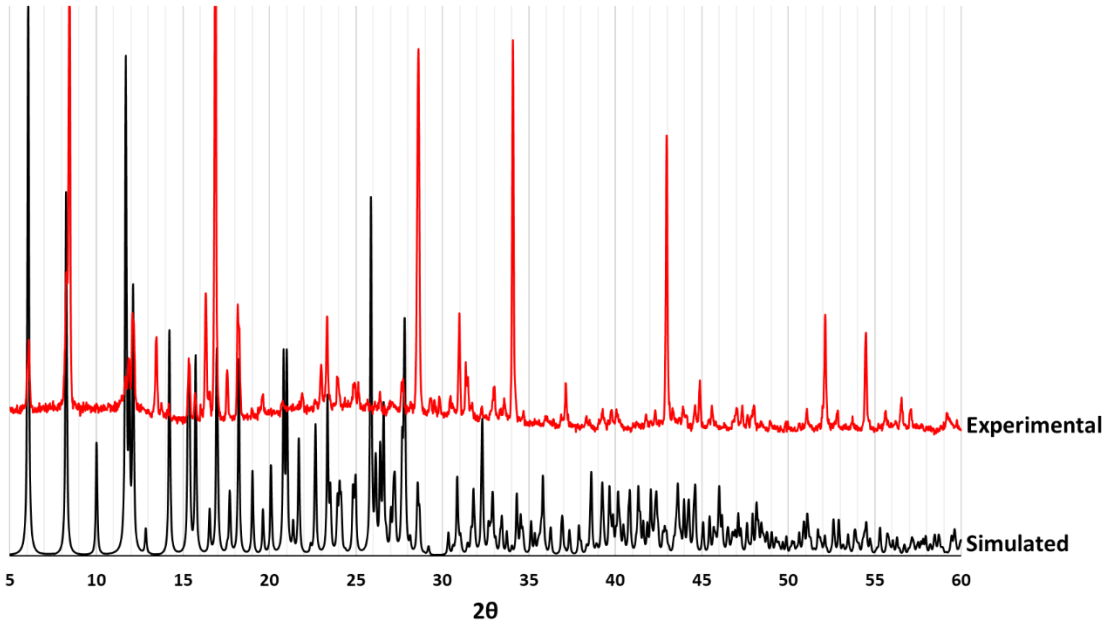

Figure 2.12. The PXRD pattern for compound **1** alongside that simulated from the single-crystal data.

2.2.2 Synthesis and characterisation of [Cd(Hcmai)(H_2O)$_2$] (**2**)

Compound **2** was synthesised in the hydrothermal reaction between $CdCl_2 \cdot 2.5H_2O$ and H_3cmai at 90 °C. After three days large brown plate crystals were recovered via vacuum filtration. PXRD analysis showed the pattern did not match any known structure and consequently a single-crystal X-ray diffraction experiment was carried out.

Compound **2** crystallises in the triclinic space group *P*-1. The asymmetric unit is composed of one cadmium centre, one Hcmai linker and two water ligands. The asymmetric unit along with the coordination sphere of the cadmium centre are shown in **Figure 2.13**.

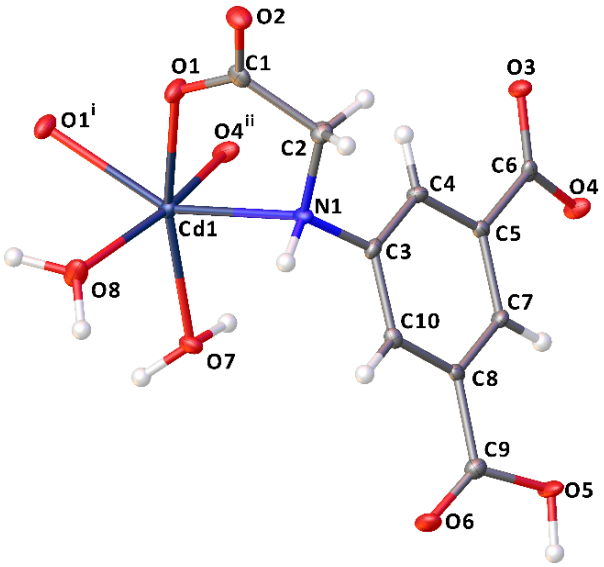

Figure 2.13. The asymmetric unit and cadmium coordination sphere in compound **2.** (i, 2 – *x*, 1 – *y*, – *z*; ii, 2 – *x*, 1 – *y*, 1 – *z*.) (ADPs plotted at 50%).

Cd1 is 6-coordinate by virtue of bonding to three different Hcmai linkers and to two water molecules. One of the Hcmai linkers coordinates in a κ^2 bidentate manner through N1 and O1, the second coordinates in a κ^1 mode via O4 and the third binds through O1. This latter oxygen coordinates both as part of the κ^2 binding mode with N1 but also in a μ_2 bridging mode to a second Cd1 centre, forming a dimer SBU as shown in **Figure 2.14**. It can also be seen that the SBU is supported by the formation of S(6) hydrogen bonds between H7B and O3.[104] The dimer is formed from the same combination of interactions as seen in compound **1**, with two bridging carboxylate oxygens (O7 in compound **1** and O1 in compound **2**) that are also part of κ^2 bidentate interactions. The dimer in compound **2** differs in that the cadmium centres bear water ligands which are not present in the compound **1** dimer.

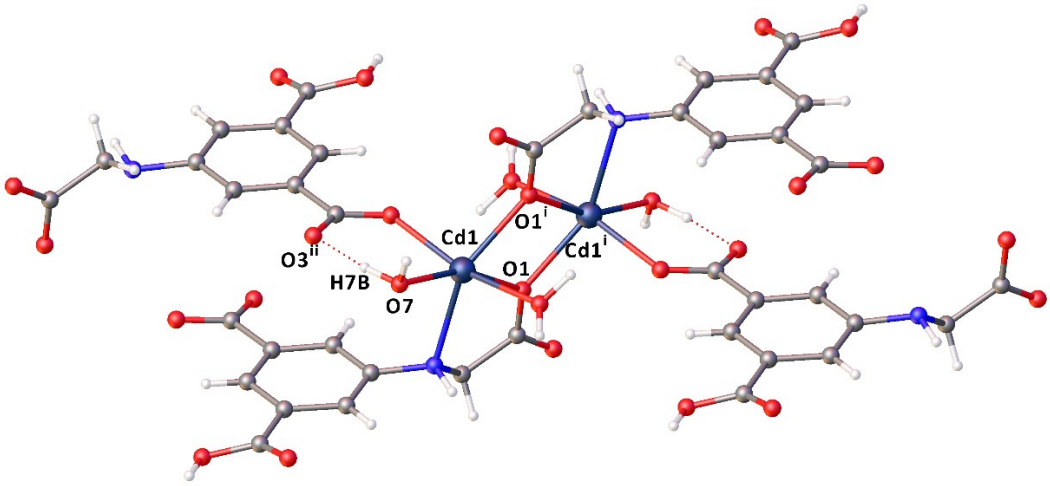

Figure 2.14. The Cd1 dimer formed in compound **2**. (i, 2 – *x*, 1 – *y*, – *z*; ii, 2 – *x*, 1 – *y*, 1– *z*.)

The SBUs and organic linkers propagate forming a 1-D chain running parallel to the *c*-axis as shown in **Figure 2.15**.

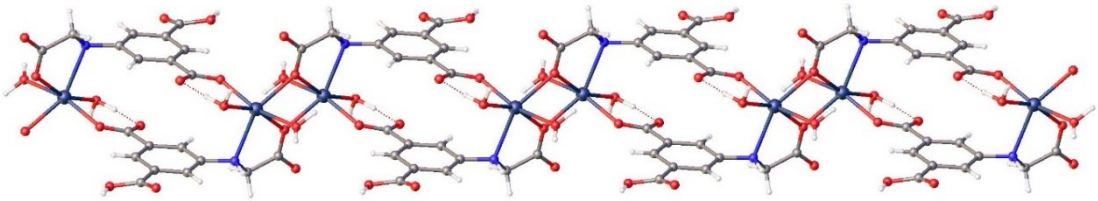

Figure 2.15. A 1-D polymeric chain running in the direction of the *c*-axis in compound **2**.

The 1-D chains form a dense 3-D structure by virtue of an extensive hydrogen-bonding network between adjacent chains. There are 5 unique inter-chain hydrogen bonds, three donated from water ligands, donor–hydrogen···acceptor: O7–H7A···O2, O8–H8A···O6 and O8–H8B···O7. One originating from the secondary amine, N1–H1···O2, and one originating from the carboxylic acid, O5–H5···O3. As in compound **1**, the presence of one non-deprotonated carboxylic acid on the linker may be explained by the preference to form a hydrogen bond.

2.2.3 Synthesis and characterisation of $[Cd_3(cmai)_2(H_2O)_4]\cdot 4H_2O$ (**3**) and $[Cd_3(cmai)_2]$ (**4**)

Compound **3** was synthesised in the reaction between $Cd(OAc)_2\cdot 2H_2O$ and H_3cmai in water at 90 °C for three days and formed as small colourless block crystals. The material crystallises in the triclinic space group *P*-1 with the asymmetric unit and cadmium coordination spheres shown in **Figure 2.16**. The asymmetric unit contains one full cadmium centre, one half occupancy cadmium centre that resides on a centre of inversion, one cmai linker, two water ligands and two guest water molecules. In compound **3** the linker is triply deprotonated and as such carries a 3- charge. This has implications not only on the cadmium:linker ratio, which is 3:2 instead of 1:1 as in compounds **1** and **2**, but also provides an extra coordination site, allowing the network formed to extend in three dimensions.

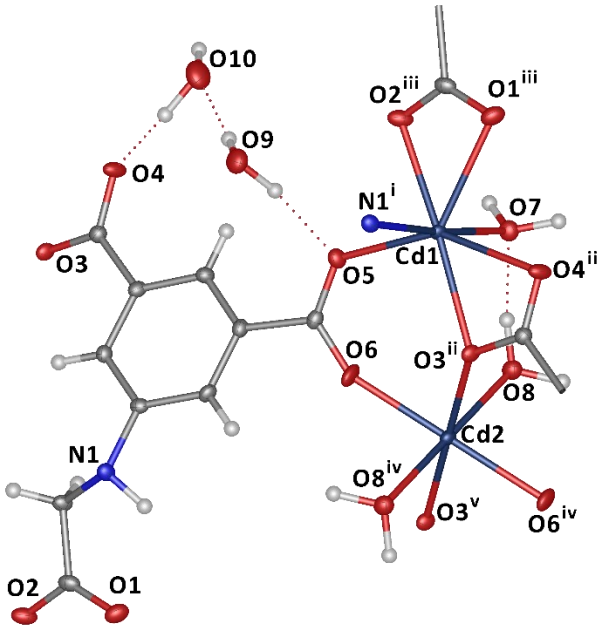

Figure 2.16. The asymmetric unit and coordination sphere of the cadmium centres in compound **3**. (i, 1 – *x*, – *y*, 2 – *z*; ii, 1 + *x*, – 1 + *y*, + *z*; iii, 1 + *x*, + *y*, – 1 + *z*; iv, – *x*, – *y*, 2 – *z*; v, 1 – *x*, – 1 – *y*, 2 – *z*) (ADPs represented at 50% probability).

Cd1, which is full occupancy, is 7-coordinate and coordinated to 4 different cmai linkers and one water ligand. Two of the linkers bind through a κ^2 coordination mode through carboxylates based on O1 and O2, and O3 and O4. O3 is also a μ_2 bridging atom between Cd1 and Cd2 centres. The third linker is coordinated though O5 in a κ^1 mode and the final linker coordinates just through N1.

Cd2 is 6-coordinate and octahedral in geometry. It has a site occupancy of a half as it resides on an inversion centre. It is ligated by four cmai linkers, two binding through O6 in κ^1 modes and

two though μ_2-O3 atoms which bridge between Cd1 and Cd2 centres. The SBU of compound **3** is formed by virtue of these linking O3 atoms and bridging carboxylates based on O5 and O6. It contains two Cd1 and one Cd2 centres as shown in **Figure 2.17**, in which the bulk of the ligands have been removed for clarity. The SBU is an 8 connected node, being coordinated to 8 different cmai linkers. It is further supported by S(6) hydrogen bonds formed between H8A and O7 of the water ligands.

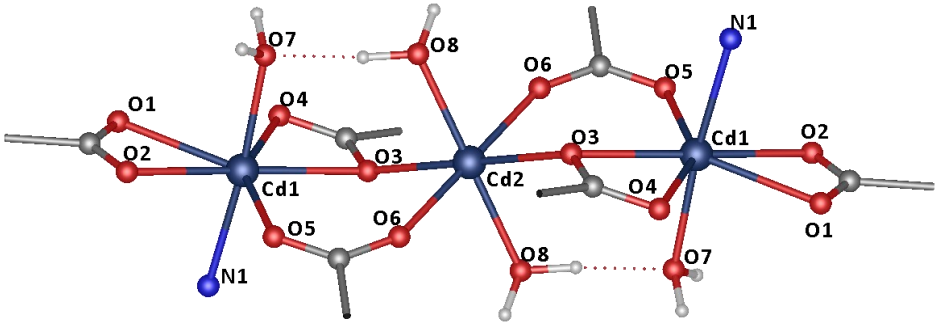

Figure 2.17. The SBU in compound **3**.

Each cmai linker is co-ordinated to 6 different cadmium centres in 4 different SBUs, extending the structure into three dimensions. The network contains channels running along the direction of the *a*-axis, which can be seen in **Figure 2.18.** The guest water molecules reside in these channels and are involved in 5 distinct hydrogen bonds, 4 with the framework and one between one another.

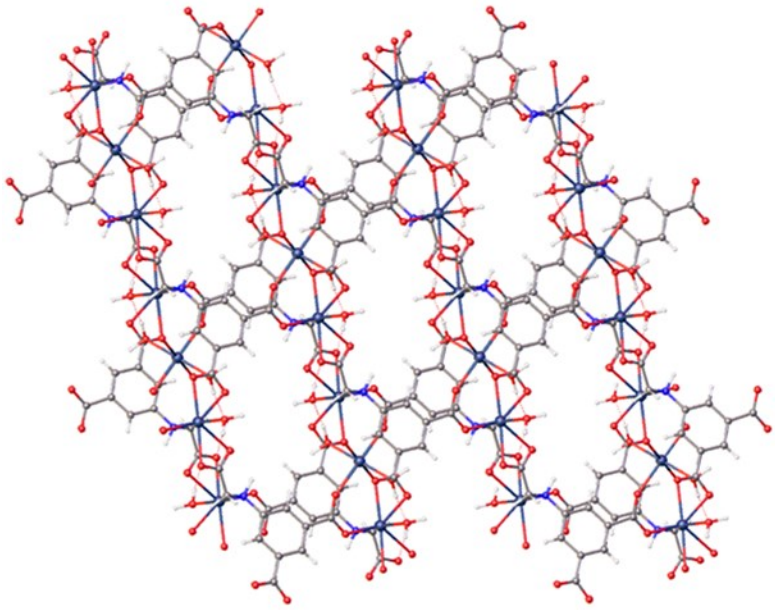

Figure 2.18. The structure of compound **3** viewed down the *a*-axis, with the guest water removed for clarity.

The presence of channels and guest solvent shows this structure has the potential for porosity. In order to probe this property further, TGA was carried out on a sample of **3**, the results of which are presented alongside the derivative in **Figure 2.19**. The plot shows two overlapping mass loss events centred at 120 °C. This mass lost can be attributed to the departure of water from the framework. The percentage mass lost between the two flat regions (30 – 160 °C) is 14.7%, however, the percentage mass of the framework that is guest water is only 7.6%. This suggests that the framework is also losing the coordinated water ligands, which explains the presence of two distinct mass loss events. The percentage mass of both coordinated and guest water is 15.1% which agrees well with the 14.7% determined experimentally.

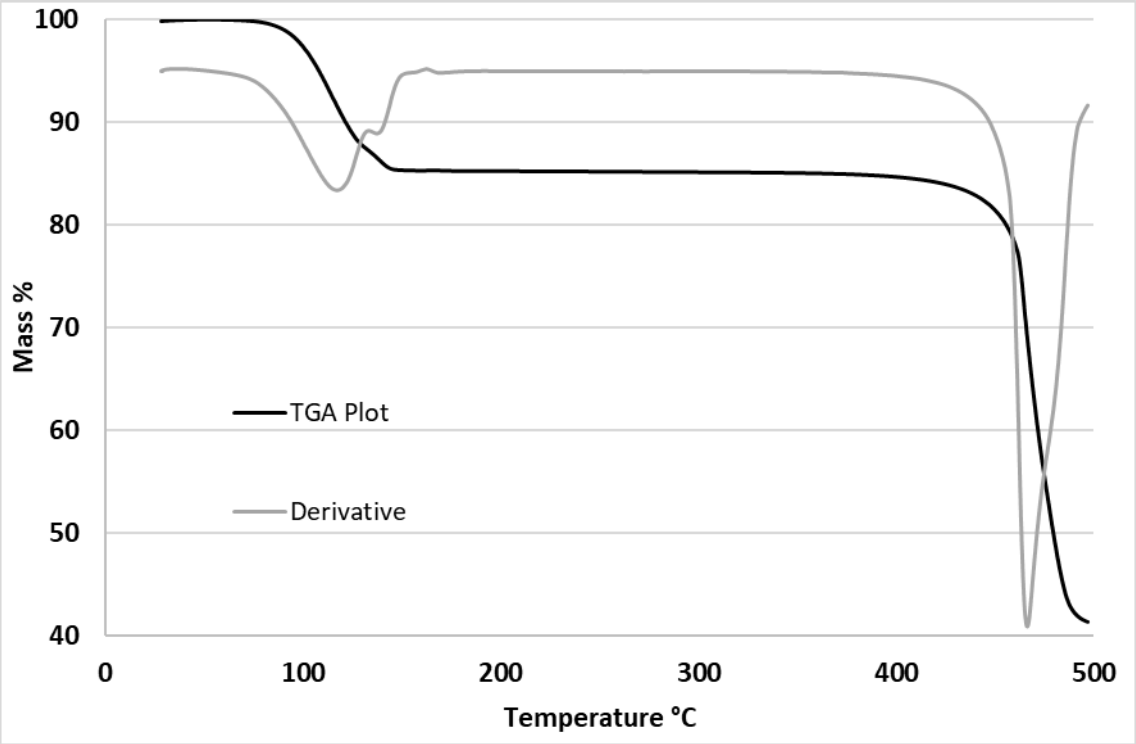

Figure 2.19. TGA plot including curve derivative for compound **3**.

Several efforts were made to activate the MOF without also removing the co-ordinated water using solvent exchanges and mild conditions, unfortunately, these were unsuccessful. Interestingly upon removal of all water from the MOF a new solid form, compound **4**, is produced, which is evidenced via PXRD as shown in **Figure 2.20.** This new solid form was obtained by heating compound **3** under reduced pressure at 100 °C for 6 hours.

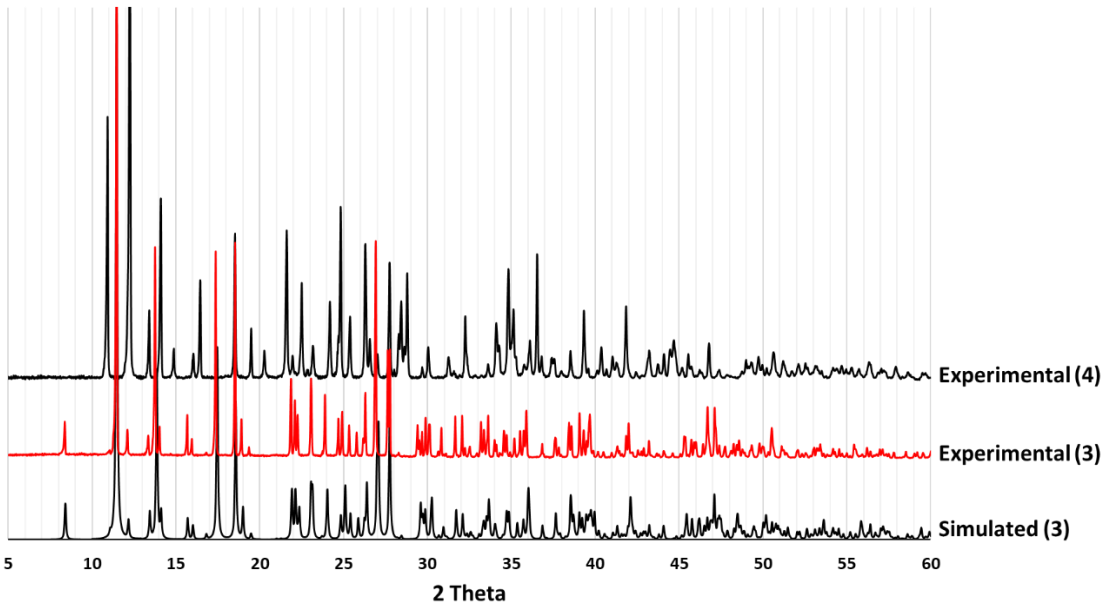

Figure 2.20. The PXRD patterns of compound **3** simulated from single-crystal data and collected experimentally and the pattern of compound **4.**

By comparison of the IR spectra of compound **3** and **4**, as shown in **Figure 2.21,** it can be seen that the broad peak between 2700-3500 cm^{-1} associated with the O-H band from water in compound **3** is absent in compound **4**. This supports the evidence from the TGA suggesting that all water, guest and ligated, was removed in the formation of compound **4.** It is also noted that in the spectrum for compound **4** the amine peak at 3320 cm^{-1} is very sharp, suggesting that it is not involved in hydrogen bonding.

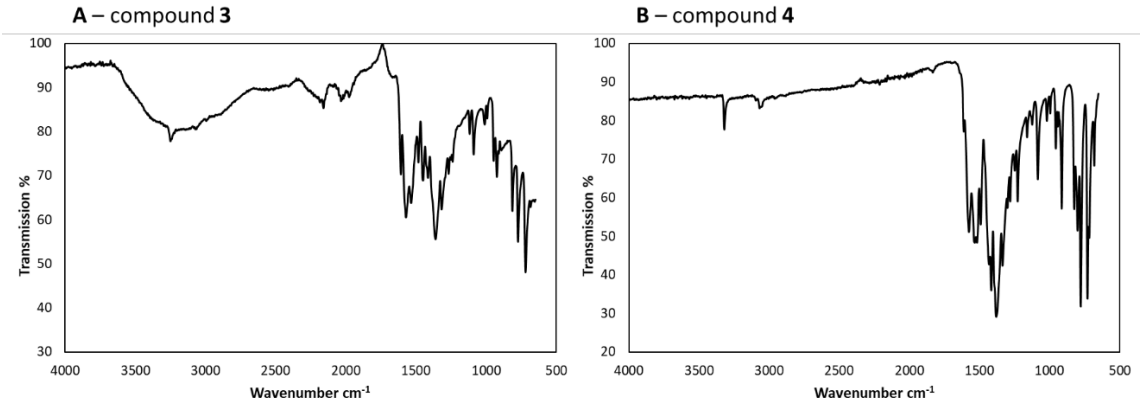

Figure 2.21. The IR spectra for compound **3** and compound **4**.

The process of removal of water from compound **3** caused the crystals to fracture making single-crystal X-ray diffraction analysis of compound **4** challenging to implement. An experiment was carried out on a small shard of **4**, however, although the data were of low quality giving poor

resolution, the connectivity was able to be determined giving insight into this solid-state transformation.

Compound **4** crystallises in the triclinic space group *P*-1 and its asymmetric unit contains one full occupancy cadmium centre, one half occupancy cadmium centre and one cmai linker. Consistent with the results of the TGA and IR experiments, the structure contains no water either as a guest or as a ligand. The asymmetric unit and coordination sphere of the two cadmium centres are shown in **Figure 2.22**.

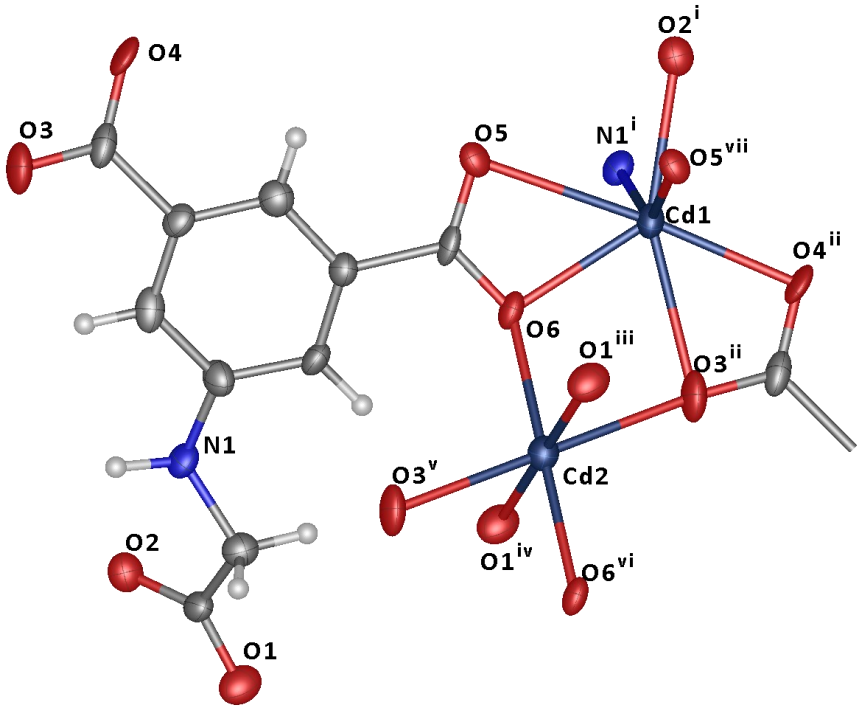

Figure 2.22. The asymmetric unit of compound **4** with coordination spheres of Cd1 and Cd2. (i, 1 – *x*, 1 – *y*, – *z*; ii, + *x*, 1 + *y*, – 1 + *z*; iii, – 1 + *x*, 1 + *y*, + *z*; iv, 2 – *x*, 1 – *y*, – *z*; v, 1 – *x*, 1 – *y*, 1 – *z*; vi, 1 – *x*, 2 – *y*, – *z*; vii, – *x*, 2 – *y*, – *z*) (ADPs represented at 50% probability).

The full occupancy cadmium centre, Cd1, is 7-coordinate and is bonded to 4 different cmai ligands. One bonds through N1 and O2 in a κ^2 binding mode. Another is bound through the carboxylate based on O5 and O6 in a κ^2 binding mode; both O5 and O6 are also involved in μ_2 bridging modes to symmetry related Cd1 and Cd2 centres respectively. This second bridging $O5^{vii}$ interaction comes from the third cmai ligand. Finally, the O3 and O4 from a carboxylate of the fourth linker are coordinated in a κ^2 binding mode.

Cd2 is half occupancy as it resides on a centre of inversion. It is distorted octahedral in geometry and is coordinated to 6 different cmai species. Two linkers bind to Cd2 through O1 and do so via a κ^1 interaction with the second carboxylate oxygen, O2, coordinating to an adjacent Cd1 centre.

The other 4 linkers all coordinate via μ_2 bridging modes via either O3 or O6, bridging between Cd1 and Cd2 centres. The bridging between adjacent Cd1 and Cd2 centres leads to the formation of chains running parallel to the *a*-axis. Part of a chain is shown in **Figure 2.23**, with the bulk of the ligands removed for clarity.

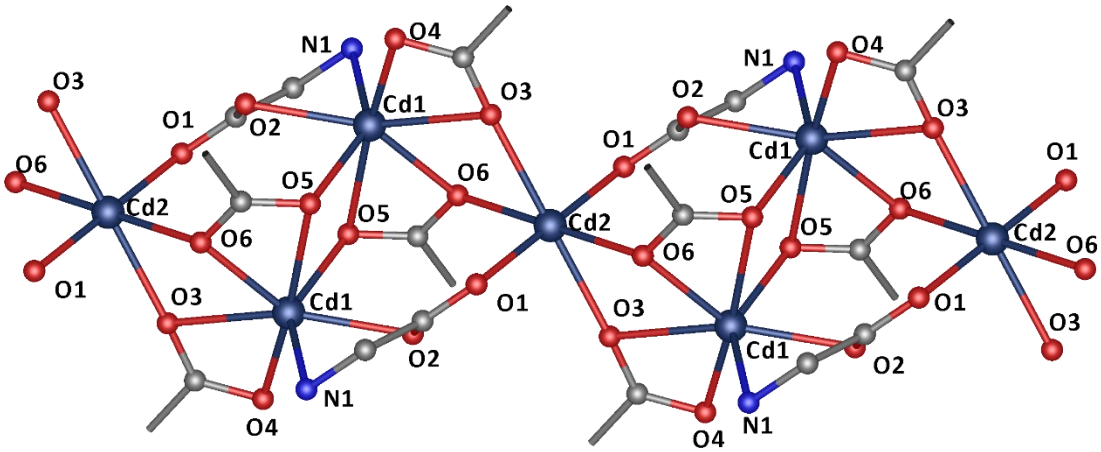

Figure 2.23. The 1-D chain SBU in compound **4.**

Each 1-D chain SBU is connected to six surrounding chains by virtue of the organic linkers, creating the 3-D network. The structure is densely packed and contains no channels, pores or void space.

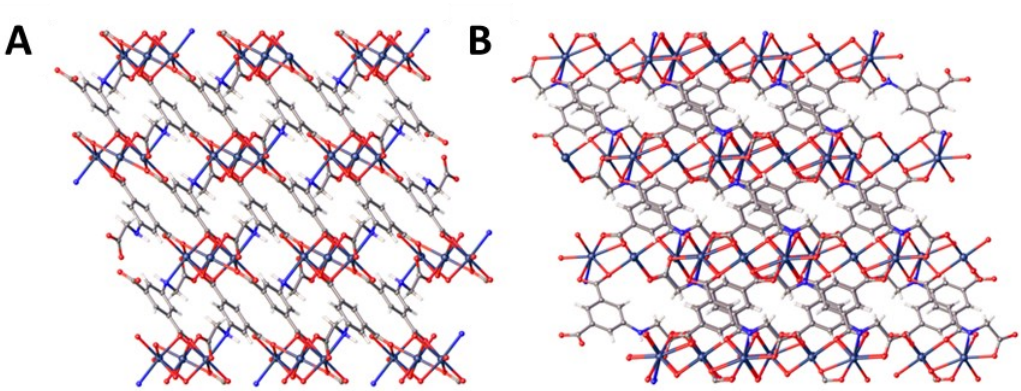

Figure 2.24. The structure of **4** as viewed down the: **A**, *a*-axis and **B**, *c*-axis.

Comparing the structures of compound **3** and **4**, several observations and assumptions can be made about the nature of the solid state transformation. The unit cell volume in compound **3** is 690.95(5) Å^3, and that of **4** is 488.97(15) Å^3 which suggests significant contraction upon loss of the water. This is also reflected by an increase in the calculated density from 2.292 g m^{-3} in compound **3** to 2.749 g m^{-3} in compound **4**. This is consistent with the lack of pores and channels in the dehydrated structure.

The Cd1 centres in both structures are 7-coordinate and are coordinated to four cmai ligands. There is a rearrangement in the binding modes, the coordination with O1 and the water ligand based on O7 are lost, additional bonds are formed between an O5 and O6 atom and Cd1. In compound **4** the O5 and O6 atoms bridge between cadmium centres, this changes the SBU from a tri-metal node to an infinite 1-D chain.

The Cd2 centre also retains its coordination geometry upon dehydration as well as still residing on an inversion centre. The bonds to both O6 and both O3 atoms are preserved, although the O6 atoms have an additional μ_2 bridging mode interaction with the adjacent Cd1 centres. The two water ligands based on O8 were replaced by coordination from O1 atoms and increases the number of cmai ligands coordinating Cd2 from 4 to 6.

Compound **3** has been shown to form compound **4** upon dehydration. In order to investigate whether this process was reversible a sample of **4** was submerged in water for a period of 5 days. After this time period a PXRD pattern of the crystalline powder was collected, this is presented in **Figure 2.25** alongside the simulated and experimental patterns for compounds **3** and **4**. Remarkably, the PXRD data showed that all of compound **4** had rehydrated and converted back to compound **3.**

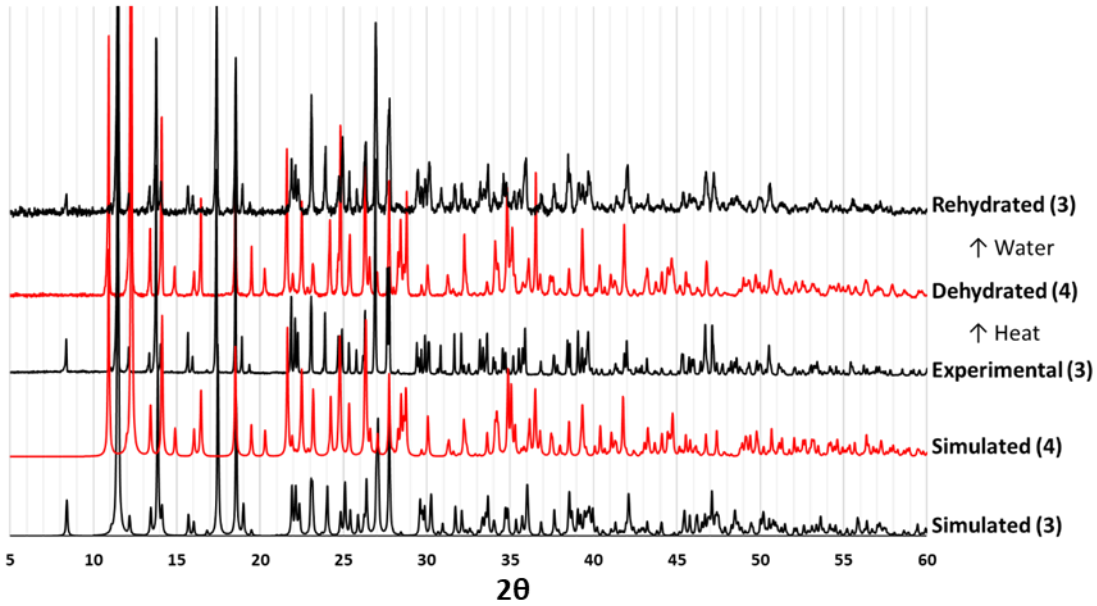

Figure 2.25. A PXRD overlay containing: the simulated pattern of compound **3**, the simulated trace for compound **4**, the experimental trace of compound **3**, the trace of dehydrated compound **3** (compound **4**) and the trace collected for the rehydrated sample of compound **4** (compound **3**).

Structural changes on exposure to an external stimulus in a MOF is known as 'breathing'. Although many examples of 'breathing' MOFs are now known, it is still a property that is

possessed by only a small minority of MOFs.[40, 105-107] Although not technically breathing as the topology of the network is not retained, the structural change presented in this case is very interesting, as it is not only characterised by a change in pore volume and unit cell size but also by the breaking of bonds and formation of new bonds. Given this, it is surprising that the process is reversible.

Two possible mechanisms for a transition like this to occur are a gradual continuous conversion from one form to the other or transition between two or more discrete structures. The breaking and formation of bonds is a discrete, non-continuous process which suggests that the transition from **3** to **4** occurs via the second mechanism. The rehydration of compound **4** could proceed by a third mechanism, a dissolution followed by reprecipitation of compound **3**. This cannot be ruled out but is unlikely as there was no visible change in the amount of solid in the vial during rehydration.[108-110]

The way in which the structural change propagates through the crystals can also be postulated. In the transition from **3** to **4** water leaves the framework causing rearrangement to a dense non-porous structure. This means that on rehydration of compound **4** the MOF must undergo an 'unzipping' mechanism whereby the surface and then outer layer of the crystals are rehydrated first, becoming porous, allowing water to travel towards the inner part of the solid where rehydration can continue, ultimately resulting in rehydration of the entire crystal. This type of structural change propagation will only occur in conversion of non-porous materials to porous ones.[111-113]

Transition from compound **3** to compound **4** was further interrogated using variable temperature X-ray powder diffraction. A sample of compound **3** was subjected to a heating profile that involved ramping the temperature up to 150 °C over the course of 90 min and then maintaining at 150 °C for 30 min before cooling back to room temperature. The plateau temperature was selected on the basis of the TGA data which showed that mass loss was complete at this temperature. PXRD patterns were collected at different points throughout the experiment; these are presented in **Figure 2.26**.

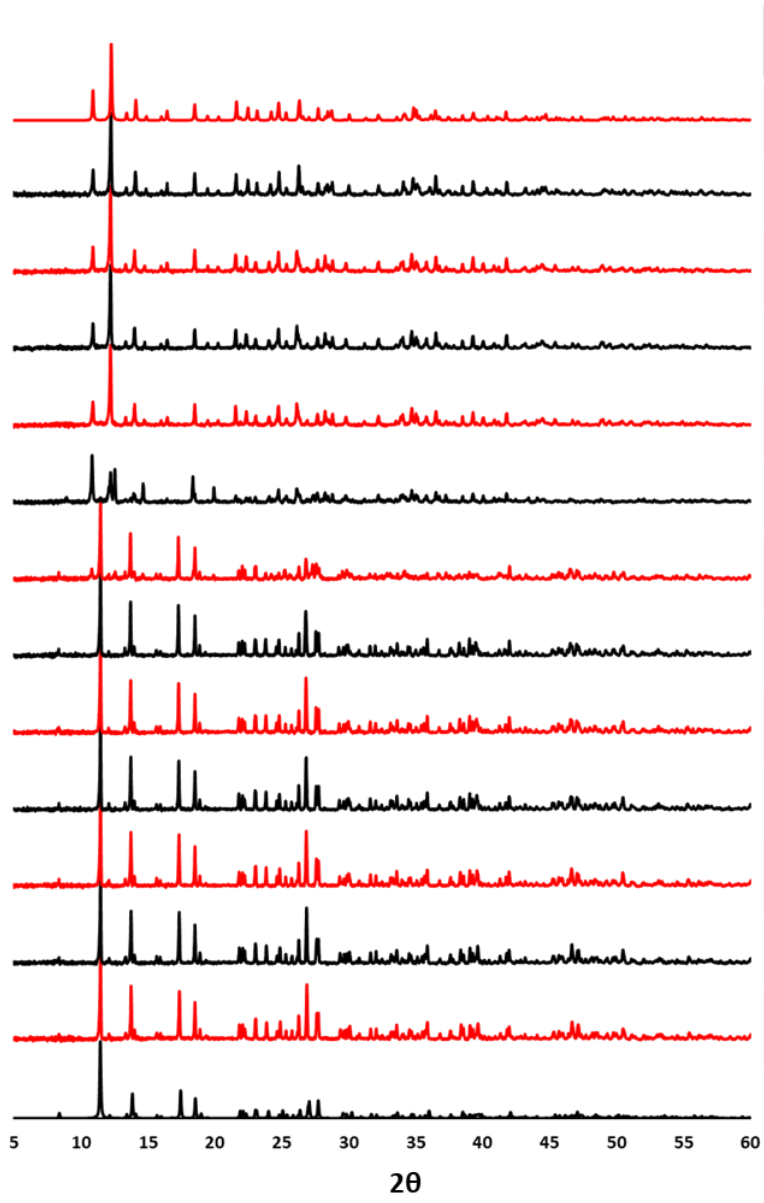

Temp (°C)	Time (mins)	PXRD Number
Compound **(4)** simulated pattern		
20	167	12
150	138	11
150	122	10
150	107	9
150	92	8
140	75	7
120	62	6
100	50	5
80	37	4
60	25	3
40	12	2
20	0	1
Compound **(3)** simulated pattern		

Figure 2.26. Variable temperature PXRD experimental results for compound **3** and **4.**

The results show that in PXRD patterns 1-6 the structure of compound **3** is retained, which represents the temperature ramping to 120 °C. At 140 °C, in PXRD pattern 7, the majority of the sample is compound **3** but there are some small extra peaks at 10° and 12° 2θ that suggest a phase change is starting to occur. At 150 °C, in pattern 8, it can be seen that a phase change has occurred as the pattern no longer matches that of compound **3.** This is in agreement with the TGA data, **Figure 2.19**, in which the loss of the water was observed to finish at 150 °C. However, the pattern does not match that for compound **4** although some of the peaks do align. PXRD patterns 9-12 match compound **4.** This suggests that the PXRD pattern 8 has captured an intermediate form in the transition between compound **3** and **4**, which, without the *in situ* monitoring, could not have been identified.

2.2.4 Synthesis and characterisation of $[Cd_6(cmai)_4(H_2O)_{9.75}(DMF)_{2.25}]\cdot 20H_2O\cdot 2.6$ DMF (**5**)

Compound **5** was obtained via an evaporative crystallisation from a solution of $Cd(NO_3)_2\cdot 4H_2O$ and H_3cmai in a 50:50 mixture of water and DMF. The product crystallised as colourless blocks in the monoclinic space group $P2_1$. Inherent diffraction weaknesses, most likely related to pseudosymmetry involving the cadmium centres and their dominance in the reflection intensities, led to an initial, albeit incorrect, solution in space group $C2$, along with a reduction in size of the asymmetric unit but concomitant obscuring of the electron density associated with the guest solvent and ligated DMF. Ultimately, examination of the raw data frames led to the identification of the correct space group.

The asymmetric unit, shown in **Figure 2.27** contains 6 full cadmium centres, 4 cmai linkers, 9 full and 2 partial water ligands, 1 full and 2 partial DMF ligands and a partial occupancy DMF guest. There is a substantial amount of unresolved guest solvent, which was treated using a solvent mask. The amount of unresolved guest solvent has been assigned as 20 H_2O and 2 DMF molecules based on the residual electron density removed using the solvent mask and parts of solvent found in the residual electron density peaks. As in compound **3** and **4**, the linker in compound **5** is triply deprotonated, carrying a 3- charge. Compound **5** also has a cadmium:linker ratio of 3:2 instead of the 1:1 ratio found in compounds **1** and **2**.

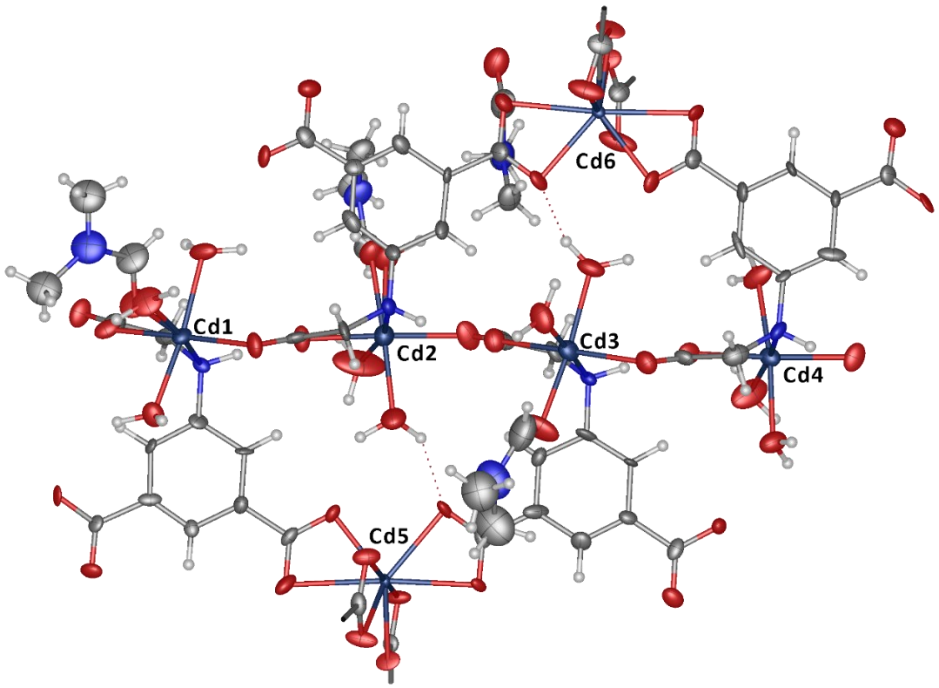

Figure 2.27. The asymmetric unit of compound **5**, along with the coordination sphere of the cadmium centres. (ADPs at 50% probability).

Cd1, Cd2, Cd3 and Cd4 are all 6-coordinate and distorted octahedral in geometry. Each centre is bonded to two cmai ligands, the first via a κ^2 bidentate binding mode involving the nitrogen of the secondary amine and carboxylate oxygen of the flexible arm. The second linker binds through the second carboxylate oxygen atom on the flexible arm. This forms a continuous 1-D chain SBU of Cd1 – Cd4 centres linked via the flexible arm portion of the cmai linkers. The other three coordination sites are occupied by different ratios of DMF and water ligands. Cd3 along with its coordination sphere is shown in **Figure 2.28**. The Cd–O bond distances in the structure vary from 2.117(13) Å to 2.344(11) Å, both of which are formed by water ligands. The Cd–N distances are generally longer, ranging from 2.342(14) Å to 2.410(11) Å.

Cd5 and Cd6 are 8-coordinate and are bound by 4 crystallographically distinct carboxylate groups in κ^2 bidentate binding modes from 4 different cmai ligands, this gives the cadmium centres pseudo tetrahedral geometry. Cd6 along with its coordination sphere is shown in **Figure 2.28**. The κ^2 binding modes are not symmetrical with the largest difference between Cd–O bond lengths observed for Cd5 bonding with O3 and O4 with distances of 2.259(7) Å and 2.619(10) Å respectively. Despite the unsymmetrical nature of the ligation, the carboxylates involved in these binding modes are all fully delocalised, evidenced by the C–O bond lengths being similar in each carboxylate group.

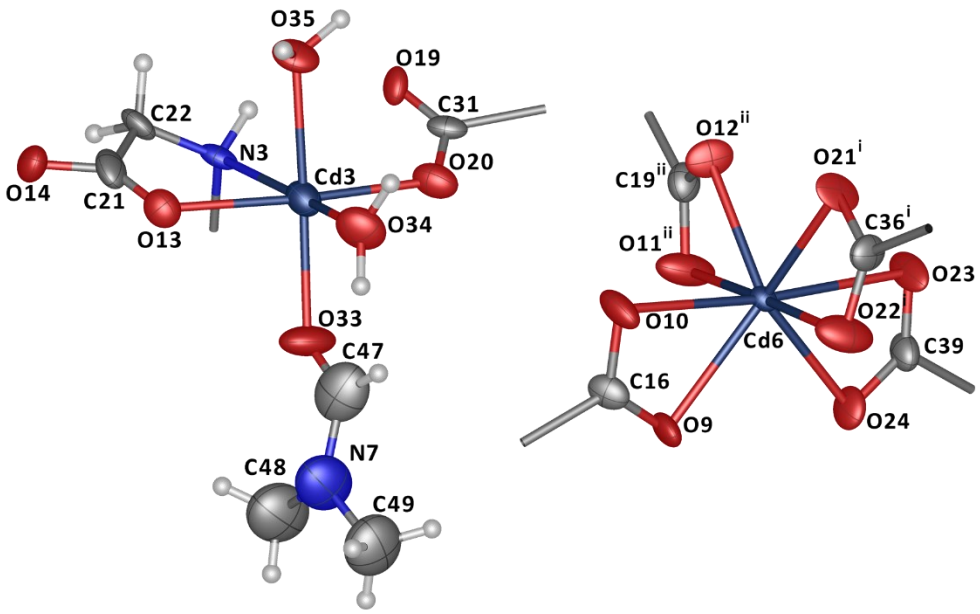

Figure 2.28. The coordination spheres of Cd3 and Cd6 in compound **5**. (i, – *x*, 1/2 + *y*, 2 – *z*; ii, 1 – *x*, -1/2 + *y*, 2 – *z*) (ADPs represented at 50% probability).

The 3-D structure of the MOF builds up from the construction of extended 1-D chains formed from the interactions between Cd1 – Cd4 and the flexible arm of the cmai linkers. These 1-D

chains are bound to perpendicular chains in the direction of the *c*-axis by virtue of the Cd5 and Cd6 centres along with the isophthalate portion of the cmai linkers. This creates a 3-D grid, shown schematically in **Figure 2.29**, with alternating planes of parallel chains running in the direction of the *a*-axis and *b*-axis.

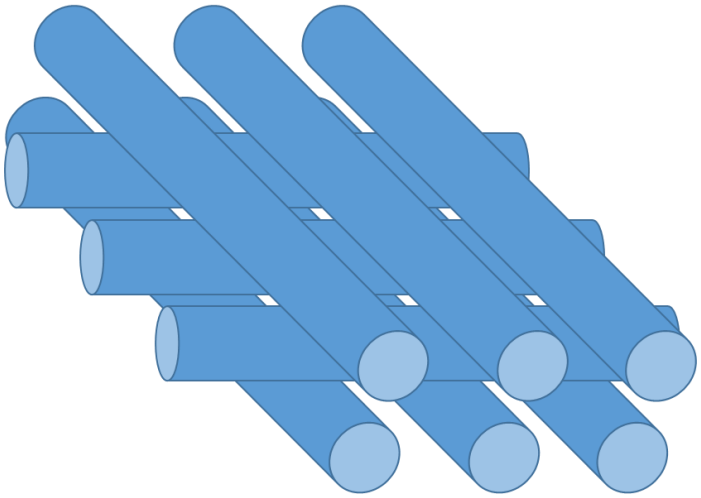

Figure 2.29. Representation of the 3-D structure of compound **5** with Cd1 - Cd4 and cmai chains represented by blue cylinders.

The 3-D structure of the framework contains a large amount of potential void space. During the structural solution a total of 19 oxygen atoms and one (additional) DMF molecule were located in the pore space per asymmetric unit. These molecules were poorly defined and very disordered and as such a solvent mask was used to treat the associated electron density. The mask showed the removal of 483 electrons per unit cell, the equivalent of approximately 4 molecules of DMF and 40 molecules of water, which is in good agreement with the amount of solvent located before applying the solvent mask. The number of electrons removed by the solvent mask is for the entire unit cell, which contains two asymmetric units, equating to 2 DMF guests and 20 water molecules removed per asymmetric unit.

The amount of guest was also interrogated using thermogravimetric analysis, the plot of which is presented in **Figure 2.30**. There is a mass loss event between 30 – 175 °C equating to 21.1%. This mass loss represents the guest solvent being removed from the framework, 20 molecules of H_2O and 2.6 molecules of DMF, this value is in good agreement with the TGA data for which these guests give a theoretical mass loss of 21.9%. Interestingly this suggests that the majority of the coordinated H_2O and DMF remains part of the framework until decomposition at above 300 °C.

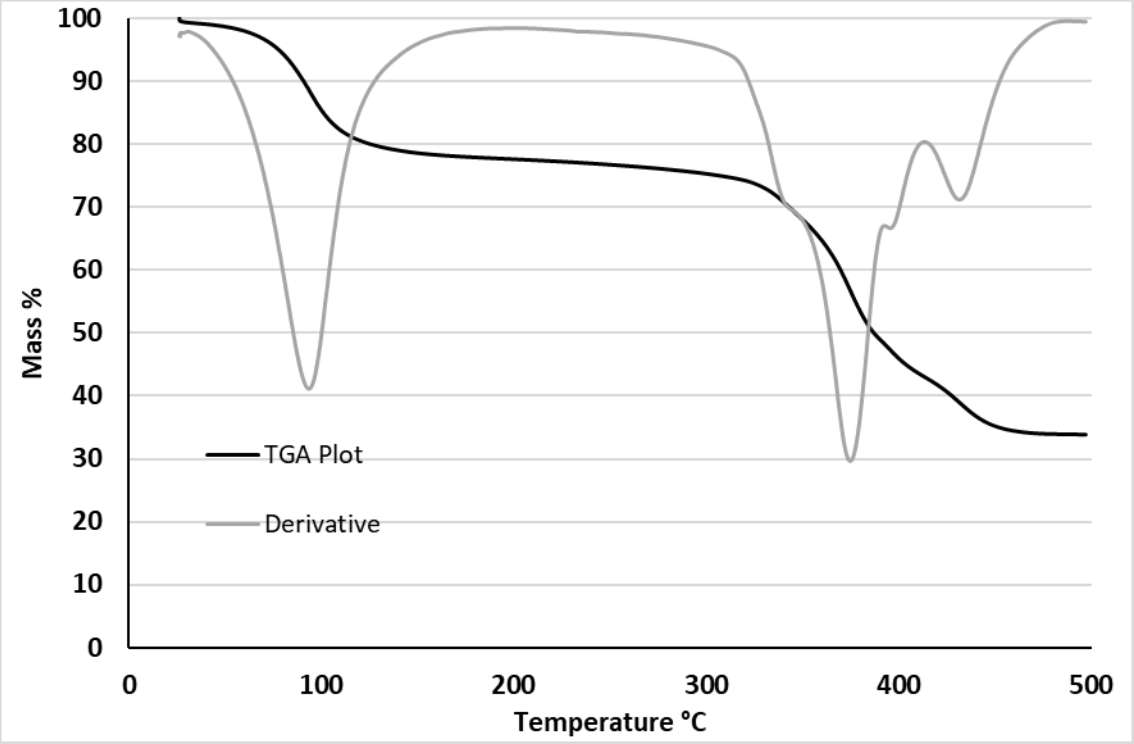

Figure 2.30. The thermogravimetric analysis for compound **5**.

A further method of evaluating the amount of guest solvent is using elemental microanalysis (CHN). The expected values for $[Cd_6(cmai)_4(H_2O)_{9.75}(DMF)_{2.25}]\cdot 20H_2O\cdot 2.6DMF$ are: C 26.11%, H 4.72%, N 4.94%. The experimental values found were: C 26.25%, H 4.24%, N 4.92%. The theoretical and experimental results are a good match, lending further support to the guest assignment.

All efforts to remove the solvent resulted in loss of crystallinity and ultimately breakdown of the framework. This may limit the MOF's applications to those in the liquid phase such as ion sequestration, small molecule inclusion and sensing.

2.2.5 Synthesis and characterisation of $[Cd_3(cmai)_2(H_2O)_3]\cdot 6H_2O$ (**6**)

Compound **6** was synthesised in the reaction of $Cd(NO_3)_2\cdot 4H_2O$ and H_3cmai in a mixture of water and DMF which was acidified using 0.5 mL of 1M HNO_3. The reaction was carried out at 120 °C for 2 days after which time colourless plate crystals had formed. Compound **6** crystallised in the monoclinic space group $P2_1$ and was refined as an inversion twin with the major component making up 57.4(12)% of the crystal.

The asymmetric unit, shown in **Figure 2.31**, contains three cadmium centres, two cmai linkers, three water ligands and six guest water molecules, one of which was disordered over two positions.

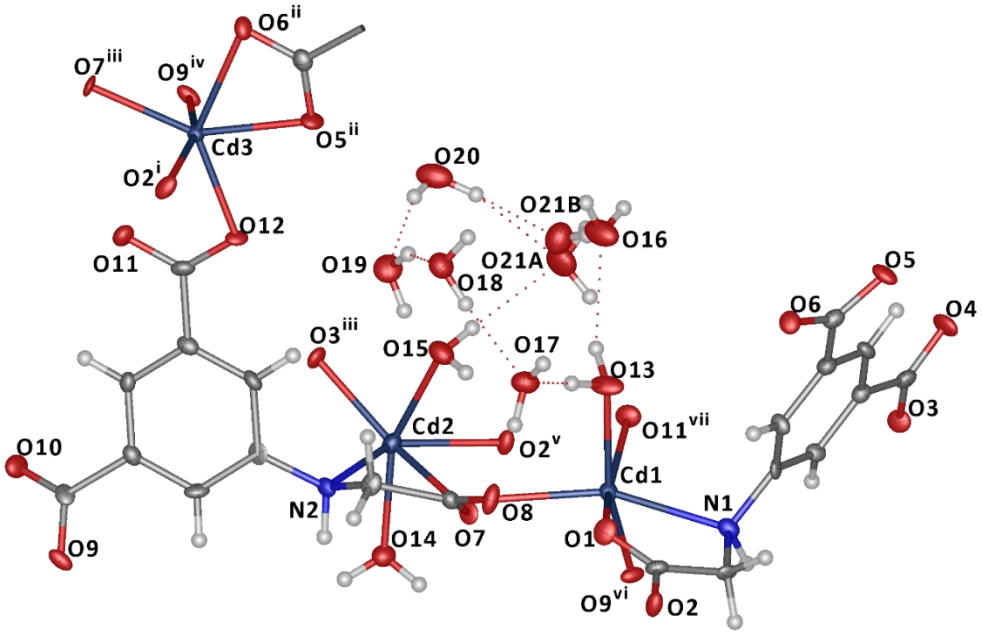

Figure 2.31. The asymmetric unit of compound **6** along with the coordination spheres of the cadmium centres. (i, 1 – *x*, 1/2 + *y*, 1 – *z*; ii, – *x*, 1/2 + *y*, 1 – *z*; iii, 1 – *x*, 1/2 + *y*, 2 – *z*; iv, – 1 + *x*, + *y*, + *z*; v, + *x*, + *y*, 1 + *z*; vi, 2 – *x*, – 1/2 + *y*, 2 – *z*; 1 – *x*, – 1/2 + *y*, 2 – *z*) (ADPs shown at 50% probability).

Cd1 is 6-coordinate and distorted octahedral in geometry. It is coordinated by four different cmai ligands and one water ligand, based on O13. The first of the cmai linkers binds through N1 and O1 of the flexible arm in a κ^2 mode. The two bound through O8 and O10 do so via κ^1 interactions and the ligand bound through O9 is part of a μ^2 bridging interaction with Cd3.

Cd2 is also 6-coordinate and distorted octahedral in geometry. However, it is bound by three cmai linkers and two water ligands. The first of the cmai ligands is bound through a κ^2 mode via N2 and O7 of the linker's flexible arm, with O7 also coordinating to a neighbouring Cd3 centre in a $\mu_2$mode. The second is coordinated in a μ_2 bridging mode via O2 also involving Cd3. The final

cmai species is bound via a κ^1 bond through O3. The two water ligands based on O14 and O15 sit axial to one another.

Cd3 is 6-coordinate and bound to 5 different cmai ligands. One bonds in a κ^2 mode through O5 and O6, another binds through O12 in a κ^1 mode. The other three are all involved in bridging between cadmium centres. O2 and O7 bridge from Cd3 to Cd2 and O9 is coordinated to both Cd3 and Cd1.

The combination of the μ_2 bridging interactions and bridging carboxylates leads to the formation of a tri-metal containing aggregate SBU which can be seen in **Figure 2.32**.

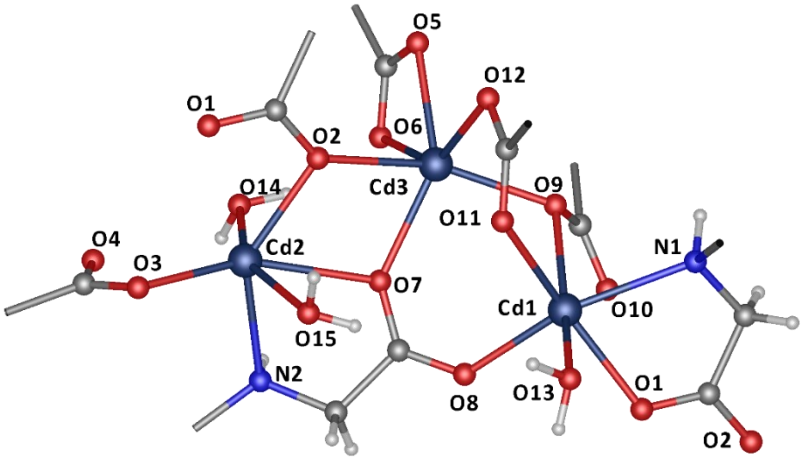

Figure 2.32. The aggregate of cadmium centres present in compound **6**.

The trimers in the structure are bound to two neighbouring trimers via O1 and O2 creating a chain, which runs in the direction of the *c*-axis, forming the SBU for compound **6** and can be seen in **Figure 2.33**.

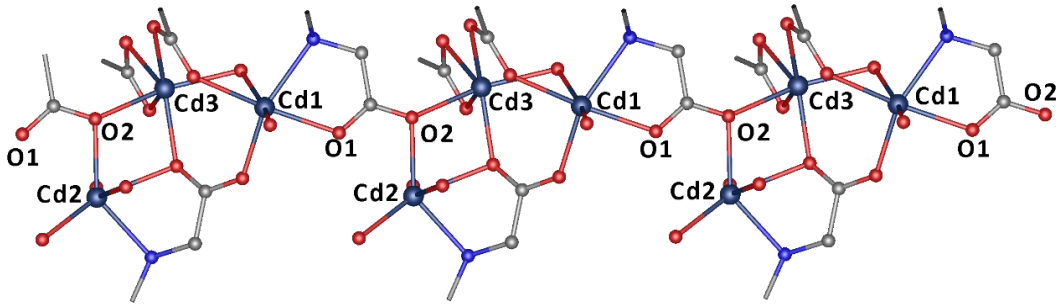

Figure 2.33. The 1-D chain SBU in compound **6**.

The chain SBUs are each connected via the bulk of the cmai linkers to 6 neighbouring SBUs, with each of the cmai molecules coordinating to 3 SBU chains. This forms a honeycomb like structure

containing channels running in the direction of the 1-D SBUs and crystallographic *c*-axis as shown in **Figure 2.34**.

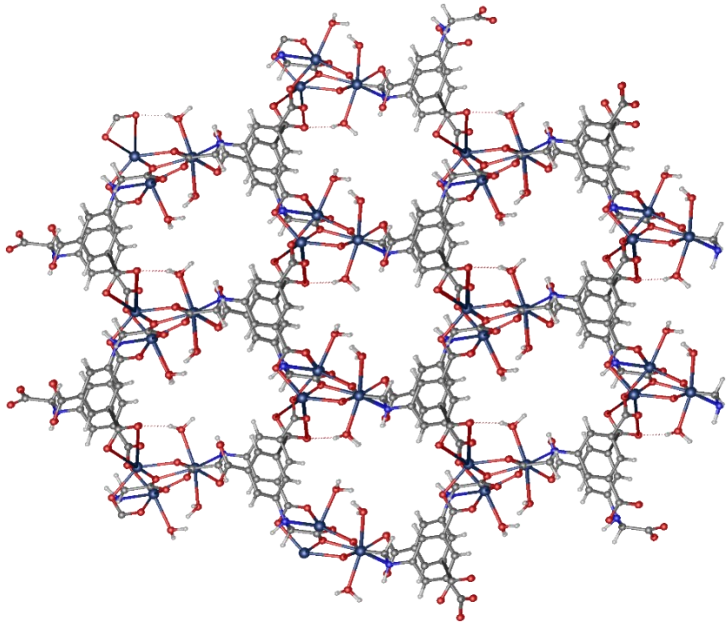

Figure 2.34. The 3-D honeycomb structure of compound **6** looking down the *c*-axis, the guest water molecules have been removed for clarity.

The guest water molecules reside in the channels of the structure and form a complex hydrogen bonding network. The structure contains a total of 21 distinct hydrogen bonds, 20 of which involve the guest solvent as either a hydrogen bond donor or acceptor. Some of these are presented in **Figure 2.35**.

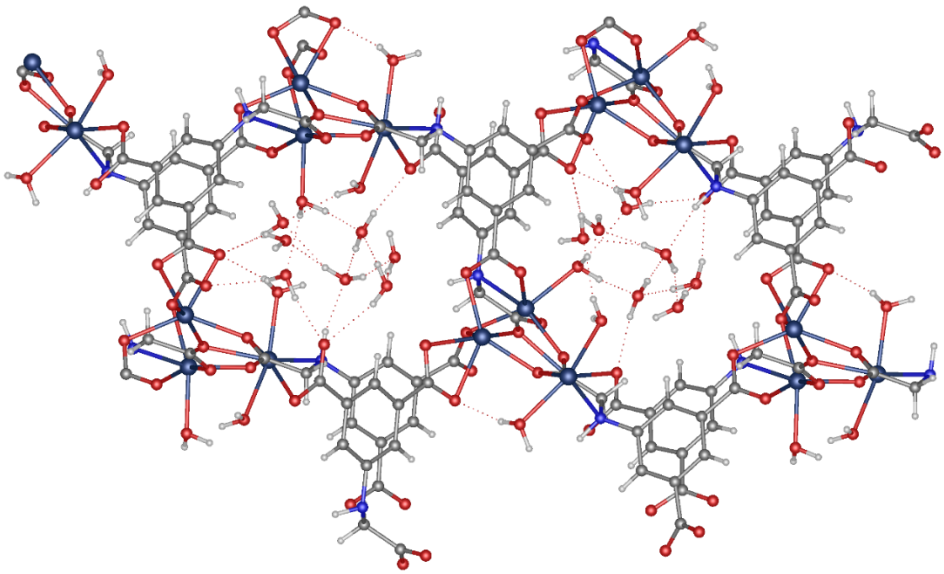

Figure 2.35. The guest water in compound **6**, showing hydrogen bonding network.

The guest-framework interaction can be probed further using TGA, a plot of the results of which is shown in **Figure 2.36**. The guest water is lost in the region 30 – 190 °C with a mass loss of 11.2% which agrees well with the theoretical value of 11.1%. Interestingly not all the guest water is lost in the same mass loss event, with two peaks in the derivative trace at 108 °C and a shallower peak at 148 °C. This is likely caused by differences in hydrogen bonding environment. The mass loss from 190 – 345 °C is only 2.3%, which equates to just over one water molecule, suggesting that some of the water ligands remain part of the framework until it starts to breakdown above 345 °C.

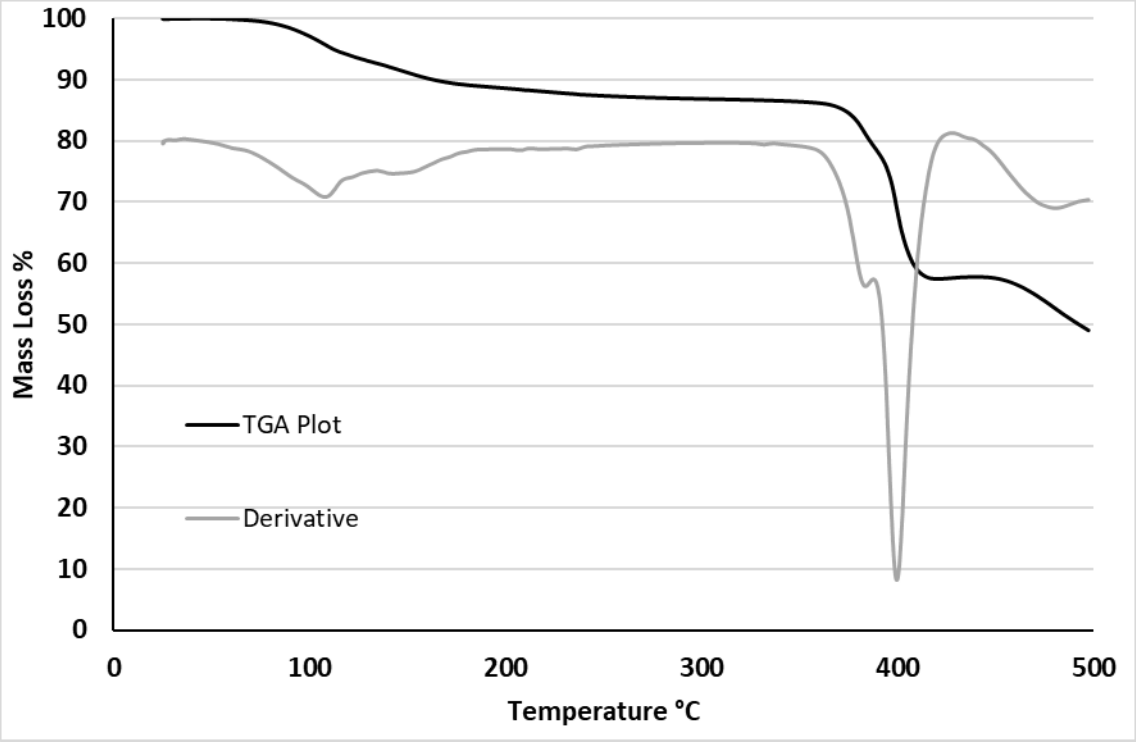

Figure 2.36. Thermogravimetric analysis for compound **6**.

2.2.6 Discussion

The combination of cadmium(II) salts and the novel linker H_3cmai under a range of different conditions has led to the synthesis six new coordination polymers. Despite containing the same constituent parts, the coordination polymers show a great deal of diversity in their gross structures. The crystallographic data and refinement details for compounds **1**-**6** can be found in **Table 2.2** at the end of this discussion.

The range of different structures were obtained by varying the synthetic conditions, a summary of which are presented in **Table 2.1**. Compounds **1**, **2** and **3** were synthesised under the same conditions but using different salts as the cadmium source. One suggestion for why compound **3** contains a fully deprotonated linker is because the acetate anion is more basic than nitrate or chloride used in the preparation of **1** and **2.** The DMF in compound **5** and the DEF/bipy in compound **6** act as bases, allowing the formation of fully deprotonated linkers in these structures. Also of note is the presence of water in all the reactions (other than compound **4**, formed by dehydration of compound **3**). The consistent use of water as the solvent or as part of the solvent system was due to the insolubility of the linker precursor in other widely used polar solvents, such as DMF and DEF.

Table 2.1. A summary of the synthetic procedures used in the synthesis of compounds **1**-**6**.

Compound	Cadmium Salt	Metal:linker ratio	Solvent System	Temperature °C	Reaction Time	Additional Information
1	$Cd(NO_3)_2{\cdot}4H_2O$	10:3	H_2O	90	3 days	
2	$CdCl_2{\cdot}2.5H_2O$	3:1	H_2O	90	3 days	
3	$Cd(OAc)_2{\cdot}2H_2O$	3:1	H_2O	90	3 days	
4	-	-	-	-	-	-
5	$Cd(NO_3)_2{\cdot}4H_2O$	3:1	DMF/H_2O	RT	2 days	Evaporative
6	$Cd(NO_3)_2{\cdot}4H_2O$	3:1	DEF/H_2O/ HNO_3	120	3 days	4,4'-bipy

Compound **1** is composed of 2-D sheets which are hydrogen bonded to adjacent sheets, forming its gross structure. Compound **2** comprises of 1-D chains, these chains pack into a dense arrangement and contains an extensive inter-chain hydrogen bonding network. Compounds **3**, **4, 5** and **6** are all 3-D networks. The most notable difference between the 3-D structures and ones of lower dimensionality is the charge on the organic linker. In the 1-D and 2-D structures the linker, Hcmai, is doubly deprotonated and carries a 2- charge. The lack of deprotonation on the third carboxylic acid means that the linker loses a potential coordination site and as a result

the network does not extend into the third dimension. The presence of a carboxylic acid functionality in compounds **1** and **2** promotes the formation of hydrogen bonds that build the chains and planes into their gross structure. In the 3-D MOFs, compounds **3**, **4, 5** and **6,** the linker, cmai, is fully deprotonated and as such carries a 3- charge. The extra carboxylate coordination site allows the structures to propagate in an extra dimension, forming 3-D topologies.

The presence of the carboxylic acid groups can be clearly seen in the IR spectra for compounds **1** and **2**, shown in **Figure 2.37**. The carboxylic acid bands, circled in red, occur at 1706 cm^{-1} and 1680 cm^{-1} in compound **1**, at 1692 cm^{-1} in compound **2**, and are absent in the spectra of the other compounds. The fact that compound **1** has two carboxylic acid bands is consistent with the presence of two crystallographically distinct Hcmai ligands in the crystal structure whereas compound **2** contains one crystallographically distinct Hcmai molecule and as such only shows one band.

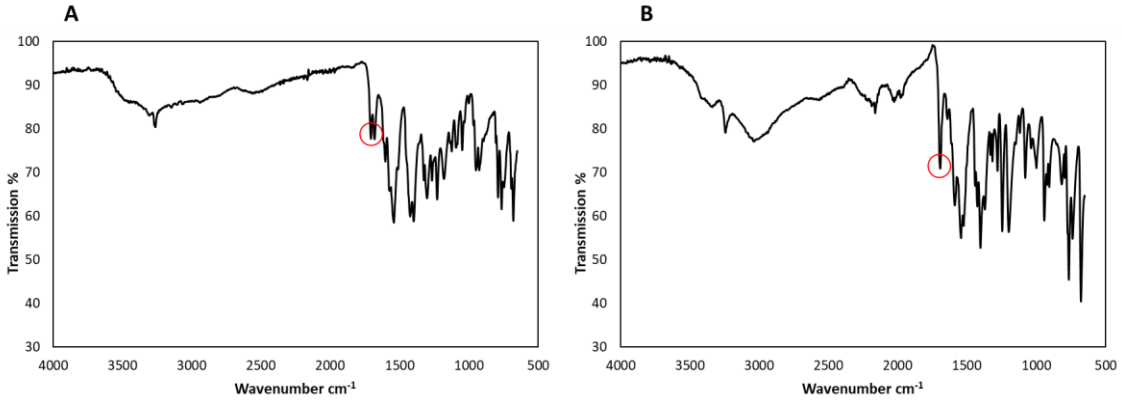

Figure 2.37. The IR spectrum for **A** – compound **1** and **B** – compound **2.**

The six compounds also contain a variety of different cadmium coordination environments, ranging from 6 to 8 in coordination number. This is not surprising as cadmium(II) is a d^{10} metal centre and as such has no directional electronic preference for a particular geometry. The relatively large size of cadmium(II) (compared with first row d-block ions) allows for higher coordination numbers to be accessed. This ability of cadmium(II) to form such a wide array of coordination geometries is a key factor in the formation of such a large variety of structures containing the same building blocks.

In all the compounds other than compound **4**, which was formed via dehydration, water ligands are present on at least one of the cadmium centres in the structure. The inclusion of water as a ligand on a metal centre allows for a wider range of coordination geometries and by extension,

network topologies to be accessed. This is because the water ligand is able to fill what would otherwise be vacant coordination sites in the MOF without changing the topology. Water ligands fulfil this role well as they are small and have the added advantage of supporting the framework via hydrogen bond formation. The presence of water ligands does have drawbacks, making the synthesised frameworks difficult to activate and the porosity challenging to access, as well as making structural prediction harder. The water ligands form hydrogen bonded networks with guest water, this makes it more difficult to remove the guests by both solvent exchange and thermally. In order to address this, reactions were undertaken in DMF and DEF, however, these were unsuccessful due to poor linker precursor solubility in these solvents.

All six compounds contain different SBUs although some similarities can be drawn between them. Compounds **1** and **2** both contain a cadmium dimer as part of their SBU, in both cases the dimer is formed by virtue of a κ^2 interaction with the secondary amine and carboxylate oxygen on the flexible arm, combined with a μ_2 bridging interaction from the same oxygen. The dimer contains two of these binding motifs, related by a centre of inversion, this can be seen in **Figure 2.38**.

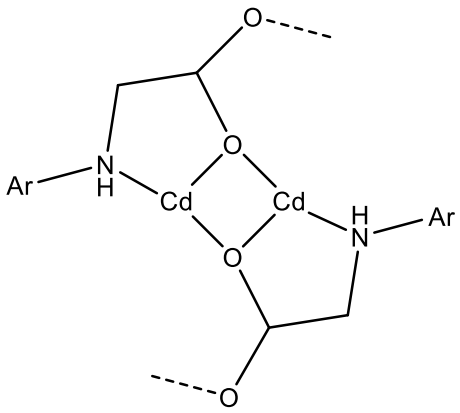

Figure 2.38. The dimer motif formed in compound **1** and **2.**

Compounds **3** and **4** contain SBUs that can be related to one and other via new bond formation, prompted by the loss of water ligands. The SBU of compound **3** is a tri-metal agglomerate which on the additional bridging mode interactions formed by O5 and O6 becomes a 1-D chain SBU in compound **4**.

Compounds **4**, **5** and **6** all contain 1-D chain SBUs, however, these differ in their composition and connectivity. The SBU chain in compound **4** is highly connected, with multiple bridging interactions between adjacent cadmium centres. In contrast, the chain in compound **5** is formed from cadmium centres linked only to 2 adjacent cadmium centres via a single connection each.

In compound **6** the SBU is formed of highly connected tri-metal aggregates which are linked in a chain to 2 neighbouring aggregates via a single connection each. Schematic representations of each of these different chain SBUs are shown in **Figure 2.39**. The differing number of bonds within the SBUs will affect the stability and flexibility of the frameworks.

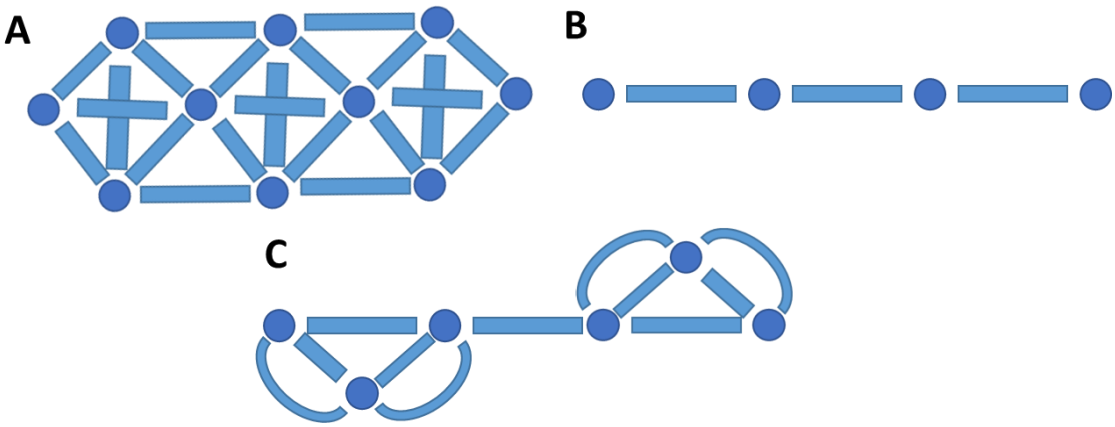

Figure 2.39. A representation of the chain SBUs in **A** – compound **4**, **B** – compound **5**, and **C** – compound **6.**

The semi-rigid linkers Hcmai and cmai have been observed to adopt a wide variety of different coordination modes when used in the synthesis of cadmium(II) based coordination polymers. The 13 different binding modes adopted by the linkers in compounds **1-6** are shown in **Figure 2.40**.

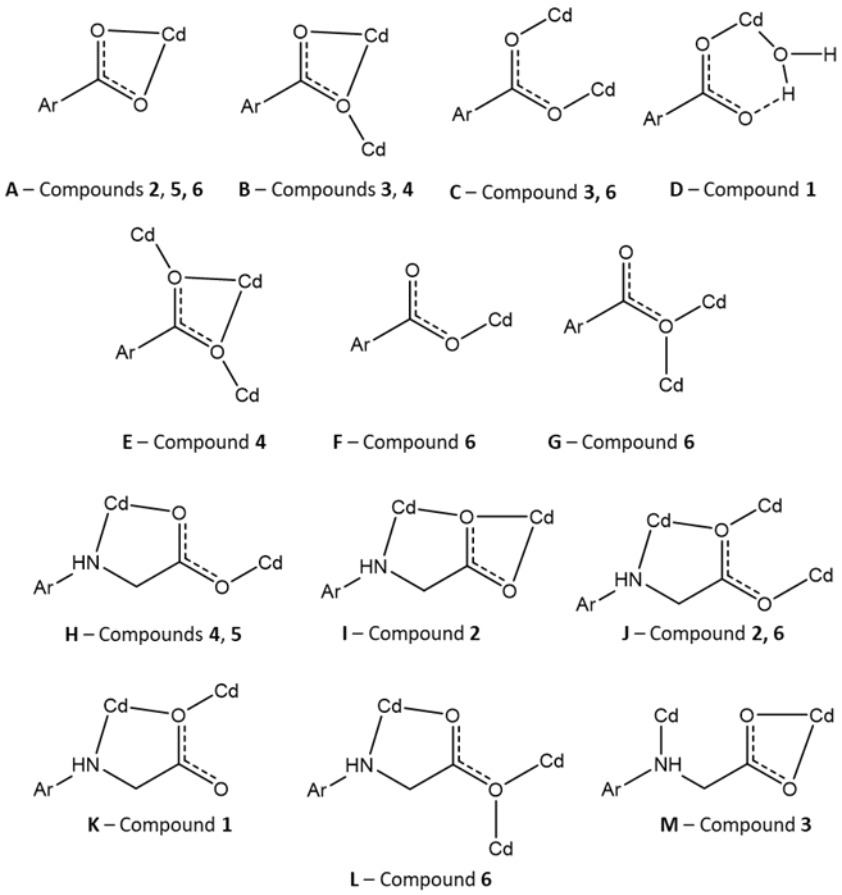

Figure 2.40. The coordination modes adopted by cmai in compound **1**-**6**, the bulk of the ligand is represented by Ar.

The large number of different coordination modes observed is one of the reasons why six different compounds have been synthesised from the same component parts. The modes can be divided into two categories, those that involve the aromatic carboxylates and those that involve the flexible arm containing the secondary amine and terminal carboxylate. The majority of the binding modes involve more than one cadmium(II) centre, forming the secondary building units in the structures. The most common binding mode motif which is present in compounds **1**, **2**, **4, 5** and **6** involves the flexible arm of the linker forming κ^2 bidentate coordination mode via the secondary amine nitrogen and one of the carboxylate oxygens on the end of the flexible arm, this can be seen in **H, I, J, K, and L**. A different type of binding mode involving the flexible arm is observed in compound **3**, in which the secondary amine coordinates to a different cadmium(II) centre than the carboxylate oxygens, this can be seen in **M**. Interestingly this less common binding mode is lost in the transformation of compound **3** to compound **4**.

Compounds **1**, **3**, **5** and **6** all contain varying amounts of guest solvent, occupying pores or channels in the structures. A method of assessing how much space there is inside a framework

is using void space analysis. This method considers the framework with the guest solvent removed and attempts to fit a sphere with radius 1.2 Å (representing a hydrogen atom) at points along a theoretical grid, using 0.2 Å steps, in the unit cell. A surface can be constructed where this sphere does not contact the van der Waals radii of the framework atoms. The volume of the space contained by the surface can be calculated and used to assess the amount of potential void space in the structure. The analysis has been carried out using the CCDC program Mercury.

Compound **1,** which contains just one guest water per asymmetric unit, has a void space of 90.74 $Å^3$ which is just 2% of the unit cell. The void space itself forms a sphere centred around the position at which the guest water resides.

Compound **3**, which contains two guest water molecules per asymmetric unit, contains a void space of 67.42 $Å^3$ which is 10% of the unit cell volume. When the void space is visualised, it resides in the channels running in the *a*-axis as shown in **Figure 2.41 A**. However, what was not initially clear based on visual inspection of the channel is that it is not uniform in diameter and has wider and narrower portions. This has a dramatic effect when considering potential voids as narrower portions of the channel do not have sufficient width to fit the 1.2 Å radius probe sphere. The result of this is multiple discrete voids in the channels rather than one long pore running throughout, this can be seen in **Figure 2.41 B**. The bottleneck that separates the discrete pores in the channel is 1.1 Å wide and only just too narrow to allow the probe sphere to pass through. The bottlenecks in the channel are likely the reason that high temperature and low pressure is required to remove the guest water from the structure.

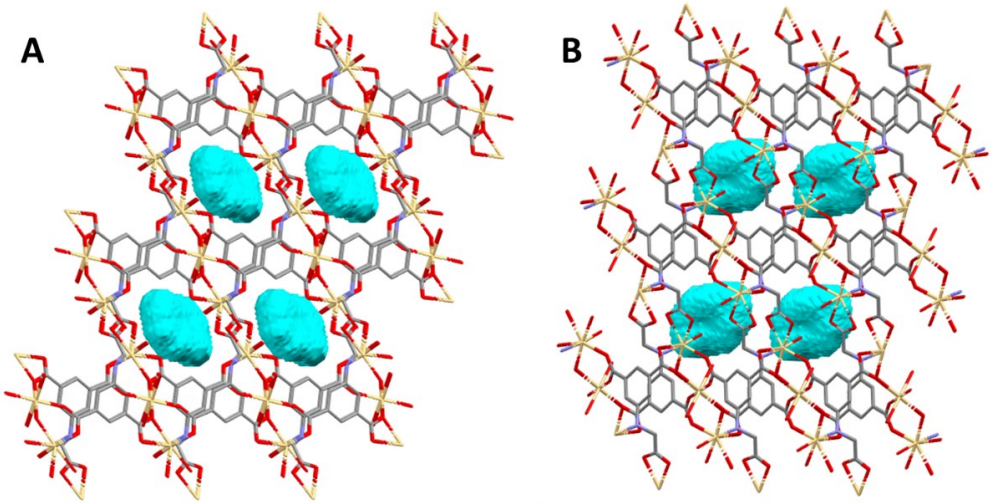

Figure 2.41. The void space in compound **3** as viewed down the **A.** *a*-axis and **B**. *b*-axis. (Cd = yellow, O = red, N = blue, C = grey, H = removed for clarity, Void space = cyan).

Compound **5** has over 20 guest solvent molecules per asymmetric unit which is far more than compound **1** or **3.** Unsurprisingly this leads to a large void space of 1513.18 $Å^3$, 32% of the unit cell volume. This value is an underrepresentation of the actual void space, this is due to the partial occupancy DMF ligands, which for the purposes of these calculation are treated as if they were full occupancy. The void volume, which is shown in **Figure 2.42**, consists of convoluted channels in all directions.

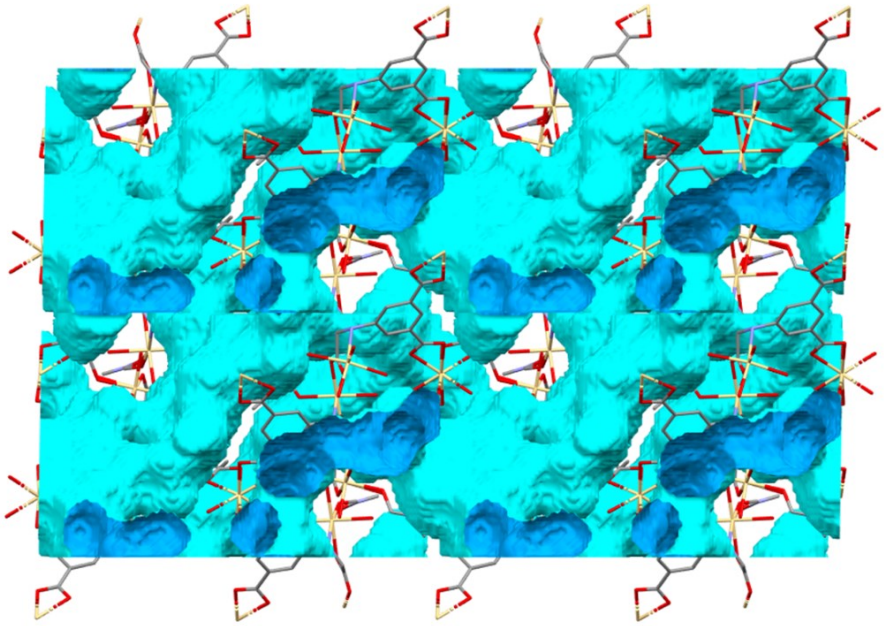

Figure 2.42. The void space in compound **5** viewed down the *b*-axis. (Void space exterior = Cyan, Void space interior = blue).

Compound **6** contains six molecules of guest water per asymmetric unit. The void space analysis showed a void volume of 287.77 $Å^3$, which is 19% of the unit cell. Unsurprisingly, the voids fill the channels in the structure, in the location of the guest water molecules. A model with the void space represented in blue is shown in **Figure 2.43**.

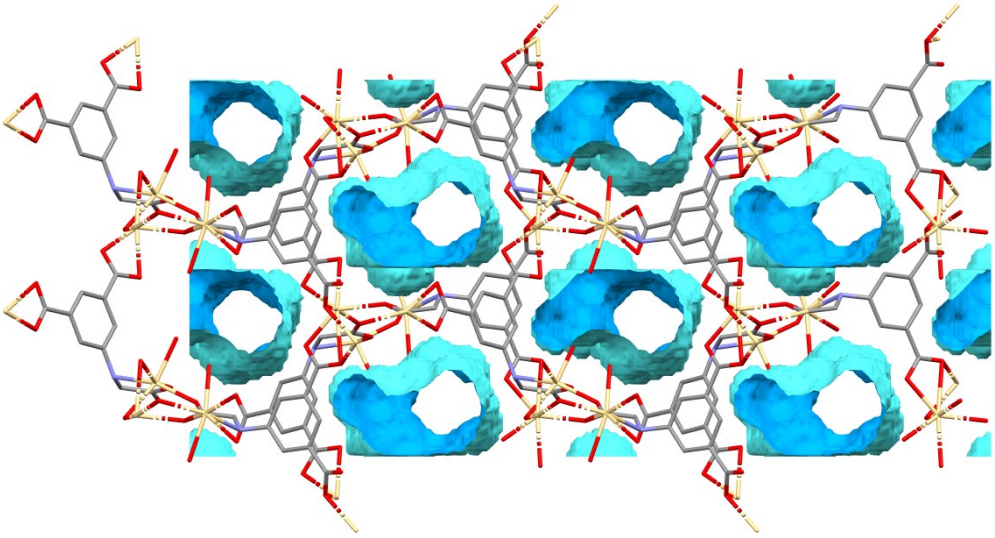

Figure 2.43. The void space in compound **6** viewed down the *c*-axis. (Void space exterior = Cyan, Void space interior = blue).

The wide array of binding modes available to the cmai based linker in combination with cadmium(II), which is itself coordinatively diverse, has given rise to six different compounds made from the same component building blocks. Whilst allowing for the generation of a large number of new structures, the variety of possible geometries adopted by the ligand makes predicting possible network structures difficult. This precludes the use of reticular chemistry in designing frameworks using this ligand and cadmium(II).

Table 2.2. Crystal data and structural refinement for compounds **1** – **6**.

Compound	**1**	**2**	**3**	**4**	**5**	**6**
Empirical formula	$C_{20}H_{20}Cd_2N_2O_{15}$	$C_{10}H_{11}CdNO_8$	$C_{20}H_{28}Cd_3N_2O_{20}$	$C_{20}H_{12}Cd_3N_2O_{12}$	$C_{51.25}H_{105.75}Cd_6N_{7.75}O_{55.5}$	$C_{20}H_{30}Cd_3N_2O_{21}$
Formula weight	753.18	385.60	953.64	809.52	2393.08	971.66
Temperature/K	150.0(3)	150.0(2)	150.00(10)	293(2)	220.00(10)	150.00(10)
Crystal system	monoclinic	triclinic	triclinic	triclinic	monoclinic	monoclinic
Space group	*I*2/a	*P*-1	*P*-1	*P*-1	$P2_1$	$P2_1$
a/Å	13.7701(4)	7.2467(6)	7.7777(2)	8.0862(15)	14.10810(10)	9.01260(10)
b/Å	11.5100(3)	8.5509(7)	8.9715(4)	8.1863(13)	14.3068(2)	18.66240(10)
c/Å	29.1745(7)	10.9978(6)	11.4851(4)	8.4893(11)	23.1617(3)	9.16440(10)
α/°	90	101.892(6)	67.353(4)	72.651(13)	90	90
β/°	90.088(2)	95.728(5)	75.848(3)	81.681(13)	90.9450(10)	103.4670(10)
γ/°	90	114.776(8)	70.505(3)	65.767(17)	90	90
Volume/Å^3	4624.0(2)	592.04(8)	690.98(5)	488.97(15)	4674.36(10)	1499.04(3)
Z	8	2	1	1	2	2
ρ_{calc}g/cm^3	2.164	2.163	2.292	2.749	1.700	2.153
μ/mm^{-1}	1.925	1.886	19.211	26.648	11.633	17.751
F(000)	2960.0	380.0	466.0	386.0	2399.0	952.0
Crystal size/mm^3	0.291 × 0.231 × 0.063	0.344 × 0.24 × 0.083	0.038 × 0.028 × 0.025	0.064 × 0.033 × 0.015	0.11 × 0.085 × 0.031	0.218 × 0.104 × 0.036
Radiation/ Å	MoKα (λ = 0.71073)	MoKα (λ = 0.71073)	CuKα (λ = 1.54184)	CuKα (λ = 1.54184)	CuKα (λ = 1.54184)	CuKα (λ = 1.54184)
2Θ range for data collection/°	7.034 to 60.686	6.696 to 60.678	8.418 to 146.698	12.006 to 136.352	6.266 to 146.148	9.478 to 146.104
Index ranges	-18 ≤ h ≤ 15, -16 ≤ k ≤ 13, -41 ≤ l ≤ 39	-10 ≤ h ≤ 9, -8 ≤ k ≤ 12, -15 ≤ l ≤ 15	-9 ≤ h ≤ 9, -11 ≤ k ≤ 11, -12 ≤ l ≤ 14	-8 ≤ h ≤ 9, -9 ≤ k ≤ 9, -10 ≤ l ≤ 10	-16 ≤ h ≤ 17, -17 ≤ k ≤ 15, -28 ≤ l ≤ 28	-11 ≤ h ≤ 7, -23 ≤ k ≤ 20, -11 ≤ l ≤ 11
Reflections collected	21531	5470	13561	2549	66896	10096
Independent reflections, R_{int}	6180, 0.0246	2988, 0.0323	2755, 0.0386	1632, 0.0286	17026, 0.0446	5352, 0.0376
Data/restraints/parameters	6180/19/390	2988/6/205	2755/12/241	1632/1/173	17026/219/1020	5352/3/449
Goodness-of-fit on F^2	1.074	1.069	1.026	1.045	1.013	1.072
Final R_1, wR_2 indexes [I>=2σ (I)]	0.0321, 0.0638	0.0335, 0.0636	0.0199, 0.0489	0.0488, 0.1187	0.0626, 0.1711	0.0418, 0.1045
Final R_1, wR_2 indexes [all data]	0.0373, 0.0659	0.0376, 0.0668	0.0216, 0.0496	0.0614, 0.1273	0.0648, 0.1735	0.0418, 0.1045
Largest diff. peak/hole / e Å^{-3}	1.66/-3.60	0.95/-0.71	0.51/-0.62	1.88/-1.31	3.79/-1.51	2.10/-1.13
Flack parameter					0.419(13)	0.426(12)

2.3 Results and Discussion: Reactions of H_3cmai with zinc(II), copper(II) and cobalt(II) salts

In order to provide more predictability and potentially allow a movement towards the use of reticular chemistry in the formation of frameworks synthesised using H_3cmai, first row d-block metal(II)-containing materials were targeted. These ions are smaller in size than cadmium(II) ions and as such should be less coordinatively diverse. The metal(II) centres, other than zinc(II), should also have more geometrical preference for bonding, again leading to more predictable coordination spheres and potentially predictable SBU formation.

2.3.1 Synthesis and characterisation of [Zn(Hcmai)(H_2O)$_2$] (**7**)

Compound **7** was synthesised from the reaction of $Zn(NO_3)_2 \cdot 6H_2O$ and H_3cmai in water at 90 °C and crystallised as colourless rods. The crystal structure was solved in the monoclinic space group $P2_1$ with an asymmetric unit containing one zinc(II) centre, one Hcmai linker and two water ligands, as shown in **Figure 2.44.**

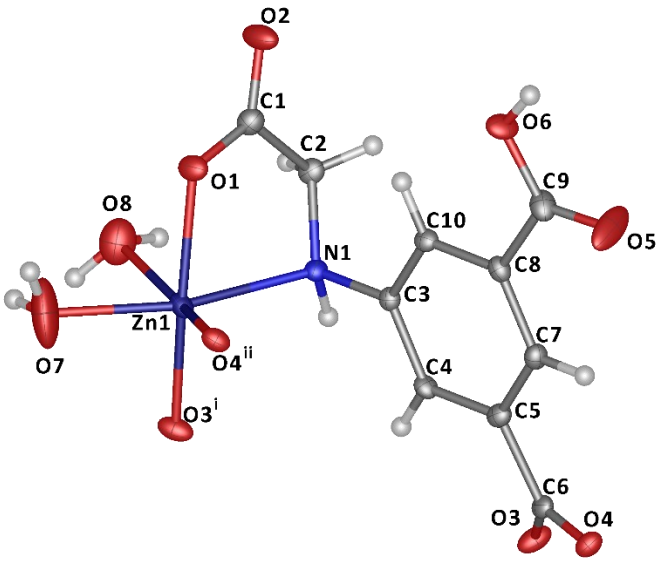

Figure 2.44. The asymmetric unit and coordination sphere in Zn1 of compound **7**. (i, 2 – *x*, – 1/2 + *y*, 2 – *z*; ii, 1 – *x*, – 1/2 + *y*, 2 – *z*). (ADPs shown at 50% probability).

Zn1 is 6-coordinate and has slightly distorted octahedral geometry. The main origin of the distortion is the bidentate binding mode of the flexible arm of the linker which coordinates through O1 and N1 with an O1 – Zn1 – N1 angle of 78.67(13) °. The metal is coordinated to three separate Hcmai linkers, the first through the κ^2 mode involving O1 and N1, the second through O3 and third through O4.

The carboxylate based on O3 and O4 bridges between adjacent Zn1 atoms and this leads to an infinite 1-D chain of carboxylate linked zinc centres which runs in the direction of the *a*-axis, shown in **Figure 2.45**.

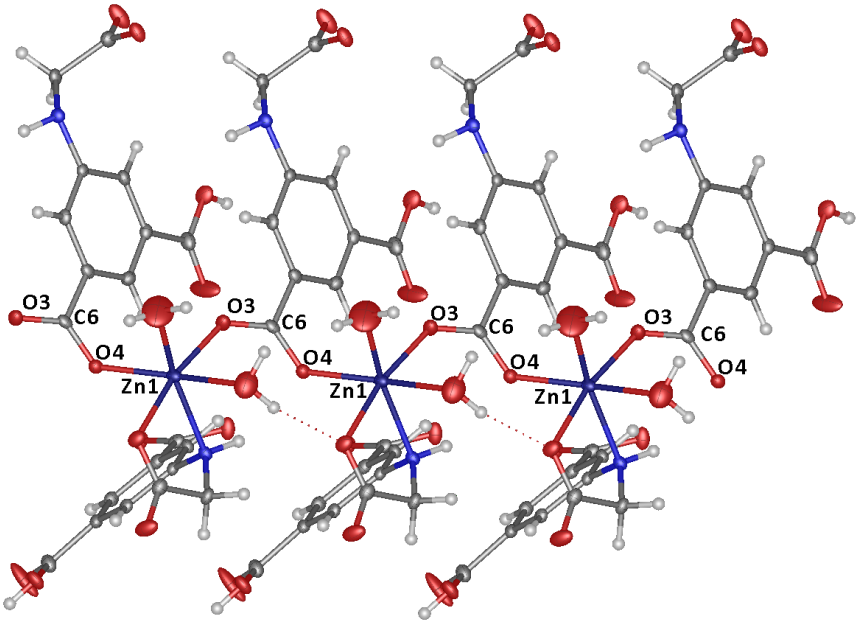

Figure 2.45. Carboxylate linked chain of Zn1 centres in compound **7**.

Each 1-D chain is connected to the two adjacent chains by virtue of the flexible arm of the Hcmai linker and the carboxylate based on O3 and O4, creating a 2-D sheet structure. The 120° angle between the carboxylate based on O3 and O4 and the flexible arm of the linker means that the sheet is corrugated as shown in **Figure 2.46**.

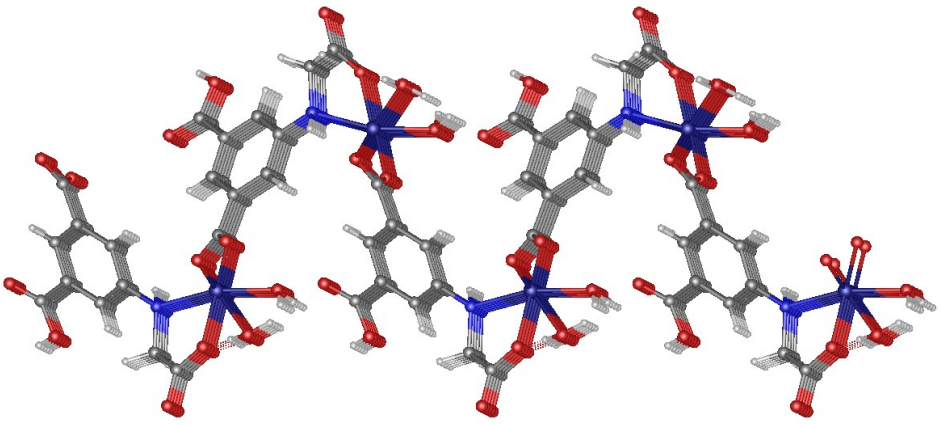

Figure 2.46. A 2-D sheet in the structure of compound **7** as viewed down the *a*-axis.

When viewed down the *c*-axis, the normal to the 2-D planes, there are no channels that pass through the sheet structure, as shown in **Figure 2.47 A**. The connectivity of the framework can

be represented by its reduced net, where the linker and metal nodes are represented at single points, this is shown in **Figure 2.47 B.** As the linker and zinc centres are both 3-connected nodes, for the purposes of network analysis, they can be considered the same. This leads to the assignment of a 3-connected uninodal network with a point symbol of 6^3, which is also known as a hcb net.

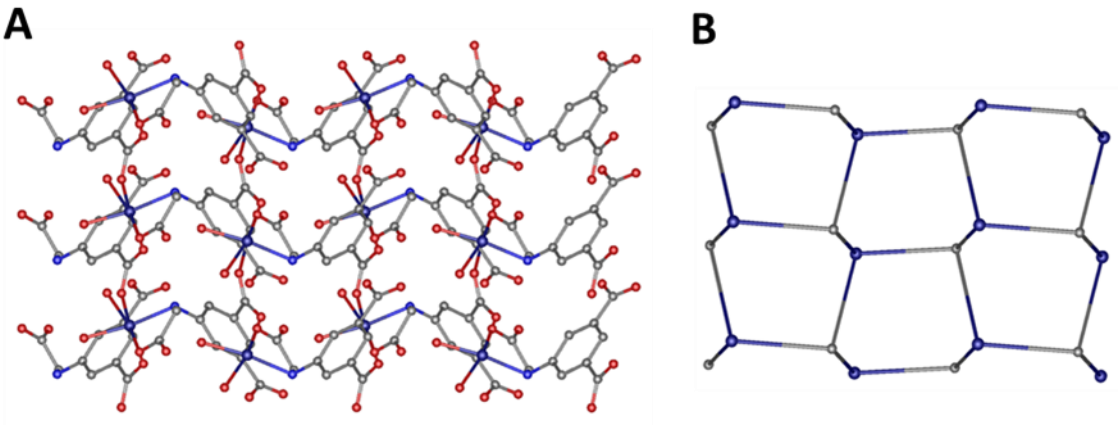

Figure 2.47. A - A 2-D plane in compound **7** viewed down the *c*-axis (hydrogen atoms removed for clarity), **B** – the reduced net of compound **7**.

The 2-D sheets stack and are supported by hydrogen bonds, which are shown in **Figure 2.48**, to produce a dense arrangement with no voids or potential for porosity.

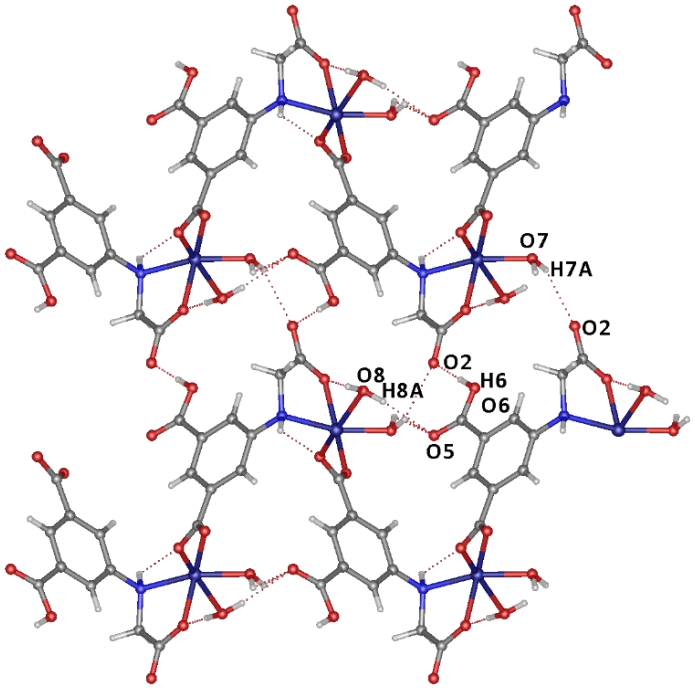

Figure 2.48. The inter-plane hydrogen bonds in compound **7**.

2.3.2 Synthesis and characterisation of [Cu(Hcmai)(H_2O)$_{1.2}$] (**8**)

The solvothermal reaction of $Cu(NO_3)_2 \cdot 2.5H_2O$ with H_3cmai in a mixture of water and ethanol at 120 °C led to the formation of green shard-like crystals. Upon the collection of the PXRD pattern it was noticed that the pattern closely matched that of compound **7** suggesting an isostructural material.

A suitable crystal was selected for single-crystal X-ray diffraction. Analysis of the crystal data revealed the crystal was twinned with the second component making up 21.3(3)% of the crystal and related to the main component by a rotation of -179.9814 about (1, 0, 0). Like compound **7**, compound **8** also crystallised in the monoclinic space group $P2_1$. The asymmetric unit contains one copper(II) centre, one Hcmai linker, one full water ligand and one 0.2 occupancy water ligand, as is shown in **Figure 2.49**.

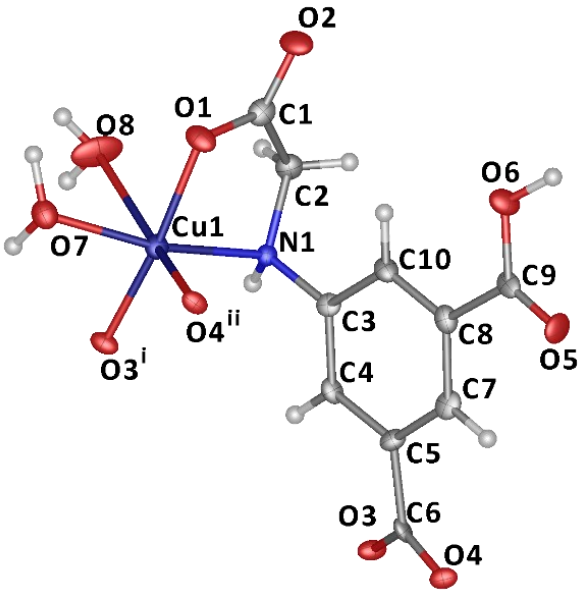

Figure 2.49. The asymmetric unit of compound **8** and coordination sphere of Cu1. (i, 2 – *x*, – 1/2 + *y*, 1 – *z*; ii, 1 – *x*, – 1/2 + *y*, 1 – *z*). (ADPs shown at 50%).

The gross structure is similar to that of compound **7**, containing stacked corrugated sheets formed from 1-D chains of carboxylate linked metal(II) centres, in this case copper(II). The most noteworthy structural difference is the presence of a partial occupancy water ligand, based on O8, rather than the full occupancy one in compound **7.** This means that the copper(II) centre is only 5-coordinate and square pyramidal in geometry ($\tau = 0.10$)[114] at 80% of atom sites and 6-coordinate octahedral at the other 20%. The reduction in water content also means that there is less hydrogen bonding within the framework.

2.3.3 Synthesis and characterisation of [Co(Hcmai)(H_2O)$_2$] (**9**)

Compound **9** was synthesised from the reaction between $Co(NO_3)_2 \cdot 6H_2O$ and H_3cmai, in water, at 90 °C and crystallised as pink-purple plate crystals. The PXRD pattern for compound **9** closely resembled that of compound **7** and **8**, suggesting it also shared the same topology. A comparison of the three diffraction patterns can be seen in **Figure 2.50**.

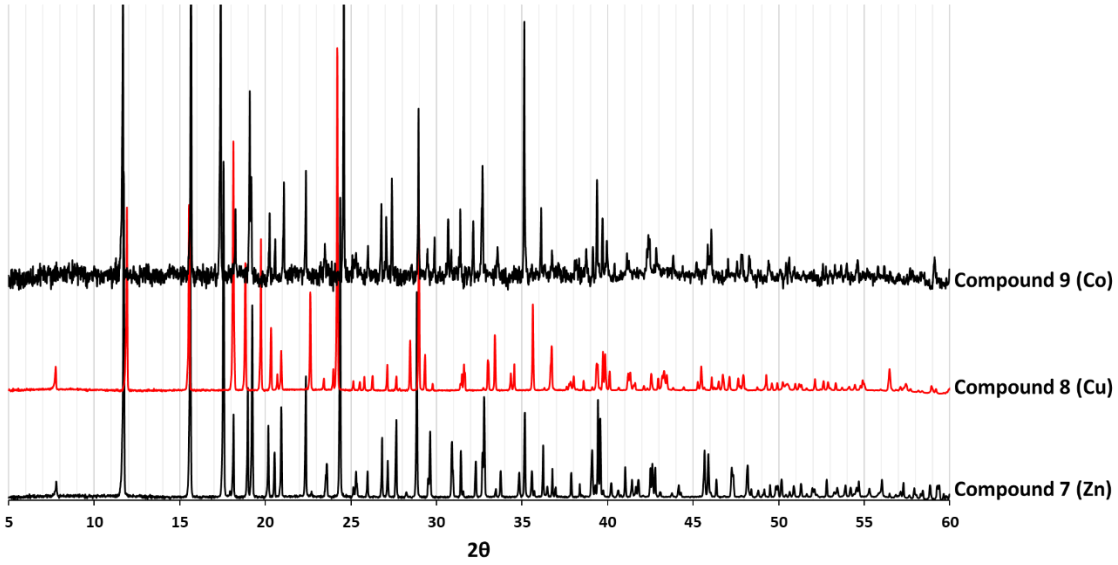

Figure 2.50. A comparison of the experimental PXRD patterns for compound **7**, **8** and **9**.

The structure has comparable unit cell parameters to those of compounds **7** and **8**, also solving in the space group $P2_1$. The asymmetric unit contains one cobalt(II) centre, one Hcmai ligand and two water ligands, this is shown along with the cobalt coordination sphere in **Figure 2.51**.

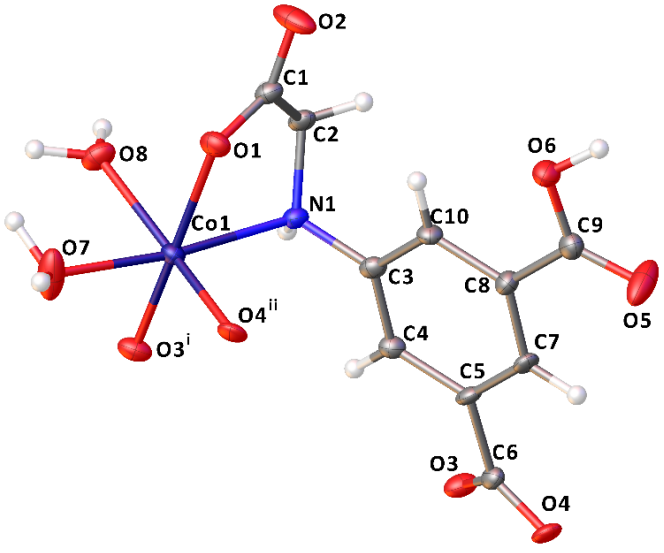

Figure 2.51. The asymmetric unit of compound **9** and coordination sphere of Co1. (i, 2 – *x*, – 1/2 + *y*, 1 – *z*; ii, 1 – *x*, – 1/2 + *y*, 1 – *z*).

Once again, the gross structure of compound **9** is similar to that observed in **7** and **8**. It is dominated by the same stacked corrugated sheets formed from 1-D chains of carboxylate linked metal(II) centres, in this case cobalt(II).

Although the structures have the same overall topology there are subtle differences between them. **Table 2.3** contains the unit cell parameters for the three compounds, those for compounds **7** and **9** are relatively similar while those for compound **8** show a smaller unit cell volume as well as notably shorter *b*-axis and larger β angle. This is likely a reflection on the lower coordination number on the copper centre along with lower atom count.

Table 2.3. The unit cell parameters for compound **7**, **8** and **9**.

Compound	*a* /Å	*b*/Å	*c*/Å	α/°	β/°	γ/°	V (Å^3)
7	4.89590(10)	10.0630(3)	11.3009(4)	90	95.584(3)	90	554.12(3)
8	4.9056(5)	9.7392(10)	11.4649(14)	90	97.117(10)	90	543.53(10)
9	4.8412(2)	10.1675(4)	11.3320(4)	90	95.158(4)	90	555.54(4)

The metal coordination sphere is the other main structural difference between the three compounds. The zinc(II) centre and cobalt(II) centre in compounds **7** and **9** respectively are both octahedral while the copper(II) centre in compound **8** is square pyramidal in 80% of sites and distorted octahedral in the other 20%. In both the octahedral and square pyramidal case the copper(II) centre has long axial bonds, consistent with a Jahn-Teller distortion. The Zn1–O4 and Co1–O4 distances are 2.063(3) Å and 2.077(4) Å respectively and the Cu1–O4 distance is longer at 2.263(6) Å. The Zn1–O8 and Co1–O8 distances are 2.287(4) Å and 2.160(5) Å whereas the Cu1–O8 distance (in the 20% of cases where the water is present) is 2.59(4) Å. This very long Cu1–O8 distance is postulated to be the reason for the partial occupancy of water as the interaction will be relatively weak. The lower average coordination number in compound **8** also influences the relative geometries of the ligands. For example, the bite angle of the bidentate flexible arm of the Hcmai linker (coordinating through N1 and O1) is larger in compound **8** (84.0°) compared with compound **7** and **9** (78.7° and 78.6°).

The IR spectra for the three isoreticular compounds are shown in **Figure 2.52**. Unsurprisingly, they are all very similar with the exception of the carbonyl stretch at 1697 cm^{-1}, which arises from the carboxylic acid containing C9 and O5. For the copper containing compound **8** the intensity of this band is stronger than for compound **7** or **9.** Structurally in compounds **7** and **9,** O5 acts as a hydrogen bond acceptor from the water ligand based on O8. However, in **8** this

water molecule only has an occupancy of 0.2 meaning that this hydrogen bond is not present in 80% of the framework.

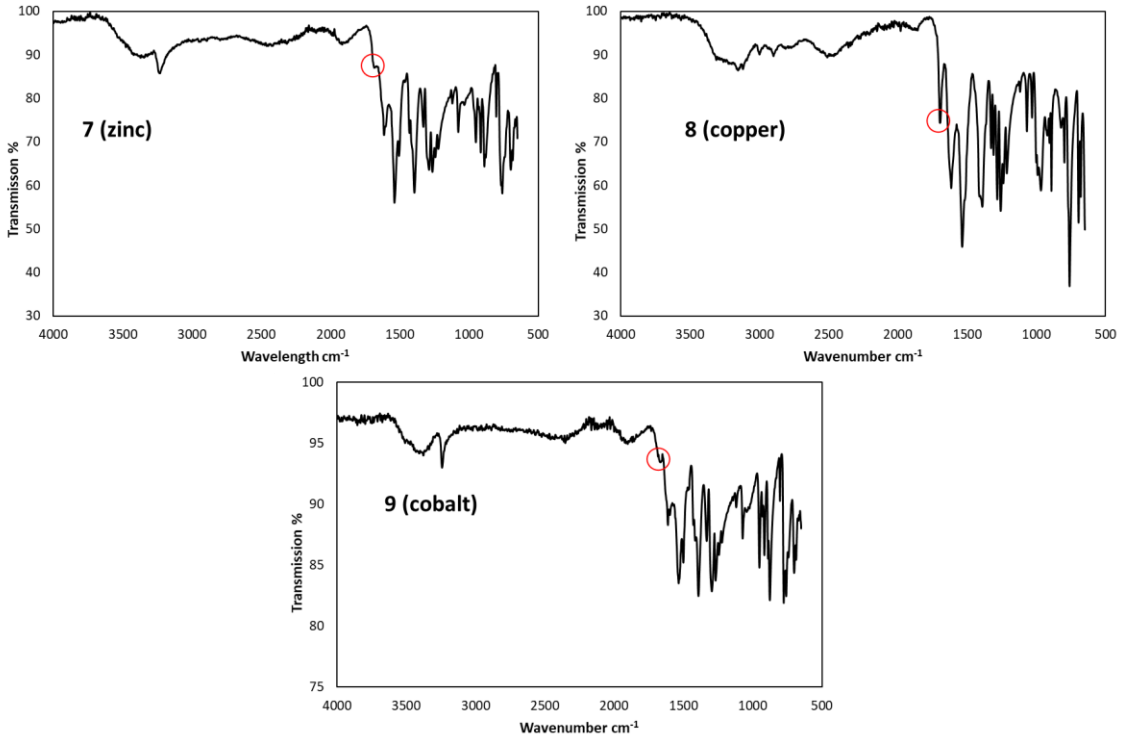

Figure 2.52. The IR spectra for compound **7**, **8** and **9**.

The isoreticular nature of compounds **7**, **8** and **9** presents a unique opportunity to probe the catalytic influence of changing the metal centre within the structure. A preliminary photocatalytic experiment involving the degradation of the dye Rhodamine B (RhB), shown in **Figure 2.53**, was carried out. The dye is used in industrial processes such as printing and dyeing but poses an environmental risk as it is a suspected carcinogen and neurotoxin, thus methods of breaking down the dye are of interest.[115]

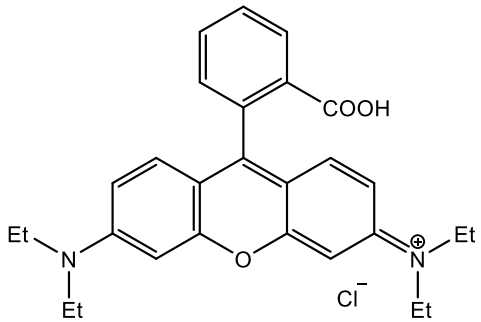

Figure 2.53. The structure of Rhodamine B.

UV-Vis spectroscopy was used to track the degradation of RhB in the presence of each of the three different compounds in an aqueous solution, the arising spectra are presented in **Figure 2.54**. In each experiment a mixture of aqueous RhB and MOF was stirred for an hour in the dark and no degradation of RhB occurred, evidenced spectroscopically. The reaction mixture was then illuminated for 30 minutes before addition of an artificial electron acceptor, H_2O_2. The experiment was continued under illumination. In the cases of compound **7** and **9** no photocatalytic activity is seen, even in the presence of H_2O_2. In contrast the spectra for compound **8** show a large drop in the intensity of the RhB peak after 30 minutes, indicating that compound **8** is photocatalytically active.

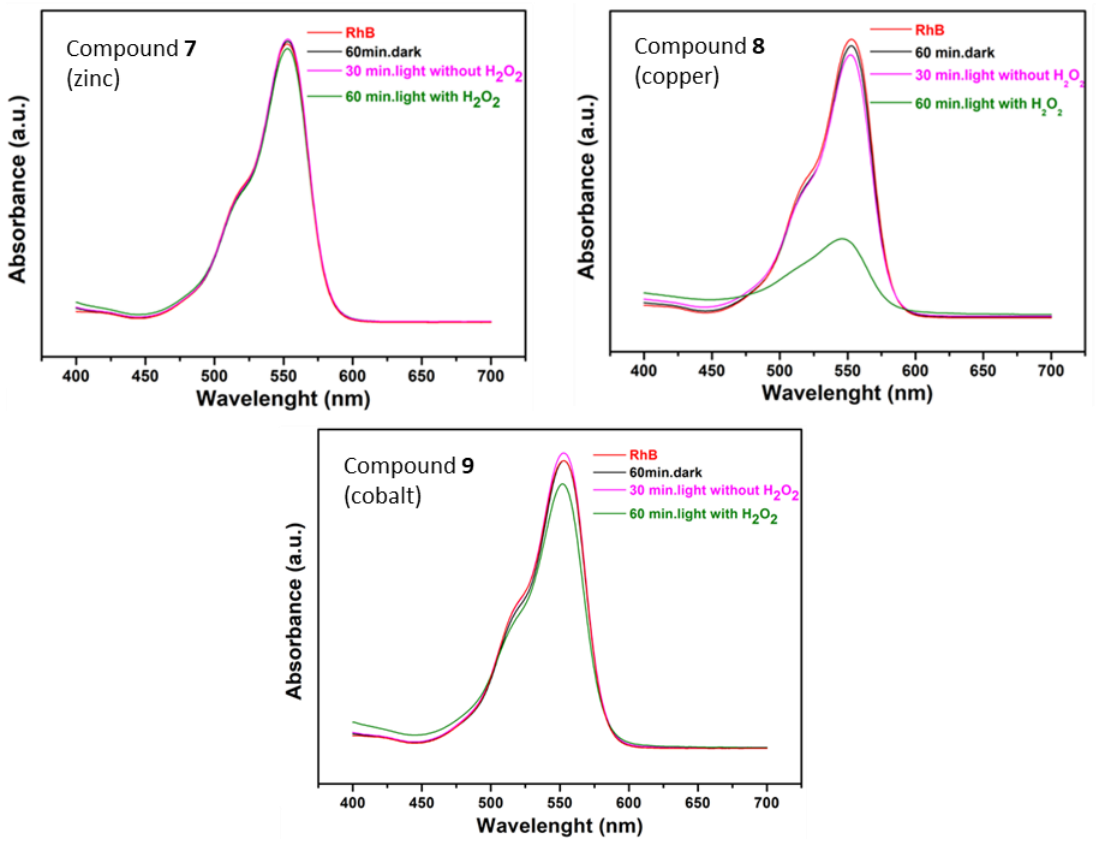

Figure 2.54. UV-Vis spectra for RhB degradation using compounds **7**, **8** and **9**.

It is notable that in the cases of compound **7** and **9**, no solid was present in the reaction mixture at the end of the experiment, suggesting that these frameworks were not stable in the presence of the H_2O_2 and this may have been the reason for their apparent lack of catalytic activity. The experiment has shown the potential for compound **8** to be used as a heterogeneous photocatalyst. Given that compound **8** is non-porous, this reaction is believed to take place on the surface of the crystallites.

2.3.4 Synthesis and characterisation of $[Zn_2(cmai)(OH)(H_2O)_2]\cdot 3H_2O$ (**10**)

The reaction of $Zn(OAc)_2\cdot 2H_2O$ and H_3cmai in a mixture of water and DEF at 120 °C yielded light tan crystals of compound **10**, which crystallised in the monoclinic space group $P2_1/n$. The asymmetric unit, shown in **Figure 2.55**, contains two zinc(II) centres, one cmai linker, one hydroxide ion, two water ligands, one full guest water molecules and two further guest water molecules that are disordered over 5 positions.

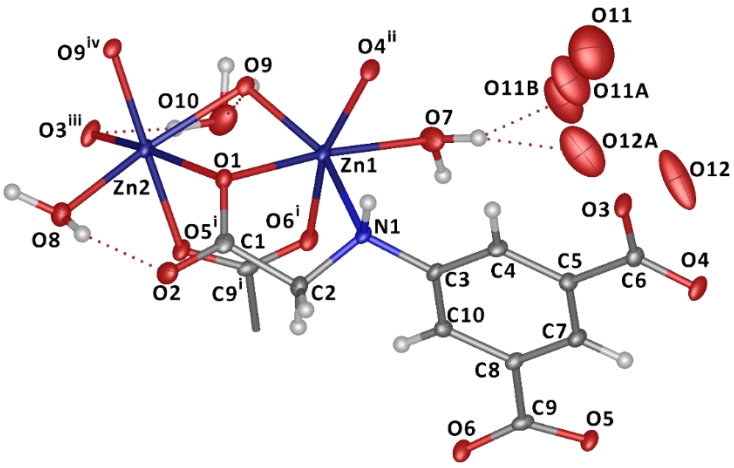

Figure 2.55. The asymmetric unit of compound **10** and the coordination spheres of Zn1 and Zn2. (i, 1 – *x*, 1 – *y*, – *z*; ii, 1/2 + *x*, 3/2 – *y*, 1/2 + *z*; iii, 3/2 – *x*, – 1/2 + *y*, 1/2 – *z*; iv, 2 – *x*, 1 – *y*, 1 – *z*).

Both Zn1 and Zn2 are 6-coordinate. Zn1 is coordinated to three cmai linkers, a water ligand (O7) and a hydroxide ion (O9). The first of the cmai linkers binds through a κ^2 bidentate mode via N1 and O1, the second binds through a κ^1 interaction through O4 and the third coordinates via a κ^1 interaction through O6.

Zn2 is also octahedral in geometry and is bound by three cmai linkers, two hydroxide ions and one water ligand. The first of the linkers is bound in a μ_2 bridging mode interaction with O1 which is also coordinated to Zn1. The second and third linkers are coordinated through κ^1 interactions through O3 and O5 respectively. The hydroxide ions coordinate via a μ_3 mode, capping a triangular arrangement of two Zn2 centres and one Zn1 centre. This arrangement forms the core of an SBU involving 4 zinc(II) centres and interactions from a total 6 cmai linkers which can be seen in **Figure 2.56**.

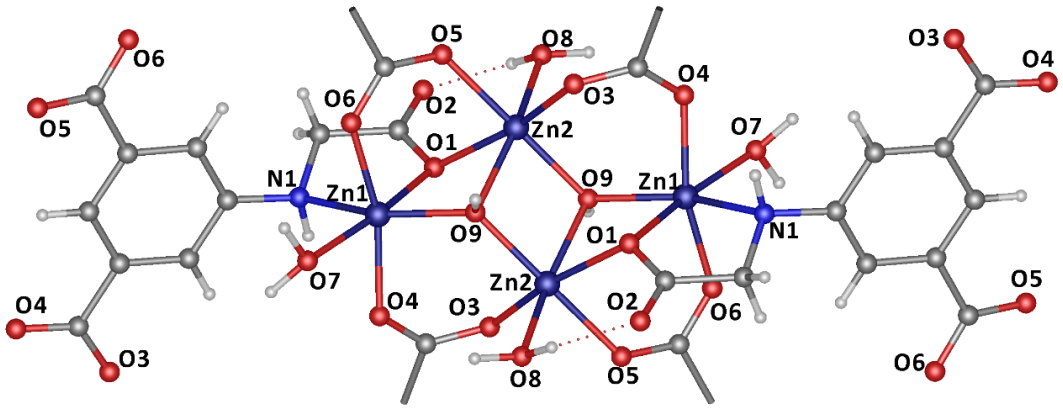

Figure 2.56. The SBU of compound **10**.

This SBU is supported by the interactions of 6 different cmai linkers, each of which are coordinated to three different SBUs. This combination of connections forms a 2-D sheet in the (1, 0, −1) plane, which can be seen in **Figure 2.57 A.** The 2-D plane can be simplified by considering the SBU as a 6-connected node and the cmai linker as a 3-connected node, the visual representation of this reduced net is shown in **Figure 2.57 B**. The net is binodal with the point symbol ($4^6.4^3$), which is also known as a kgd net.

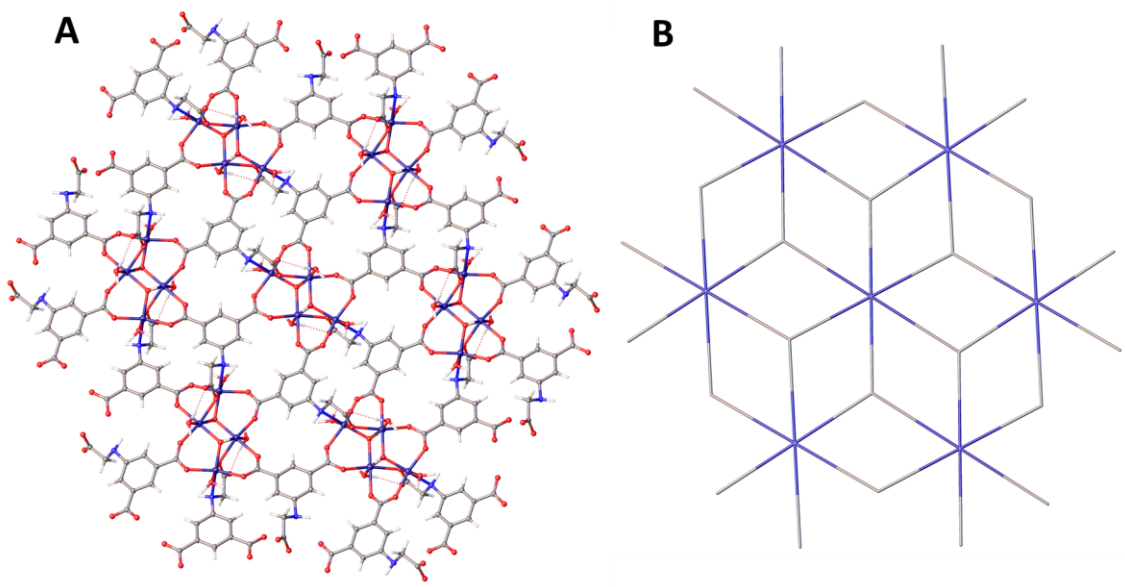

Figure 2.57. A – The 2-D plane structure of compound **10**, **B** – the reduced net of compound **10.**

The 2-D sheets stack in the gross structure in an aligned manner. The SBUs protrude out of the plane of the individual sheets, creating channels in the structure between the layers. These channels can be seen in **Figure 2.58**, in which, alternating layers of the structure have been coloured green and orange to highlight the distinct sheets.

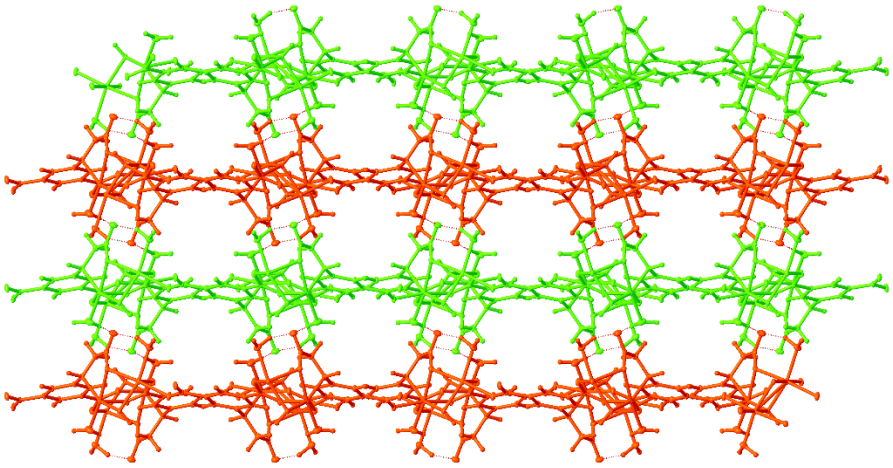

Figure 2.58. The layered structure of 2-D planes in compound **10**, as viewed from the (1, 0, 1) plane, alternating planes have been coloured green and orange.

The channels are filled with guest water. The water molecule based on O10 acts as a hydrogen bond donor to both O3 and O7, and an acceptor to H8A and H9. Participating in 4 hydrogen bonds is likely the reason that the water atom based on O10 is well resolved. The other two guest water molecules are disordered over 5 positions within the channel.

The potential void space has been plotted in **Figure 2.59** and as expected resides in the channels between the 2-D sheets. The void space has a volume of 252.49 $Å^3$, 16% of the total unit cell volume.

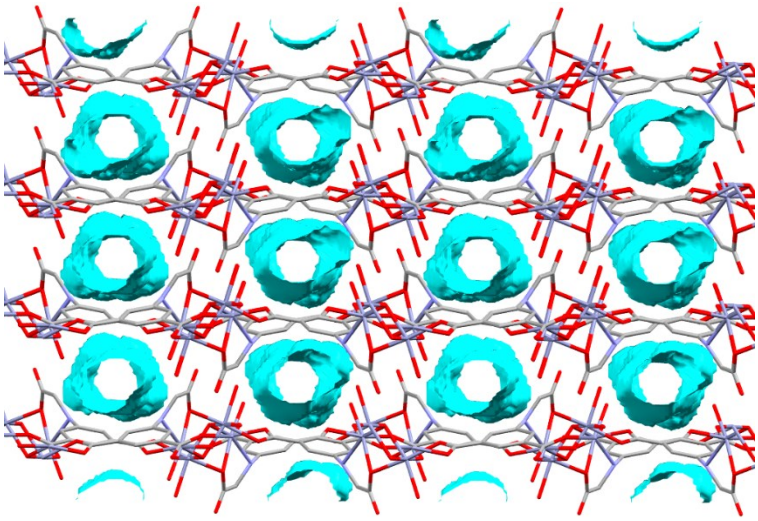

Figure 2.59. The void space in compound **10**.

The identity of the bulk material was confirmed as compound **10** using PXRD. Thermal analysis of the material was carried out to further probe the guest-framework relationship. The results of the TGA are presented in **Figure 2.60**. The mass loss between 30 °C and 200 °C is 17.6%, this

equates to 4.6 water molecules per asymmetric unit, which is in good agreement with the 5 modelled in the crystal structure. The TGA trace also shows that this mass loss contains two overlapping events, namely, loss of the guest water and loss of the coordinated water. The fact that the events overlap is the reason that this material could not be activated while maintaining the crystal structure. All attempts to remove the guest water also resulted in the removal of coordinated water leading to collapse of the framework and complete loss of crystallinity, evidenced by PXRD.

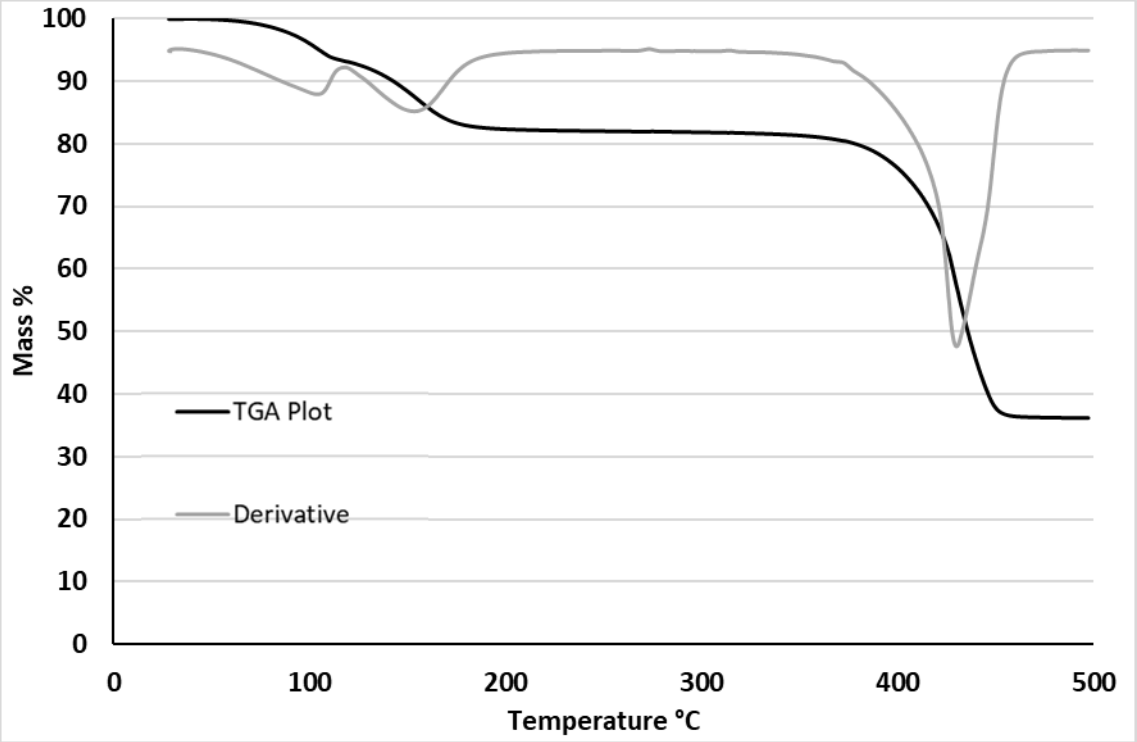

Figure 2.60. The results of the TGA of compound **10.**

2.3.5 Discussion

Four new MOFs have been synthesised using H_3cmai-derived linkers in combination with 3d metal(II) salts. Materials based on first row d-block metals were targeted in an effort to give a greater degree of control over the SBU and arising network topology formed, than that observed for the MOFs based on cadmium(II) centres. The synthesis of a series of isoreticular MOFs, namely compounds **7**, **8** and **9**, has shown that this control was indeed achieved. These compounds contain the same 1-D chain SBU and comprise of uninodal 6^3 nets, with different metal centres, zinc(II), copper(II) and cobalt(II) respectively. A second zinc-based MOF, compound **10**, was also synthesised, the crystal and structural refinement data for these compounds are shown in **Table 2.4** at the end of this discussion.

The structure of the copper-based compound **8** was subtly different to that of the zinc and cobalt containing materials, compounds **7** and **9.** Compound **8** contained a partial occupancy water ligand which was full occupancy in the other materials. The partial occupancy was attributed to a Jahn-Teller distortion, lengthening the copper-water bond to the point that the water ligand was no longer present 80% of the time.

The three isostructural compounds were investigated for their photocatalytic activity in the degradation of Rhodamine B. It was shown that only the copper-based compound **8** could catalyse the breakdown of the dye. This is a promising result for MOFs synthesised using H_3cmai and further investigation of these compounds in the area of catalysis would be an interesting line of future study.

The second zinc MOF, compound **10**, was synthesised with the introduction of a DEF/H_2O solvent system and using an acetate salt rather than a nitrate. This framework contains a different SBU to that of compound **7** but does contain 6-coordinate zinc(II) centres in an octahedral geometry. It appears that the reduced size of zinc(II) over cadmium(II) has led to a preference in formation of 6-coordinate centres rather than the range of 6-8 coordinate centres observed in the cadmium-based materials. With less coordinative diversity, the resultant coordination spheres and SBUs can be better predicted.

The coordination modes adopted by the H_3cmai-derived linkers in compounds **7**-**10** were less diverse than was observed in the cadmium compound **1**-**6,** with only four different modes observed in compounds **7**-**10** verses 13 observed in the cadmium compounds. This is due to the fact that there were only two different topologies of framework observed in compounds **7**-**10**, whereas six different structures were observed in compound **1**-**6**. The four different binding modes are presented in **Figure 2.61**. Binding mode **A** was also present in compounds **2**, **5** and **6,**

while binding mode **B** was also present in compounds **3** and **6**. Binding modes **C** and **D** were not observed in the cadmium MOFs, however, both contain the common bidentate κ^2 mode involving the secondary amine and carboxylate oxygen of the flexible linker arm. The bite angle of this bidentate binding mode is larger in the 3d metal(II)-based MOFs than in the cadmium(II)-based MOFs, with average angles across the two groups of MOFs of 79.1° and 71.5° respectively. This larger bite angle is due to the smaller radii of the 3d metal centres.

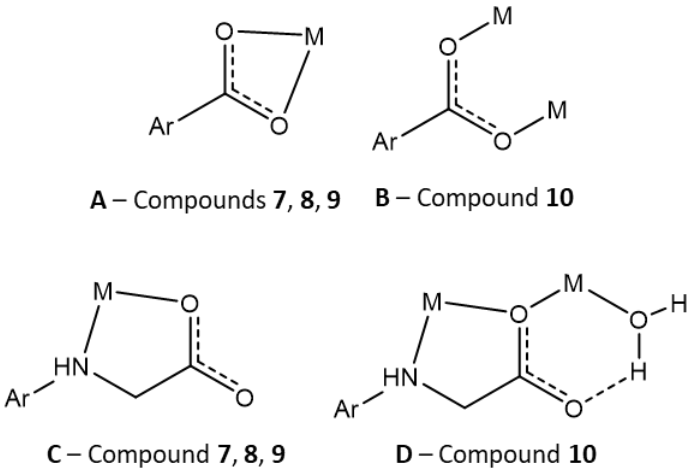

Figure 2.61. The coordination modes present in compounds **7**-**10**.

Both of the observed topologies of the first row d-block compounds were composed of 2-D sheet structures. Compound **7**, **8** and **9** contained the doubly-deprotonated linker, Hcmai. The cadmium compounds **1** and **2**, which comprised of 2-D sheets and 1-D chains respectively, also contained Hcmai as the linker. This suggests that if the (H)cmai linker is doubly deprotonated a 3-D framework is unlikely to form. Compound **10** contains the fully deprotonated linker, cmai, but formed sheets, this is in contrast to the cadmium structures in which a fully deprotonated linker led to a 3-D framework.

Compounds **7**, **8** and **9** formed dense structures containing no guest solvent, while **10** contains 3 molecules of disordered guest water per unit formula of the MOF. This equates to a potential void space of 16% of the unit cell. The potential voids take the form of channels running in-between the 2-D sheets that make up the structure of the MOF. The internal void space is limited in compounds **6**-**10**, in part, by their 2-D structure.

Table 2.4. Crystal data and structural refinement for compounds **7** – **10**.

Compound	**7**	**8**	**9**	**10**
Empirical formula	$C_{10}H_{11}NO_8Zn$	$C_{10}H_{9.4}CuNO_{7.2}$	$C_{10}H_{11}CoNO_8$	$C_{10}H_{17}NO_{12}Zn_2$
Formula weight	338.57	322.32	332.13	473.98
Temperature/K	149.9(3)	150.1(4)	150.00(10)	150.00(10)
Crystal system	monoclinic	monoclinic	monoclinic	monoclinic
Space group	$P2_1$	$P2_1$	$P2_1$	$P2_1/n$
a/Å	4.8959(1)	4.9056(5)	4.8412(2)	7.4213(3)
b/Å	10.0630(3)	9.7392(10)	10.1675(4)	19.3205(6)
c/Å	11.3009(4)	11.4649(14)	11.3320(4)	10.8081(4)
α/°	90	90	90	90
β/°	95.584(3)	97.117(10)	95.158(4)	96.871(3)
γ/°	90	90	90	90
Volume/Å^3	554.12(3)	543.53(10)	555.54(4)	1538.57(10)
Z	2	2	2	4
ρ_{calc}g/cm^3	2.029	1.969	1.986	2.046
μ/mm^{-1}	3.538	2.044	12.568	3.186
F(000)	344.0	326.0	338.0	960.0
Crystal size/mm^3	0.141 × 0.041 × 0.023	0.316 × 0.089 × 0.019	0.183 × 0.046 × 0.033	0.277 × 0.239 × 0.105
Radiation	CuKα (λ = 1.54184)	MoKα (λ = 0.71073)	CuKα (λ = 1.54184)	MoKα (λ = 0.71073)
2Θ range for data collection/°	7.86 to 146.822	7.164 to 55.04	7.834 to 146.51	6.664 to 54.958
Index ranges	-6 ≤ h ≤ 6, -10 ≤ k ≤ 12, -14 ≤ l ≤ 13	-3 ≤ h ≤ 6, -12 ≤ k ≤ 12, -14 ≤ l ≤ 14	-5 ≤ h ≤ 6, -12 ≤ k ≤ 12, -13 ≤ l ≤ 14	-9 ≤ h ≤ 9, -24 ≤ k ≤ 25, -14 ≤ l ≤ 14
Reflections collected	4616	2564	2451	12808
Independent reflections, R_{int}	1628, 0.0321	2564, 0.0541	1637, 0.0292	3507, 0.0393
Data/restraints/parameters	1628/2/189	2564/5/198	1637/10/204	3507/40/278
Goodness-of-fit on F^2	1.068	0.953	1.044	1.081
Final R_1, wR_2 indexes [I>=2σ (I)]	0.0308, 0.0803	0.0481, 0.0958	0.0461, 0.1224	0.0323, 0.0774
Final R_1, wR_2 indexes [all data]	0.0314, 0.0810	0.0611, 0.0989	0.0472, 0.1241	0.0391, 0.0808
Largest diff. peak/hole / e Å^{-3}	0.66/-0.49	0.56/-1.00	0.69/-0.61	1.60/-0.49
Flack parameter	-0.09(3)	-0.01(3)	-0.001(6)	

2.4 Conclusions

A new polycarboxylic acid linker precursor, H_3cmai, has been designed and synthesised. The semi-rigid molecule contains a 1,3-benzenedicarboxylic acid backbone and a flexible arm in the 5 position, made up of a secondary amine and a terminal carboxylic acid. The combination of this species with metal(II) salts under a variety of conditions has led to the formation of 10 new metal-organic frameworks all of which have been structurally characterised.

Six cadmium MOFs were synthesised, **1** $[Cd_2(Hcmai)_2(H_2O)_2]\cdot H_2O$, **2** $[Cd(Hcmai)(H_2O)_2]$, **3** $[Cd_3(cmai)_2(H_2O)_4]\cdot 4H_2O$, **4** $[Cd_3(cmai)_2]$, **5** $[Cd_6(cmai)_4(H_2O)_{9.75}(DMF)_{2.25}]\cdot 20H_2O\cdot 2.6DMF$ and **6** $[Cd_3(cmai)_2(H_2O)_3]\cdot 6H_2O$. The structural diversity among these compounds was extensive considering they are formed using the same building block units. They varied in dimensionality, linker deprotonation ($Hcmai^{2-}$ vs. $cmai^{3-}$), topology, guest solvent present and potential void space. Within the structures a wide array of cadmium coordination environments was observed, ranging from 6-coordinate to 8-coordinate. A total of 13 different binding modes were observed for the cmai-based linker. The combination of the flexibility and adaptability of both the metal centre and organic linker is what allows so many different structures to form.

An interesting crystal to crystal transformation was observed upon heating of compound **3**, forming compound **4**. The flexibility of the cmai ligand and cadmium centres allowed for a structural rearrangement upon the loss of ligated and guest water molecules from compound **3**. The transformation was shown to be reversible upon submerging the material in water, which is significant due to the number of bonds being broken and formed in the rearrangement from one structure to the other. The fact that such a rearrangement can take place, highlights a property associated with materials synthesised using semi-rigid linkers. The inherent flexibility allows for response to external stimuli (in this case, concomitant heating and water loss) resulting in a change in structure, this could be exploited in applications such as sensing.

Four MOFs were also synthesised using metal(II) centres from the first row of the d-block, **7** $[Zn(Hcmai)(H_2O)_2]$, **8** $[Cu(Hcmai)(H_2O)_{1.2}]$, **9** $[Co(Hcmai)(H_2O)_2]$ and **10** $[Zn_2(cmai)(OH)(H_2O)_2]\cdot 3H_2O$. The associated structures exhibited less structural diversity than the cadmium-based MOFs, with three of them, compounds **7**, **8** and **9** being isostructural. This was attributed to the reduced size of the metals, leading to the formation of exclusively 6-coordinate centres. An initial study into the photocatalytic behaviour of the isostructural compounds **7**, **8** and **9** was carried out. The degradation of the environmentally persistent and toxic dye Rhodamine B was interrogated. The copper-containing compound **8**, showed a good level of activity and was the

only compound that did not dissolve in the reaction mixture, suggesting that more robust cmai-based MOFs may have potential for use in heterogeneous catalysis.

Accessing permanent porosity was found to be a challenge for this series of structures. The reason for this is 2-fold. The structures formed from the doubly deprotonated linker (Hcmai), compounds **1**, **2**, **7**, **8**, **9** and **10**, formed one- or two-dimensional networks. These were densely packed and contained little or no guest solvent. The lower dimensionality arises from the diminished number of ligating groups from which the coordination network can extend, the impact of which is that structures were able to pack more efficiently to minimize cavities in the material.

Also notable is that all the structures, except compound **4**, contain water ligands along with the guest solvent. The water ligands, often involved in the formation of a hydrogen bonding network with guest molecules, were lost from the structures at similar temperatures to the guest solvent, making it hard to remove the guests while retaining the ligated water. In compound **5**, **6** and **10**, the removal of the ligated water caused the framework to collapse, in compound **3**, it resulted in a structural rearrangement to a denser form, neither leading to permanent porosity in the MOF. The presence of the water in the structures was attributed primarily to the fact that water was used as part of the solvent system in all cases. This was due to the poor solubility of the linker in other polar solvents.

MOF synthesis using H_3cmai in combination with metal(II) salts has resulted in the formation of 10 new compounds, displaying a range of structural features and properties. The facile combination of this linker precursor with metal centres to form networks highlights the potential for this linker to be used in the synthesis of further interesting and diverse structures.

2.5 Experimental

2.5.1 Generic Procedures – Utilised across all chapters

2.5.1.1 Single-crystal X-ray Diffraction

Single-crystal X-ray diffraction data were collected on either a Rigaku Oxford Diffraction Supernova diffractometer (Kα, λ = 1.54184 Å) or a Rigaku Oxford Xcalibur diffractometer (Kα, λ = 0.71073 Å). Both diffractometers use a graphite monochromator, a four-circle kappa goniometer and an EosS2 detector. Data processing and reduction was carried using CrysAlisPro software. Crystal structures were solved using SHELXT[116] and refined using full-matrix least-squares methods using SHELXL-2015.[117] These programs were executed and structures visualised in Olex2.[118]

2.5.1.2 Powder X-ray Diffraction

Powder X-ray diffraction (PXRD) patterns were recorded on either a Bruker AXS D8 Advance diffractometer using copper Kα radiation (λ = 1.5406 Å) at 298 K or on a STOE Powder Diffraction System using copper Kα radiation (λ = 1.540589 Å) at 298 K. On the D8 the beam slit was set to 1 mm, detector slit to 0.2 mm and anti-scattering slit set to 1 mm. Samples were dried on a filter paper and then lightly ground between two slides, before being mounted on a glass slide for the measurement. Data was collected on a flat-plate in reflection mode between 5-60° with a step size of 0.024° and a scan speed of 0.3 s/step. On the STOE instrument patterns were collected in transmission mode using a multi-MYTHEN detector with a step size of 0.015° and 600 s/step (detector). Samples were dried on a filter paper prior to the measurement and then ground using a pestle and mortar. The powder was immobilised between two acetate sheets in the sample holder with the aid of resin/IPA based glue if necessary.

2.5.1.3 Nuclear Magnetic Resonance Spectroscopy

Nuclear Magnetic Spectroscopy was carried out at 298 K on either a Bruker Advance 300 MHz Ultrashield NMR spectrometer or an Agilent 500 MHz NMR spectrometer. All peaks were referenced to residual proton peaks from the solvent.

2.5.1.4 Infrared Spectroscopy

ATR-FTIR spectroscopy was carried out on solid samples using a Perkin Elmer Spectrum 100 spectrometer mounted on a diamond/gem platform.

2.5.1.5 Elemental Microanalysis (CHN)

Elemental analysis samples were sent to and experiments conducted by London Metropolitan University or Exeter Analytical UK Ltd.

2.5.1.6 Adsorption/Desorption Isotherm Measurements

Gas sorption measurements were carried out on a BELSORP Mini-II (BEL Japan) gas sorption analyser. In a typical experiment 50 mg of activated sample was placed in a pre-weighed tube. The sample was heated at 150 °C under reduced pressure for 1000 mins prior to the experiment, at this point the sample was re-weighed to obtain an accurate sample mass. The adsorption and desorption isotherms were collected at 77 K with the aid of a liquid nitrogen bath.

2.5.1.7 MOF Synthesis

MOF syntheses were carried out in microwave reaction tubes (10 mL or 30 mL) and sealed with a Teflon-lined cap. Where higher pressures were generated, Parr acid digestion bombs were utilised. In general, the synthesised materials were stored under solvent to maintain pore solvent content and crystallinity. All reported materials were synthesised in good yields (40%-90%), exact values are not given due to the ambiguity of pore solvent mass and the need to keep the material under solvent.

2.5.1.8 Thermogravimetric Analysis

TGA analysis was conducted using a Setsys Evolution TGA 16/18. Once the instrument had been calibrated, a small powdered sample (5 - 20 mg) was placed into a 170 µL aluminium crucible which was placed onto the internal instrument balance. The sample was then subject to a pre-programmed heating profile at 10 °C/min under a flow of air and the mass loss of the sample was recorded with respect to the temperature. The data collection and processing were carried out using Calisto.

2.5.2 Synthesis of 5-((carboxymethyl)amino)isophthalic acid (H_3cmai)

5-Aminoisophthalic acid (25 mmol, 4.53 g) was dissolved in MeOH (150 mL). To this solution was added glyoxalic acid monohydrate (30 mmol, 2.76 g). The reaction mixture was stirred at room temperature for 5 hours after which $NaCNBH_3$ (32 mmol, 2.01 g) was added in one portion. The reaction mixture was left stirring at room temperature overnight in which time an off-white product had precipitated. This was collected by vacuum filtration and dried in an oven for 6 hours. (Yield 4.27 g, 71.4%). The identity of the product was confirmed via ^{1}H-NMR, **Figure 2.62**, (500 MHz, DMSO-d_6); δ (ppm) 7.68 (1H, s), 7.23 (2H, s), 3.56 (2H, s) and $^{13}C\{^{1}H\}$-NMR, **Figure 2.63**, (125.7 MHz, DMSO-d_6); δ (ppm) 173.1, 168.8, 148.7, 134.3, 118.4, 116.3, 46.7.

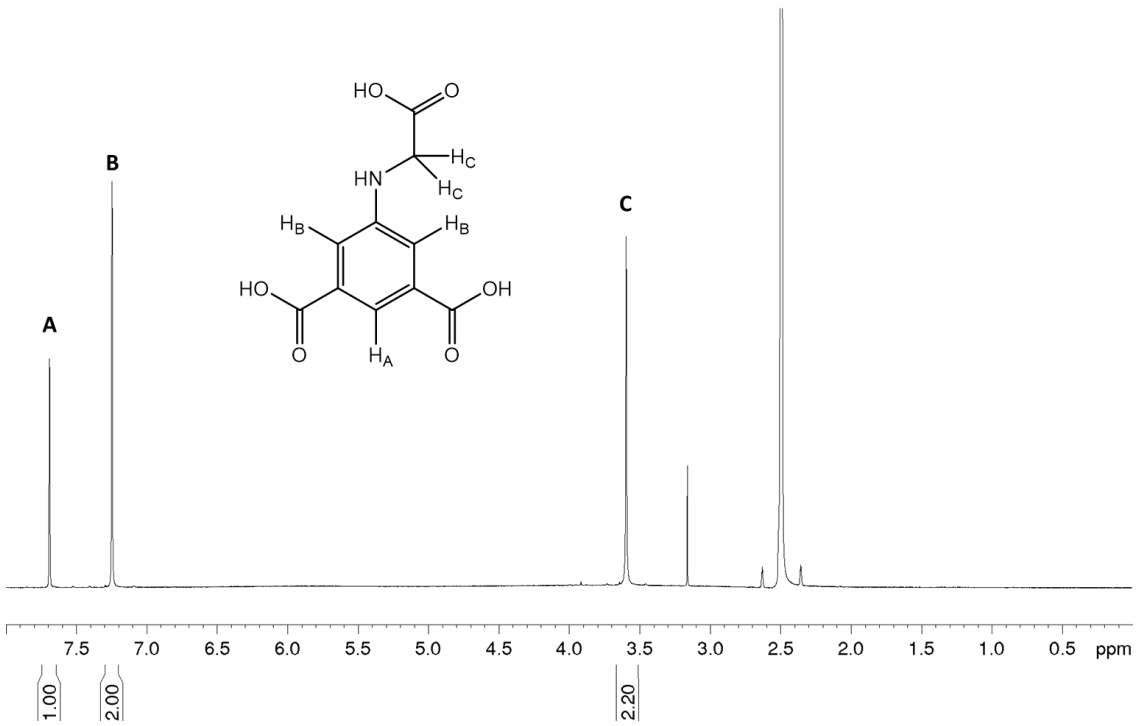

Figure 2.62. ^{1}H-NMR spectrum of H_3cmai.

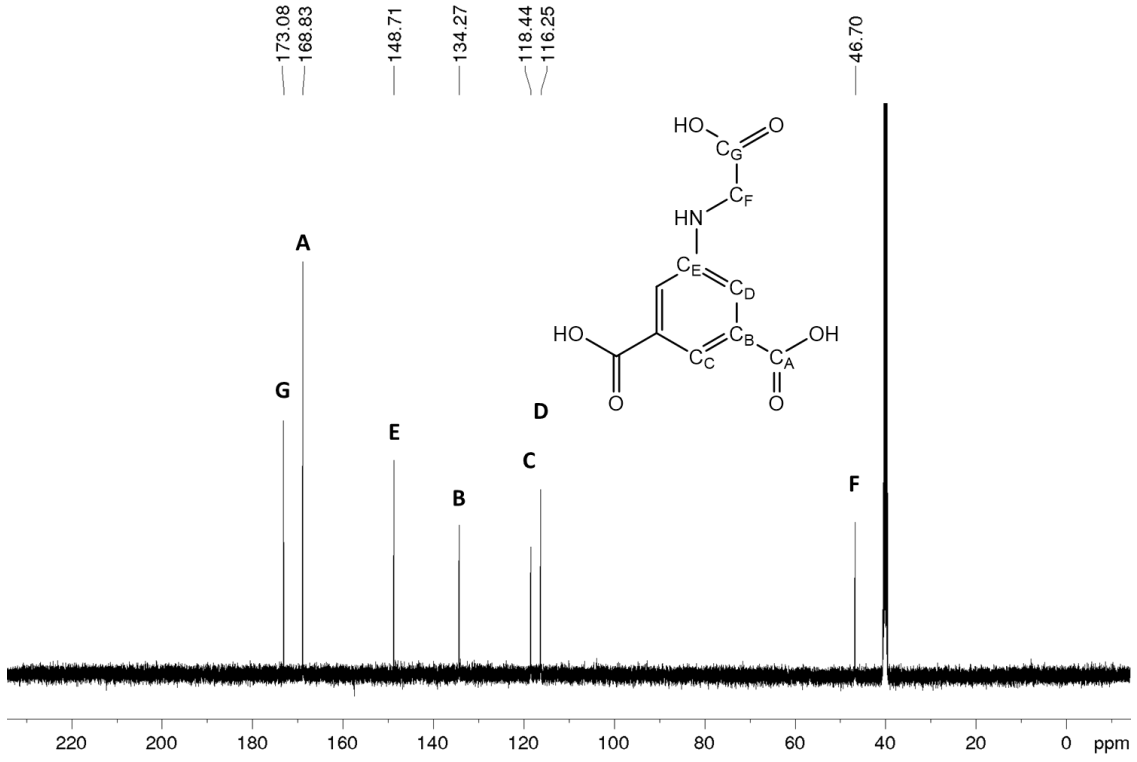

Figure 2.63. ^{13}C{^{1}H}-NMR spectrum of H_3cmai.

2.5.3 Synthesis of $[Cd_2(Hcmai)_2(H_2O)_2]\cdot H_2O$ (**1**)

$Cd(NO_3)_2\cdot 4H_2O$ (1 mmol, 0.3085 g) and H_3cmai (0.3 mmol, 0.0717 g) were placed in a 30 mL microwave reaction vessel. 18 mL of deionised water was added, and the mixture magnetically stirred for 15 minutes after which it was sealed with a Teflon-lined cap and placed in an oven at 90 °C for three days. After removal from the oven and cooling under ambient conditions large light brown plate crystals were collected via vacuum filtration, washed with deionised water and stored in fresh deionised water until required. The material was analysed by PXRD, **Figure 2.12**, and compared to the pattern simulated from the single-crystal data which confirmed compound **1** as the major component of the solid.

Thermogravimetric analysis was carried out on compound **1**, with the results presented in **Figure 2.64**. A mass loss between 30 and 195 °C 7.3%, matches well with the theoretical loss of 7.2% for 3 water molecules. After 195 °C, there is a sharp drop in mass, which is attributed to the breakdown of the framework.

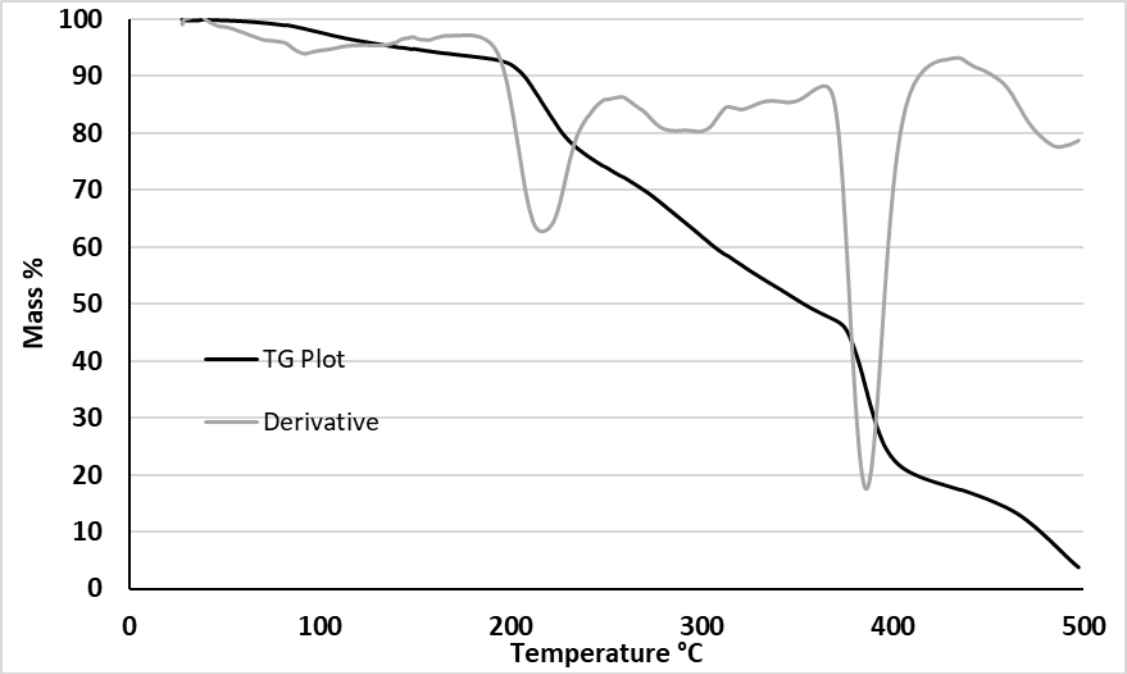

Figure 2.64. Thermogravimetric analysis plot of compound **1**.

The IR spectrum for compound **1** is shown in **Figure 2.65**. (solid, cm^{-1}) 3306s (br), 3260w, 1706w, 1680w, 1602m (sh), 1540s, 1420s, 1398s, 1301s, 1228s, 948m, 924m, 763s, 678s.

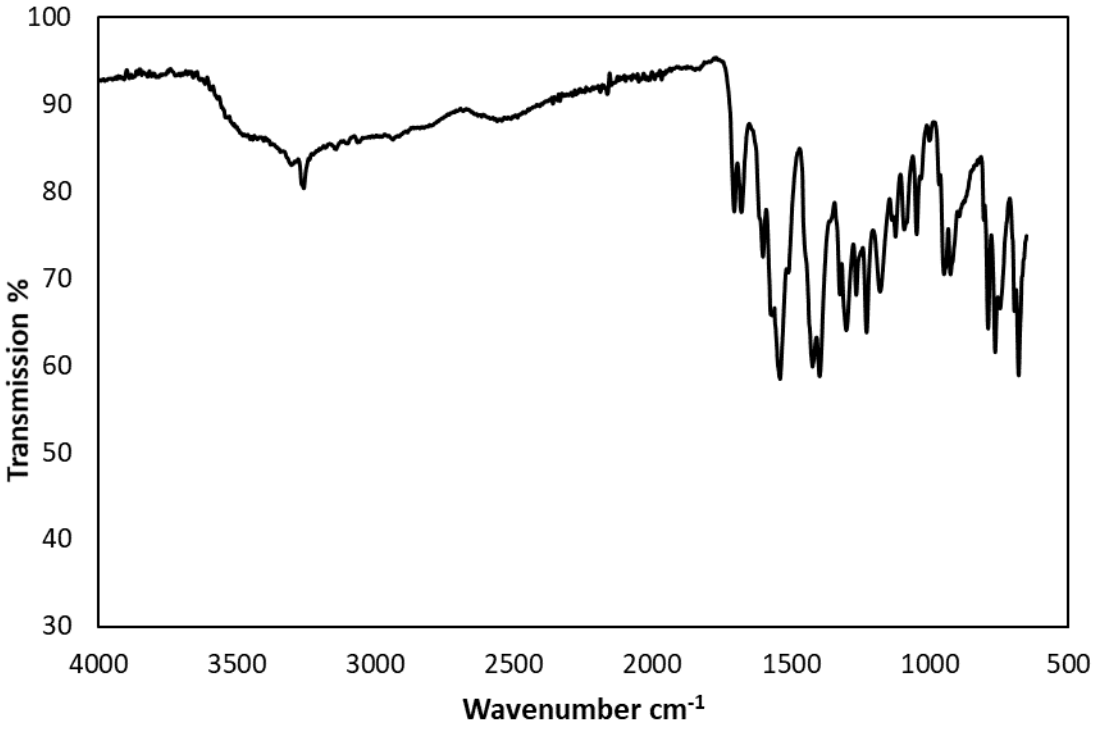

Figure 2.65. Infrared spectrum for compound **1**.

2.5.4 Synthesis of [Cd(Hcmai)(H_2O)$_2$] (**2**)

$CdCl_2 \cdot 2.5H_2O$ (0.6 mmol, 0.1370 g) and H_3cmai (0.2 mmol, 0.0478 g) were put into to a 10 mL microwave vial containing 8 mL of H_2O and sonicated for 15 minutes. The vial was then placed in an oven for three days at 90 °C. After removal from the oven and cooling under ambient conditions, the intergrown brown blocks were collected using vacuum filtration, washed with deionised water and stored in fresh deionised water until required.

PXRD analysis was conducted and is presented in **Figure 2.66**. The experimental pattern for compound **2** shows good agreement with the simulated pattern, the discrepancy in the intensities of the patterns can be attributed to preferred orientation, with the extra peaks suggesting the presence of a minor second phase. Elemental microanalysis (CHN) was also carried out and showed good agreement with the theoretical values based on the solved structure for compound **2**. Expected based on crystal structure: C 31.15%, H 2.88%, N 3.63%. Found: C 31.02%, H 2.77%, N 3.43%.

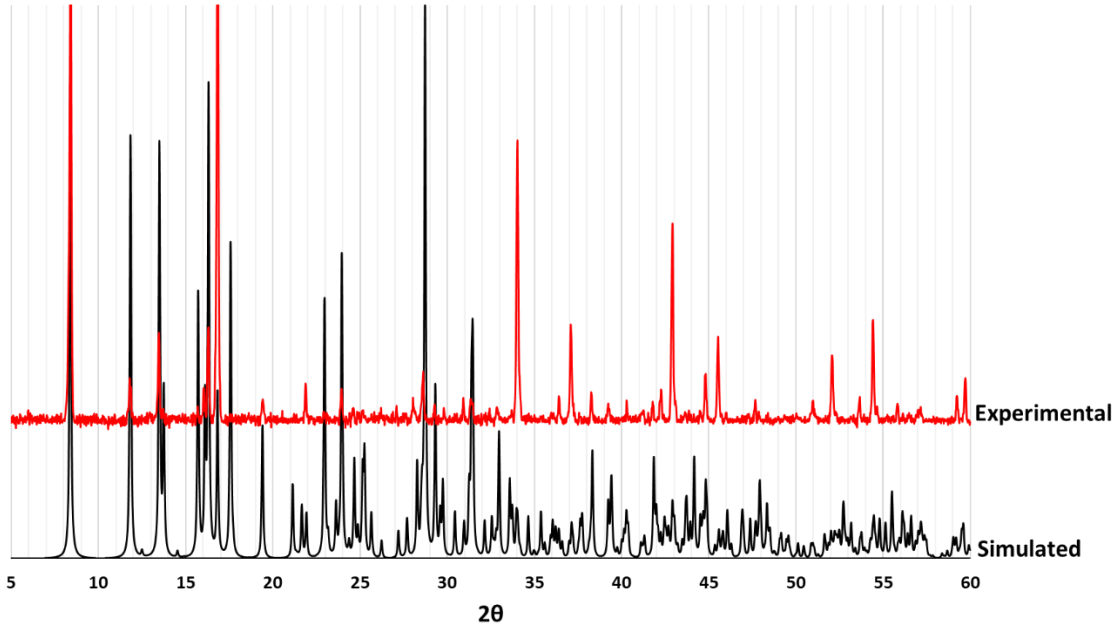

Figure 2.66. Comparison of simulated and experimental PXRD for compound **2**.

Thermogravimetric analysis was carried out on compound **2** and the results are presented in **Figure 2.67**. The mass loss between 175-220 °C was 7.53%. The loss of the two ligated water molecules from the structure would give a mass loss of 9.35% so the observed mass loss is slightly lower than expected in this region, possibly due to the presence of a second phase.

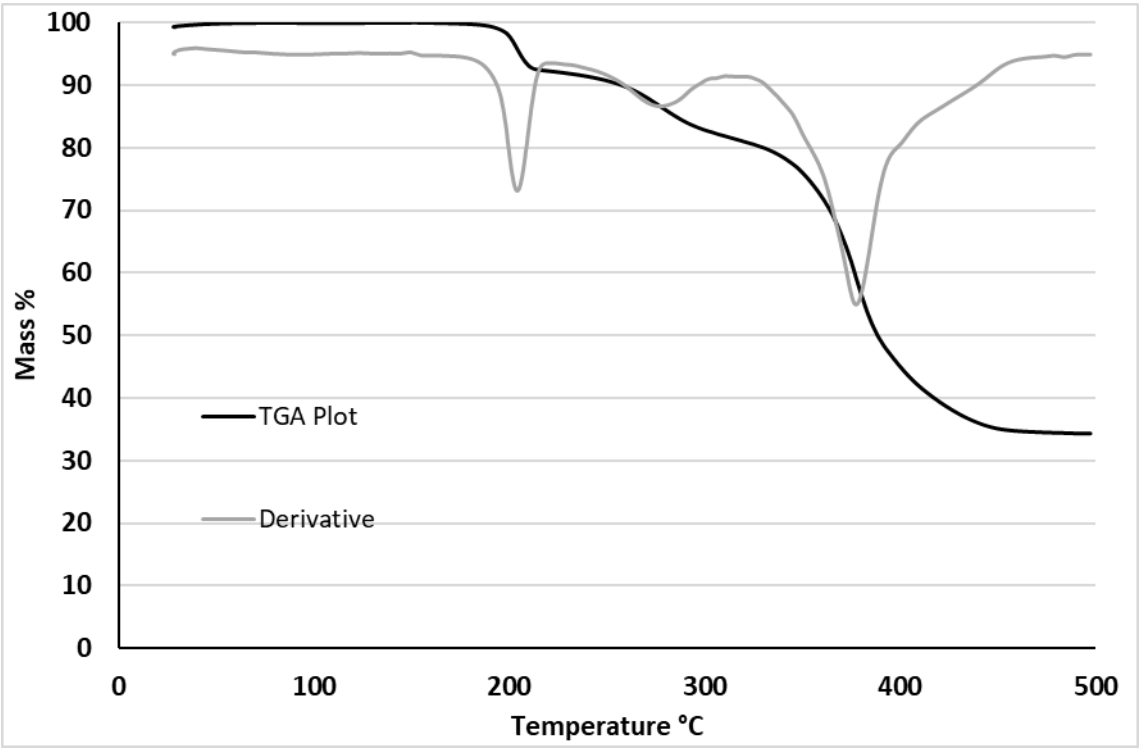

Figure 2.67. Thermogravimetric analysis plot of compound **2**.

The IR spectrum for compound **2** is shown in **Figure 2.68**. (solid, cm^{-1}) 33243w, 3030s (br), 1693w, 1590m, 1542s, 1402s, 1246s, 1198s, 942s, 765s, 677s.

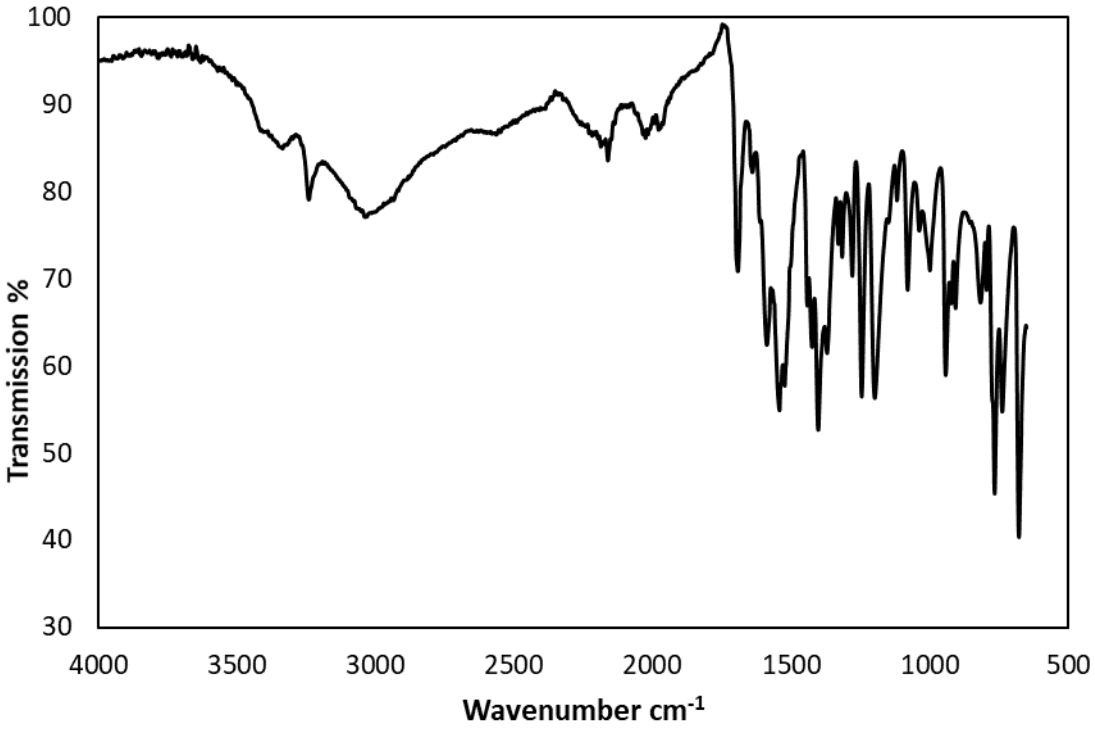

Figure 2.68. Infrared spectrum for compound **2**.

2.5.5 Synthesis of $[Cd_3(cmai)_2(H_2O)_2]\cdot 4H_2O$ (**3**)

$Cd(OAc)_2\cdot 2H_2O$ (0.6 mmol, 0.1599 g) and H_3cmai (0.2 mmol, 0.0478 g) were placed in a 10 mL microwave vial containing 9 mL of H_2O and sonicated for 15 minutes. The vial was sealed and then placed in an oven at 90 °C for three days. After removal from the oven and cooling under ambient conditions, the colourless rhombohedral block shaped crystals were collected by vacuum filtration and washed with deionised water and stored in fresh deionised water until required.

PXRD analysis was conducted and is presented in **Figure 2.69**. The simulated and experimental patterns align very closely confirming that the single-crystal is representative of the bulk. Elemental microanalysis (CHN) was also carried out and showed good agreement with the theoretical values based on the solved structure for compound **3**. Expected: C 25.19%, H 2.96%, N 2.94%. Found: C 25.31%, H 2.83%, N 2.91%.

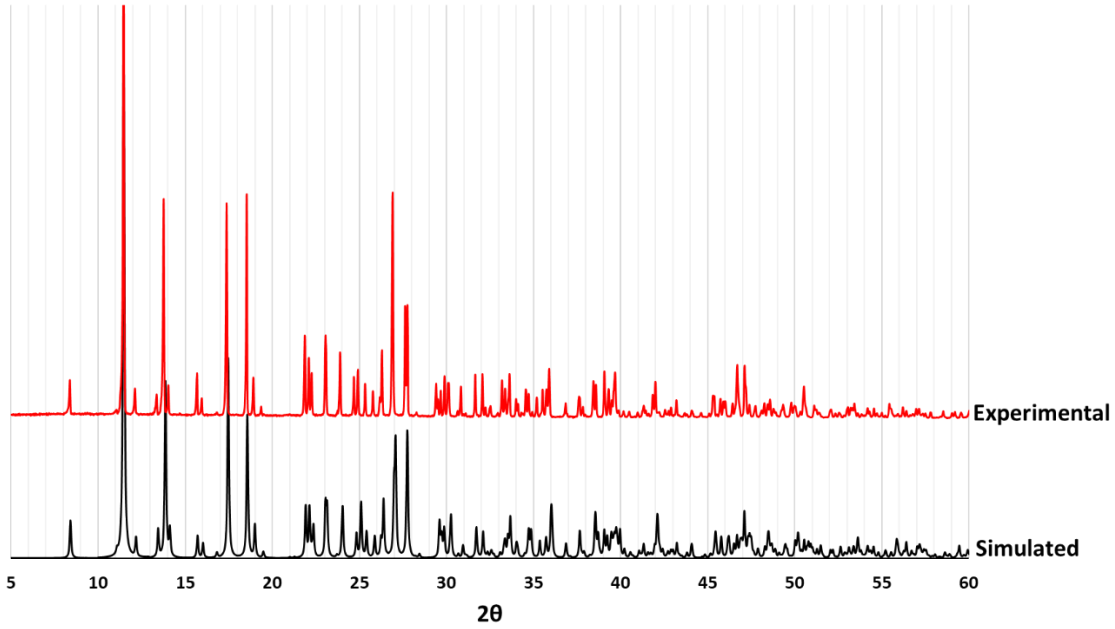

Figure 2.69. Comparison of simulated and experimental PXRD for compound **3**.

The IR spectrum for compound **3** is shown in **Figure 2.70**. (solid, cm^{-1}) 3251w, 3184s (br), 1608m, 1572s, 1534m, 1362s, 1318m, 1090w, 813m, 774s, 721s.

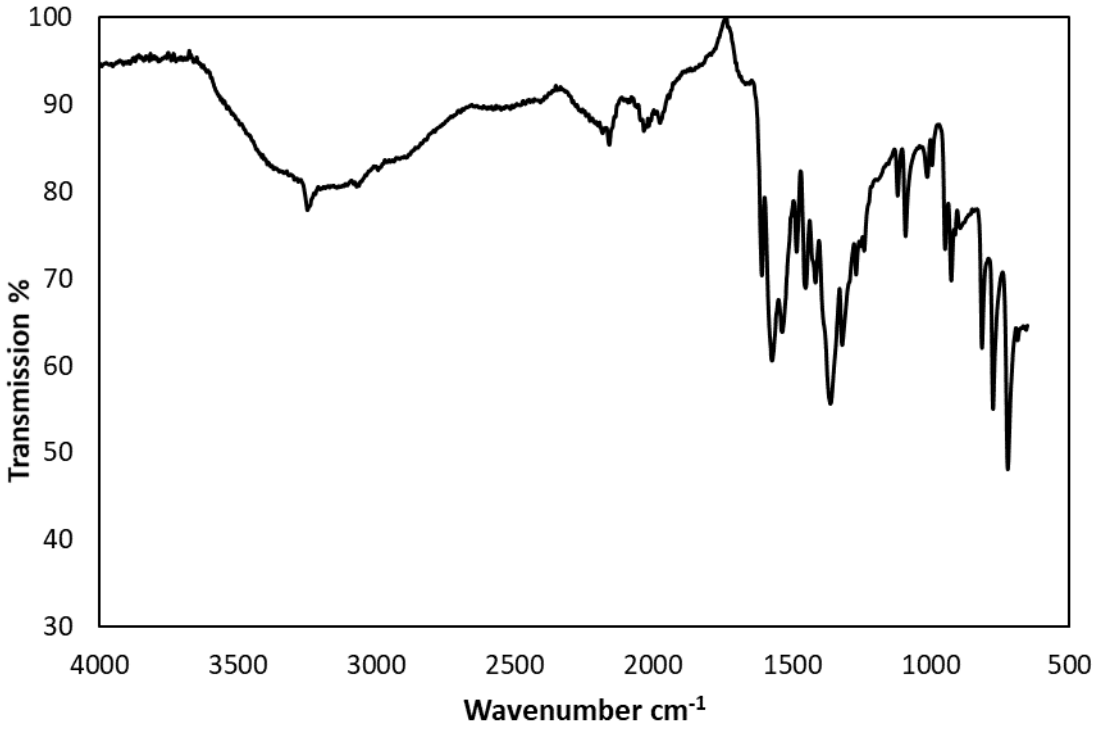

Figure 2.70. Infrared spectrum of compound **3**.

2.5.6 Synthesis of $[Cd_3(cmai)_2]$ (**4**)

A small sample of compound **3** (*ca.* 40 mg) was heated to 100 °C under reduced pressure using a high vacuum line for a period of 6 hours. During this time, compound **4** was formed and analysis was carried out without further purification. PXRD analysis of compound **4**, presented in **Figure 2.71**, shows the bulk material identity is the same as the single-crystal data collected for compound **4.**

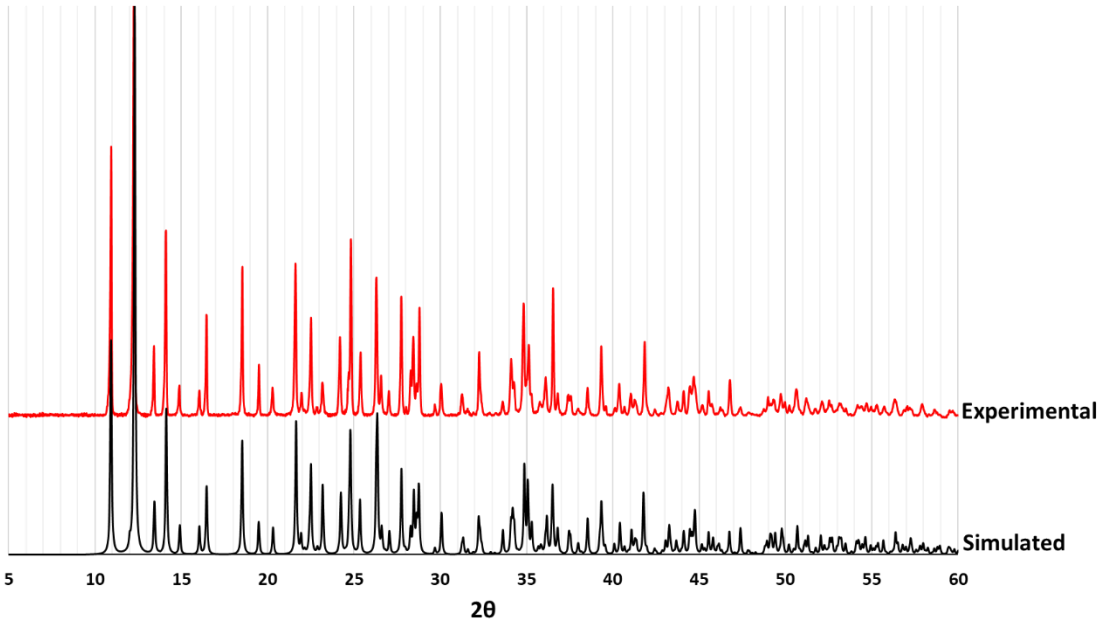

Figure 2.71. Comparison of the simulated and experimental PXRD patterns for compound **4**.

The IR spectrum for compound **4** is shown in **Figure 2.72**. (solid, cm^{-1}) 3319w, 3028w, 1612w (sh), 1572m, 1531m, 1515m, 1490m, 1414s, 1379s, 1083w, 912m, 776s, 728s.

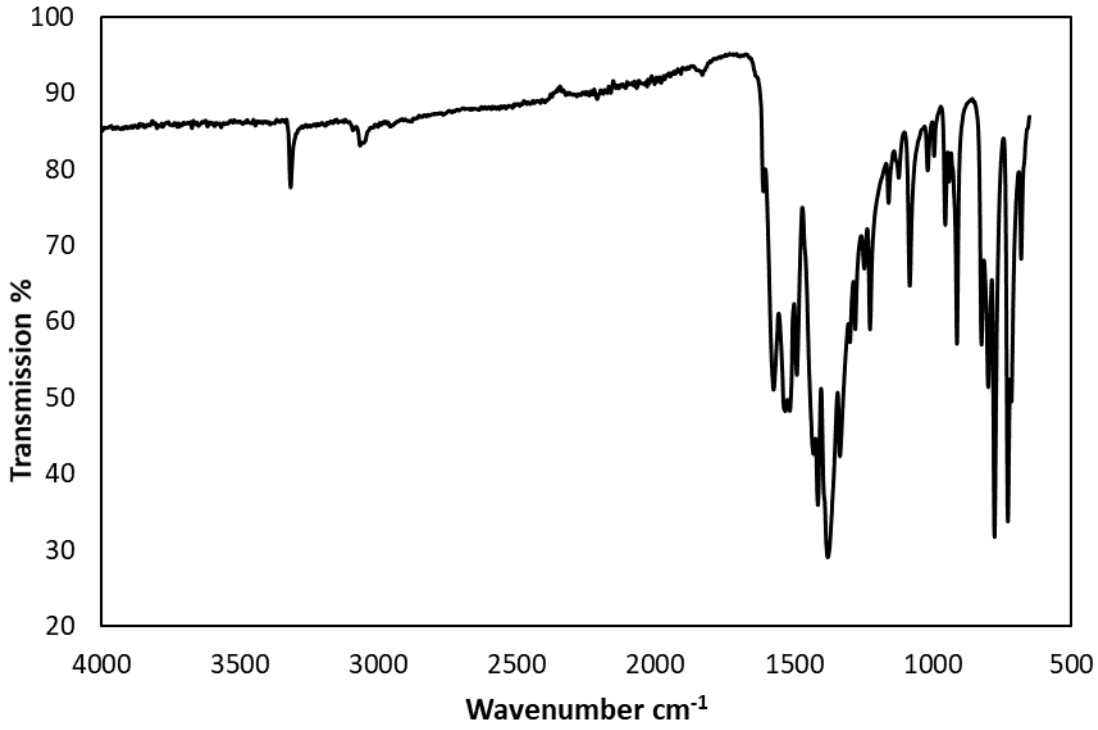

Figure 2.72. The Infrared spectrum of compound **4**.

2.5.7 Variable Temperature Powder Diffraction Experiment

A sample of compound **3** was ground into a fine powder and mounted into a capillary. The capillary was placed into the furnace of a STOE Powder Diffraction System outfitted with a Eurotherm 2416 high temperature device. Scans were collected throughout the experiment using copper radiation in Debye-Scherrer mode and a Multi-MYTHEN detector with a collection time of 10 minutes per trace. During the collection of each pattern the temperature was maintained at a constant value. The temperature profile and collections are described in **Table 2.5**.

Table 2.5. The temperature profile and collections for VT-PXRD on compound **(3)**.

Time (mins)	Collection /Ramp	Temperature (°C)		Time (mins)	Collection /Ramp	Temperature (°C)
0-10	1	20		75-85	7	140
10-12	Ramp	40		85-87	Ramp	150
12-22	2	40		87-92	Hold	150
22-25	Ramp	60		92-102	8	150
25-35	3	60		102-107	Hold	150
35-37	Ramp	80		107-117	9	150
37-48	4	80		117-122	Hold	150
48-50	Ramp	100		122-132	10	150
50-60	5	100		132-138	Hold	150
60-62	Ramp	120		138-148	11	150
62-73	6	120		148-167	Ramp	20
73-75	Ramp	140		167-177	12	20

2.5.8 Synthesis of $[Cd_6(cmai)_4(H_2O)_{9.75}(DMF)_{2.25}]\cdot 20H_2O\cdot 1.6DMF$ (**5**)

H_3cmai (0.4 mmol, 0.0960 g) was added to 16 mL of DMF and sonicated for 15 mins after which time 16 mL of H_2O was added causing dissolution of the acid. To the solution was added $Cd(NO_3)_2\cdot 4H_2O$ (1.2 mmol, 0.0960 g). The solution remained slightly cloudy and was split between 7 smaller vials to facilitate evaporation and left for 48 hours in a fume hood after which time large colourless block shaped crystals had formed. The samples were combined, and the crystals collected via vacuum filtration, washing with deionised water and then stored in fresh deionised water until required.

The PXRD analysis is presented in **Figure 2.73**. The simulated and experimental patterns correspond closely confirming that the bulk material is compound **5**. Elemental microanalysis

(CHN) was also carried out. Expected: C 26.11%, H 4.72%, N 4.94%, Found: C 26.25%, H 4.24%, N 4.92%. The slightly higher than expected percentages for carbon and nitrogen suggest that the DMF pore content may be, on average, greater than that suggested by the data collected for the selected single-crystal.

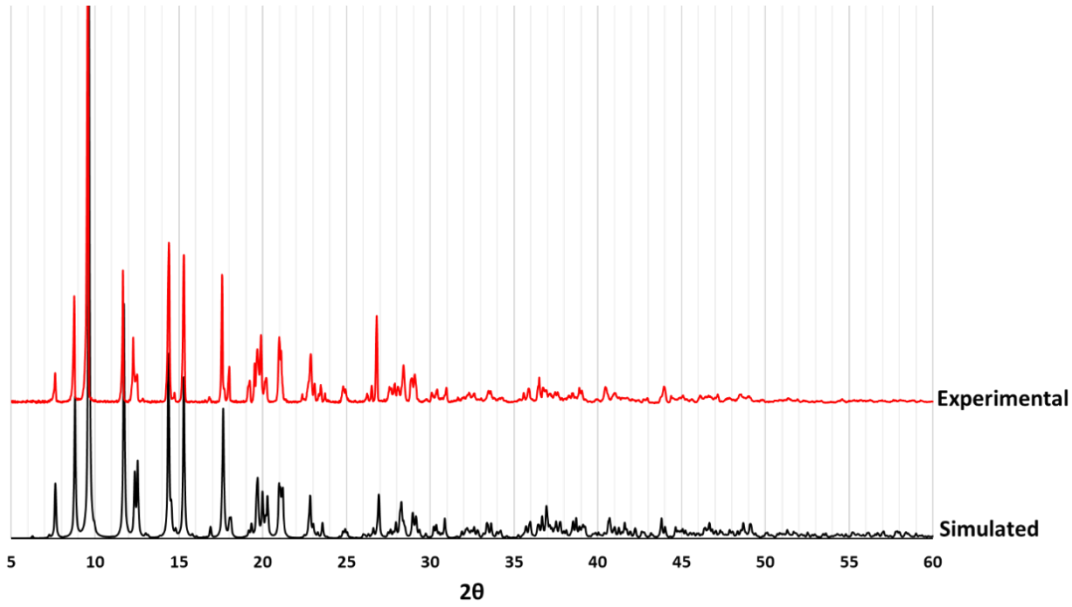

Figure 2.73. Comparison of simulated and experimental PXRD patterns for compound **5**.

The IR spectrum for compound **5** is shown in **Figure 2.74**. (solid, cm^{-1}) 3283vs (br), 1648m, 1574s, 1372s, 1305s, 1109w, 919w, 779s, 735s.

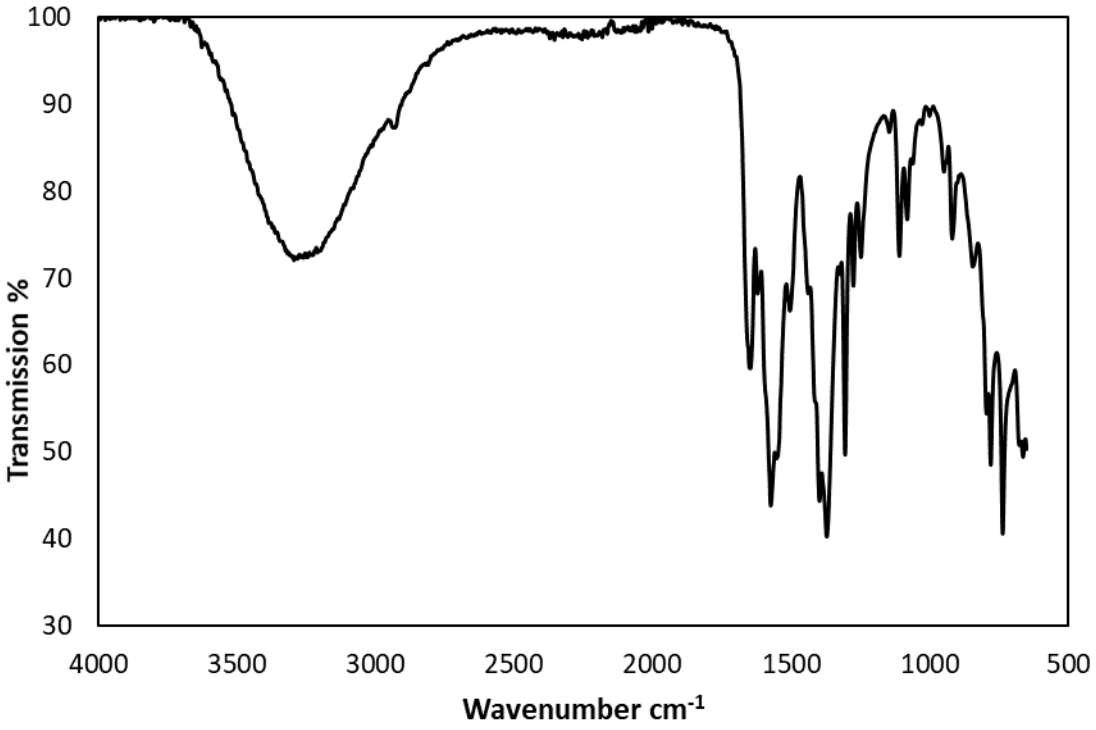

Figure 2.74. The IR spectrum of compound **5**.

2.5.9 Synthesis of $[Cd_3(cmai)_2(H_2O)_3]\cdot 6H_2O$ (**6**)

H_3cmai (0.1 mmol, 0.0239 g) was placed in a 10 mL microwave vial containing 4 mL of DEF and the mixture was sonicated for 15 minutes. To this was added 4 mL of water, causing the acid to fully dissolve. 4,4'-bypyridine (bipy) (0.1 mmol, 0.0154 g) followed by $Cd(NO_3)_2\cdot 4H_2O$ (0.3 mmol, 0.0925 g) were added and the vial was sealed, then placed in an oven at 120 °C for three days. After removal from the oven and cooling under ambient conditions, the colourless plate crystals were collected by vacuum filtration and washed with deionised water and stored in fresh deionised water until required.

The bulk material of compound **6** was analysed by PXRD and the trace compared to that simulated from the single-crystal data. As can be seen in **Figure 2.75**, the patterns match very closely confirming the identity of the bulk as compound **6**.

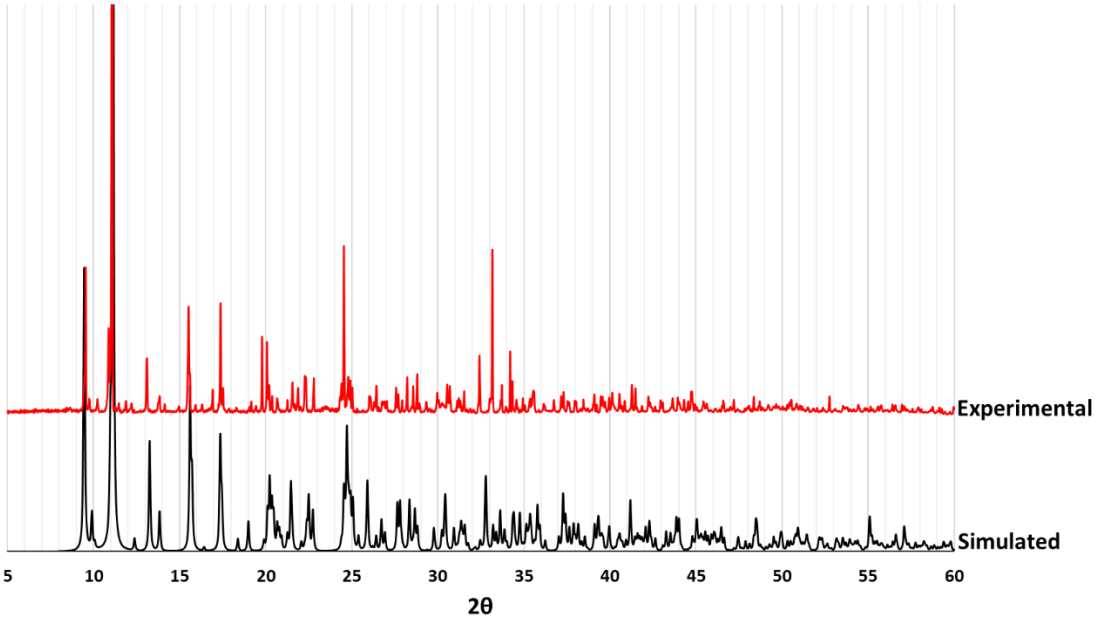

Figure 2.75. A comparison of the experimental PXRD pattern of compound **6** and the pattern simulated from single-crystal data.

The IR spectrum for compound **6** is shown in **Figure 2.76**. (solid, cm^{-1}) 3282s (br), 1578m (sh), 1545s, 1425m (sh), 1365s, 1308s, 778s, 727s.

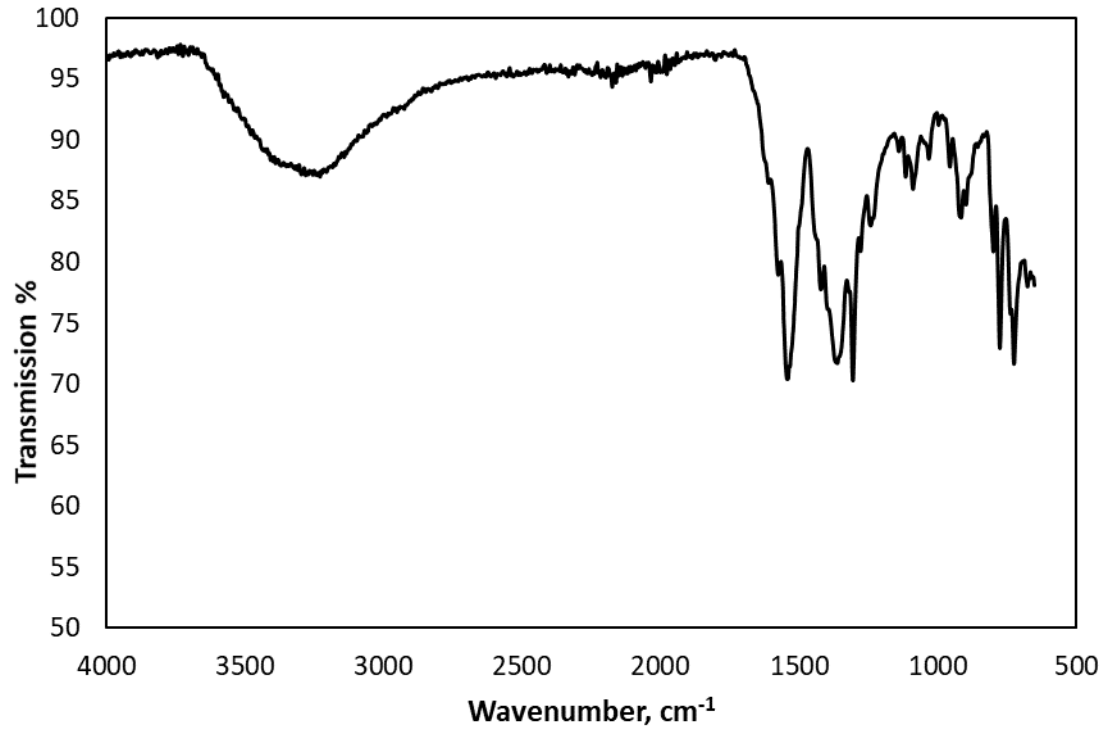

Figure 2.76. The IR spectrum for compound **6.**

2.5.10 Synthesis of [Zn(Hcmai)(H_2O)$_2$] (**7**)

$Zn(NO_3)_2 \cdot 6H_2O$ (0.6 mmol, 0.1785 g) and H_3cmai (0.2 mmol, 0.0478 g) were added to a 10 mL microwave vial containing 8mL of H_2O and sonicated for 15 minutes. The vial sealed with a Teflon-lined cap was then placed in an oven for 3 days at 90 °C. After removal from the oven and cooling under ambient conditions, the colourless rod shaped crystals were collected by vacuum filtration and washed with deionised water and stored in fresh deionised water until required.

A PXRD pattern was collected for compound **7** and compared to one generated from single-crystal data as shown in **Figure 2.77**. The two patterns match closely confirming the identity of the bulk as compound **7**. Elemental microanalysis was also conducted and showed good agreement between the experimental result and the theoretical values. Expected: C 35.47%, H 3.27%, N 4.14%. Found: C 35.40%, H 3.11%, N 3.96%.

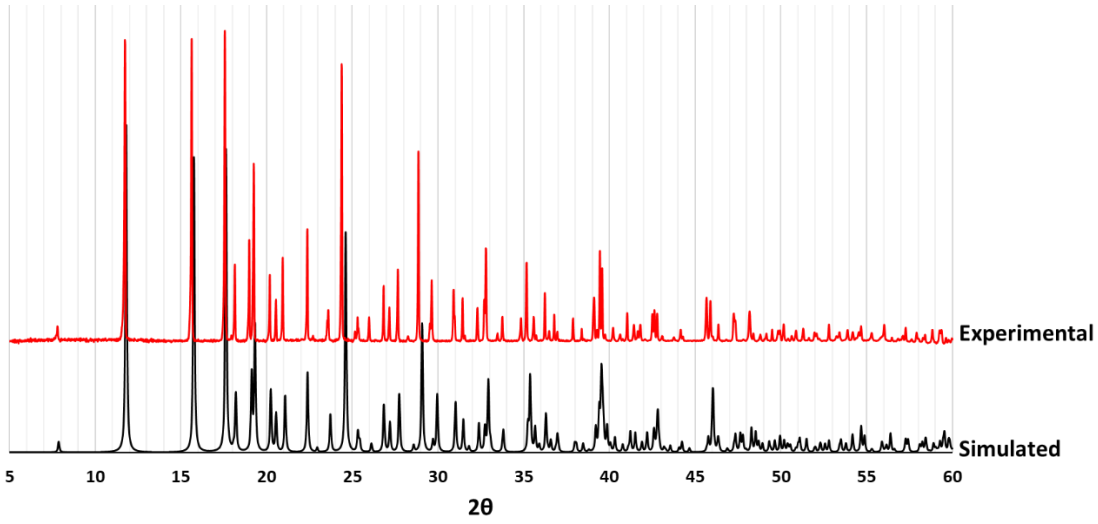

Figure 2.77. The experimental and simulated PXRD patterns for compound **7.**

Thermogravimetric analysis was carried out on compound **7**, the results are presented in **Figure 2.77**. The mass loss between 60-195 °C is 4.1%, the expected mass loss for both the coordinated water molecules would be 10.64% suggesting that the majority of the coordinated water remains in the framework until the next mass loss event in the range 225-325 °C of 15.81% The latter represents the remainder of the guest water and some of the organic component of the MOF starting to break down.

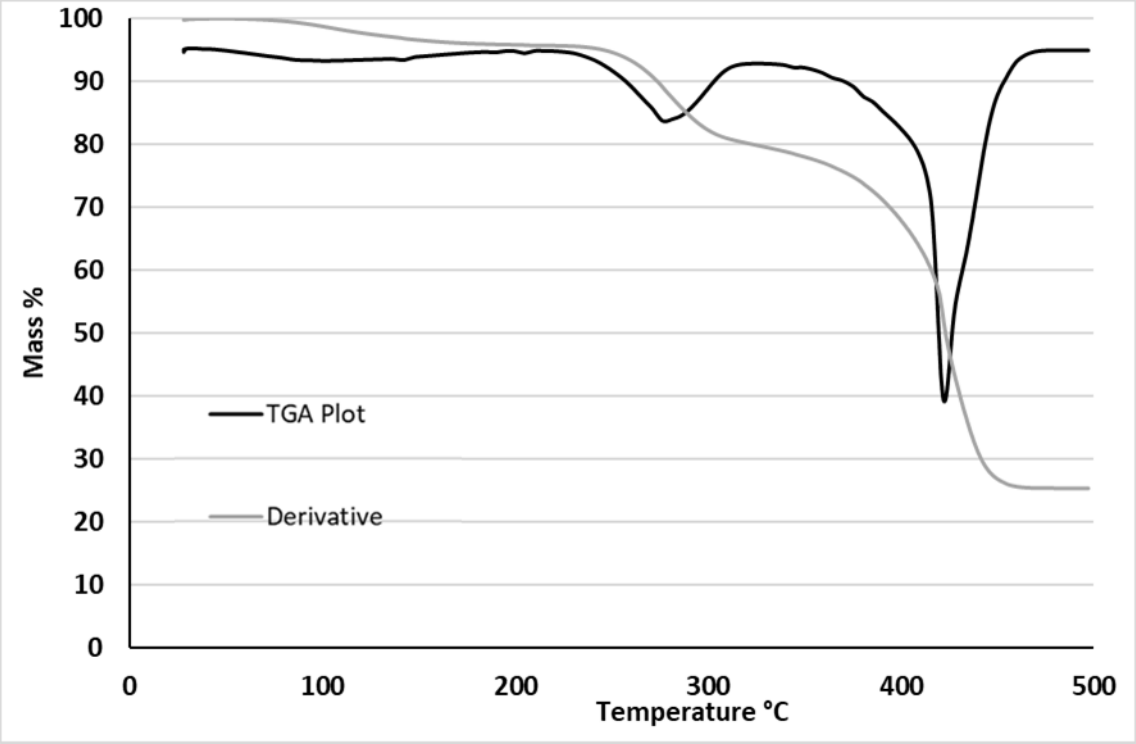

Figure 2.78. The TGA plot for compound **7**.

2.5.11 Synthesis of [Cu(Hcmai)(H_2O)$_{1.2}$] (**8**)

$Cu(NO_3)_2 \cdot 2.5H_2O$ (0.6 mmol, 0.1396 g) and H_3cmai (0.2 mmol, 0.0476 g) were added to 10 mL mixture of EtOH and H_2O in a 1:1 ratio in a Teflon insert for an Parr acid digestion bomb. The mixture was stirred for 15 minutes in the Teflon liner before removing the stirrer bar and sealing the autoclave. The autoclave was heated in an oven at 120 °C for 48 hours. After removal from the oven and cooling under ambient conditions, the clusters of green shard-like crystals were collected by vacuum filtration and washed with deionised water (3 x 3 mL) and fresh ethanol (3 x 3 mL). The crystals were stored in deionised water until required.

A PXRD pattern was collected for compound **8** and compared to a pattern simulated from the single-crystal data as shown in **Figure 2.77**. The two patterns match closely confirming the identity of the bulk as compound **8**. Elemental microanalysis was carried out, good agreement was found between the experimental result and the theoretical values. Expected: C 37.26%, H 2.94%, N 4.35%. Found: C 37.09%, H 3.12%, N 4.32%.

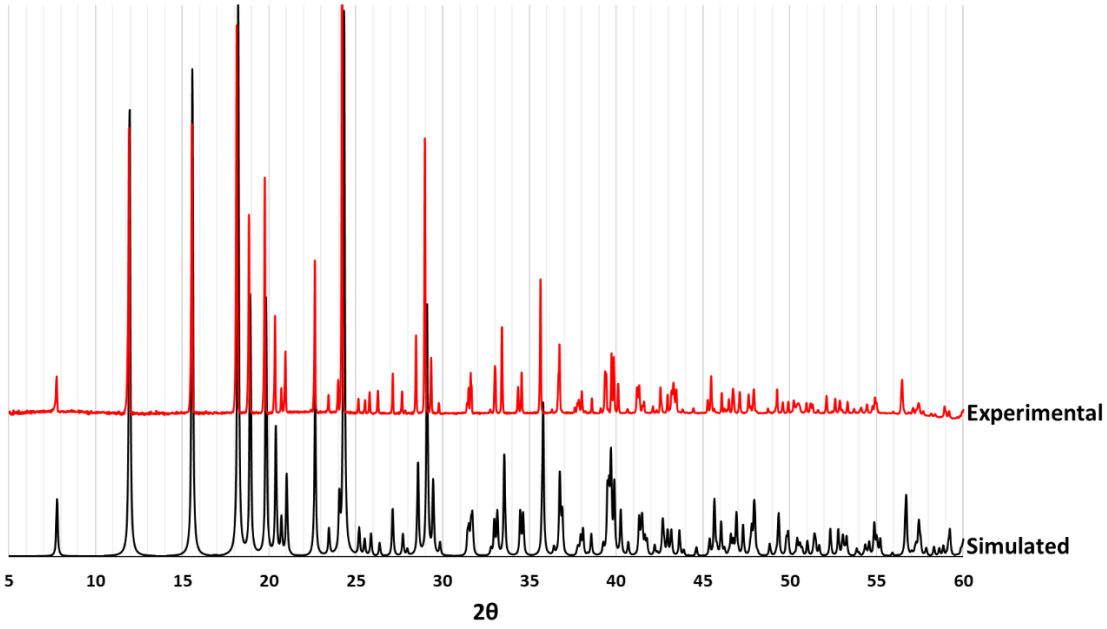

Figure 2.79. The simulated and experimental PXRD patterns for compound **8**.

Thermogravimetric analysis was carried out on compound **8**, the results are presented in **Figure 2.80.** The plot shows no mass loss until 200 °C at which point there are three successive events centred on 225 °C, 280 °C, and 320°C which represent water loss (6.7 wt.% based on 1.2 water molecules) from the structure followed by framework decomposition.

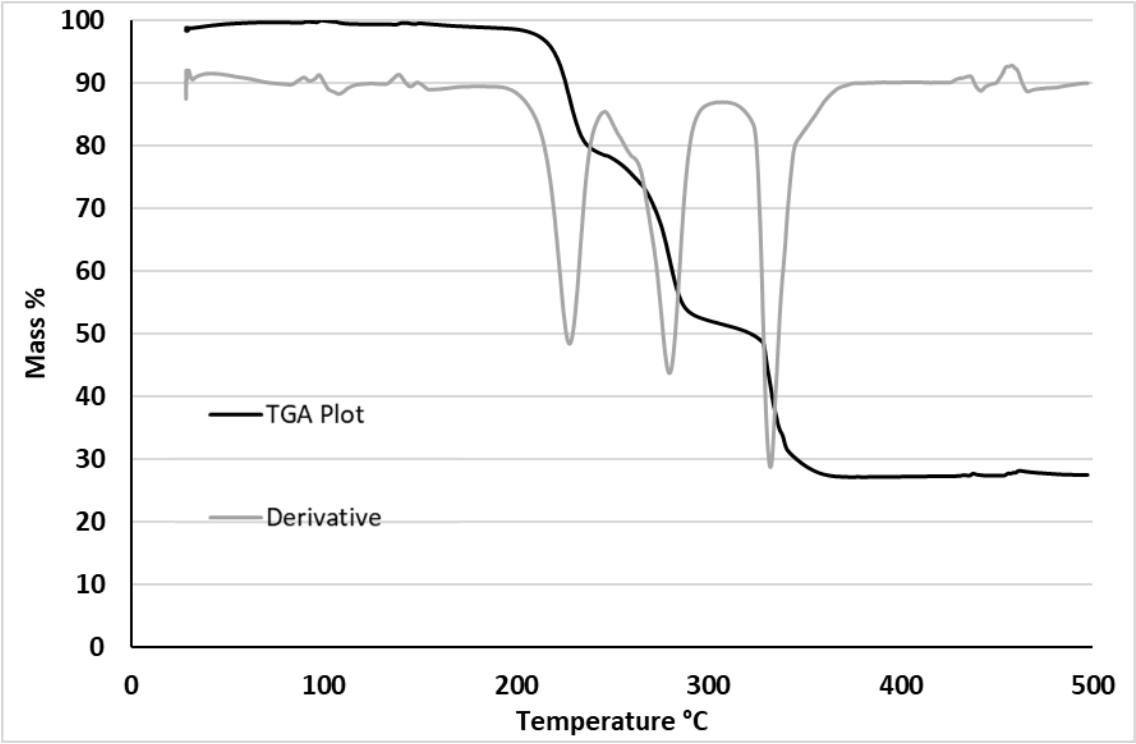

Figure 2.80. TGA result for compound **8**.

2.5.12 Synthesis of [Co(Hcmai)(H_2O)$_2$] (**9**)

$Co(NO_3)_2 \cdot 6H_2O$ (0.5 mmol, 0.1455 g) and H_3cmai (0.15 mmol, 0.0359 g) were added to a 10 mL microwave vial containing 8mL of H_2O and the mixture was sonicated for 15 minutes. The vial sealed with a Teflon-lined cap was then placed in an oven for 18 hours at 90 °C. After removal from the oven and cooling under ambient conditions, the pink plate crystals were collected by vacuum filtration and washed with deionised water (3 x 3 mL) and stored in deionised water until required.

Analysis of the bulk material was carried out using PXRD. The collected diffraction pattern was compared to a pattern simulated from the single-crystal data and is shown in **Figure 2.81**. The two patterns match closely confirming the identity of the bulk as compound **9**.

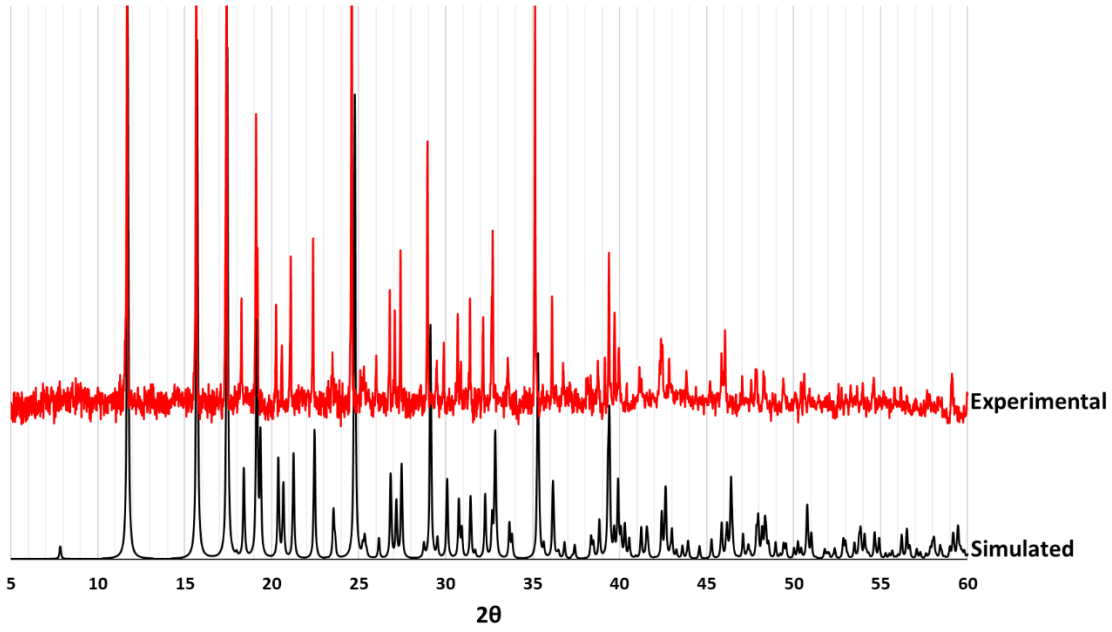

Figure 2.81. The simulated and experimental PXRD traces for compound **9**.

Thermogravimetric analysis results for compound **9** are presented in **Figure 2.82**. It can be seen that there is no mass loss observed in the material until 150 °C. There is a slow mass loss between 150–340 °C, equating to 19.1%. This suggests that, as well as the release of the guest water, (which makes up 10.85% of the mass of the material) some of the organic component also decomposes. After 340 °C there is a sharp increase in the rate of mass loss equating to full decomposition of the remaining linker and residue formation.

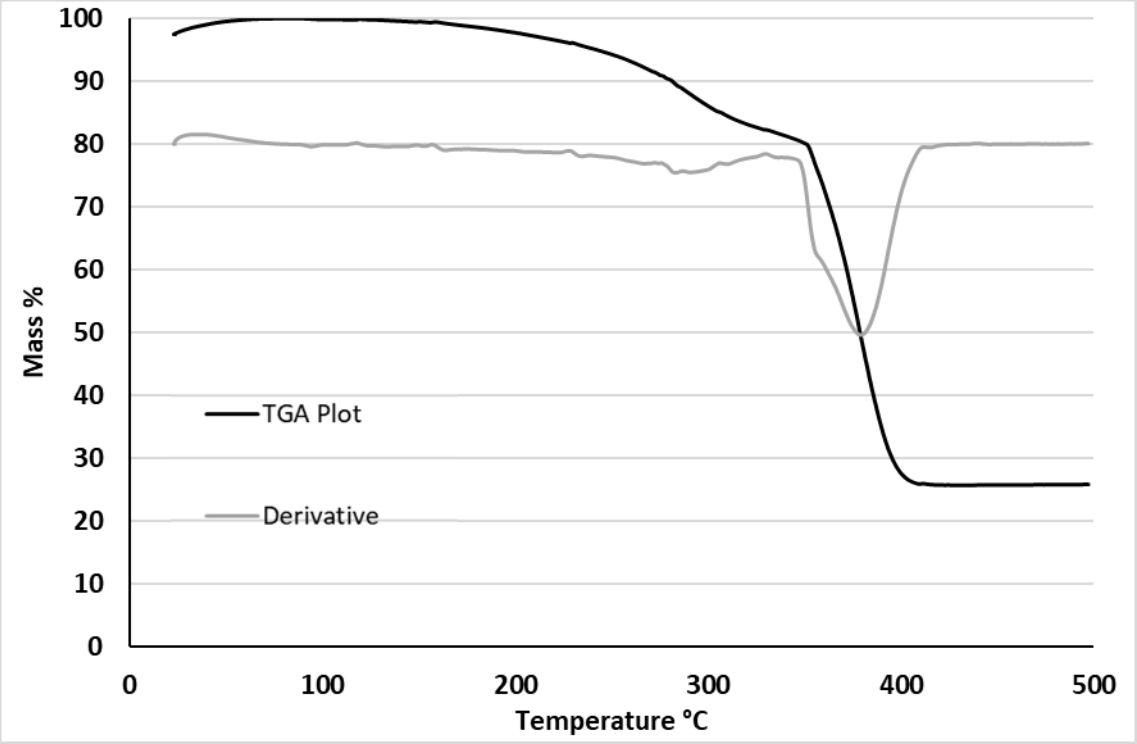

Figure 2.82. The TGA results for compound **9**.

2.5.13 Synthesis of $[Zn_2(cmai)(OH)(H_2O)_2]\cdot 3H_2O$ (**10**)

$Zn(OAc)_2\cdot 2H_2O$ (0.5 mmol, 0.1098 g) and H_3cmai were added to a 12 mL of a 50:50 mixture of DEF:water in a 30 mL microwave reaction vial. The vial was sealed, and the mixture sonicated for 15 minutes before being placed in an oven for 72 hours at 120 °C. After removal from the oven and cooling under ambient conditions, the light tan crystals were washed with fresh water (3 x 3 mL) and collected via vacuum filtration at which point they were stored in deionised water until required.

A PXRD pattern was collected for compound **10** and compared to a pattern simulated from the single-crystal data as shown in **Figure 2.83**. The peak positions in the two patterns match well confirming the bulk material as compound **10**. Elemental microanalysis was carried out; good agreement was found between the experimental result and the theoretical values. Expected: C 25.34%, H 3.61%, N 2.95%. Found: C 25.21%, H 3.34%, N 2.90%.

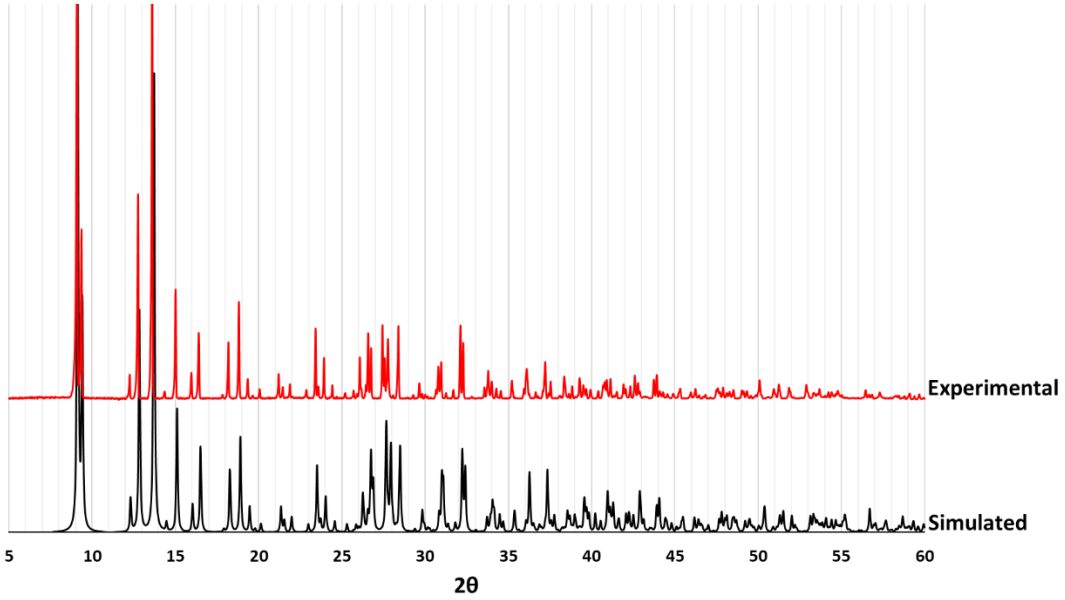

Figure 2.83. The simulated and experimental PXRD traces for compound **10**.

The IR spectrum for compound **10** is presented in in **Figure 2.84**. (solid, cm^{-1}) 3284s (br), 1616m (sh), 1561s, 1407s, 1365s, 1238w, 1090w,1047w, 921w, 780m, 723s.

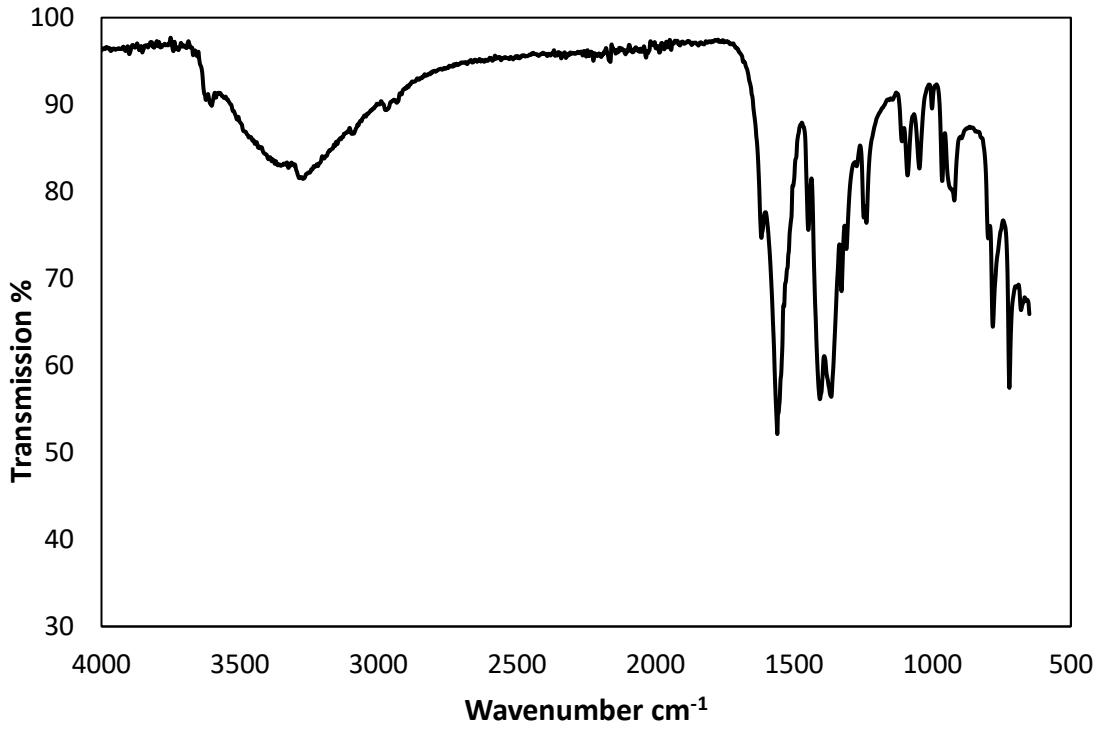

Figure 2.84. The IR spectrum for compound **10**.

Chapter 3 - Synthesis of Cadmium and Zinc Metal-Organic Frameworks Using 5-((carboxymethyl)amino)isophthalic Acid and Neutral N-donor Ligands.

3.1 Introduction

The results of the investigation into MOFs synthesised from H_3cmai, presented in **Chapter 2**, highlighted that the majority of the frameworks contained only a small amount of potential void space. One possible reason for this is the flexibility of the cmai linker, allowing a large number of coordination modes and environments. This facilitates the thermodynamic drive to reduce empty space leading to densely packed structures with small pores. A way to circumvent this problem is to add a second rigid linker to the framework, increasing the portion of the MOF that is completely rigid, favouring open frameworks with larger cavities.

Neutral linkers, such as those derived from pyridine are an attractive option. The inclusion of both cmai and the co-ligands into a framework is favourable, as the anionic cmai linker allows the charges to balance with the metal cations without the need for guest anions. Use of an anionic co-linker could potentially form competing frameworks that do not incorporate the target cmai ligand. The addition of a second linker may also provide a route to higher dimensionality frameworks which generally have larger surface areas and internal cavities. Two linear neutral linkers were targeted for investigation, 4,4'-bypyridine (bipy) and 1,2-bis(4-pyridyl)ethylene (bpe), shown in **Figure 3.1**.

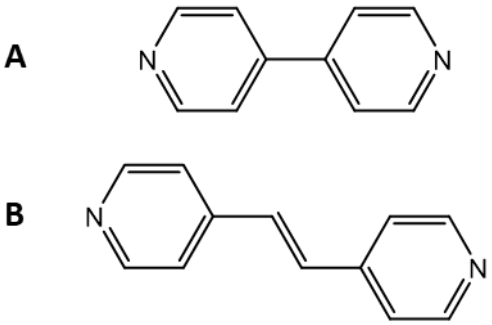

Figure 3.1. The structure of **A** – 4,4'-bypyridine (bipy) and **B** – 1,2-bis(4-pyridyl)ethylene (bpe).

These pyridine-based linkers are both linear, the main difference between them is the distance between the coordinating nitrogen atoms, which are approximately 7.0 Å and 9.4 Å apart in bipy and bpe respectively. There are many examples of the combination of bipy and polycarboxylates in the formation of MOFs.[85, 119-121] One example of this in the formation of a cadmium containing MOF was reported by Zaworotko *et al.*[122] who synthesised [Cd(bdc)(bipy)] from $Cd(NO_3)_2{\cdot}4H_2O$, H_2bdc and bipy in a mixture of DMF/DEF at 85 °C. The structure consists of cadmium dimer SBUs

that are supported by the interactions from four bdc linkers and four bipy linkers, as shown in **Figure 3.2 A.** The cadmium ions and bdc linkers form a 2-D network, which is transferred into three dimensions by the pillaring bipy linkers, as can be seen in **Figure 3.2 B.** The bipy linkers act as spacers between the two layers, creating channels in the structure.

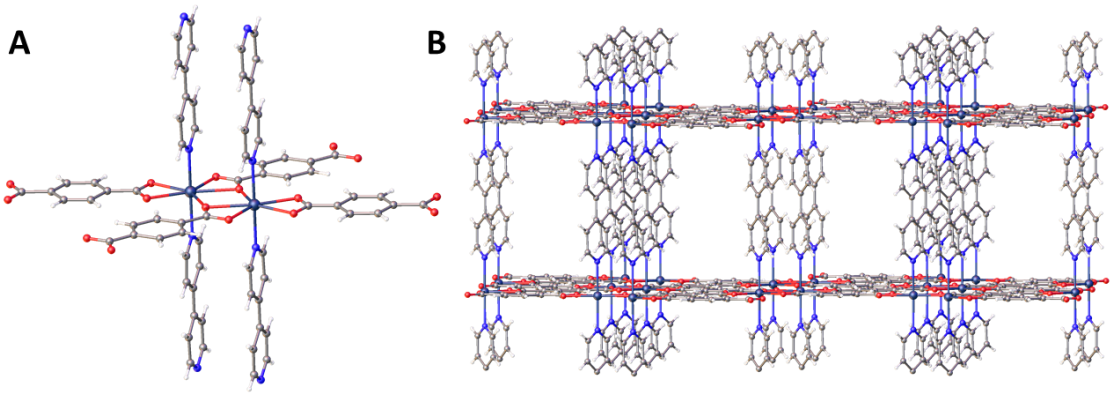

Figure 3.2. A – The cadmium dimer SBU in [Cd(bdc)(bipy)] and **B** – The 3-D structure of [Cd(bdc)(bipy)].[122]

A third neutral ligand, 1,10-phenanthroline (phen), shown in **Figure 3.3**, was also selected for investigation in this chapter. This ligand was selected as part of a different strategy towards the synthesis of functional MOFs. A highlighted issue in **Chapter 2** was the incorporation of water as a ligand in majority of the frameworks. This caused problems when attempting to activate them, as ligated water was lost along with the guest solvent, causing collapse of the framework. The bidentate coordination mode of phen acts as a capping ligand when coordinated to a metal centre. The phen may compete with water as a capping ligand, producing frameworks with no water ligands which will be more robust to activation.

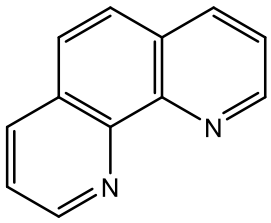

Figure 3.3. 1,10-phenanthroline (phen).

This linker was used by Roa and Thirumurugan in the synthesis of [Cd(bdc)(phen)]·H_2O.[123] The structure of the MOF is shown in **Figure 3.4** and consists of 2-D square net sheets. The sheets stack, giving a structure with pores in which guest water molecules resides.

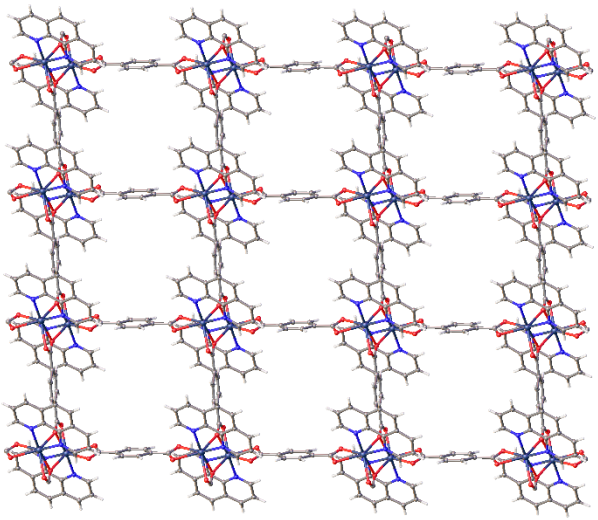

Figure 3.4. The structure of [Cd(bdc)(phen)]·H_2O.[123]

3.2 Results and Discussion: Cadmium MOFs containing cmai-based linkers and neutral N-donor ligands

As discussed in **Chapter 2**, cadmium coordination polymers and MOFs are attractive materials for a number of applications. The high number of novel cadmium-based MOFs containing cmai obtained in **Chapter 2** suggest that the affinity between cadmium and cmai is good. Combining the two components with neutral ligands provides a potential route to higher dimensionality frameworks via pillaring, increasing the likelihood of forming high surface area, high porosity structures.

3.2.1 The synthesis and characterisation of $[Cd_3(cmai)_2(bipy)(H_2O)_4]\cdot 6H_2O\cdot 2DMF$ (**11**)

Compound **11** was formed in the reaction between $Cd(NO_3)_2\cdot 4H_2O$, H_3cmai and bipy in an 1:1 DMF and water solution to which nitric acid had been added. The addition of the acid dissolved any remaining linker or salt that was still present or had formed before heating the reaction. The reaction was carried out at 90 °C for 18 hours, forming very large (5 mm long) colourless obelisk-shaped crystals. Single-crystal X-ray diffraction was carried out on a small block cut from one of these obelisks.

The crystal structure was solved in the polar tetragonal space group $P4_32_12$. The asymmetric unit contains one full occupancy and one half occupancy cadmium centre, one cmai linker, half of a bipy linker, two water ligands, one of which is disordered over three positions, and one guest water molecule. The asymmetric unit along with the coordination spheres of the cadmium centres are presented in **Figure 3.5**.

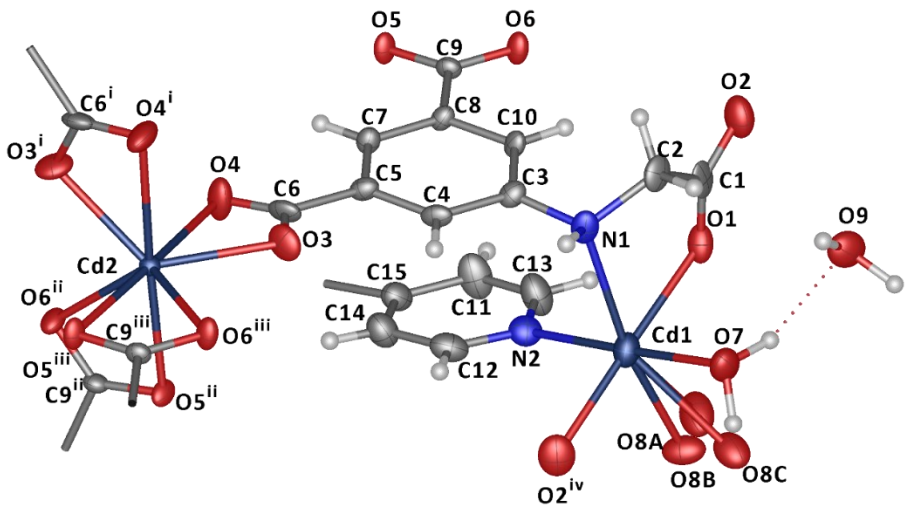

Figure 3.5. The asymmetric unit of compound **11**, with the coordination spheres of Cd1 and Cd2. (i, – *x*, – *y*, 1/2 – *z*; ii, – *x*, 1 – *y*, 1/2 – *z*; iii, + *x*, – 1 + *y*, + *z*; 1/2 – *x*, – 1/2 + *y*, 3/4 – *z*) (ADPs represented at 50% probability).

Cd1 is 6-coordinate, distorted octahedral in geometry, and is bound by two different cmai linkers, a bipy ligand, and two water ligands, with one of the water molecules being disordered over three sites. The first cmai ligand is bound via a κ^2 bidentate mode through N1 and O1 of the flexible arm of the linker. The second cmai ligand binds through O2, which is the other carboxylate oxygen on the flexible arm. The bipy ligand coordinates through N2 and the full occupancy water through O7. The disordered water ligands based on O8A, O8B and O8C have occupancies of 0.45, 0.35 and 0.2 respectively.

Cd2 is 8-coordinate and bound by four different cmai linkers. All the ligands are bonded to Cd2 in the same way, a bidentate κ^2 coordination via the two oxygen atoms of an aryl carboxylate, two based on O3 and O4, and two based on O5 and O6. The coordination geometry of the four carboxylates is pseudo-tetrahedral (τ_4 = 0.69). The distortion in the tetrahedral geometry can be explained by considering the symmetry of the carboxylate ligating groups. The bonds of the carboxylate groups based on O3 and O4 are asymmetrical with Cd–O distances of 2.267(4) Å and 2.586(5) Å respectively. In contrast the carboxylate containing O5 and O6 coordinates symmetrically with Cd–O bond lengths of 2.420(4) Å and 2.414(4) Å for O5 and O6 respectively.

The SBU in compound **11** is formed from chains of Cd1 centres linked through their coordination with carboxylate oxygens O1 and O2. One of these chains is shown in **Figure 3.6**.

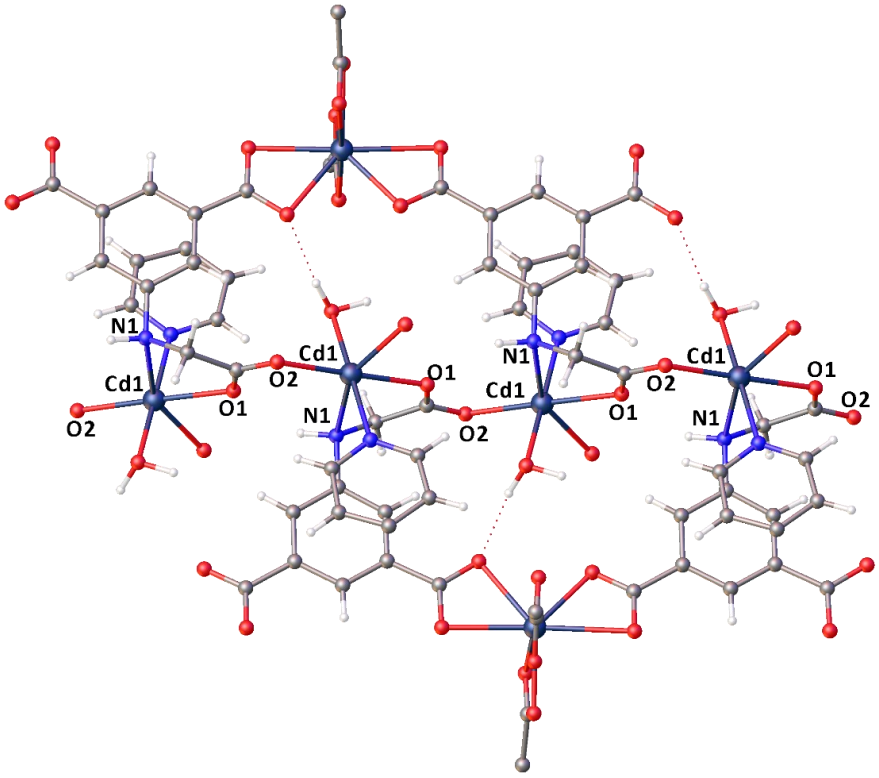

Figure 3.6. The 1-D chain SBU and surrounding linkers in compound **11**.

The chains run in the direction of the *a*-axis and the *b*-axis in alternating layers. Adjacent chains in the same layer are not directly connected, instead Cd2 centres serve to bind the chains in the layers above and below together, perpendicular to one another. The neutral bipy ligands also fulfil the same role as Cd2, binding SBU chains at right angles to chains in the layer above or below. This forms a square-based network of chains which is shown schematically in **Figure 3.7**.

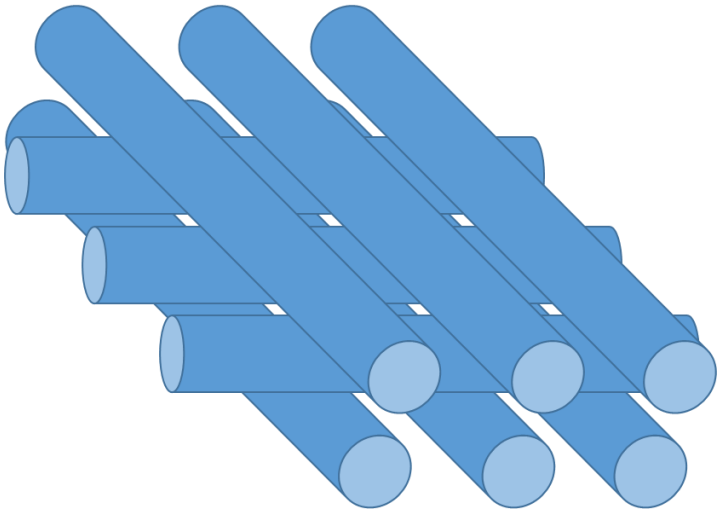

Figure 3.7. A schematic representation of the 3-D structure of compound **11**.

This 3-D structure is very similar to that of compound **5**. It contains the same 1-D chain SBUs and the same 8-coordinate pseudo-tetrahedral cadmium centres, which link adjacent perpendicular chains. It even has the same conformation of cmai linkers. An overlay of a portion of the two structures is shown in **Figure 3.8**. The main difference between the two structures is the presence of bipy in compound **11,** at coordination sites which are occupied by either DMF or water in compound **5**. The bipy linker pillars between adjacent layers of the structure, binding neighbouring SBU chains at right angles to one another.

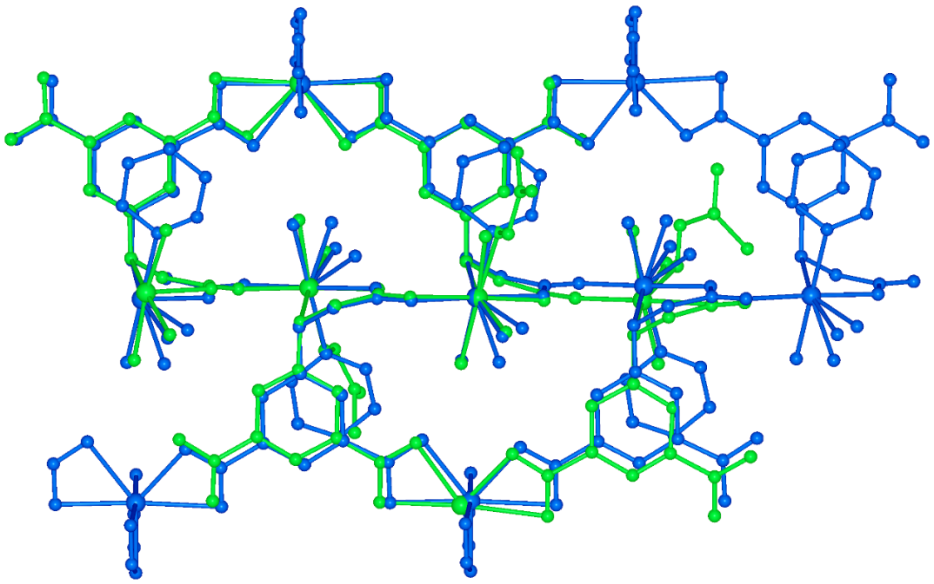

Figure 3.8. An overlay of part of the structures of compound **5** (green) and compound **11** (blue).

The structure contains channels in between the chain SBUs in each of the layers. These channels run both in the direction of the *a*-axis and *b*-axis as can be seen in **Figure 3.9**. The channels are linked to one another, forming a convoluted network of cavities inside the framework. These voids and channels are where the disordered guest solvent resides.

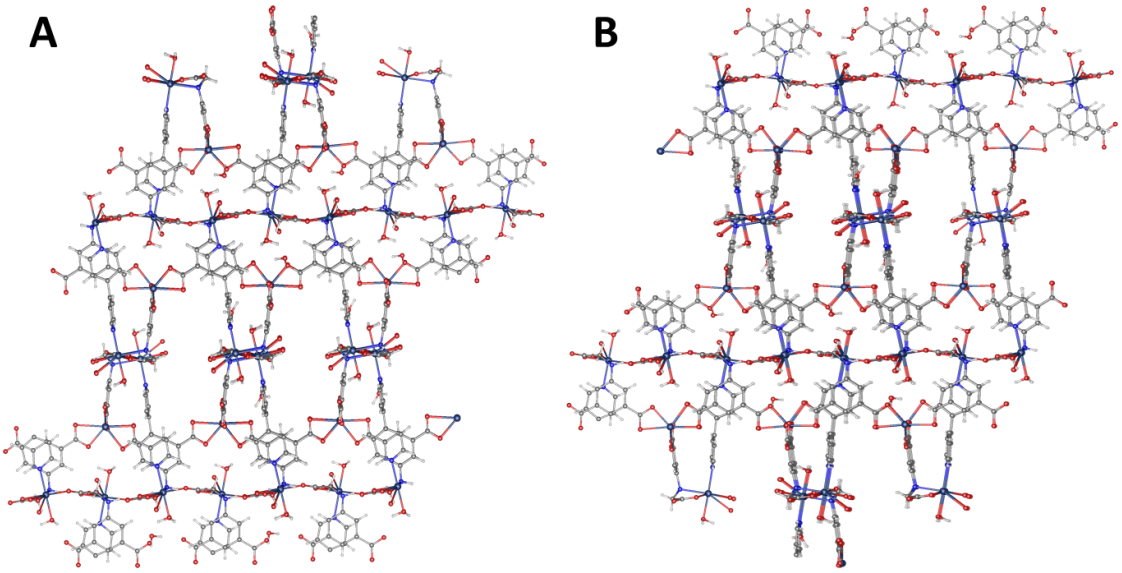

Figure 3.9. The structure of compound **11** viewed down the **A** - *a*-axis and **B** - *b*-axis.

Guest solvent was located in pores of the structure and equated to 1 DMF and 2 water molecules per asymmetric unit. Due to its disordered nature it was ultimately treated using a solvent mask. The assignment of this guest solvent was corroborated by elemental microanalysis (CHN), for which the theoretical expected value was: C 33.47%, H 4.21%, N 6.50%. This matches very closely to the values found experimentally: C 33.59%, H 3.93%, N 6.46%.

The thermogravimetric analysis, shown in **Figure 3.10**, showed three mass loss events centred at 90 °C, 112 °C and 158 °C, which had a total mass loss of 13.5%. Between 190 °C and 320 °C there is gradual loss of an additional 5.25% mass. The guest solvent makes up 19.7% of the mass of the framework so the TGA results suggest that some of the guest solvent remains in the framework up until the framework decomposition at 320 °C.

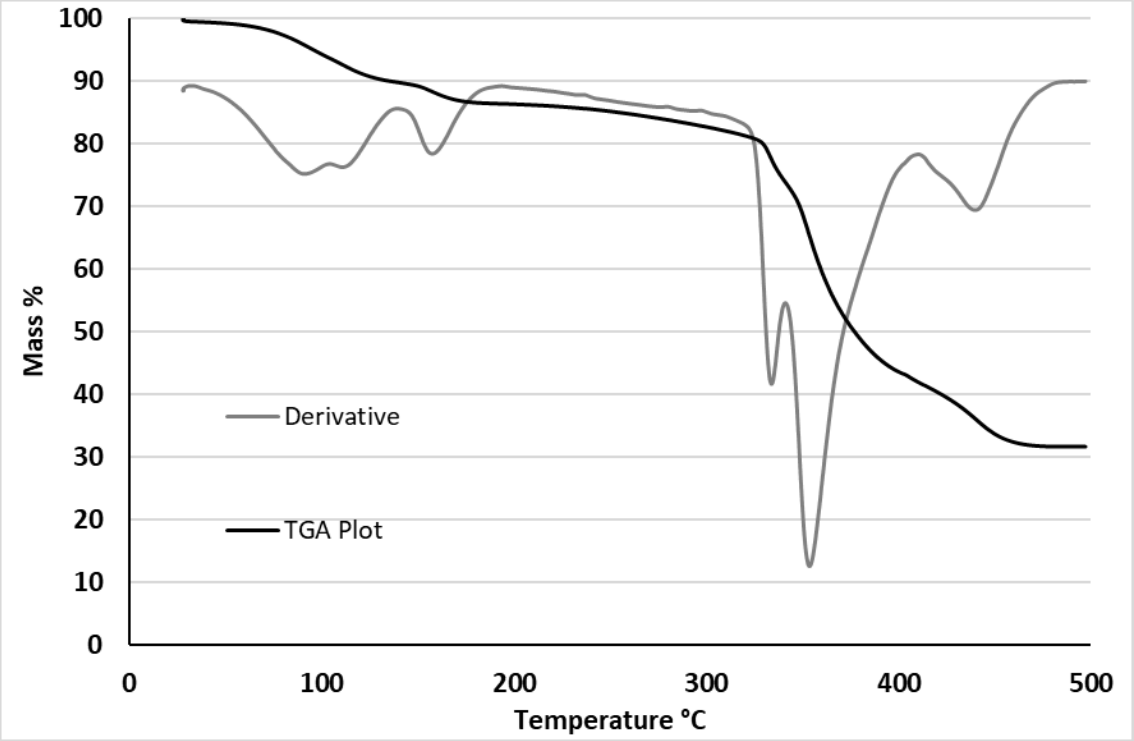

Figure 3.10. The thermogravimetric analysis for compound **11**.

While attempting to activate the compound it was noticed that when heating at 90 °C for 24 hours the material changed colour from colourless to yellow. This prompted further investigation into what had caused the colour change. The PXRD pattern for the yellow 'activated' sample is shown in **Figure 3.11** alongside the pattern for as-synthesised compound **11.** The patterns are almost identical suggesting that the gross structure of the framework remains intact on heating at 90 °C. There is a slight loss of crystallinity evidenced by the broadening of some of the peaks.

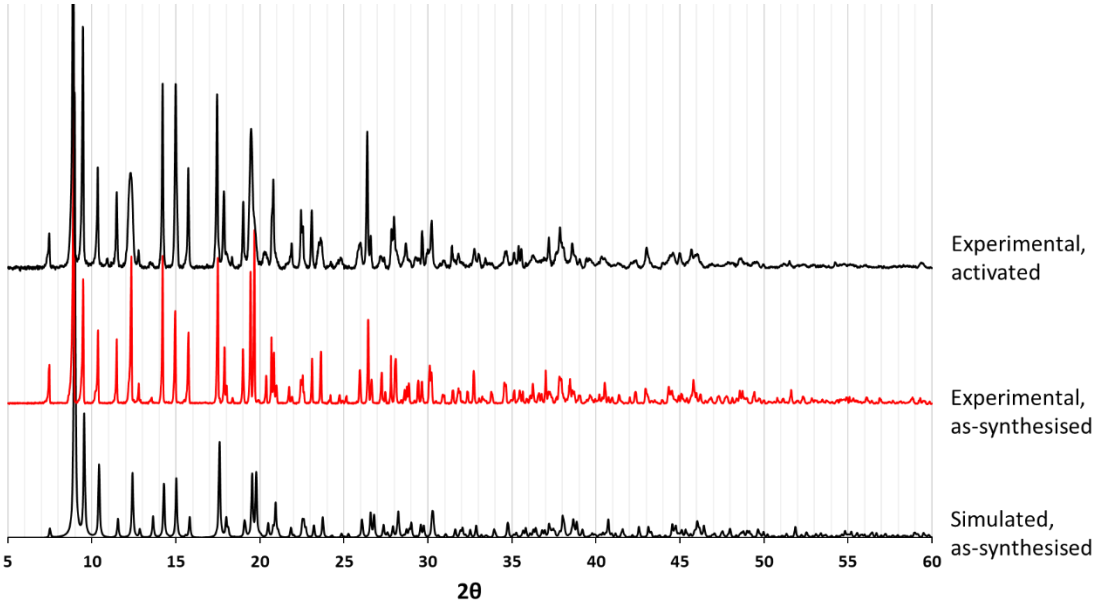

Figure 3.11. The simulated and experimental PXRD patterns for compound **11**, along with the pattern for the 'activated' material.

In order to assess whether the guest solvent in the pores was still present, a single-crystal of the yellow 'activated' compound **11** was selected for X-ray analysis. The activation process had caused significant degradation of the single-crystals, which had cracked and fragmented. Data were collected for a small yellow tablet, the quality of which were less than optimal, nonetheless, the structure was still resolved.

The unit cell for the yellow material, referred to as compound **11-A,** is slightly smaller than compound **11**. The structure was solved in the space group $P4_12_12$, while compound **11** was solved in $P4_32_12$. The asymmetric unit, shown in **Figure 3.12**, contains one full occupancy and one half occupancy cadmium centre, one cmai linker, half a bipy ligand, one water ligand and one DMF ligand with one guest water. This gives compound **11-A** the formula $[Cd_3(cmai)_2(bipy)(H_2O)_2(DMF)_2]\cdot 2H_2O$.

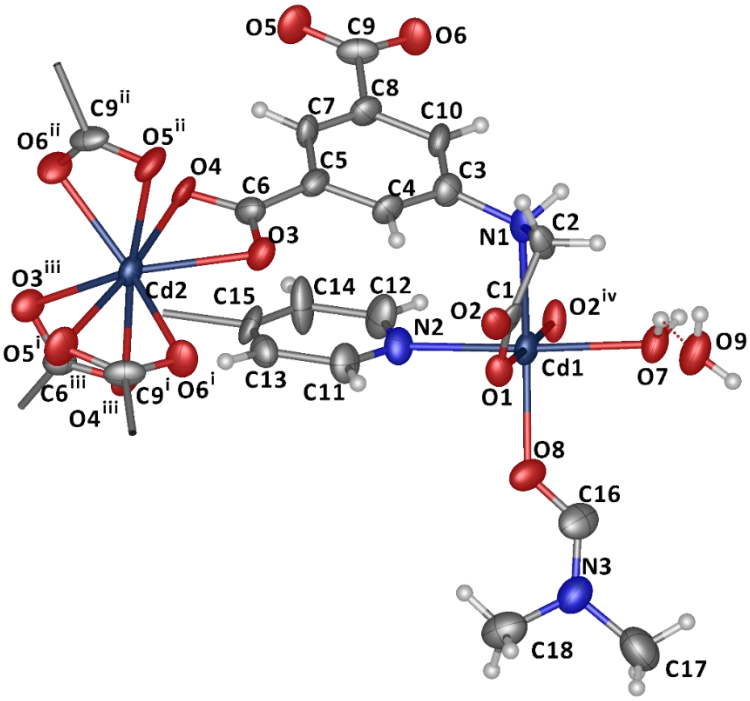

Figure 3.12. The asymmetric unit and cadmium coordination spheres in compound **11-A**. (i, *x*, 1 + *y*, *z*; ii 1 – *x*, – *y*, 3/2 – *z*; iii, 1 – *x*, 1 – *y*, 3/2 – *z*; iv, 1/2 – *x*, – 1/2 + *y*, 5/4 – *z*) (ADPs represented at 30% probability).

In contrast to the structural refinement for as-synthesised compound **11** there was no evidence of disordered solvent within the pores of **11-A**. The other difference is that compound **11-A** contains a DMF ligand on Cd1, whereas in the as-synthesised material, this coordination site was occupied by disordered water ligands. This suggests that during the 'activation' process a ligand exchange occurs on Cd1, exchanging water for DMF. Interestingly it appears that the guest water based on O9 has sufficiently strong hydrogen bonds that it is retained in compound **11-A**.

A simulated PXRD pattern for **11-A** was compared to the experimental trace collected for the bulk material. These traces can be seen in **Figure 3.13** and unsurprisingly the two match very closely showing that the structural solution is representative of the bulk material.

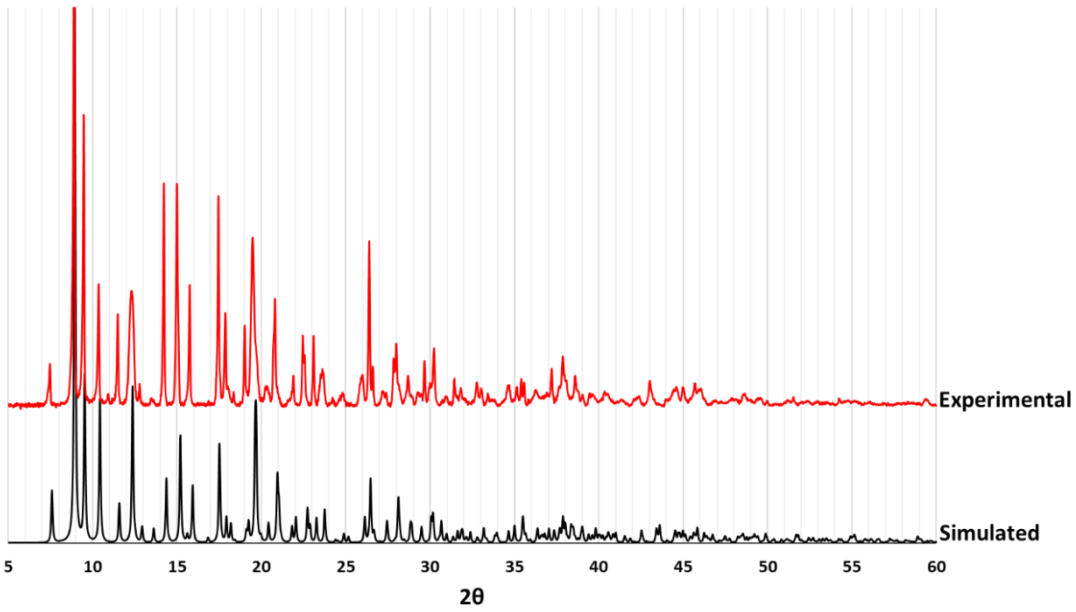

Figure 3.13. The PXRD pattern of compound **11-A** simulated from the single-crystal data and the experimental pattern.

The solvent remaining in **11-A** was interrogated further using TGA, the plot of which is presented in **Figure 3.14**. The analysis revealed one mass loss event between 30 – 210 °C equating to 15.4% of the mass of the material. The removal of one DMF and two water molecules per asymmetric unit equates to a mass loss of 18.4% (i.e. all the water and DMF molecules found in the crystal structure), whereas the removal of one DMF and one water molecule equates to a mass loss of 15.4%. This suggests that one water molecule remains in the framework up to the decomposition temperature of 320 °C. This is consistent with the TGA results for compound **11**, which also suggested that some solvent remains in the framework until decomposition.

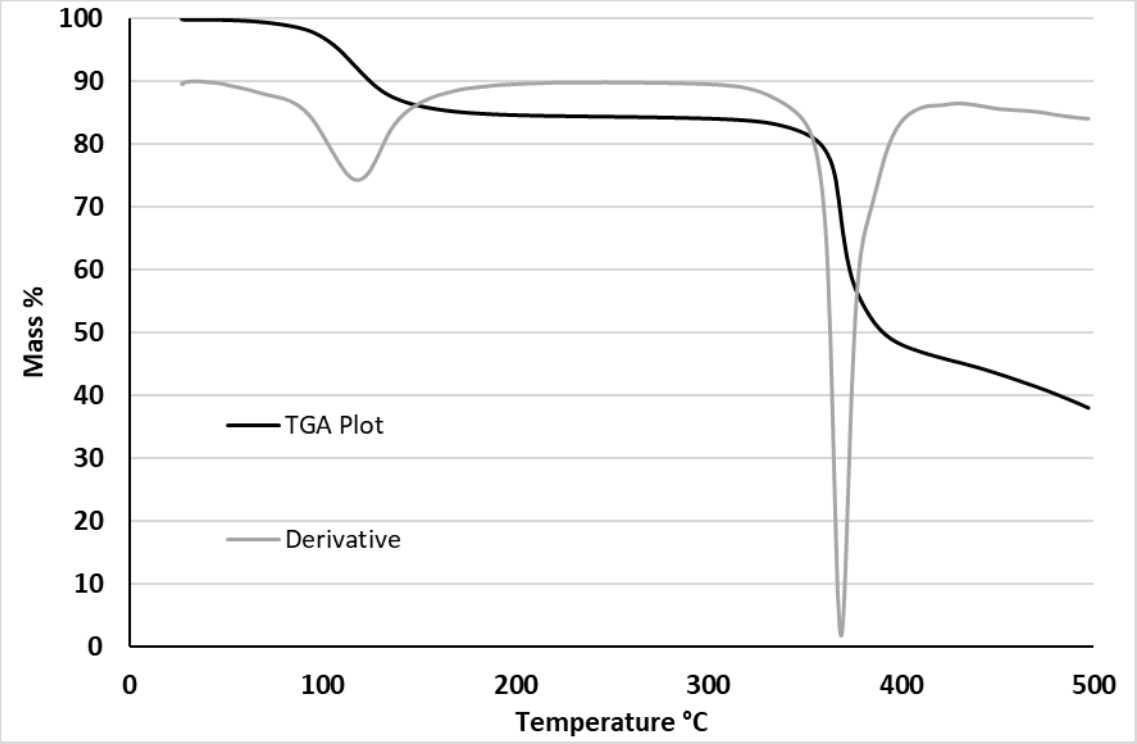

Figure 3.14. TGA plot for compound **11-A**.

In order to see if the water-DMF ligand exchange was reversible a sample of compound **11-A** was submerged in water for 24 hours. After this time the material had changed colour from yellow to colourless, suggesting it had reverted to the structure of compound **11**. The PXRD pattern of the re-hydrated material is presented in **Figure 3.15** alongside the experimental pattern for the compound **11** and compound **11-A**. The pattern is very similar showing the overall structure of the framework remains unchanged. The peak at 19.5° (circled in blue in **Figure 3.15**) may be an indicator of the presence of the disordered water ligands on Cd1 in compound **11**. It is present in the simulated and experimental patterns for **11** but has considerably less intensity in the simulated and experimental patterns for compound **11-A**. This feature of the material's diffraction needs to be further studied to confirm its use in detection of ligand exchange.

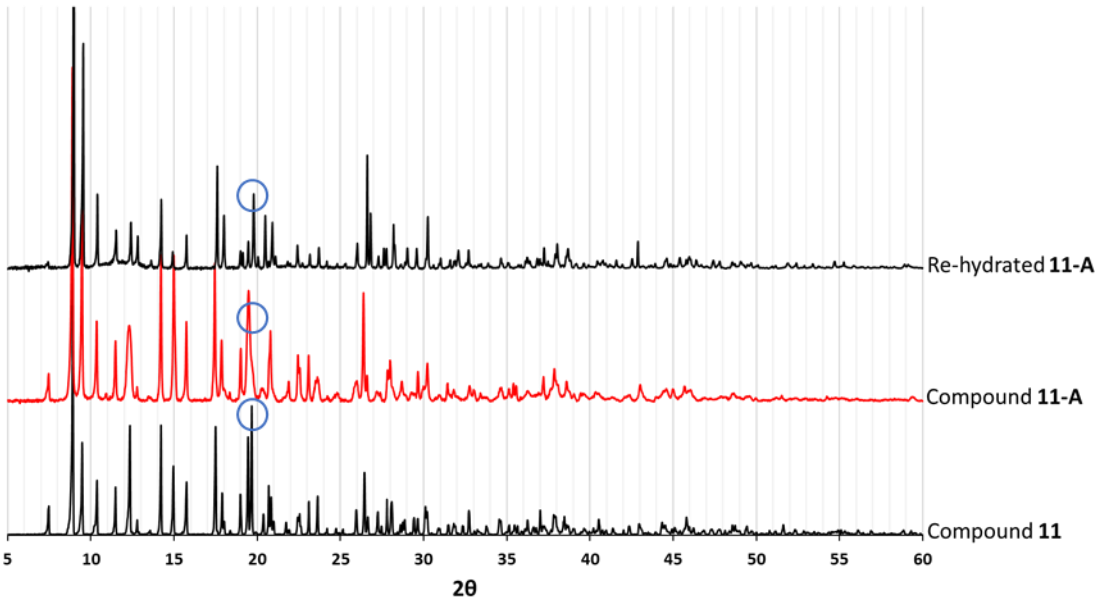

Figure 3.15. The experimental PXRD patterns for compound **11**, **11-A** and the material collected after re-hydration of compound **11-A**

Void space analysis was conducted on compound **11** to assess the potential space that could be utilised inside the framework if all the solvent were removed whilst maintaining the framework structure. As can be seen from **Figure 3.16**, the voids form convoluted channels running throughout the crystal lattice and represent 35% of the volume of the structure.

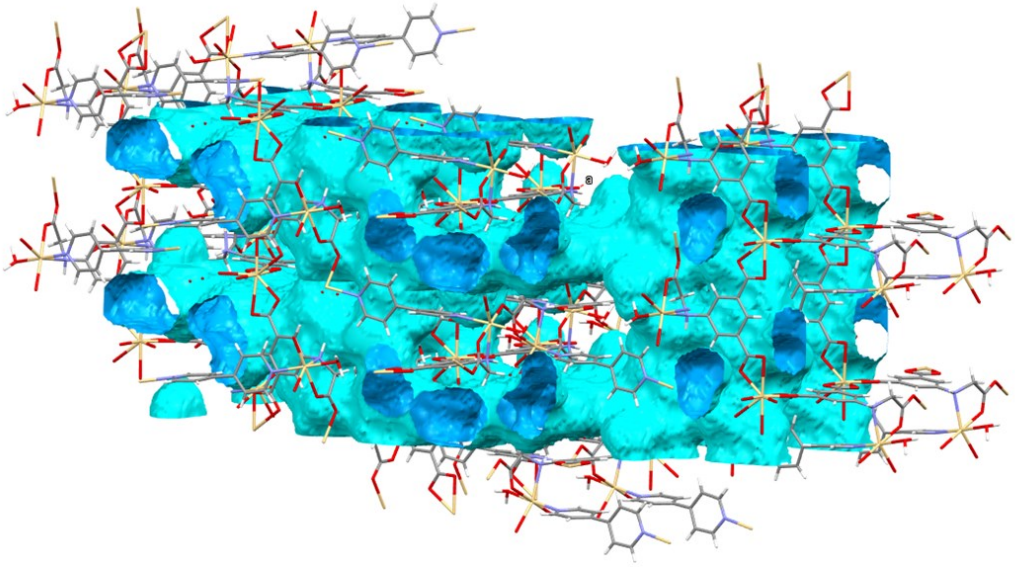

Figure 3.16. The voids in the structure of compound **11**.

The role of bipy in the structure of compound **11** can be interrogated by comparison with compound **5**. **Figure 3.17** shows a portion of the two structures with some of the DMF solvent

and hydrogen atoms removed for clarity. It can be seen that the structures are topologically identical other than the bipy linkers which are highlighted in green in **Figure 3.17 B**. This suggests that the bipy ligand does not play a key role in the formation of the base MOF structure.

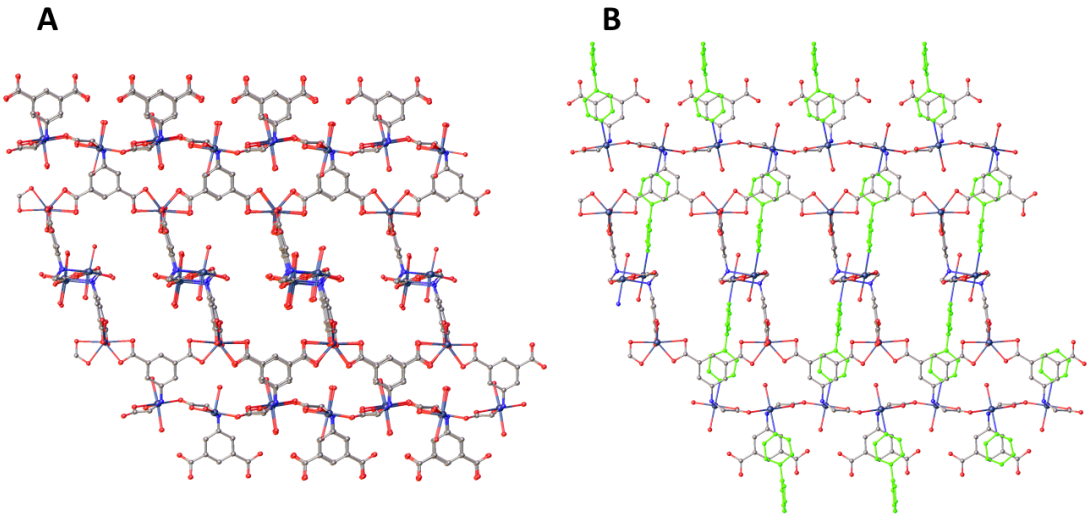

Figure 3.17. A – Structure of compound **5** with DMF ligands and hydrogen atoms hidden for clarity. **B** – Structure of compound **11** with hydrogen atoms hidden and bipy linkers highlighted in green.

The importance of the bipy ligand is realised when activating the materials. In the case of compound **5**, the application of even very mild heat led to complete breakdown of the framework. In contrast, application of heat on compound **11** led to the formation of an activated form, **11-A**. This suggests that although the bipy had little influence on the base structure of the MOF, its pillaring between layers stabilises the framework, allowing for some solvent to be removed without loss of the underlying structure. The bipy does not increase the porosity or surface area but it does allow for it to be accessed.

The additional bipy ligands in compound **11** would be thought to reduce the size of the channels inside the MOF. However, when conducting void space analysis for compounds **5** and **11**, they have percentage void volumes of 32% and 35% of their respective unit cells. The higher value for compound **11** is due to the number of bulky DMF ligands in compound **5** which take up more space in total than the bipy linkers.

3.2.2 The synthesis and characterisation of $[Cd_2(Hcmai)_2(bpe)]\cdot 2DMF$ (**12**)

Compound **12** was formed from the reaction between $Cd(OAc)_2\cdot 2H_2O$, H_3cmai and bpe in 4:4:1 mixture of DMF, water and 1M HNO_3. The reaction was carried out at 90 °C for 18 hours, during which colourless long block crystals had formed. After collection via vacuum filtration and washing with deionised water a suitable crystal was selected for single-crystal X-ray diffraction analysis.

Compound **12** crystallises in the triclinic space group *P*-1. The asymmetric unit, which is shown in **Figure 3.18**, comprises of one cadmium centre, one doubly deprotonated Hcmai linker, half a bpe linker, and one guest DMF molecule which is disordered over two positions.

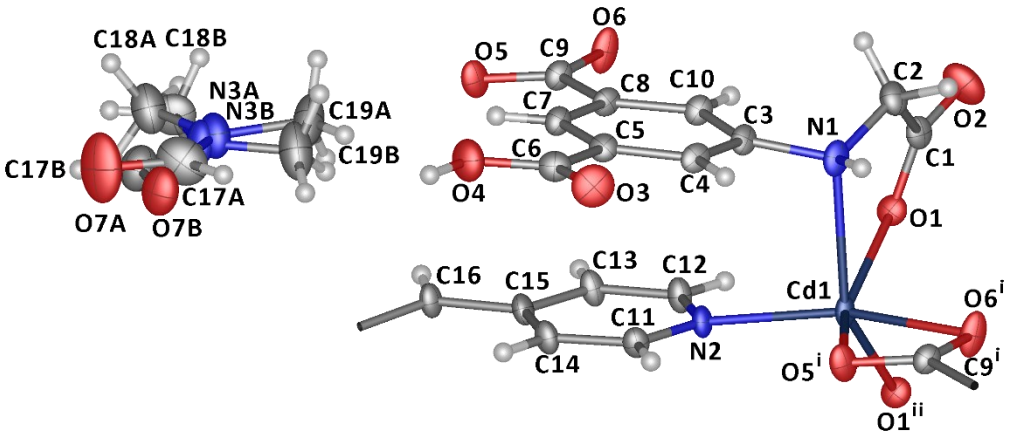

Figure 3.18. The asymmetric unit of compound **12**, along with the coordination sphere of the cadmium centre. (i, 1 + *x*, + *y*, + *z*; ii, 2 – *x*, 2 – *y*, – *z*)(Atomic displacement parameters are represented at 50% probability).

The SBU of compound **12** is a cadmium dimer, formed by the interaction of two Cd1 centres and the flexible arms of two Hcmai linkers. The linkers each bond to a Cd1 centre in a κ^2 bidentate manner through N1 and O1. O1 is also bound to the other Cd1 centre in a μ_2 bridging mode interaction, as can be seen in **Figure 3.19**.

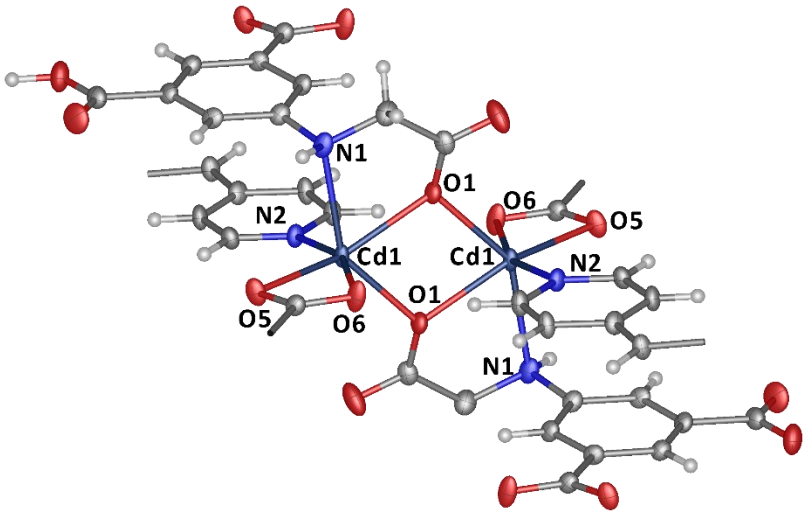

Figure 3.19. The cadmium dimer SBU and surrounding atoms in compound **12**.

The SBUs are connected into 1-D tapes by virtue of the Hcmai linkers, as shown in **Figure 3.20**. The tapes propagate in the direction of the *a*-axis via coordination through the flexible arm on one side of the linker and also through a carboxylate, based on O5 and O6. Each SBU is bound to the adjacent two SBUs in the tape, with two Hcmai ligands forming each link.

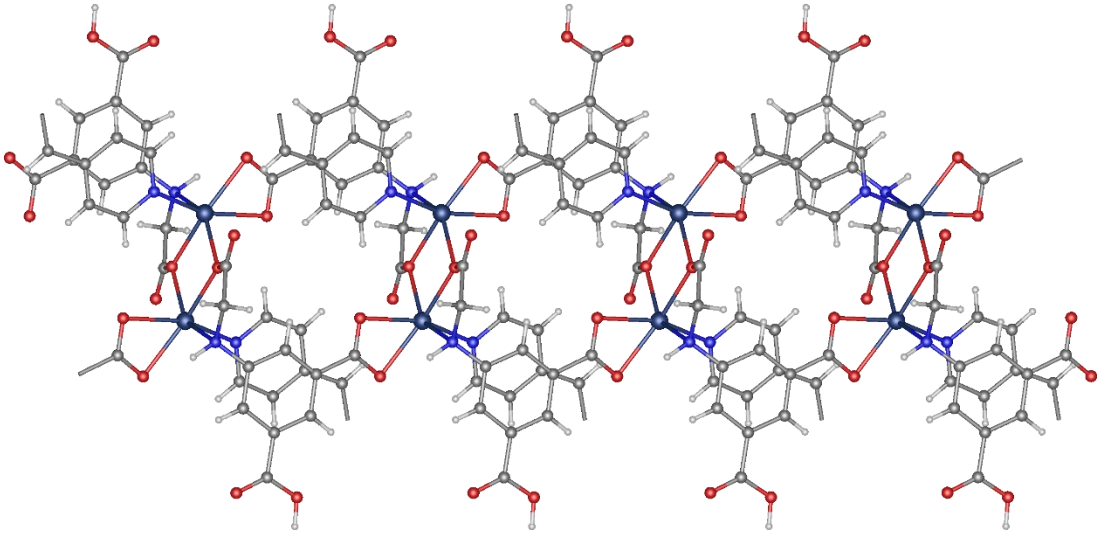

Figure 3.20. The 1-D tapes formed between the cadmium dimer SBUs and Hcmai linkers in compound **12**.

The bpe linkers connect adjacent tapes into 2-D sheets. The sheets sit parallel to the *ab*-plane in the structure, one of these is shown in **Figure 3.21**.

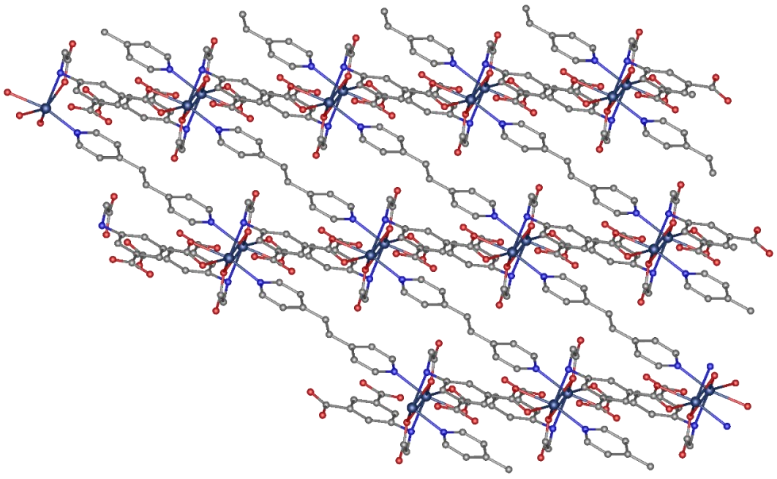

Figure 3.21. A 2-D sheet in compound **12**. Hydrogen atoms have been removed for clarity.

The sheets stack to form the gross structure. Two sheets are shown in **Figure 3.22**, viewed looking down the *a*-axis, the guest DMF can be seen in the channels formed between sheets. Compound **12** contains two distinct hydrogen bonds both involving the carboxylic acid on the Hcmai linker, these can be seen in **Figure 3.22**. The guest DMF, which is disordered over two positions in a ratio of 0.55:0.45, accepts a hydrogen through O7A/O7B from the carboxylic acid donor, O4–H4. Both the orientations of DMF molecule form hydrogen bonds with the same carboxylic acid. The second hydrogen bond in the structure is donated from the secondary amine N1–H1 and accepted by the carbonyl carboxylic acid oxygen O3, and this serves to connect adjacent sheets in the structure.

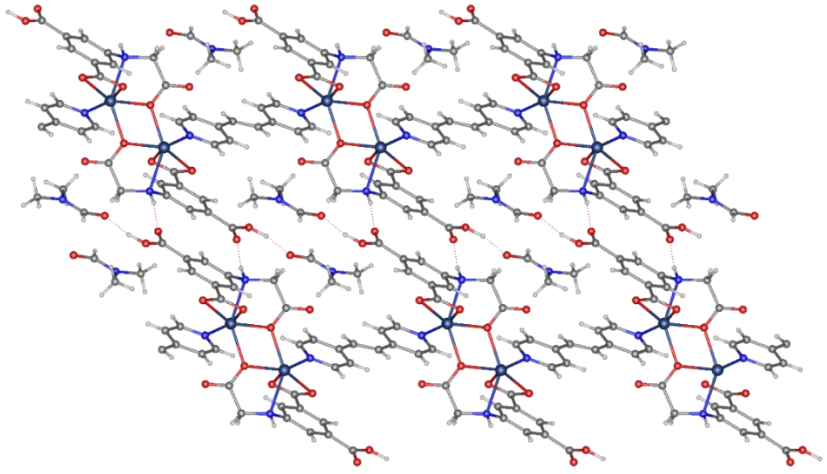

Figure 3.22. The guest DMF in compound **12**, showing hydrogen bonding between layers of the framework and solvent. Only one orientation of the DMF guest is shown for clarity.

Analysis of **12** with the guest DMF molecules removed revealed that the potential void space in the 'activated' MOF is in the region of 26% of the structure volume. The depiction of this space

can be seen in **Figure 3.23** and shows that the voids take the form of channels in the structure in the direction of the *a*-axis.

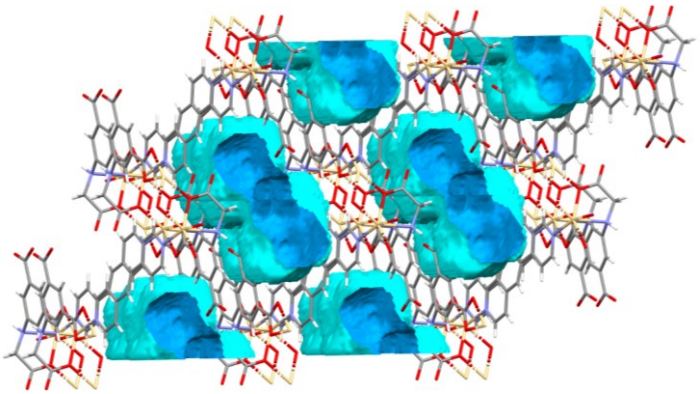

Figure 3.23. The potential void space in compound **12**.

Attempts to activate compound **12** were unsuccessful even under very forcing conditions such as heating at 180 °C for 24 hours and heating at 150 °C under reduced pressure for 24 hours. Solvent exchange with methanol and chloroform were also unsuccessful in removing the DMF molecules from the pores. None of the treatment had any noticeable effect on the PXRD pattern for the material; the framework retaining its structure and DMF guest solvent molecules. The reason for this becomes apparent when looking at the TGA data shown in **Figure 3.24**. There is less than 2% mass loss between 30 °C and 275 °C and the removal of the guest DMF, in the event centred around 300 °C, is almost immediately followed by framework decomposition. The very high temperature needed to remove the guest DMF in the TGA is an indication of the strength of the guest's interaction with the framework and is likely why the activation attempts failed.

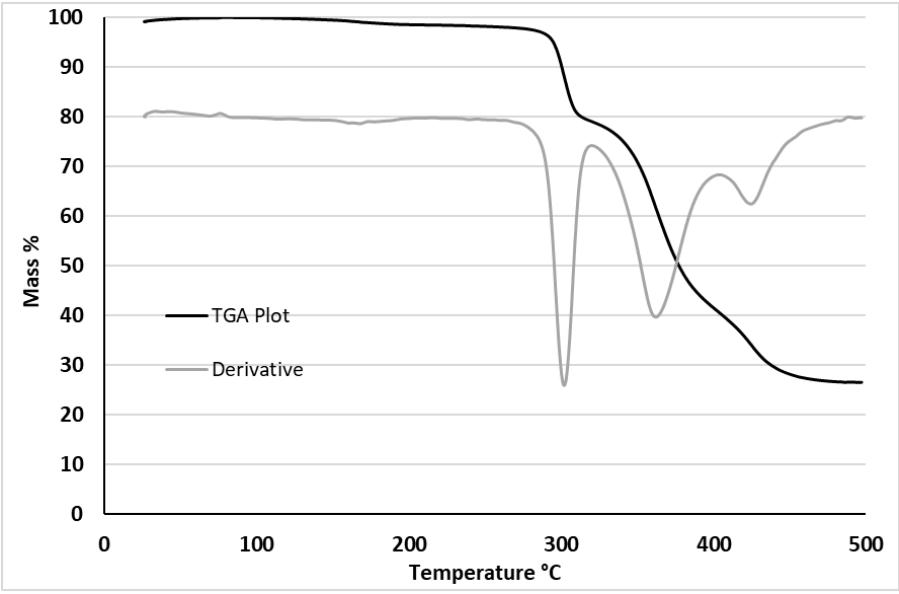

Figure 3.24. The thermogravimetric analysis for compound **12**.

3.2.3 The synthesis and characterisation of $[Cd_3(cmai)_2(bpe)_2(H_2O)_3]\cdot 6H_2O$ (**13**)

Compound **13** was synthesised from the reaction between $Cd(OAc)_2\cdot 2H_2O$, H_3cmai and bpe in water at 90 °C for three days and formed as small colourless block crystals. A crystal suitable for single-crystal X-ray diffraction was selected for analysis. The data were integrated to account for twinning in the crystal, in a 51:49 ratio by virtue of a 180° rotation about the *b*-axis.

The structure of compound **13** was solved in the monoclinic space group *C*2/*c*. The asymmetric unit contains one full occupancy and one half occupancy cadmium centre, one cmai linker, one bpe linker, one and a half water ligands, and three guest water molecules, one of which is disordered over two positions. The asymmetric unit along with the cadmium coordination spheres are shown in **Figure 3.25**.

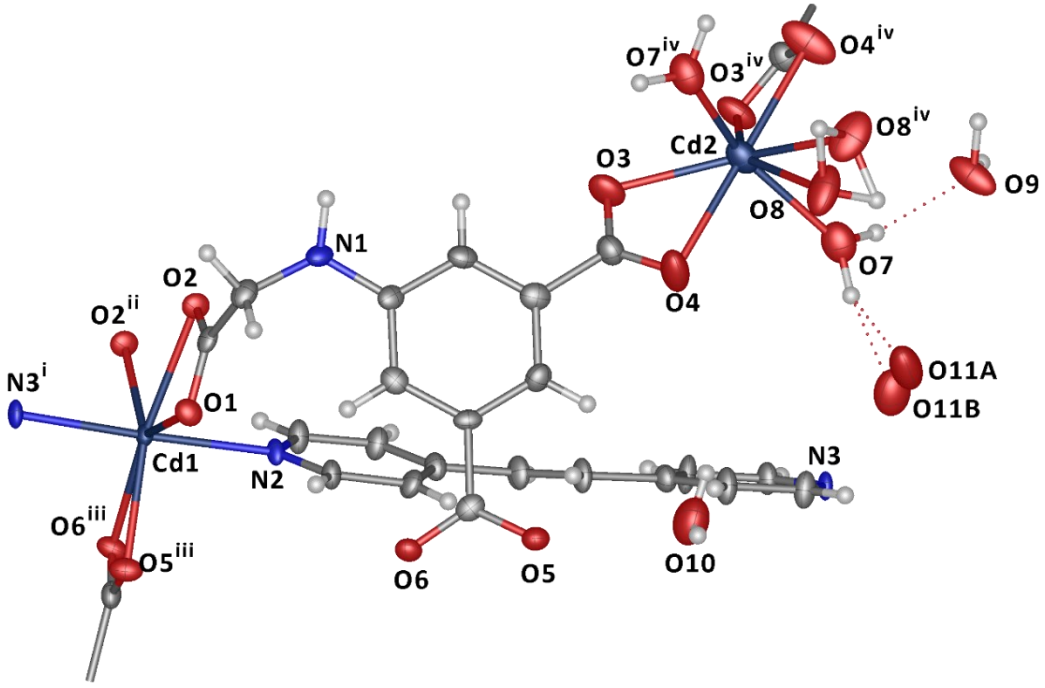

Figure 3.25. The asymmetric unit with cadmium coordination spheres in the structure of compound **13**. (i, – 1/2 + *x*, 1/2 + *y*, + *z*; ii, 1/2 – *x*, 3/2 – *y*, 1 – *z*; iii, 1/2 – *x*, 1/2 + *y*, 1/2 – *z*; iv, 1 – *x*, + *y*, 3/2 – *z*) (Atomic displacement parameters are presented at 50% probability).

Cd1 is 7-coordinate and pentagonal bipyramidal in geometry. It is coordinated by three cmai linkers and two bpe linkers. The first cmai ligand coordinates in a κ^2 mode via the carboxylate on the flexible arm of the linker, based on O1 and O2. The O2 atom is also part of a μ_2 bridging mode interaction to a second Cd1 centre, which is how the second cmai linker binds. The final cmai ligand coordinates in a κ^2 mode through the carboxylate based on O5 and O6. The axial coordination sites are each occupied by a bpe linker, binding through N2 and N3 respectively.

Cd2 is half occupancy and resides on a 2-fold rotation axis running in the direction of the *b*-axis. It is 7-coordinate and is bound by two cmai linkers and three water ligands, one of which is disordered over two positions. The two cmai ligands both coordinate in a κ^2 mode through the carboxylate based on O3 and O4 and are related by 2-fold rotation. Two of the water ligands are based on O7 and are also related by the rotation. The final water ligand based on O8 is disordered over two positions. It is half occupancy in the asymmetric unit and resides just off of the rotation axis, which generates the second position.

The SBU in compound **13** is a cadmium dimer, containing two Cd1 centres as shown in **Figure 3.26**. The dimer is formed by virtue of the μ_2 bridging mode from O2 atoms of two different cmai linkers.

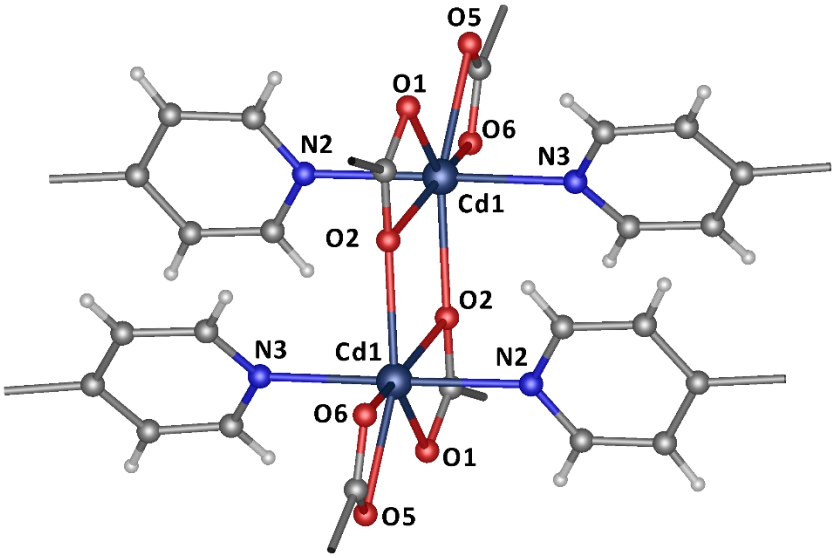

Figure 3.26. The Cd1 dimer SBU in compound **13**.

The SBU involves four different cmai ligands, each of these linkers binds to an adjacent SBU. Considering only these ligands and the SBU a 2-D square network is produced as shown in **Figure 3.27**.

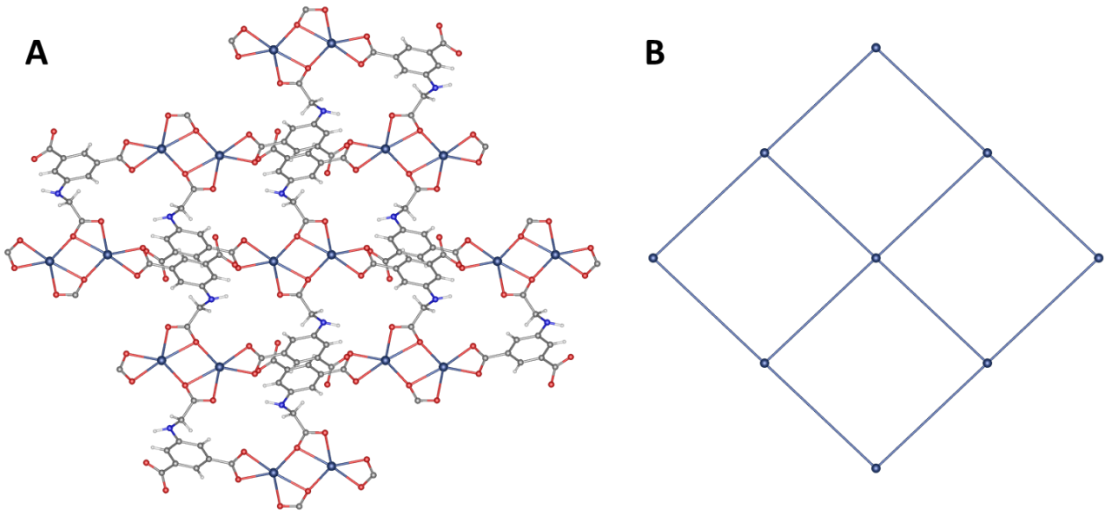

Figure 3.27. A - The square based topology formed by the interaction of the Cd1 dimer SBU and cmai ligands in compound **13**. **B** – The reduced net for this square topology.

Each of the 4 cmai ligands also coordinates to a Cd2 centre. This serves to bridge adjacent sheets together into a 3-D network. **Figure 3.28** shows the 3-D structure with the SBU sheets highlighted in blue, the Cd2 centres can be seen halfway between each layer bridging them via cmai linkers. The bpe ligands also perform a similar function within the structure. Each SBU is bound to an SBU in the layers above below by a pair of bpe linkers. These can be seen in **Figure 3.28** binding the layers at two different angles.

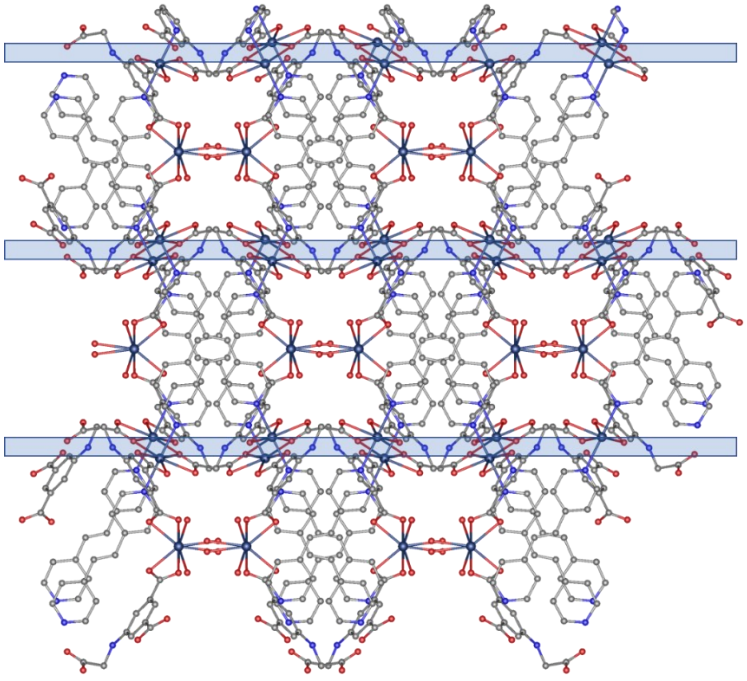

Figure 3.28. The 3-D structure of compound **13** as viewed down the *b*-axis. The layers formed by the SBU and cmai interaction are highlighted by the blue bars. (Hydrogen atoms and guest solvent molecules have been removed for clarity).

It can be seen in **Figure 3.28** that small channels exist between the SBU layers, around the Cd2 centres, this space is occupied by the guest solvent. There are a total of three guest water molecules per asymmetric unit based on O9, O10 and O11. The water based on O11 is disordered over two positions with equal occupation at each site. Due to the diminished amount of electron density associated with the half occupancy hydrogen atoms those associated with O11A and O11B were not modelled. The structure contains a total of seven unique hydrogen bonds, all of which involve the guest water molecules.

The interaction of the guest water with the framework was probed further using thermogravimetric analysis, the results of which can be seen in **Figure 3.29**. The mass loss between 30 °C and 180 °C is 9.5% which suggests that 3.5 molecules of water per asymmetric unit are lost from the structure, equating to 0.5 molecules of coordinated water plus the guest water. The remaining coordinated water presumably remain part of the framework until the next mass loss event begins at 270 °C and is concurrent with breakdown of the framework.

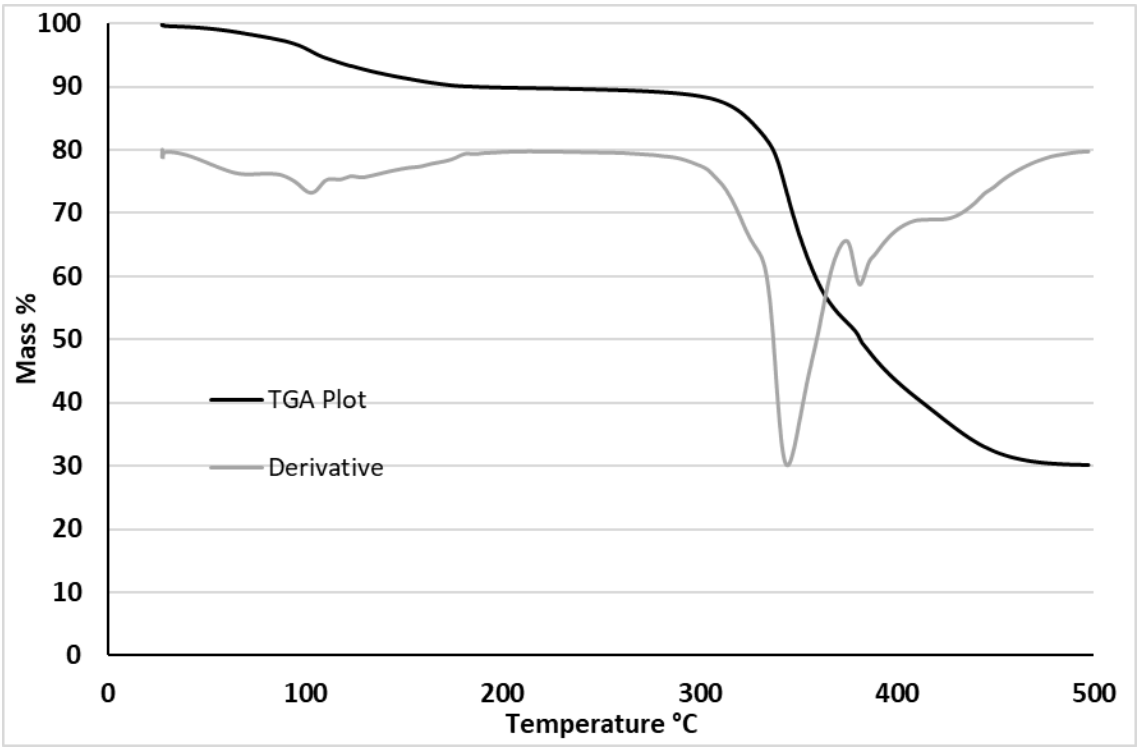

Figure 3.29. Thermogravimetric analysis of compound **13**.

The amount of potential void space in the structure of **13** was probed after removing the guest water molecules and interrogating the cavities that remain. These revealed that the only space remaining were the exact positions of the water molecules removed for the analysis and equated to just 2.5% of the structure volume.

3.2.4 The synthesis and characterisation of $[Cd_2(cmai)(bpe)_2]NO_3 \cdot DMF$ (**14**)

Compound **14** was synthesised in the reaction between $Cd(NO_3)_2 \cdot 4H_2O$, H_3cmai and bpe in a mixture of DMF, water and 1M HNO_3. The synthesis was carried out at 90 °C for 36 hours and yielded colourless block crystals. A suitable crystal was selected for single-crystal X-ray diffraction analysis.

Compound **14** crystallises in the triclinic space group *P*-1. The asymmetric unit contains two cadmium centres, one cmai linker, two bpe linkers, a nitrate ion and a guest DMF molecule. The framework itself is positively charged and is charge balanced by the presence of a nitrate anion in the pores. The asymmetric unit is shown in **Figure 3.30** along with the coordination spheres of the cadmium centres.

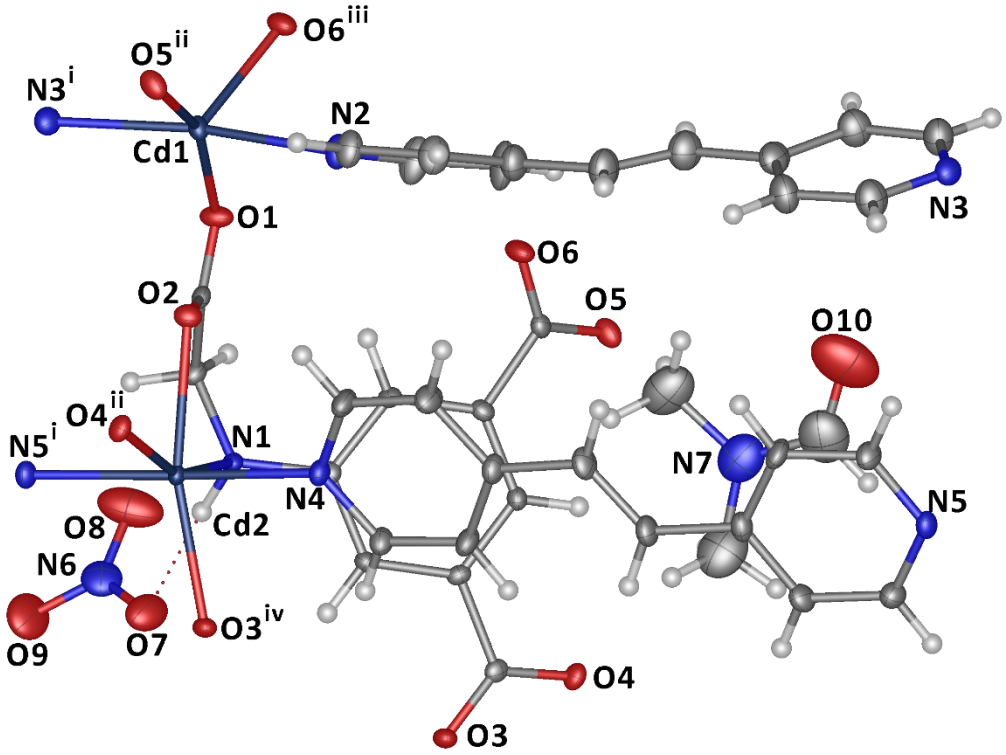

Figure 3.30. The asymmetric unit and cadmium coordination spheres in compound **14**. (i, 1 + *x*, – 1 + *y*, + *z*; ii, 1 + *x*, + *y*, + *z*; iii, 1 – *x*, 1 – *y*, 1 – *z*; iv, 1 – *x*, 1 – *y*, – *z*) (Atomic displacement parameters represented at 50% probability).

Cd1 is 5-coordinate and distorted square pyramidal in geometry (τ_5 = 0.16), with Cd1–O6^{iii} as the axial bond. It is coordinated to three cmai linkers and two bpe linkers. All three of the cmai ligands bond in a κ^1 mode through carboxylate oxygens based on O1, O5 and O6. The two bpe linkers bind through N3 and N4 respectively and sit opposite one another.

Cd2 is 6-coordinate and distorted octahedral in geometry. It is bound by three different cmai linkers and two different bpe linkers. One of the cmai ligands binds in a κ^2 binding mode through N1 and O2 of the flexible arm. The other two coordinate through O3 and O4 respectively, in κ^1 modes. The two bpe molecules bond through N4 and N5 respectively and sit axial to one another.

The SBU in compound **14** is a 1-D chain made up of alternating Cd1-Cd1 and Cd2-Cd2 dimers. The two dimer types share a broadly similar structure as can be seen in **Figure 3.31**.

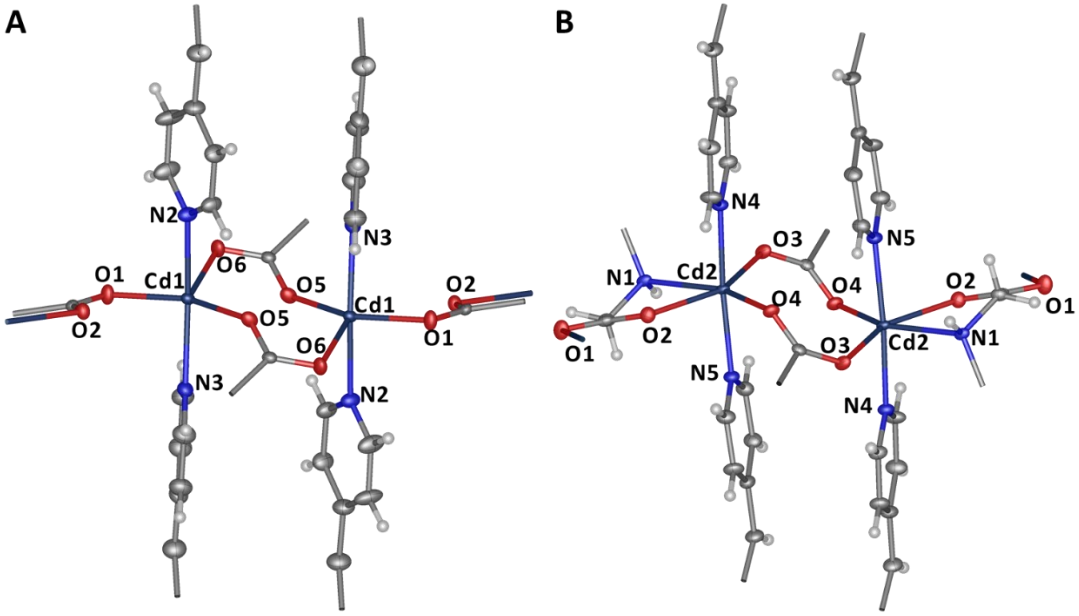

Figure 3.31. A – The Cd1 dimer that forms part of the SBU in compound **14**. **B** – The Cd2 dimer that forms part of the SBU in compound **14**.

Both contain two bridging carboxylates, based on O5 and O6 for the Cd1 dimer and on O3 and O4 for the Cd2 dimer. Both also have bpe ligands at coordination sites approximately 180° from each other, four per dimer. The main difference between the two dimers is that the Cd1 dimer propagates in the structure via O1 whereas Cd2 propagates by a κ^2 interaction involving N1 and O2. These link the dimers together into the chain SBUs like that shown in **Figure 3.32**.

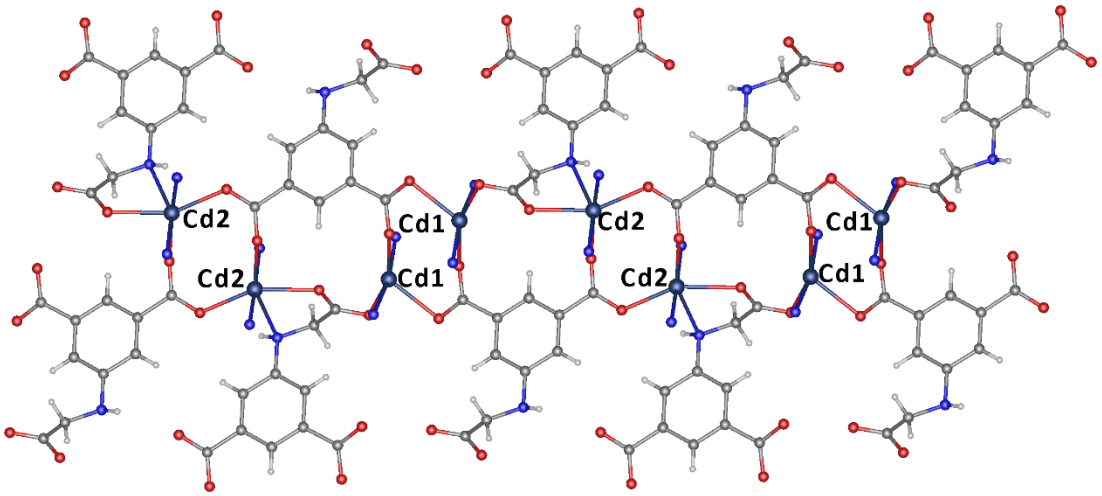

Figure 3.32. The 1-D chain SBU and participating cmai linkers in compound **14,** viewed down the *b*-axis.

The SBU chains are linked together by the cmai linkers forming 2-D sheets which sit parallel to the *ac* plane. One of these sheets is shown in **Figure 3.33** with the chains highlighted in blue.

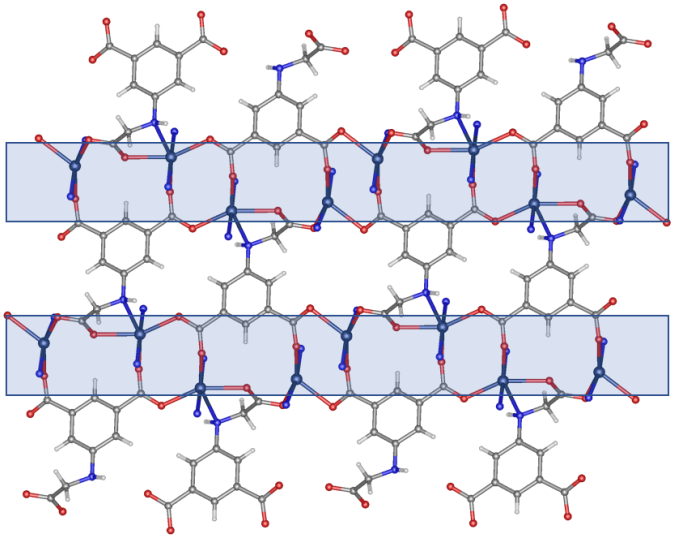

Figure 3.33. The 2-D planes formed by the SBU and cmai linkers in compound **14**, viewed down the *b*-axis. The SBU chains are highlighted in blue.

Adjacent sheets are connected by pillaring bpe linkers into the 3-D network shown in **Figure 3.34**.

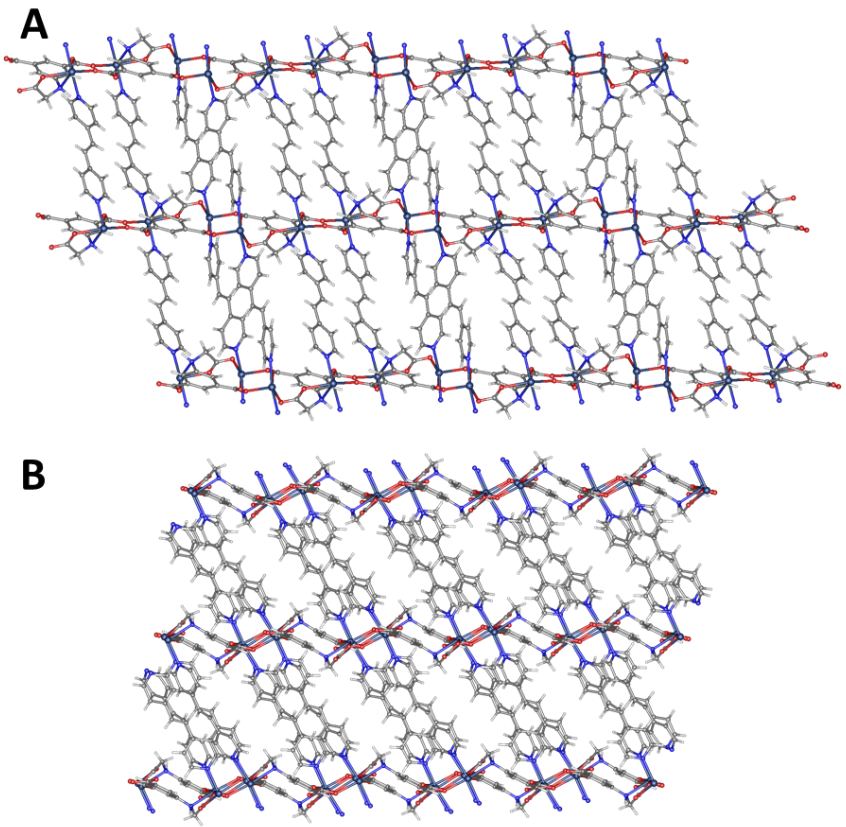

Figure 3.34. The 3-D structure of compound **14** as viewed down the **A** – *a*-axis and **B** – *c*-axis.

Cavities in the structure exist between the cadmium-cmai layers and the pillaring bpe linkers. These are filled by nitrate ions and guest DMF molecules, as shown in **Figure 3.35**. The nitrate ion participates in the formation of the only hydrogen bonds in the structure. N1 from the cmai linker acts as the hydrogen bond donor and O7 of the nitrate ion acts as the acceptor with a H···A distance of 1.929(6) Å, a D···A distance of 2.904 Å and D–H···A angle of 176(2)°.

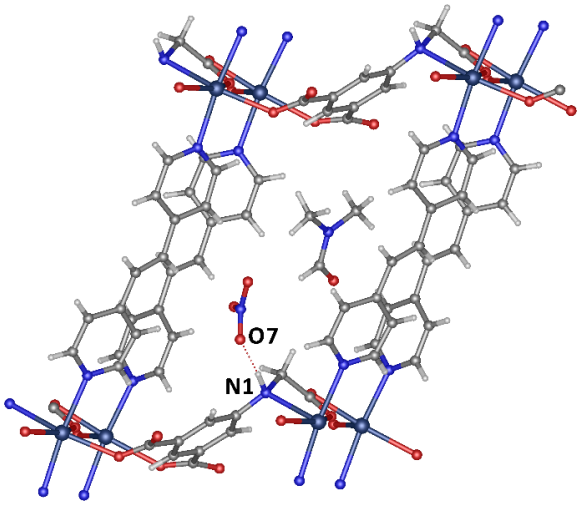

Figure 3.35. The guest DMF and nitrate counter ion in compound **14**.

The thermal behaviour of compound **14** was interrogated using thermogravimetric analysis, the results of which are shown in **Figure 3.36**. The material shows a mass loss event between 175 °C and 275 °C equating to 7.2% of the total mass, this matches well with the loss of a DMF molecule for which the theoretical mass loss is 7.6%. The framework then degrades at temperatures exceeding 300 °C.

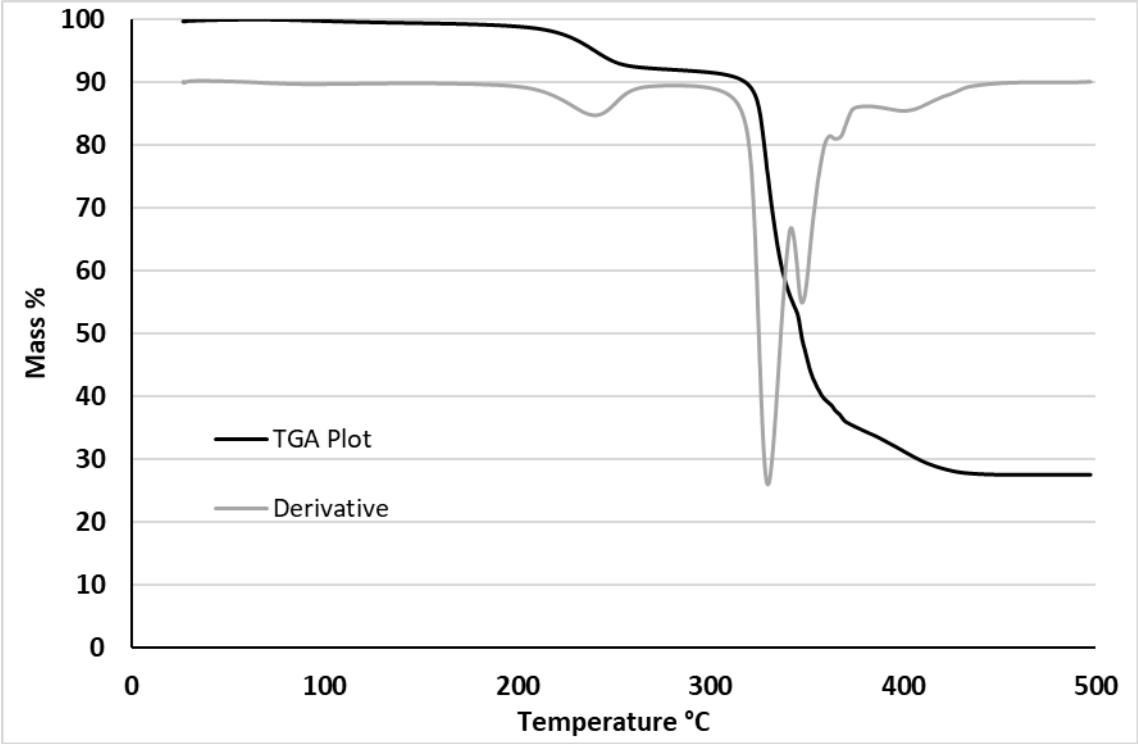

Figure 3.36. The TGA results for compound **14**.

The potential void space of compound **14** was analysed with the guest DMF removed. The analysis showed that the structure contains discrete voids rather than possessing channels. This likely contributes to the high temperature at which the guest DMF was lost in the TGA. The cavities, which can be seen in **Figure 3.37**, represent 15% of the structure volume.

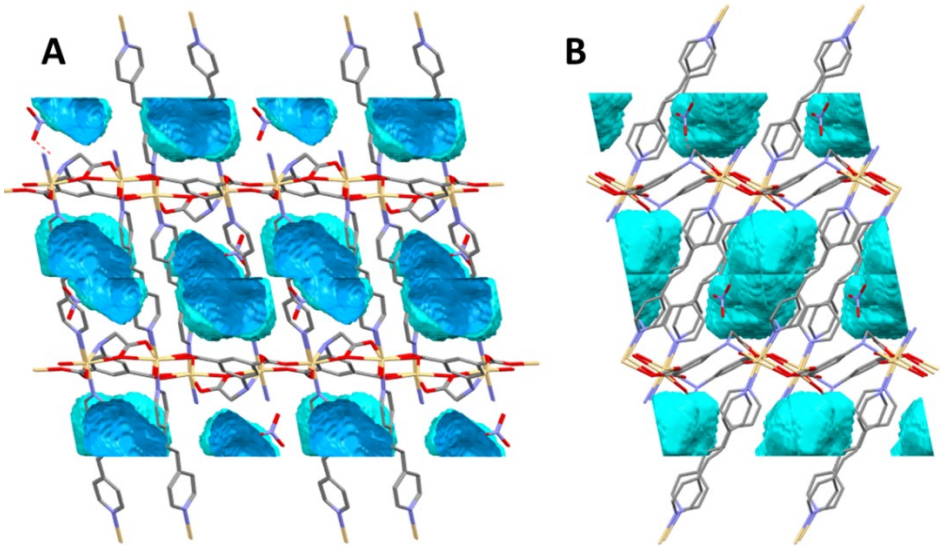

Figure 3.37. The cavities in the pore space analysis for compound **14**, as viewed down the **A** – *a*-axis and **B** – *c*-axis.

3.2.5 The synthesis and characterisation of $[Cd_6(cmai)_4(phen)_6(H_2O)_2]\cdot 12.5H_2O\cdot 0.75DMF$ (**15**)

Compound **15** was formed from the reaction between $Cd(NO_3)_2\cdot 4H_2O$, H_3cmai and 1,10-phenanthroline (phen) in a 1:1 mixture of DMF and water. The reaction was carried out at 90 °C for 48 hours, during which colourless plate crystals formed. After collection via vacuum filtration and washing with distilled water a suitable crystal was selected for single-crystal X-ray diffraction analysis.

The structure of compound **15** was solved in the orthorhombic space group *Pca*2_1. The asymmetric unit, shown in **Figure 3.38**, contains 6 cadmium centres, 4 cmai linkers, 6 phen ligands and two water ligands, one of which is disordered over two sites. There was evidence of guest solvent in the refinement but due to its disordered nature, it was addressed using a solvent mask.

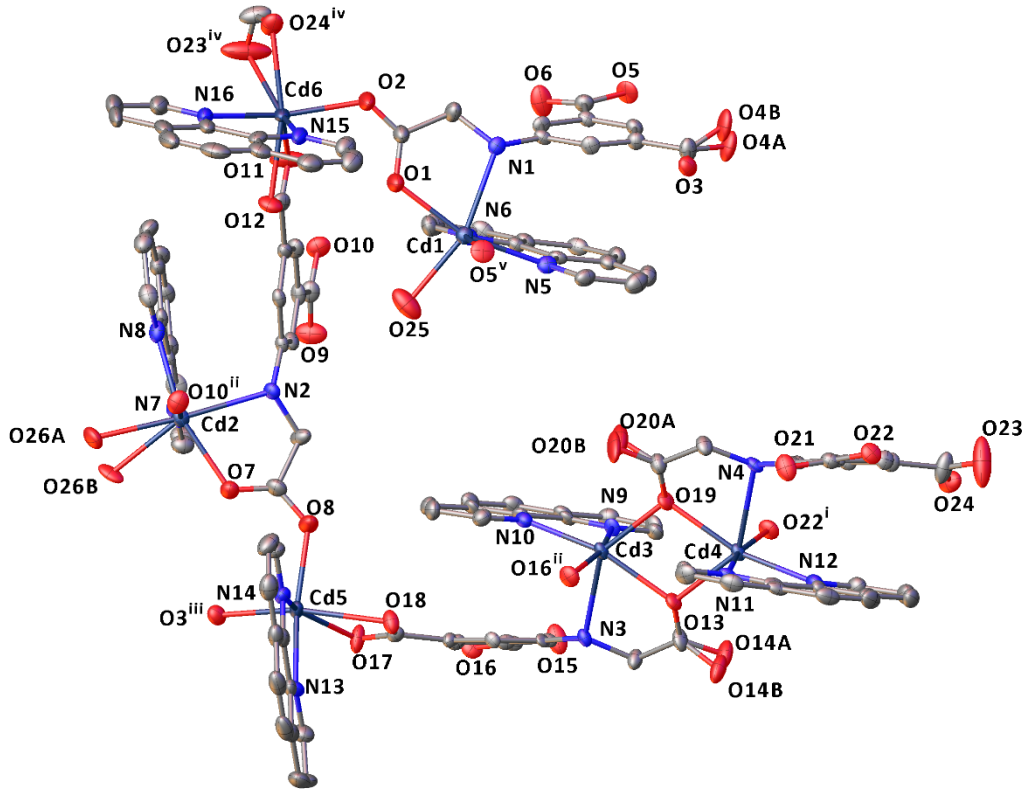

Figure 3.38. The asymmetric unit and cadmium coordination spheres in compound **15**. (i, 1/2 + *x*, 2 – *y*, + *z*; ii, – 1/2 + *x*, 1 – *y*, + *z*; iii, + *x*, – 1 + *y*, + *z*; iv, 1 – *x*, 2 – *y*, – 1/2 + *z*; v, – 1/2 + *x*, 2 – *y*, + *z*). (Atomic displacement parameters are represented at 50% probability).

Although the asymmetric unit is very large there is some pseudo-symmetry present between pairs of cadmium centres. Cd1 and Cd2, which can be seen in **Figure 3.39 A** and **B** respectively, are both 6-coordinate, distorted octahedral in geometry and have the same coordination

environments. They are both coordinated by two cmai linkers, one phen ligand and one water ligand. One of the cmai linkers binds through a κ^2 mode involving the secondary amine nitrogen and carboxylate oxygen of the flexible arm of the linker, while the second binds through a κ^1 mode through an aryl carboxylate, supported by acceptance of a hydrogen bond from the secondary amine. The two centres have a pseudo-enantiotropic relationship, with all cadmium to ligating atom distances being similar. The main difference between the two centres is that the water ligand coordinated to Cd2 based on O26, is disordered over two positions with a 0.7:0.3 occupancy, while the comparative water bonded to Cd1, based on O25 is full occupancy.

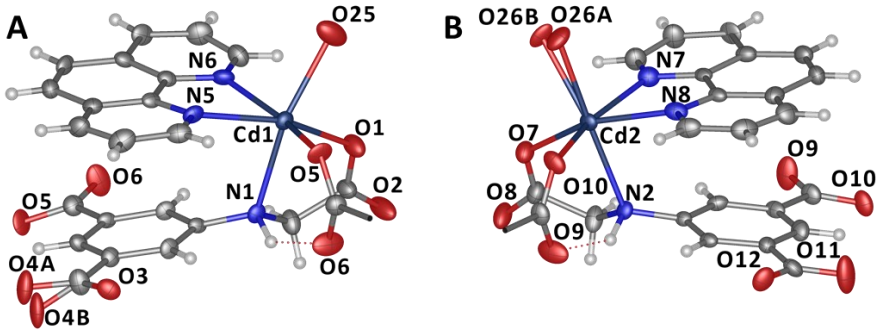

Figure 3.39. The coordination spheres of Cd1 and Cd2 in compound **15**. (Atomic displacement parameters are represented at 50% probability).

Cd3 and Cd4 are both 6-coordinate and are each bound by three cmai linkers and one phen ligand. As with Cd1 and Cd2, there appears to be a pseudo-enantiotropic relationship between the Cd3 and Cd4 coordination spheres, leading to the formation of a dimer which can be seen in **Figure 3.40**. As such, each centre is bound by one cmai linker in a κ^2 mode involving the secondary amine nitrogen and carboxylate oxygen of the flexible linker arm. This carboxylate oxygen (O13 and O19) is also part of a μ_2 interaction bridging between the Cd3 and Cd4 centres. The third cmai linker coordinates via a κ^1 mode through an aryl carboxylate and is supported by a hydrogen bond donated by the secondary amine. The source of the pseudo-symmetry is also apparent as a non-crystallographic inversion centre lying between Cd3 and Cd4.

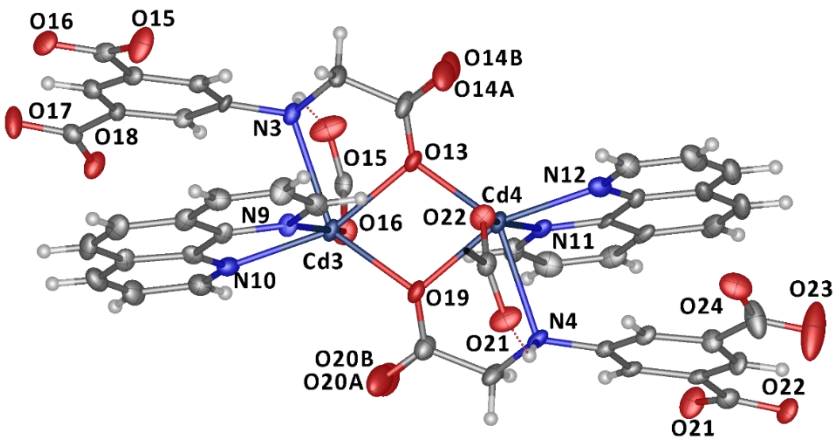

Figure 3.40. The coordination spheres of, and dimer formed by, Cd3 and Cd4 in compound **15**. (Atomic displacement parameters are represented at 50% probability).

Although the same enantiotropic relationship is present between the coordination spheres of Cd5 and Cd6, there is more deviation between those atoms, Cd5 is 6-coordinate whereas Cd6 is 7-coordinate. The origin of the extra coordination bond can be seen in **Figure 3.41**, the carboxylate based on O3 and O4 only coordinates to Cd5 through O3 in a κ^1 mode, whereas the comparative carboxylate based on O11 and O12 coordinates to Cd6 in a κ^2 mode. The other coordination modes are the same to both centres, one κ^1 bond from the carboxylate oxygen on the flexible arm of the cmai linker, one κ^2 interaction from an aryl carboxylate from another cmai linker and the κ^2 mode associated with the phen linker.

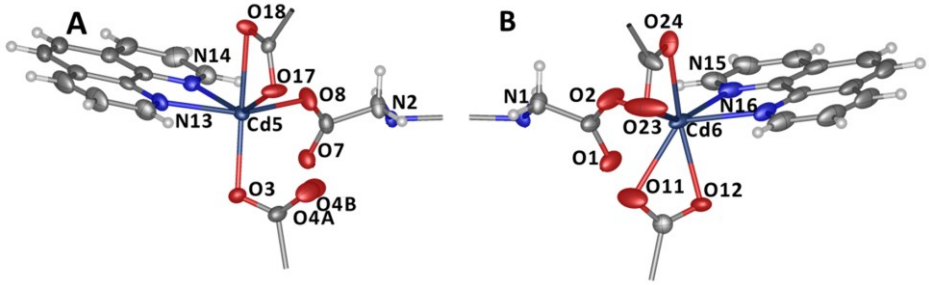

Figure 3.41. The coordination spheres of Cd5 and Cd6 in compound **15**. (Atomic displacement parameters are represented at 50% probability).

The structure of compound **15** contains three different SBUs. The first is the dimer formed between Cd3 and Cd4, as shown in **Figure 3.40**, and involves μ_2 bridging carboxylate oxygens based on O13 and O19.

The second and third SBUs are pairs of Cd1 and Cd6 centres and Cd2 and Cd5 centres respectively. Due to the pseudo-symmetry in the structure both take the same form which is

illustrated in **Figure 3.42**. The pair of centres are only connected by virtue of one bridging carboxylate and so it is unlikely this arrangement will give the structure any additional stability.

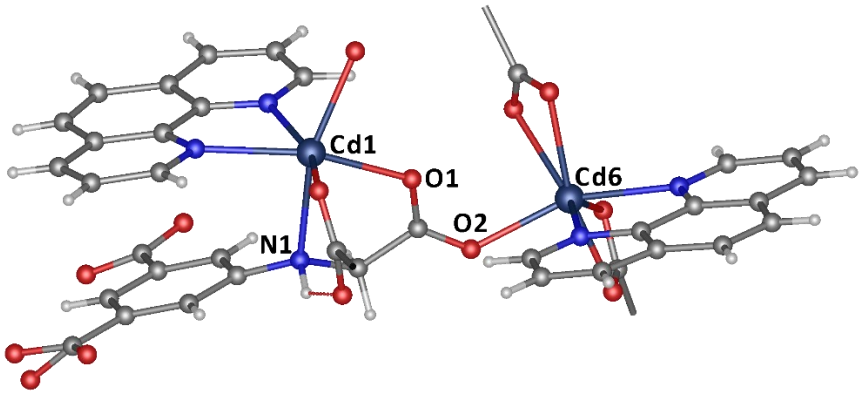

Figure 3.42. A pair of Cd1 and Cd6 centres along with their coordination spheres in compound **15**.

The 3-D structure can be constructed by considering each of the centres and their function in turn. Cd1 and Cd2 along with their coordination spheres propagate into 1-D chains running in the direction of the *a*-axis, which can be seen in **Figure 3.43**. The chains alternate and sit in the *ab* plane, forming a sheet-like structure.

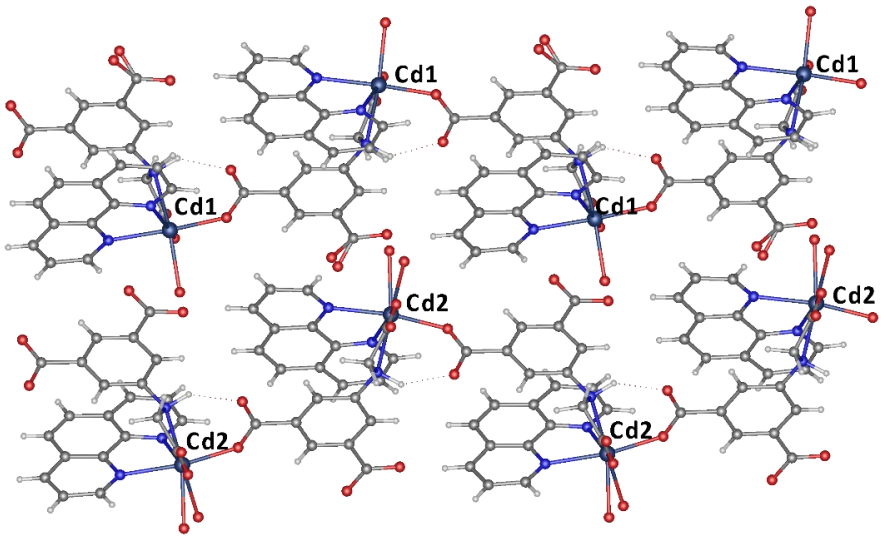

Figure 3.43. The 1-D chains formed by Cd1 and Cd2, running in the direction of the *a*-axis, sitting in the *ab* plane (viewed down the *c*-axis).

The chains in the Cd1-Cd2 plane are linked by virtue of the Cd5 and Cd6 centres forming a 2-D sheet that also lies in the *ab* plane. The structure of one of these planes is shown in **Figure 3.44**, looking down the direction of the chains in the *a*-axis.

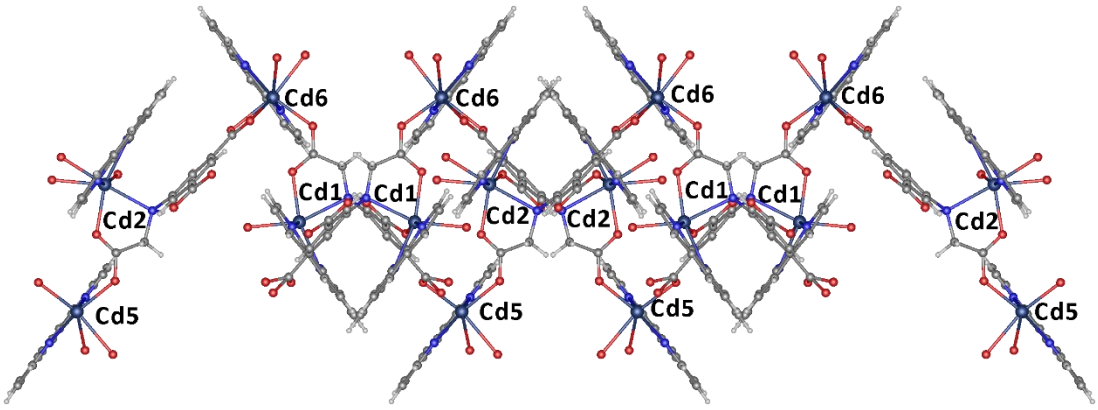

Figure 3.44. 2-D sheet formed in compound **15** as viewed down the *a*-axis.

A second 2-D sheet structure is formed from Cd3 and Cd4 dimers and their coordination sphere and is shown in **Figure 3.45**. This sheet also sits in the *ab* plane, parallel to the sheet formed by Cd1, Cd2, Cd5 and Cd6.

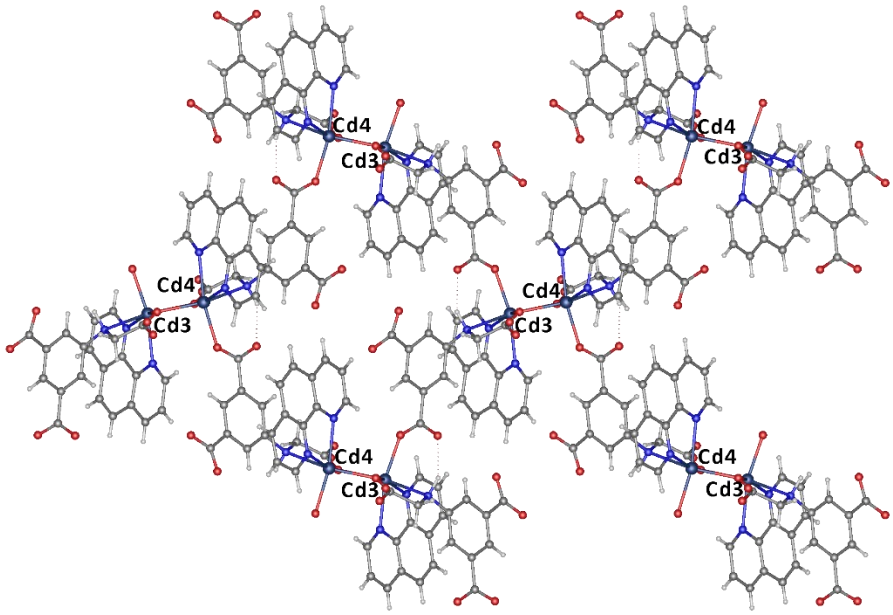

Figure 3.45. The 2-D sheet formed by Cd3 and Cd4 dimers and their coordination sphere as viewed down the *c*-axis.

The two different sheet structures stack in an alternating manner and are linked together via Cd5 and Cd6 centres forming the 3-D network. This is shown in **Figure 3.46**, where the Cd1 and Cd2 planes are highlighted in green, Cd3 and Cd4 planes in orange and, Cd5 and Cd6 in blue.

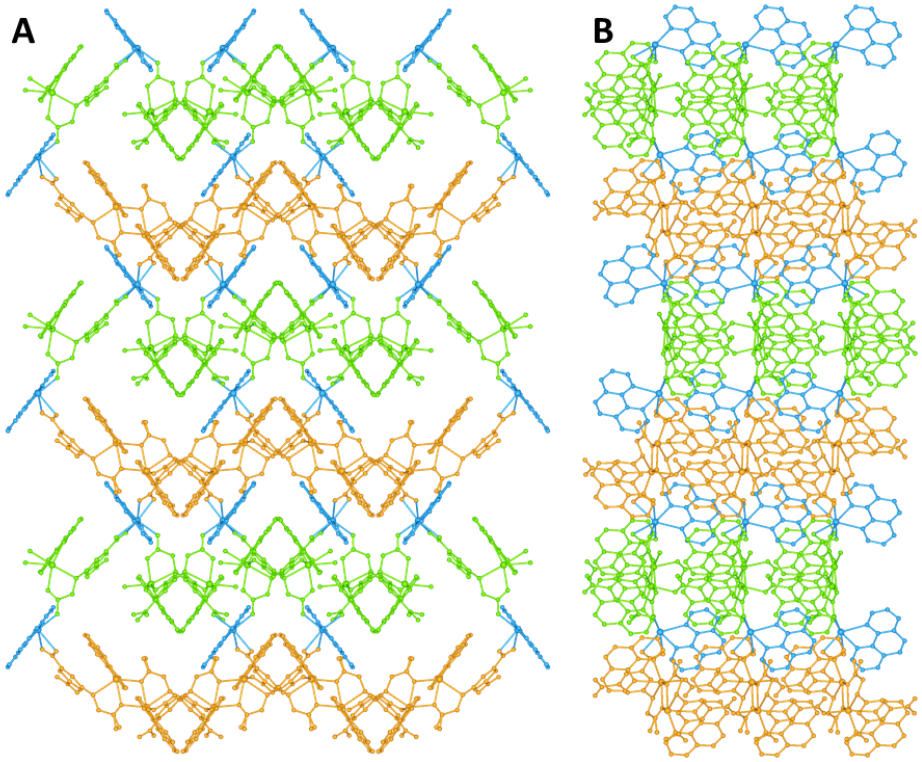

Figure 3.46. The 3-D structure of compound **15** viewed along the **A** – *a*-axis and **B** – *b*-axis. Cd1 and Cd2 planes are highlighted in green, Cd3 and Cd4 planes in orange and, Cd5 and Cd6 in blue. (Hydrogens omitted for clarity).

The amount of guest solvent in the pores of the framework can be assessed using several different techniques. The number of electrons related to the solvent mask was 523 per unit cell. There are four asymmetric units per unit cell in the space group $Pca2_1$ so 130.75 electrons per asymmetric (and formula) unit for the MOF.

^{1}H-NMR spectroscopy revealed the presence of approximately 0.75 molecules of DMF per asymmetric unit, accounting for 30/130.75 of the electrons associated with guest solvent. The remaining guest solvent must be water and has therefore been assigned as 12.5 molecules of H_2O. This gives a formula of $[Cd_6(cmai)_4(phen)_6(H_2O)_2]\cdot 12.5H_2O\cdot 0.75DMF$.

Using the formula for compound **15** established from a combination of X-ray and ^{1}H-NMR analyses, the theoretical elemental microanalysis values would be: C 45.49%, H 3.55%, N 7.78%. The experimental results were: C 45.50%, H 3.56%, N 7.27% and are in good agreement with the calculated values, giving credence to the guest solvent assignment.

The thermogravimetric analysis, shown in **Figure 3.47**, can also be used to interrogate the pore solvent. The mass loss between 35 °C and 260 °C is 8.44%, this can be assigned as the loss of 12.5 molecules of guest water and the 2 water ligands, which gives 8.66%. The DMF solvent is presumably lost at temperatures above 300 °C at which point the framework starts to decompose.

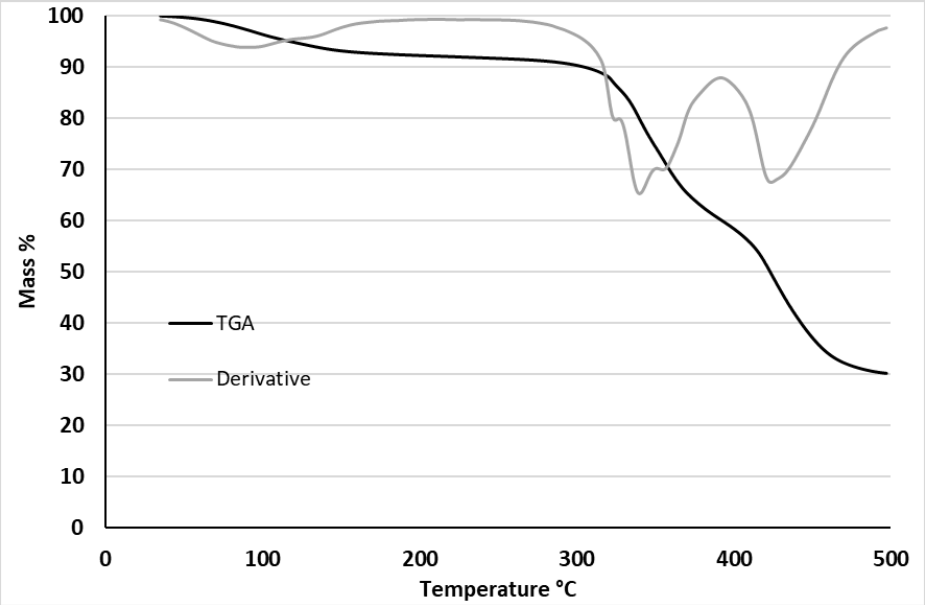

Figure 3.47. The TGA for compound **15**.

An assessment of potential porosity of compound **15** using void space analysis showed that the cavities take the form of convoluted channels running in the 110 direction and account for 14% of the structure volume.

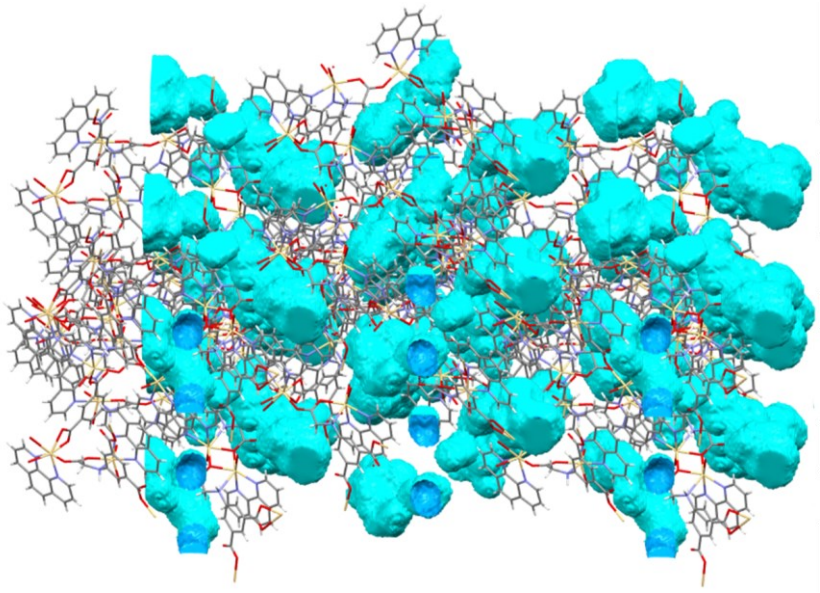

Figure 3.48. The voids in compound **15**.

3.2.6 Discussion

Five new cadmium based MOFs have been synthesised using a mixed ligand approach, combining H_3cmai derived linkers with the neutral ligands bpe, bipy and phen. One MOF was synthesised using bipy as the secondary linker, three were synthesised using bpe and one was synthesised using phen. The crystal and structural refinement data for compounds **11**-**15** are shown in **Table 3.3** at the end of this discussion.

A variety of synthetic conditions were utilised in the preparation of compounds **11**-**15**, these have been summarised in **Table 3.1**.

Table 3.1. A summary of the synthesis of cadmium MOFs containing neutral ligands.

Compound	Cadmium Salt	Co-ligand	Metal:cmai: co-ligand	Solvent System	1M Nitric Acid
11 - $[Cd_3(cmai)_2(bipy)(H_2O)_4]\cdot 6H_2O\cdot 2DMF$	$Cd(NO_3)_2\cdot 4H_2O$	Bipy	3:1:1	DMF/H_2O	0.2 mL
12 - $[Cd_2(Hcmai)_2(bpe)]\cdot 2DMF$	$Cd(OAc)_2\cdot 2H_2O$	Bpe	3:1:1	DMF/H_2O	1 mL
13 - $[Cd_3(cmai)_2(bpe)_2(H_2O)_3]\cdot 6H_2O$	$Cd(OAc)_2\cdot 2H_2O$	Bpe	6:1:1	H_2O	-
14 - $[Cd_2(cmai)(bpe)_2]NO_3\cdot DMF$	$Cd(NO_3)_2\cdot 4H_2O$	Bpe	3:1:1	DMF/H_2O	0.5 mL
15 - $[Cd_6(cmai)_4(phen)_6(H_2O)_2]\cdot 12.5H_2O\cdot 0.75DMF$	$Cd(NO_3)_2\cdot 4H_2O$	phen	3:1	DMF/H_2O	-

Nitric acid was used as an additive in compounds **11**, **12** and **14** to afford a clear solution before placing the reaction in the oven, dissolving any remaining linker or salts that were present. The larger amount of nitric acid added in the synthesis of compound **14** could be the driving force behind the formation of a charged framework and the source of the nitrate counter ion. The more acidic conditions could also be a contributing factor to the formation of a Hcmai linker in compound **12** rather than the a fully deprotonated cmai linker found in the other four compounds.

Compounds **11**, **13**, **14** and **15** are all composed of 3-D networks, whereas compound **12** is only 2-D. The reason for this is that the anionic linker in compound **12** is not fully deprotonated, being present as Hcmai. In the other 3-D structures the linker is fully deprotonated, providing an extra binding site and therefore allowing extension of the network into the third dimension. This relationship between dimensionality and ligand deprotonation was also observed in the structures presented in **Chapter 2**. Given this, it appears likely that the linker deprotonation plays a larger role than the addition of a neutral linker in the formation of a 3-D network.

Although a large number of the variables within the syntheses of these compounds have been investigated there is still a substantial amount of the research space that has not been explored, such as varying the reactant ratios and changing the reaction temperature.

As was found in **Chapter 2**, the cadmium centres in compound **11**-**15** possess a variety of coordination numbers and geometries, ranging from 5-coordinate trigonal bipyramidal to 8-coordinate dodecahedral. There is also significant variation within the same structure, with compound **11** containing both 6-coordinate and 8-coordinate centres, compound **14** containing both 5-connected and 6-connected centres and compound **15** containing 6-coordinate and 7-coordinate centres. Cadmium(II) centres possess the ability to vary their coordination environment due to their size, being in the second row of the d-block, and by having a d^{10} configuration, imparting no electronic directional preference for coordination.

The variety of coordination environments adopted by cadmium centres means that a range of different SBUs were observed. One that has been previously observed and is present in two of these structures, **12** and **15**, is a cadmium dimer supported by two bridging μ_2-O atoms that are also part of a κ^2 bidentate interaction with the secondary amine of the (H)cmai linker. The general arrangement can be seen in **Figure 3.49**. Compound **13** also contains a cadmium dimer containing two bridging μ_2-O atoms but does not have the κ^2 mode associated with the flexible arm.

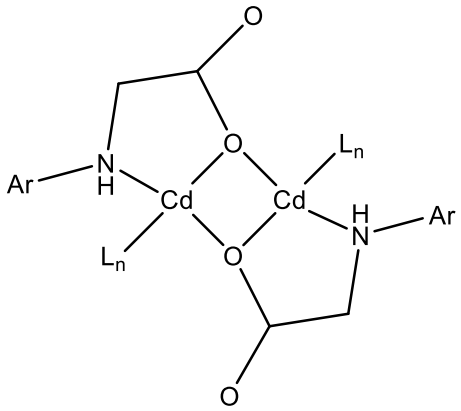

Figure 3.49. The structure of the cadmium dimer motif.

Compounds **11** and **14** both contain chains of cadmium centres that are linked by just a single bridging carboxylate group. In compound **11** the chains are solely comprised of carboxylate-linked cadmium centres whereas in compound **14** the chains are comprised of carboxylate-linked dimers. These two 1-D chain SBUs are depicted in **Figure 3.50**.

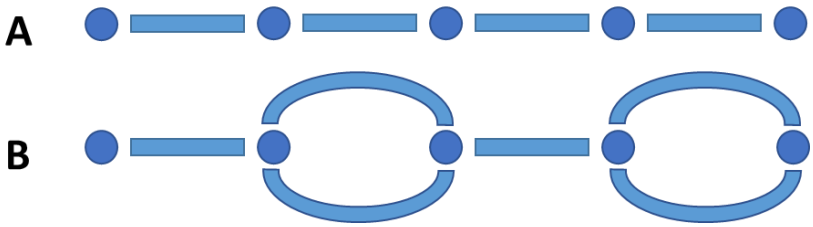

Figure 3.50. A representation of the 1-D chain SBUs in **A** – compound **11** and **B** – compound **14**. The blue circles represent single cadmium centres and the bars are bridging carboxylate groups.

As well as structural variety being intrinsic to the cadmium centres, the cmai linker was also shown to adopt a wide range of coordination modes in **Chapter 2**. The coordination modes observed in compounds **11**-**15** are shown in **Figure 3.51**. The 7 modes observed in compounds **11**-**15** is considerably fewer than the 13 modes seen in compounds **1**-**6** suggesting that the presence of a neutral N-donor linker reduces the number of interactions that tend to form between cadmium(II) and cmai based linkers.

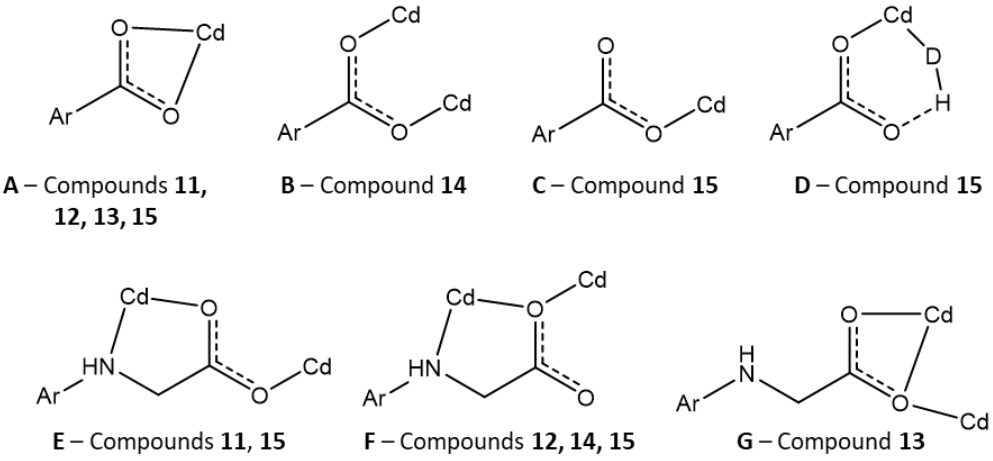

Figure 3.51. The coordination modes adopted by the (H)cmai linkers in compounds **11**-**15**.

The binding modes A-F had been observed previously in compounds **1**-**6**, only mode G had not been seen before. The coordination mode **G** seen in compound **13**, is interesting as it is the first example of a cmai linker not coordinating through the secondary amine. The binding mode involving a κ^2 bidentate coordination through the secondary amine and carboxylate oxygen is a very prevalent interaction, seen in all but two compounds investigated thus far.

All compounds **11**-**15** contained guest solvent in pores or channels of varying sizes, unlike compounds **1, 7, 8** and **9**. This suggests that the presence of a neutral ligand is significant in the formation of porous structures. The volume of the potential cavities that are present within the framework structures are summarised using void space in **Table 3.2**.

Table 3.2. The void space in compounds **11**-**16**.

Compound	**11**	**12**	**13**	**14**	**15**
Void Space	35%	26%	2%	15%	14%

The largest potential void space of 35% was observed for compound **11**, the pores therein take the form of convoluted channels. The lowest void space was observed for compound **13** of just 2%. The network topology of compound **15** allows for the formation of multiple channels running through the structure, however, due to the bulk of the capping phen ligands on all the cadmium centres, the void space is significantly reduced. This represents a clear disadvantage to the use of a capping bidentate ligand.

The presence of water ligands was highlighted as one of the reasons for the difficulty in activating the frameworks reported in **Chapter 2**. Addition of neutral linkers into the synthesis was anticipated to provide a competing coordinating species for water ligands, and, indeed, these were not so prevalent in the structures formed. Compounds **11**, **13** and **15**, have water ligands on one or more of their cadmium centres. Compounds **12** and **14**, however, contain no water ligands. This shows that the addition of the neutral linkers was, in part, successful in this aim. The TGA analysis showed that compounds **12** and **14** needed to be heated to very high temperatures (>200 °C) to remove the guest DMF molecules. The use of solvent exchange methodologies may allow more facile access to the activated structures. Another benefit of neutral linkers was observed in compound **11** where the pillaring linker bipy was shown, by comparison with analogous compound **5**, to impart extra stability to the MOF. This allowed the structure to be retained on heating, allowing partial access to the porosity of the MOF which was inaccessible in compound **5**.

Table 3.3. Crystal data and structural refinement for compounds **11 – 15**.

Compound	**11**	**12**	**13**	**14**	**15**
Empirical formula	$C_{18}H_{27}Cd_{1.5}N_3O_{12}$	$C_{19}H_{19}CdN_3O_7$	$C_{44}H_{50}Cd_3N_6O_{21}$	$C_{37}H_{33}Cd_2N_7O_{10}$	$C_{112}H_{76}Cd_6N_{16}O_{26}$
Formula weight	646.02	513.77	1336.10	960.50	2736.28
Temperature/K	150.01(10)	150.00(10)	150.00(10)	150.01(10)	150.01(10)
Crystal system	tetragonal	triclinic	monoclinic	triclinic	orthorhombic
Space group	$P4_32_12$	$P\text{-}1$	$C2/c$	$P\text{-}1$	$Pca2_1$
a/Å	10.07444(5)	7.8646(2)	24.3237(4)	9.4809(3)	15.6432(1)
b/Å	10.07444(5)	11.1931(2)	13.6310(2)	12.9396(6)	17.0869(1)
c/Å	47.1409(3)	12.5150(4)	14.6680(2)	15.9797(7)	41.3209(2)
α/°	90	64.999(3)	90	76.056(4)	90
β/°	90	78.190(3)	100.285(2)	75.834(3)	90
γ/°	90	77.837(2)	90	75.621(3)	90
Volume/Å^3	4784.54(5)	967.70(5)	4785.12(13)	1807.01(14)	11044.82(11)
Z	8	2	4	2	4
ρ_{calc}g/cm^3	1.794	1.763	1.855	1.765	1.646
μ/mm^{-1}	11.379	9.480	11.361	1.247	9.771
F(000)	2592.0	516.0	2672.0	960.0	5424.0
Crystal size/mm^3	0.182 × 0.154 × 0.099	0.215 × 0.058 × 0.039	0.088 × 0.039 × 0.028	0.487 × 0.276 × 0.166	0.226 × 0.14 × 0.037
Radiation/Å	CuKα (λ = 1.54184)	CuKα (λ = 1.54184)	CuKα (λ = 1.54184)	MoKα (λ = 0.71073)	CuKα (λ = 1.54184)
2Θ range for data collection/°	7.502 to 146.156	7.862 to 146.142	7.388 to 146.43	6.58 to 60.762	6.712 to 146.836
Index ranges	-12 ≤ h ≤ 12, -12 ≤ k ≤ 12, -57 ≤ l ≤ 35	-9 ≤ h ≤ 9, -13 ≤ k ≤ 11, -15 ≤ l ≤ 15	-30 ≤ h ≤ 30, -15 ≤ k ≤ 16, -17 ≤ l ≤ 17	-13 ≤ h ≤ 13, -18 ≤ k ≤ 18, -20 ≤ l ≤ 22	-19 ≤ h ≤ 15, -21 ≤ k ≤ 20, -51 ≤ l ≤ 51
Reflections collected	60307	8746	6482	26673	149631
Independent reflections, R_{int}	4783, 0.0438	3852, 0.0314	6482, 0.0296	9452, 0.0292	22103, 0.0529
Data/restraints/parameters	4783/25/287	3852/64/328	6482/5/369	9452/1/511	22103/1026/1476
Goodness-of-fit on F^2	1.043	1.041	1.161	1.047	1.032
Final R_1, wR_2 indexes [I>=2σ (I)]	0.0320, 0.0850	0.0281, 0.0707	0.0419, 0.1173	0.0278, 0.0579	0.0346, 0.0857
Final R_1, wR_2 indexes [all data]	0.0321, 0.0851	0.0292, 0.0717	0.0475, 0.1291	0.0358, 0.0616	0.0350, 0.0860
Largest diff. peak/hole / e Å^{-3}	1.12/-0.96	0.93/-1.12	1.64/-2.18	0.53/-0.43	0.90/-1.03
Flack parameter	0.007(5)				0.044(3)

3.3 Results and Discussion: Zinc MOFs containing cmai-based linkers and neutral N-donor ligands

In order to provide a comparison with the zinc-containing compounds **7** and **10** discussed in **Chapter 2**, experiments were conducted to synthesise zinc-based MOFs containing both cmai and a neutral ligand. Zinc based MOFs have the benefit of a smaller metal centre than cadmium which allows for less coordinative diversity and therefore a larger element of control over the SBU and the topologies formed. Zinc is also much less toxic than cadmium which can be an important consideration depending on the intended application of the MOF.

3.3.1 The synthesis and characterisation of $[Zn_3(cmai)_2(bipy)(H_2O)_4]\cdot 2H_2O$ (**16**) and $[Zn_3(cmai)_2(bipy)]$ (**17**)

Compound **16** was formed in the reaction of H_3cmai and bipy with $Zn(NO_3)_2\cdot 6H_2O$ in a 1:1 mixture of DMF and water at 90 °C. During the two day reaction compound **16** crystallises as light purple blocks in the triclinic space group *P*-1. The asymmetric unit, shown in **Figure 3.52**, contains one full occupancy zinc centre, one half occupancy zinc centre, one cmai linker, half a bipy linker, two water ligands and one disordered guest water molecule.

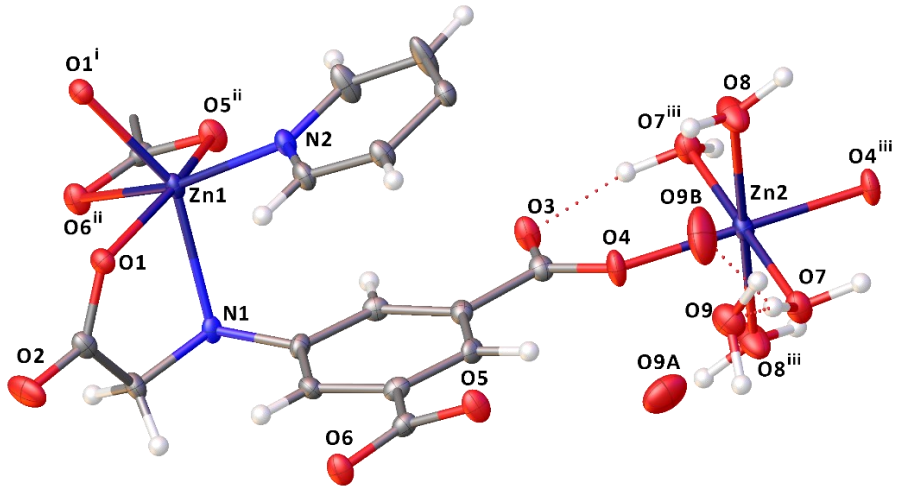

Figure 3.52. The asymmetric unit and zinc coordination spheres in compound **16**. (i, 1 – *x*, 1 – *y*, – *z*; ii, – 1 – *x*, + *y*, + *z*; iii, – *x*, – *y*, 1 – *z*)(Atomic displacement parameters are represented at 50%).

Zn1 is full occupancy, 6-coordinate and is bound by three cmai and one bipy linker. The three cmai linkers all coordinate in different modes. One coordinates in a κ^2 mode through N1 of the secondary amine and O1 of the carboxylate of the flexible arm. O1 is also part of a μ_2 bridging mode interaction involving a second Zn1 centre, this is how the second cmai linker coordinates,

through O1. The third cmai linker coordinated via a κ^2 mode through the carboxylate oxygens, O5 and O6.

Zn2 is half occupancy, 6-coordinate, octahedral in geometry and resides on an inversion centre. It is coordinated by two symmetry related cmai linkers, both in a κ^1 mode through O4. This interaction is supported by a hydrogen bond formed between the water ligand based on O7 and the other carboxylate oxygen O3. Zn2 has four water ligands, two based on O4 and two on O7.

The SBU in compound **16** is a zinc dimer formed from two Zn1 centres that are linked by bridging μ_2 mode O1 atoms, as shown in **Figure 3.53**.

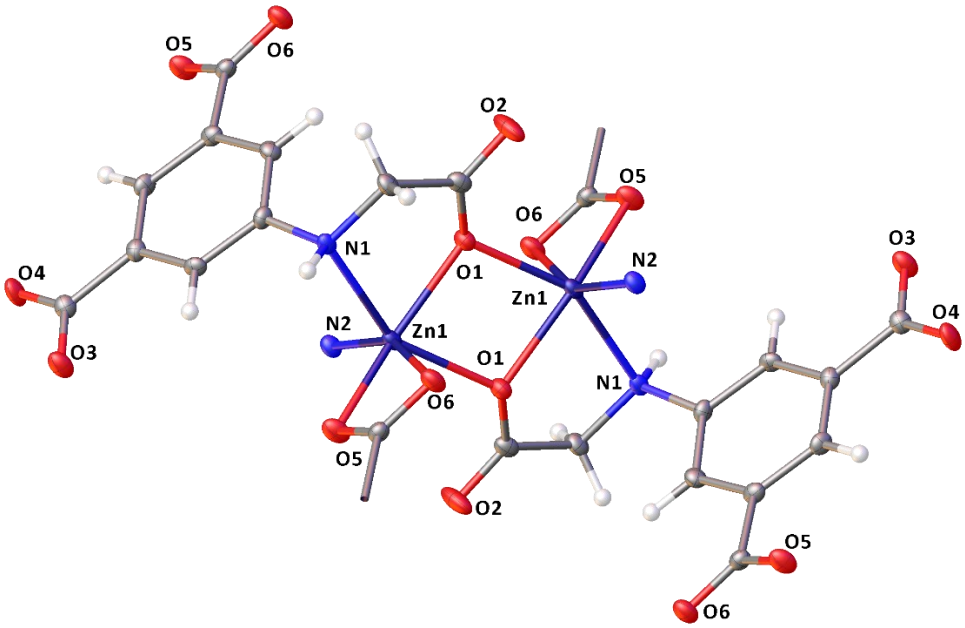

Figure 3.53. The zinc dimer SBU in compound **16**.

The interaction of the Zn1 dimer SBU and the cmai linkers forms 1-D tapes running in the direction of the *a*-axis. One of these chains is shown in **Figure 3.54**.

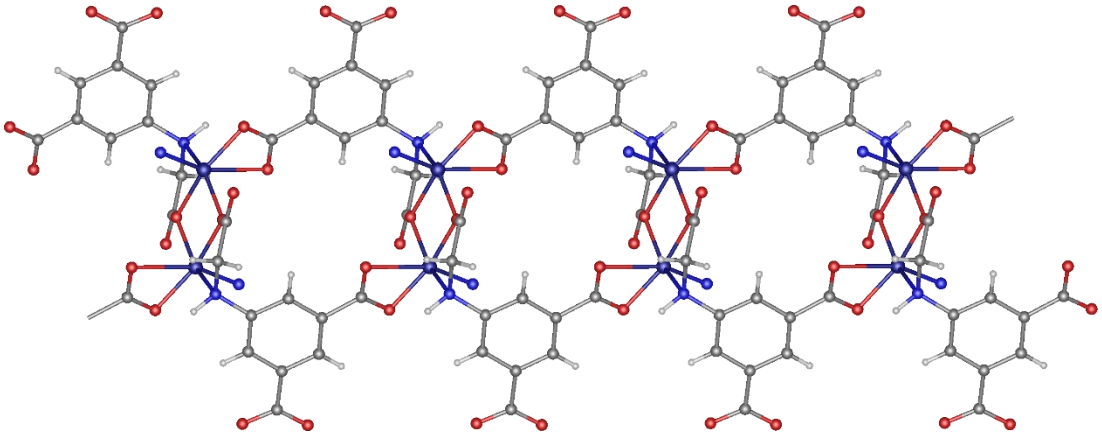

Figure 3.54. 1-D chain formed by zinc dimers and cmai linkers in compound **16**. (Only the N-atom of the bipy linkers are shown for clarity).

The chains are linked to their neighbours through the bipy ligands, forming 2-D sheets which lie parallel the *ab* plane. One of these sheets is shown looking down the length of the 1-D tapes, and from perpendicular to the plane, in **Figure 3.55 A** and **B** respectively.

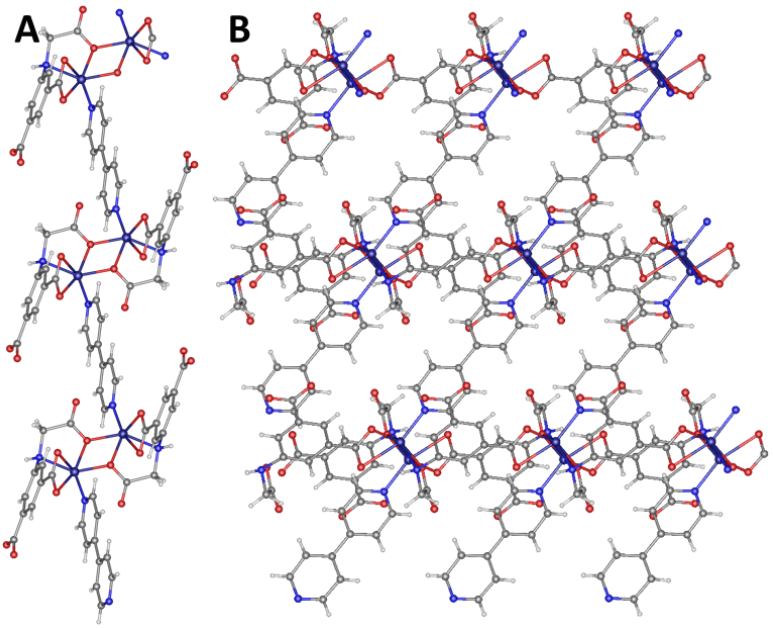

Figure 3.55. The 2-D planes formed by Zn1-dimers, and the cmai and bipy linkers. Viewed looking down the **A** – *a*-axis and **B** – *c*-axis.

Adjacent planes are linked via the coordination of O4 carboxylate oxygens to Zn2 centres. This forms the overall 3-D structure of compound **16**, which can be seen in **Figure 3.56**.

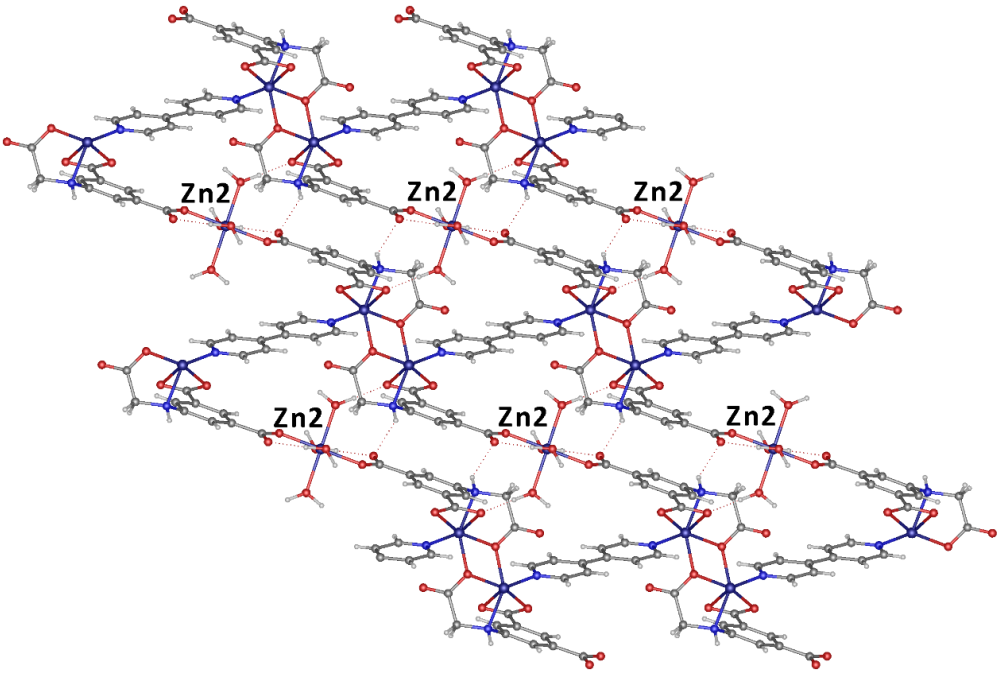

Figure 3.56. The 3-D structure of compound **16**, viewed down the *a*-axis.

Compound **16** contains one molecule of guest water per formula unit which is disordered over 3 positions in a ratio of 0.88:0.07:0.05. Due to the low occupancy of the minor positions only the hydrogen atoms of the major position, O9, were included in the refinement. The water based on O9 is heavily involved in hydrogen bonding with the framework, donating two hydrogen bonds, to O2 and O3, and accepting one from the water ligand based on O7. The other two hydrogen bonds in the structure are donated from the water ligand based on O8 and accepted by the carboxylate oxygen O6, and donated from the secondary amine, N1, and accepted by O3. These hydrogen bonds all span between the adjacent 2-D sheets formed from the Zn1-dimers, cmai and bipy linkers, helping support the 3-D structure along with the Zn2 centres.

The guest solvent and thermal behaviour of compound **16** were investigated using thermogravimetric analysis, and the results are shown in **Figure 3.57**.

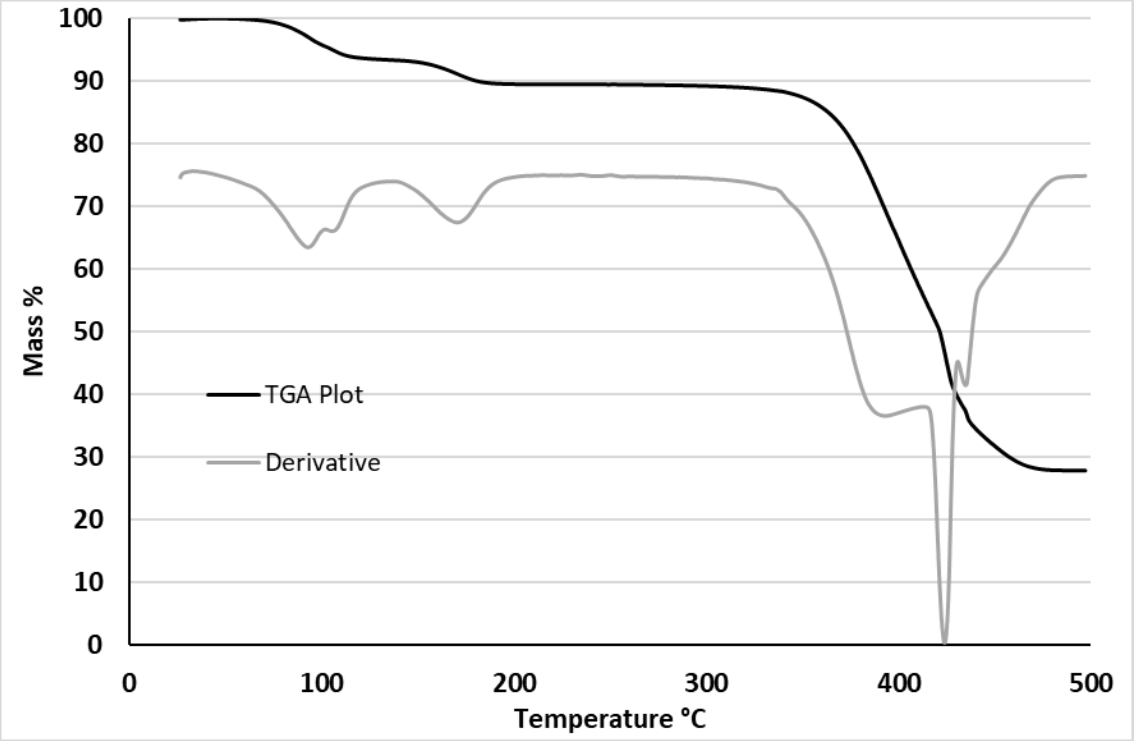

Figure 3.57. The TGA results for compound **16**.

The mass loss between 30 °C and 200 °C is 10.5%, which likely represents complete dehydration of compound **16**, including water ligands, for which the theoretical mass lost would be 11.6%. The derivative shows that this mass loss occurs in three events, two of which overlap between 30 °C and 130 °C and the third takes place between 130 °C and 200 °C. In the two overlapping mass losses between 30 °C and 130 °C a total of 6.5% of the compound's mass is lost, equivalent to 3.4 molecules of water. A further 4.0% of the compound's mass is lost between 130 °C and 200 °C, equating to 2.1 molecules of water.

These events suggest that the guest water and some of the water ligands are lost simultaneously. They also show that Zn2 undergoes partial dehydration before losing the rest of its water ligands. This suggests that a rearrangement of the structure might occur to address reduced coordination number of the Zn2 centres. To investigate this further, a variable temperature PXRD experiment was carried out in order to ascertain the structural changes in **16** as water ligands are lost from the compound. A sample of compound **16** was exposed to a heating profile consisting of a ramp up to 200 °C over a period of 50 minutes, followed by a hold at 200 °C for 6 hours before returning to room temperature. The results are presented in **Figure 3.58**.

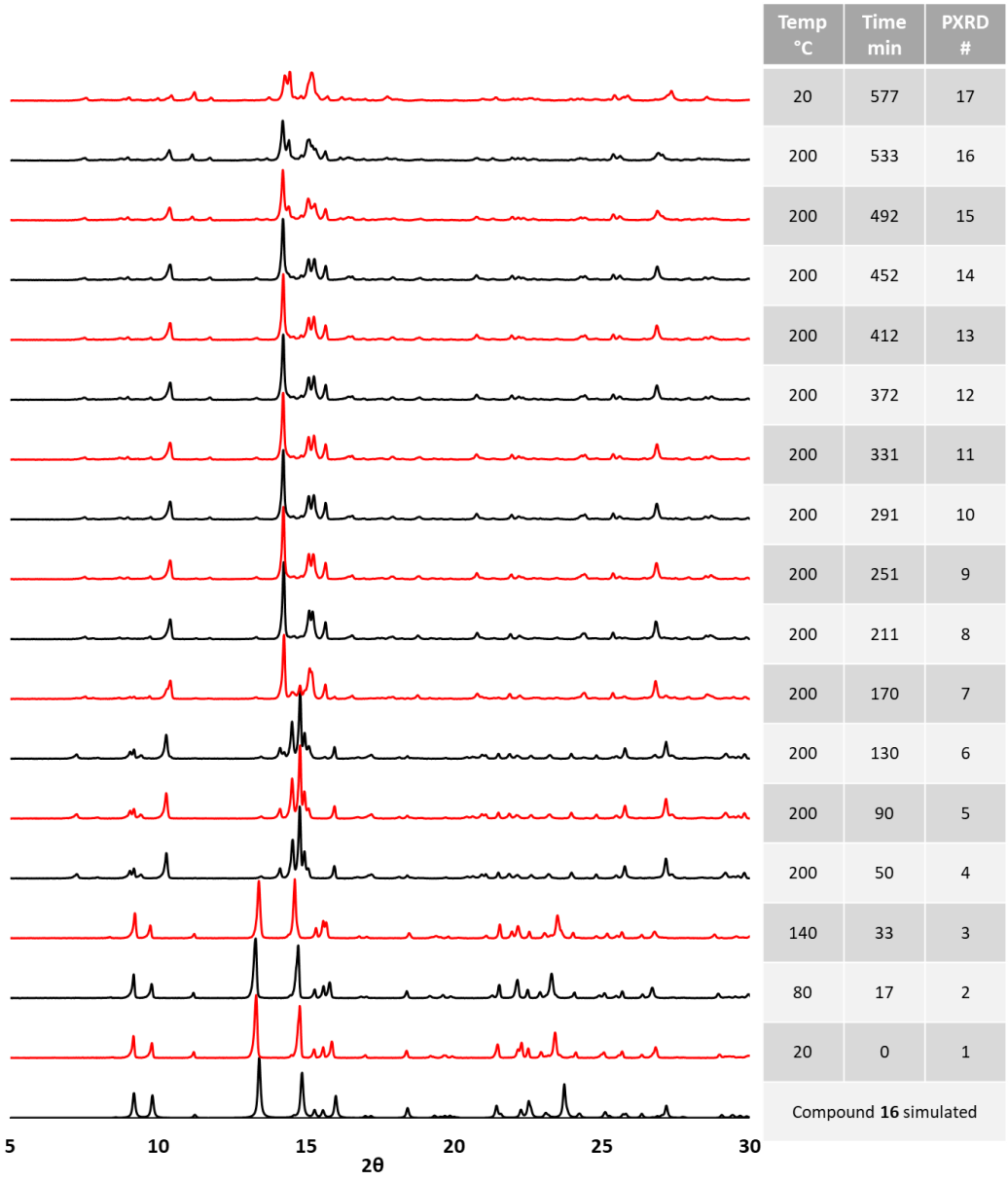

Temp °C	Time min	PXRD #
20	577	17
200	533	16
200	492	15
200	452	14
200	412	13
200	372	12
200	331	11
200	291	10
200	251	9
200	211	8
200	170	7
200	130	6
200	90	5
200	50	4
140	33	3
80	17	2
20	0	1
Compound **16** simulated		

Figure 3.58. Variable temperature PXRD results for compound **16**.

The VT-PXRD experiment has revealed the existence of several different forms related to compound **16**. In PXRD patterns 1-3, ranging from 20 °C to 140 °C, the structure of compound **16** is preserved. A new pattern is observed in PXRD 4-6, for which the temperature was held at 200 °C for 80 mins, indicating a structural change. Further change is observed in pattern 7 and this phase is maintained until pattern 14, over a temperature plateau of 200 °C for 282 mins. Traces 15 and 16 appear to be very similar to those of 7-14 but there are some minor changes such as an emergence of a peak at 14.5° and the merger of the peaks at 15.1° and 15.3°. Upon the return of the material to room temperature, the pattern for the material remains very similar, indicating the structure obtained at elevated temperatures does not revert back to the original compound **16** structure.

Based on the TGA and VT-PXRD the second observed phase in PXRD 4-6 is likely to be a partially dehydrated form that has lost guest water and some of the water ligands. The structure obtained at temperatures higher than this is a fully dehydrated form.

In an attempt to isolate the high temperature/dehydrated forms of compound **16** a sample of the material was placed under vacuum and heated at 170 °C for 2 hours. After this period a PXRD pattern was collected which showed a change of form to a mixture of the three phases identified in traces 1, 5 and 10 of the variable temperature PXRD experiment, as can be seen in the comparison in **Figure 3.59**.

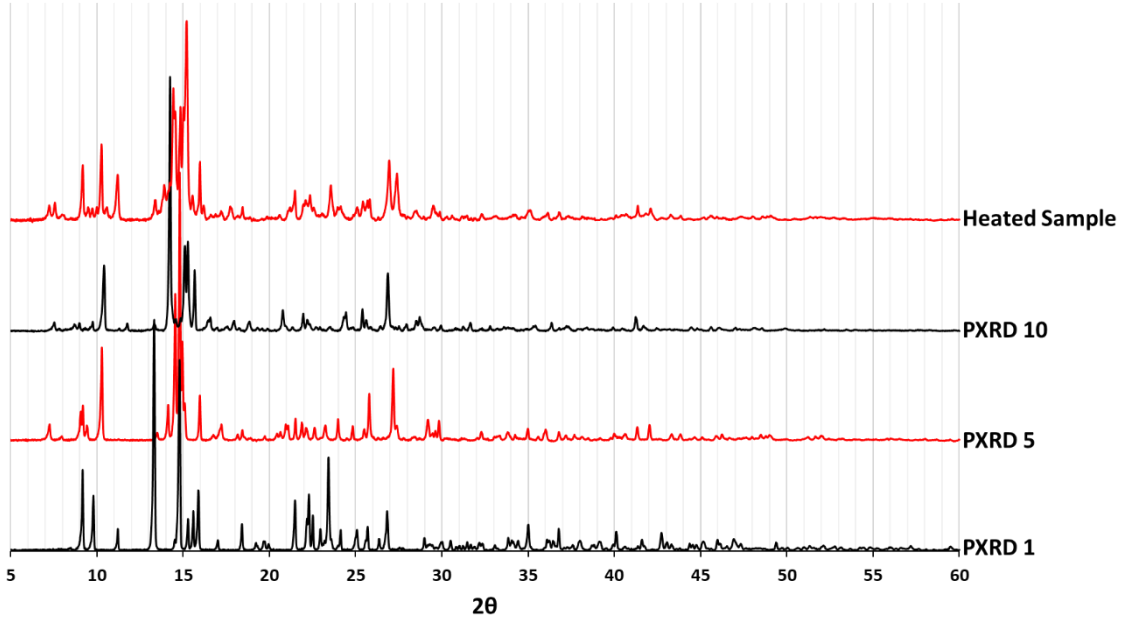

Figure 3.59. PXRDs 1, 5 and 10 compared to the pattern collected for the heat/vacuum treated sample of compound **16**.

Screening experiments using a single-crystal diffractometer were carried out. It was found that some of the crystals had a similar unit cell as that of compound **16**, while others had a very different unit cell. A full data collection was carried out on one of the latter crystals, giving the structure for $[Zn_3(cmai)_2(bipy)]$ (**17**).

The crystal structure of compound **17** was solved in the triclinic space group *P*-1 and has an asymmetric unit containing three zinc centres, two cmai linkers and one bipy linker. This can be seen along with the coordination spheres of the zinc centres in **Figure 3.60**.

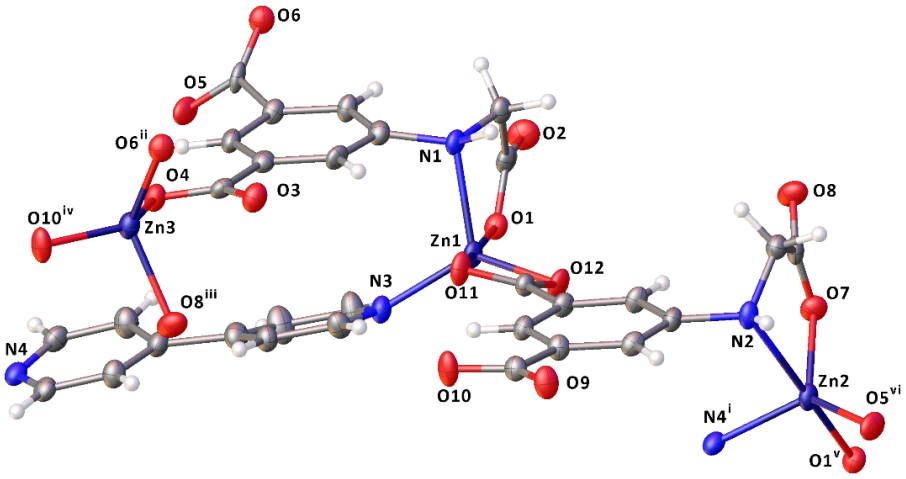

Figure 3.60. The asymmetric unit and zinc coordination in compound **17**. (i, – *x*, 1 – *y*, 1 – *z*; ii, 1 – *x*, 1 – *y*, – *z*; iii, + *x*, 1+ *y*, + *z*; iv, 1 – *x*, 1 – *y*, 1 – *z*; v, – *x*, – *y*, 1 – *z*; vi, + *x*, – 1 + *y*, 1 + *z*)(ADPs shown at 50%).

The zinc-dimer SBU from compound **16** does not persist in compound **17**, instead the dimer is altered by loss of one of the μ_2-bridging interactions. This results in breakdown of the symmetry of the compound, thus, in compound **17** the two zinc centres are crystallographically distinct. A comparison of the two related SBUs is shown in **Figure 3.61**.

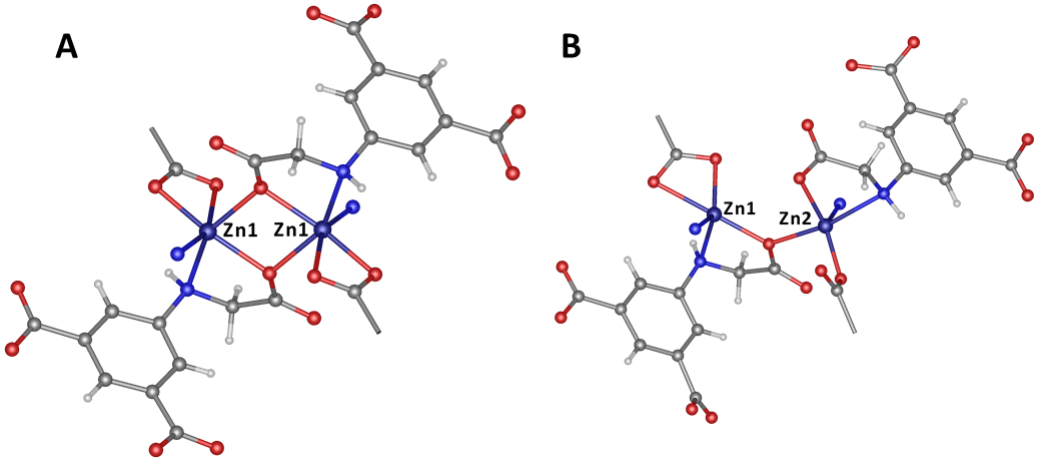

Figure 3.61. The SBU in **A** - compound **16** and **B** - compound **17**.

During the single-crystal to single-crystal transformation of compound **16** to compound **17**, Zn2 from compound **16** is transformed into Zn3 in compound **17**, the coordination sphere of both centres is shown in **Figure 3.62**. Loss of water ligands around Zn2 in **16** results in the alteration of the coordination number from 6 to 4 during the transformation. It can be seen that the Zn-O4 bonds are retained in the transformation while the water ligands are lost. The unsaturated coordination of the Zn3 upon loss of the water ligands is satisfied by additional bonds formed to O6 and O8.

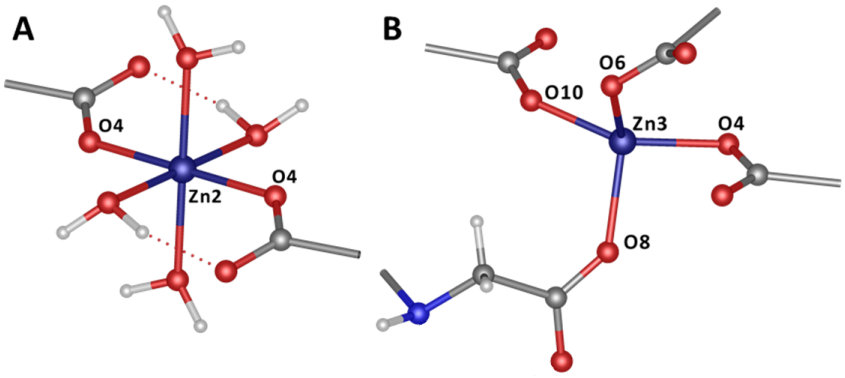

Figure 3.62. The coordination environment of **A** – Zn2 from compound **16** and **B** – Zn3 from compound **17.**

The gross structure of compound **17** builds up in a very similar way to compound **16**. The SBU formed by Zn1 and Zn2 in combination with the cmai linkers form 1-D chains. Adjacent chains are connected via the bipy linkers forming 2-D sheets parallel to the *bc* plane. Similar to compound **16** the 2-D planes in compound **17** are connected to adjacent planes via a zinc centre, in this case Zn3. This results in a 3-D network as shown in **Figure 3.63**.

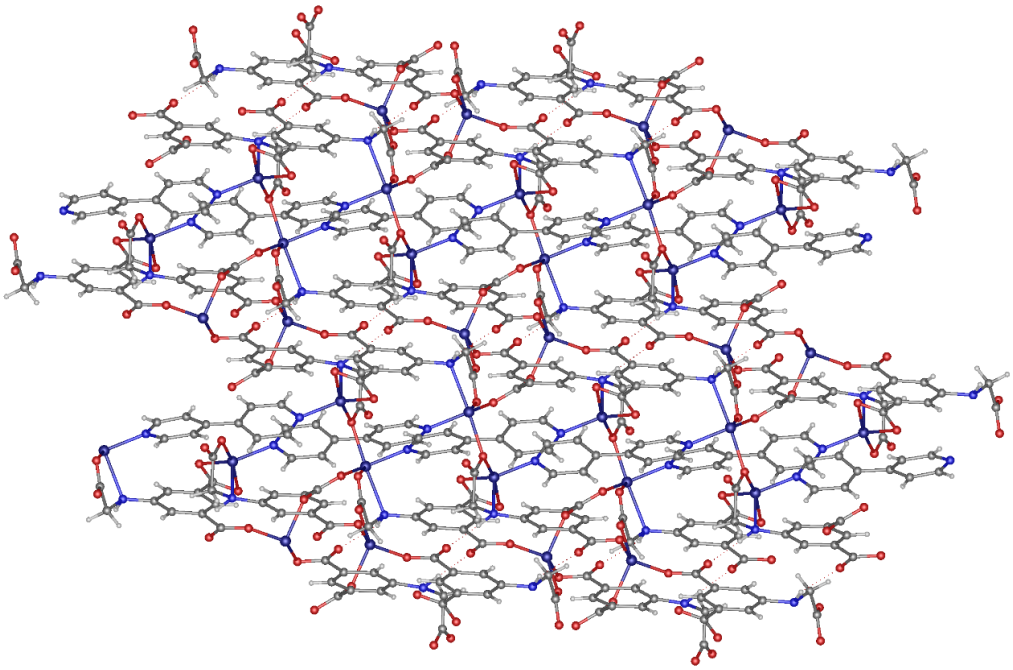

Figure 3.63. The 3-D structure of compound **17**.

Interestingly compound **17** is only slightly denser than compound **16** with calculated densities of 1.859 g cm^{-3} and 1.807 g cm^{-3} respectively. The void space analysis for the two materials also reveals an interesting result, the visual representations of which can be seen in **Figure 3.64**. Compound **17**, despite rearrangement upon loss of the water from the structure has a higher

percentage potential void space than compound **16**, 6.5% and 4.1% respectively. This increase in void space after dehydration and structural rearrangement is due to the loss of the water ligands, which no longer take up space in the structure.

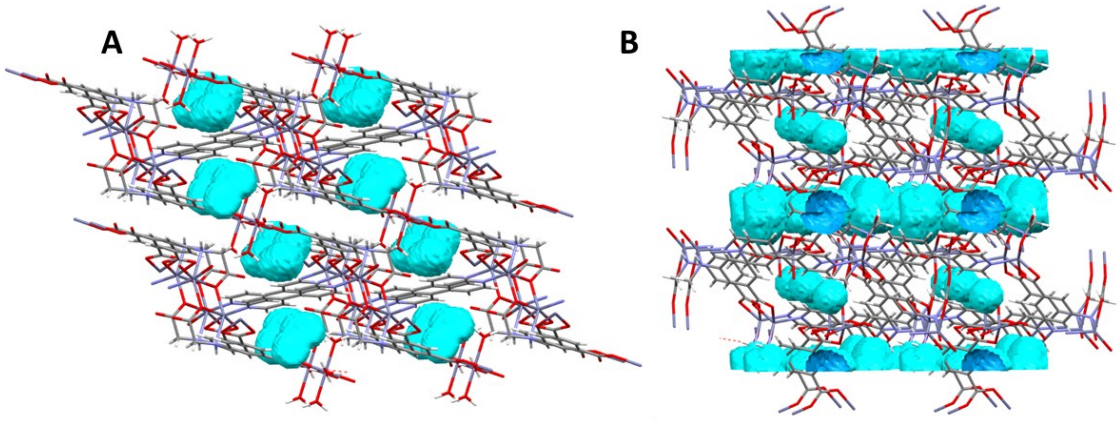

Figure 3.64. Potential void space analysis for **A** – compound **16** and **B** – compound **17**.

A PXRD pattern was generated from the single-crystal data for compound **17** and compared to traces collected during the VT-PXRD experiment to elucidate which form compound **17** represents, this is shown in **Figure 3.65**.

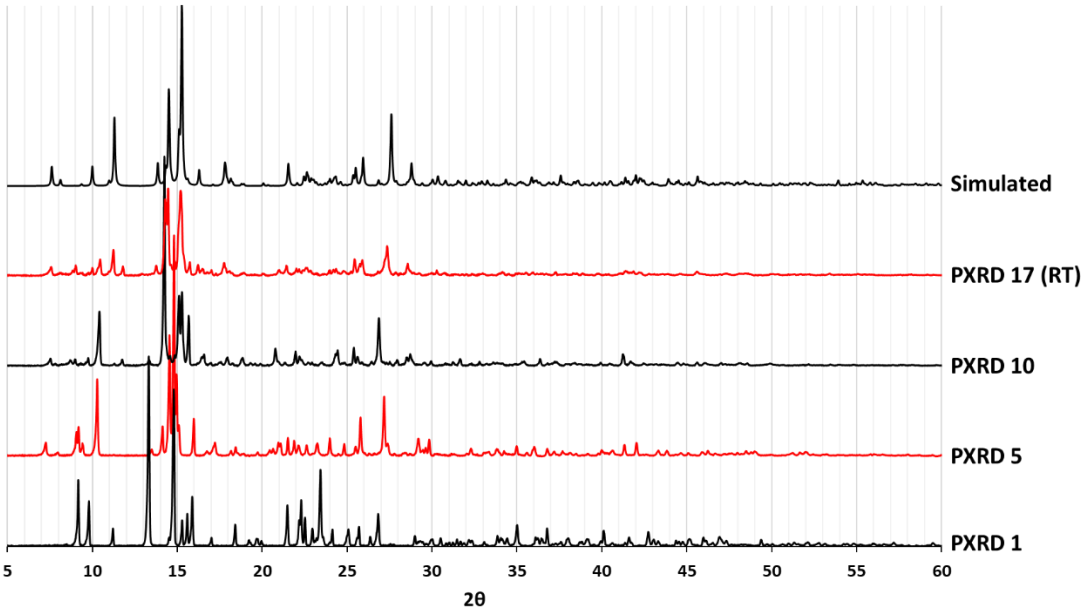

Figure 3.65. Comparison of VT-PXRD patterns with the simulated pattern for compound **17**.

The simulated pattern matches PXRD 17 most closely, which is the trace collected of the material once it has returned to room temperature. The pattern is also similar to PXRDs 7-16 suggesting these represent a related high temperature form of compound **17**. The simulated pattern is

markedly different to patterns 4-6, which is presumably a partially dehydrated intermediate whose structure is somewhere in-between those of compound **16** and **17.**

The reversibility of the dehydration was investigated by submerging the heat and vacuum treated material in water for a period of 18 hours, after which a PXRD pattern for the material was collected, this is shown in **Figure 3.66**. The heat treated material, which appears to be a mixture of compound **16**, **17** and a partially dehydrated intermediate, after submersion in water, converts to compound **16**, indicating the dehydration/rehydration is reversible.

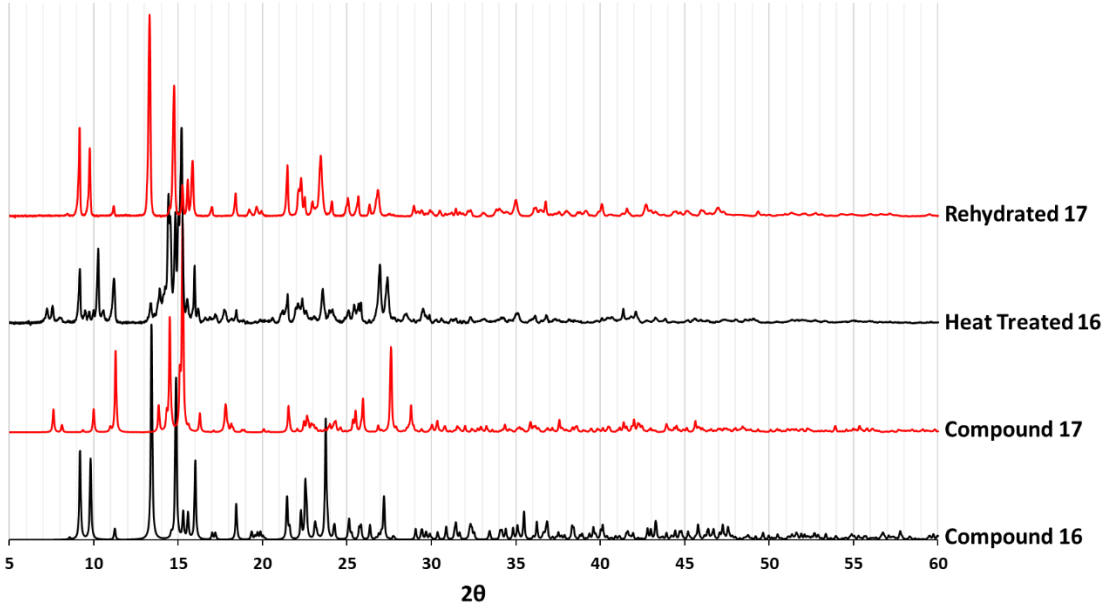

Figure 3.66. Simulated PXRD patterns for compound **16** and **17**, the experimental pattern for heat-treated compound **16** and experimental pattern for the rehydrated material.

3.3.2 The synthesis and characterisation of $[Zn_2(Hcmai)_2(bpe)]\cdot 2DMF$ (**18**)

In an analogous synthesis to that for compound **12**, $[Cd_2(Hcmai)_2(bpe)]\cdot 2DMF$, compound **18** was synthesised in the reaction between $Zn(NO_3)_2\cdot 6H_2O$, H_3cmai and bpe in a mixture of DMF, water and concentrated nitric acid. The reaction was carried out at 90 °C for 3 days, in which time colourless long block crystals had formed. After collection via vacuum filtration and washing with fresh H_2O a suitable crystal was selected for single-crystal X-ray diffraction analysis.

The unit cell found for compound **18** resembled that of the previously determined structure, compound **12**. This suggested that the two materials could be isostructural, though compound **12** is a cadmium based MOF and compound **18** is zinc based. Therefore, a full collection and structural determination was carried out. The structure of compound **18** was solved in the triclinic space group *P*-1. The asymmetric unit, shown in **Figure 3.67** along with the zinc coordination sphere, contains one zinc centre, one Hcmai linker, half a bpe linker and a disordered guest DMF molecule. This is the same asymmetric unit seen for compound **12** with the cadmium centre exchanged for zinc.

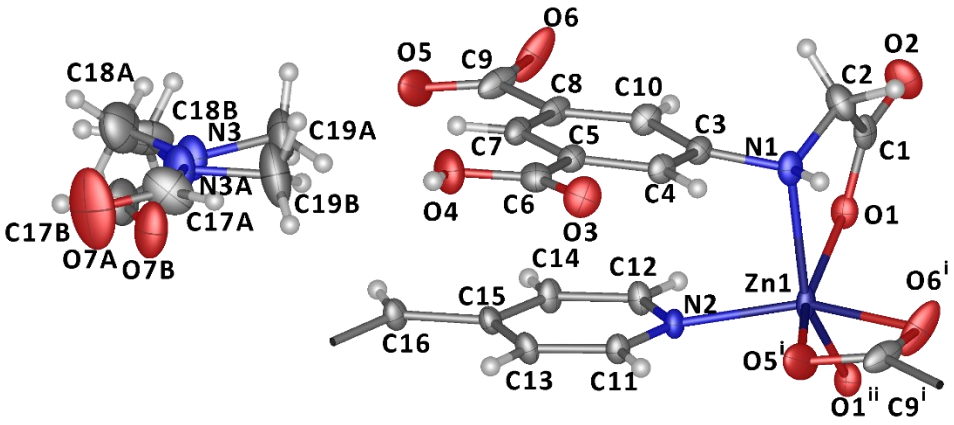

Figure 3.67. The asymmetric unit in compound **18**, along with the zinc coordination sphere. (i, 1 + *x*, + *y*, + *z*; ii, – 1 – *x*, – *y*, 2 – *z*)(ADPs are shown at 50% probability).

The structure of compound **18** builds up in the same manner as compound **12**. The Zn1 centres form dimers by virtue of two bridging μ_2-O1 atoms from two different Hcmai linkers, these atoms also partake in a κ^2 mode with N1. The dimers are formed in to 2-D tapes in combination with the Hcmai linkers. The tapes are joined into sheets lying in the *ab* plane by the bpe ligands, with the carboxylic acid groups projecting from either face of each plane. The structure of these planes is shown in **Figure 3.68**.

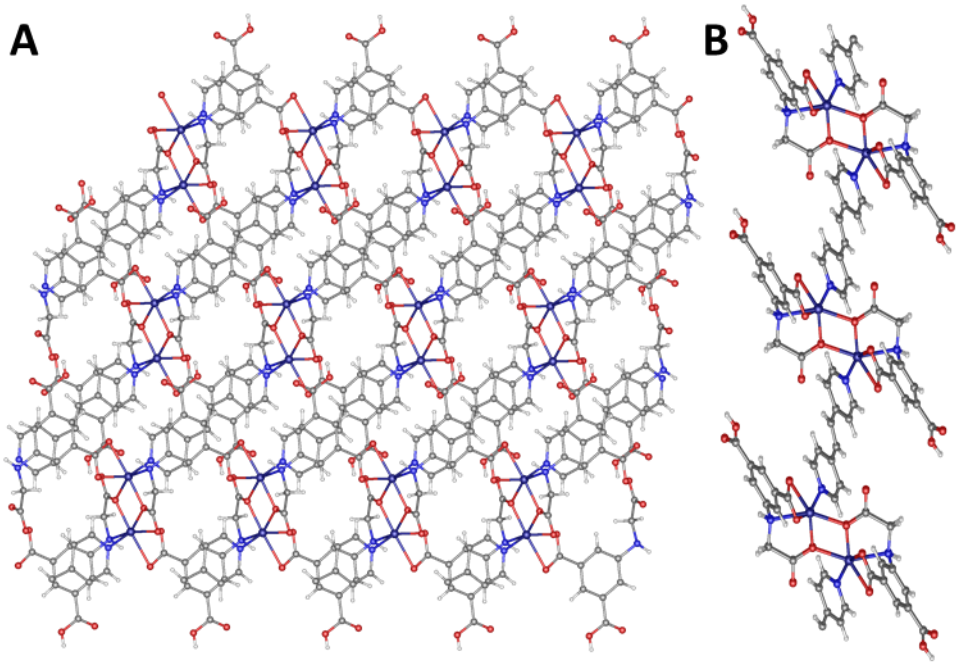

Figure 3.68. The 2-D planes in compound **18** as viewed looking down the **A –** *c*-axis and **B** – *a*-axis.

As in compound **12** the overall structure is supported by hydrogen bonds which are donated by the secondary amine, N1, and accepted by O3 on the carboxylic acid of the Hcmai linker. The interaction of two of these sheets can be seen in **Figure 3.69**. The packing of the sheets leaves channels running between them in the direction of the *a*-axis, these are where the guest DMF molecules resides, with both orientations of DMF forming a hydrogen bond with H4 that has been donated by the carboxylic acid oxygen, O4. The ratio the two positions is 55:45, the same found for the cadmium analogue, compound **12**.

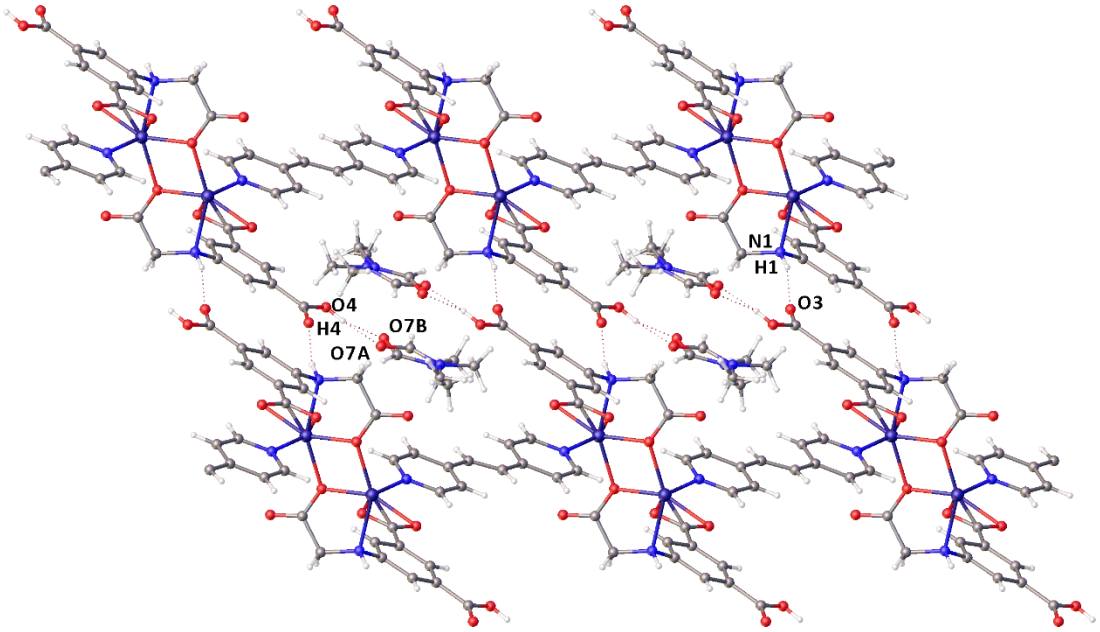

Figure 3.69. Two sheets in the structure of compound **18** showing hydrogen bonding, viewed looking down the *a*-axis.

The guest solvent and thermal behaviour of the system was interrogated using thermogravimetric analysis, the results of which are presented in **Figure 3.70**. The percentage mass of guest DMF in the structure assigned from the X-ray data is 15.7%. The TGA results show that between 215 °C and 320 °C 18.0% of the mass of the material was lost. The higher than expected value suggests that the framework has started to decompose before complete loss of the DMF solvent. This is further supported by the fact the TGA plot does not plateau after the DMF loss event, transitioning straight into framework decomposition.

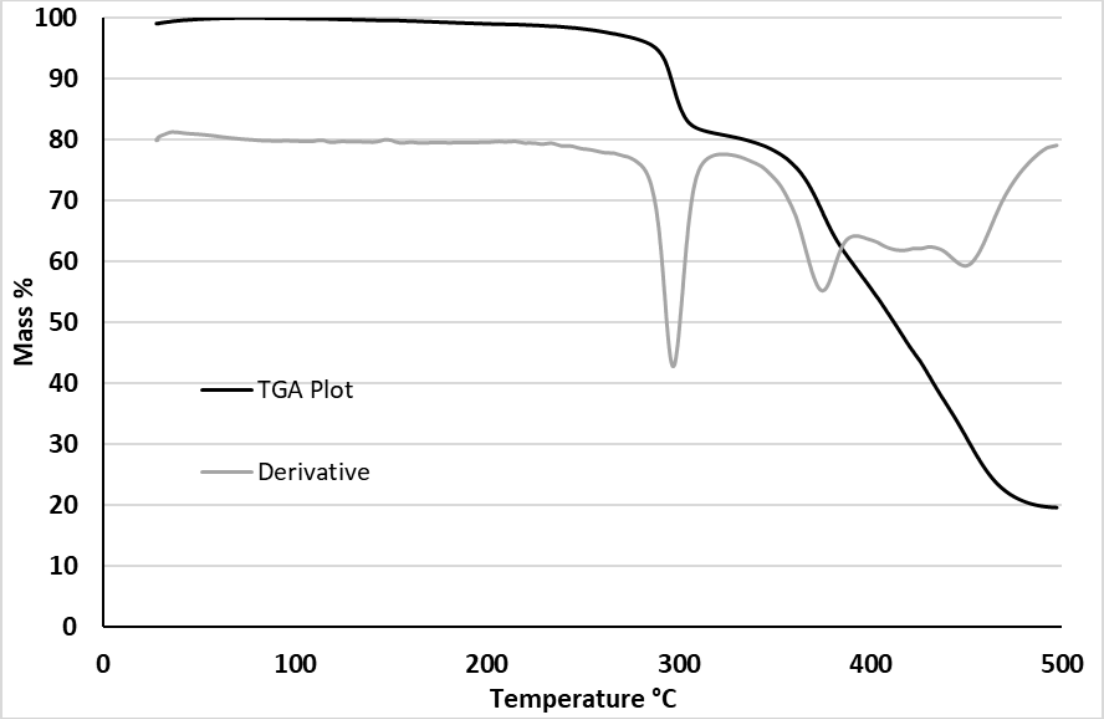

Figure 3.70. The thermogravimetric analysis results for compound **18**.

Void space analysis was carried out on the framework with the guest DMF removed from the structure. The channels found can be seen in **Figure 3.71** and represent 24% of the unit cell volume. The high temperature needed to remove the solvent from the pores, evidenced by TGA, is expected to make accessing the porosity of the material difficult.

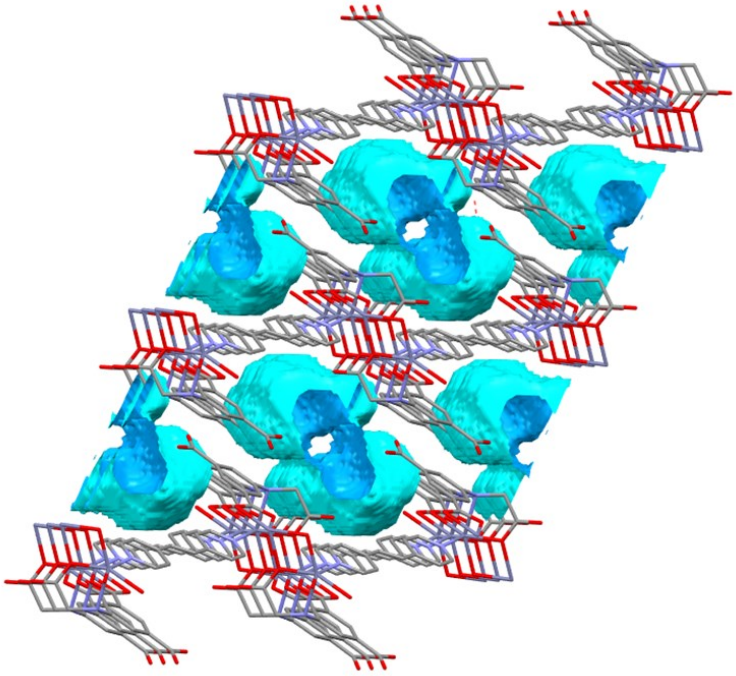

Figure 3.71. The void space in compound **18** with guest solvent removed.

3.3.3 The synthesis and characterisation of $[Zn_3(cmai)_2(phen)_2(H_2O)_3]\cdot 3H_2O$ (**19**)

Compound **19** was synthesised from the reaction of $Zn(NO_3)_2\cdot 6H_2O$ with H_3cmai and phen in a mixture of water and DMF at 90 °C for 7 days. The yellow block crystals were collected by filtration and a suitable crystal selected for single-crystal X-ray diffraction analysis.

Compound **19** crystallises in the orthorhombic space group *Pbca* and has an asymmetric unit containing three zinc centres, two cmai linkers, two phen ligands, three water ligands and three guest water molecules. The asymmetric unit along with the coordination sphere of the zinc centres are shown in **Figure 3.72**.

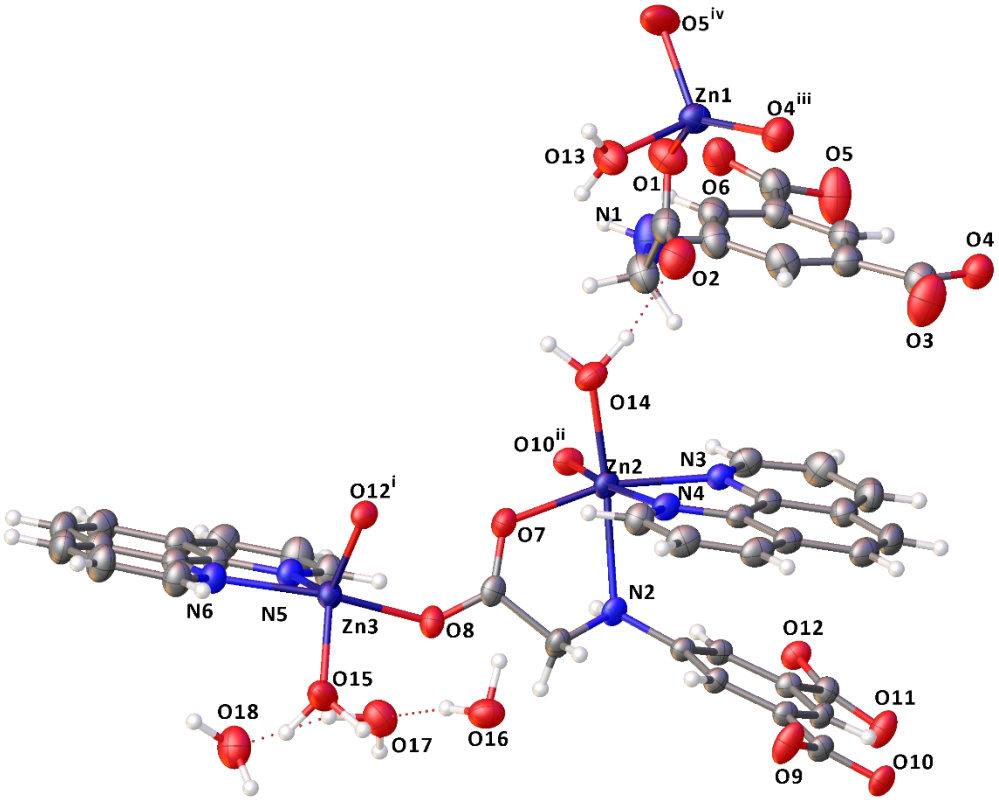

Figure 3.72. The asymmetric unit of compound **19** along with the coordination spheres of the zinc centres. (i, 1/2 + *x*, + *y*, 1/2 – *z*; ii, 1/2 – *x*, – 1/2 + *y*, + *z*; iii, 1 – *x*, 1 – *y*, 1 – *z*; iv, 1/2 + *x*, 1/2 – *y*, 1 – *z*)(Atomic displacement parameters are represented at 50% probability).

The structure of compound **19** is unusual as it contains two distinct frameworks in the same crystal structure. The first is an anionic framework, $[Zn(cmai)(H_2O)]^-$ and the second is cationic, $[Zn_2(cmai)(phen)_2(H_2O)_2]^+$. the two frameworks exist in a 1:1 ratio, so no charge-balancing counter ions are observed in the structure.

The anionic framework $[Zn(cmai)(H_2O)]^-$ contains one crystallographically independent zinc(II) centre, Zn1, one fully-deprotonated cmai ligand and one water ligand. Zn1 displays distorted

tetrahedral geometry (τ_4 = 0.74) and is bonded to three different cmai species, all of which bind through κ^1 modes via carboxylate oxygens O1, O4 and O5. The anionic framework contains no SBU and the network extends through primary building units in the form of the single zinc centres, Zn1. Each of the cmai linkers is bound to three Zn1 centres, which produces a 2-D network as shown in **Figure 3.73. A**. The network can be simplified and as both cmai and Zn1 are three-connected nodes, the resultant net is uninodal with a point symbol (4.8^2), also known as a fes type net. This can be seen in **Figure 3.73. B**.

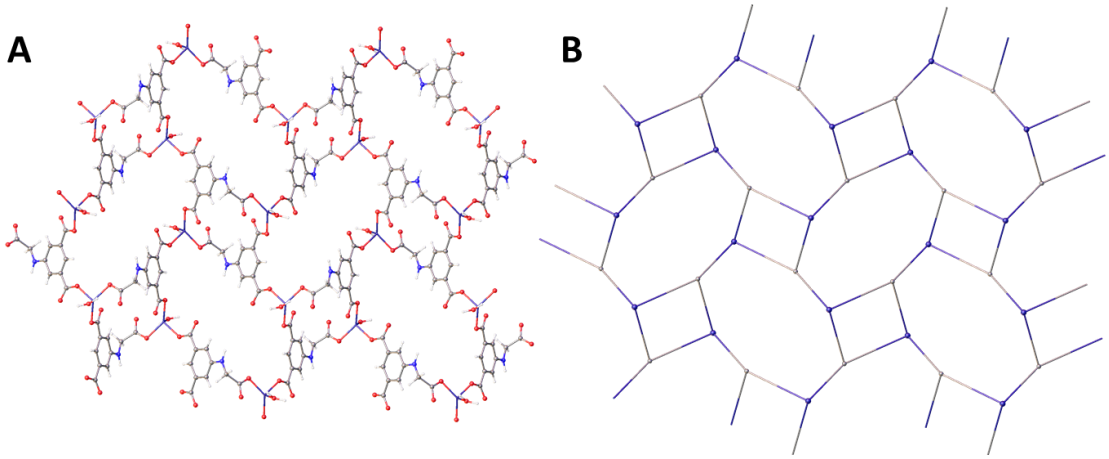

Figure 3.73. A – The 2-D structure of the anionic framework in compound **19**. **B** – The reduced net for the anionic framework.

The cationic framework, $[Zn_2(cmai)(phen)_2(H_2O)_2]^+$, contains two crystallographically distinct zinc centres. Zn2 is 6-coordinate and slightly distorted octahedral in geometry. It is coordinated by two cmai linkers, a phen ligand and one water ligand. One of the cmai linkers coordinates in a κ^2 mode through N2 of the secondary amine and the carboxylate oxygen of the flexible arm of the linker, O7. The other coordinates in a κ^1 mode involving an aryl carboxylate oxygen, O10, and is supported by the formation of a hydrogen bond donated by the secondary amine to the other carboxylate oxygen, O9. The phen linker coordinates in the expected bidentate κ^2 mode through N3 and N4 and the water ligand coordinates through O14.

Like Zn2, Zn3 is bound by two cmai linkers, one phen linker and one water ligand, however, it is 5-coordinate and distorted trigonal bipyramidal in geometry (τ_5 = 0.71). The cmai linkers each bind in κ^1 modes involving carboxylate oxygens, O8 and O12. The phen linker binds though N5 and N6 and the water ligand binds through O15.

The Zn2 and Zn3 centres are linked by a single bridging carboxylate, based on O7 and O8, forming a very simple SBU. The pair of zinc centres are coordinated by three cmai linkers, so act as a three-connected node. Each of the cmai linkers coordinates to three different zinc-containing

nodes so is also a three-connected node. The combination of these building blocks leads to the formation of a 2-D sheet, the structure of which is shown in **Figure 3.74. A**. The reduced net of the framework, shown in **Figure 3.74. B**, is a uninodal hcb type net with the point symbol 6^3.

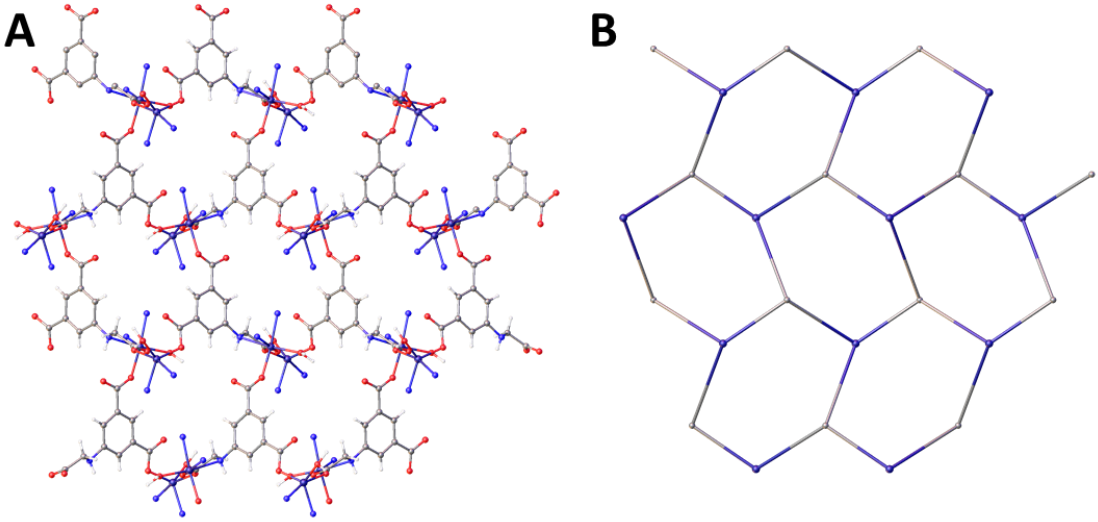

Figure 3.74. A – The 2-D structure of the cationic framework in compound **19**, the bulk of the phen ligands has been remove for clarity. **B** – The reduced net for the cationic framework.

The two charged frameworks are layered in an ABAB manner with the three crystallographically distinct guest water molecules lying between the sheets, as shown in **Figure 3.75**.

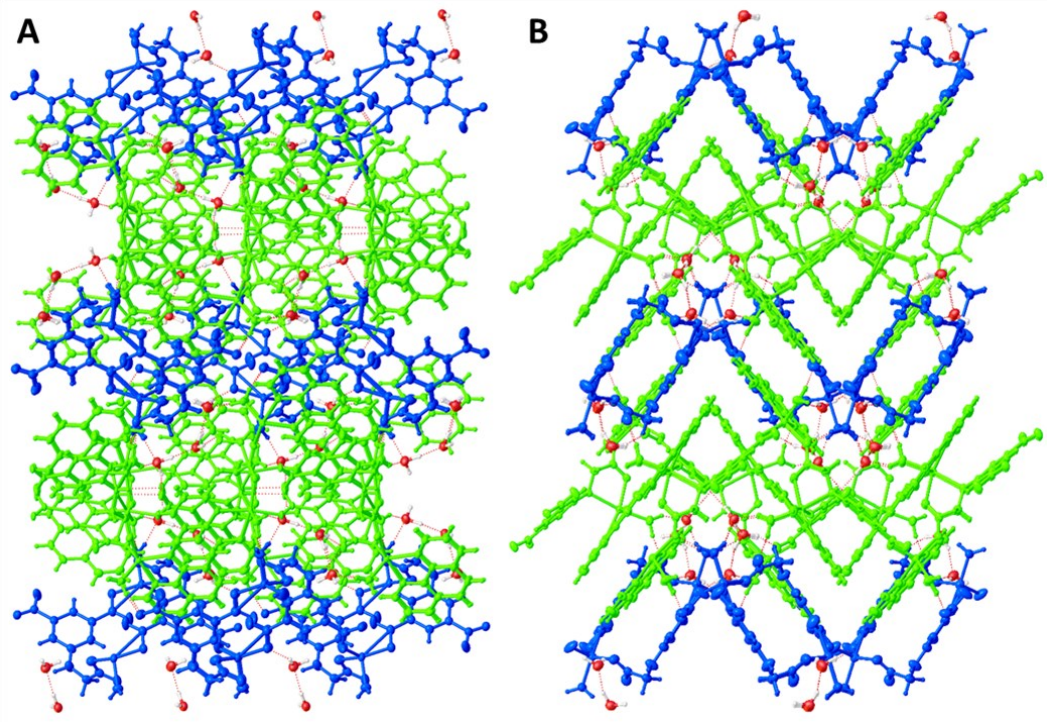

Figure 3.75. The layered structure of compound **19** viewed down the **A** – *a*-axis and **B** – *b*-axis. The anionic framework is shown in blue and the cationic framework in green.

The guest water molecules are extensively hydrogen bonded, both as donors and acceptors, to and from each of the charged frameworks. There are a total of 13 independent hydrogen bonds in the structure. One of these is involved in an intra-network interaction in the cationic framework involving the secondary amine, N2 donating to the carboxyl oxygen, O9. There are four hydrogen bonds directly between the frameworks, three of which originate from water ligands and the final one involving N1–H1···O11. The remaining eight hydrogen bonds all involve the guest water molecules, with the water molecules based on O16 and O18 both donating and accepting two hydrogen bonds while that based on O17 is a donor twice and acceptor once.

The extensive hydrogen bonding network involving the guest water molecules together with the presence of coordinated water suggests that this MOF will be difficult to activate and it did not retain crystallinity on attempts to do so. The thermal behaviour of the MOF and its guests were investigated further using TGA, the results of which are presented in **Figure 3.82**. 6.8% of the compound's mass was lost between 80 °C and 140 °C, which is consistent with loss of four of the six water molecules present in the formula unit (calc. 6.3%). The remaining two water molecules are lost more slowly between 140 °C and 250 °C, which is consistent with the high degree of hydrogen bonding observed within the structure and the aforementioned difficulty of activation.

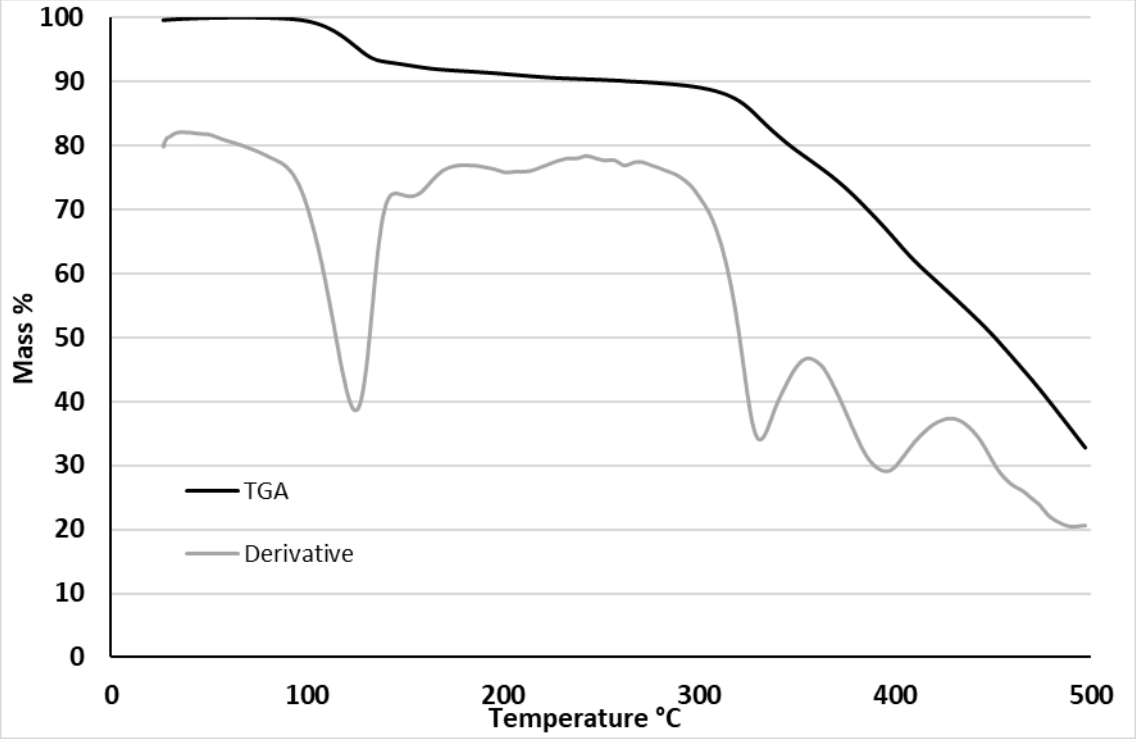

Figure 3.76. The TGA results for compound **19**.

Potential void space analysis of compound **19,** with the guest water molecules removed, shown in **Figure 3.77**, has revealed that the structure contains discrete cavities. Unsurprisingly, these

cavities are located where the guest water resides. The voids make up 5% of the total volume of the structure.

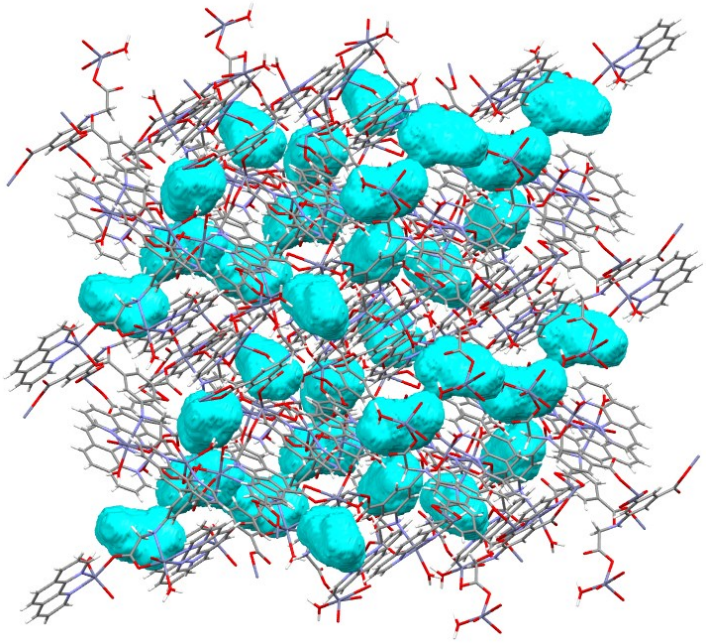

Figure 3.77. The potential voids inside compound **19.**

3.3.4 Discussion

The combination of zinc salts with H_3cmai and the neutral linkers bipy, bpe and phen leads to the formation of three new MOFs, compounds **16**, **18** and **19**, one with each co-ligand. A fourth structure was obtained upon dehydration of compound **16**, forming compound **17**. The crystal and structural refinement data for these materials are presented in **Table 3.5** at the end of this discussion.

The three structures formed from solution were all synthesised in very similar reactions, with the main variation being the reaction time and identity of the co-linker, as summarised in **Table 3.4**. Many more experiments could be designed to investigate the formation of new structures, for example using different zinc salts and varying the reaction temperature.

Table 3.4. A summary of synthetic conditions for compounds **16**-**19**.

Compound	Zinc Salt	Co-ligand	Metal:cmai: co-ligand	Solvent System	Temp °C	Reaction Time	Comment
16	$Zn(NO_3)_2{\cdot}6H_2O$	bipy	3:1:1	DMF/H_2O	90	2 days	-
17	$Zn(NO_3)_2{\cdot}6H_2O$	bipy	3:1:1	-	-	-	Dehydration product
18	$Zn(NO_3)_2{\cdot}6H_2O$	bpe	4:2:1	DMF/H_2O	90	3 days	0.05 mL Conc. HNO_3
19	$Zn(NO_3)_2{\cdot}6H_2O$	phen	3:1:1	DMF/H_2O	90	7 days	-

Compound **16** and its dehydration product, compound **17**, form 3-D networks, whilst compounds **18** and **19** form 2-D sheet structures. Both the zinc compounds synthesised in **Chapter 2** formed sheets, so the addition of a neutral linker has allowed the formation of a 3-D framework but does not appear to guarantee the generation of a higher dimensionality topology.

The coordination of the zinc centre in compounds **16**-**19** varies from 4-coordinate to 6-coordinate. Compound **19** contains three different zinc centres with different coordination numbers. This degree of variation is surprising considering the zinc compounds in **Chapter 2** only contained 6-coordinate octahedral zinc centres.

Despite the varying zinc coordination numbers, compounds **16**-**19** display only one type of SBU, if one is formed. Compounds **16** and **18** both contain a zinc dimer SBU, which is supported by two bridging μ_2-O atoms that are also part of a κ^2 bidentate interaction with the secondary

amine of the (H)cmai linkers. This SBU was seen in some of the cadmium structures both in **Chapter 2** and **Chapter 3**, its form is shown in **Figure 3.78**.

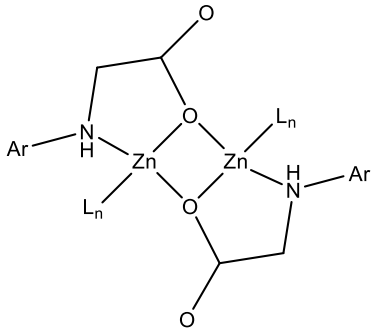

Figure 3.78. The structure of the zinc dimer motif observed in compound **16** and **18**.

In the single-crystal to single-crystal transformation from compound **16** to compound **17** the zinc dimer SBU is partially broken, losing one of the μ_2-O interactions, so while still technically a dimer the symmetry of the unit has been reduced. Compound **19** contains a pair of zinc centres linked by a single bridging carboxylate, so although it can be considered an SBU it is unlikely to provide any significant structural support to the framework. The formation of zinc and cadmium dimer SBUs when combined with neutral linkers suggests that this is a favourable arrangement of ligands and metal centres in these types of MOFs.

The ligand cmai has been shown in **Chapter 2** to adopt a wide range of coordination modes, and these mixed-linker zinc MOFs are no different. The range of different binding modes adopted in compounds **16**-**19** are presented in **Figure 3.79**. The binding modes are the same as those observed in the mixed-linker cadmium compounds **11**-**15**, shown in **Figure 3.51**, other than the mode shown in **Figure 3.79. G**, which has the carboxylate bound in κ^1 mode. **Figure 3.79 G** is observed in the anionic network of compound **19** and is only the second example of a cmai linker in which the secondary amine does not coordinate to a metal centre. The fact that the same coordination modes are observed in both the cadmium and zinc mixed-ligand MOFs, and that these modes are less diverse than the modes observed for compounds **1**-**10**, suggests that presence of the N-donor ligands promote the formation of these specific arrangements of species. With less binding modes observed, a greater degree of control and predictability can be gained over the systems synthesised by introducing a neutral N-donor co-linker.

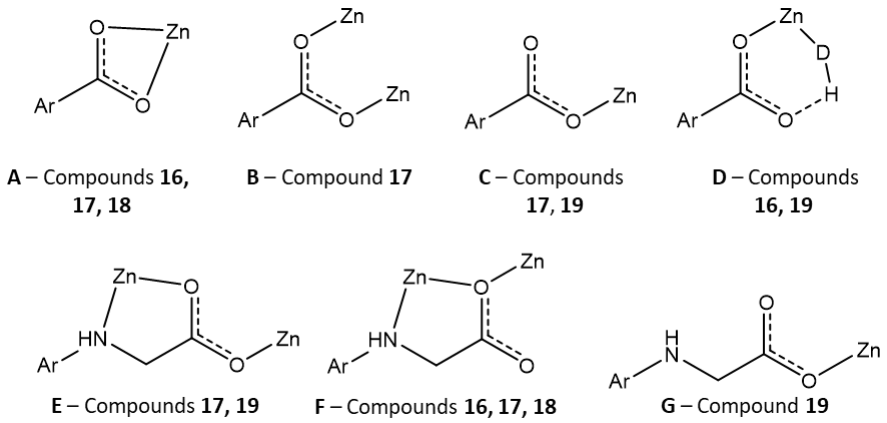

Figure 3.79. The coordination modes present in compounds **16**-**19**.

Neither the structures of compounds **17** nor **18** contain any water ligands. In compound **17** the lack of water is not surprising as the material is formed by heating under reduced pressure, causing dehydration. Compound **18** contains no water ligands despite being synthesised in a DMF/H_2O solvent mixture. The structure formed is isoreticular to cadmium-based compound **12** and like the cadmium analogue the structure must be heated to very high temperatures (>250 °C) to remove the guest DMF. This is the only example of the formation of zinc/cadmium isoreticular structures in this work. Compound **18** is also the only zinc-based MOFs to exhibit a substantial amount of potential porosity, with a void space of 24% of the structure's volume.

The single-crystal to single-crystal transformation observed between compound **16** and its dehydrated form compound **17** is very interesting. This is a similar type of transformation to that seen between the cadmium-based compounds **3** and **4** suggesting that it maybe concomitant with the semi-rigid nature of the cmai linker. One of the driving forces for the structural rearrangements observed is likely the unsaturated nature of the vacant coordination sites left on removal of water ligands. The transformation was shown to be reversible despite it involving the breaking and formation of bonds.

The structure of compound **19** is also interesting and represents the first example of two charge-balancing 2-D frameworks crystallising as part of the same structure. The closest system previously reported involves a zinc MOF that was formed from a tetracarboxylate linker and contains two 3-D interpenetrating charged nets. The two components were very similar in topology and composition with the charge difference arising from missing zinc centres in the anionic framework.[124] In contrast, the alternating nets in compound **19** are structurally very different, with the anionic net adopting a fes-type topology with 4-coordinate zinc centres and the cationic network adopting a hcb-type net with 5 and 6-coordinate zinc centres.

Table 3.5. Crystal data and structural refinement for compounds **16**-**19**.

Compound	**16**	**17**	**18**	**19**
Empirical formula	$C_{15}H_{15.76}N_2O_9Zn_{1.5}$	$C_{30}H_{20}N_4O_{12}Zn_3$	$C_{19}H_{19}N_3O_7Zn$	$C_{44}H_{40}N_6O_{18}Zn_3$
Formula weight	466.11	824.61	466.74	1136.93
Temperature/K	150.01(10)	150.00(10)	150.00(10)	150.00(10)
Crystal system	triclinic	Triclinic	triclinic	orthorhombic
Space group	*P*-1	*P*-1	*P*-1	*Pbca*
a/Å	7.9590(7)	11.6706(3)	7.6676(4)	16.72968(10)
b/Å	10.5220(13)	11.9926(3)	11.1769(5)	15.76472(8)
c/Å	11.2100(13)	12.5606(3)	12.3443(6)	32.93520(17)
α/°	112.467(11)	82.140(2)	65.576(4)	90
β/°	93.024(8)	67.531(2)	80.618(4)	90
γ/°	96.773(8)	65.140(2)	78.608(4)	90
Volume/Å^3	856.57(18)	1473.40(7)	940.33(9)	8686.29(8)
Z	2	2	2	8
ρ_{calc}g/cm^3	1.807	1.859	1.648	1.739
μ/mm^{-1}	2.172	3.518	2.267	2.704
F(000)	474.0	828.0	480.0	4640.0
Crystal size/mm^3	0.301 × 0.225 × 0.114	0.345 × 0.18 × 0.121	0.184 × 0.072 × 0.055	0.191 × 0.078 × 0.059
Radiation/Å	MoKα (λ = 0.71073)	CuKα (λ = 1.54184)	CuKα (λ = 1.54184)	CuKα (λ = 1.54184)
2Θ range for data collection/°	6.72 to 54.964	7.62 to 145.158	7.898 to 146.168	5.366 to 146.218
Index ranges	-7 ≤ h ≤ 10, -13 ≤ k ≤ 12, -13 ≤ l ≤ 14	-14 ≤ h ≤ 14, -14 ≤ k ≤ 14, -15 ≤ l ≤ 15	-9 ≤ h ≤ 9, -13 ≤ k ≤ 13, -15 ≤ l ≤ 14	-17 ≤ h ≤ 20, -16 ≤ k ≤ 19, -40 ≤ l ≤ 40
Reflections collected	7208	61049	9303	83683
Independent reflections, R_{int}	3926, 0.0246	5826, 0.0404	3753, 0.0305	8672, 0.0456
Data/restraints/parameters	3926/20/296	5826/2/450	3753/15/325	8672/13/704
Goodness-of-fit on F^2	1.017	1.185	1.046	1.107
Final R_1, wR_2 indexes [I>=2σ (I)]	0.0344, 0.0718	0.0771, 0.2282	0.0341, 0.0877	0.0446, 0.1172
Final R_1, wR_2 indexes [all data]	0.0456, 0.0775	0.0827, 0.2331	0.0370, 0.0902	0.0458, 0.1183
Largest diff. peak/hole / e Å^{-3}	0.51/-0.50	1.85/-0.93	0.76/-0.47	1.38/-0.50
Flack parameter	-	-	-	-

3.4 Conclusions

A total of nine new MOFs have been synthesised using novel linkers based on H_3cmai, along with neutral N-donor ligands and zinc(II) or cadmium(II) centres. The N-donor ligands used were 4,4'-bypyridine (bipy) and 1,2-bis(4-pyridyl)ethylene (bpe), both of which are linear pyridine-based linkers, and 1,10-phenanthroline (phen), which is a bidentate ligand. Four of the structures contained bpe, three contained bipy and two contained phen.

The introduction of a neutral ligand into the synthesis of MOFs containing cmai was targeted for several reasons. In the first instance, it provides a way of increasing the proportion of the framework that is rigid, promoting the maintenance of permanent porosity on the removal of guest solvent. The presence of the extra ligands was also anticipated to increase competition with water ligands, reducing the number which bound to metal sites in the arising structures. Finally, bipy and bpe were anticipated to increase the dimensionality of the arising frameworks, as 50% of those described in **Chapter 2**, containing just cmai as a linker, were one or two dimensional.

In general, it was found that the nine structures that contain an N-donor ligand had a higher dimensionality than those from **Chapter 2**, with three of the compounds exhibiting 2-D topologies and six having 3-D networks. Isostructural compounds **12** and **18**, along with compound **14** did not contain any water ligands, showing that the addition of the neutral ligands lead to a reduction of the prevalence of coordinating water. In the case of compound **11**, the supporting bipy pillaring linker allowed for a partially activated form to be accessed, which was not possible in compound **5**, which has an analogous structure but without the structurally supporting bipy linker.

In **Chapters 2** and **3** a total of 19 new MOFs have been synthesised using linkers based on H_3cmai. With such a large group of structures some clear patterns and trends emerge that can be attributed to this MOF family.

The degree of deprotonation on the cmai-based linker dictates the dimensionality of the framework formed. In all cases where the linker was only doubly deprotonated, with one of the aryl carboxylic acids remaining protonated in each case, the framework formed was either one or two dimensional. This could provide an additional strategy when trying to synthesise three dimensional frameworks, using more basic conditions to ensure the cmai linker is fully deprotonated.

11 of the 19 MOFs made contained cadmium as the metal centre. The large number of structures formed from a limited number of building blocks has been ascribed to the flexibility in coordination number and geometry of cadmium(II) centres, with coordination numbers between 5 and 8 observed. Having a d^{10} electron configuration means that cadmium(II) centres have no electronic directional preference in the coordination geometry formed which, as such, is very varied. These features combined with the fact that cmai can adopt a large number of different coordination modes leads to many combinations of the building blocks, resulting in structural diversity.

A key feature of H_3cmai is the flexible arm of the ligand, consisting of a secondary amine and a CH_2 linked carboxylic acid. This flexible portion of the linker exhibited a similar binding mode in all but three of the structures found. This is a κ^2 bidentate binding mode, involving the secondary amine and one of the carboxylate oxygens on the end of the arm and is depicted in **Figure 3.80**. The prevalence of this mode reflects the chelate effect via the favourable five-membered metallocycle formation.

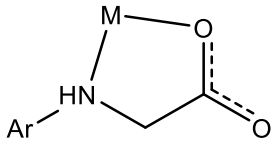

Figure 3.80. Bidentate binding of flexible arm of cmai.

The difficulty in activating these materials whilst retaining the framework structure was highlighted as a common theme. This was mainly attributed to the presence of water ligands which were lost from the structures at similar temperatures to the guest solvent. The arising unsaturated metal coordination sites, appeared to have caused framework collapse or structural rearrangement.

Instances of structural rearrangement were observed in three of the structures, compounds **3**, **11** and **16**. In the case of compound **11**, a ligand exchange was observed where a guest DMF molecule was able to displace a water ligand on heating. In the case of compound **3** and **16**, full dehydration occurred accompanied by a change in connectivity of the linkers and topology of the framework. These rearrangements were shown to be reversible in all cases, a surprising property considering it requires the breaking and formation of large numbers of bonds.

Overall the cmai linker has shown a remarkable affinity for the formation of coordination polymers and MOFs. These have displayed a range of interesting structural features and

properties. These include reversible structural rearrangement on dehydration and photocatalytic activity, suggesting that these materials may find uses in catalysis and sensing.

3.5 Future Work – Chapter 2 and 3

The natural continuation of this part of the project will look at investigating the properties of the new MOFs in more depth with a view to establishing applications for which they may be suited. Preliminary photocatalytic studies highlighted compound **8** as active for the degradation of the dye rhodamine B, suggesting that catalysis may be an area of study to investigate further. It has also been noted that some of the compounds exhibited luminescence under UV light, so characterisation of this property could lead to potential applications in sensing.

Several interesting structural changes caused by heating and water loss were observed in the synthesised MOFs. Further investigation of these phenomena should be carried out to confirm that this is a common feature of materials containing this linker. This initially could be studied by carrying out VT-PXRD experiments on all of the frameworks. It would also be interesting to see if the frameworks exhibit similar structural rearrangements when exposed to solvents other than water.

The unique structure of compound **19**, composed of two charged balancing 2-D nets, stacked in alternate layers, should be investigated further. The synthesis of materials similar to this could be targeted, using similar conditions and other bidentate N-donor ligands. Equally important is understanding if this type of layered material with its unique charge distribution can be exploited in an application.

As this thesis presents the first investigation into the compounds formed containing H_3cmai, it is probable that additional MOFs could be synthesised using this linker. Specific synthetic targets that would be of interest are MOFs containing lanthanide metals, which have not been explored in this work. The lanthanide ions are larger than cadmium(II) so more variation in coordination mode and structural arrangement are expected. The metal to ligand ratio would also be expected to change due to the stability of lanthanide(III) centres. Lanthanide-based MOFs are known to have luminescent properties, amenable to applications in sensing.

The synthesis of H_3cmai was realised by addition of glyoxalic acid to 5-amino-1,3-benzenedicarboxylic acid, resulting in the production of a semi-rigid linker with a flexible arm consisting of a secondary amine and CH_2 linked carboxylic acid. The reaction of glyoxalic acid in combination with other phenylamines will result in the formation of species containing the same flexible arm as H_3cmai. The ideal starting place to investigate the class of ligands containing this coordination site would be in the formation of 4-((carboxymethyl)amino)benzoic acid and 3,5-di((carboxymethyl)amino)benzoic acid, the structures of which are shown in **Figure 3.81**, as they

are structurally similar to H_3cmai. Comparable binding modes would be expected to be present in MOFs synthesised from these linkers as in cmai, and as such, a similar level of structural variety would be expected.

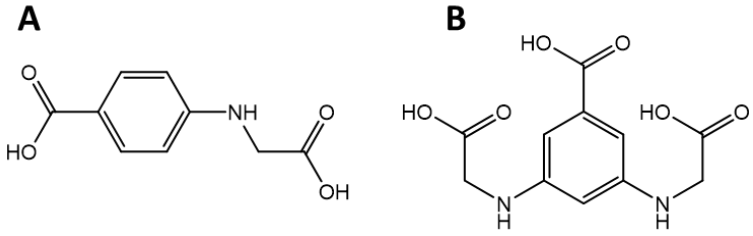

Figure 3.81. A - 4-((carboxymethyl)amino)benzoic acid and **B** – 3,5-di((carboxymethyl)amino)benzoic acid.

3.6 Experimental

General procedures are presented in the experimental section of **Chapter 2.**

3.6.1 The synthesis of $[Cd_3(cmai)_2(bipy)(H_2O)_4]\cdot 6H_2O\cdot 2DMF$ (**11**)

H_3cmai (0.1 mmol, 0.0239 g) was added to 4 mL of DMF in a 10 mL microwave reaction vessel and the mixture sonicated for 15 min. To this was added 4 mL of deionised water which caused the acid to dissolve. 4,4'-bipy (0.1 mmol, 0.0154 g) was dissolved in the reaction solution and then $Cd(NO_3)_2\cdot 4H_2O$ (0.3 mmol, 0.0925 g) was added, causing a precipitate to form. Finally, 0.2 mL of 1M HNO_3 was added dissolving the precipitate and the vial was then sealed using a Teflon-lined cap. The reaction vessel was placed in an oven at 90 °C for 18 hours during which very large colourless obelisk-shaped crystals formed. After removal from the oven and cooling under ambient conditions, these were collected using vacuum filtration and washed with deionised water (3 x 3 mL). The material was stored under deionised water until required.

The identity of the bulk material was interrogated using PXRD. The experimental pattern is presented alongside the pattern simulated from single-crystal data in **Figure 3.82**. The two patterns match very closely confirming the phase purity of the material as compound **11.** Elemental microanalysis was carried out; good agreement was found between the experimental result and the theoretical values. Expected: C 33.47%, H 4.21%, N 6.50%. Found: C 33.59%, H 3.93%, N 6.46%.

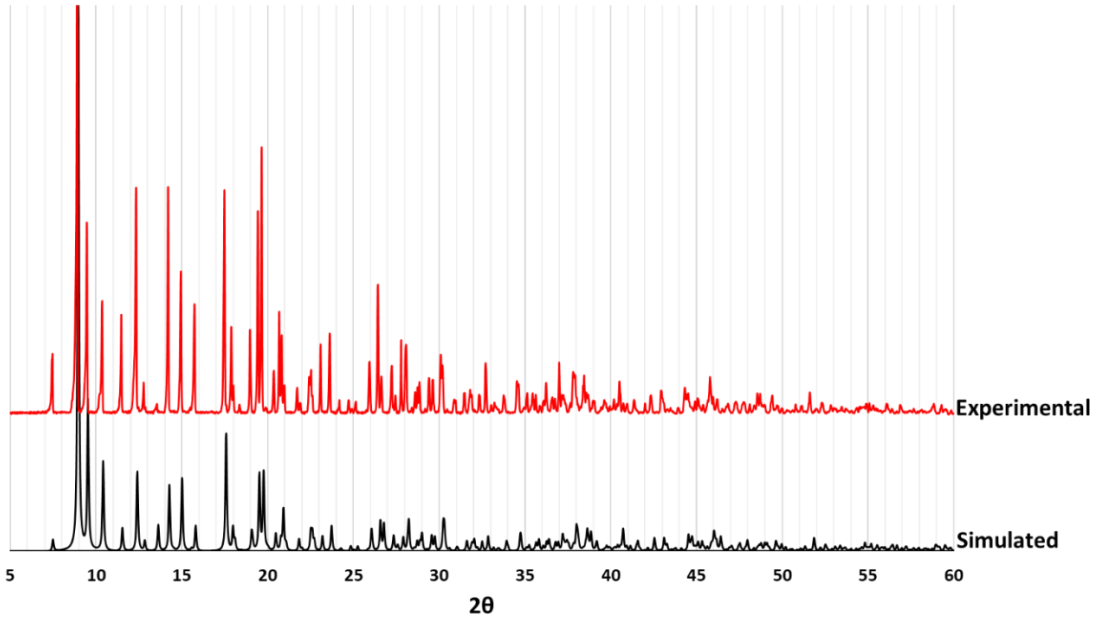

Figure 3.82. The experimental PXRD pattern for compound **11** compared to the pattern simulated from the single-crystal data.

The IR spectrum was collected for a sample of compound **11** and is shown in **Figure 3.83**. (solid, cm^{-1}) 3321s (br), 1649m, 1625m (sh), 1574s, 1377s (sh), 1370s, 1305s, 1106w, 1076w, 779s, 736s.

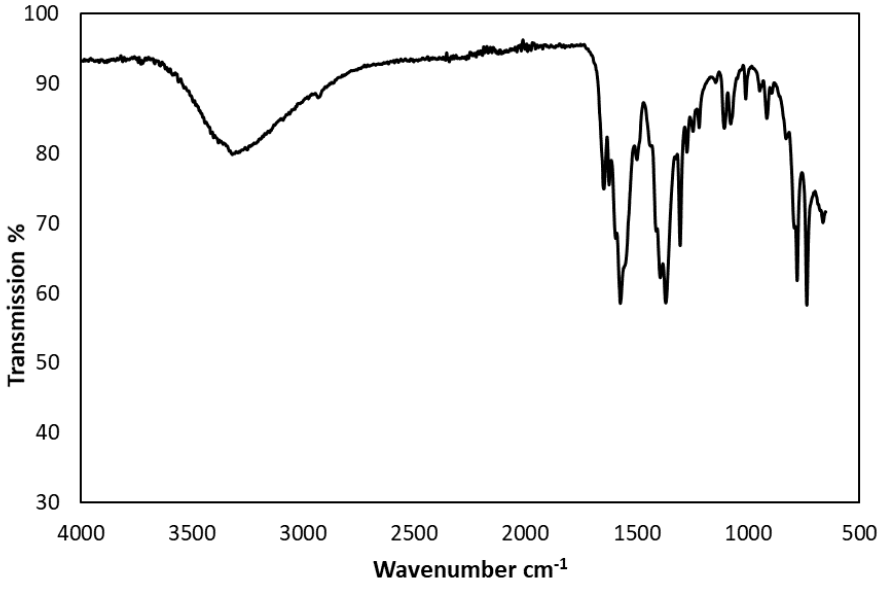

Figure 3.83. The IR spectrum for compound **11**.

A ^{1}H-NMR experiment was conducted on a sample of compound **11** digested in a D_2SO_4/D_2O/DMSO-d^6 mixture and is presented in **Figure 3.84**. The spectrum showed the expected ratio of 2:1 for cmai linker to bipy.

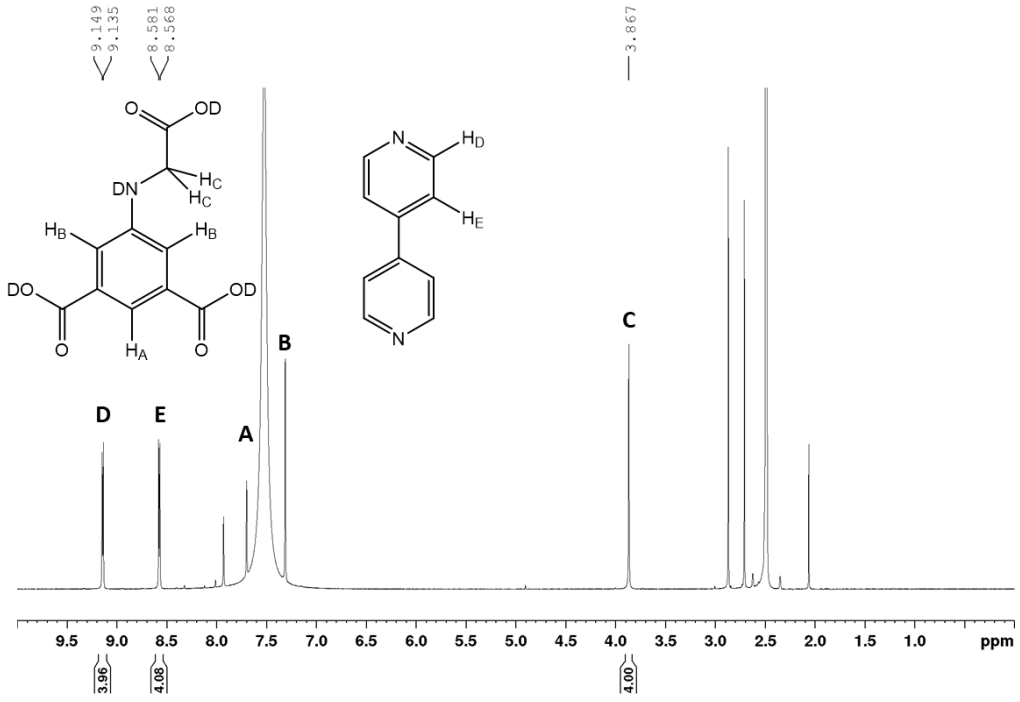

Figure 3.84. The ^{1}H-NMR spectrum of digested compound **11**.

3.6.2 The synthesis of $[Cd_2(Hcmai)_2(bpe)]\cdot 2DMF$ (**12**)

H_3cmai (0.1 mmol, 0.0239 g) was added to 4 mL of DMF in a 10 mL microwave reaction vessel and the mixture sonicated for 15 min. To this was added 4 mL of water which caused the acid to dissolve. bpe (0.1 mmol, 0.0184 g) was dissolved in the reaction solution then $Cd(OAc)_2\cdot 2H_2O$ (0.3 mmol, 0.080 g) was added, causing a precipitate to form. Finally, 1 mL of 1M HNO_3 was added which caused the precipitate to dissolve and the vial was then sealed using a Teflon-lined cap. The reaction vessel was placed in an oven at 90 °C for 18 hours during which time colourless block crystals had formed. After removal from the oven and cooling under ambient conditions, these were collected using vacuum filtration and washed with deionised water (3 x 3 mL). The material was stored under deionised water until required.

The identity of the bulk material was probed by PXRD. The experimental pattern was compared to the pattern simulated from the single-crystal data, presented in **Figure 3.85**, and showed good agreement. The bulk material was further interrogated by elemental microanalysis for which the theoretical values matched well with the experimental ones. Expected: C 44.42%, H 3.73%, N 8.18%. Found: C 43.40%, H 3.70%, N 7.92%.

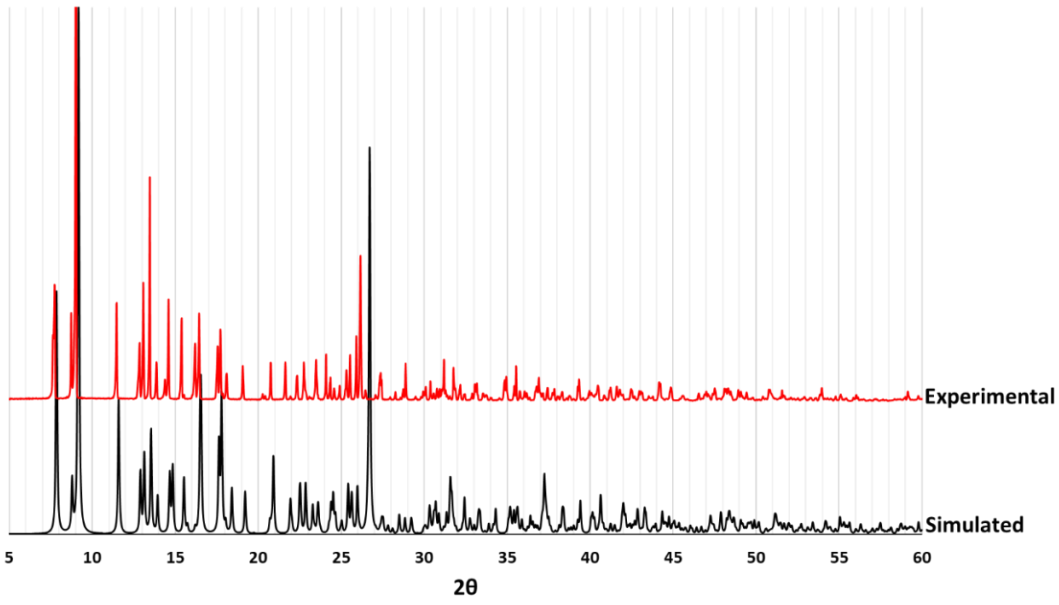

Figure 3.85. The experimental PXRD trace for compound **12**, compared the trace simulated from single-crystal data.

The IR spectrum was collected for a sample of compound **12** and is shown in **Figure 3.86**. (solid, cm^{-1}) 3295w, 1689m, 1635m, 1608s, 1536m, 1336s, 1305s, 1021m, 1076w, 897m, 837m, 766s, 670s.

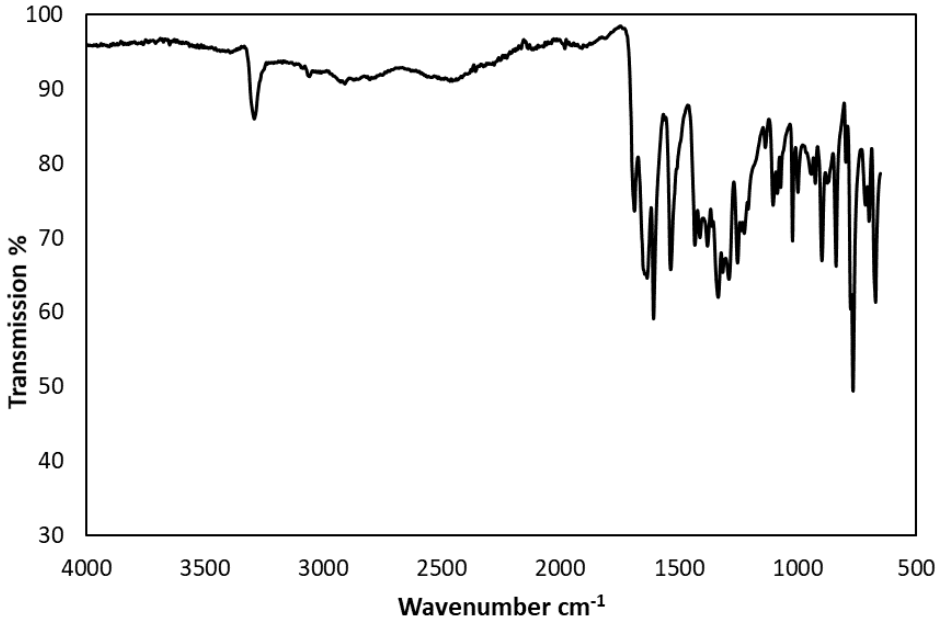

Figure 3.86. The IR spectrum for compound **12**.

A ^{1}H-NMR experiment was conducted on a sample of compound **12** digested in a D_2SO_4/D_2O/DMSO-d^6 mixture and is presented alongside assigned molecular structures of the linkers in **Figure 3.87**. The spectrum showed the expected ratio of 2:1 for cmai linker to bpe.

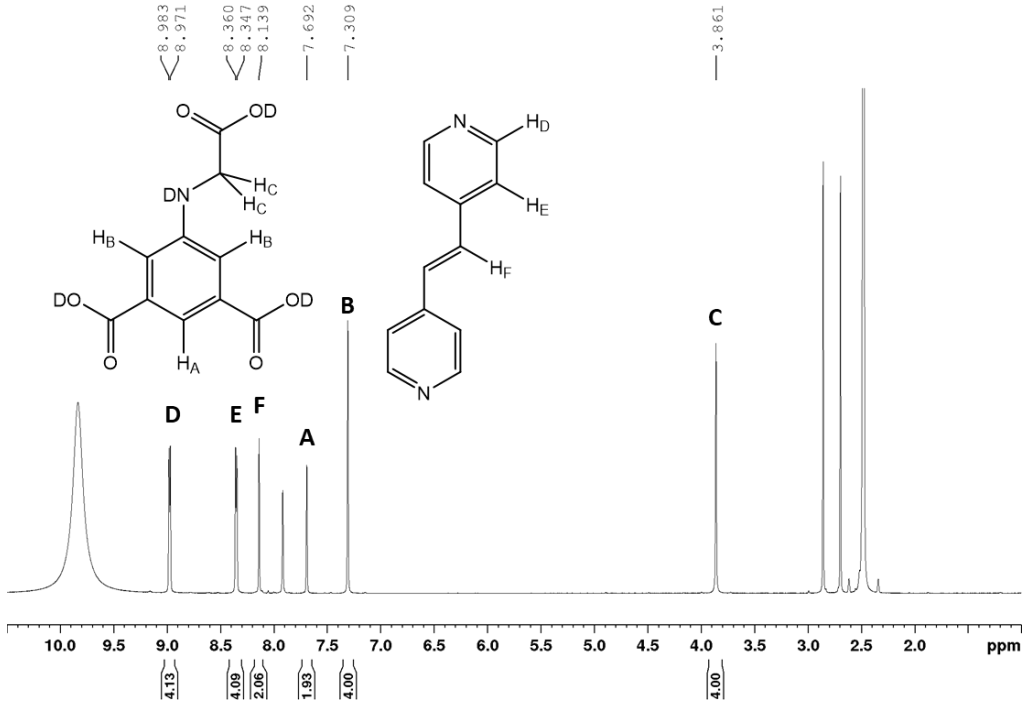

Figure 3.87. The ^{1}H-NMR spectrum of digested compound 1**2.**

3.6.3 Synthesis of $[Cd_3(cmai)_2(bpe)_2(H_2O)_3]\cdot 6H_2O$ (**13**)

$Cd(OAc)_2\cdot 2H_2O$ (0.6 mmol, 0.1599 g), H_3cmai (0.1 mmol, 0.0238 g) and bpe (0.1 mmol, 0.0182 g) were placed in a 30 mL microwave vial containing 12 mL of deionised water and the mixture sonicated for 15 minutes. The vial was sealed and then placed in an oven at 90 °C for three days. After removal from the oven and cooling under ambient conditions, the light yellow rod crystals were collected by vacuum filtration and washed with deionised water (3 x 3 mL) and then stored in deionised water until required.

PXRD analysis was carried out to assess the phase of the bulk material. The experimental pattern is presented alongside the pattern generated from the single-crystal data in **Figure 3.88**. The patterns match very closely confirming the bulk material as compound **13**. Elemental microanalysis was also carried out and the experimental results were in good agreement with those calculated based on the formula assigned for compound **13** based on the single-crystal data. Expected: C 39.55%, H 3.77%, N 6.29%. Found: C 38.91%, H 3.53%, N 6.24%.

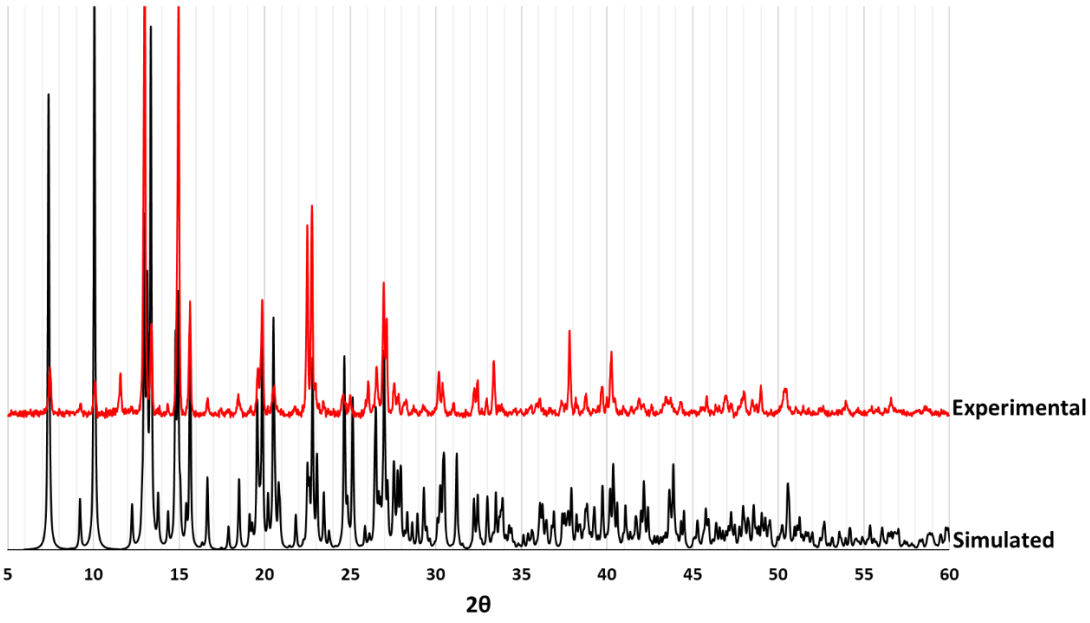

Figure 3.88. The experimental PXRD pattern for compound **13**, compared to that generated from the single-crystal data.

The IR spectrum was collected for a sample of compound **13** and is shown in **Figure 3.89**. (solid, cm^{-1}) 3325s, 1608m, 1537s, 1427s, 1375s, 1320m, 1018w, 781m, 1076w, 897m, 775s, 736s.

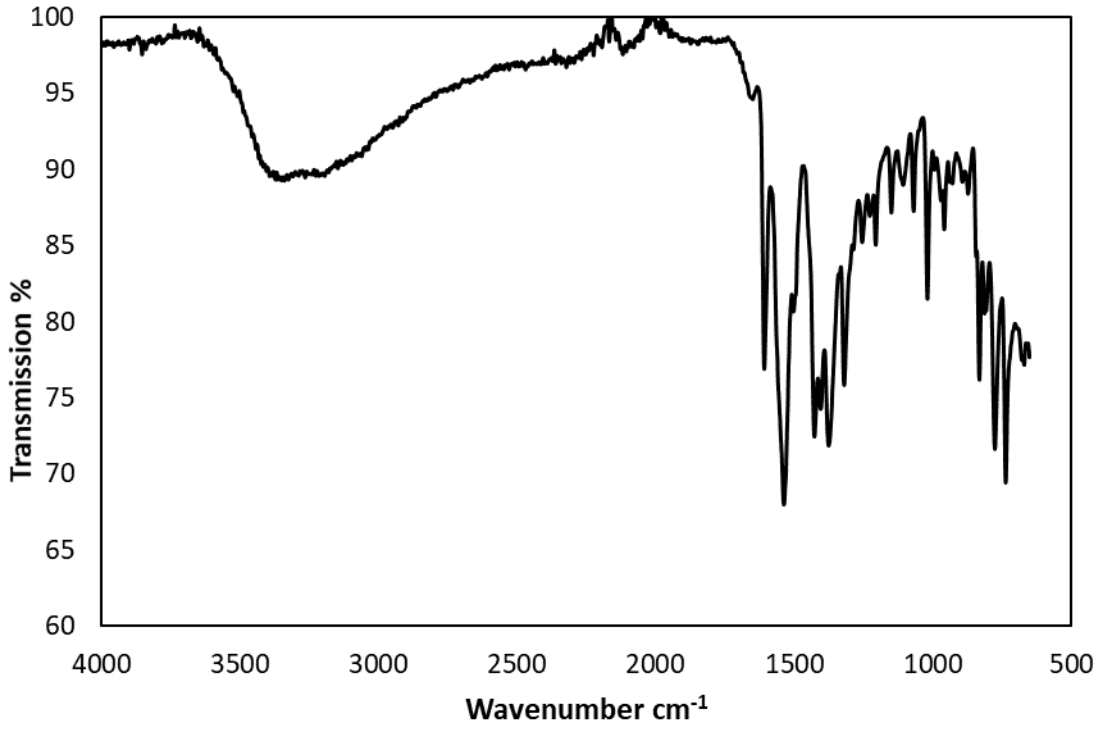

Figure 3.89. The IR spectrum for compound **13**.

3.6.4 The synthesis of $[Cd_2(cmai)(bpe)_2]\cdot(NO_3)\cdot DMF$ (**14**)

H_3cmai (0.1 mmol, 0.0239 g) was added to 4 mL of DMF in a 10 mL microwave reaction vessel and the mixture sonicated for 15 min. To this was added 4 mL of water which caused the acid to dissolve. bpe (0.1 mmol, 0.0184 g) was dissolved in the reaction solution then $Cd(NO_3)_2\cdot 4H_2O$ (0.3 mmol, 0.0925 g) was added. Finally, 0.5 mL of 1M HNO_3 was added and the vial was sealed using a Teflon-lined cap. The reaction vessel was placed in an oven at 90 °C for 36 hours during which colourless block crystals had formed. After removal from the oven and cooling under ambient conditions, these were collected via vacuum filtration and washed with deionised water (3 x 3 mL) and then stored in deionised water until required.

Characterisation of the bulk material was carried out using PXRD. The experimental trace is presented alongside the trace simulated from the single-crystal structure in **Figure 3.90**, showing the synthesised bulk material is compound **14**.

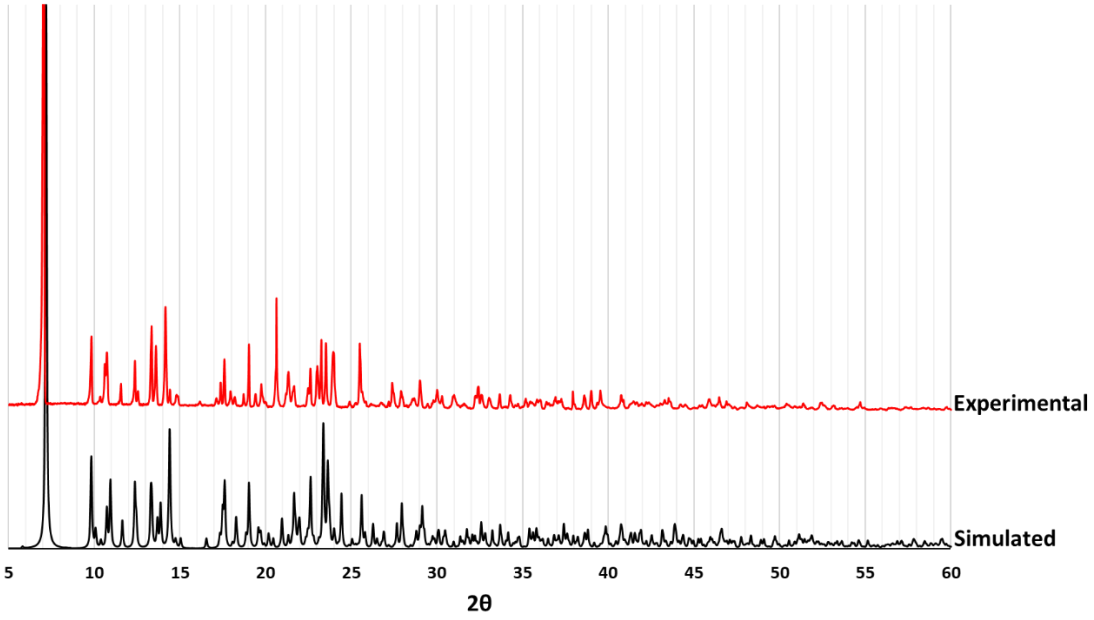

Figure 3.90. The experimental and simulated pattern for compound **14**.

The IR spectrum was collected for a sample of compound **14** and is shown in **Figure 3.91**. (solid, cm^{-1}) 1664m, 1609m, 1548s, 1332s, 1328m, 915mw, 829s, 777s, 719m.

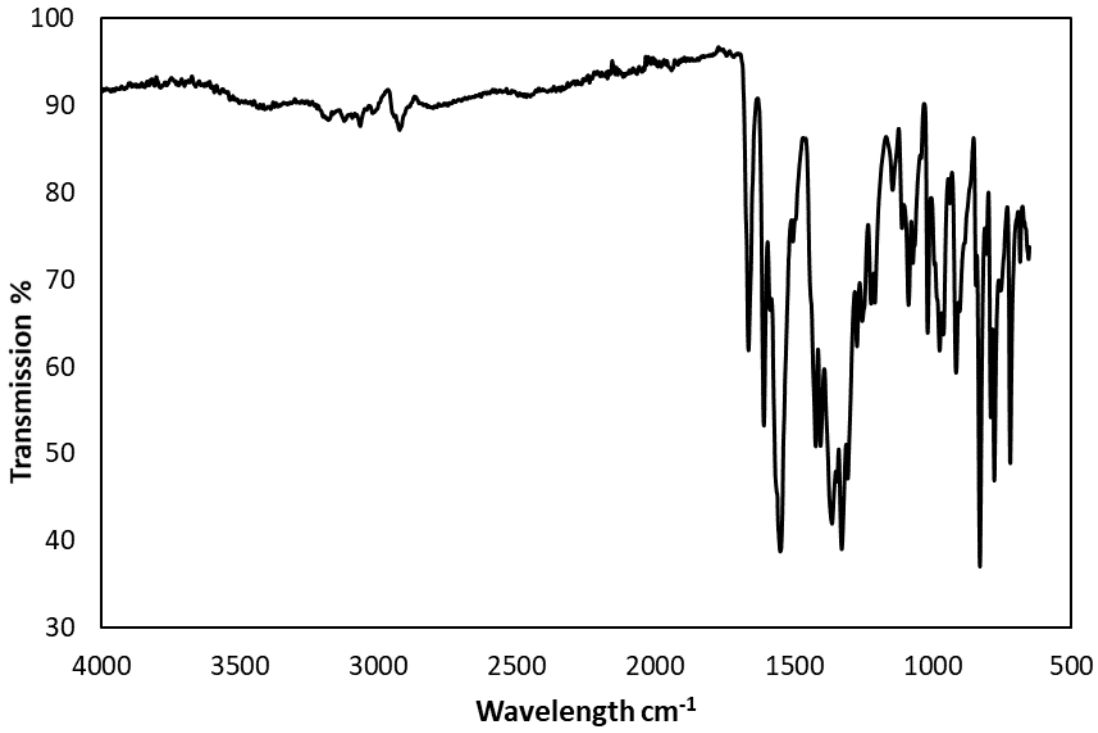

Figure 3.91. The IR spectrum for compound **14**.

A ^{1}H-NMR experiment was conducted on a sample of compound **14** digested in a D_2SO_4/D_2O/DMSO-d^6 mixture and is presented in **Figure 3.92**. The spectrum shows the expected 1:2:1 ratio for cmai to bpe to DMF that is present in the structure.

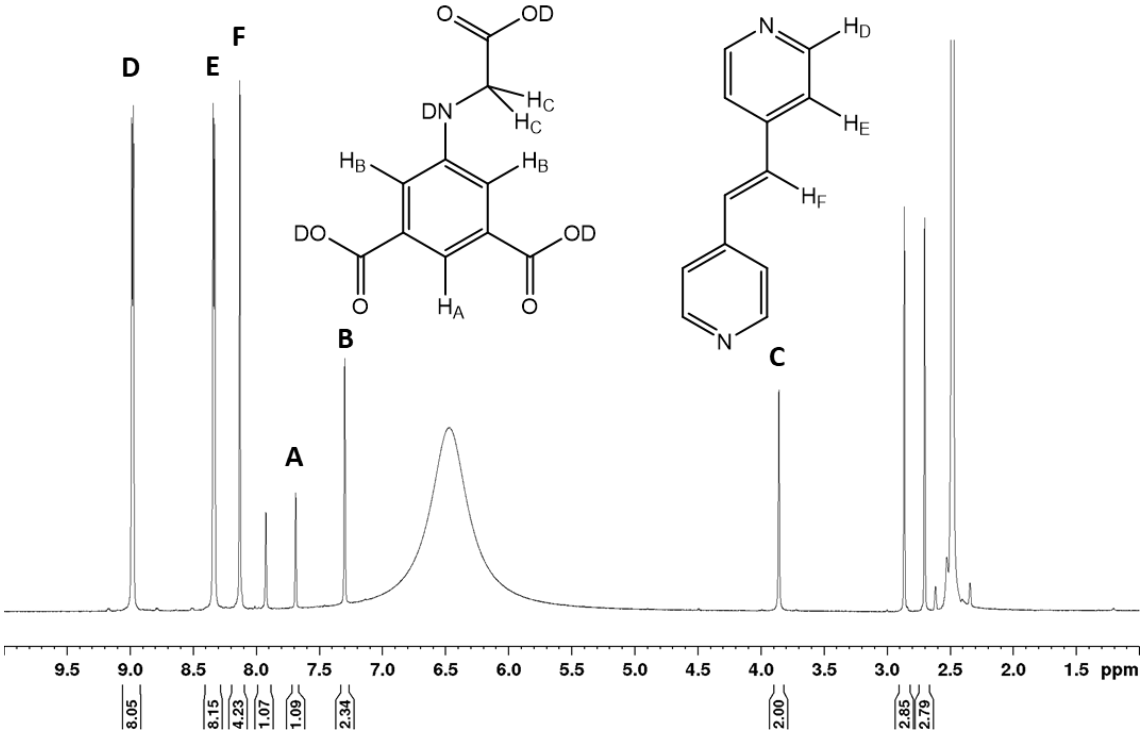

Figure 3.92. ^{1}H-NMR spectrum for digested compound **14**.

3.6.5 The synthesis of $[Cd_6(cmai)_4(phen)_6(H_2O)_2]\cdot 12.5H_2O\cdot 0.75DMF$ (**15**)

H_3cmai (0.2 mmol, 0.048 g) was added to 8 mL of DMF in a 10 mL microwave reaction vessel and sonicated for 15 min. To this was added 8 mL of H_2O which caused the acid to dissolve. phen (0.2 mmol, 0.036 g) was dissolved in the reaction solution at which point $Cd(NO_3)_2\cdot 4H_2O$ (0.6 mmol, 0.018 g) was added. The vial was sealed using a Teflon-lined cap and placed in an oven at 90 °C for 48 hours in which time colourless plate crystals had formed. After removal from the oven and cooling under ambient conditions, these were collected via vacuum filtration and washed with deionised water (3 x 3 mL) and then stored in deionised water until required.

The product was analysed using PXRD. The pattern simulated from the single-crystal data is shown in **Figure 3.93** compared to the experimental data. The two match very closely confirming the bulk material as compound **15**. Elemental microanalysis was carried out and the experimental results were in good agreement with those calculated based on the formula assigned for compound **13** based on the single-crystal data. Expected: C 45.49%, H 3.55%, N 7.78%. Found: C 45.50%, H 3.56%, N 7.27%.

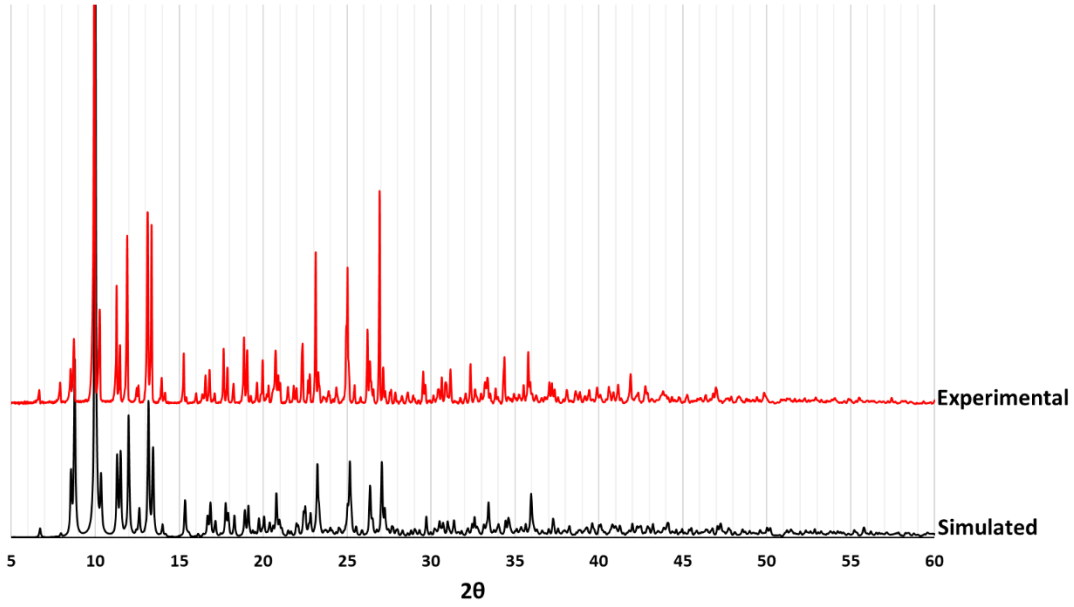

Figure 3.93. The experimental PXRD pattern for compound **15**, presented alongside the pattern simulated from the single-crystal data.

The IR spectrum was collected for a sample of compound **15** and is shown in **Figure 3.94**. (solid, cm^{-1}) 3195s (br), 1555s, 1359s, 1100w, 847m, 778s, 722s.

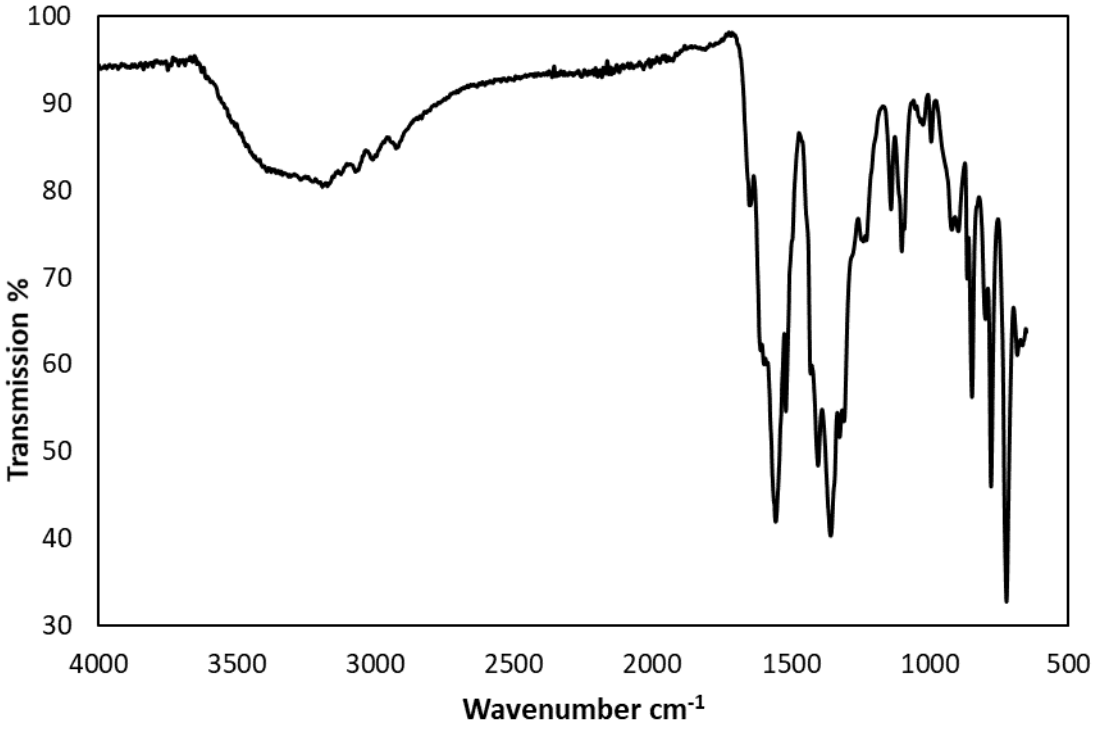

Figure 3.94. The IR spectrum of compound **15**.

The ^{1}H-NMR spectrum for digested compound **15,** shown in **Figure 3.95**, suggests that the ratio between cmai and phen is 1:1. This disagrees with the structure obtained from the single-crystal diffraction data. There are several smaller peaks in the aromatic region that may be associated with a second form of the phen linker, possibly due to the acidic digestion conditions. Taking these peaks into account, the ratio moves closer towards that implied by the single-crystal and elemental analysis experiments.

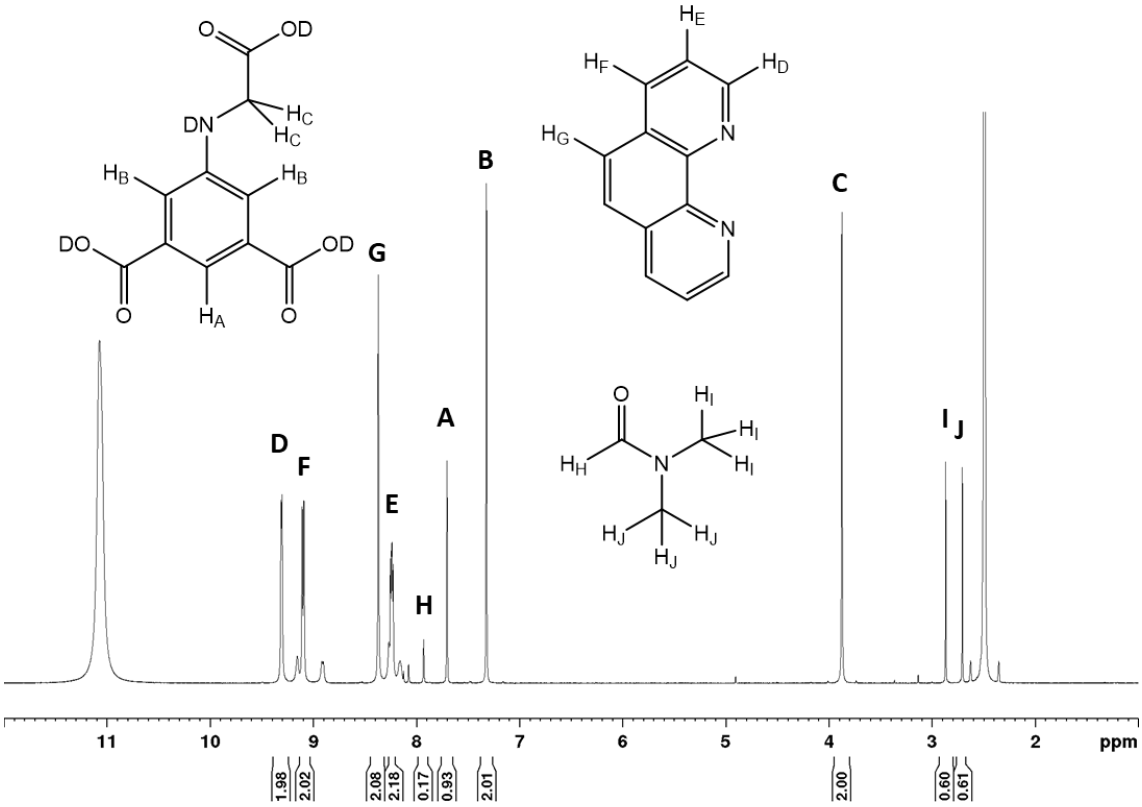

Figure 3.95. The ^{1}H-NMR spectrum for digested compound **15.**

3.6.6 The synthesis of $[Zn_3(cmai)_2(bipy)(H_2O)_4]\cdot 2H_2O$ (**16**)

H_3cmai (0.1 mmol, 0.0239 g) was added to 3 mL of DMF in a 10 mL microwave reaction vessel and sonicated for 15 min. To this was added 3 mL of water causing the acid to dissolve. bipy (0.1 mmol, 0.0156 g) was dissolved in the reaction solution then $Zn(NO_3)_2\cdot 6H_2O$ (0.3 mmol, 0.0893 g) was added. The vial was sealed using a Teflon-lined cap and placed in an oven at 90 °C for 48 hours during which time light purple block crystals formed. After removal from the oven and cooling under ambient conditions, these were collected via vacuum filtration and washed with deionised water (3 x 3 mL) and then stored in deionised water until required.

The identity of the bulk material was confirmed by comparison of the experimentally collected PXRD pattern to the trace generated from the single-crystal data, as shown in **Figure 3.96**. The

bulk material was further analysed by elemental microanalysis (CHN), the experimental results were in good agreement with those calculated based on the formula assigned for compound **16** based on the single-crystal data. Expected: C 38.63%, H 3.46%, N 6.01%. Found: C 38.35%, H 3.44%, N 6.06%.

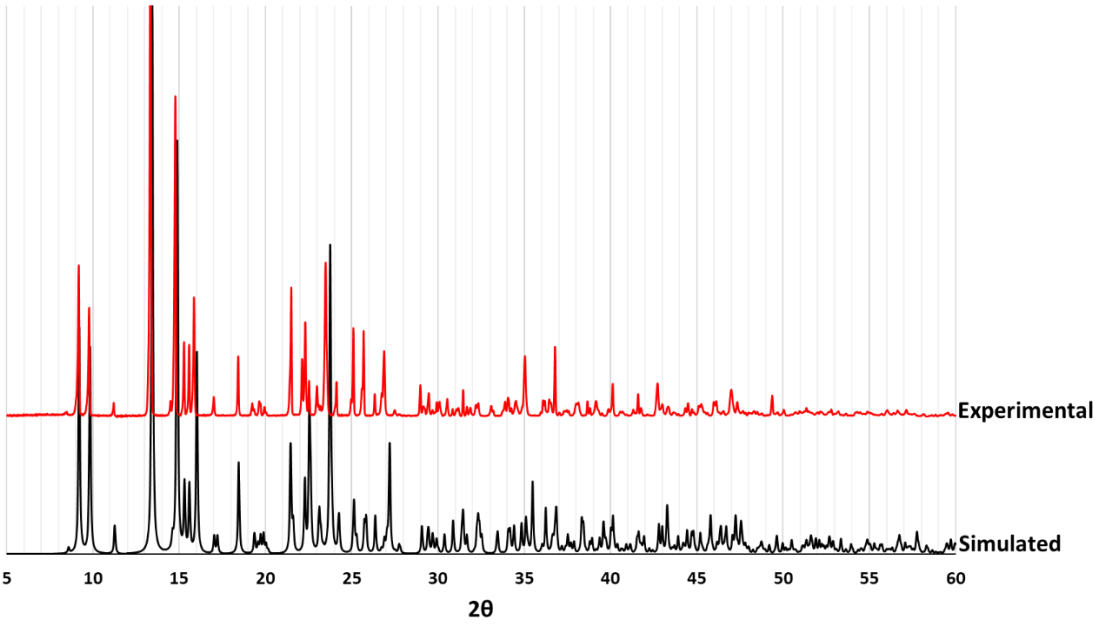

Figure 3.96. The PXRD pattern for compound **16** compared to that simulated from the single-crystal data.

The IR spectrum was collected for a sample of compound **16** and is shown **Figure 3.97**. (solid, cm^{-1}) 3253s (br), 1611m, 1539s, 1348s, 1320s, 1229w, 1079w, 911w, 794w, 777s, 725s.

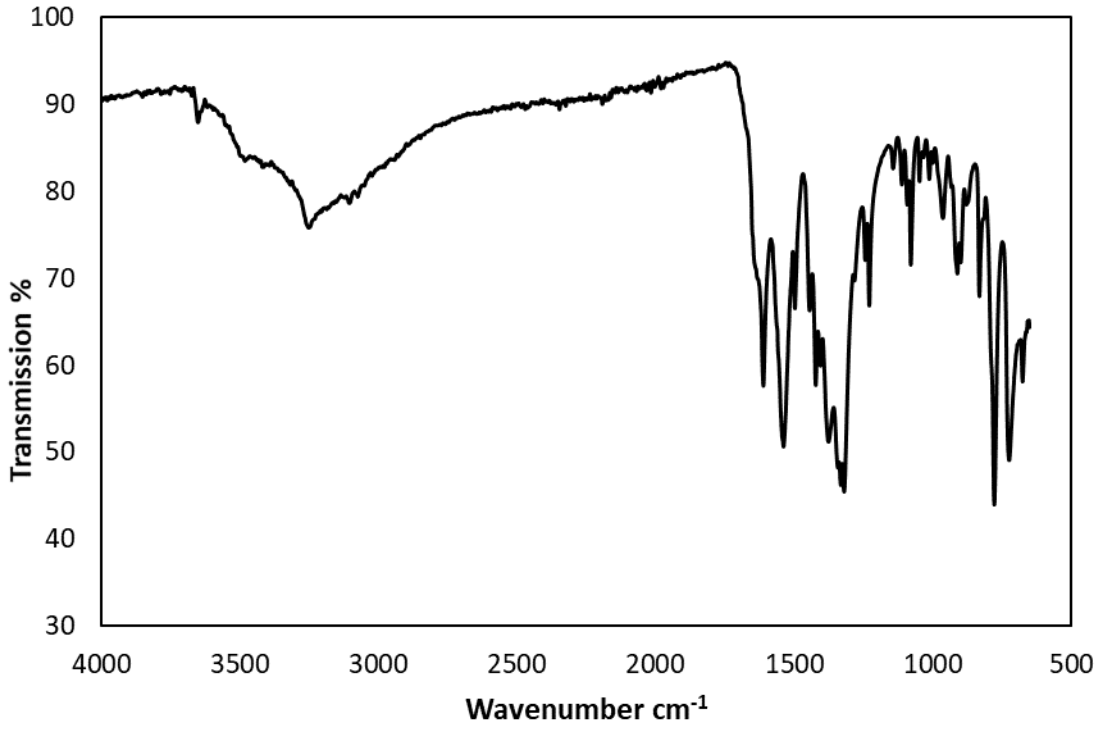

Figure 3.97. The IR spectrum for compound **16**.

3.6.7 The synthesis of $[Zn_3(cmai)_2(bipy)]$ (**17**)

Compound **17** was obtained on heating a sample of compound **16** at 170 °C under reduced pressure for a period of 2 hours. The resultant material was not phase pure and contained a mixture of compound **16, 17** and a third phase as evidenced by PXRD shown in **Figure 3.59**.

3.6.8 The synthesis of $[Zn_2(Hcmai)_2(bpe)]\cdot 2DMF$ (**18**)

H_3cmai (0.3 mmol, 0.0717 g) was added to 3 mL of DMF in a 10 mL microwave reaction vessel and sonicated for 15 min. To this was added 3 mL of water which caused the acid to dissolve. bpe (0.15 mmol, 0.0273 g) was dissolved in the reaction solution then $Zn(NO_3)_2\cdot 6H_2O$ (0.6 mmol, 0.1785 g) was added, causing a precipitate to form. Finally, 0.05 mL of conc. HNO_3 was added which caused the precipitate to dissolve. The vial was sealed using a Teflon-lined cap and placed in an oven at 90 °C for three days during which colourless block crystals formed. After removal from the oven and cooling under ambient conditions, these were collected via vacuum filtration and washed with deionised water (3 x 3 mL) and then stored in deionised water until required.

The bulk material was analysed using PXRD, the trace of which is shown in **Figure 3.98** along with the pattern simulated from the single-crystal data. The peaks in the two patterns match very well confirming the bulk as compound **18**. Elemental microanalysis was also carried out and

good agreement was found between the experimental and theoretical values. Expected: C 48.89%, H 4.10%, N 9.00%. Found: C 48.28%, H 4.10%, N 8.80%.

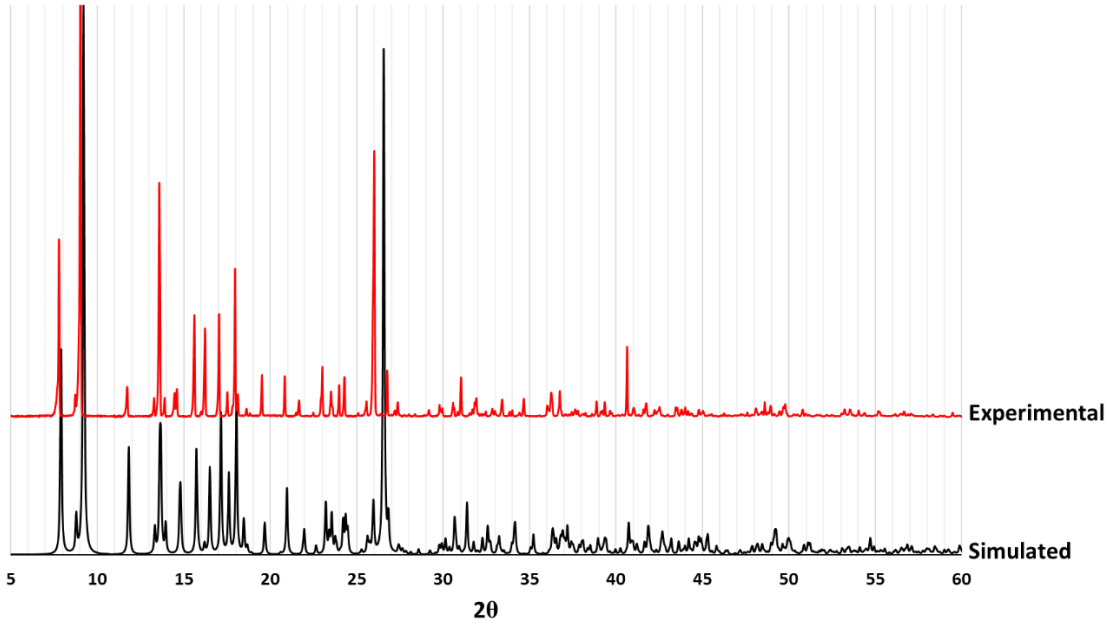

Figure 3.98. The experimental PXRD pattern for compound **18** and the pattern simulated from the single-crystal data.

3.6.9 The synthesis of $[Zn_3(cmai)_2(phen)_2(H_2O)_3]\cdot 3H_2O$ (**19**)

In a 10 mL glass microwave tube, H_3cmai (0.048 g, 0.2 mmol) was sonicated in DMF (4 mL) for 15 min, then deionised water (4 mL) was added, dissolving the acid. To this solution was added 1,10-phenanthroline (0.036 g, 0.2 mmol) and $Zn(NO_3)_2\cdot 6H_2O$ (0.179 g, 0.6 mmol). The solution was sealed and sonicated for a further 5 minutes before being placed in an oven at 90 °C for 7 days. After removal from the oven and cooling under ambient conditions, the yellow block-shaped crystals were recovered by vacuum filtration, washed with deionised water (3 x 3 mL) and then stored in deionised water until required.

The material was analysed using PXRD with the collected pattern and that simulated from the single-crystal data shown in **Figure 3.99**. The material was also investigated using elemental analysis. The calculated values based on the crystal structure are: C 46.48%, H 3.55%, N 7.39%, whereas the experimental values are: C 45.50%, H 3.56%, N 7.27%. The calculated and the experimental have a slight discrepancy which is rectified by the presence of an additional molecule of water, $[Zn_3(cmai)_2(phen)_2(H_2O)_3]\cdot 4H_2O$ calculated values: C 45.76%, H 3.67%, N 7.28%.

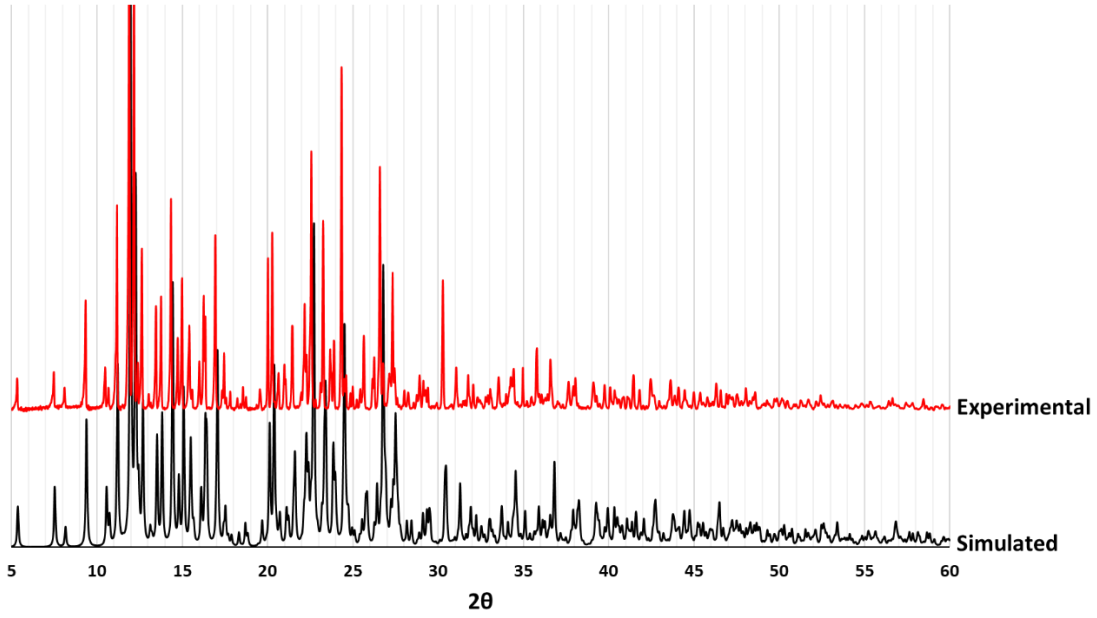

Figure 3.99. The experimental PXRD pattern for compound **19**, compared to the pattern simulated from the single-crystal data.

The IR spectrum was collected for a sample of compound **19** and is shown **Figure 3.100**. (solid, cm^{-1}) 3225w (br), 1562m, 1419s, 1392m, 1360m, 1328m, 770mw, 723s.

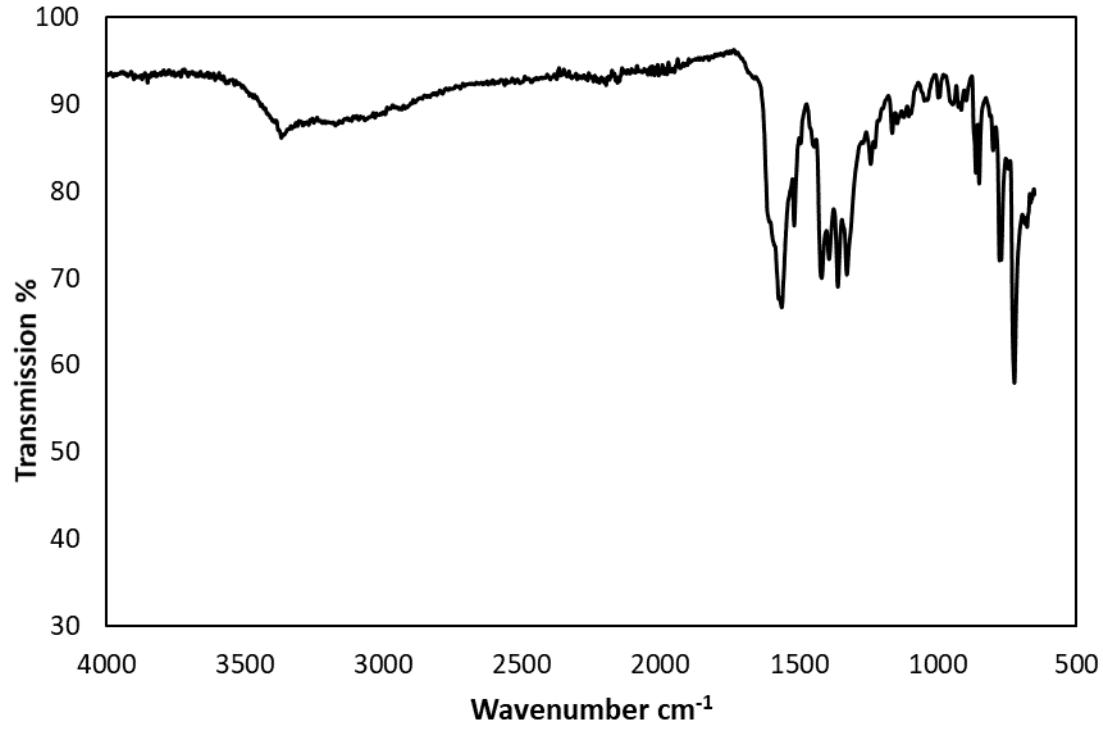

Figure 3.100. The IR spectra for compound **19**.

Chapter 4 - Synthesis of Cross-Linked MOFs Using A Functionalised Semi-Rigid Terephthalic Acid Derivative

4.1 Introduction

The semi-rigid linker, cmai, discussed in **Chapter 2** and **3**, derives its flexibility from the carboxylic acid terminated arm, the flexibility arises from the degrees of freedom intrinsic to the secondary amine and CH_2 group. This grouping of atoms arose from the product of the reductive amination used in the synthesis. Rather than introducing another coordinating group directly, as in the case of H_3cmai, reductive amination can be used to couple two linker precursors together. This strategy generates organic ligands which contain some flexibility, an increased number of binding sites and are also novel, presenting an unexplored research space.

Reductive amination has been used to synthesise a novel tetracarboxylic acid from 2-amino-1,4-benzenedicarboxylic acid and a dialdehyde. The semi-rigid linker precursor, 2,2'-((1,4-phenylenebis(methylene))bis(azanediyl))diterephthalic acid (H_4tpat), was synthesised using terephthalaldehyde to couple together a pair of 2-amino-1,4-benzenedicarboxylic acid units, the reaction scheme is shown in **Figure 4.1**. The linker tpat is semi-rigid due to the presence of the secondary amine and CH_2 groups that bridge between the aromatic rings.

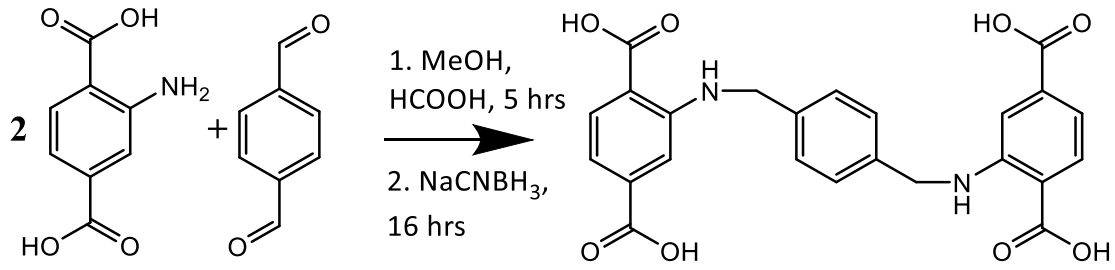

Figure 4.1. The synthesis of H_4tpat.

In a typical reaction for the formation of H_4tpat, 2-amino-1,4-benzenedicarboxylic acid was dissolved in MeOH and to this was added terephthalaldehyde and a small amount of formic acid. The reaction mixture was stirred at room temperature for 5 hours at which point it was cooled and $NaCNBH_3$ was added. After stirring at room temperature overnight the product was precipitated by the addition of HCl and H_2O. The product identity was confirmed via ^{1}H-NMR and $^{13}C\{^1H\}$-NMR spectroscopy, the assigned spectra for which are shown in **Figure 4.2** and **Figure 4.3**.

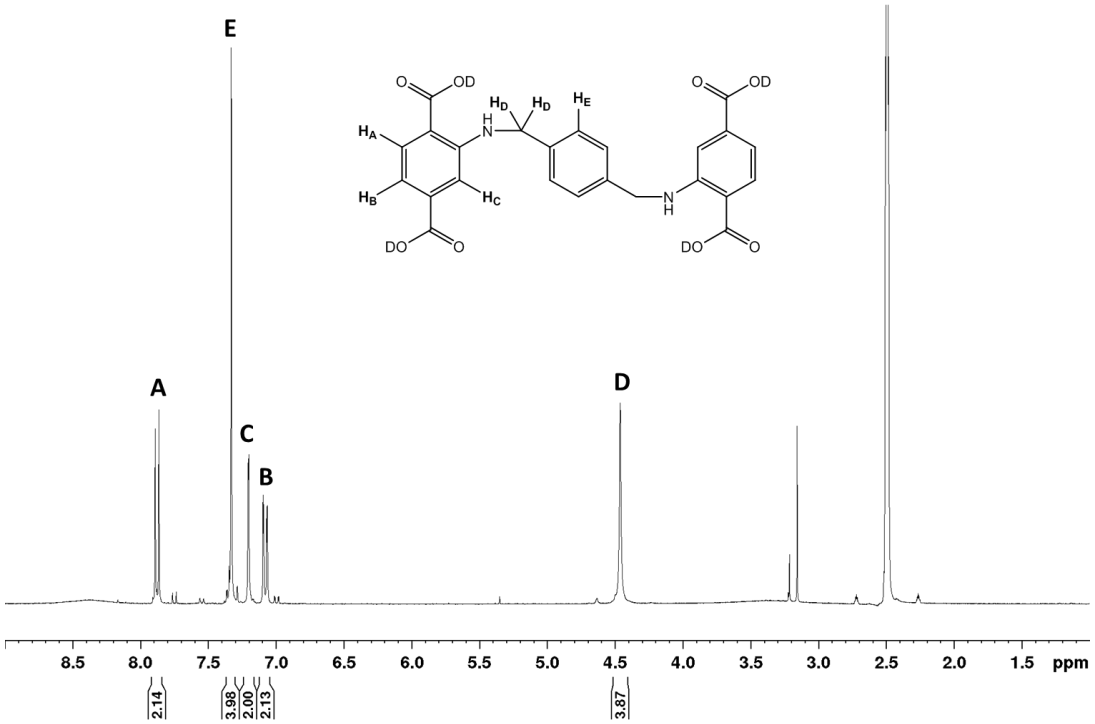

Figure 4.2. The ^{1}H-NMR spectrum for D_4tpat dissolved in DMSO-d^6.

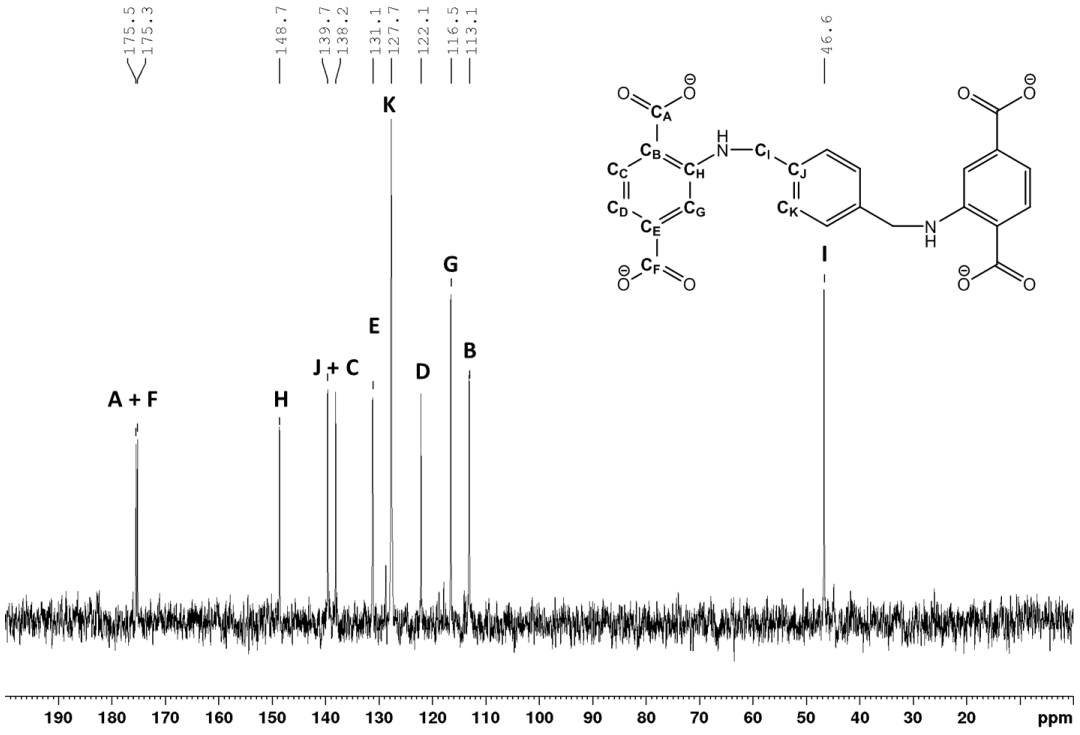

Figure 4.3. ^{13}C{^{1}H}-NMR spectrum of tpat dissolved in D_2O/NaOD.

4.2 Results and Discussion

4.2.1 The synthesis and structure of $[Zn_8(tpat)_3(NO_3)_4(H_2O)_4]$ (**20**)

H_4tpat and $Zn(NO_3)_2 \cdot 6H_2O$ were dissolved in DMF and placed in an oven at 80 °C for four days leading to the formation of yellow intergrown hexagonal prism shaped crystals. The structure was interrogated using single-crystal X-ray analysis. The crystals did not diffract beyond a resolution of 1.2 Å. This was judged to reflect symmetrical disorder as the crystals were single. However, despite the resolution a unit cell, space group and broad connectivity was established.

The structure of compound **20** was solved in the hexagonal space group *P*6/*mmm*. The SBU is a zinc dimer that is supported by the interactions from three carboxylate groups shown in **Figure 4.4. A**. The axial positions in the dimer were modelled as oxygen atoms, which could be water ligands. Each SBU extends in three directions 120° to one another via the 2-amino-1,4-benzenedicarboxylate linkers, which can be seen in **Figure 4.4. B.** The amine is disordered over the four positions around the benzene ring, and at each position is also disordered either side of the aromatic ring. The para-xylene tethering group was not resolved in the crystal data. This is likely due to a combination of crystallographic disorder, high symmetry and consequent crystal data quality. The presence of the tethering group is proved unequivocally in the following discussion.

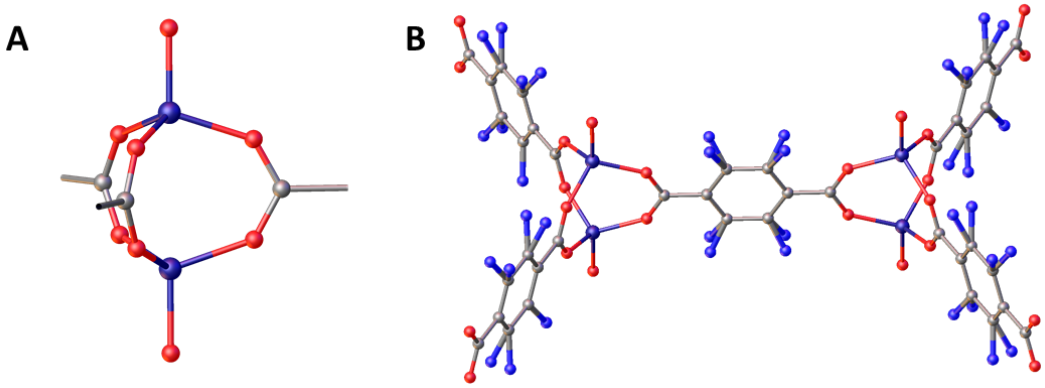

Figure 4.4. A – Zinc dimer SBU in compound **20**. **B –** 2-amino-1,4-benzene dicarboxylate linking two SBUs.

The 120° 3-connected nodes formed by the SBU extends into a hexagonal sheet structure, with a hcb type net. The 2-D sheets stack in an aligned manner so there are hexagonal channels running through the structure in the direction of the *c*-axis as can be seen in **Figure 4.5**.

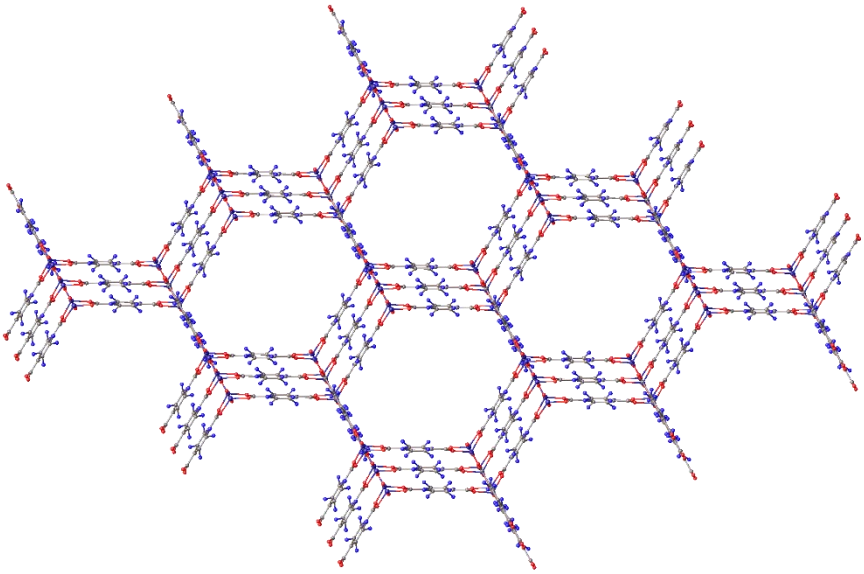

Figure 4.5. The stacking of 2-D sheets in compound **20**.

As the framework is cationic, counter ions are needed to balance the charge. However, these could not be resolved due to disorder. The ions are likely either nitrates, from the zinc salt, or formate, which is a known decomposition product of DMF.

A CSD search for structures with similar unit cell parameters as compound **20** revealed that a MOF with the formula $[Zn_4(bdc\text{-}NH_2)_3(NO_3)_2(H_2O)_2]$ had been previously reported. This MOF was synthesised from $Zn(NO_3)_2{\cdot}6H_2O$ and 2-amino-1,4-benzenedicarboxylic acid in combination with a polymer templating agent and was named PNMOF-3. A comparison of the unit cell information for compound **20** and PNMOF-3 is shown in **Table 4.1**[125]

Table 4.1. A comparison of the unit cell of compound **20** and PNMOF-3.

MOF	Space Group	*a*	*b*	*c*	*α*	*β*	*γ*
20	*P6/mmm*	18.326 (5)	18.326 (5)	14.2983 (11)	90	90	120
PNMOF-3	*P6/mmm*	18.3385 (7)	18.3385(7)	14.2657 (14)	90	90	120

A PXRD pattern for compound **20** was collected and compared to the pattern for PNMOF-3 simulated from the single-crystal data, this is shown in **Figure 4.6**. The two patterns match very closely, confirming that compound **20** is isostructural with PNMOF-3.

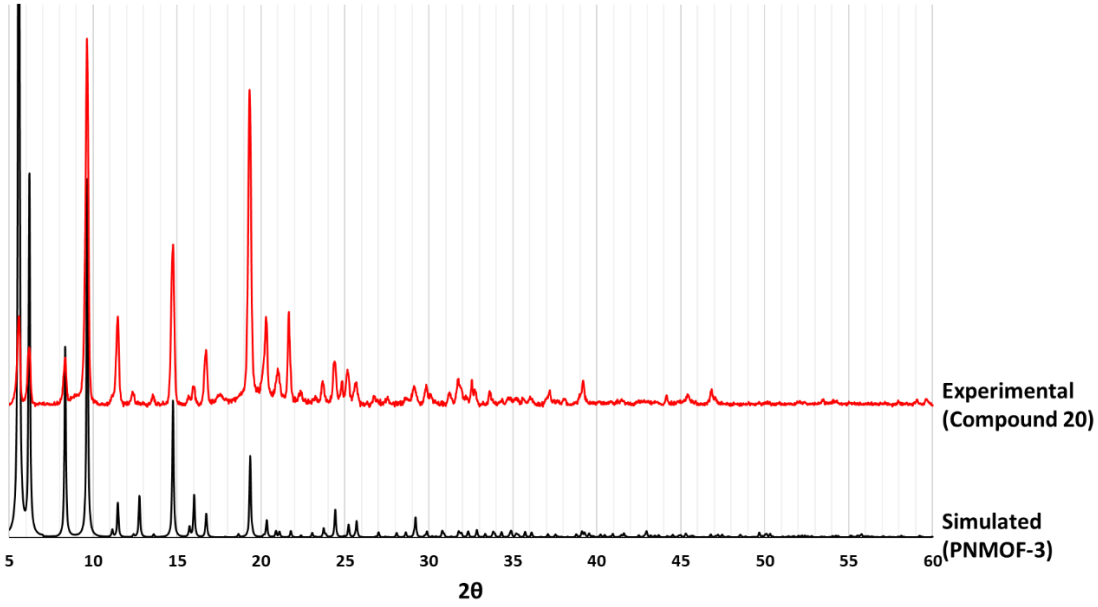

Figure 4.6. The PXRD pattern collected for compound **20** along with the pattern simulated from the single-crystal data for PNMOF-3.

The gross structure in PNMOF-3 is similar to that determined from the single-crystal data for compound **20,** other than the axial coordination site of the SBUs. The data collected and published for PNMOF-3 were of sufficient quality to model the axial site, as disordered water and nitrate ligands in a 1:1 ratio, these are depicted, one on each zinc in the SBU shown in **Figure 4.7**. Due to the similarity in the structures it is reasonable to suggest that the axial ligands in compound **20** might also be a similar mixture of nitrate ions and water ligands.

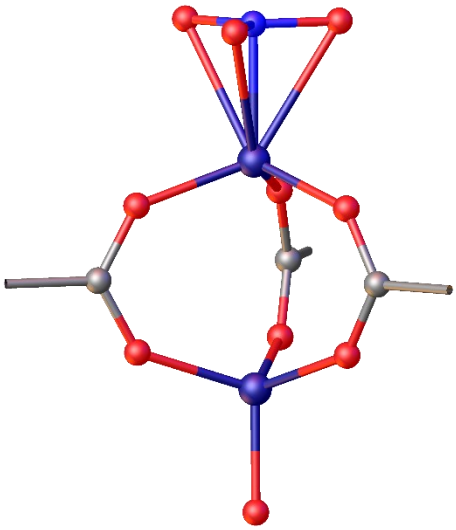

Figure 4.7. An SBU in PNMOF-3.

As 2-amino-1,4-benzenedicarboxylic acid is both the starting material in the synthesis of H_4tpat and also a reactant in the synthesis of PNMOF-3, it was vital to prove that compound **20** contains tpat as a linker and not bdc-NH_2, which could conceivably be a degradation product of H_4tpat. The presence of tpat in compound **20** was analysed using several different techniques including infrared spectroscopy, ^{1}H-NMR spectroscopy and mass spectrometry.

IR spectroscopy was used to probe the presence of the N-H stretches that usually occur in the region 3500-3200 cm^{-1}. **Figure 4.8** shows the IR spectra of PNMOF-3, IRMOF-3 and 2-amino-1,4-benzenedicarboxylic acid, all of which have two N-H stretches between 3500 cm^{-1} and 3300 cm^{-1}. These stretches correspond to the fact that a primary amine is present.

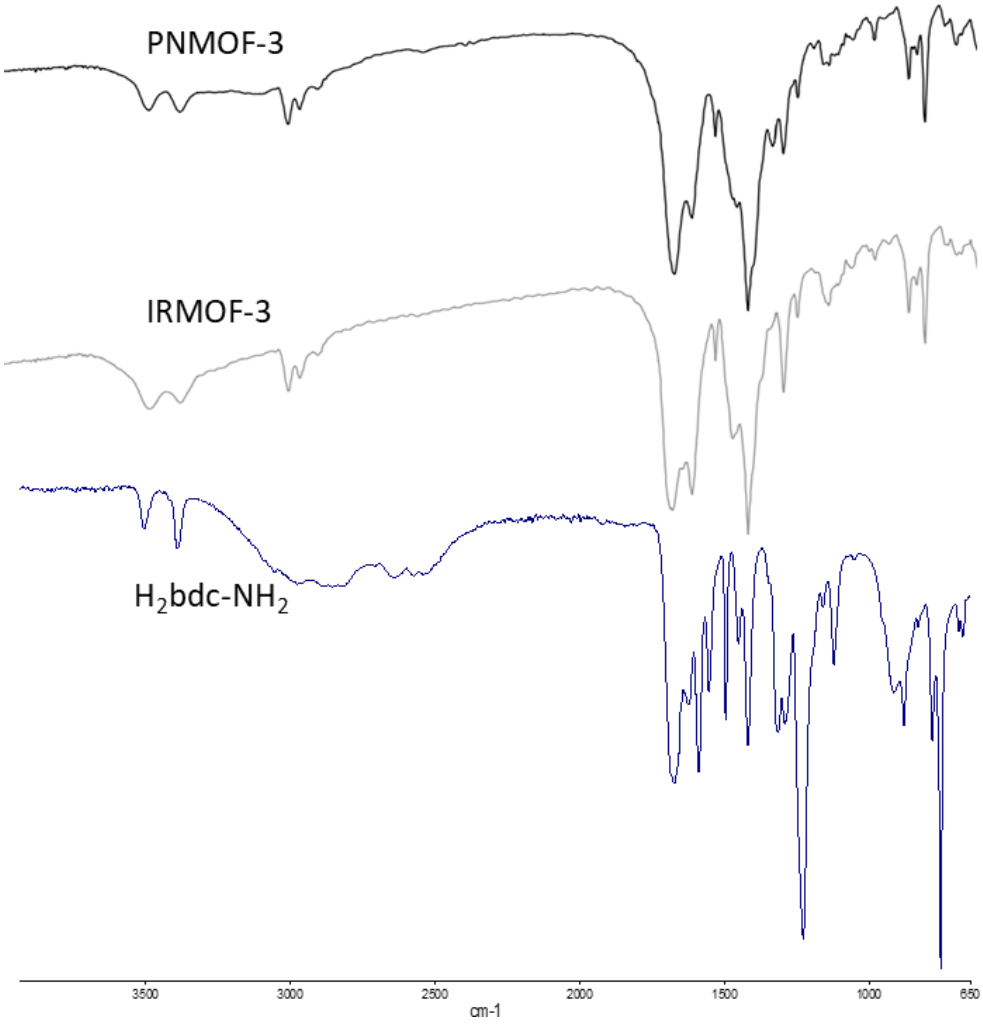

Figure 4.8. IR spectra for PNMOF-3 and H_2bdc-NH_2.

The IR spectrum collected for H_4tpat and compound **20** are shown in **Figure 4.9**. They each exhibit only one peak in the amine region, at 3375 cm^{-1} and 3350 cm^{-1} respectively. The

presence of only one peak is indicative of a secondary amine being present and confirms that bdc-NH_2 is not present in compound **20**.

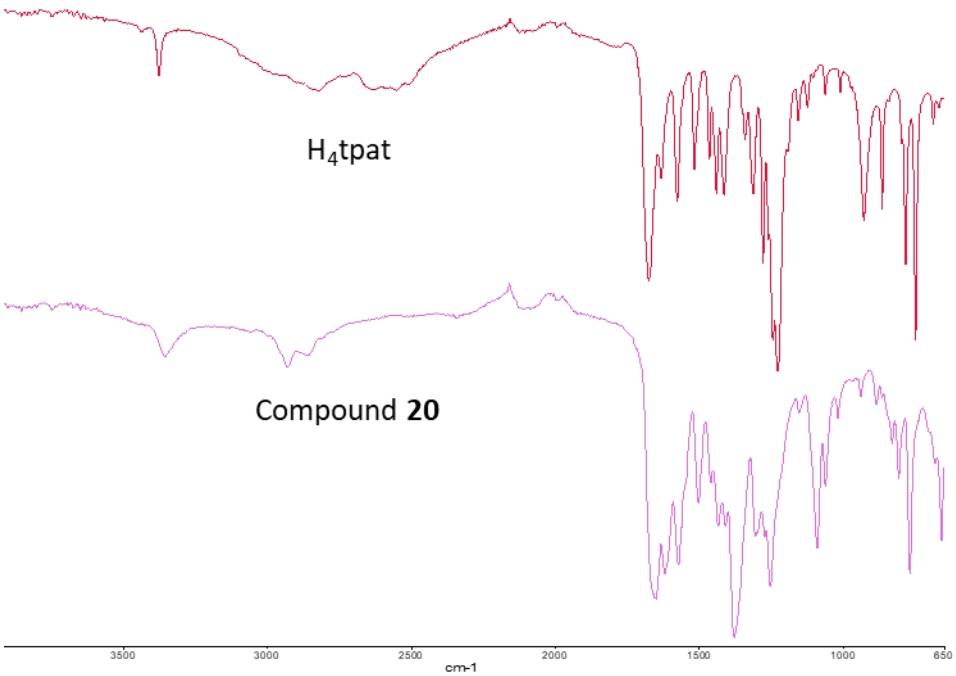

Figure 4.9. The IR spectra of H_4tpat and compound **20**.

A sample of compound **20** was digested in dilute aqueous NaOH solution in order to decompose the polymeric framework into its component parts. A mass spectrometry experiment was conducted on this solution using a time of flight (TOF) instrument and negative electrospray as the ionisation technique. The spectrum is presented in **Figure 4.10** and shows a molecular ion peak at 463.1185 and is expected at 463.1147 for $[H_3tpat]^-$, confirming the presence of tpat in compound **20.**

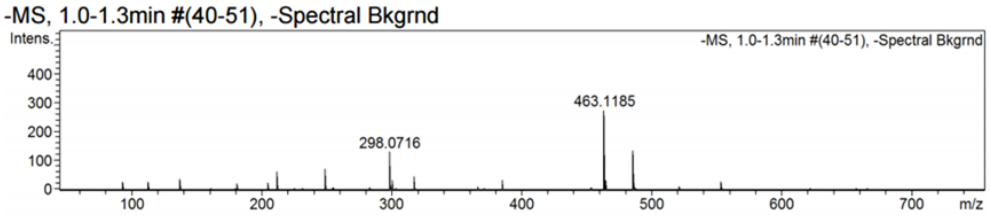

Figure 4.10. The mass spectrum for compound **20** digested in dilute NaOH(aq).

A sample of compound **20** was digested in a NaOD/D_2O solution and a ^{1}H-NMR spectrum was collected which is shown in **Figure 4.11** alongside the assignment for tpat. The data further confirms the presence of tpat in compound **20**.

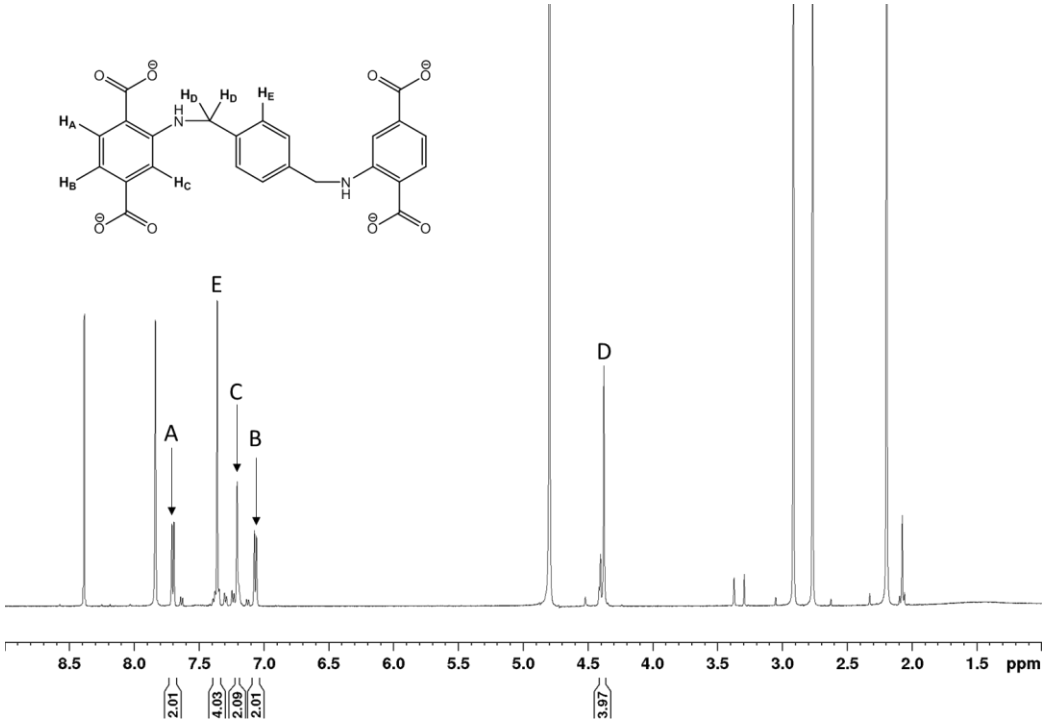

Figure 4.11. ^{1}H-NMR spectrum of digested compound **20** digestated in NaOD/D_2O.

In summary a combination of mass spectrometry, IR and ^{1}H-NMR spectroscopy has demonstrated that compound **20** contains tpat. The X-ray diffraction data, both powder and single-crystal, suggest that the MOF has the same layered hcb topology as the previously reported material PNMOF-3. The location of the *p*-xylene tether could not be ascertained crystallographically due to the disordered nature of the group and the quality of the data. The tether locations can be proposed by considering the length of the bridging group and where this could be accommodated into the solid-state structure. There are several conceivable positions in which the tether could reside, with the most likely these depicted in **Figure 4.12**. Coordination mode **A** places the tether bridging adjacent hexagonal layers of the MOF framework, mode **B** puts the tether bridging adjacent dicarboxylate units within the same 2-D sheet and **C** has the tether and bdc unit directed into the cavity space, such that tpat acts as a bidentate linker only. The validity of these coordination modes can be assessed by considering the distances involved in each case and comparing these with the structure metrics.

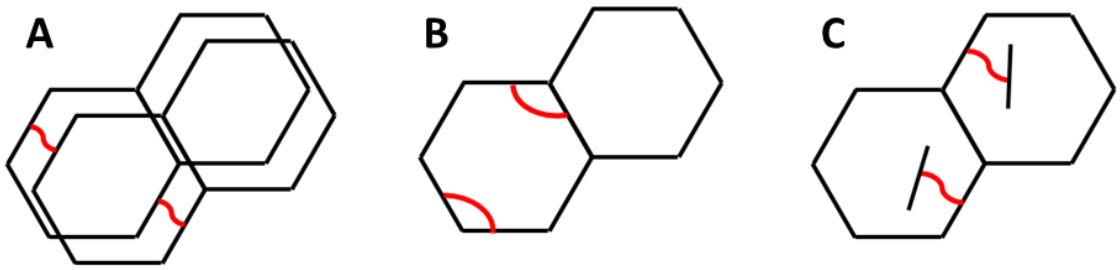

Figure 4.12. A diagram showing: **A** – tpat bridging two adjacent MOF layers, **B** – tpat bridging two adjacent dicarboxylate units in the same layer and **C** – tpat with only one dicarboxylate unit incorporated into the framework.

In order to assess whether the diamino-*p*-xylene tether has sufficient dimension to conform to these binding modes, the length of the tether must be determined. This was effected using Chem3D from PerkinElmer, treating the tether as a free diamino-*p*-xylene molecule. The maximum and minimum lengths were determined by placing the tether in both an anti and syn conformation, as shown in **Figure 4.13**, and this yielded N···N distances of 7.3 Å and 6.7 Å respectively.

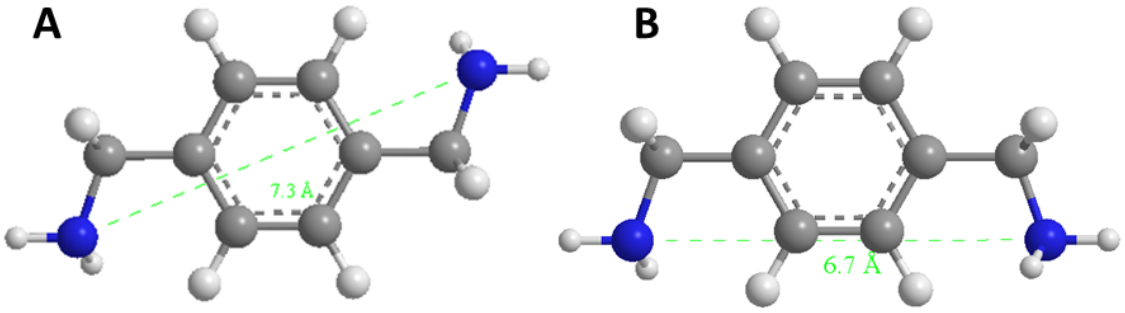

Figure 4.13. Chem3D models for diamino-*p*-xylene, **A –** anti conformation, **B –** syn conformation.

The distances pertaining to the different co-ordination modes can be assessed from the crystal structure of compound **20**. For mode **A**, the shortest distance between layers is from the nitrogen atom of one aminobenzenedicarboxylate unit to the aminobenzenedicarboxylate directly below in the adjacent layer. This distance is 9.47(4) Å and is shown in **Figure 4.14**. This N···N distance is significantly larger than the N···N distance in the tether (7.3 Å) so it is not possible for this coordination mode to be present in compound **20**.

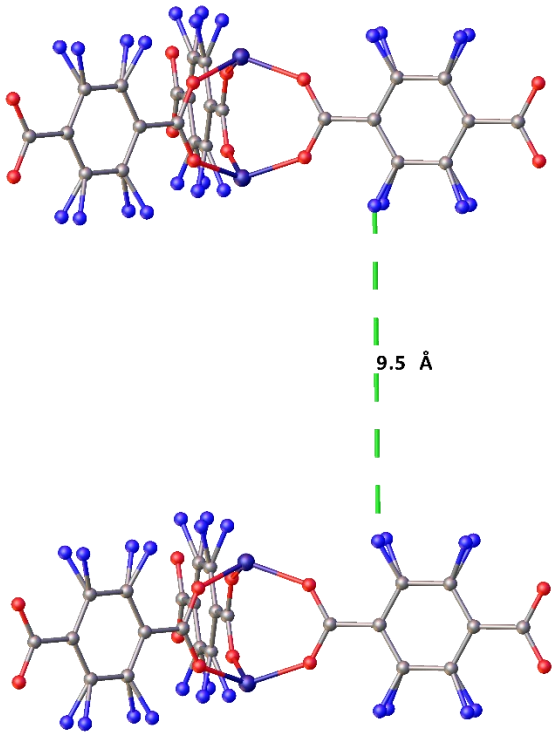

Figure 4.14. The shortest N···N distance between dicarboxylate units in adjacent planes of compound **20**.

In coordination mode **B** (**Figure 4.12**), the *p*-xylene bridge links two dicarboxylate units in the same 2-D hexagonal layer. The shortest distance, in compound **20**, between the amine nitrogen atoms of adjacent dicarboxylate units in the same plane is 6.57(16) Å, as shown in **Figure 4.15**. This metric is similar to the N···N distance in the syn-conformer of diamino-*p*-xylene (6.7 Å) giving credence to coordination mode **B**'s presence in compound **20**.

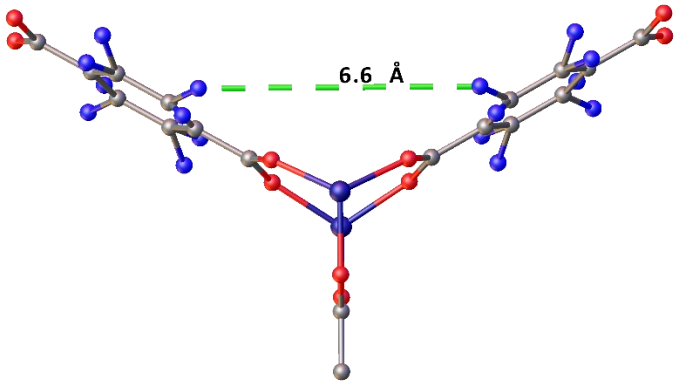

Figure 4.15. The shortest N···N distance between dicarboxylate units in the same 2-D sheet in compound **20**.

Coordination mode **C** shown in **Figure 4.12** has only one of the dicarboxylate units of tpat coordinating to zinc atoms and participating in the formation of the framework. The bridging

group and other bdc unit sit in the pores of the MOF structure as a very bulky pendent group. In order for this mode to be feasible geometrically the pendent xylene and bdc unit simply need to fit in the pores of the framework. Due to the large hexagonal channels (21.1765(6) Å diameter) running in the direction of the *c*-axis and the large inter-sheet distances (9.47(4) Å) there is adequate space for this to be a possibility.

In order to ascertain whether coordination mode **B** or **C** dominates in compound **20** the pores in the structure need to be interrogated. Methods of choice are gas adsorption to measure the materials surface area and thermogravimetric analysis to look at guest solvent properties. The associated logic in determination of the tpat binding mode relies on comparisons of results with those for the non-tether/pendent group containing PNMOF-3.

The reported synthesis for PNMOF-3 used $Zn(NO_3)_2{\cdot}6H_2O$ and H_2bdc-NH_2 as well as a polymer additive to template the formation of the MOF. The reaction was carried out at 100 °C for 24 hours but the product formed was not phase pure, as it contained some IRMOF-3, so would not be a suitable sample to use for comparison studies with compound **20**.[125] A phase pure sample of PNMOF-3 was prepared by adapting the procedure used for the synthesis of compound **20**. $Zn(NO_3)_2{\cdot}6H_2O$ and H_2bdc-NH_2 were reacted in DMF at 80 °C for four days. The product and its phase purity were confirmed by PXRD, the matching PNMOF-3 simulated pattern and experimental pattern are shown in **Figure 4.16**. Interestingly, this experiment has shown that phase pure PNMOF-3 can be synthesised without the use of a polymer additive.

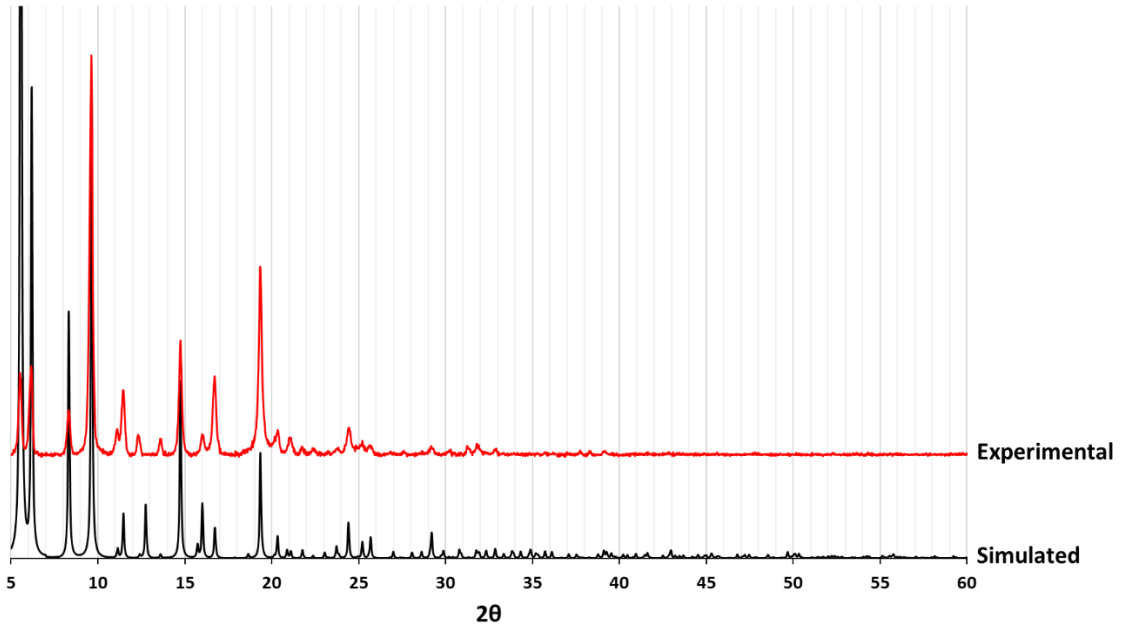

Figure 4.16. The experimental pattern for PNMOF-3 alongside the trace simulated from the single-crystal data.

Both PNMOF-3 and compound **20** were unstable to activation which ruled out access to measuring adsorption isotherms. The results for the thermogravimetric analysis are presented in **Figure 4.17**. It can be seen that there is very little difference in the percentage mass of volatiles lost from the two materials. This was somewhat surprising as it suggests that the pore volumes are similar. However, this finding provides strong evidence for the presence of coordination mode **B** with the *p*-xylene groups tethering adjacent dicarboxylate units in the same 2-D sheet. Mode **C** would be expected to accompany a very large difference in volatile mass due to the bulk of the linker occupying space in the pores. Additionally, guest solvent loss occurs more quickly from PNMOF-3 than compound **20.** This is due to the extra *p*-xylene groups inhibiting the movement of solvent within the pores.

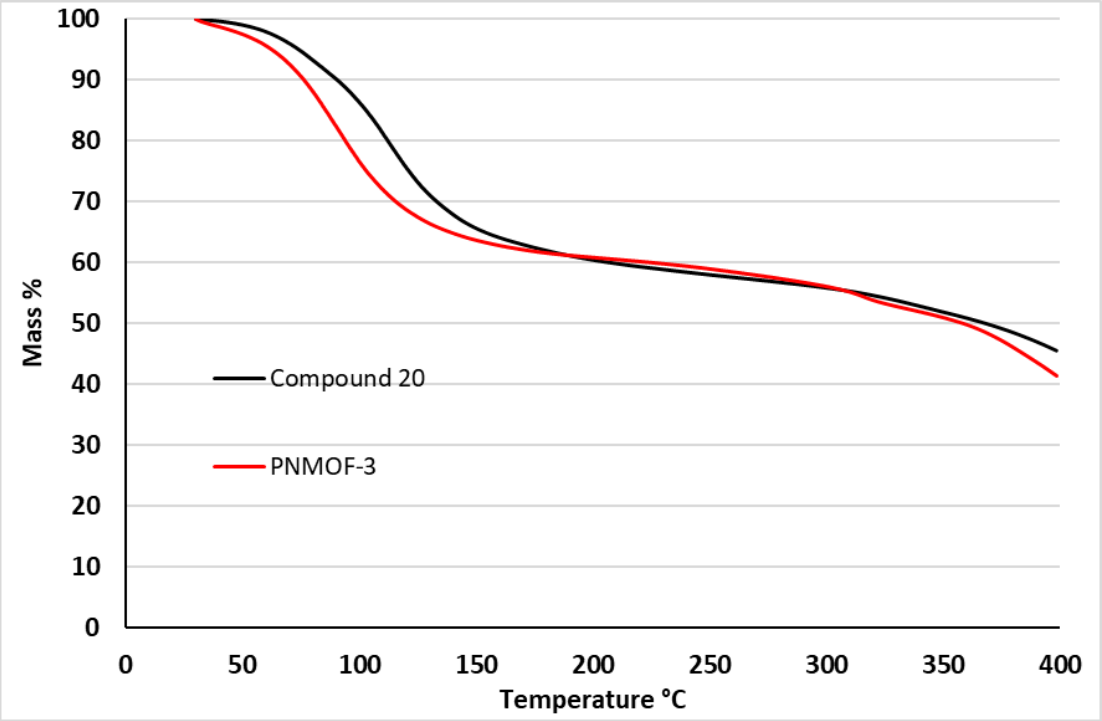

Figure 4.17. The TGA results for compound **20** and PNMOF-3.

4.2.2 The synthesis and structure of $[Zn_8O_2(tpat)_3]$ (**21**)

When the temperature was increased from 80 °C to 100 °C in synthetic conditions mirroring that used to make compound **20**, a new material was obtained. Compound **21** crystallised as large yellow cubic crystals, immediately distinguishable from those for compound **20**, which are hexagonal.

A single-crystal X-ray diffraction experiment was carried out on a tablet cut from one of the cubic crystals. Compound **21** was found to have a cubic unit cell that was similar to the cell for the

previously reported IRMOF-3, $[Zn_4O(bdc\text{-}NH_2)_3]$.[16] A comparison of the two unit cells is shown in **Table 4.2**.

Table 4.2. The unit cells of compound **21** and IRMOF-3.

MOF	Space Group	*a*	*b*	*c*	*α*	*β*	*γ*
Compound **21**	*Fm*-3*m*	25.7467(5)	25.7467(5)	25.7467(5)	90	90	90
IRMOF-3	*Fm*-3*m*	25.7465(14)	25.7465(14)	25.7465(14)	90	90	90

The structure of compound **21** was solved in the cubic space group *Fm*-3*m* with the labelled atoms in **Figure 4.18** representing the asymmetric unit**.** This is a very similar asymmetric unit to that of IRMOF-3 and unsurprisingly gives rise to the formation of the same SBU, comprising of a tetrahedral arrangement of 4-coordinate zinc centres around a central oxygen anion. Each of the edges of this tetrahedron are bridged by carboxylate groups from the organic linkers, in this case tpat.

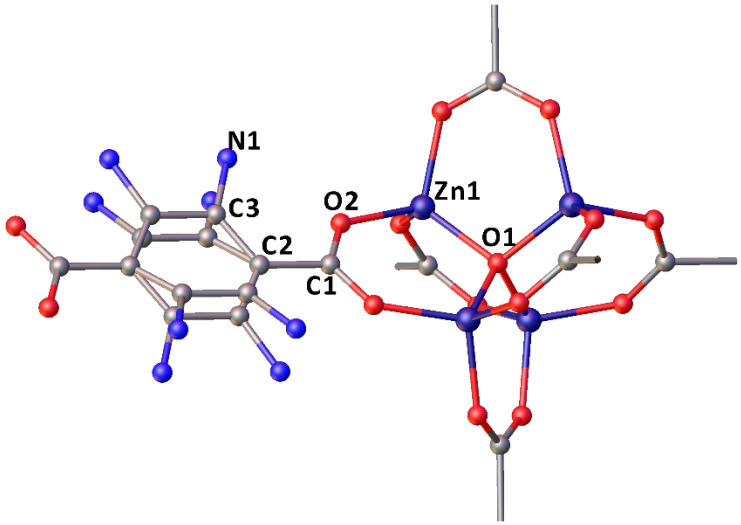

Figure 4.18. The asymmetric unit in compound **21** (labelled atoms) along with the SBU.

The structure extends in to a 3-D cubic network as shown in **Figure 4.19**. The C3 atom is disordered over two positions, which results in two different orientations of the linker benzene ring.

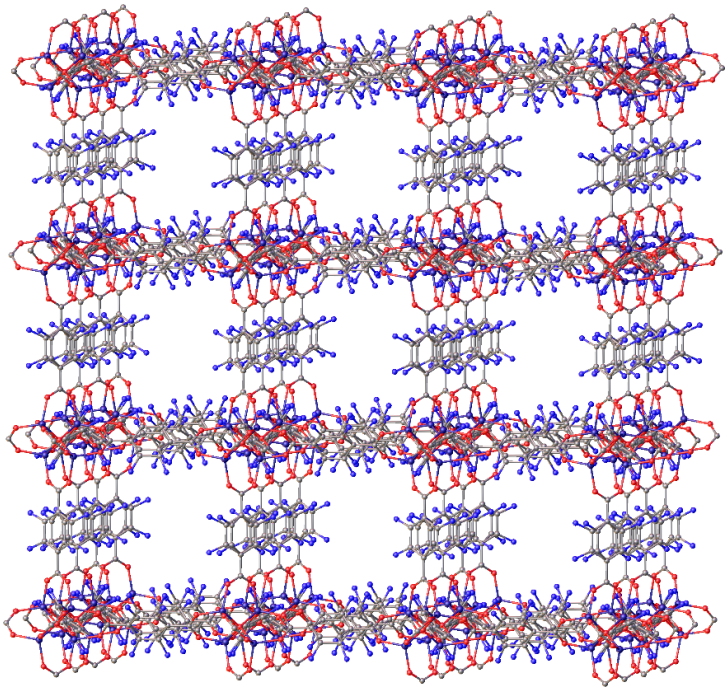

Figure 4.19. The cubic network structure of compound **21**.

The *p*-xylene groups could not be located using the single-crystal data. This is due to a number of reasons, the first of these being that the amine nitrogen, and therefore the rest of the *p*-xylene group, are statistically disordered over the 4 positions around the benzene ring. Thus each position has only a 1/4 of the electron density associated with these atoms. This problem is compounded as the benzene ring itself resides in two different orientations, leaving just 1/8th of the atom electron density at each locus. Considering the increased degrees of freedom associated with atoms further along the tether, spreading their electron density even more, it is not surprising the tether could not be located.

As for compound **20**, mass spectrometry and ^{1}H-NMR spectroscopy were needed to establish the presence of tpat rather than bdc-NH_2. Under the same conditions used for compound **20** the mass spectra showed the molecular ion peak at 463.1159, as seen in **Figure 4.20**. This is in good agreement with expected ion mass at 463.1147, confirming tpat as present in compound **21**.

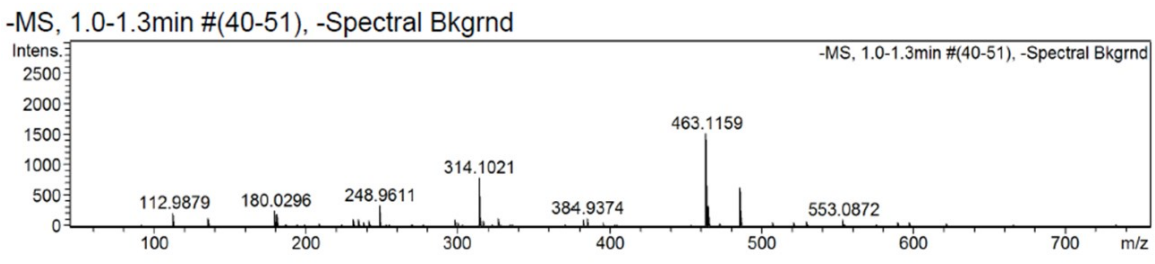

Figure 4.20. The mass spectrum for digested compound **21**.

A sample of compound **21** was digested in a $NaOD/D_2O$ solution and a ^{1}H-NMR spectrum collected. The spectrum and assignment are shown in **Figure 4.21** and confirms the presence of tpat and absence of bdc-NH_2 in the compound **21**.

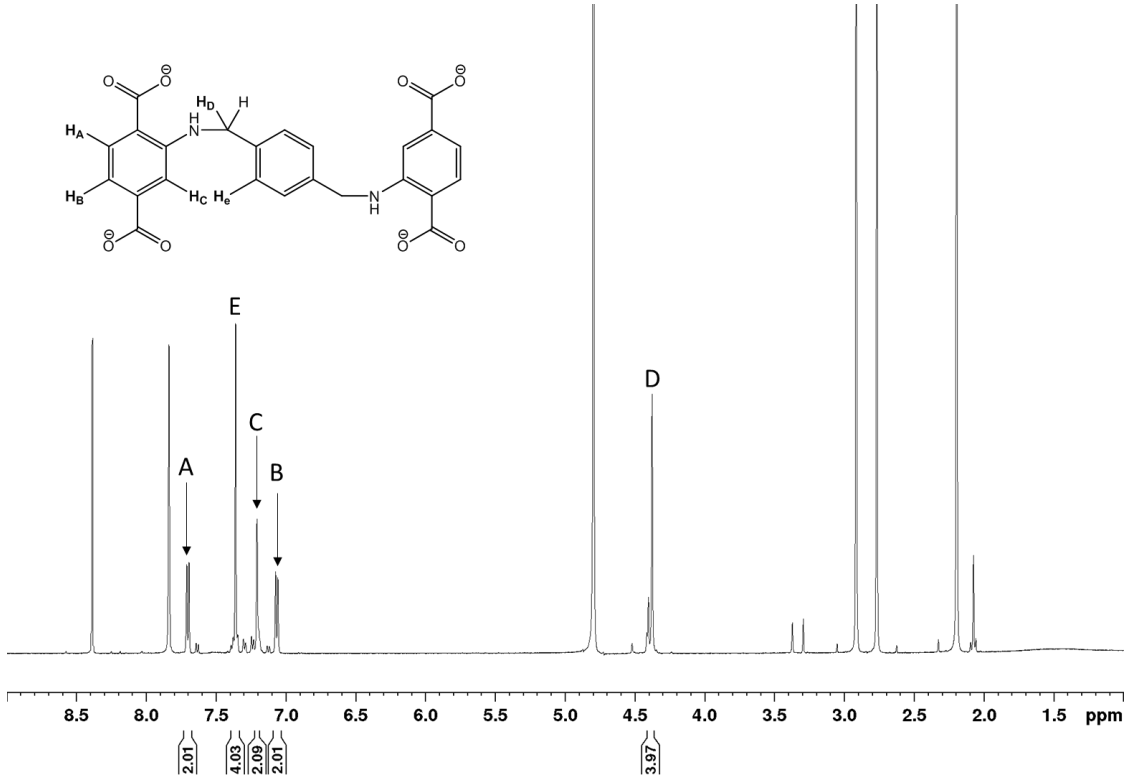

Figure 4.21. The ^{1}H-NMR spectrum of digested compound **21**.

The tpat species has been shown to be present in compound **21** by both mass spectrometry and ^{1}H-NMR spectroscopy, giving a formula of $[Zn_8O_2(tpat)_3]$ for the MOF. As with compound **20,** it is possible to postulate where in the MOF the tether is located by considering the geometry and distances between bdc fragments in the framework.

The tether could potentially span the cubic pores in three arrangements, which are represented by the dashed lines in **Figure 4.22**. Line **A** represents the tether bisecting the middle of the cavity, linking the bdc units which are diagonally opposed in the cubic pore. **B** represents the tether linking opposite bdc units across the same face of the pore and **C** represents the linking of adjacent bdc units across a corner. A fourth possibility is that only one of the bdc units coordinates as part of the framework and the other unit, along with the tethering diamino-p-xylene group, act as a very large pendent group. However, due to the size of this pendent group and the size of the pores it is highly unlikely that this is possible.

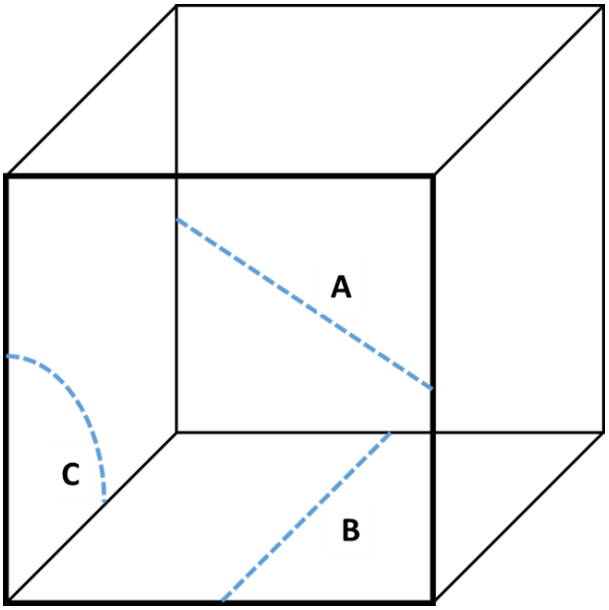

Figure 4.22. Representation of the tethering modes in the cubic IRMOF pore. **A** – Diagonally opposite. **B** – Opposite on the same face. **C** – Adjacent across a corner.

From the single-crystal data for compound **21**, it is possible to measure the minimum (and maximum) distances that the tether would need to span in order to form the three different coordination modes shown in **Figure 4.22**. As was shown in **Figure 4.13** the maximum distance the diamino-*p*-xylene group could span is approximately 7.3 Å and the minimum distance it could span is 6.7 Å. The shortest N···N measured distances for coordination mode **A** and **B** are 13.43(3) Å and 8.67(4) Å respectively, too large to accommodate the bridging tether. **Figure 4.23** shows both the maximum and minimum value for the corner tethering mode represented by **C**. The maximum distance at 9.07(5) Å is too long to be viable, and the minimum distance at 4.36(3) Å is too short. Intermediate distances are possible due to the disordered nature of the nitrogen atom location. Out of the three tethering modes discussed only **C**, linking adjacent bdc units across a corner, is likely to be present in the crystal structure, although, there could be some variation in the location of the tether within this binding mode.

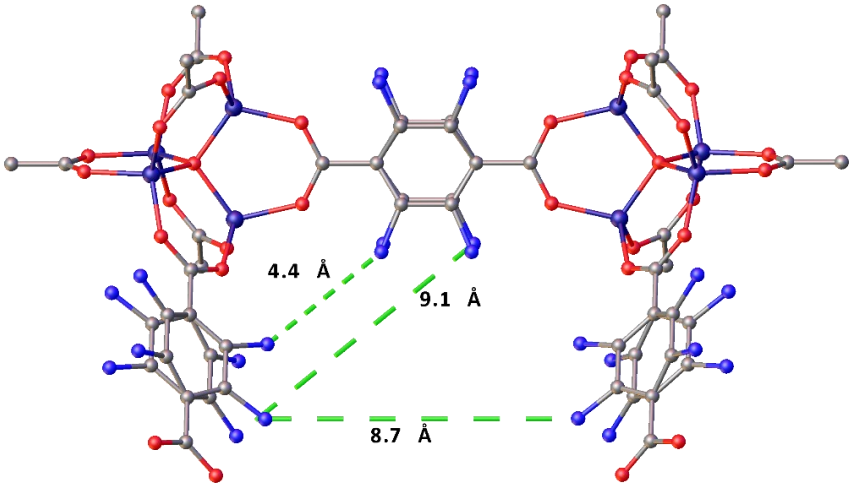

Figure 4.23. The N···N distances for coordination mode **B** and **C**.

The thermal behaviour of compound **21** and its guest solvent was interrogated via thermogravimetric analysis. In order to provide a comparison, the same analysis was carried out on a sample of IRMOF-3, the results are shown in **Figure 4.24**. The results indicate guest DMF leaves more quickly and at lower temperatures from IRMOF-3 than from compound **21**. This is due to the bulky tethering group preventing solvent from moving as freely about the framework and provides extra interactions between the framework and guest solvent. The results also suggest that compound **21** contains a lower percentage mass of volatiles, this is consistent with it having a smaller internal void space as some of the space is taken up by the *p*-xylene tether.

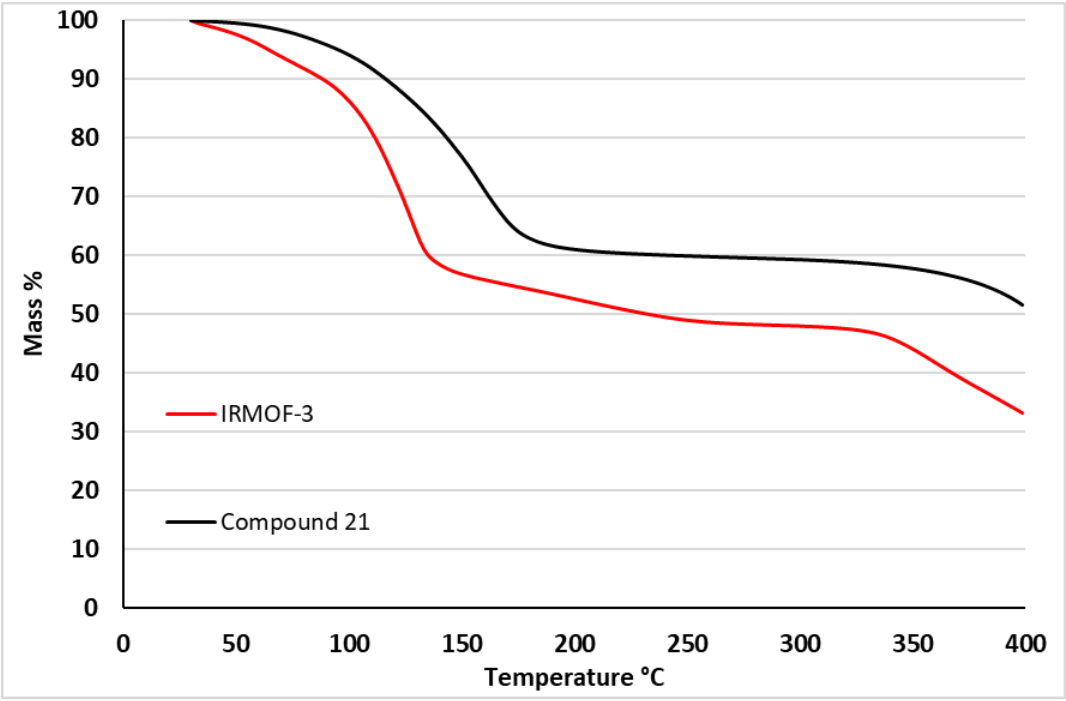

Figure 4.24. The TGA data for compound **21** and IRMOF-3.

In order to determine the surface area of compound **21** a nitrogen adsorption isotherm was collected. Activation of the material was carried out after solvent exchange with $CHCl_3$ then a nitrogen adsorption/desorption isotherm was collected at 77 K. Using the BET isotherm gave a surface area for compound **21** of 1847 $m^2 g^{-1}$. This surface area is consistent with those observed for other bdc based IRMOF structures with pendent groups of comparable size to the xylene tether. This provides further evidence that the tpat linker is coordinating via both bdc units and not just one, for which the expected surface area would be much lower.[126-129]

A series of structures related to compound **21** have been reported by Cohen *et al.* These were formed using linkers that consist of two 1,4-benznedicarboxylate units joined by a tether, much like tpat, but with amide or ether groups, not amines. When reacted with a zinc salt these form MOFs with the IRMOF topology. The linkers used were a series of alkyl tethered amido-1,4-benzenedicarboxylates and xylene-tethered ether-1,4-benzenedicarboxylates, the structures of which are presented in **Figure 4.25**.[127, 128]

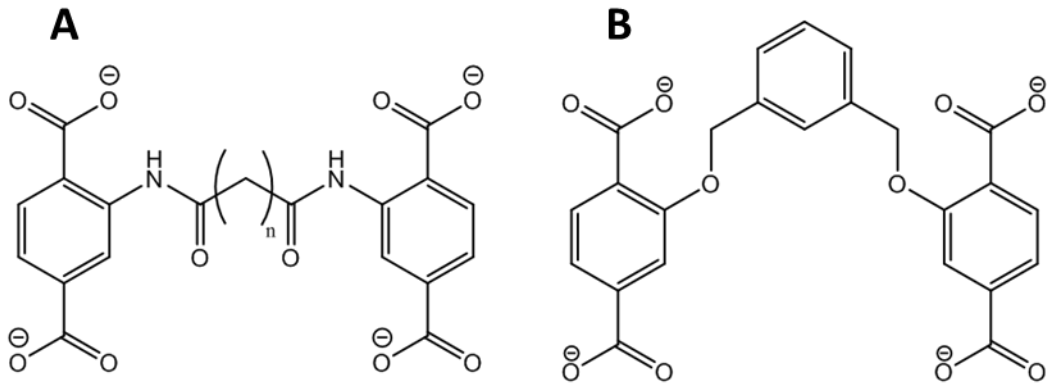

Figure 4.25. A – Tetradentate linkers used to construct IRMOFs (n = 3-7). **B** – meta-xylene ether based tetradentate linker used to construct IRMOFs.

As found with compounds **20** and **21**, the electron density for the tethering groups could not be assigned in any of the single-crystal experiments conducted by Cohen's group. The structures formed exhibited enhanced solvent entrapment within the crystal structure, this was evidenced by incomplete activation of the MOFs at 105 °C when n was larger than three. In these MOFs, residual solvent was found in the structure whereas, in IRMOF-3 and when n was equal to three, complete activation was achieved at 105 °C. This solvent entrapment was observed for compound **21** in the TGA results, where compound **21** lost its pore solvent at a higher temperature and over a larger range than IRMOF-3. This suggests that the different tethers may impart similar properties in this regard to the frameworks.[127]

As well as the linker shown in **Figure 4.25 B**, the *o* and *p*-xylene equivalents were also synthesised in Cohen's work. Interestingly only the reaction utilising the *m*-xylene containing linker was shown to form an IRMOF topology. This is in contrast to what was observed with tpat, which contains a *p*-xylene tether and forms the IRMOF topology when used in the synthesis of compound **21**. The reported BET surface area for the *m*-xylene IRMOF was 2121 $m^2 g^{-1}$ which was slightly higher than the 1847 $m^2 g^{-1}$ for compound **21**.[128]

4.2.3 Mixed-linker MOFs based on compounds **20** and **21**

A mixed-linker MOF contains two or more different but interchangeable linkers performing the same structural role. A reticular synthesis of a series of mixed linker MOFs based on the topology exhibited by compound **20** and PNMOF-3 was undertaken. The creation of a mixed-linker system allows for control over the amount of tether present in the MOF, therefore allowing for fine tuning of properties such as guest retention and surface area. As H_2bdc-NH_2 has already been used to form a MOF with this topology it is an ideal candidate to use in a mixed-linker system along with the cross-linking tpat.

The relative concentration of the two linker precursors were systematically varied in the starting reaction mixture over eight experiments. The reaction conditions for each experiment were kept similar, with the linker precursors and $Zn(NO_3)_2 \cdot 6H_2O$ being dissolved in DMF and heated at 80 °C for four days. The relative proportions of each linker in the products were analysed using ^{1}H-NMR spectroscopy, after digestion in a D_2O/NaOD solution, with the results shown in **Table 4.3**.

Table 4.3. The proportions of the tpat vs. bdc-NH_2 in the reaction mixture and in the product of the mixed-linker MOFs.

Experiment Number	Proportion of tpat in reaction mixture	Proportion of tpat in MOF	MOF Formula
7 (Compound **20**)	1	1	$[Zn_4(tpat)_3(NO_3)_2(H_2O)_2]$
6	0.60	0.83	$[Zn_4(bdc\text{-}NH_2)_{0.27}(tpat)_{1.365}(NO_3)_2(H_2O)_2]$
5	0.33	0.60	$[Zn_4(bdc\text{-}NH_2)_{0.75}(tpat)_{1.125}(NO_3)_2(H_2O)_2]$
4	0.25	0.39	$[Zn_4(bdc\text{-}NH_2)_{1.30}(tpat)_{0.85}(NO_3)_2(H_2O)_2]$
3	0.175	0.41	$[Zn_4(bdc\text{-}NH_2)_{1.25}(tpat)_{0.875}(NO_3)_2(H_2O)_2]$
2	0.10	0.17	$[Zn_4(bdc\text{-}NH_2)_{2.14}(tpat)_{0.43}(NO_3)_2(H_2O)_2]$
1 (PNMOF-3)	0	0	$[Zn_4(bdc\text{-}NH_2)_3(NO_3)_2(H_2O)_2]$

The data in **Table 4.3** are presented graphically in **Figure 4.26**. Overall, these experiments have shown preferential inclusion of tpat over bdc-NH_2 into the MOF products. This can be seen as

the red plotted line for the tpat inclusion sits above the black line simulating a proportional uptake. The reasons for the preferential uptake of tpat is likely due to the entropic gain associated with the higher number of coordinating groups. Each tpat coordinates to four different SBUs while bdc-NH_2 only coordinates to two.

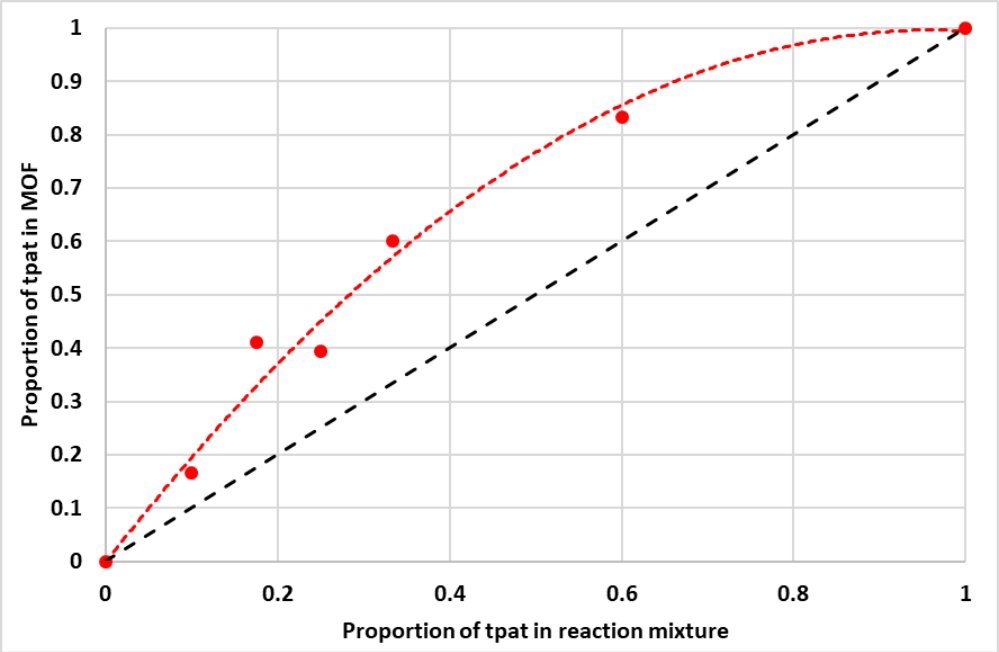

Figure 4.26. The amount of tpat included into MOFs based on the amount present in the reaction mixture. The results are shown in red, with the black line simulating an even uptake.

PXRD analysis was conducted on a sample of each of the mixed-linker products, the results of which are shown in **Figure 4.27**. All the samples present here showed the expected hexagonal sheet structure associated with compound **20** and PNMOF-3. At very low concentrations of tpat in the reaction mixture (0.025) a different phase was observed, further study is needed to ascertain whether this result is an anomaly.

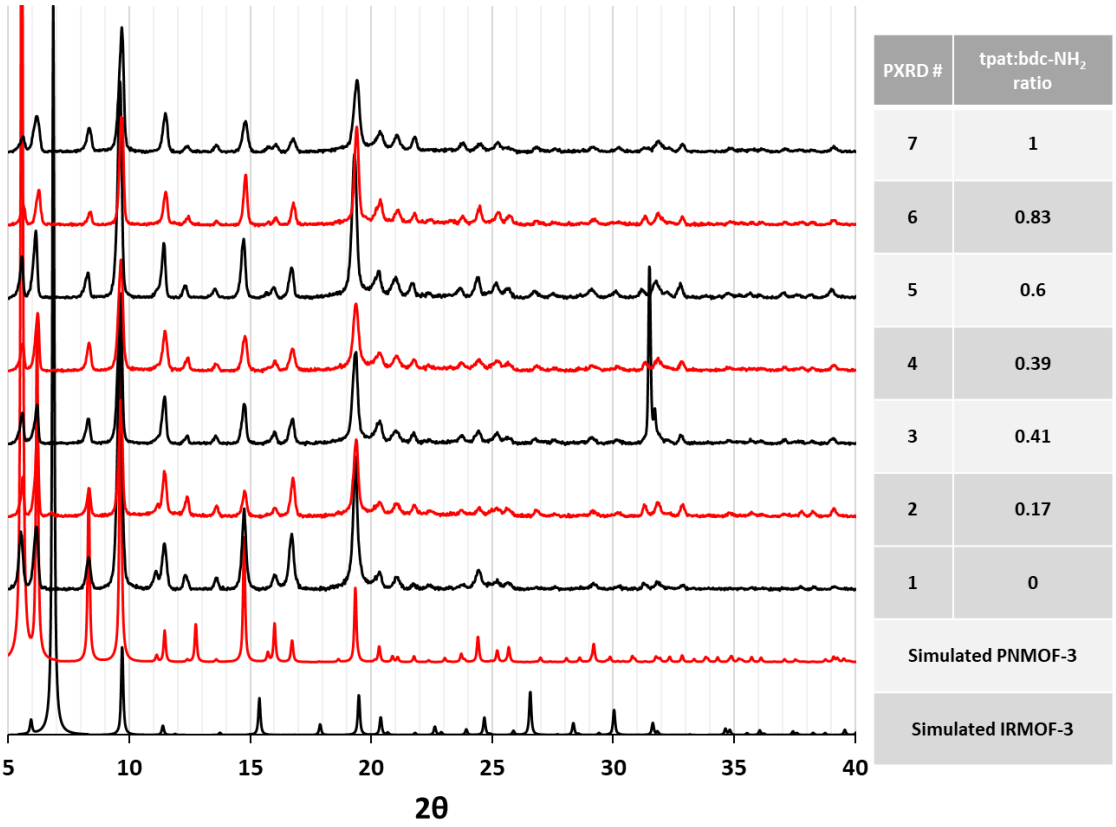

Figure 4.27. The PXRD patterns for the mixed-linker materials synthesised using zinc(II), H_4tpat, and H_2bdc-NH_2.

Two of the mixed linker MOFs from the previous experiment, with the formula $[Zn_4(bdc\text{-}NH_2)_{0.75}(tpat)_{1.125}(NO_3)_2(H_2O)_2]$ (5) and $[Zn_4(bdc\text{-}NH_2)_{2.14}(tpat)_{0.43}(NO_3)_2(H_2O)_2]$ (2), were subjected to thermogravimetric analysis, the results of which can be seen in **Figure 4.28**.

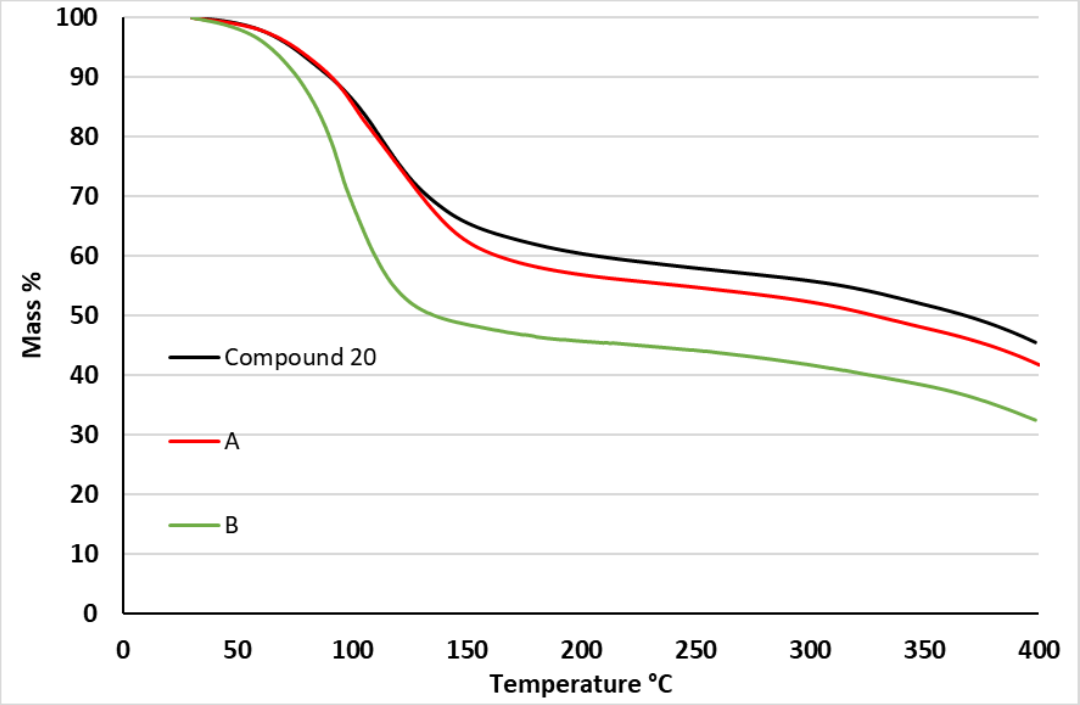

Figure 4.28. The TGA results for mixed-linker MOFs based on the compound **20** topology. A – $[Zn_4(bdc\text{-}NH_2)_{0.75}(tpat)_{1.125}(NO_3)_2(H_2O)_2]$, B – $[Zn_4(bdc\text{-}NH_2)_{2.14}(tpat)_{0.43}(NO_3)_2(H_2O)_2]$.

The proportion of tpat present in the MOF decreases from experiment 7 to 5 to 2, this is concurrent with an increase in the mass of guest solvent present in the structures. This is due to the tethering group occupying space within the pores, reducing the space available for solvent to fill. It can also be seen, particularly in the case of experiment 2 where the MOF contains a low proportion of tpat, that the guest solvent is lost at lower temperatures. This is due to the decreased amount of interaction between guest and framework when compared to 5 or compound **20** (7).

These data are in disagreement with TGA collected for PNMOF-3, shown in **Figure 4.17**, that suggested that PNMOF-3, containing no tethering group, had a very similar percentage mass of volatiles as compound **20**. These results suggest that PNMOF-3 would be expected to have a higher percentage mass of solvent than **B** (experiment 2). This discrepancy could be caused by rapid loss of solvent from PNMOF-3 during sample preparation or could indicate that the system contains further complexities with the coordination modes and pendent linker groups.

4.3 Conclusions

A new semi-rigid tetracarboxylic acid containing linker precursor, H_4tpat, has been designed and synthesised. The linker features two 2-amino-1,4-benzenedicarboxylate units tethered by a semi-rigid *p*-xylene group. The use of this ligand in combination with zinc(II) salts has led to the discovery of two new MOFs.

The first of these, compound **20**, was determined to have a formula of $[Zn_8(tpat)_3(NO_3)_4(H_2O)_4]$. The single-crystal data revealed that the structure was composed of sheets of 1,4-benzenedicarboxylate linked 3-connected zinc nodes, with the nodes taking the form of zinc dimers, leading to a hexagonal hcb net. The sheets are aligned leaving channels running in the direction of the *c*-axis. Interestingly the bulk of the tether could not be located in the crystal data so its presence was unequivocally proven using a combination of ^{1}H-NMR spectroscopy, IR spectroscopy and mass spectrometry. The location of the tether was deduced using geometric considerations, placing the tether spanning between two adjacent linkers in the same sheet.

Compound **20** was found to have a similar structure to a previously reported MOF, PNMOF-3, which has the formula $[Zn_4(bdc\text{-}NH_2)_3(NO_3)_2(H_2O)_2]$. This framework contains the same hcb sheet topology but has no tethering *p*-xylene group between bdc-NH_2 linking units. A new synthesis for PNMOF-3 was designed, allowing for access to phase pure material, something which had not previously been achieved. This allowed for comparisons of thermal behaviour of PNMOF-3 and compound **20.**

A second new MOF, compound **21**, with the formula $[Zn_8O_2(tpat)_3]$, was found to form in analogous synthetic conditions to compound **20** but at higher temperatures. The structure and topology of the framework were elucidated using single-crystal X-ray diffraction. The structure was found to be a cubic structure with octahedral $Zn_4O(CO_2)_6$ SBU nodes linked by 2-amino-1,4-benzenedicarboxylate units. As in the case with compound **20**, the tethering *p*-xylene groups were not located in the data. Using the same methodology and geometric considerations the tethering groups were shown to be present and likely bridged adjacent bdc units across the corners of the cubic pores.

Compound **21** was found to have a similar structure to the previously reported IRMOF-3, $[Zn_4O(bdc\text{-}NH_2)_3]$. Through comparative experiments, this allowed for elucidation of the impact on material properties intrinsic to the tethering group. It was shown that compound **20** has a lower surface area than that of IRMOF-3 (1847 $m^2\ g^{-1}$ vs. 2069 $m^2\ g^{-1}$), also containing a lower

mass of guest solvent within the pores. Compound **20** exhibited enhanced solvent entrapment, leading to solvent loss at higher temperatures and at a slower rate.

The cross-linked MOFs have shown an ability to enhance guest-entrapment within the frameworks. This could be advantageous in applications where controlled release of a guest species is important, such as in drug delivery or other biological molecules. Control of the degree of guest entrapment can be achieved with the use of mixed-linker MOFs. A series of mixed-linker MOFs containing tpat and bdc-NH_2 were synthesised. PXRD showed that the structures were based on the hexagonal sheet topology of compound **20**. It was found that the amount of guest solvent and the temperature range of release can be controlled by substituting some of the cross-linking tpat for bdc-NH_2. Future study of this area would focus on synthesis of mixed-ligand systems exhibiting the IRMOF and compound **21** topology. These MOFs, which are more robust than the compound **20** related systems, could be investigated for uptake and release of drug molecules. Exploring the benefits imparted on the materials performance as a drug delivery system by the presence of the tethering group.

4.4 Experimental

General procedures are presented in the experimental section of **Chapter 2.**

4.4.1 Synthesis of H_4tpat

2-amino-1,4-benzenedicarboxylic acid (10 mmol, 1.812 g) and terephthalaldehyde (5 mmol, 0.671 g) were dissolved in 300 mL of MeOH. 5 drops of formic acid were added, then the reaction mixture stirred at room temperature for 5 hours. The reaction mix was placed in an ice bath and $NaCNBH_3$ (14 mmol, 0.880 g) was added in one portion. The reaction was then stirred at room temperature for a further 16 hours before being acidified using 1M HCl, which resulted in precipitation of a yellow solid which was collected by vacuum filtration and oven dried at 60 °C for 4 hours. Total yield, 1.50 g (65%).

The product identity was confirmed via ^{1}H-NMR (300 MHz, DMSO-*d*^{6}); 4.46 (4H, s), 7.08 (2H, dd, *J* = 8.2, 1.4 Hz), 7.20 (2H, d, *J* = 1.3 Hz), 7.33 (4H, s), 7.88 (2H, d, *J* = 8.2 Hz) and ^{13}C{^{1}H}-NMR (125 MHz, D_2O); 175.5, 175.3, 148.7, 139.7, 138.2, 131.1, 127.7, 122.1, 116.5, 113.1, 46.6. The NMR spectra are shown in **Figure 4.2** and **Figure 4.3** respectively.

4.4.2 Synthesis of $[Zn_8(tpat)_3(NO_3)_4(H_2O)_4]$ (**20**)

In a glass vial, $Zn(NO_3)_2{\cdot}6H_2O$ (0.6 mmol, 0.1785 g) and H_4tpat (0.2 mmol, 0.0928 g) were dissolved in 16 mL of DMF with the aid of a sonicator. The vial was sealed and then heated in an oven at 80 °C for 4 days. After removal from the oven and cooling under ambient conditions, the yellow intergrown hexagonal prism crystals were separated by vacuum filtration, then washed with dry DMF (3 x 5 mL) and stored in dry DMF.

4.4.3 Synthesis of PNMOF-3 $[Zn_4(bdc\text{-}NH_2)_3(NO_3)_2(H_2O)_2]$

In a glass vial, $Zn(NO_3)_2{\cdot}6H_2O$ (0.6 mmol, 0.1785 g) and H_2bdc-NH_2 (0.3 mmol, 0.0545 g) were dissolved in 16 mL of DMF with the aid of a sonicator. The vial was sealed and then heated in an oven at 80 °C for 4 days. After removal from the oven and cooling under ambient conditions, the yellow-brown intergrown hexagonal prism crystals were separated by vacuum filtration, then washed with dry DMF (3 x 5 mL) and stored in dry DMF.

4.4.4 Synthesis of $[Zn_8O_2(tpat)_3]$ (**21**)

In a glass vial, $Zn(NO_3)_2{\cdot}6H_2O$ (0.6 mmol, 0.1785 g) and H_4tpat (0.2 mmol, 0.0928 g) were dissolved in 16 mL of DMF with the aid of a sonicator. The vial was sealed and then heated in an oven at 100 °C for 4 days. After removal from the oven and cooling under ambient conditions, yellow cubic crystals were separated by vacuum filtration, then washed with dry DMF (3 x 5 mL)

and stored under dry DMF until required. The data for the refinement of the single-crystal structure collection is shown in **Table 4.4**.

Table 4.4. Crystal data and structural refinement for compound **21**.

Compound	**21**
Empirical formula	$C_{24}H_9N_3O_{13}Zn_4$
Formula weight	808.76
Temperature/K	240.00(10)
Crystal system	cubic
Space group	*Fm*-3*m*
a/Å	25.7467(5)
b/Å	25.7467(5)
c/Å	25.7467(5)
α/°	90
β/°	90
γ/°	90
Volume/Å^3	17067.3(10)
Z	8.00064
ρ_{calc}g/cm^3	0.630
μ/mm^{-1}	1.490
F(000)	3184.0
Crystal size/mm^3	0.275 × 0.166 × 0.146
Radiation/Å	CuKα (λ = 1.54184)
2Θ range for data collection/°	5.946 to 145.81
Index ranges	-31 ≤ h ≤ 27, -31 ≤ k ≤ 18, -28 ≤ l ≤ 31
Reflections collected	14049
Independent reflections, R_{int}	916, 0.0327
Data/restraints/parameters	916/7/37
Goodness-of-fit on F^2	1.175
Final R_1, wR_2 indexes [I>=2σ (I)]	0.0590, 0.2121
Final R_1, wR_2 indexes [all data]	0.0630, 0.2222
Largest diff. peak/hole / e Å^{-3}	0.37/-0.21

The phase purity of the material was confirmed using PXRD, as shown in **Figure 4.29**.

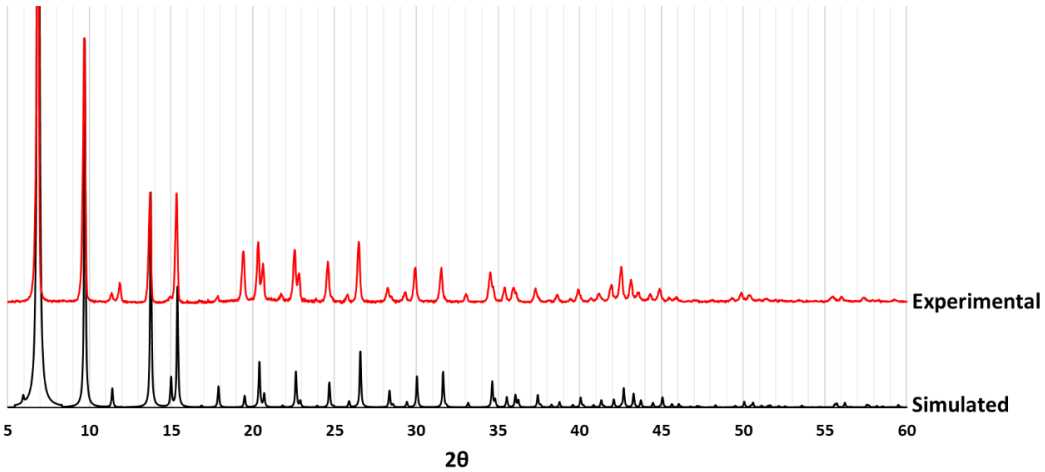

Figure 4.29. The PXRD pattern collected for compound **21**, along with the pattern simulated from the single-crystal data.

The material was activated by performing a solvent exchange with $CHCl_3$ over three days, exchanging for fresh $CHCl_3$ every 24 hours. A sample of the solid was then heated under reduced pressure for 24 hours at 100 °C. Nitrogen adsorption and desorption isotherms were collected at 77 K, shown in **Figure 4.30**. The data were used to construct a BET plot, shown in **Figure 4.31**. From this an estimate for the surface area was calculated as 1847 $cm^2\ g^{-1}$.

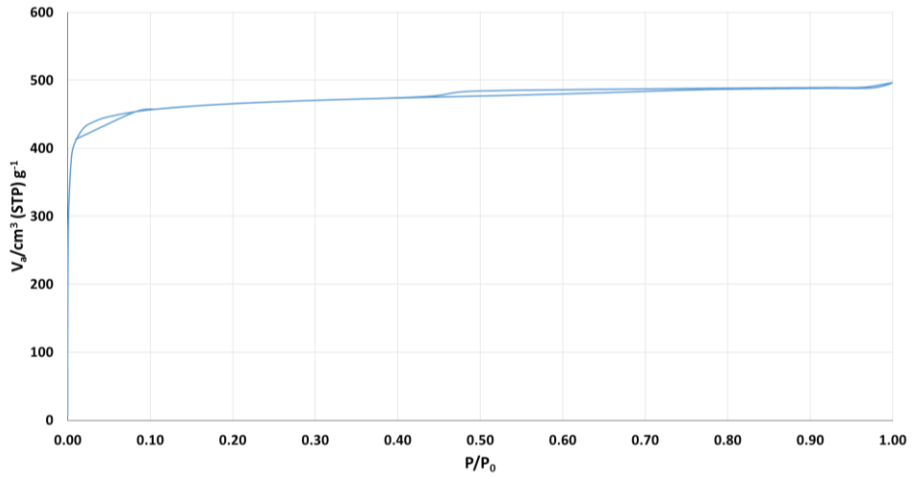

Figure 4.30. The N_2 adsorption and desorption isotherm for compound **21**.

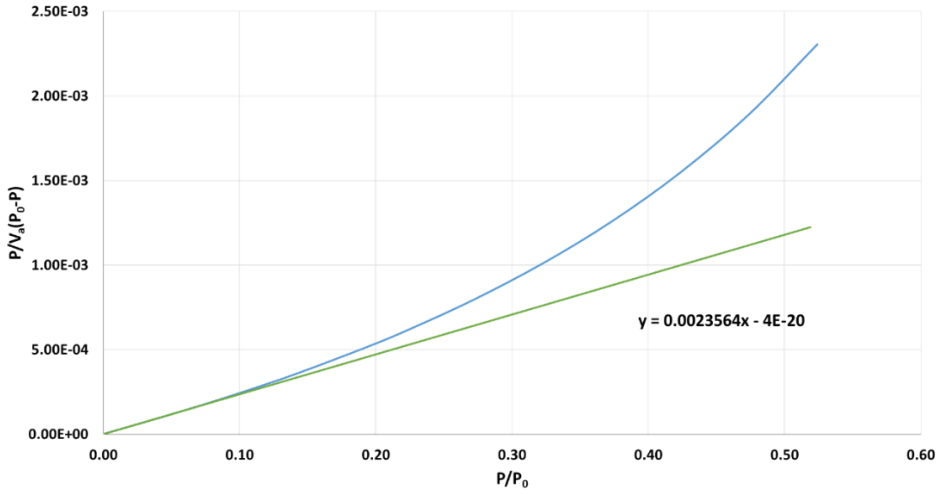

Figure 4.31. BET plot for compound **21.**

4.4.5 Synthesis of Mixed-Linker Systems.

In a glass vial $Zn(NO_3)_2{\cdot}6H_2O$ (0.6 mmol, 0.1785 g), H_4tpat and H_2bdc-NH_2 in varying ratios (see **Table 4.3**) were dissolved in 16 mL of DMF with the aid of a sonicator. The vial was sealed and then heated in an oven at 80 °C for 4 days. After cooling under ambient conditions, the yellow crystals were separated by vacuum filtration, then washed with dry DMF (3 x 5 mL) and stored in dry DMF until required.

Chapter 5 - The Inclusion and Release of Semiochemicals from Metal-Organic Frameworks

5.1 Introduction

The ability of MOFs to adsorb small molecules into pores and subsequently release them has been extensively investigated, with the majority of the species explored being either gases or active pharmaceutical ingredients.[87, 130-134] There has been comparatively little research into the storage of other biologically active molecules. One such group of potential guests are those associated with agriculture, namely insecticides, fungicides, herbicides and pheromones. These are a very important group of chemicals used to protect crops from destruction or competition which would otherwise decrease their yield.

The planet's population is set to exceed 9 billion by 2050, placing unprecedented pressure on agriculture to provide for an ever increasing populace.[135] Agricultural land is finite and therefore the need to increase the efficiency of the land available is essential. A part of rising to this challenge is providing effective methods for reducing loss of crops to pests.[136] Methods of pest control can be split into four categories: biological, chemical, mechanical and physical. Biological control uses the introduction of either a predator or micro-organism to regulate the population of a pest species. Chemical control can be the use of pesticides to kill unwanted organisms or the use of a semiochemical (a chemical which effects a change in a species) to disrupt the natural behaviour of the pest. Mechanical control is the movement of the pest species and/or their environment to remove a local population, whereas physical control constitutes the use of physical barriers to prevent pest movement to the crops.[137]

A common method of chemical control utilizes pheromones in pest management. Pheromones, which are a subset of semiochemicals, are substances which are secreted outwardly by one member of a species and received by a second member, triggering a specific response. Population control using these chemical signals can be achieved by mass trapping, lure and kill, mating disruption or disruption to other pest habits. Mass trapping is conceptually the simplest method, using an attractant pheromone to lure pests into a trap, like a cage or sticky pad. Lure and kill works in a similar way but the pest is eliminated at the source of the attractant. Pheromones can also be used to disrupt mating cycles so the population of the pest falls. Other pest habits such as feeding and migration can also be targeted using pheromones to give similar results.[138 139]

An inherent problem with pheromone-based lure traps is their short lifespan, requiring repeated and frequent replacement. Their lifespan is limited by the volatility of the pheromone attractant, as once all the lure has evaporated into the environment the trap ceases to function. This is an issue as pheromones are volatile by nature. The lifetimes of these traps can be improved by introducing a method to release the semiochemical in a controlled manner. One novel method of introducing the desired control is through the use of porous materials. The semiochemical can be adsorbed inside the pores of the material. The interaction between the pheromone and the pore walls then decreases the rate at which the pheromone is released into the environment. With a slower rate of release, the lifetime of the lure trap can be increased.

5.1.1 Pheromones and Semiochemicals in Porous Materials

There are several examples in the literature where porous materials have been used as host media for pheromones and semiochemicals with a view to creating improved lure traps. Zeolites, a class of porous aluminosilicates, have been used as materials to house semiochemicals. Two zeolites, faujasite and ZSM-5 were used in a study along with the pheromones 1-decanol, a female sex pheromone from *Agrotis segetum* (turnip moth) and *Cydia pomonella* (codling moth), and trimedlure, a synthetic attractant for male *Ceratitis capitata* (Mediterranean fruit fly). The structures of these lures are shown in **Figure 5.1**. The research showed that not only could the two substances be adsorbed but they were also released at a controlled rate for a period of over a month. The release was also optimized for the two different pheromones both by varying the pore diameter, which was achieved by changing the zeolite used and varying the polarity and polarizability of the network, achieved by altering the silicon/aluminium ratio.[140]

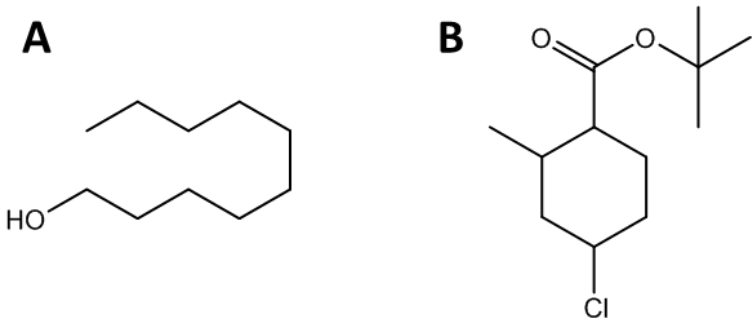

Figure 5.1. The structures of semiochemicals: **A,** 1-decanol and **B,** trimedlure.

Zeolites have also been used to create pheromone traps targeting *Riptortus pedestris* (soybean bug) which is a well-known pest of soybean fields and fruit trees. In this study the surface of zeolite 4A was modified with a surfactant in order to maximize adsorption of pheromones. The

lure targeted in this study was an aggregation pheromone and consists of a complex ternary mixture of three components, (E)-2-hexenyl-(Z)-3-hexenoate, (E)-2-hexenyl-(E)-2-hexenoate and myristyl isobutyrate, the structures of which are shown in **Figure 5.2**. The semiochemicals were used in the ratio of 7:5:1 respectively and it was shown that the small proportion of myristyl isobutyrate was key to the pheromone working effectively. In a field test it was found that the zeolite-based trap outperformed a commercial product, trapping over double the number of soybean bugs over a period of 20 weeks.[141]

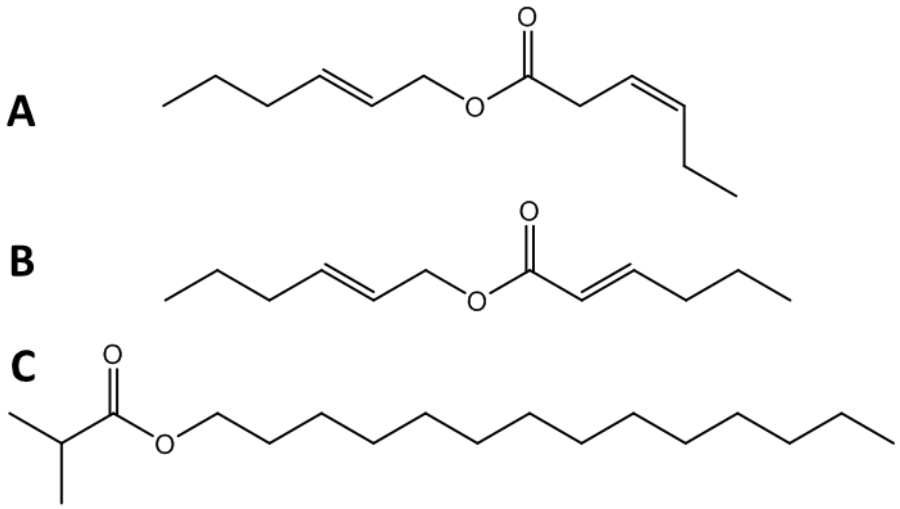

Figure 5.2. The structures of the 3 components of the soybean bug pheromone, **A** (E)-2-hexenyl-(Z)-3-hexenoate, **B** (E)-2-hexenyl-(E)-2-hexenoate and **C** myristyl isobutyrate.

Porous Vycor Glass (PVG), a commercial porous silica glass, has been successfully impregnated with a number of different pheromones and used in two different field tests. In the first, the PGV was loaded with 5,9-dimethylpentadecane, a pheromone for *Leucoptera coffeela* (coffee leaf miner) and placed in a coffee plantation along with commercial rubber septa lures loaded with the same pheromone. The second test was carried out in an apple orchard and used a complex ternary mixture of pheromones, (Z)-8-dodecenyl acetate, (E)-8-dodecenyl acetate and (Z)-8-dodecen-1-ol. These are the sex pheromones for *Grapholita molesta* (oriental fruit moth) which is a pest of apples and other fruit in the tropics. Rubber septa loaded with pheromone were also placed in the orchard in order to give a comparison with a common commercial method of release. The results showed that in both field tests the PGV had a similar performance to the rubber septa over the six week monitoring period. It was also seen that the ratio of the components in the complex ternary mixture released from the PGV was, on average, close to the ideal proportion, demonstrating that a complex mixture of semiochemicals could still be employed effectively in a porous material.[142]

Another example of utilizing silica in a pheromone dispenser is by the formation of sol-gel matrices. Sol-gels are inorganic polymers, made from silicates in this case, which are amorphous and produce a 3-D porous network. The pore sizes and distribution are determined by the extent of cross-linking during the polymer formation. In contrast to the aforementioned systems, the pheromone is not adsorbed into already formed pores, but added before the sol-gel has formed. The gel then sets with the pheromone impregnated in the material. It was shown that a large number of pheromones could be included in this system with field results demonstrating constant release rates for up to a month.[143]

Mesoporous silicates containing the *Cydia pomonella* (codling moth) pheromone (E,E)-8,10-dodecadien-1-ol have been synthesised. These are hierarchical structures formed using surfactants and silicates followed by calcination. As with the sol-gel formation, the pheromone was added during the synthesis of the silicate and was shown to have a drastic effect on the structure formed. The silicates formed ranged in structure from hexagonally arranged channels to lamellar sheets and amorphous materials, schematics of which are shown in **Figure 5.3**. Unsurprisingly, these different structures had different uptake and release properties. The lamellar and amorphous structures contained more pheromone with the amorphous material releasing the pheromone at a slower rate than the more ordered structures.[144]

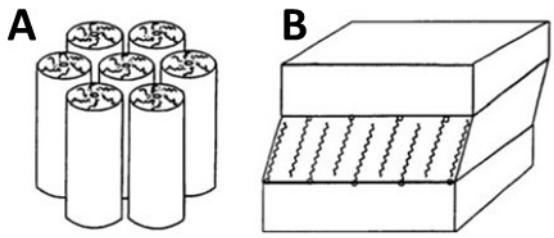

Figure 5.3. Mesoporous silica structure synthesised: **A**, MCM-41(hexagonal) and **B**, MCM-50 (lamellar).[144]

5.1.2 Biological Molecules in Metal-Organic Frameworks

Although there are no previous reports concerning the adsorption or release of pheromones in MOFs, there are examples of other families of biologically active molecules being included into MOFs.

One of these groups are hormones. These are chemicals that are produced in an organism, that are transported to another tissue in the same organism to elicit a response. An example of where a hormone has been included in a MOF is ethylene, **Figure 5.4 A.**[145] Ethylene is a plant ripening hormone; a fruit exposed to the gas will ripen. This can be utilised by allowing fruit to be picked

and stored before it is ripe, after which it can be artificially ripened by exposing it to ethylene when it is required for sale and consumption. Ethylene is already used commercially to stimulate ripening of a wide range of fruit but is highly flammable and, as such, costly safety precautions must be taken with its handling. The inclusion and storage of the gas inside MOFs allows for a safer method of storage and release into the environment.

The MOF used in this report was named CuTPA [Cu(bdc)(DMF)] and is made up of copper paddle-wheel SBUs and bdc linkers. The SBU and linear linker combine to make a 2-D square network, as shown in **Figure 5.4 B**, with the axial positions on the copper paddle-wheel occupied by DMF solvent molecules. The 2-D sheets align in an ABC type manner so that every third layer is aligned. It was found that, once activated, this MOF could adsorb and release significant amounts of ethylene; a 50 mg sample released 654 µL/L of ethylene in a 4 L container. It was then used in tests to ripen avocados and bananas. The presence of the MOF encapsulated ethylene facilitated ripening of both fruits, reducing firmness and eliciting the anticipated colour change.[145]

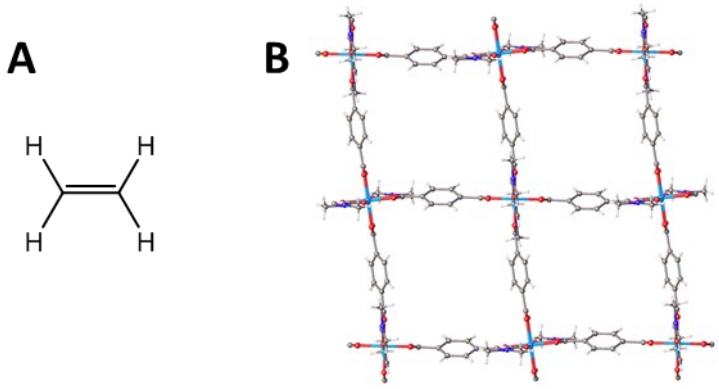

Figure 5.4. Structures of **A** – the plant hormone ethylene and **B** – a sheet from the MOF CuTPA.

Another system for the controlled release of ethylene has recently been reported. This system uses an aluminium-based MOF MIL-96(Al), which is a 3-D framework made up of octahedral Al(III) centres linked by 1,3,5-benzenetricarboxylate ligands.[146] This MOF is used in combination with a Fe(III)-alginate matrix to form an ethylene delivery system. Sodium alginate is a natural polysaccharide that in combination with a metal ion (Fe(III)) forms a solid matrix. The core is made up of the ethylene loaded MIL-96(Al) with the Fe(III)-alginate matrix forming around the MOF. The ethylene is released when the system is submerged in water in the presence of a sodium citrate promoter. The latter breaks down the Fe-alginate matrix exposing the ethylene-impregnated MOF which then releases the gas. This process is depicted in **Figure 5.5**. The system released approximately 365 µL/L of ethylene in a 4 L container over 3 hours.[147]

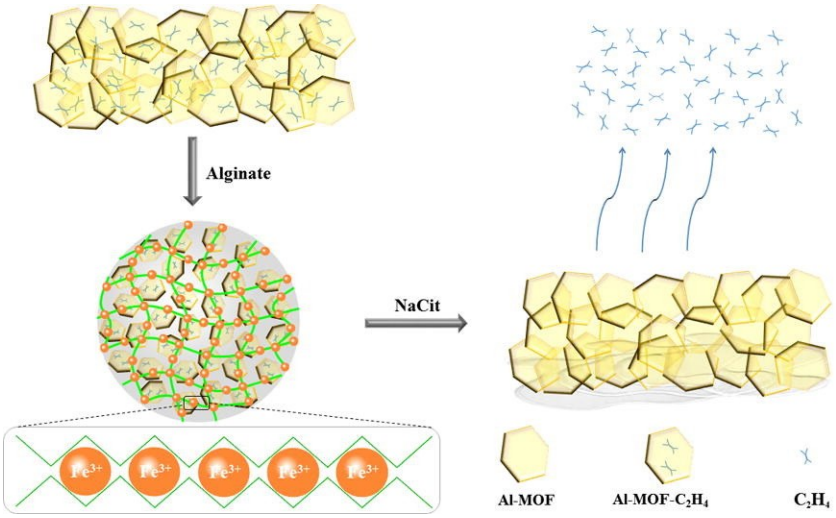

Figure 5.5. A schematic diagram showing the process for ethylene release from the MIL-96@Alginate system.[147]

1-methylcyclopropene (1-MCP), the structure of which is shown in **Figure 5.6**, is a plant hormone that also regulates growth in plants. It is used commercially to slow the ripening of fruit and also to stop ornamental plants from wilting. Its presence causes the opposite effect to ethylene, this is because it is a competitive inhibitor of the ethylene receptor. 1-MCP blocks the ethylene receptors so the ripening hormone cannot bind and therefore the chemical pathway leading to ripening is not triggered.[148]

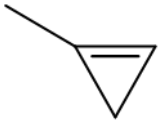

Figure 5.6. The structure of 1-methylcyclopropene (1-MCP).

The storage and controlled release of this hormone from a MOF is at the core of a fruit packaging technology called TruPick. This is one of the first commercial uses of MOFs with the MOF material supplied by a spin-out company from Queen's University Belfast called MOF Technologies and utilised by Decco, a post-harvest solutions company. The identity of the MOF has not been made public for commercial reasons but is delivered in the form of a sachet with the framework contained within a water soluble gel. Once released into the sealed environment of a storage container the hormone slows ripening, reducing the amount of waste from food spoilage. This is beneficial from both an environmental and commercial perspective.[149]

The gas nitric oxide, NO, is a signalling molecule in humans and is involved in a wide range of physiological processes in the body. These include but are not limited to, vasodilation, neural transmission and as part of an immune response.[150]

The study of NO in porous materials is attractive as a delivery system utilizing its anti-bacterial, anti-thrombotic and wound healing properties. The main area of delivery concentrates on smart wound dressings, with the NO actively preventing infection and promoting healing. A wide variety of different MOFs have been studied and reported for NO uptake and release, most of these focus on the interaction of NO with coordinatively unsaturated metal sites within the framework.[151-154]

An example of one of these frameworks is MOF-74, also known as CPO-27, which was prepared with either cobalt or nickel metal centres. The organic linker used was 2,5-dioxido-1,4-benzenedicarboxylate (dobdc), shown in **Figure 5.7**, giving a MOF formula of $[M_2(dobdc)]\cdot 2DMF$. The framework has been reported with a wide range of M^{2+} ions (M = Mg, Fe, Co, Ni, Cu, Zn).[155, 156]

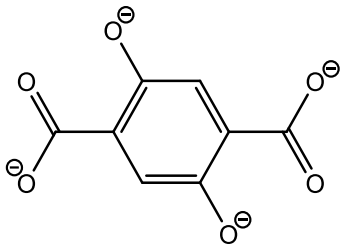

Figure 5.7. The organic linker in MOF-74, 2,5-dioxido-1,4-benznedicarboxylate (dobdc).

The framework topology is a honeycomb structure, with oxido and carboxylate linked metal centres forming long 1-D chain SBUs. These are bridged to three neighbouring chains by the bulk of the linker to form a hexagonal honeycomb with channels running along the same axis as the SBUs. All the metal centres in the structure are symmetry related and all possess a labile co-ordination site extending into the pore channel. In the as-synthesised MOF this site is occupied by a solvent molecule, usually DMF. Upon MOF activation, this site becomes vacant and when NO is introduced to the system it coordinates to the metal via the nitrogen atom. The NO saturated MOF can then release the gas into the environment. This process and the MOF structure are depicted in **Figure 5.8**.

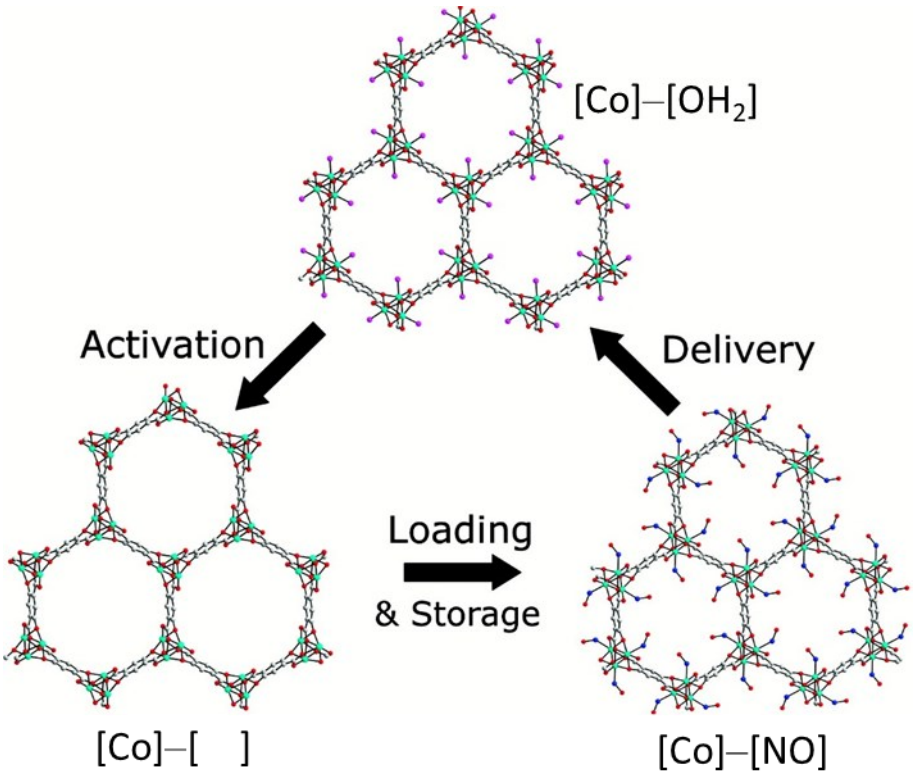

Figure 5.8. The activation, loading and delivery cycle for NO in Co-MOF-74. (Co, cyan; O, red; C, white; O (water), purple).[152]

The NO-loaded MOF was tested to examine the rate at which the gas was released, the results showed that both the cobalt and nickel based materials were still releasing NO after 14 hours. Interestingly, there was an initial spike in the rate of release in the first 10 minutes, which was attributed to the liberation of NO gas in the pores which are not bound to the metal centre and therefore are only held by comparatively weak physisorption.

5.1.3 Project Scope

This part of the thesis aimed to investigate the incorporation of several semiochemicals into different MOFs with a view to creating lure traps targeted at pest species of the agriculture industry.

The semiochemicals chosen for investigation were 3-octanone (oct), 4-methyl-3-heptanone (mhp), 1-hexanol (hex) and isoamyl acetate (iaa). The structures of these semiochemicals are shown in **Figure 5.9**.

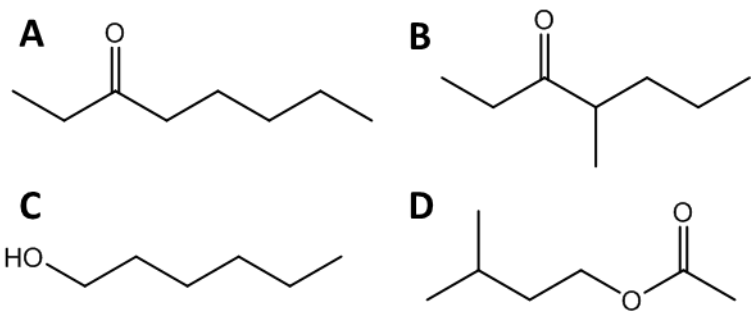

Figure 5.9. Semiochemicals under study: **A**, 3-octanone (oct); **B**, 4-methyl-3-heptanone (mhp); **C**, 1-hexanol (hex) and **D**, isoamyl acetate (iaa).

3-Octanone and 4-methyl-3-heptanone are alarm pheromones for species of leaf-cutting ants (*Atta* and *Acromyrmex* genera). These ants are agricultural pests in the neotropics, affecting coffee, cocoa, sugar cane and forestry industries. The use of alarm pheromones for a lure seems counterintuitive but it has been shown that an ant colony will attack the source of an alarm pheromone over long distances. This is in contrast to trail pheromones which only act over short distances.[157-159] Of the two pheromones, 3-octanone is far cheaper and is commercially available so was used in preference to 4-methyl-3-heptanone for the majority of studies.

1-Hexanol is an attractant for the German cockroach (*Blatella germanica*) and a known volatile released by decomposing lipids. Cockroaches are pests in human buildings and urban areas, they are carriers of human pathogens such as *Staphylococcus aureus*, *Escherichia coli*, and *Salmonella spp.* Cockroach-derived allergens are also associated with allergic reactions and asthma. As such pest management is required and 1-hexanol has been identified as a suitable attractant for a lure-based trap.[160, 161]

The spotted wing drosophila (*Drosophila suzukii)* is an invasive pest native to Asia and has been detected across North America and Europe. It is a fruit fly that has become a pest to soft skinned fruit such as raspberries, cherries and strawberries. Unlike other fruit flies, it feeds on ripening fruit not just damaged or decomposing fruit so poses a more substantial financial threat to the agricultural industry. Isoamyl acetate is an attractant for the spotted wing drosophila and it is emitted by ripe fruit. This compound is ideal for a lure trap as, despite the fly being a pest to pre-ripened fruit, it is more strongly attracted to the semiochemicals released by ripe fruit.[162-164]

5.1.4 Previous Work

Previous work in the Burrows group carried out by Dr Amer Hamzah has shown that the leaf cutting ant pheromones 3-octanone and 4-methyl-3-heptanone could be taken up into the pores

of several different MOFs. The research programme investigated the IRMOF family, and the MOFs investigated were IRMOF-1 (MOF-5), IRMOF-3, which has a primary amine functionalisation, and other alkyl functionalised derivatives of IRMOF-3. The IRMOF structure has been described in **Section 1.1.3** and can be seen in **Figure 1.10**. The IRMOFs have the generic formula $[Zn_4O(L)_3]$, where L is a linear dicarboxylate. The dicarboxylates used by Dr Hamzah are shown in **Figure 5.10***.* The linkers were selected to provide a range of different functionalities within the MOF pores with which the pheromones could interact. The rationale for the choice of amines with alkyl chains was that the polar ketone group of the pheromones should interact strongly with the amine on the linkers and that the alkyl chains on both the linkers and pheromone would also interact. The combination of interactions should maximise uptake and slow down release.[31]

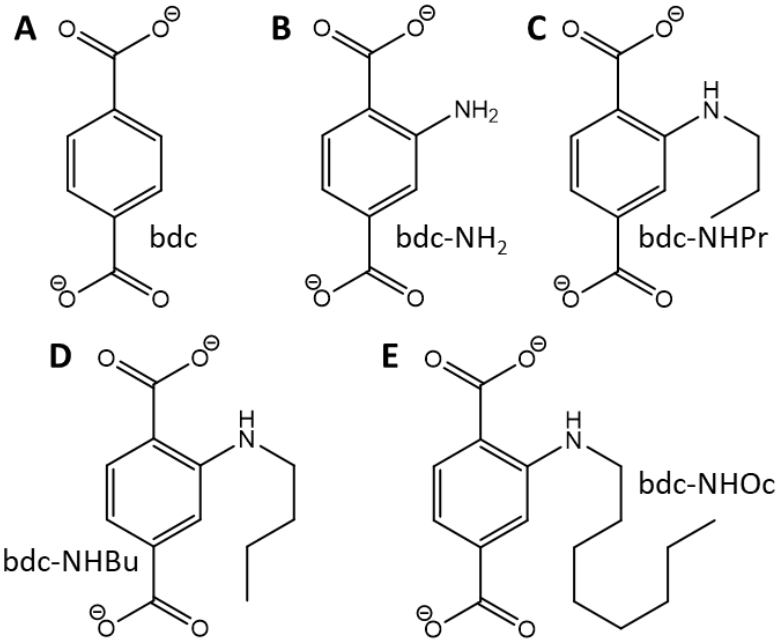

Figure 5.10. The structures of the benzene dicarboxylates used in the synthesis of the IRMOFs in the pheromone uptake experiments. **A** bdc, **B** bdc-NH_2, **C** 2-propylamino-1,4-benzenedicarboxylate (bdc-NHPr), **D** 2-butylamino-1,4-benzenedicarboxylate (bdc-NHBu) and **E** 2-octylamino-1,4-benzenedicarboxylate (bdc-NHOc).

The majority of the research was carried out using 3-octanone due to cost and availability. It was shown that by weight percentage, 3-octanone was taken up into the MOFs in the order IRMOF-NHPr > IRMOF-NHBu > IRMOF-3 > IRMOF-1 > IRMOF-NHOc. The maximum uptake value observed for IRMOF-NHPr was 36.8 wt.% which equates to a formula of $[Zn_4O(bdc\text{-}NHPr)_3]\cdot 2.7oct$. The decrease in uptake in MOFs containing the ligands bdc-NHBu and bdc-NHOc was rationalised as reflecting that more pore space is occupied with the alkyl arms of the linkers,

and in the case of IRMOF-NHOc almost no uptake was observed at all. This premise was supported by the lower measured surface area values for activated versions of these MOFs.

Other results from this work highlighted the effects of repeated washing of the pheromone-loaded MOF crystals. It was shown that successive washing of the crystals drastically lowered the measured amount of 3-octanone held in the MOF, with a loss of 10 wt.% over three washes. It was also shown that significant loadings of 3-octanone (23.2 wt.%) could still be achieved using 4:1 equivalents of 3-octanone to MOF in DMF rather than neat 3-octanone. This is a more cost-effective way of loading the MOFs and would be particularly relevant if using a more expensive pheromone.

A UiO-66 (**Figure 1.27**) analogue of the IRMOF-NHPr was synthesised using bdc-NHPr as a linker. This MOF was targeted due to its previously reported moisture stability. It was shown to have a very similar 3-octanone uptake of 35.1 wt.%.

Following the success of 3-octanone inclusion in MOF systems, 4-methyl-3-heptanone was successfully adsorbed into the pores of IRMOF-NHPr. The loaded MOF was then used in a field study using leaf-cutting ants and loaded bait piles, where it was shown to have a similar and significant effect on the attraction of ants to the bait pile treated with neat pheromone. The results are summarised in **Figure 5.11**.

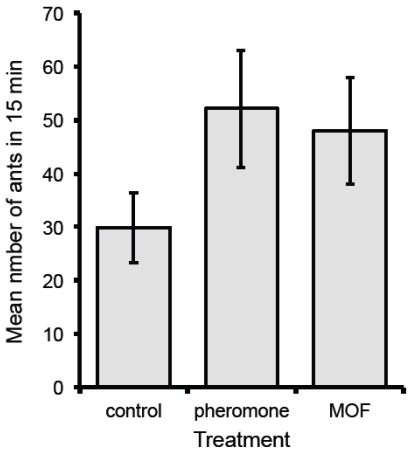

Figure 5.11. A plot showing the number of ants attracted to bait piles enhanced with either pheromone loaded MOF or a pheromone treatment.[31]

In summary, former research in the Burrows group has identified that two different leaf cutting ant pheromones (3-octanone and 4-methyl-3-heptanone) could be taken up, in significant quantities, into several different MOFs. The addition of an aminopropyl arm to the organic linker, functionalising the pores of the MOF, led to an increase in the amount of pheromone that

could be loaded into the pores. It was also shown that a MOF loaded with 4-methyl-3-heptanone attracted ants to a bait pile with comparative frequency to a bait pile laced with just the pheromone. This initial result demonstrated that the MOF could effectively release the pheromone in concentrations suitable for a pheromone lure trap.

5.2 Results and Discussion

5.2.1 Inclusion and Release of 3-Octanone from IRMOFs

Following on from the results obtained by Dr Amer Hamzah it was necessary to repeat some of the experiments she conducted in order to provide a baseline and point of reference for comparison between the two sets of data. The importance of this was highlighted in Dr Amer Hamzah's work which showed that successive washings of the MOF crystals had a large impact on the measured amount of 3-octanone contained within the pores. Although experimental details such as washing procedure were kept as similar as possible, slight variation is unavoidable. These repeat studies were carried out on some of the IRMOFs previously investigated.

Dr Amer Hamzah investigated a range of IRMOFs including those containing linkers **A**-**C** in **Figure 5.12**, the MOFs formed in combination with these linkers are named MOF-5 [$Zn_4O(bdc)_3$], IRMOF-3 [$Zn_4O(bdc\text{-}NH_2)_3$] and IRMOF-NHPr [$Zn_4O(bdc\text{-}NHPr)_3$]. To extend the study, a fourth novel MOF using the linker 2-propoxy-1,4-benzenedicarboxylate (bdc-OPr) was synthesised and was designated IRMOF-OPr. All four MOFs were investigated for their ability to include 3-octanone.

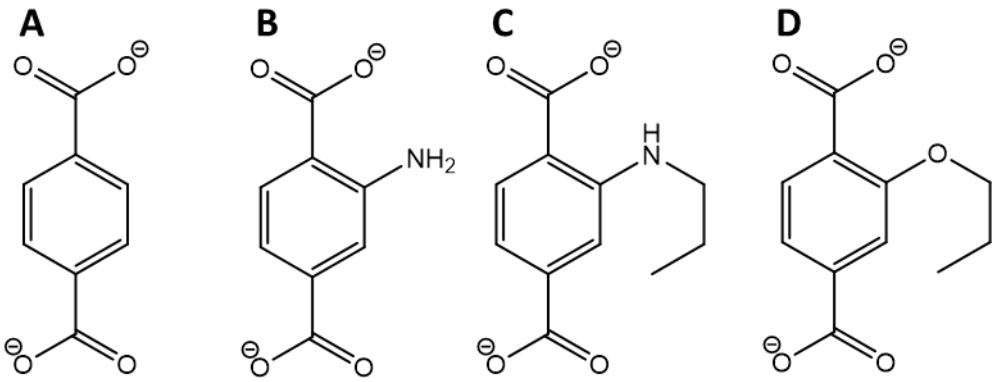

Figure 5.12. The dicarboxylates used to form IRMOFs for pheromone loading. **A** – bdc, **B** – bdc-NH_2, **C** – bdc-NHPr, **D** – bdc-OPr.

MOF-5 and IRMOF-3 were synthesised according to previously reported syntheses.[165, 166] IRMOF-NHPr and IRMOF-OPr were synthesised in analogous procedures based on that for IRMOF-3 replacing the H_2bdc-NH_2 in the preparation with H_2bdc-NHPr and H_2bdc-OPr respectively. The synthetic procedures produced colourless, orange-brown, yellow and colourless large cubic crystals respectively. The identities of the crystalline products were confirmed using PXRD.

Once synthesised, the crystals in each batch were washed with fresh DMF then collected via vacuum filtration before being immersed in neat 3-octanone. The vials were sealed and left for 72 hours and during this time period exchange occurred inside the framework whereby DMF diffuses out of the pores and the 3-octanone diffuses in. Based on past studies, the exchange was assumed to reach equilibrium after three days. After this time each crystalline product was recovered by vacuum filtration and rinsed with n-hexane (3 x 3 mL). This washing step was undertaken to ensure no pheromone remained on the surface of the crystals, which would skew measurements of the amount of 3-octanone in the pores. The removal of 3-octanone from the crystal surface can be conveniently tracked by visual means, as the crystals go from being tacky when wet to free flowing once surface 3-octanone has been removed.

To assess the loading of 3-octanone into the MOFs, a sample of the 3-octanone loaded MOF was digested in a solution of either DCl/D_2O in DMSO-d_6 or D_2SO_4/D_2O in DMSO-d_6. This digestion breaks the MOF down into its component parts, the ratio between linker and 3-octanone can then be used to ascertain how much 3-octanone was in the pores. Three NMR samples were taken for each of the MOFs to allow an average to be calculated and to give insight into the variance of the uptake within a batch of crystals.

Figure 5.13 shows the ^{1}H-NMR spectrum for one of the digested samples of 3-octanone loaded IRMOF-3. The relevant peaks have all been labelled, A-C for the linker peaks and D-J for the peaks pertaining to the 3-octanone. H_C was chosen as the resonance used to determine the relative amount of dicarboxylate and H_G was selected to determine the relative amount of 3-octanone as it is the only 3-octanone peak that does not overlap with another resonance.

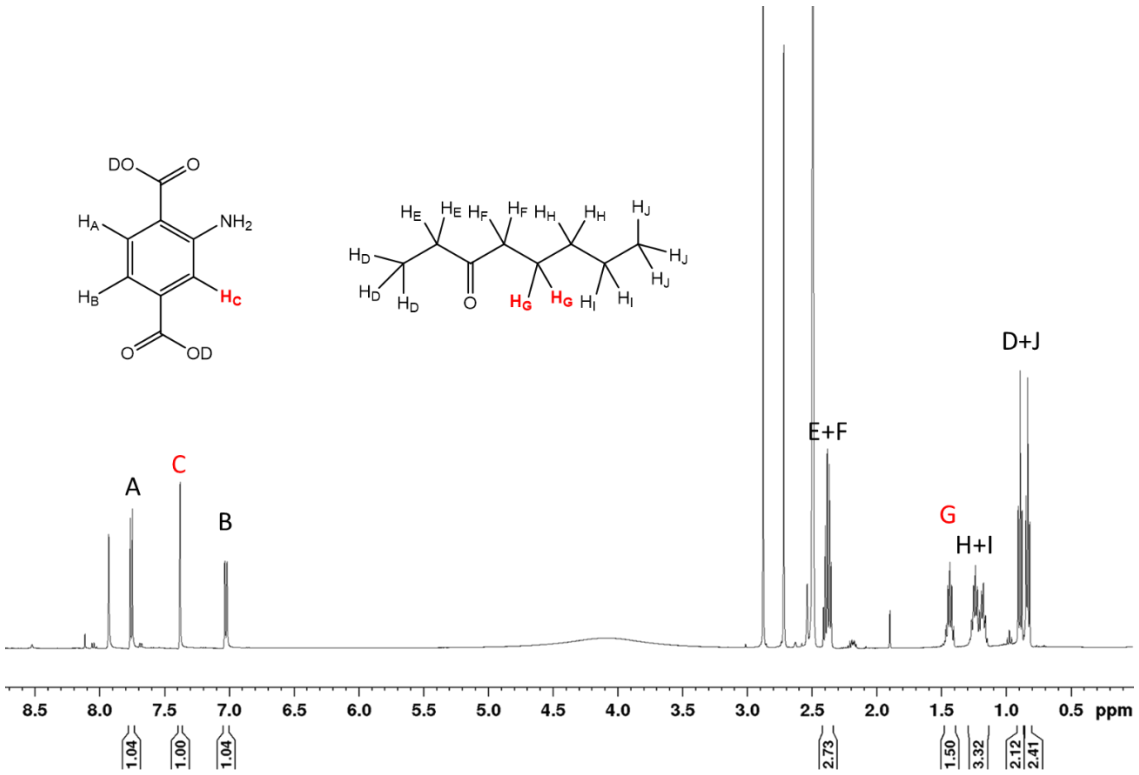

Figure 5.13. The ^{1}H-NMR spectrum of digested, 3-octanone loaded, IRMOF-3.

For this sample it can be seen that the ratio between H_C and H_G is 1:1.50, however, there are two H_G protons present per 3-octanone molecule and so the ratio between bdc-NH_2 and 3-octanone in the loaded MOF is 1:0.75. This ratio can be related back to the formula for the loaded MOF which gives a composition for this sample as $[Zn_4O(bdc\text{-}NH_2)_3]\cdot 2.25oct$.

The weight percentage uptake of 3-octanone is a useful metric as it allows comparison between different frameworks. This represents the amount of 3-octanone in the framework as a percentage of the empty framework weight. The formula is:

$$\text{Weight \% Uptake} = \frac{\text{M}_\text{w}\text{ of oct} \times \text{Number of moles of oct}}{\text{M}_\text{w}\text{ of MOF}} \times 100$$

A summary of the results obtained from the uptake of 3-octanone into MOF-5, IRMOF-3, IRMOF-NHPr and IRMOF-OPR are shown in **Table 5.1**.

Table 5.1 A summary of the inclusion of 3-octanone into IRMOFs.

MOF	Linker : 3-octanone	Loaded MOF Formula	Wt.% of oct
MOF-5	1 : 0.306	$[Zn_4O(bdc)_3]\cdot 0.92oct$	15%
IRMOF-3	1 : 0.737	$[Zn_4O(bdc\text{-}NH_2)_3]\cdot 2.21oct$	35%
IRMOF-NHPr	1 : 1.127	$[Zn_4O(bdc\text{-}NHPr)_3]\cdot 3.38oct$	46%
IRMOF-OPr	1 : 1.215	$[Zn_4O(bdc\text{-}OPr)_3]\cdot 3.65oct$	50%

Comparing these results highlights several characteristics of this system. Amine-functionalised IRMOF-3 was able to include over double the amount of 3-octanone per unit formula of MOF when compared to MOF-5 (35 wt.% vs 15 wt.%). This suggests that having a polar group on the surface of the pores is important when considering how much 3-octanone will be included. As 3-octanone contains a polar ketone group it is unsurprising that it interacts more strongly with the polar functionalised pore wall. There is also the potential for hydrogen bond formation between the amine protons and the ketone oxygen.

The addition of a propyl group to the amine functionality in the ligand, forming IRMOF-NHPr, showed a marked increase in the quantity of 3-octanone included in the MOF. This indicates that the interaction between 3-octanone and the MOF is further strengthened by the presence of the alkyl group. 3-octanone possesses an alkyl chain which can interact with the non-polar propyl chain on the bdc-NHPr. There are also polar interactions occurring between the amine and ketone groups, with the possibility of hydrogen bonding between the secondary amine proton and ketone oxygen.

The amount of 3-octanone included in IRMOF-NHPr and the newly synthesised material IRMOF-OPr is very similar, with slightly more being included in the latter (46 wt.% vs. 50 wt.%). The most notable difference between the two frameworks is a lack of hydrogen bond donor groups in IRMOF-OPr. This means that there cannot be hydrogen bonding interactions between IRMOF-OPr and 3-octanone. However, the lack of this interaction has not diminished the amount of 3-octanone included in the system, suggesting that hydrogen bonding is either not present or is of a comparable strength to the dipole–dipole interactions between the IRMOF-OPr framework and 3-octanone.

5.2.2 Inclusion of 3-Octanone in γ-CDMOFs

Cyclodextrins are a class of cyclic sugar molecules, with the most common, α, β, γ containing 6, 7 and 8 glucose units respectively. The structure of γ-cyclodextrin (γ-CD) is shown in **Figure 5.14 A**, with the glucose units linking in a 1, 4 manner. This linking gives rise to a 3-D toroidal conformation that has two distinct faces and a cavity in the centre of the ring, as can be seen in **Figure 5.14 B**. The primary and secondary faces have primary and secondary alcohol groups on their surfaces, respectively, making them hydrophilic, in contrast the centre of the toroid which is lipophilic. This disparity in hydrophobicity in the macromolecule leads to some interesting and useful properties.[167]

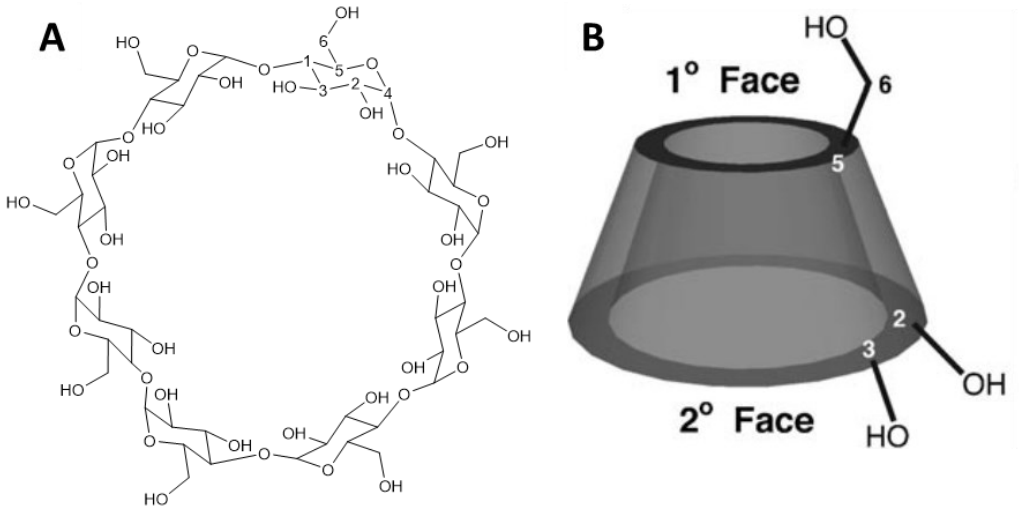

Figure 5.14. A - The structure of γ-cyclodextrin. **B** – The 3-D conformation formed by γ-cyclodextrin.[168]

The lipophilic cavity in combination with the hydrophilic exterior allows for the formation and dissolution of inclusion complexes. These complexes are of particular interest in the area of drug delivery. γ-Cyclodextrin can form inclusion complexes with drug molecules, aiding the drugs stability, solubility, and bioavailability in the process. Inclusion complexes of this type are already marketed by pharmaceutical companies.[169, 170]

More recently, γ-cyclodextrin has received interest as a linker used in MOF synthesis. MOFs based on γ-cyclodextrin (CDMOFs) have been reported with group 1 metal ions (Na^+, K^+, Rb^+, Cs^+), the network formed varies depending on the reaction conditions and metal ion used.[168, 171-173] These frameworks are of particular interest to this project because of their previously reported success in inclusion complex formation with small molecules and their green and sustainable nature. The end use of the MOF will be in the environment and, as such, the material should be as environmentally friendly as possible. CDMOFs contain environmentally compatible metal ions and the naturally occurring sugar γ-cyclodextrin. They are synthesised using alcohol and water which is preferable to DMF and related dipolar aprotic solvents that are commonplace in MOF synthesis. This green nature has been highlighted by the production of an 'edible' CDMOF, made using food grade reagents.[168, 173]

Two different CDMOFs were investigated, K-CDMOF [$K_2(OH)_2$(γ-CD)] and Na-CDMOF [Na(OH)(γ-CD)]. K-CDMOF is composed of 8 coordinate K^+ ions, each ligated by 4 γ-CD molecules. The crystal structure is composed of repeating cubic units containing 6 γ-CD molecules, which form the faces of the cubes. Two different representations of this motif are presented in **Figure 5.15.** The motifs stack so that the 3-D structure has channels running along all three axes as well as the pore spaces at the centre of the cubes.

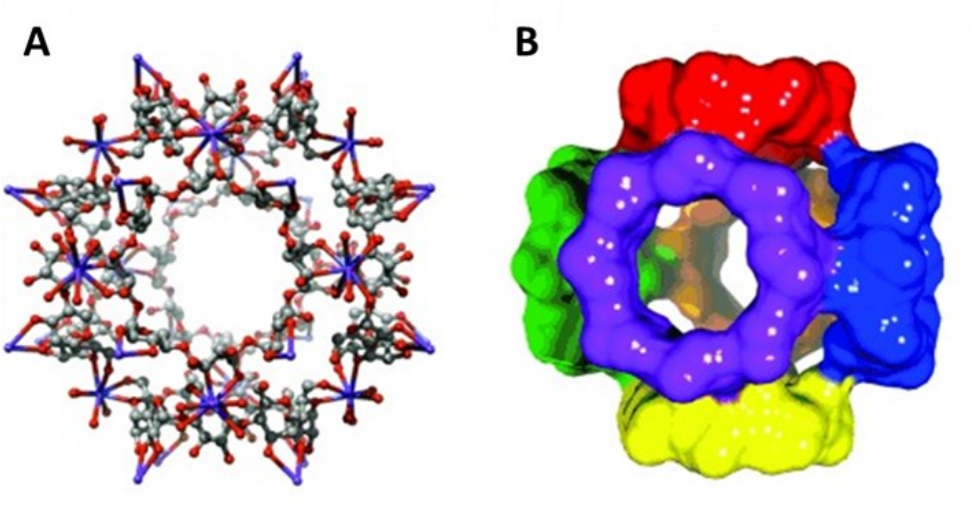

Figure 5.15. A - A ball and stick representation of the repeating cubic motif in K-CDMOF. Potassium is shown in purple, oxygen in red and carbon in grey. **B -** A surface representation of the cubic motif, with each γ-CD molecule shown in a different colour.

Na-CDMOF is composed of two crystallographically distinct 6 coordinate Na^+ centres that bridge between the secondary faces of adjacent γ-CD molecules. The structure formed is a 2-D bilayer of linked γ-CD molecules, the conformation of these is shown in the crystal structure and schematically in **Figure 5.16 A** and **B** respectively. The 2-D sheets stack so that the cavities in the γ-CD molecules of adjacent sheets align, giving rise to channels that run throughout the gross structure.

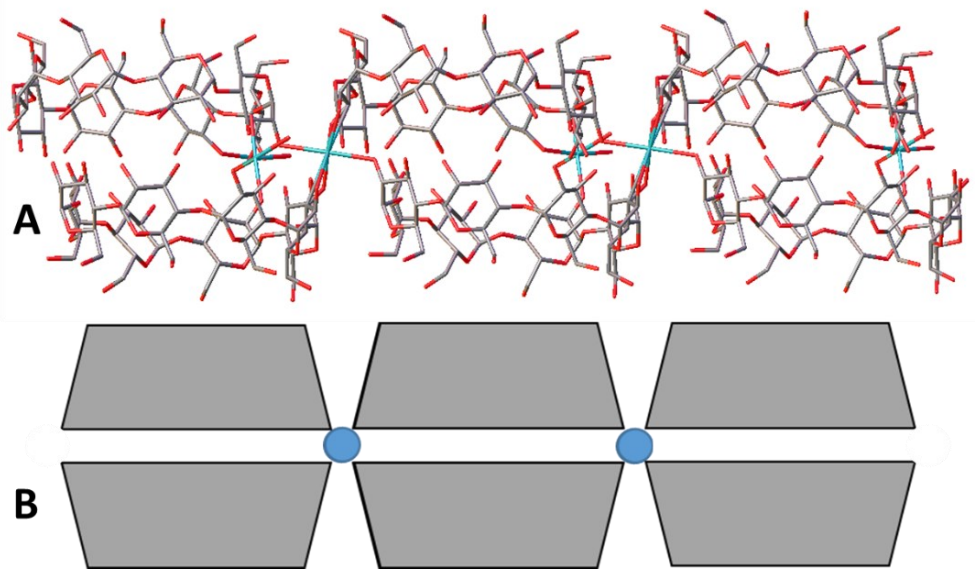

Figure 5.16. A c The 2-D bilayer sheet in crystal structure of Na-CDMOF with sodium shown in cyan, oxygen in red and carbon in grey. **B** – A diagram of the bilayer.

Both CDMOFs were synthesised using modified versions of previously reported procedures.[168, 173] The syntheses involved the vapour diffusion of methanol into an aqueous solution of the

metal hydroxide and γ-CD over the course of 7 days promoting crystallisation of the MOFs. The crystalline products were collected by vacuum filtration and their identity was confirmed via PXRD.

Both of the MOFs were submerged in neat 3-octanone in the same manner as the IRMOF samples. After the three day exchange period the MOFs were recovered via vacuum filtration and rinsed with n-hexane (3 x 3 mL). Three samples were taken from each batch, digested using a deuterated acid solution and ^{1}H-NMR spectroscopy experiments were conducted to obtain a ratio between γ-CD and 3-octanone, a sample spectrum is shown in **Figure 5.17**. Protons H_G were selected for the analysis of 3-octanone as in the IRMOF experiments. H_A was selected for the γ-CD as this peak has least overlap with other signals. There are 16 H_A protons per γ-CD molecule, and 2 H_G protons per 3-octanone which gives a formula for the loaded sample in **Figure 5.17** as $[K_2(OH)_2(\gamma\text{-CD})]\cdot 1.54oct$.

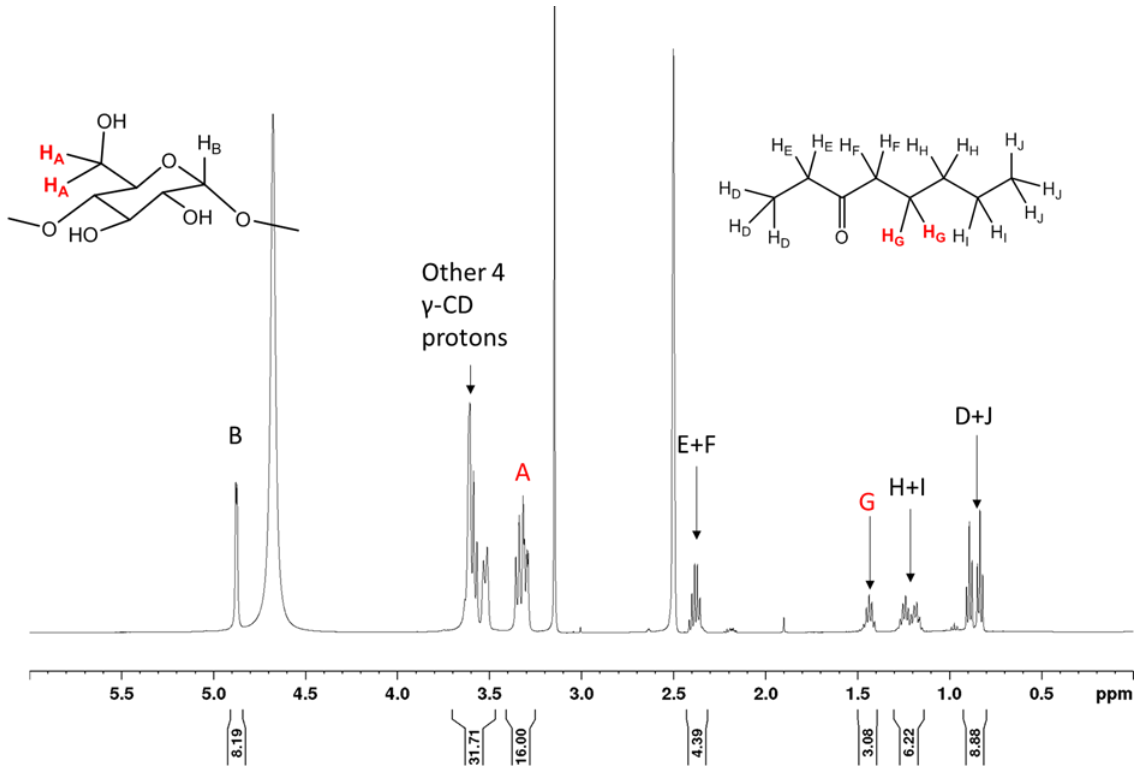

Figure 5.17. ^{1}H-NMR spectrum of a digested sample of 3-octanone loaded K-CDMOF.

For each MOF, an average of the three samples was taken. This was used to establish the weight percent uptake of 3-octanone, the results of the inclusion experiment are summarised in **Table 5.2**. It can be seen that the two MOFs included a very similar amount of 3-octanone. This is surprising as the crystal structures are very different. K-CDMOF was expected to have much

higher uptake than Na-CDMOF due to its higher surface area (1220 $m^2 g^{-1}$ vs. 376 $m^2 g^{-1}$)[168, 173], meaning it should have more space within its pores to house the 3-octanone molecules.

Table 5.2. A table summarising the 3-octanone inclusion experiments into K-CDMOF and Na-CDMOF.

MOF	Linker : 3-octanone	Loaded MOF Formula	Wt.% of oct
K-CDMOF	1 : 1.59	$[K_2(OH)_2(\gamma\text{-CD})]\cdot 1.59$oct	15%
Na-CDMOF	1 : 1.80	$[Na(OH)(\gamma\text{-CD})]\cdot 1.80$oct	17%

5.2.3 Inclusion of 3-Octanone in Zn-MOF-74

Computational modelling of 3-octanone in the pores of IRMOF-3, carried out by members of the Düren group at the University of Bath, suggested that the ketone oxygen of 3-octanone had a stronger interaction with the zinc metal centres in the SBU rather than the amine of the linker.[174] To capitalise on this stronger interaction MOF-74 [M_2(dobdc)] was selected as a potential host for the pheromone. MOF-74 was chosen as it has a very high metal to ligand ratio and also has the potential for a vacant metal site upon activation, both of these factors should promote metal-guest interaction.

MOF-74 [M_2(dobdc)], previously discussed in **Section 5.1.2** can be formed from a variety of M^{2+} ions (M = Zn, Cu, Ni, Co, Mg) and the ligand 2,5-dioxodo-1,4-benznedicarboxylate (dobdc). In this study zinc was selected as the metal of interest as it is relatively non-toxic which is an important consideration when thinking about the end use of materials in the environment. The SBU is an infinite 1-D chain of metal ions linked by carboxylate and oxido oxygens. These 1-D chains are bridged to three adjacent chains in a trigonal arrangement by the dobdc linker, this gives an overall hexagonal honeycomb structure with channels running parallel to the 1-D chains through the structure. The linker, SBU and framework structure are all depicted in **Figure 5.18**.

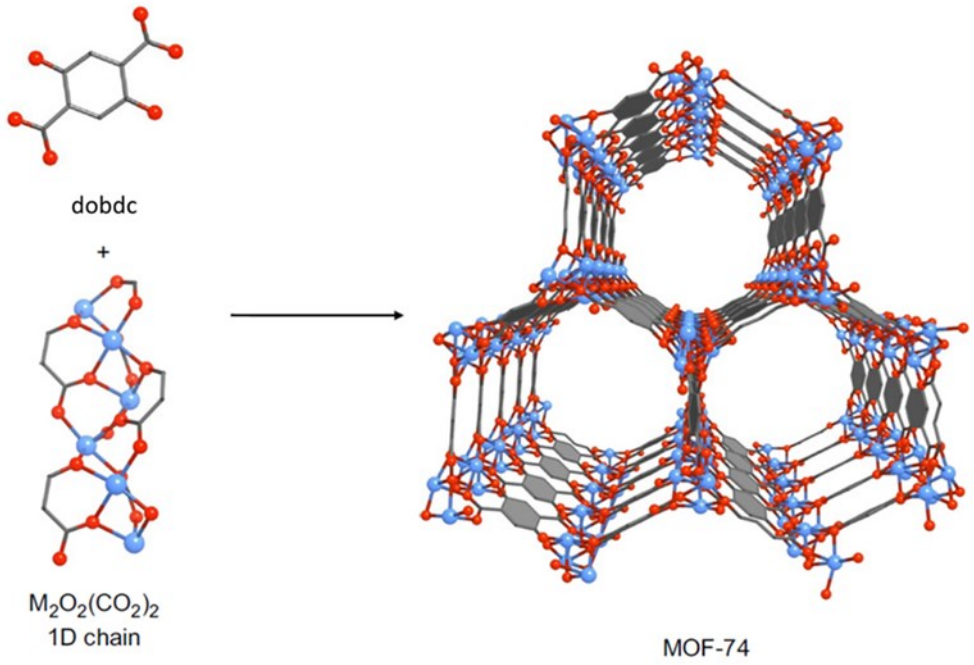

Figure 5.18. The linker dobdc, 1-D SBU and structure of MOF-74.

The as-synthesised MOF has the formula [M_2(dobdc)]·2DMF, with the zinc centres in an octahedral geometry. One of the coordination sites, which is occupied by a DMF molecule, points into the channels of the MOF. This solvent molecule is labile and can be removed either

by solvent exchange or by activation, allowing access to the metal centre. This process was anticipated to allow the 3-octanone to interact with these metal centre.

The MOF was synthesised using a modified version of a previously reported synthesis.[175] The crystalline product was rinsed using fresh DMF before being submerged in 3-octanone for three days. After this period the crystals were retrieved via filtration and washed with n-hexane (3 x 3 mL) before being digested in DCl/DMSO-d_6. Interestingly, under these loading conditions, no uptake of 3-octanone was observed. This is attributed to the labile coordination site in the channels of the MOF being occupied by DMF solvent from the synthesis. **Figure 5.19** shows a space-filling image of the crystal structure of a channel in Zn-MOF-74 with DMF coordinated to the zinc centres. It can be seen that the remaining space in the channel is small, approximately 5.5 Å in diameter. 3-octanone has approximate dimensions of 13.0 Å x 5.5 Å x 4.2 Å and thus would be unlikely to pass into the pore channel.

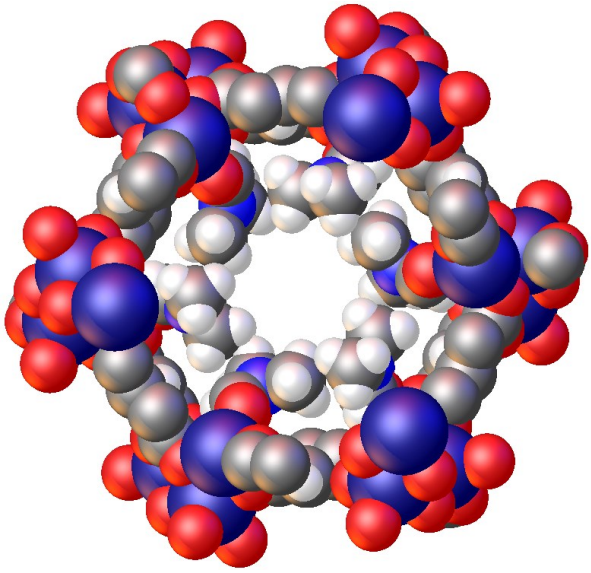

Figure 5.19. A space-filling model of Zn-MOF-74 with DMF ligands.

In order to circumvent this issue an additional solvent exchange step was added after the synthesis of the MOF and before 3-octanone loading. After synthesis, the Zn-MOF-74 crystals were submerged in MeOH for a period of three days, exchanging the supernatant with fresh MeOH every 24 hours. This drives most of the coordinated DMF to exchange with MeOH molecules. This was evidenced by the small amount DMF present in the NMR of the digested MOF, with a linker to DMF ratio of 1:0.15. The absence of the DMF ligands creates a larger channel space, with approximate diameter of 11 Å, this allows for 3-octanone to enter the framework more easily. At this point the MOF-74 crystals were recovered using filtration before being submerged in 3-octanone for the standard three day period, after which they were

washed with n-hexane and separate samples digested in a DCl/DMSO-d_6 solution. The ^{1}H-NMR spectrum of one of these samples is shown in **Figure 5.20**. The organic linker only has one proton resonance from H_A and proton H_G was used from 3-octanone to establish the ratio of linker to pheromone. The results are summarised in **Table 5.3**. The amount of 3-octanone per unit formula of MOF is much lower for MOF-74 than the IRMOF or CDMOF series, though this low value is partially due to the small unit formula for Zn-MOF-74. The formula for MOF-74 is small and contains only one linker moiety and two metal ions and it's 3-octanone uptake is more comparable when presented as a weight percentage uptake, 14 wt.%.

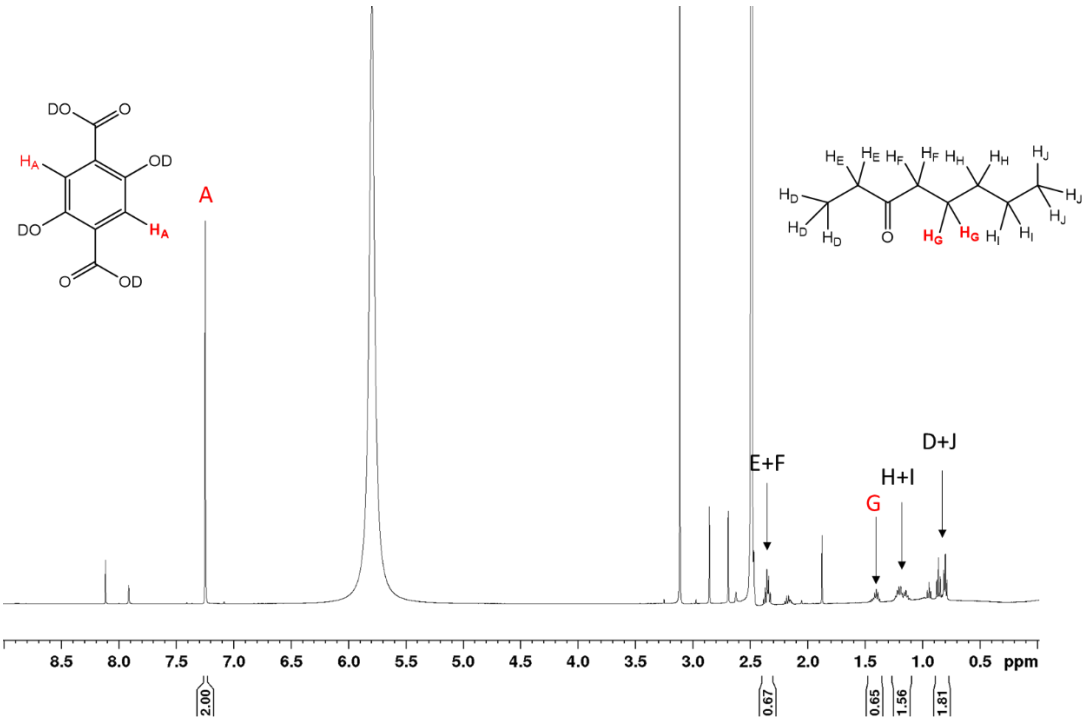

Figure 5.20. ^{1}H-NMR spectrum of a digested sample of 3-octanone loaded Zn-MOF-74.

Table 5.3. A table summarising the 3-octanone inclusion experiments into Zn-MOF-74

MOF	Linker : 3-octanone	Loaded MOF Formula	Wt.% of oct
Zn-MOF-74	1 : 0.35	$[Zn_2(dobdc)]\cdot 0.35oct$	14%

5.2.4 Discussion of 3-Octanone Inclusion

The 3-octanone inclusion results are summarised in **Table 5.4**. The best performing MOFs in terms of wt.% uptake are IRMOF-NHPr and IRMOF-OPr (46 wt.% and 50 wt.% respectively) with IRMOF-3 following closely behind (35 wt.%). All the other MOFs performed very similarly, including approximately 15 wt.% of 3-octanone. From the data it is clear that the IRMOF topology offers the greatest scope for the inclusion of large amounts of 3-octanone from those studied. It can also be seen that the inclusion of a polar functionality greatly enhances the amount of 3-octanone loaded into the pores of the MOF. The addition a non-polar propyl chain also increased the amount of 3-octanone taken into the framework. This suggests that the combination of the polar nitrogen/oxygen and non-polar alkyl chain are both interacting favourably with the polar ketone oxygen and non-polar alkyl tail on 3-octanone.

Table 5.4. A summary of the results of the 3-octanone inclusion experiments

MOF	Linker : 3-octanone	Loaded MOF Formula	Wt.% of oct	BET Surface Area ($m^2 g^{-1}$)
MOF-5	1 : 0.306	$[Zn_4O(bdc)_3]\cdot 0.92oct$	15%	3800[165]
IRMOF-3	1 : 0.737	$[Zn_4O(bdc\text{-}NH_2)_3]\cdot 2.21oct$	35%	2069
IRMOF-NHPr	1 : 1.127	$[Zn_4O(bdc\text{-}NHPr)_3]\cdot 3.38oct$	46%	1561
IRMOF-OPr	1 : 1.215	$[Zn_4O(bdc\text{-}OPr)_3]\cdot 3.65oct$	50%	1695
K-CDMOF	1 : 1.59	$[K_2(OH)_2(\gamma\text{-CD})]\cdot 1.59oct$	15%	1220[168]
Na-CDMOF	1 : 1.80	$[Na(OH)(\gamma\text{-CD})]\cdot 1.80oct$	17%	339[173]
Zn-MOF-74	1 : 0.35	$[Zn_2(dobdc)]\cdot 0.35oct$	14%	496[175]

Interestingly the trend in 3-octanone inclusion does not follow that of BET surface areas. Although the surface area gives a representation of the amount of space inside a MOF and therefore potential space for 3-octanone, the strength of interaction between 3-octanone and the framework also needs to be considered. The method of loading the 3-octanone into the MOF is via a solution-phase exchange. This means that upon immersion in 3-octanone an equilibrium is established, with 3-octanone diffusing into the pores and the synthesis solvent diffusing out of the framework. Based on previous studies, equilibrium is assumed to be reached after three days, the position of this equilibrium is governed by the relative strength of interactions between the framework and 3-octanone as well as the strength of the interaction between the framework and the synthesis solvent.

3-Octanone Loading of Activated MOFs

From the loading of MOFs via a solution-phase exchange method, a trend in the strength of interaction between the frameworks and 3-octanone has been established. However, it was highlighted in the ^{1}H-NMR spectra of the digested MOFs, that in all cases, some of the synthesis solvent remained in the pores. This causes two issues, the first is that DMF is toxic therefore not environmentally compatible and not aligned with the intended end use of the MOF system. The second issue is that the residual DMF takes up space inside the pores of the framework, leaving less space for 3-octanone. In order to solve these issues, the DMF can be removed before the 3-octanone is loaded, which is done by activating the MOF. Due to issues with stability and moisture sensitivity, MOF-5 and the CDMOFs were not carried forward to this part of the investigation.

IRMOF-3, IRMOF-NHPr and IRMOF-OPr were activated via solvent exchange with $CHCl_3$ over the course of at least three days before being heated under reduced pressure at 100 °C overnight. Zn-MOF-74 was activated in a similar manner but using MeOH as the exchange solvent. Once activated the vial was back filled with N_2 and then the crystals submerged in 3-octanone for a period of three days. After this time period the crystals were recovered using vacuum filtration and washed with n-hexane (3 x 3 mL). The MOFs were digested in a deuterated acid solution then solution-phase ^{1}H-NMR experiments carried out.

The results of these experiments are summarised in **Table 5.5**. As expected, the amount of 3-octanone included in all the frameworks increased dramatically when compared to the non-activated frameworks. The largest increases were seen for IRMOF-3 and Zn-MOF-74 both of which were loaded with over twice as much 3-octanone using this method.

Table 5.5. A summary of the inclusion of 3-octanone into activated MOFs.

MOF	Linker : 3-octanone	Loaded MOF Formula	Wt.% of oct	BET Surface Area ($m^2 g^{-1}$)
IRMOF-3	1 : 1.59	$[Zn_4O(bdc\text{-}NH_2)_3]\cdot 4.78oct$	75%	2069
IRMOF-NHPr	1 : 1.52	$[Zn_4O(bdc\text{-}NHPr)_3]\cdot 4.58oct$	62%	1561
IRMOF-OPr	1 : 1.34	$[Zn_4O(bdc\text{-}OPr)_3]\cdot 4.02oct$	55%	1695
Zn-MOF-74	1 : 0.71	$[Zn_2(dobdc)]\cdot 0.71oct$	29%	496[175]

The weight percent uptake of 3-octanone in the activated MOFs follows a different trend to that of the same frameworks using the solvent exchange method of loading. The activated samples follow a trend that appears to be influenced more by surface area, with IRMOF-3 showing the

highest uptake along with the highest surface area, and MOF-74 showing lowest uptake and the lowest surface area. IRMOF-NHPr and IRMOF-OPr have similar surface areas and only a small difference in uptake.

The amount of 3-octanone included was also be measured using thermogravimetric analysis. A plot showing the analysis for a sample of IRMOF-NHPr, loaded with 3-octanone using the activation method is shown in **Figure 5.21**. The weight percent uptake and formula of this sample, as determined by ^{1}H-NMR, are 63 wt.% and $[Zn_4O(bdc\text{-}NHPr)_3]\cdot 4.65oct$. The TGA indicates a mass loss of 35.9% between 25 °C and 295 °C, which is attributed to the loss of 3-octanone from the pores. This equates to a weight percentage uptake of 56 wt.% and a MOF formula of $[Zn_4O(bdc\text{-}NHPr)_3]\cdot 4.11oct$. These values are in reasonable agreement with the values obtained from the ^{1}H-NMR digestion experiments given the ambiguity of the TGA in determining the precise temperature at which all the included pheromone has been released.

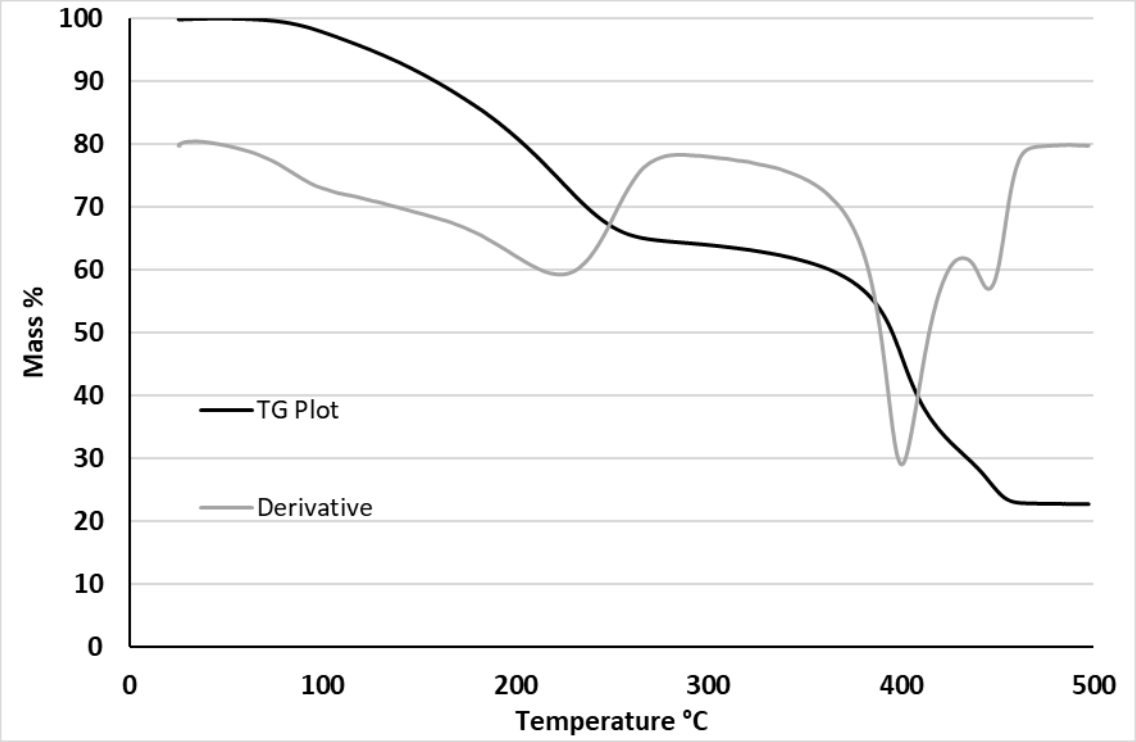

Figure 5.21. The TGA plot of IRMOF-NHPr loaded with 3-octanone using the activation method.

An alternative way of using TGA to evaluate the amount of volatiles present is by considering the remaining material at the end of the analysis, which for IRMOFs is known to be ZnO.[176] The percentage mass of ZnO remaining at the end of the experiment can be used to work out the percentage of zinc that was present in the starting material, which in turn can be used to assign a value to the initial molecular weight and therefore the amount of 3-octanone present. The percentage of mass of ZnO is 22.7%, this results in an initial material with a formula of $[Zn_4O(bdc\text{-}$

NHPr)$_3$]·3.82oct. This method of evaluation gives a value that is marginally lower than both the ^{1}H-NMR result and the result gained from interrogating the mass loss. This slight discrepancy could be explained by the presence of defects in the material, thus leading to inaccurate calculations involving proton integrals or mass losses.

The use of TGA to determine the amount of pheromone in the pores has some significant drawbacks compared to ^{1}H-NMR spectroscopy. TGA requires significantly more sample (*ca.* 10 mg vs 1 mg), takes significantly more time per experiment (120 mins vs. 2 mins) and therefore is more costly to run per sample. TGA is only useful for samples which have only one type of guest molecule, as different guests cannot necessarily be distinguished from each other in the thermal analysis. Due to these considerations ^{1}H-NMR spectroscopy was used as the primary means of semiochemical loading analysis.

5.2.5 Release of 3-octanone from MOFs

Arguably, the most important property of a pheromone dispensing material is the rate and volume of pheromone able to be released into the environment. This release profile will dictate the effectiveness and lifetime of the end use lure trap. An ideal release profile for a material would be a consistent (linear) release extending over a period of several months. This would permit for the lifetime of the traps to be extended (compared to current commercial products) and for them to be equally effective throughout their lifetimes.

The release profile of 3-octanone from a MOF can be measured indirectly using ^{1}H-NMR spectroscopy. To do this a sample of MOF is loaded with 3-octanone using either the solution-phase exchange method or the activation method. Once loaded with pheromone a small sample of this material is digested and ^{1}H-NMR spectroscopy carried out to ascertain the amount of 3-octanone in the pores, this is the day 0 measurement. The rest of the loaded MOF is left on the bench in an open vial where pheromone is free to diffuse into the environment. A second small sample of MOF is taken after two days, digested and ^{1}H-NMR spectroscopy used to probe the amount of 3-octanone that remains in the pores. The decrease in 3-octanone between the day 0 and day 2 measurement shows the amount of pheromone that has been released into the environment. The experiment can be extended, taking additional samples and assessing the 3-octanone content every few days using ^{1}H-NMR spectroscopy. This allows the amount of 3-octanone lost from the pores to be tracked over the course of the investigation.

The release profile for IRMOF-NHPr loaded with 3-octanone using the solution-phase exchange method is shown in **Figure 5.22**. Each data point represents a sample being taken on a specific day, the number of molecules of 3-octanone per unit formula of the MOF that are still present are probed via a ^{1}H-NMR experiment. As can be seen from the curve of best fit, the data follow the expected downward trend as the 3-octanone diffuses out of the MOF and into the environment. Although the trend is not linear appreciable amounts of 3-octanone are consistently released up to 50 days. This is a promising result, and a trap with this lifetime would be at the top end of the range of commercially available ones in terms of longevity.

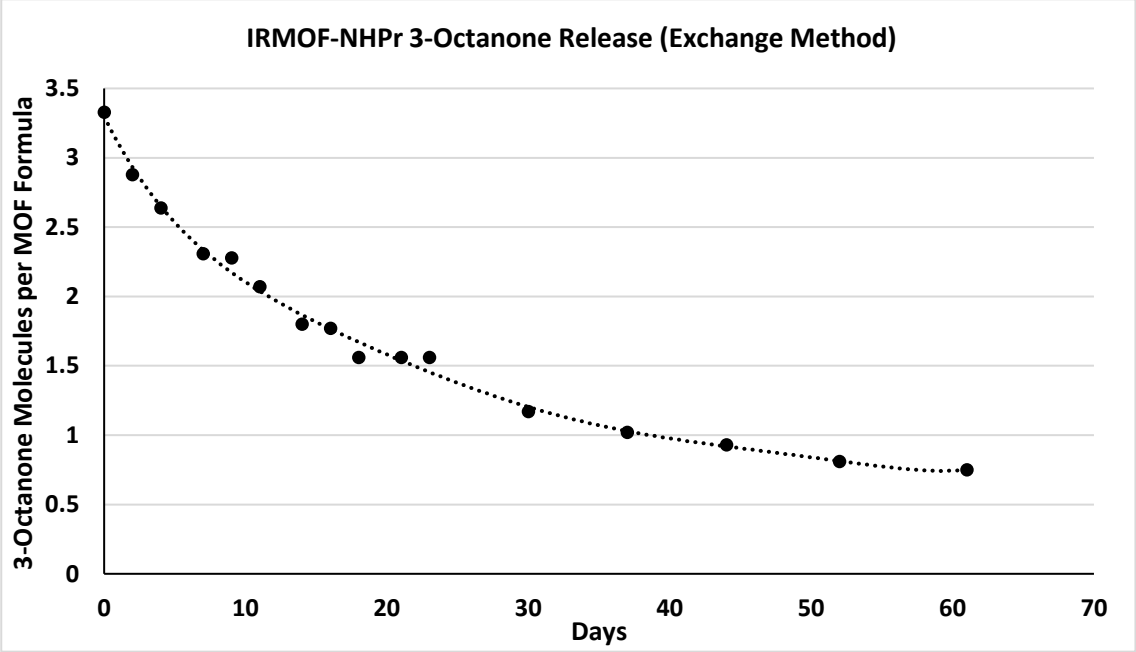

Figure 5.22. The release profile of 3-octanone from IRMOF-NHPr (solution exchange method).

The release profile of 3-octanone from IRMOF-3 and IRMOF-OPr, loaded using the solution exchange method, were also measured. The traces are shown in comparison to the result for IRMOF-NHPr in **Figure 5.23**. It can be seen that IRMOF-OPr and IRMOF-NHPr have comparable release profiles. They start with approximately the same amount of 3-octanone in the pores and release at a similar rate for a similar amount of time. This indicates that the interactions between the two frameworks and 3-octanone are very similar and suggests that hydrogen bonding between IRMOF-NHPr and the 3-octanone is unimportant.

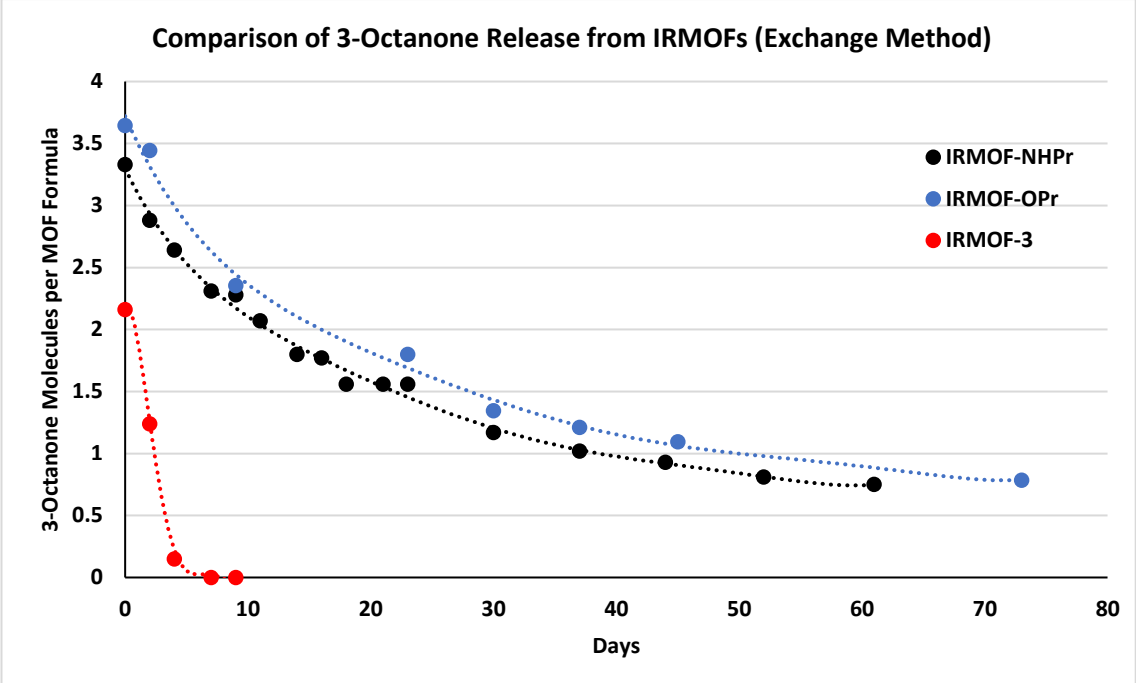

Figure 5.23. The release profiles of 3-octanone from IRMOF-NHPr, IRMOF-OPr and IRMOF-3 (solution exchange method).

The release profile for IRMOF-3 is markedly different from both IRMOF-NHPr and IRMOF-OPr. The day 0 loading is lower as expected following the inclusion experiments in which it was shown that with the solution-phase exchange method of loading, IRMOF-3 included less 3-octanone than the other two MOFs. The release profile shows that IRMOF-3 releases all of the 3-octanone in its pores more quickly than the other IRMOFs, with all of the loaded 3-octanone being released within 7 days. This fast release indicates that the interactions between the 3-octanone and the IRMOF-3 framework are weaker than those for IRMOF-NHPr and IRMOF-OPr. The increased rate of release may also stem from the fact that IRMOF-3 is less stable than IRMOF-NHPr and IRMOF-OPr, and as such may be losing crystallinity and porosity, expelling 3-octanone more quickly. The final consideration is the location of the 3-octanone as well as the residual DMF within the pores of the framework. As the DMF was present before the 3-octanone was introduced into the pores, it may occupy the more favourable and stronger binding sites within the framework. In loaded IRMOF-3 there is comparatively less 3-octanone and therefore more DMF in the pores, it is likely that more of the strong binding sites are occupied by DMF such that the 3-octanone is then relegated to occupying the less favourable and weaker binding sites, leading to its faster release. In reality these factors are most likely all contributing and a combination of them leads to the 3-octanone being released more quickly in IRMOF-3 compared to IRMOF-NHPr and IRMOF-OPr.

The release profile of MOFs loaded using the activation method was also explored. The same methodology was used for tracking the release of the 3-octanone from the MOFs. A comparison of the release profiles for IRMOF-NHPr loaded through the solution-phase exchange method and the activation method is shown in **Figure 5.24**. The day 0 measurement for the activated method is substantially higher than that for the exchange method, this was expected following the results of the inclusion experiments. The IRMOF-NHPr (activated) releases the included 3-octanone at a steady rate with the last measurement being recorded at over 110 days. This release period is about double that of the IRMOF-NHPr (exchange) sample. The increased release period can be attributed to a combination of there being more 3-octanone within the pores of the MOF to be released, and an increase in the interactions of 3-octanone with the framework as it is not in competition with DMF, which was removed during the activation step.

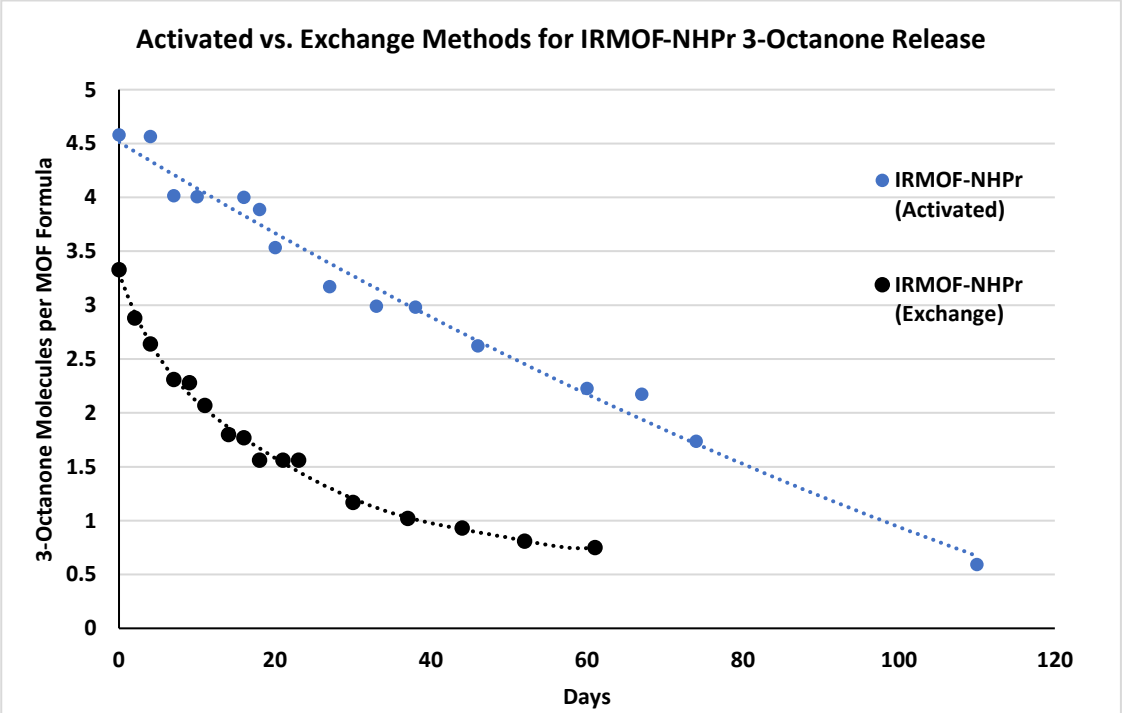

Figure 5.24. The release profiles of 3-octanone from IRMOF-NHPr (Exchange) and IRMOF-NHPr (Activated).

A final measurement taken on day 346 for the IRMOF-NHPr sample loaded via the activation method, showed that there were still 0.52 molecules of 3-octanone per unit formula of MOF in the pores of the framework. This result was omitted from the graph in **Figure 5.24** for clarity. As this value is only very slightly lower than the measurement at day 110, which had a value of 0.59, this suggest that this system is unlikely to fully release all of the 3-octanone contained within the pores. This is in agreement with the apparent trends of IRMOF-NHPr and IRMOF-OPr (exchange method loading) which appear to retain a near constant amount of 3-octanone in

their respective pores past the day 50 measurement, also at values just above 0.5 molecules of 3-octanone per unit formula of MOF.

In order to ascertain whether the structure of IRMOF-NHPr was still intact after day 346 a PXRD pattern of the sample was collected, this is plotted in **Figure 5.25**, against the pattern collected after the MOF was loaded with 3-octanone and against the pattern for IRMOF-3 simulated from single-crystal data. As can be seen from the matching peaks the MOF structure is still intact. The crystallinity of the MOF may have deteriorated slightly, evidenced by the peaks being slightly broader and the background being noisier.

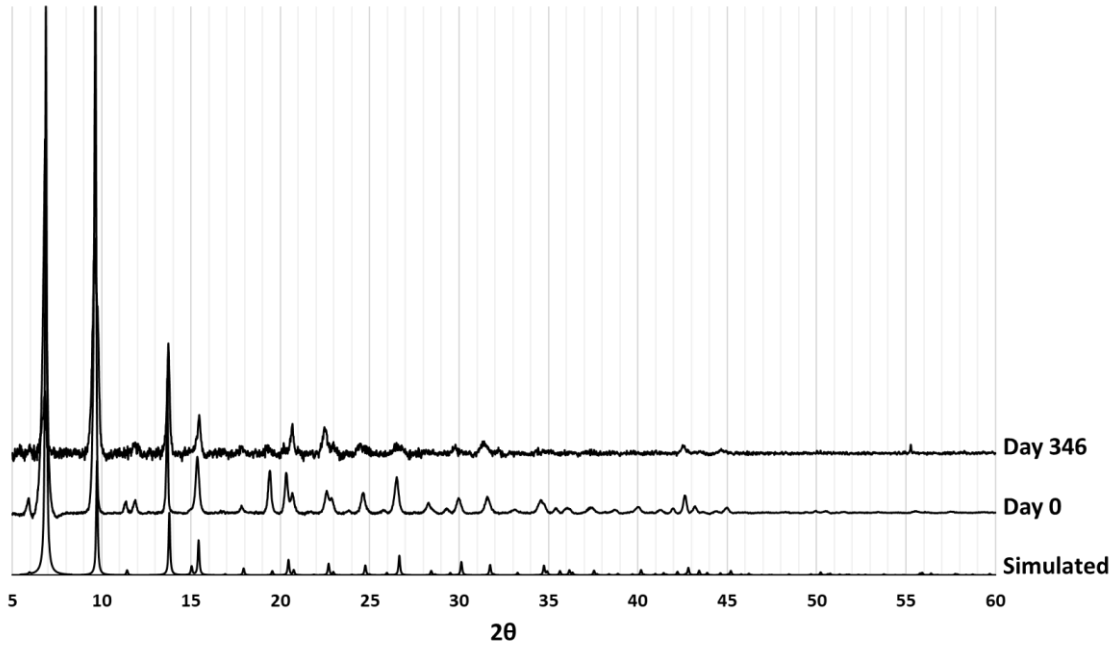

Figure 5.25. The PXRD patterns of IRMOF-NHPr loaded with 3-octanone via the activation method at day 0 and day 346 along with the diffraction pattern simulated from the single-crystal data for IRMOF-3.

The fact that IRMOF-NHPr was still intact after almost a year is an important result. This is a long time for an IRMOF to survive being exposed to atmospheric moisture, with MOF-5 and IRMOF-3 typically degrading within hours.[177] The remarkable stability of this sample stems from the hydrophobic environment within the framework, preventing water from accessing the vast majority of the metal sites within the structure. There are two contributing factors to the hydrophobic nature of the pores. The first is the propyl chain on the organic linker, which being non-polar is naturally hydrophobic. The second is the 3-octanone guest molecules, which like the organic linkers, have non-polar regions and are insoluble in water further adding to the hydrophobicity of the pores. The introduction of hydrophobic functional groups and/or hydrophobic guests could be a useful strategy for stabilising otherwise water sensitive MOFs.

5.2.6 Uptake and Release of 1-Hexanol

After the successful application of the IRMOF systems in the incorporation and release of 3-octanone, the next logical step was to investigate whether this strategy could be extended to other semiochemicals. 1-Hexanol, an attractant of the German cockroach, was selected due to its comparable size to 3-octanone, industrial relevance and commercial availability. 1-Hexanol provides a good contrast to 3-octanone as it is of a similar size, but the former contains an alcohol functionality rather than a ketone. It was anticipated that different interactions formed by an alcohol with MOFs would yield insightful results.

Uptake and release experiments were conducted on IRMOF-3 and IRMOF-NHPr as these emerged as successful frameworks in the 3-octanone investigation and are easily synthesised. Both the solution exchange method and activation method were used to load the semiochemical into the MOFs. The procedure for each experiment was kept as similar as possible to that used in the 3-octanone experiment, though using 1-hexanol instead. The analysis of the 1-hexanol uptake was also conducted as before, using ^{1}H-NMR spectroscopy on digested samples of the semiochemical loaded MOFs. Shown in **Figure 5.26** is a sample spectrum of IRMOF-3 loaded with 1-hexanol using the solution based exchange method. The proton resonance used to determine the amount of 1-hexanol present was H_D as it does not overlap with any other signals. The ratio between the peaks H_C and H_D is 1.00:3.66, this ratio is equivalent to a MOF formula of $[Zn_4O(bdc\text{-}NH_2)_3]\cdot 5.49hex$ and a weight percent uptake of 68.8 wt.%.

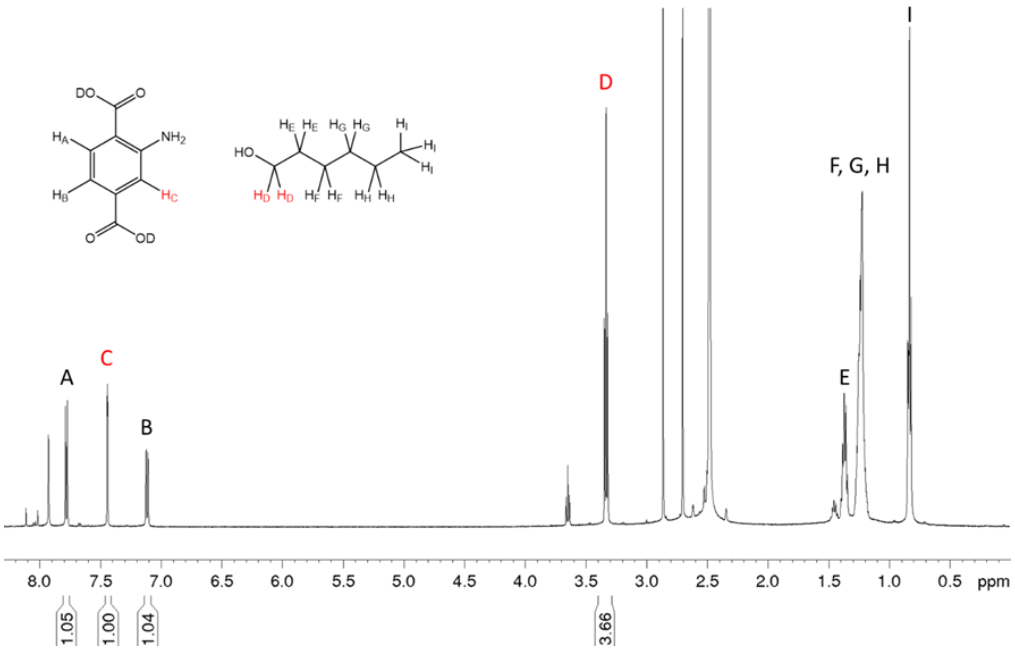

Figure 5.26. The 1H-NMR spectrum of IRMOF-3 loaded with 1-hexanol using the solution exchange method.

The results from other uptake experiments are summarised in in **Table 5.6**, the prefix 'A' before the MOF name represents those materials that were activated before being loaded, those without a prefix were loaded via the solution exchange method.

Table 5.6. A summary of the uptake of 1-hexanol into various IRMOFs.

MOF	Linker : 1-Hexanol	Loaded MOF Formula	Wt.% of hex
MOF-5	1 : 2.05	$[Zn_4O(bdc)_3]\cdot 3.08$ hex	41%
IRMOF-3	1 : 3.66	$[Zn_4O(bdc\text{-}NH_2)_3]\cdot 5.49$hex	69%
IRMOF-NHPr	1 : 3.06	$[Zn_4O(bdc\text{-}NHPr)_3]\cdot 4.59$hex	50%
A-IRMOF-3	1 : 3.87	$[Zn_4O(bdc\text{-}NH_2)_3]\cdot 5.80$hex	73%
A-IRMOF-NHPr	1 : 3.65	$[Zn_4O(bdc\text{-}NHPr)_3]\cdot 5.47$hex	59%

IRMOF-3 showed the highest wt.% uptake of 1-hexanol using both the solution exchange method and activation method of semiochemical loading. IRMOF-NHPr exhibited a higher uptake than MOF-5 when loaded via the solution exchange method. The wt.% uptake of 1-hexanol for both IRMOF-3 and IRMOF-NHPr increased when using the activation method over the solution exchange method.

Interestingly, 1-hexanol uptake does not follow the same trend as observed for 3-octanone concerning the amounts of semiochemical incorporated within the MOFs using the solution exchange method of loading. IRMOF-3 uptakes a larger amount of 1-hexanol than IRMOF-NHPr, suggesting that 1-hexanol has a stronger affinity for the IRMOF-3 framework than for that of IRMOF-NHPr. This is surprising as 1-hexanol does contain a non-polar alkyl chain of comparable in size to that in 3-octanone, which was attributed to the preference of 3-octanone for IRMOF-NHPr over IRMOF-3. Both IRMOF-3 and IRMOF-NHPr include more 1-hexanol than MOF-5 but the difference between MOF-5 and the functionalised frameworks is less than that was observed for 3-octanone. There was difference of only 9 wt.% between MOF-5 and IRMOF-NHPr for 1-hexanol uptake, whereas the difference in 3-octanone uptake between MOF-5 and IRMOF-3 was 20 wt.%. It can also be seen that the weight percent uptake values for 1-hexanol are higher than those for 3-octanone. This is because the there is more complete exchange with the DMF in the 1-hexanol, allowing more semiochemical in the pores.

The IRMOF-3 and IRMOF-NHPr samples that were loaded via the activation method both follow the expected trend based on their surface areas. IRMOF-3 has the larger surface area so has more space within the pores to host the semiochemical and as such has the high loading per unit formula (5.80 vs. 5.47). The difference between the two systems is even more apparent

when looking at the wt.% uptake (73 wt.% vs. 59 wt.%), due to the higher weight of the IRMOF-NHPr framework.

Comparing the two different methods of loading it can be seen that the samples loaded via the activation method contain more semiochemical than those loaded via the solution exchange method. However, the difference between the two methods is much less for 1-hexanol inclusion than observed for 3-octanone inclusion. For example, with 1-hexanol IRMOF-3 saw an increase of just 5.7% when using the activation method over the solution exchange method, in the 3-octanone investigation this increase was 116.3%. This shown graphically in **Figure 5.27**.

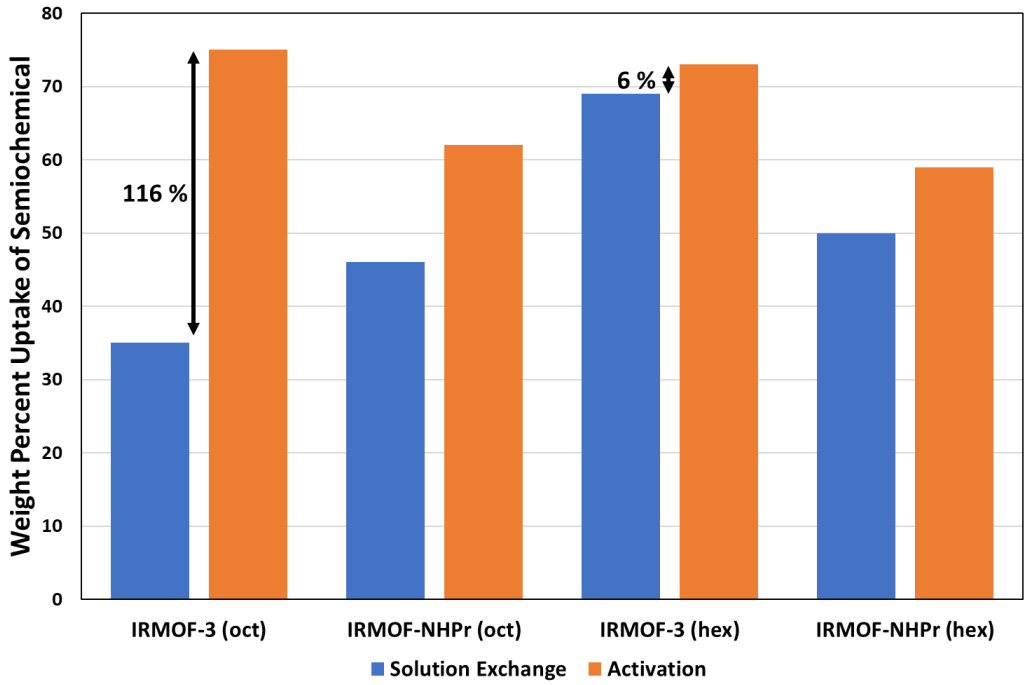

Figure 5.27. A bar chart showing the contrast in uptake capacities of 3-octanone and 1-hexanol in IRMOF-3 and IRMOF-NHPr between the two loading methods.

The small increase in the loading of 1-hexanol between methods is due to the 1-hexanol loading using the solution exchange method being far more effective than that of 3-octanone. This can be interrogated by considering the ratio of semiochemical to DMF in the loaded MOFs. In IRMOF-3 for 3-octanone the ratio was 1 : 1.07 whereas for 1-hexanol the ratio was 1 : 0.39. This means that in the 1-hexanol case the equilibrium is far closer to fully exchanging the semiochemical for DMF than in the 3-octanone case. The activation method of loading represents what complete exchange would look like as there is no competition from the DMF as it has already been removed, so the semiochemical to DMF ratio is 1 : 0. Thus the solution exchange method loading capacity for 1-hexanol into IRMOF-3 is much closer to that of the sample loaded using the activation method as the solution exchange method allowed for the

inclusion of a much larger amount than was observed in the 3-octanone case. The fact the solution based exchange was more effective suggests that 1-hexanol has a stronger interaction with the framework than 3-octanone.

Following the uptake measurements, a release profile was collected for each of the samples, treating the uptake measurement as day 0. The release profiles for MOF-5, IRMOF-3 and IRMOF-NHPr loaded via the solution exchange method are presented in **Figure 5.28**.

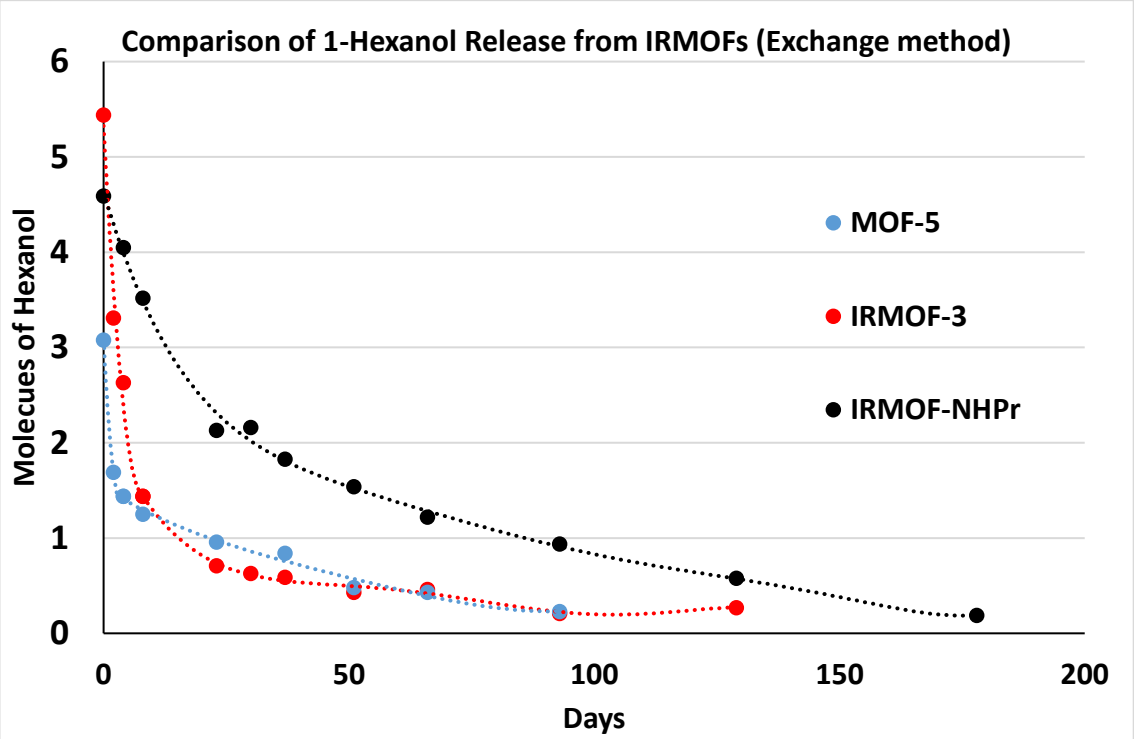

Figure 5.28. A comparison of the release of 1-hexanol from IRMOF samples loaded via the solution exchange method.

Both MOF-5 and IRMOF-3 release the majority of the included 1-hexanol very quickly over the first week after which time the release slows steadily until reaching a plateau after approximately 50 days. IRMOF-NHPr has a more controlled release profile, it still has a faster rate of release in the first 30 days but has a steady release of 1-hexanol out to 176 days, almost 6 months. This highlights that although a higher uptake is achieved using IRMOF-3, the release profile for IRMOF-NHPr is more suitable for this application and would therefore be a better choice of system.

The release profiles of IRMOF-3 and IRMOF-NHPr loaded via the activation method are shown in **Figure 5.29**. Comparing the two release profiles it can be seen that the same trend exists in the samples loaded via the activation method as those loaded via the solution exchange method. The IRMOF-3 sample releases 1-hexanol from the pores much more quickly than IRMOF-NHPr,

despite containing more 1-hexanol to start with. IRMOF-3 releases a large proportion of the included 1-hexanol in the first week after which release slows. IRMOF-NHPr appears to release at a steady and controlled pace throughout the experiment, an ideal profile for the application.

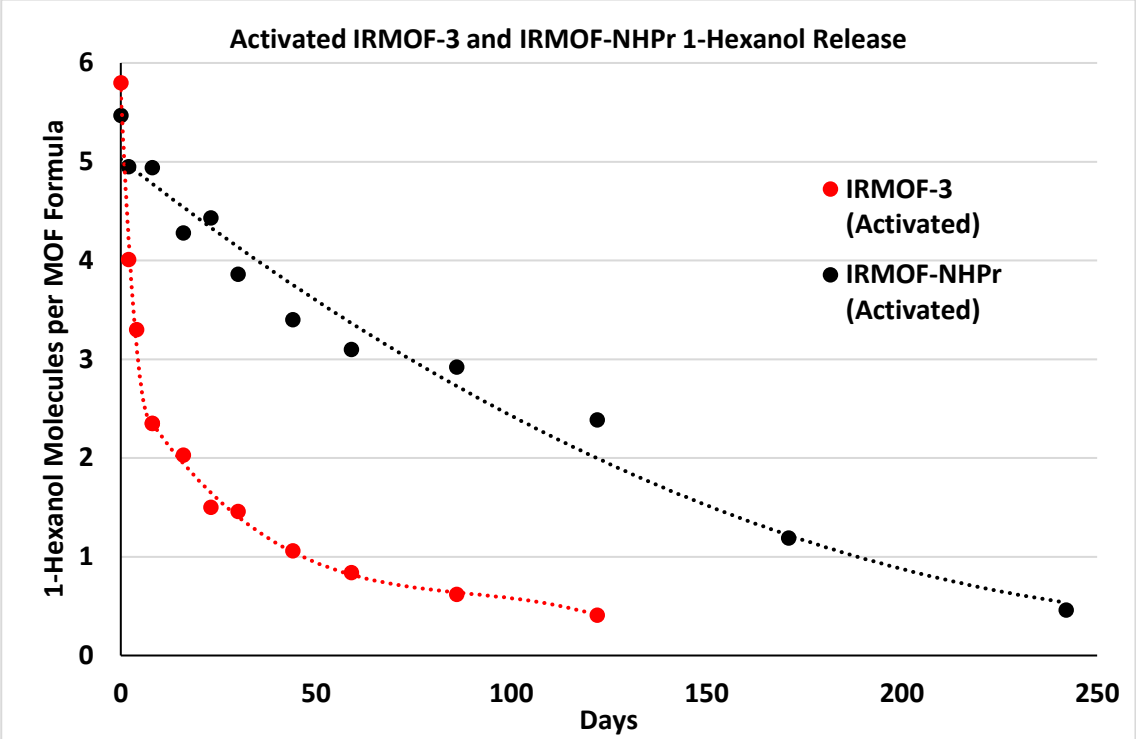

Figure 5.29. The release profiles of 1-hexanol from IRMOF-3 and IRMOF-NHPr loaded via the activation method.

These results show that, as in in the 3-octanone experiments, the addition of the propyl arm to the amine of the linker has had a significant effect on the retention of 1-hexanol within the framework. This is attributed to additional favourable interactions between the alkyl part of the 1-hexanol molecule and the propyl chain of the linker. The propyl chains may also present an additional physical barrier to the 1-hexanol moving through and out of the framework.

The combination of favourable interactions, higher loading capacities and controlled release profile has yielded a system with a release profile that extends over 8 months. The IRMOF-NHPr loaded with 1-hexanol via the activation method shows a release period over twice as long as that for the same system containing 3-octanone.

An additional benefit of using a MOF as semiochemical hosts is the potential for the framework to be reused. If the framework remains intact for the duration of its release period, then it can be reloaded with semiochemical and another release period started. This would allow for longer trap lifetimes and therefore lower material costs for the system.

On day 129 of the release experiments for IRMOF-3 and IRMOF-NHPr loaded via the solution exchange method, the samples were re-submerged in 1-hexanol for a period of 5 days. Samples of IRMOF-3 and IRMOF-NHPr loaded via the activation method were also re-submerged in 1-hexanol on day 122 of their release experiment for a period of 5 days. After the 5 day period, the samples were washed with n-hexane and PXRD patterns and release profiles were collected. The PXRD patterns revealed that both IRMOF-3 samples had decomposed but the IRMOF-NHPr samples had retained their crystalline structure. The release profiles and reloaded release profiles for the two IRMOF-NHPr samples can be seen in **Figure 5.30**.

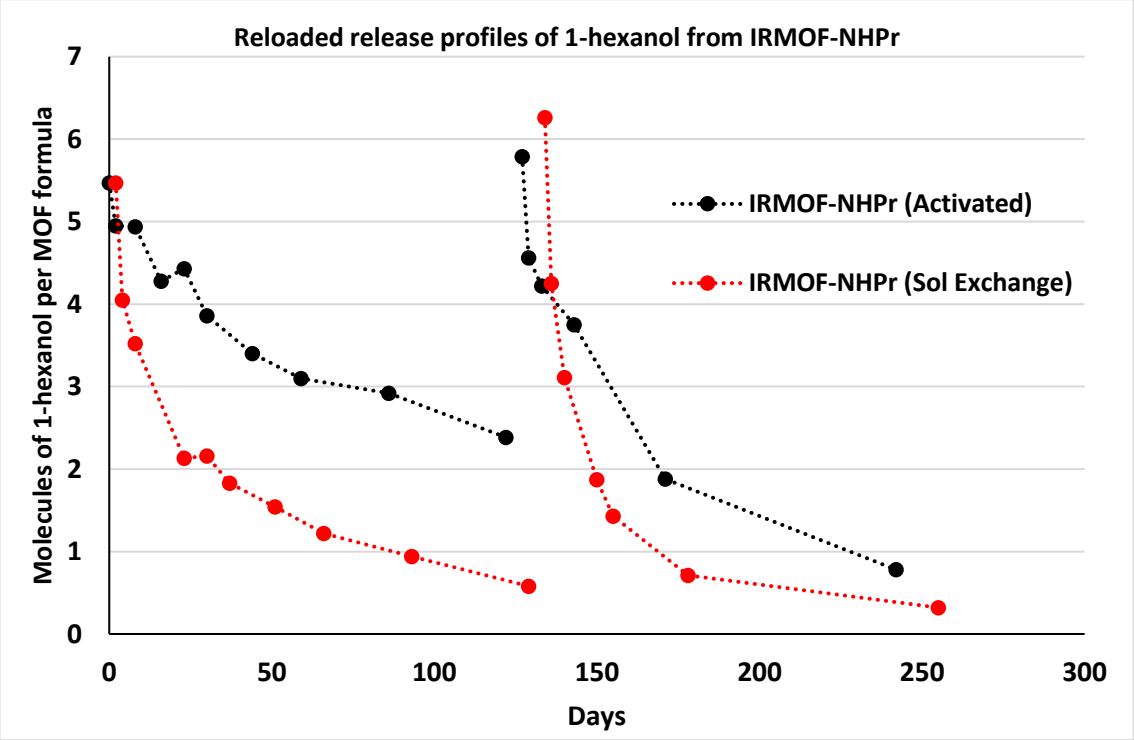

Figure 5.30. Release profile for IRMOF-NHPr samples loaded via both methods showing reloading with fresh 1-hexanol.

These show that both samples exhibit a surprisingly high second cycle 'day 0' measurement, this could be attributed to the extra 2 days of loading time. Both samples also show a much quicker release of the semiochemical than the first cycle of release data, which may reflect some degradation of the MOF and loss of crystallinity. In order to assess this hypothesis a PXRD trace was collected on the final day of each of the respective samples release measurements; these are plotted in **Figure 5.31**. It can be seen that both samples have lost the majority of their crystallinity and is likely the cause of the fast release. This shows that although repeated cycles of loading and release are possible, a more robust MOF family than the IRMOFs would need to be targeted.

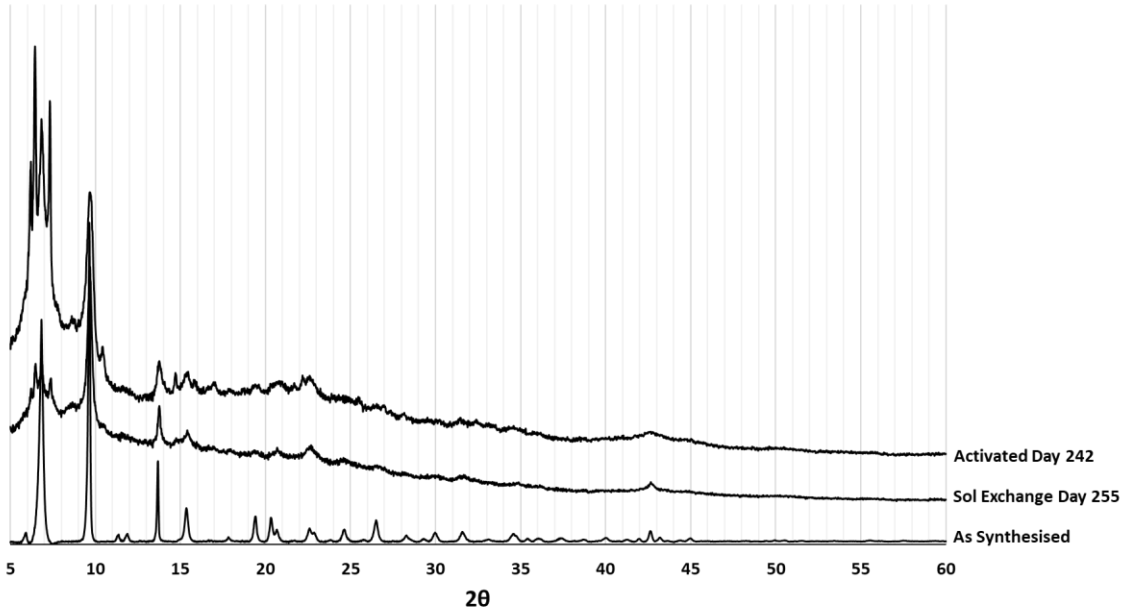

Figure 5.31. PXRD patterns of IRMOF-NHPr samples loaded with 1-hexanol via different methods after reloading at the end of their second release period.

5.2.7 Uptake and Release of Isoamyl Acetate

Isoamyl acetate (iaa) is an attractant of the spotted wing drosophila (*Drosophila suzukii)*, a pest of soft fruit orchards. The semiochemical is an ester, so its investigation allows the probing of a further functional group and the MOF systems' tolerance to that group. It has a similar molecular weight to 3-octanone but contains a branched chain so has a larger cross sectional area. Uptake and release experiments were carried out on IRMOF-3 and IRMOF-NHPr loaded using both the solution exchange method and the activation method.

The experimental procedure for loading the MOFs was kept as close as possible to that used with the other two semiochemicals. The analysis of the results was also conducted in the same way using ^{1}H-NMR spectroscopy to probe the composition of digested MOF samples. An example spectrum of isoamyl acetate loaded IRMOF-NHPr, loaded using the solution exchange method, is shown in **Figure 5.32**. H_E was used as the proton to quantify the amount of isoamyl acetate present.

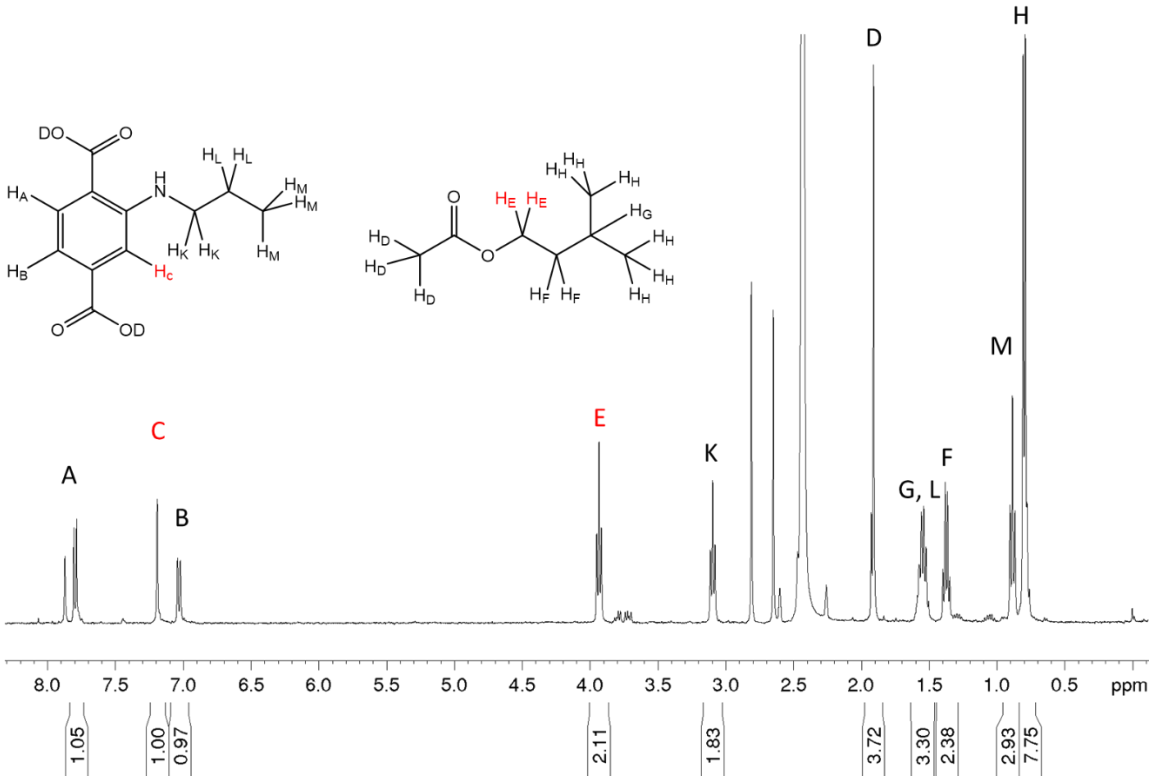

Figure 5.32. The ^{1}H-NMR spectrum for isoamyl acetate loaded IRMOF-NHPr, Day 0.

Samples of IRMOF-3 and IRMOF-NHPr were loaded with isoamyl acetate using both the solution-phase exchange method and the activation method. The values obtained, via ^{1}H-NMR spectroscopy of the digested samples, for the loading capacities are summarised in **Table 5.7**.

Table 5.7. A summary of the uptake of isoamyl acetate into various IRMOFs.

MOF	Linker : Isoamyl Acetate	Loaded MOF Formula	Wt.% of iaa
IRMOF-3	1 : 2.39	$[Zn_4O(bdc\text{-}NH_2)_3]\cdot 3.59iaa$	56%
IRMOF-NHPr	1 : 2.38	$[Zn_4O(bdc\text{-}NHPr)_3]\cdot 3.57iaa$	49%
A-IRMOF-3*	1 : 3.02	$[Zn_4O(bdc\text{-}NH_2)_3]\cdot 4.03iaa$	64%
A-IRMOF-NHPr	1 : 3.08	$[Zn_4O(bdc\text{-}NHPr)_3]\cdot 4.10iaa$	57%

(*Result was obtained on day 2 of release profile)

There is very little difference in the amount of isoamyl acetate loaded in IRMOF-3 compared to IRMOF-NHPr, this was true for samples loaded via both methods. In the solution based exchange method IRMOF-3 had more isoamyl acetate loaded than IRMOF-NHPr (56 wt.% vs. 49 wt.%). Using the activation method of loading IRMOF-3 had a slightly higher weight percent loading than IRMOF-NHPr (64 wt.% vs. 57 wt.%), however, the uptake result for IRMOF-3 in this case was taken after two days, this was due to an instrument error with the day 0 sample. Taking this into account it is likely that the IRMOF-3 had a higher uptake than the value reported. The small difference in uptake values suggests that the affinity of the two different frameworks for isoamyl acetate is similar.

As expected, an increase in the uptake of isoamyl acetate is observed when using the activation loading method over the solution based exchange method due to the lack of competition with DMF in the framework pores. However, as with 1-hexanol, the increase in the amount of semiochemical loaded via the activation method over the solution exchange method was smaller than that observed for 3-octanone.

Following the loading capacity measurements, a release profile was collected for each of the samples, using the loading capacity measurement as day 0. The release profiles for all 4 samples are plotted in **Figure 5.33**.

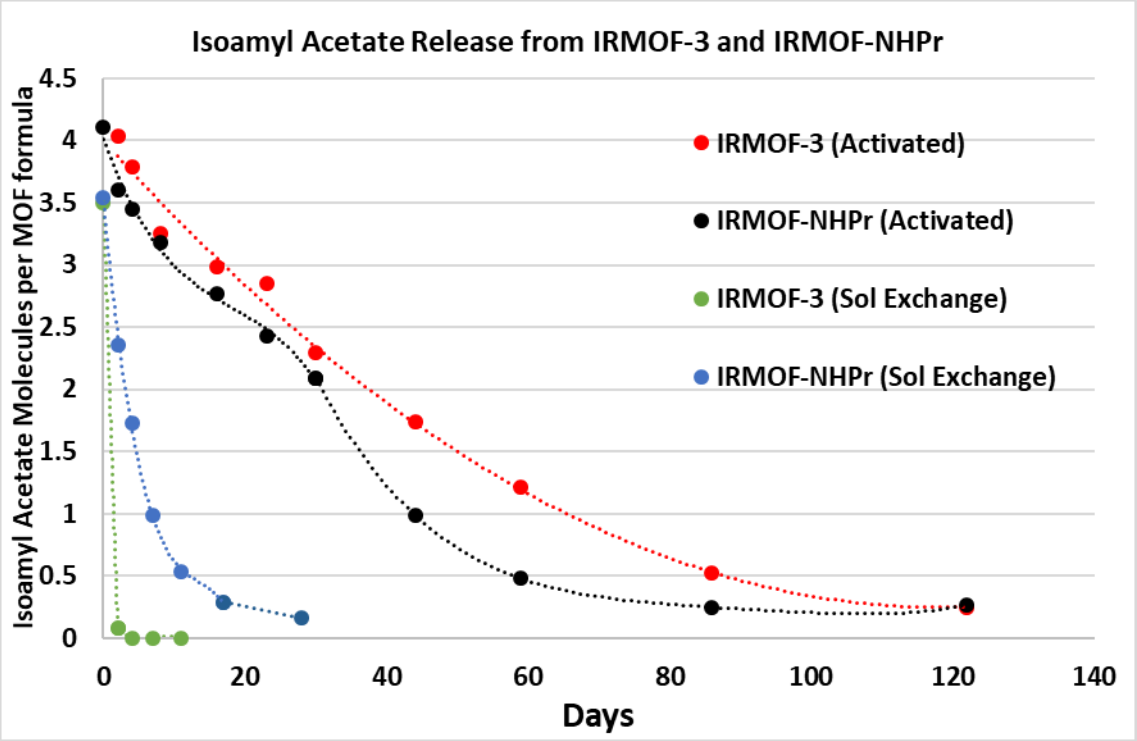

Figure 5.33. The release profiles of isoamyl acetate from IRMOF-3 and IRMOF-NHPr loaded via the activation method and solution-phase exchange method.

The release profiles for IRMOF-3 loaded using the solution-phase exchange method shows that the sample released all its loaded isoamyl acetate by day 4. This is the fastest and most complete loss of any semiochemical observed during the course of this investigation. The IRMOF-NHPr sample loaded in the same way also released isoamyl acetate very quickly, releasing nearly all of it within 20 days. Due to the speed of these releases, especially that of IRMOF-3, a PXRD pattern was collected of the samples in order to see if a loss in crystallinity was contributing to the rapid loss of semiochemical, these patterns are presented in **Figure 5.34**. It can be seen that the IRMOF-3 sample has completely degraded while the IRMOF-NHPr sample has retained the IRMOF structure.

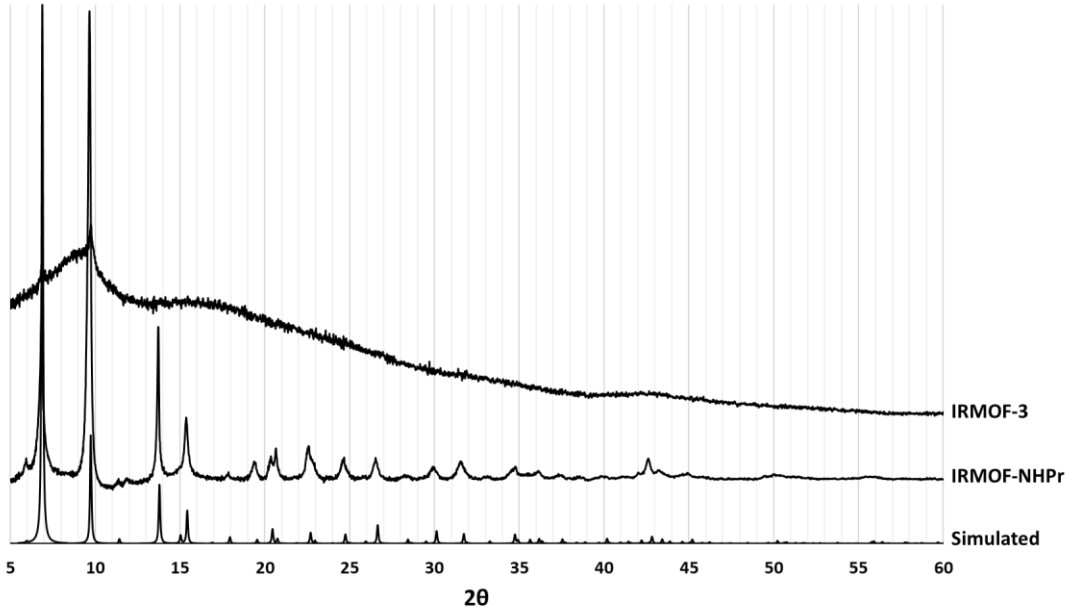

Figure 5.34. The PXRD patterns of IRMOF-3 and IRMOF-NHPr loaded via the solution exchange method after isoamyl acetate release compared with the pattern for IRMOF-3 simulated from single-crystal data.

Interestingly the samples loaded with isoamyl acetate via the activation method have a very different release profile despite having similar uptake values to the samples loaded via the solution exchange method. The IRMOF-3 sample has a steady release which starts to tail off at about 80 days while IRMOF-NHPr shows a similar steady release but starts to tail off a little earlier at about 60 days. The similarity in these release patterns suggests that the affinity of isoamyl acetate for the framework are of comparable strengths.

An attempt at reloading the IRMOF-3 and IRMOF-NHPr samples originally loaded via the activation method failed and gave no uptake at all. A PXRD pattern confirmed that this was because the samples had lost all crystallinity and so was likely no longer porous.

5.3 Conclusions

The results presented in this chapter demonstrate the potential for MOFs to be used as hosts for semiochemicals in the construction of lure traps for pest species. Three different semiochemicals, 3-octanone, 1-hexanol and isoamyl acetate, have all been successfully loaded into, and released from, different functionalised MOFs.

The ant alarm pheromone 3-octanone has been successfully loaded into a range of different MOFs including two γ-cyclodextrin MOFs, Zn-MOF-74, IRMOF-1, IRMOF-3, IRMOF-NHPr and the new MOF [Zn_4O(2-propoxy-1,4-benzenedicarboxylate)$_3$] (IRMOF-OPr). The 3-octanone was loaded via a solution-phase exchange with the synthesis solvent that resided in the pores. The amount of pheromone loaded into the pores was ascertained using ^{1}H-NMR spectroscopy of digested samples of the loaded MOF. The MOF that showed the largest uptake under these conditions was the newly synthesised MOF IRMOF-OPr with a weight percent uptake of 50%.

The synthesised series of IRMOFs allowed for the importance of functionalisation to be interrogated. IRMOF-1 with no functional group decorating the pores of the framework had the lowest uptake in the series (15 wt.%). IRMOF-3, with an amine functional group, performed significantly better (35 wt.%), this was attributed to favourable interactions between the polar amine group and polar ketone group in 3-octanone. IRMOF-NHPr, with an additional propyl group, had a larger uptake value again (46 wt.%), this was attributed to the favourable interactions between the alkyl chain in the 3-octanone and propyl chain of the ligand. Finally, substituting the propylamine group with a propoxy group in IRMOF-OPr showed a slight increase in uptake value (50 wt.%).

A new method of pheromone loading into MOFs was also developed, this involved activation of the material prior to submerging the MOF in the pheromone. This strategy resulted in an increase in the amount of semiochemical loaded in the frameworks with the largest increase seen for IRMOF-3 which increased from an uptake value of 35 wt.% to 75 wt.%. Activation prior to the semiochemical loading has the added benefit of removing the toxic DMF from the system. When using this loading procedure, it was shown that TGA could be used as a further method of quantifying the amount of 3-octanone loaded into the pores and that results were in good agreement with those obtained by ^{1}H-NMR spectroscopy.

The release of 3-octanone from the loaded MOFs into the environment was explored. This was analysed using ^{1}H-NMR spectroscopy of digested samples of pheromone-loaded MOF taken at regular intervals, to construct release profiles. As well as maximum release lifetimes, the profiles

also give an indication of the relative affinity of 3-octanone for different frameworks. It was shown that when loaded using the solution-phase exchange method, IRMOF-NHPr and IRMOF-OPr had very similar release profiles suggesting that the strength of interactions between the frameworks and 3-octanone are similar. In contrast the IRMOF-3 sample loaded in the same way released all of its 3-octanone over a much shorter period suggesting a lower affinity between 3-octanone and IRMOF-3.

A comparison between the two different loading methods highlighted that samples loaded via the activation method release for a much longer period, over 100 days for IRMOF-NHPr. This was not only because more pheromone is contained within the pores, in addition, the shape and rate of the release profile was also altered, becoming more linear. This change has been attributed to the lack of competition between 3-octanone and DMF in the pores.

In order to investigate the tolerance of the IRMOF system to different functional groups and to expand the library of semiochemicals that MOFs may host, two more candidates were investigated. The first of these was 1-hexanol, an attractant of the German cockroach. In the case of 1-hexanol, the uptake values were higher for IRMOF-3 than for IRMOF-NHPr suggesting that the propyl group is less important in this case.

It was also shown that in the case of 1-hexanol, there was less of a difference in the observed loading capacities between the two different loading methods when compared to 3-octanone. This reflects a more complete exchange occurring in the solution exchange method as evidenced by the significantly lower amount of DMF present in these samples than in the 3-octanone cases.

The release profiles for 1-hexanol showed that despite only a small increase in the loading capacity of this attractant, those samples loaded by the activation method released the guest over a longer period at a more controlled and consistent rate. It was also shown that although the IRMOF-3 sample loaded via the activation method showed the highest loading capacity it released the 1-hexanol into the environment more quickly than IRMOF-NHPr. The release rate in the IRMOF-3 was not linear, releasing over half the included semiochemical in the first week then releasing the remainder more slowly over a period of 100 days. This contrasts with the IRMOF-NHPr sample which released 1-hexanol at a steady rate for nearly 250 days. A consistent steady release is an important parameter when considering the end application, as the trap ideally needs to preform equally well throughout its lifetime.

Samples of IRMOF-NHPr loaded with 1-hexanol through both methods were suitably crystalline to be re-loaded with more 1-hexanol after a period of 122 days. The re-uptake values for the

reloaded samples were similar to those obtained for the newly synthesised samples, however, the release profiles showed a much faster release rate over a much shorter time period, perhaps due to partial framework decomposition. This result shows that reloading of frameworks with fresh semiochemicals has the potential to be a viable strategy with which to increase the economic feasibility of the systems, however, more robust MOFs need to be targeted.

A third semiochemical, isoamyl acetate, which is an attractant for the spotted wing fly was also investigated. The semiochemical was successfully loaded using both the solution-phase exchange and activation methodologies into IRMOF-3 and IRMOF-NHPr. The results for this system showed that there was very little difference between IRMOF-3 and IRMOF-NHPr in terms of loading capacities.

A comparison between the two loading methods showed that despite only a small increase in loading capacity, the activation method loaded samples released at a much slower, more controlled rate, for a longer period of time. The samples loaded via the solution-phase exchange method released the isoamyl acetate very quickly, the IRMOF-3 sample doing so within 2 days.

Figure 5.35 shows a comparison of the uptake of all three semiochemicals into IRMOF-3 and IRMOF-NHPr using both methods of loading. This highlights that in terms of weight percent uptake IRMOF-NHPr varied very little between semiochemicals, whereas IRMOF-3 exhibited a larger variance.

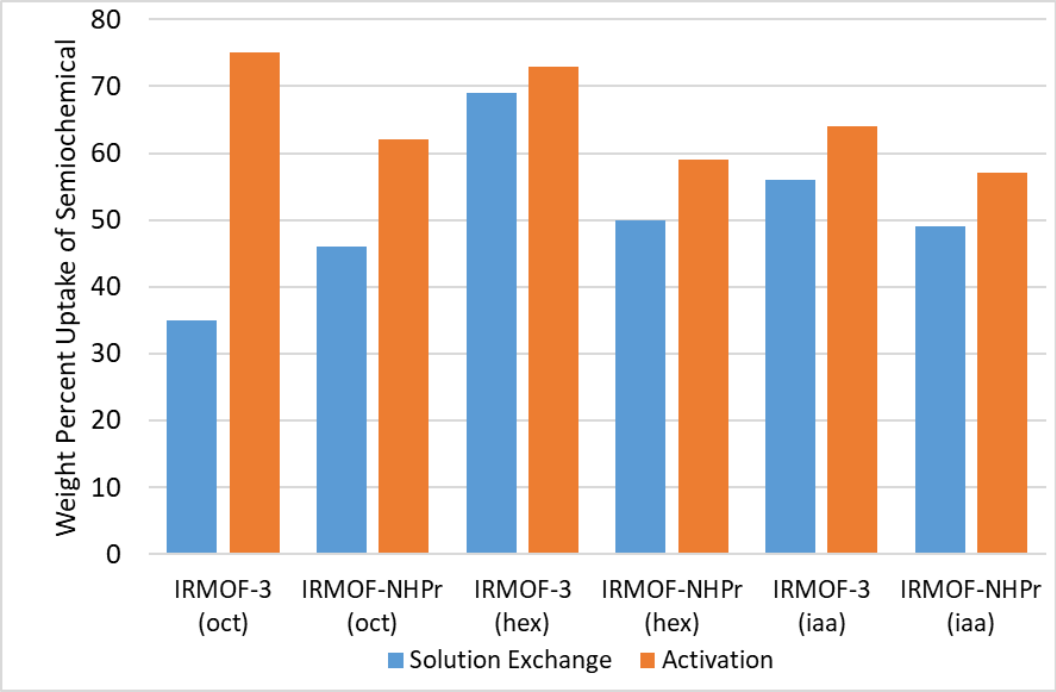

Figure 5.35. A comparison of semiochemical uptake using both methods of loading into IRMOF-3 and IRMOF-NHPr.

This research has demonstrated that, of the two different loading methodologies, the activation method achieves higher loading capacities, as seen in **Figure 5.35**, more consistent release rates and longer release periods. The method has the added advantage of removing DMF from the system which is then no longer released into the environment with the semiochemical. The only drawback of this method compared to the solution-phase exchange method is that it requires an extra solvent exchange step and heating under reduced pressure, both of which are time and energy intensive.

IRMOF-NHPr loaded by the activation method was shown to give the best performance in terms of uptake and release profile shape and length with both 3-octanone and 1-hexanol while in the isoamyl acetate it performed similarly to IRMOF-3. A comparison of the release of the three semiochemicals from IRMOF-NHPr loaded via the activation method is shown in **Figure 5.36**. This graph highlights that each semiochemical has a different release profile, despite having similar uptake values.

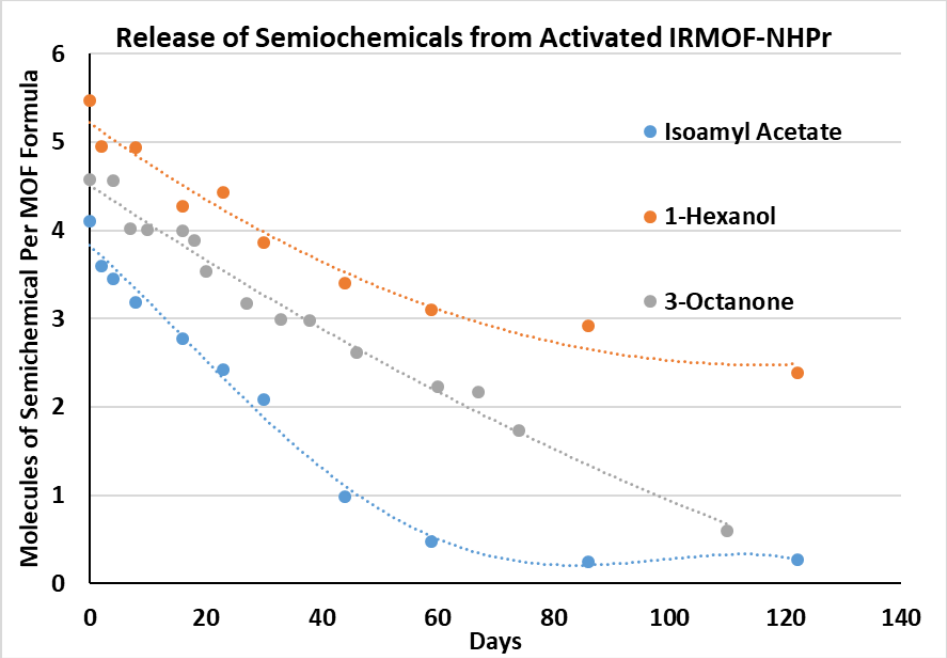

Figure 5.36. A comparison of the release of isoamyl acetate 1-hexanol and 3-octanone from IRMOF-NHPr loaded via the activation method.

Three different semiochemicals have been loaded into and released from a number of different MOFs. The uptake amount and release profile varies between each semiochemical and for each MOF. It has been shown that framework functionalisation can be exploited to improve the uptake and release profiles for the different semiochemicals. This has resulted in materials that release semiochemicals for time periods far exceeding the lifetime of commercially available lure-traps.

5.4 Future Work

The continuation of this project has several distinct, related strands. The first of these is computational modelling of the functionalised IRMOF systems. Calculations and simulations will be carried out to look at the strength of interactions between semiochemicals and the frameworks, and also determine where in the pores of the MOF the semiochemicals reside. These calculations will be carried out on a variety of functionalised IRMOFs with an aim to computationally derive the optimal functionalisations which can then be applied practically. Calculations will be carried out on a range of semiochemicals with different functional groups, such as 3-octanone, isoamyl acetate and isobutyl acetate. This would again, inform experimental work to optimise these systems.

This work has highlighted that high uptake and steady extended release periods are not necessarily concomitant. It has also been shown that each semiochemical has an optimal linker functionalisation to give an ideal release curve. Finding this optimal linker will require the in-depth interrogation of a wider range of linker functional groups such as adding or reducing the number functionalities and/or changing the alkyl chain length, some potential linkers are shown in **Figure 5.37**. Another potential strategy for controlling the pore functionalisation would be to use a mixed-ligand approach in the MOF synthesis which would permit a combination of functionalities in different distributions throughout the pores of the MOF.

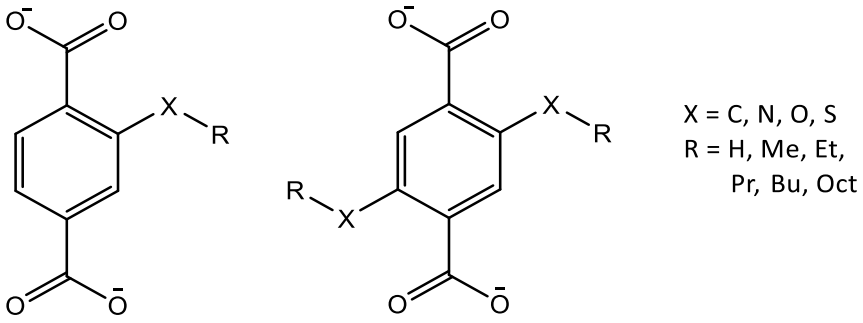

Figure 5.37. Potential functionalised linkers for IRMOF semiochemical system optimisation.

The possibility for the reloading MOFs with more semiochemicals after their first release cycle was assessed and although it was shown to be possible in the case of 1-hexanol loaded IRMOF-NHPr, loss of crystallinity limited the effectiveness of the second release and precluded loading of a third cycle. This would be an attractive property of the system as it would make it more economically viable and sustainable.

One solution will be to employ a more stable MOF. In related work carried out in the group, Dr Amer Hamzah synthesised a UiO-66 derivative using H_2bdc-NHPr and successfully loaded it with

3-octanone.[31] UiO-66 is a well-known example of a water stable MOF and can be readily functionalised so is an ideal candidate to enable reloading cycles.[80] Other possible candidates are MIL-125,[178] a titanium(IV) bdc MOF with the formula $[Ti_8O_8(OH)_4(bdc)_6]$ and (Fe)MIL-101,[179] which has the formula $[Fe_3O(H_2O)_2Cl(bdc)_3]$.

Finally, a wider selection of semiochemicals could be investigated in order to improve the scope of these systems and give wider applicability. All of the semiochemicals investigated herein have possessed varying functionality but were of similar size. Thus, in order to access the robustness of the system, larger and smaller semiochemicals will be investigated. Two possible candidates are undecanal and 2-methyl-3-buten-2-ol, the structures of which are shown in **Figure 5.38**. Undecanal is a component in the sex pheromone of the greater wax moth, which is a honeybee parasite and, as such, a pest of the honey industry.[180] 2-methyl-3-buten-2-ol is an aggregation pheromone of the spruce bark beetle, a pest in the spruce forests in Norway.[181]

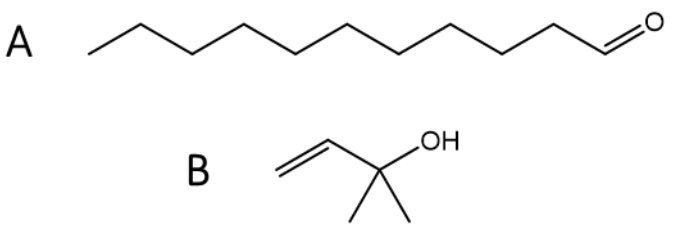

Figure 5.38. The structures of **A** – undecanal and **B** – 2-methyl-3-buten-2-ol.

5.5 Experimental Procedures

General procedures are presented in the experimental section of **Chapter 2.**

5.5.1 Synthesis of Organic Dicarboxylic Acids

5.5.1.1 Synthesis of 2-aminopropyl-1,4-benzenedicarboxylic acid

2-aminopropyl-1,4-benzenedicarboxylic acid was synthesised by a procedure developed by Dr Amer Hamzah and reported in her thesis. The reaction scheme for this reaction is shown in **Figure 5.39**.[31]

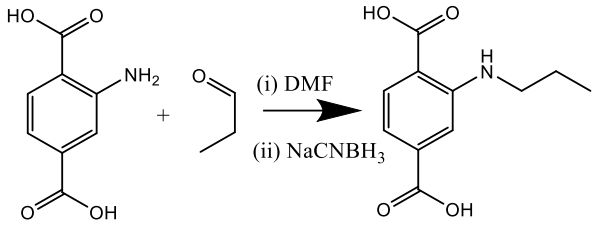

Figure 5.39. Reaction scheme for the synthesis of 2-propylamino-1,4-benzenedicarboxylic acid.

2-Amino-1,4-benzenedicarboxylic acid (2.2 mmol, 0.401 g) was dissolved in 20 mL of dry DMF. Propanal (4.4 mmol, 0.32 mL) was added to the solution which was stirred at room temperature for one hour. The reaction mixture was then cooled in an ice bath and $NaCNBH_3$ (4.5 mmol, 0.2810 g) was added. The solution was then stirred at room temperature for 24 hours. The yellow solution was acidified to pH 2 using a 1 M HCl solution. H_2O was then added until a yellow solid precipitated. The product was collected via vacuum filtration and dried in an oven at 60 °C for two hours. Yield = 0.41 g (84%)

The product identity was confirmed via ^{1}H-NMR, shown in **Figure 5.40**. (300 MHz, DMSO-d_6); δ (ppm) 7.85 (1H, d, *J* = 8.2 Hz), 7.22 (1H, d, *J* = 1.3 Hz), 7.06 (1H, dd, *J* = 8.2, 1. 5 Hz), 3.16 (2H, t, *J* = 6. 9 Hz), 1.61 (2H, m, *J* = 7.1 Hz), 0.95 (3H, t, *J* = 7.3 Hz)

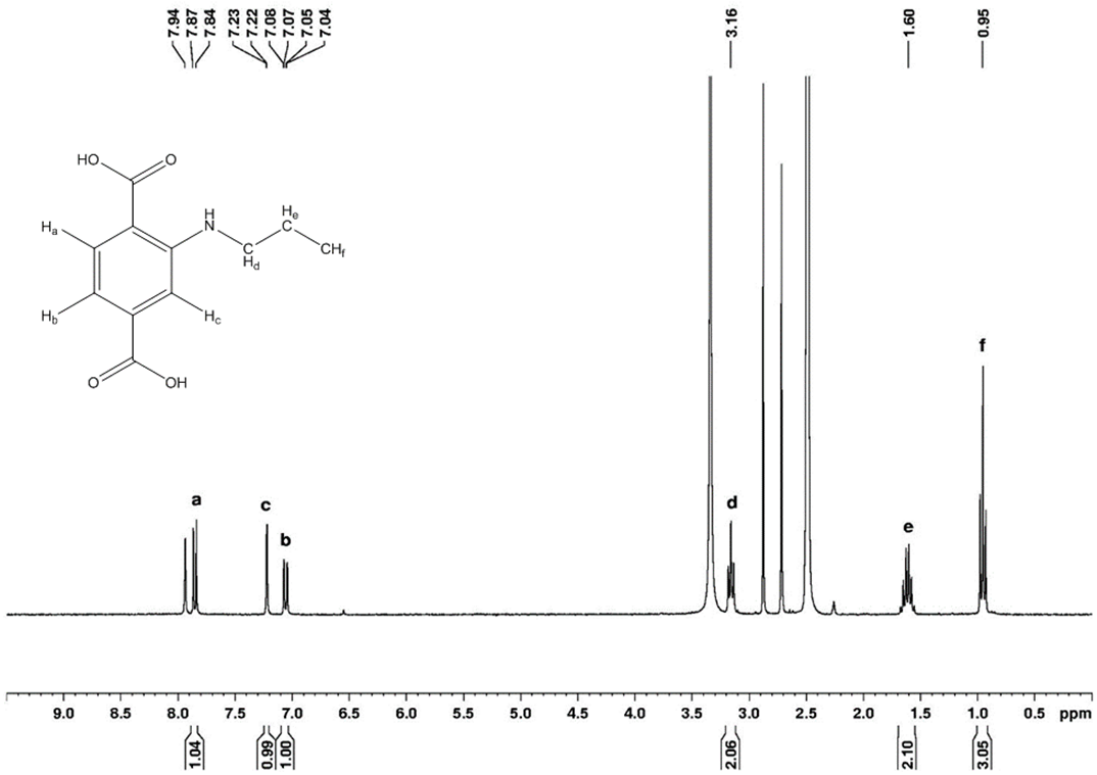

Figure 5.40. ^{1}H-NMR spectrum of 2-propylamino-1,4-benzenedicarboxylic acid.

5.5.1.2 Synthesis of 2-propoxy-1,4-benzenedicarbocylic acid

2-propoxy-1,4-benzenedicarbocylic acid (H_2bdc-OPr) was synthesised according to the procedure shown in **Figure 5.41**, the etherication was based on a literature procedure for the synthesis of the bi-functionalised analogue, 2,5-dipropoxy-1,4-benzenedicarboxylic acid.[119]

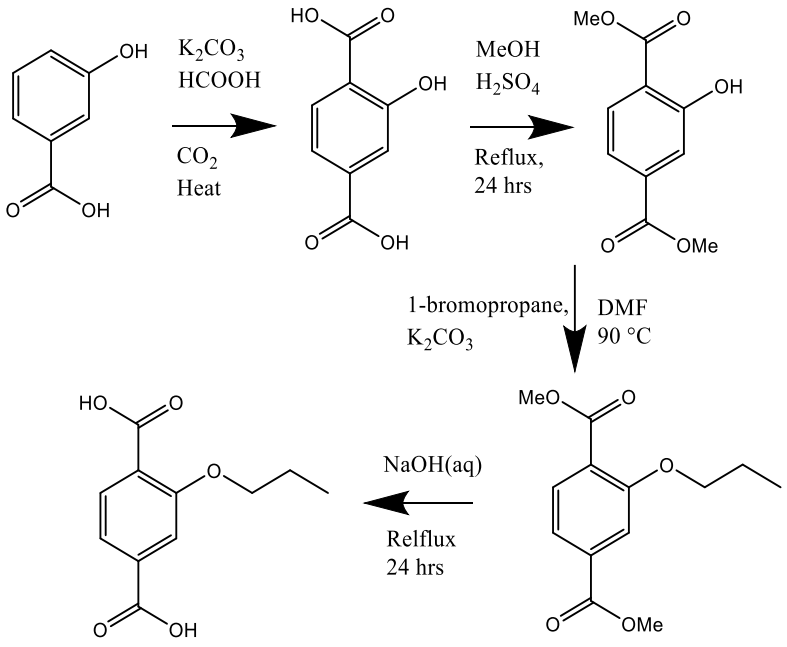

Figure 5.41. Reaction scheme for the synthesis of 2-propoxy-1,4-benzenedicarboxylic acid.

K_2CO_3 (0.35 mol, 100 g) was placed in a round bottom flask fitted with a condenser. Formic acid (40 mL) was added dropwise with vigorous stirring. The temperature of the reaction was increased to 210 °C whilst the reaction was flushed with nitrogen for 30 min. The N_2 stream was replaced by a CO_2 stream generated from 500 g of dry ice. 3-hydroxybenzoic acid (0.1 mol, 13.81 g) was added in one portion and the reaction mixture stirred at 210 °C for 6 hours. After this time the reaction mixture was allowed to cool and dissolved in 200 mL of boiling water. The product was precipitated by the addition of acid and then washed with (4 X 100 mL) of H_2O. The crude product was dried at 50 °C overnight then recrystallised from MeOH to give pure 2-hydroxy-1,4-benzenedicarboxylic acid. (Yield = 6.033 g, 33%)

2-Hydroxy-1,4-benzenedicarboxylic acid (11.26 mmol, 2.05 g) was dissolved in 200 mL of MeOH. 5 mL of conc. H_2SO_4 was added and the solution heated at reflux for 24 hours. Once cooled to room temperature the MeOH was removed under reduced pressure. The slurry was neutralised using $NaHCO_3$(aq). The product was extracted from the aqueous phase using $CHCl_3$ (3 x 50 mL). The organic phase was washed with brine and dried over $MgSO_4$ before being removed under reduced pressure to give dimethyl-2-hydroxy-1,4-benzenedicarboxylate (Yield = 1.577 g, 67%).

Dimethyl-2-hydroxy-1,4-benzenedicarboxylate (7.5 mmol, 1.577 g), 1-bromopropane (15 mmol, 1.36 mL) and K_2CO_3 (20 mmol, 2.764 g) were dissolved in 30 mL of dry DMF. The reaction mixture was heated at 90 °C for 18 hours under a nitrogen atmosphere. After cooling the reaction was quenched with the addition of 12M HCl. The mixture was filtered, and the product extracted from the filtrate with $CHCl_3$ (3 x 30 mL). The organic layer was evaporated to dryness and 100 mL of 1 M NaOH(aq) was added, then heated at reflux for 18 hours. Once cooled, acidification using 1 M HCl(aq) caused precipitation of the product which was collected via vacuum filtration. Yield (0.846 g, 50%).

The product identity was confirmed via ^{1}H-NMR, shown in **Figure 5.42**. (300 MHz, DMSO-d_6); δ (ppm) 7.64 (1H, d, *J* = 8.3 Hz), 7.53 (1H, d, *J* = 1.3 Hz), 7.50 (1H, dd, *J* = 8.3, 1.3 Hz), 4.02 (2H, t, *J* = 6.3 Hz), 1.72 (2H, m, *J* = 7.2 Hz), 0.97 (3H, t, *J* = 7.4 Hz).

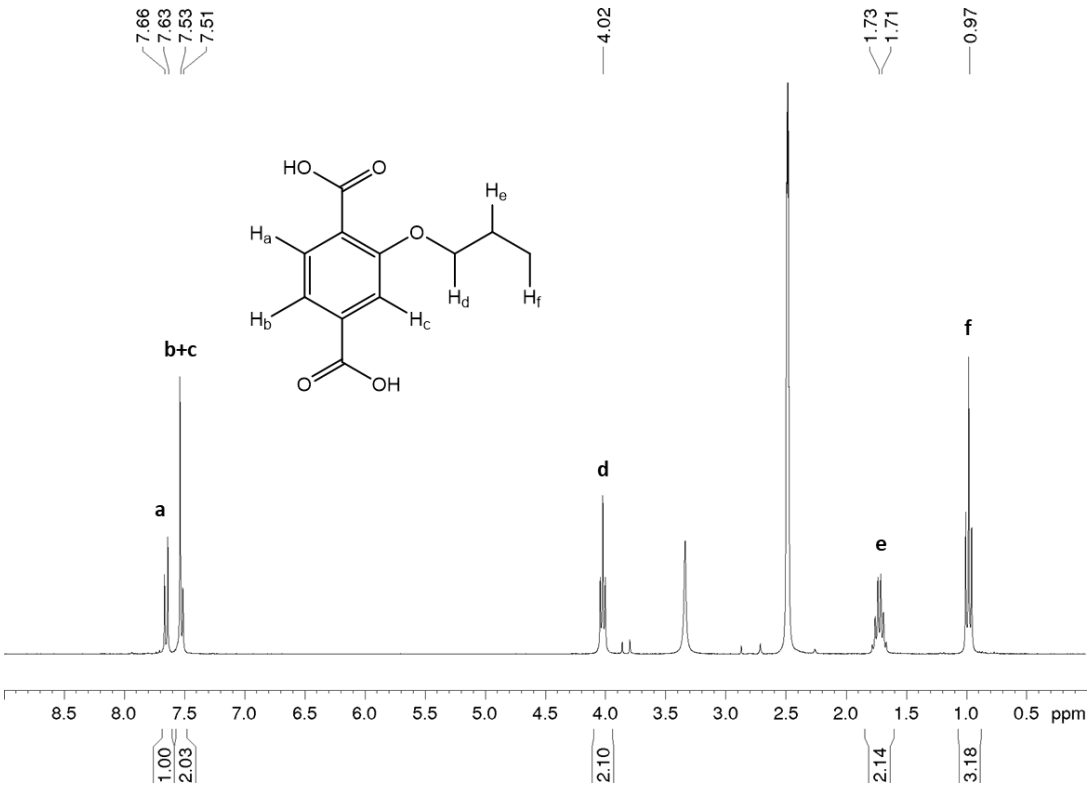

Figure 5.42. ^{1}H-NMR spectrum for 2-propoxy-1,4-benzenedicarboxylic acid.

5.5.1.3 Synthesis of 2,5-dihydroxy-1,4-benzenedicarboxylic acid

2,5-dihydroxy-1,4-benzenedicarboxylic acid (H_4dobdc) was synthesised according to a modified literature preparation, the scheme for which can be seen in **Figure 5.43**.[182]

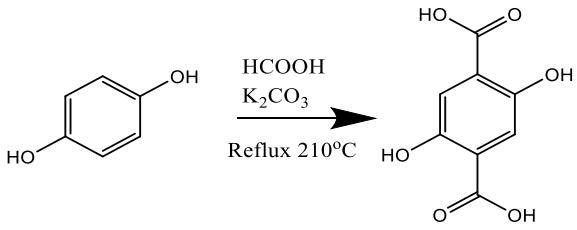

Figure 5.43. Reaction scheme for the synthesis of 2,5-dihydroxy-1,4-benzenedicarboxylic acid (H_4dobdc).

Potassium carbonate (0.71 mol, 97.989 g) was added to a round bottomed flask fitted with a condenser, formic acid (38.0 mL) was added drop wise with vigorous stirring. The reaction mixture was then heated to 210 °C forming a thick melt of potassium formate, carbonate and bicarbonate. The reaction mixture was flushed with a continuous stream of N_2 for a period of 30 min after which the N_2 stream was replaced with CO_2, sourced from a 1 L round bottomed flask filled with dry ice. Hydroquinone (0.20 mol, 22.344 g) was added in one portion and the reaction mixture held at 210 °C with vigorous stirring for 6 hours. After cooling, the reaction mixture was dispersed by adding 200 mL of boiling water. After the suspension had cooled to room

temperature the mixture was filtered and the solid residue washed with H_2O. The crude product was then suspended in 500 mL of H_2O before being acidified using 1 M HCl then separated via filtration and washed with 200 mL of fresh H_2O. After being left to air dry for 12 hours, the grey solid was dried in the oven at 80 °C for 1 hour at which point it turned yellow. Yield (6.06 g, 15%).

The low yield was due to ineffective stirring, a lot of solidified product had been lost during the dispersion with boiling water.

Product identity was confirmed by ^{1}H-NMR, **Figure 5.44**, (300 MHz, DMSO-d_6); δ (ppm) 7.26 (2H, s). ^{13}C-NM^{13}C{^{1}H}-NMR, **Figure 5.45**, (75.5 MHz, DMSO-d_6); δ (ppm) 170.4, 152.0, 119.4, 117.4. IR spectroscopy was carried out and compared to the spectrum collected for the same compound purchased from Sigma-Aldrich. The matching spectra are shown in **Figure 5.46**.

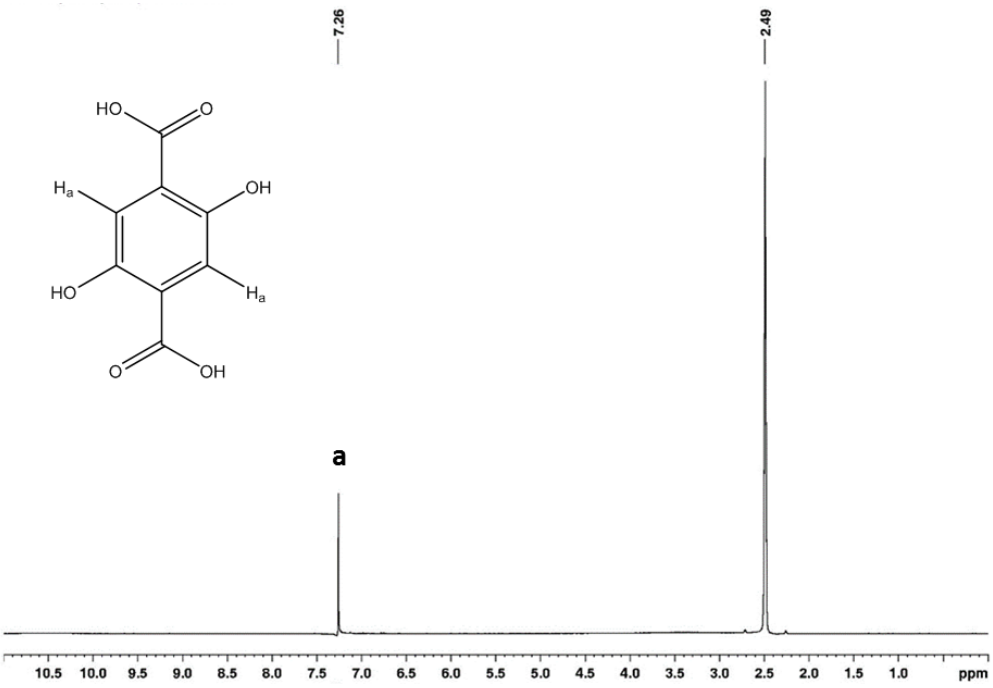

Figure 5.44. ^{1}H-NMR spectrum of H_4dobdc.

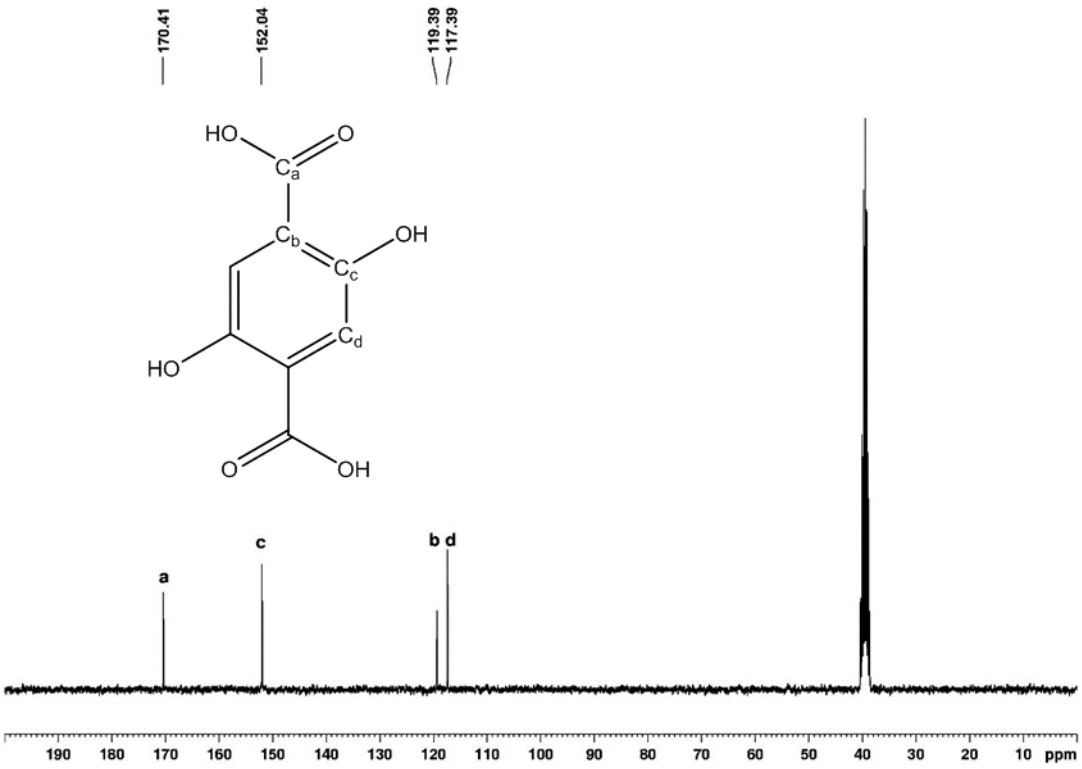

Figure 5.45. $^{13}C\{^{1}H\}$-NMR spectrum of synthesised H_4dobdc.

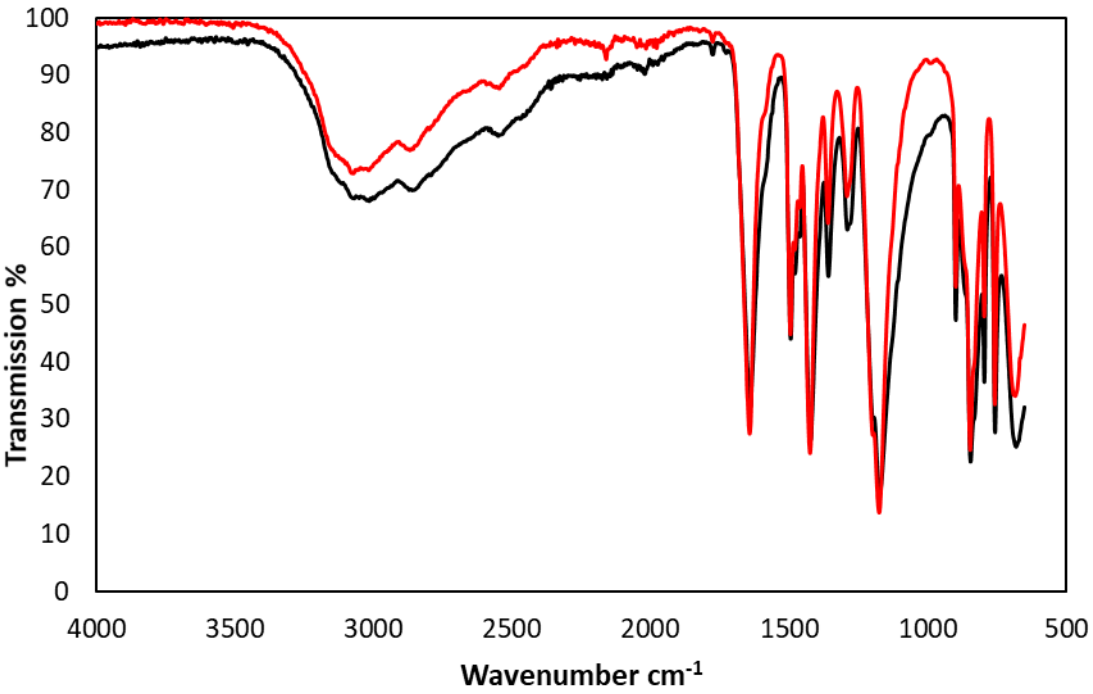

Figure 5.46. IR Spectrum of synthesised H_4dobdc (black) and purchased H_4dobdc (red).

5.5.2 Synthesis of Metal-Organic Frameworks

5.5.2.1 Synthesis of MOF-5

MOF-5 was synthesised based on a modified version of a previously reported procedure.[165] $Zn(NO_3)_2 \cdot 6H_2O$ (1.5 mmol, 0.446 g) and H_2bdc (0.5 mmol, 0.083 g) were added to 49 mL of dry DMF and 1 mL of deionised water in a 125 mL Teflon-lined steal autoclave. The mixture was stirred for 15 minutes before being sealed and placed in an oven at 100 °C for 7 hours. The reaction mixture was left to cool naturally in the powered down oven (ca. 6 hours). Once at room temperature the colourless crystals were collected by filtration and washed with dry DMF (3 X 5 mL) and then stored in dry DMF until required. The product identity was confirmed by PXRD, the pattern of which can be seen in **Figure 5.47**.

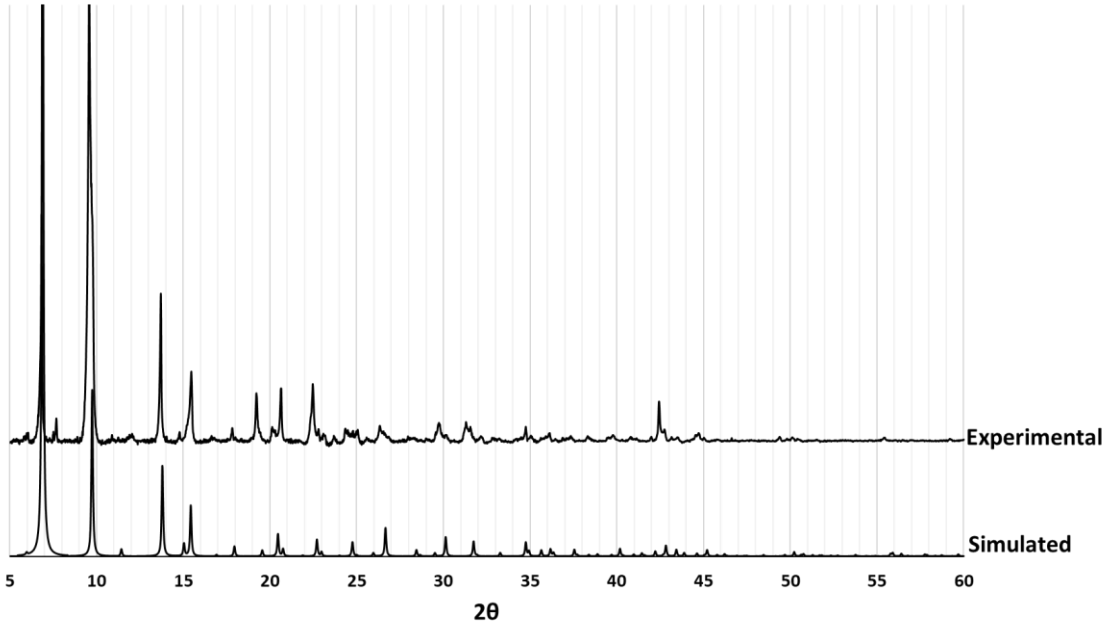

Figure 5.47. The experimental PXRD trace of MOF-5 compared to the trace simulated from single-crystal data for MOF-5.[20]

5.5.2.2 Synthesis of IRMOF-3

IRMOF-3 was synthesised using a modified synthetic procedure based on a previously reported literature preparation.[166] $Zn(NO_3)_2 \cdot 6H_2O$ (4 mmol, 1.19 g) and 2-amino-1,4-benzenedicarboxylic acid (1.6 mmol, 0.290 g) were dissolved in 40 mL of dry DMF with the aid of a sonicator. The reaction solution was decanted into 5 10 mL microwave vials which were sealed with a crimped Teflon-lined cap. The vials were placed in an oven at 105 °C for 48 hours. After removal from the oven and cooling under ambient conditions, the large orange-brown cubic crystals were collected via vacuum filtration, then washed with fresh DMF (3 X 5 mL) and stored in dry DMF

until required. The product identity was confirmed using PXRD, the trace of which can be seen in **Figure 5.48**.

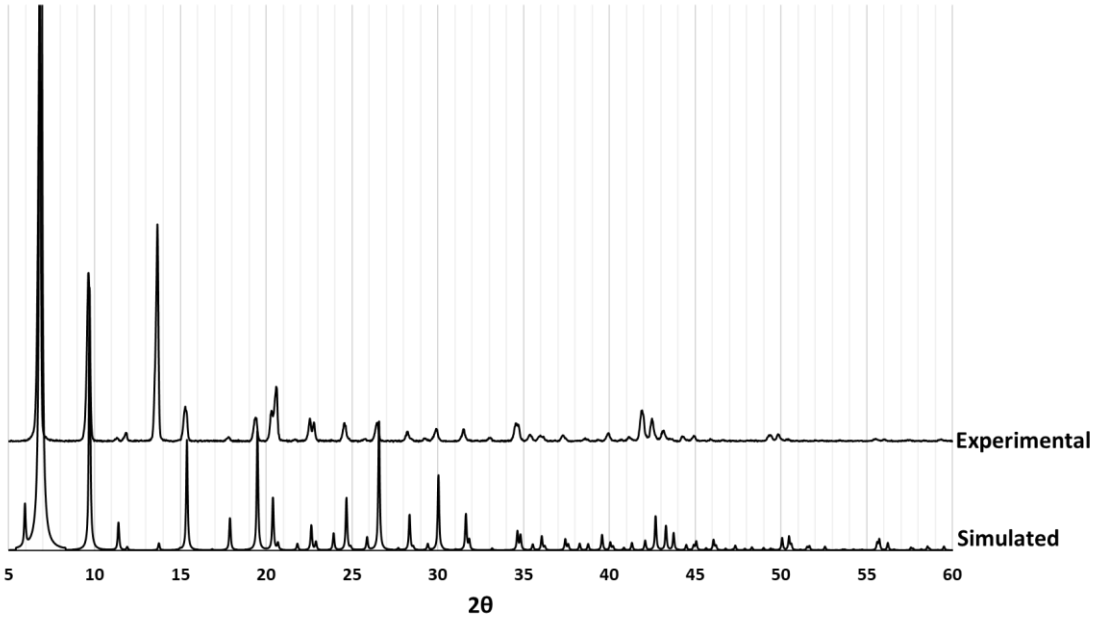

Figure 5.48. The experimental PXRD trace of IRMOF-3 compared to the trace simulated from single-crystal data for IRMOF-3.[19]

If activation of the material was required a solvent exchange with chloroform was carried out. The crystals were filtered and submerged in chloroform for a period of 3 days exchanging the chloroform for fresh chloroform every 24 hours. After this period the crystals were recovered by vacuum filtration and then heated at 100 °C under reduced pressure for 24 hours before being backfilled with N_2 gas.

A nitrogen adsorption isotherm was collected and is shown in **Figure 5.49**. This was used to create a BET plot, shown in **Figure 5.50**, which was used to estimate the surface area of IRMOF-3 as 2069 $m^2 g^{-1}$.

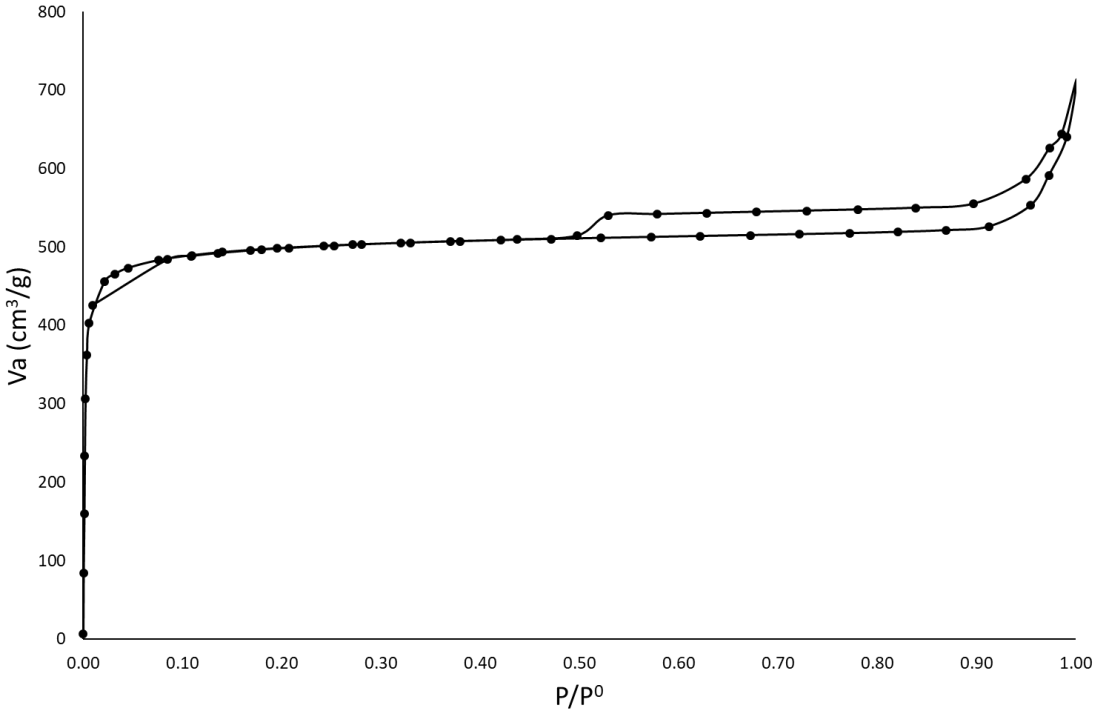

Figure 5.49. Nitrogen adsorption/desorption isotherm for IRMOF-3.

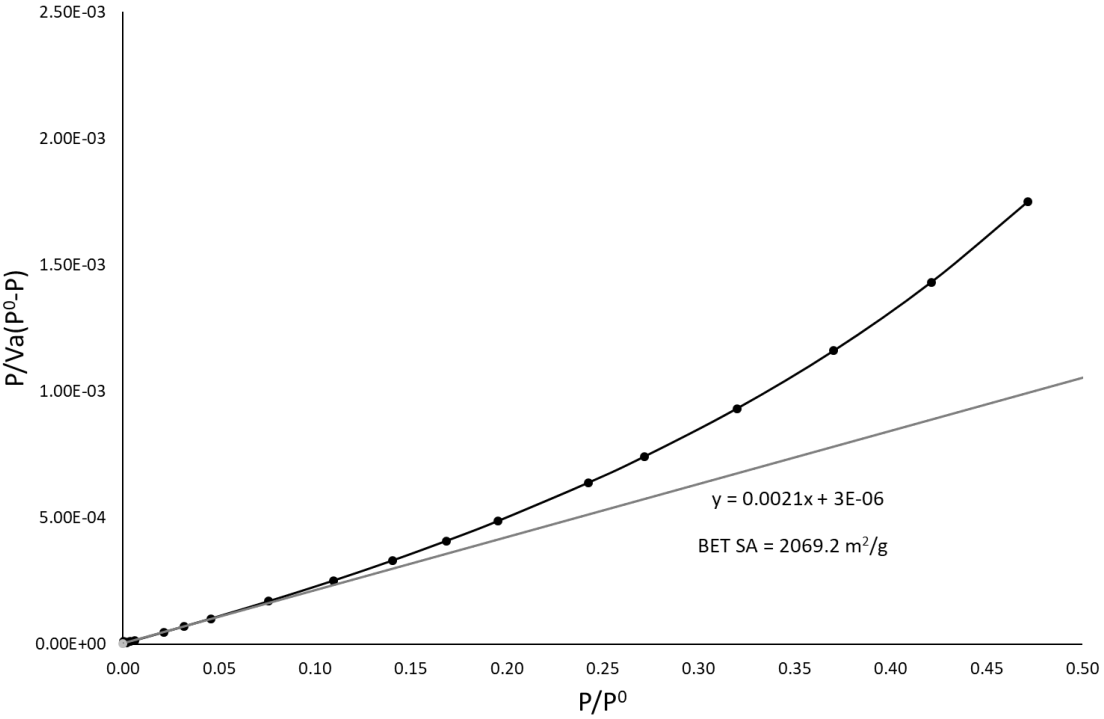

Figure 5.50. BET plot for IRMOF-3.

5.5.2.3 Synthesis of IRMOF-NHPr

IRMOF-NHPr was synthesised using a modified procedure based on that used for IRMOF-3. $Zn(NO_3)_2 \cdot 6H_2O$ (4 mmol, 1.19 g) and 2-aminopropyl-1,4-benzenedicarboxylic acid (1.6 mmol, 0.357 g) were dissolved in 40 mL of dry DMF with the aid of a sonicator. The reaction solution was decanted into 5 10 mL microwave vials which were sealed with a crimped Teflon-lined cap. The vials were placed in an oven at 105 °C for 48 hours. After removal from the oven and cooling under ambient conditions, the large yellow cubic crystals were collected via vacuum filtration, then washed with fresh DMF (3 X 5 mL) and stored in dry DMF until required. The product identity was confirmed using PXRD, the pattern of which can be seen in **Figure 5.51**. As the single-crystal structure of IRMOF-NHPr has not been reported the experimental pattern was compared to the simulated pattern generated from the single-crystal structure for IRMOF-3.

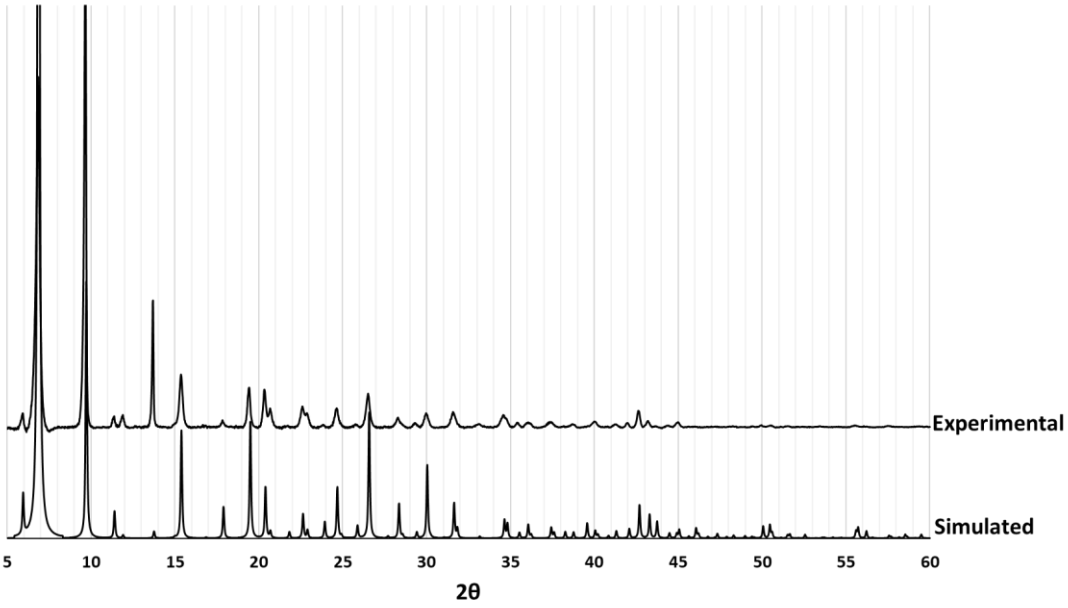

Figure 5.51. The experimental PXRD trace of IRMOF-NHPr compared to a trace simulated from single-crystal data for IRMOF-3.

Activation was carried out in an identical manner to that for IRMOF-3. A nitrogen adsorption isotherm was collected, as shown in **Figure 5.52**, and a BET plot constructed, shown in **Figure 5.53**, giving a BET surface area for IRMOF-NHPr of 1561 $m^2 g^{-1}$.

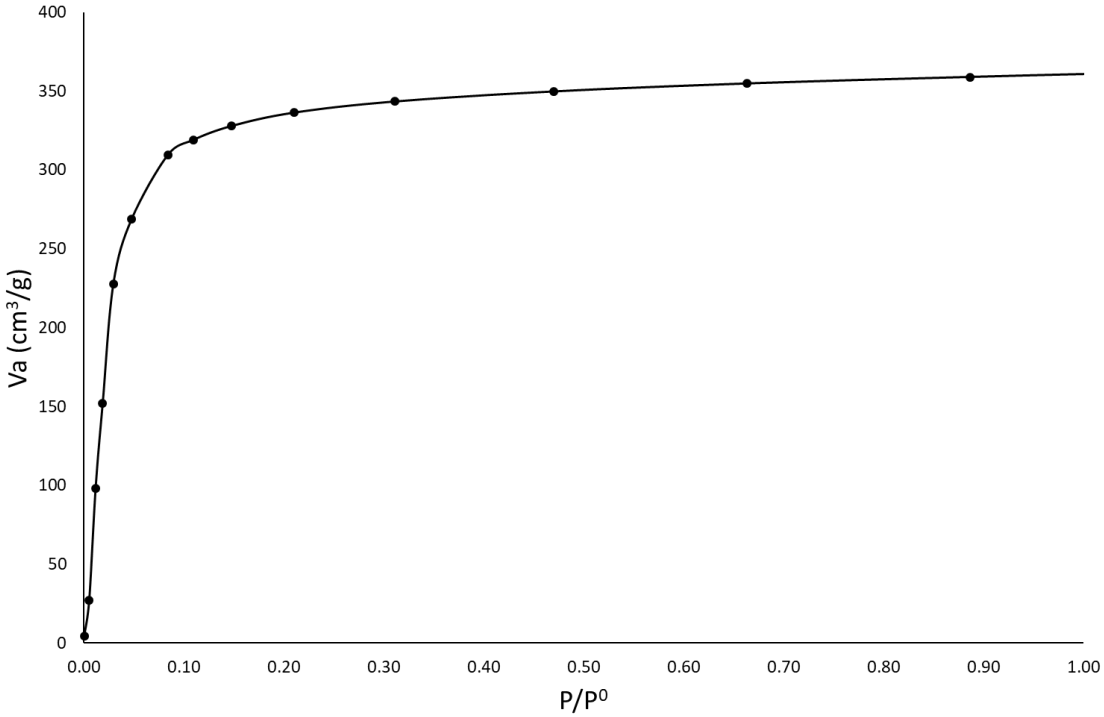

Figure 5.52. Nitrogen adsorption Isotherm for IRMOF-NHPr

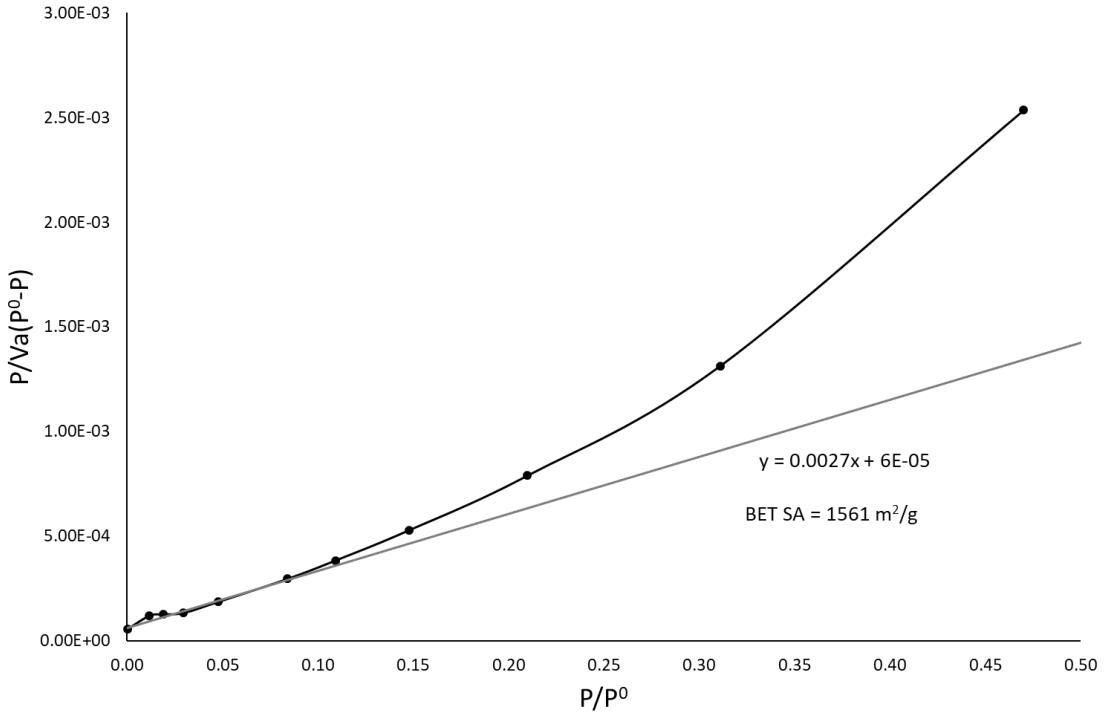

Figure 5.53. BET plot for IRMOF-NHPr.

5.5.2.4 Synthesis of IRMOF-OPr

$Zn(NO_3)_2 \cdot 6H_2O$ (0.6 mmol, 0.179 g) and 2-propoxy-1,4-benzenedicarboxylic acid (0.2 mmol, 0.045 g) were dissolved in 8 mL of dry DMF in a 10 mL microwave vial with the aid of a sonicator. The vial was sealed with a crimped Teflon-lined cap and placed in an oven at 100 °C for 72 hours. After removal from the oven and cooling under ambient conditions, the large colourless cubic crystals were collected via vacuum filtration, then washed with fresh DMF (3 x 5 mL) and stored in dry DMF until needed. The products identity was confirmed using PXRD. As with the IRMOF-NHPr the experimental pattern has been compared to that simulated from single-crystal data for IRMOF-3 as no single-crystal structure has been solved for IRMOF-OPr. This trace is shown in **Figure 5.54**.

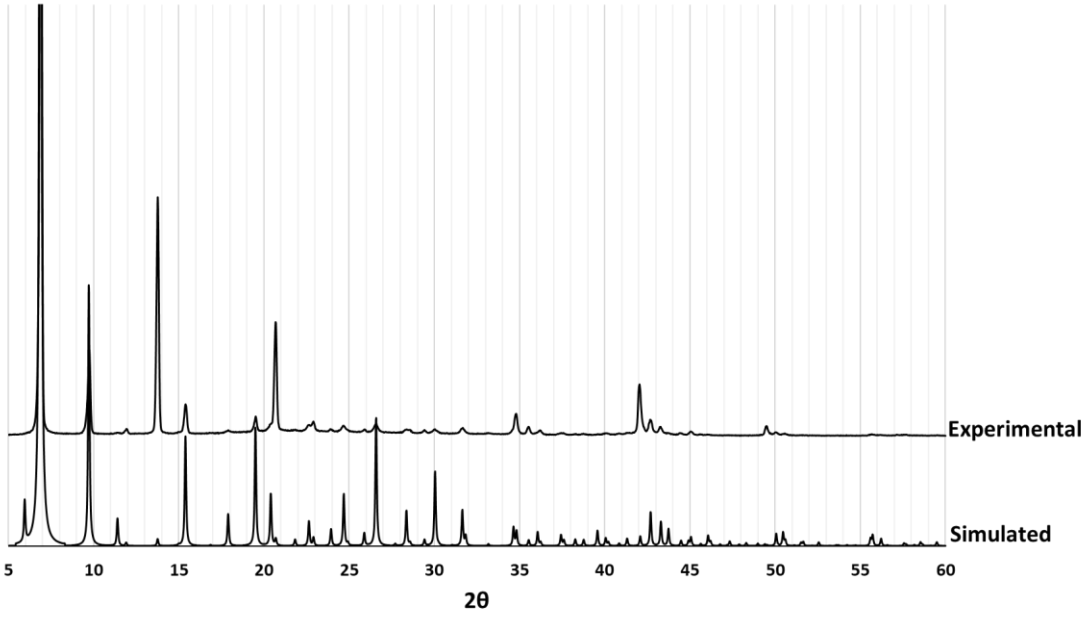

Figure 5.54. The experimental PXRD trace of IRMOF-OPr compared to a trace simulated from single-crystal data for IRMOF-3.

Activation was carried out in an identical manner to that for IRMOF-3 and IRMOF-NHPr. A nitrogen adsorption isotherm was collected, as shown in **Figure 5.55**, and a BET plot constructed, shown in **Figure 5.56Figure 5.53**, giving a BET surface area for IRMOF-OPr of 1696 $m^2 g^{-1}$.

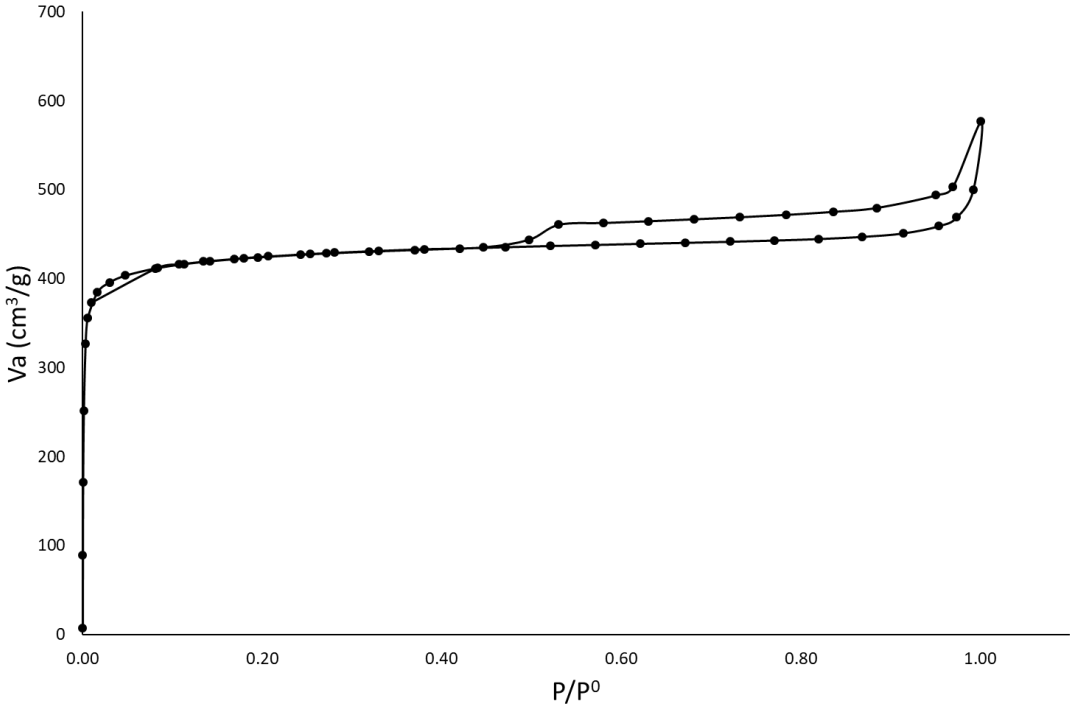

Figure 5.55. Nitrogen adsorption and desorption isotherm for IRMOF-OPr.

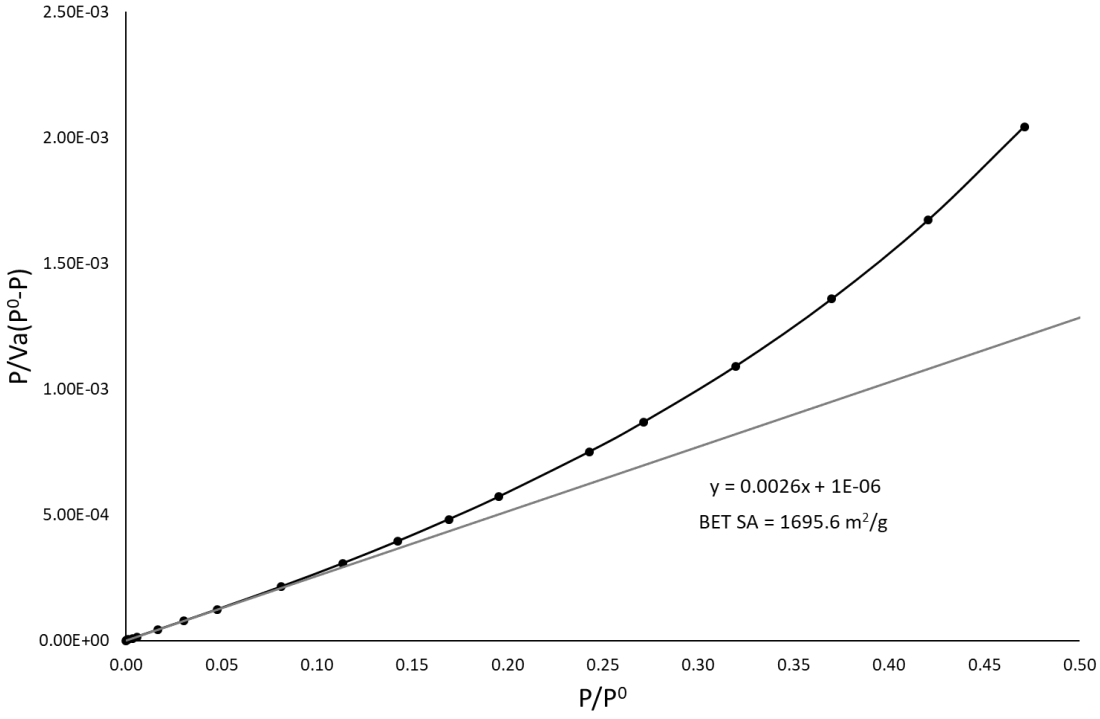

Figure 5.56. BET plot for IRMOF-OPr.

5.5.2.5 Synthesis of Zn-MOF-74

Zn-MOF-74 [$Zn_2(dobdc)_2$] was synthesised using a modified procedure based on a previously reported literature preparation.[175] $Zn(NO_3)_2 \cdot 6H_2O$ (0.76 mmol, 0.226 g) and 2,5-dihydroxy-1,4-benzenedicarboxylic acid (0.26 mmol, 0.0515 g) were added to 7 mL of dry DMF in a 10 mL microwave vial and dissolved with the aid of a sonicator. 1 mL of deionised water was added and the vial sealed with a Teflon-lined cap. The vial was heated at 105 °C for 48 hours producing clusters of small yellow-green crystals. After removal from the oven and cooling under ambient conditions, the crystals were collected by vacuum filtration and washed with excess MeOH and then stored in MeOH prior to use. The product identity was confirmed by as shown in **Figure 5.57**.

If activation of the material was required a further solvent exchange with methanol was carried out. The methanol was exchanged for fresh methanol every 24 hours for a period of 3 days. After this period the crystals were recovered by vacuum filtration and then heated at 180 °C under reduced pressure for 24 hours before being backfilled with N_2 gas.

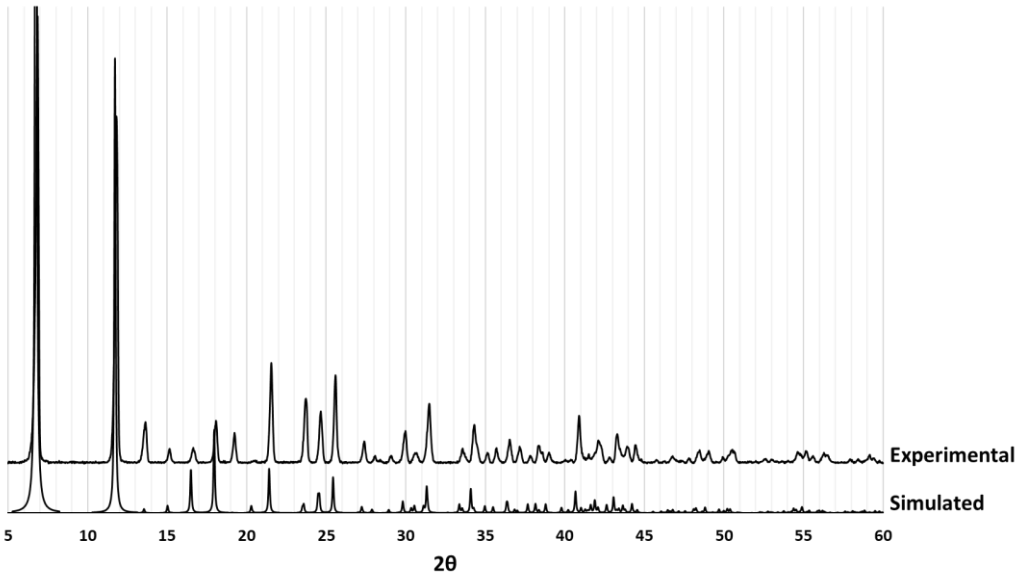

Figure 5.57. The experimental PXRD trace of Zn-MOF-74 compared to the trace simulated from single-crystal data.[183]

5.5.2.6 Synthesis of K-CDMOF

K-CDMOF was prepared according to a literature procedure.[168] In a 30 mL vial, potassium hydroxide (3.98 mmol, 0.2232 g) and γ-cyclodextrin (0.50 mmol, 0.6520 g) were dissolved in 10 mL of H_2O with the aid of a sonicator. The vial was then placed inside a beaker and 25 mL of methanol added to the beaker. The top of the beaker was covered and sealed using parafilm.

The reaction was left for 7 days for vapour diffusion to occur and crystals to grow. The crystals were stored in their mother liquor prior to use. The product identity was confirmed via PXRD as shown in **Figure 5.58**.

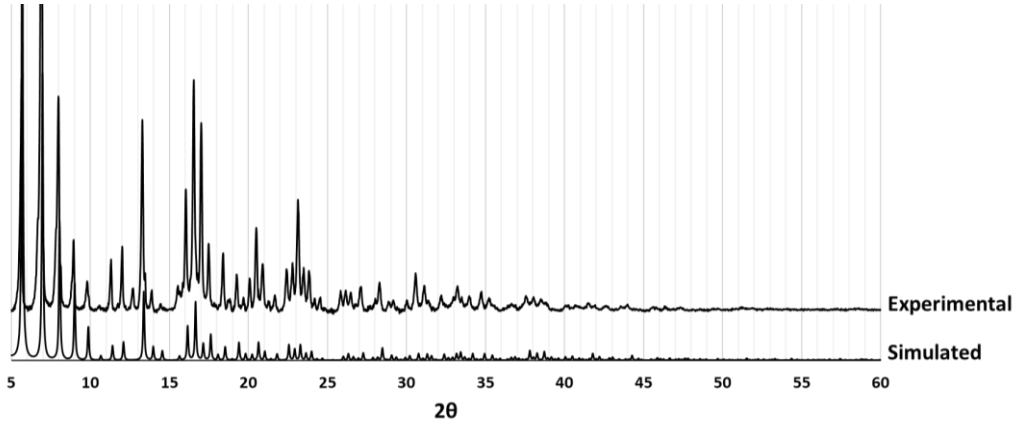

Figure 5.58. The experimental PXRD trace of K-CDMOF compared to the trace simulated from single-crystal data.[168]

5.5.2.7 Synthesis of Na-CDMOF

Na-CDMOF was prepared according to a literature procedure.[173] In a 30 mL vial, sodium hydroxide (4.39 mmol, 0.1754 g) and γ-cyclodextrin (0.50 mmol, 0.6534 g) were dissolved in 10 mL of H_2O with the aid of a sonicator. The vial was then placed inside a beaker and 25 mL of methanol added to the beaker. The top of the beaker was covered and sealed using parafilm. The reaction was left for 7 days for vapour diffusion to occur and crystals to grow. The crystals were stored in their mother liquor prior to use. The product identity was confirmed via PXRD as shown in **Figure 5.59**.

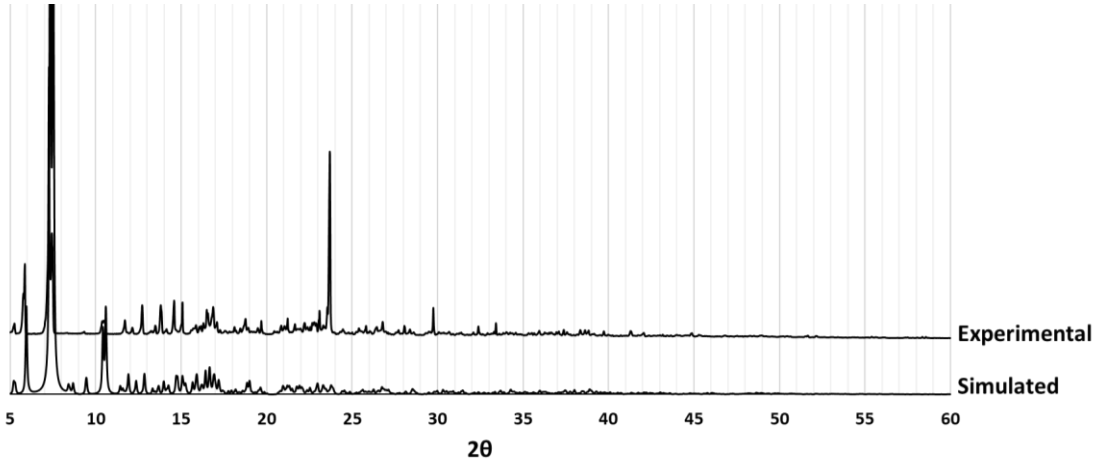

Figure 5.59. The experimental PXRD trace of Na-CDMOF compared to the trace simulated from single-crystal data.[173]

5.5.3 Semiochemical Inclusion and Release Procedures

5.5.3.1 Inclusion of Semiochemicals

For non-activated samples, the MOF crystals were separated from their storage medium via vacuum filtration. The crystals were submerged into neat semiochemical inside a sealed vial. After three days of semiochemical-solvent exchange, the crystals were again recovered using vacuum filtration and washed with (3 x 3 mL) of n-hexane. The day 0 and maximum uptake measurement was then made by digesting the MOF in deuterated solvent and collecting a ^{1}H-NMR spectrum.

For activated samples the same procedure as above was followed except that the semiochemical was introduced into the N_2 filled vial that the activated MOF crystals were being stored in, minimising exposure to moisture in the air.

5.5.3.2 Digestion of MOFs for ^{1}H-NMR

MOF-74, and the IRMOF and CDMOF derivatives were all digested using deuterated acidic solutions. Approximately 10 mg of the MOF was dissolved in either a DCl or D_2SO_4 based solution. In the DCl case, 0.4 mL of DMSO-d_6 and 0.2 mL of a stock solution were used to dissolve the MOF. The stock solution contained 0.1 mL of DCl 35 wt.% (in D_2O) and 3 mL of DMSO-d_6. In the case of D_2SO_4 the MOF was digested in a solution containing 0.5 mL of DMSO-d_6 and 0.1 mL of a stock solution. This stock solution comprised of 0.1 mL of D_2SO_4 96-98 wt.% (in D_2O) and 2.4 mL of DMSO-d_6.

5.5.3.3 Release of Semiochemicals from MOFs

Once removed from the semiochemical and washed the loaded MOFs were left in open vials on the bench in the lab. Samples of the MOF were taken, digested and analysed by ^{1}H-NMR spectroscopy at set time intervals to ascertain the loss of semiochemical from the pores of the MOF.

Chapter 6 - References

1. H. Furukawa, K. E. Cordova, M. O'Keeffe and O. M. Yaghi, *Science*, 2013, **341**, 974-987.
2. S. Kitagawa, R. Kitaura and S.-i. Noro, *Angew. Chem. Int. Ed.*, 2004, **43**, 2334-2375.
3. C. Dey, T. Kundu, B. P. Biswal, A. Mallick and R. Banerjee, *Acta Crystallogr. Sect. B*, 2014, **70**, 3-10.
4. H.-C. Zhou and S. Kitagawa, *Chem. Soc. Rev.*, 2014, **43**, 5415-5418.
5. A. U. Czaja, N. Trukhan and U. Muller, *Chem. Soc. Rev.*, 2009, **38**, 1284-1293.
6. D. N. Dybtsev, H. Chun and K. Kim, *Angew. Chem. Int. Ed.*, 2004, **43**, 5033-5036.
7. N. Prasetya and B. P. Ladewig, *ACS Appl. Mater. Interfaces*, 2018, **10**, 34291-34301.
8. P. V. Dau and S. M. Cohen, *Chem. Commun.*, 2013, **49**, 6128-6130.
9. S. Seth and A. J. Matzger, *Cryst. Growth Des.*, 2017, **17**, 4043-4048.
10. K. Biradha, A. Ramanan and J. J. Vittal, *Cryst. Growth Des.*, 2009, **9**, 2969-2970.
11. O. M. Yaghi and H. Li, *J. Am. Chem. Soc.*, 1995, **117**, 10401-10402.
12. S. R. Batten, N. R. Champness, X.-M. Chen, J. Garcia-Martinez, S. Kitagawa, L. Öhrström, M. O'Keeffe, M. P. Suh and J. Reedijk, *Pure Appl. Chem.*, 2013, **85**, 1715-1724.
13. J. L. C. Rowsell and O. M. Yaghi, *Microporous and Mesoporous Mater.,* 2004, **73**, 3-14.
14. D. J. Tranchemontagne, J. L. Mendoza-Cortes, M. O'Keeffe and O. M. Yaghi, *Chem. Soc. Rev.*, 2009, **38**, 1257-1283.
15. M. Eddaoudi, D. B. Moler, H. Li, B. Chen, T. M. Reineke, M. O'Keeffe and O. M. Yaghi, *Acc. Chem. Res.*, 2001, **34**, 319-330.
16. O. M. Yaghi, M. O'Keeffe, N. W. Ockwig, H. K. Chae, M. Eddaoudi and J. Kim, *Nature*, 2003, **423**, 705-714.
17. J. Kim, B. Chen, T. M. Reineke, H. Li, M. Eddaoudi, D. B. Moler, M. O'Keeffe and O. M. Yaghi, *J. Am. Chem. Soc.*, 2001, **123**, 8239-8247.
18. N. Stock and S. Biswas, *Chem. Rev.*, 2012, **112**, 933-969.
19. M. Eddaoudi, J. Kim, N. Rosi, D. Vodak, J. Wachter, M. O'Keeffe and O. M. Yaghi, *Science*, 2002, **295**, 469-472.
20. H. Li, M. Eddaoudi, M. O'Keeffe and O. M. Yaghi, *Nature*, 1999, **402**, 276-279.
21. N. L. Rosi, J. Eckert, M. Eddaoudi, D. T. Vodak, J. Kim, M. O'Keeffe and O. M. Yaghi, *Science*, 2003, **300**, 1127-1129.
22. G. Férey, C. Serre, C. Mellot-Draznieks, F. Millange, S. Surblé, J. Dutour and I. Margiolaki, *Angew. Chem. Int. Ed.*, 2004, **43**, 6296-6301.
23. M. Wickenheisser, F. Jeremias, S. K. Henninger and C. Janiak, *Inorg. Chim. Acta*, 2013, **407**, 145-152.
24. P. Horcajada, S. Surblé, C. Serre, D.-Y. Hong, Y.-K. Seo, J.-S. Chang, J.-M. Grenèche, I. Margiolaki and G. Férey, *Chem. Commun.*, 2007, 2820-2822.
25. C. Volkringer, D. Popov, T. Loiseau, G. Férey, M. Burghammer, C. Riekel, M. Haouas and F. Taulelle, *Chem. Mater.*, 2009, **21**, 5695-5697.
26. L. Y.-T. C. Ke-Hui, L. J. Z. J.-Q. Wang and X. T. Yun-Qi, *Chinese J. Inorg. Chem.*, 2011, **5**.
27. A. Lieb, H. Leclerc, T. Devic, C. Serre, I. Margiolaki, F. Mahjoubi, J. S. Lee, A. Vimont, M. Daturi and J.-S. Chang, *Microporous and Mesoporous Mater.,* 2012, **157**, 18-23.
28. G. Zhong, D. Liu and J. Zhang, *Cryst. Growth Des.*, 2018, **18**, 7730-7744.
29. B. Singco, L.-H. Liu, Y.-T. Chen, Y.-H. Shih, H.-Y. Huang and C.-H. Lin, *Microporous and Mesoporous Mater.*, 2016, **223**, 254-260.
30. Z. Yin, S. Wan, J. Yang, M. Kurmoo and M.-H. Zeng, *Coord. Chem. Rev.*, 2019, **378**, 500-512.
31. H. Amer Hamzah, PhD Thesis, University of Bath, 2017.
32. W. J. Gee, L. K. Cadman, H. Amer Hamzah, M. F. Mahon, P. R. Raithby and A. D. Burrows, *Inorg. Chem.*, 2016, **55**, 10839-10842.

33. K. S. Asha, R. Bhattacharjee and S. Mandal, *Angew. Chem. Int. Ed.*, 2016, **55**, 11528-11532.
34. J. E. Mondloch, O. Karagiaridi, O. K. Farha and J. T. Hupp, *CrystEngComm*, 2013, **15**, 9258-9264.
35. W. Xuan, C. Zhu, Y. Liu and Y. Cui, *Chemical Society Reviews*, 2012, **41**, 1677-1695.
36. U. Mueller, M. Schubert, F. Teich, H. Puetter, K. Schierle-Arndt and J. Pastre, *J. Mater. Chem.*, 2006, **16**, 626-636.
37. O. K. Farha and J. T. Hupp, *Acc. Chem. Res.*, 2010, **43**, 1166-1175.
38. S. Yang, X. Lin, W. Lewis, M. Suyetin, E. Bichoutskaia, J. E. Parker, C. C. Tang, D. R. Allan, P. J. Rizkallah, P. Hubberstey, N. R. Champness, K. M. Thomas, A. J. Blake and M. Schröder, *Nat. Mater.*, 2012, **11**, 710-716.
39. S. S. Han, D.-H. Jung and J. Heo, *J. Phys. Chem. C*, 2013, **117**, 71-77.
40. C. Serre, F. Millange, C. Thouvenot, M. Noguès, G. Marsolier, D. Louër and G. Férey, *J. Am. Chem. Soc.*, 2002, **124**, 13519-13526.
41. T. K. Trung, P. Trens, N. Tanchoux, S. Bourrelly, P. L. Llewellyn, S. Loera-Serna, C. Serre, T. Loiseau, F. Fajula and G. Férey, *J. Am. Chem. Soc.*, 2008, **130**, 16926-16932.
42. G. Férey, *Chem. Soc. Rev.*, 2008, **37**, 191-214.
43. M. Rubio-Martinez, C. Avci-Camur, A. W. Thornton, I. Imaz, D. Maspoch and M. R. Hill, *Chem. Soc. Rev.*, 2017, **46**, 3453-3480.
44. Y. Sun and H.-C. Zhou, *Sci. Tech. Adv. Mater.*, 2015, **16**, 054202.
45. S. S. Y. Chui, S. M. F. Lo, J. P. H. Charmant, A. G. Orpen and I. D. Williams, *Science*, 1999, **283**, 1148.
46. Parr Instrument Company - Hydrothermal Synthesis, https://www.parrinst.com/products/sample-preparation/acid-digestion/applications/hydrothermal-synthesis/, (accessed 17/12/2019).
47. J. I. Feldblyum, A. G. Wong-Foy and A. J. Matzger, *Chem. Commun.*, 2012, **48**, 9828-9830.
48. I. Thomas-Hillman, A. Laybourn, C. Dodds and S. W. Kingman, *J. Mater. Chem. A*, 2018, **6**, 11564-11581.
49. A. Martinez Joaristi, J. Juan-Alcañiz, P. Serra-Crespo, F. Kapteijn and J. Gascon, *Cryst. Growth Des.*, 2012, **12**, 3489-3498.
50. S. L. James, C. J. Adams, C. Bolm, D. Braga, P. Collier, T. Friscic, F. Grepioni, K. D. M. Harris, G. Hyett, W. Jones, A. Krebs, J. Mack, L. Maini, A. G. Orpen, I. P. Parkin, W. C. Shearouse, J. W. Steed and D. C. Waddell, *Chem. Soc. Rev.*, 2012, **41**, 413-447.
51. D. Chen, J. Zhao, P. Zhang and S. Dai, *Polyhedron*, 2019, **162**, 59-64.
52. YLK Laboratory Equipment, http://www.ylkeqpt.com/show-7-72.html, (accessed 17/12/2019).
53. W.-J. Son, J. Kim, J. Kim and W.-S. Ahn, *Chem. Commun.*, 2008, 6336-6338.
54. T. Loiseau, C. Serre, C. Huguenard, G. Fink, F. Taulelle, M. Henry, T. Bataille and G. Férey, *Chem. Eur.*, 2004, **10**, 1373-1382.
55. P. A. Bayliss, I. A. Ibarra, E. Pérez, S. Yang, C. C. Tang, M. Poliakoff and M. Schröder, *Green Chem.*, 2014, **16**, 3796-3802.
56. A. Laybourn, J. Katrib, R. S. Ferrari-John, C. G. Morris, S. Yang, O. Udoudo, T. L. Easun, C. Dodds, N. R. Champness, S. W. Kingman and M. Schröder, *J. Mater. Chem. A*, 2017, **5**, 7333-7338.
57. A. Laybourn, A. M. López-Fernández, I. Thomas-Hillman, J. Katrib, W. Lewis, C. Dodds, A. P. Harvey and S. W. Kingman, *Chem. Eng. J.l*, 2019, **356**, 170-177.
58. D. Crawford, J. Casaban, R. Haydon, N. Giri, T. McNally and S. L. James, *Chem. Sci.*, 2015, **6**, 1645-1649.
59. MOF Technologies - Manufacturing, https://www.moftechnologies.com/manufacturing/, (accessed 17/12/2019).

60. B. D. Cullity, *Elements of X-ray diffraction*, Prentice Hall, Upper Saddle River, N.J. London, 3rd ed., 2001.
61. W. Clegg, *X-ray crystallography*, Oxford University Press, Oxford, 2nd ed., 2015.
62. S. I. Brückner, J. Pallmann and E. Brunner, in *The Chemistry of Metal–Organic Frameworks*, Wiley-VCH Verlag GmbH & Co. KGaA, 2016, pp. 607-628.
63. A. Burrows, J. S. Holman, A. F. Parsons, G. Pilling, G. J. Price, in *Chemistry3*, Oxford University Press, Oxford, 3rd edn., 2017, ch. 12.2, pp. 569 - 575.
64. M. B. Johnson and M. A. White, in *Multi Length-Scale Characterisation*, John Wiley & Sons Ltd, 2014, pp. 63-119.
65. I. Senkovska, K. A. Cychosz, P. Llewellyn, M. Thommes and S. Kaskel, in *The Chemistry of Metal–Organic Frameworks*, Wiley-VCH Verlag GmbH & Co. KGaA, 2016, pp. 575-605.
66. J. U. Keller, ed. R. Staudt, Springer US, New York, NY, 1st ed., 2005, ch. 7, pp. 389-392.
67. G. Attard, ed. C. Barnes, Oxford University Press, Oxford, 1998, ch. 1.
68. L. Holyfield, PhD Theisis, University of Bath, 2018.
69. O. K. Farha, A. Özgür Yazaydın, I. Eryazici, C. D. Malliakas, B. G. Hauser, M. G. Kanatzidis, S. T. Nguyen, R. Q. Snurr and J. T. Hupp, *Nat. Chem.*, 2010, **2**, 944-948.
70. C. Montoro, E. García, S. Calero, M. A. Pérez-Fernández, A. L. López, E. Barea and J. A. R. Navarro, *J. Mater. Chem.*, 2012, **22**, 10155-10158.
71. Y. Pan, T. Li, G. Lestari and Z. Lai, *J. Membr. Sci.*, 2012, **390-391**, 93-98.
72. C. Zhang, R. P. Lively, K. Zhang, J. R. Johnson, O. Karvan and W. J. Koros, *J Phys. Chem.*, 2012, **3**, 2130-2134.
73. K. S. Park, Z. Ni, A. P. Côté, J. Y. Choi, R. Huang, F. J. Uribe-Romo, H. K. Chae, M. O'Keeffe and O. M. Yaghi, *Proc. Nat. Ac. Sci.*, 2006, **103**, 10186.
74. B. Yilmaz and U. Müller, *Top. Catal.*, 2009, **52**, 888-895.
75. B. F. Hoskins and R. Robson, *J. Am. Chem. Soc.*, 1989, **111**, 5962-5964.
76. J. Lee, O. K. Farha, J. Roberts, K. A. Scheidt, S. T. Nguyen and J. T. Hupp, *Chem. Soc. Rev.*, 2009, **38**, 1450-1459.
77. C. J. Doonan and C. J. Sumby, *CrystEngComm*, 2017, **19**, 4044-4048.
78. A. Legrand, J. Canivet and D. Farrusseng, in *The Chemistry of Metal–Organic Frameworks*, Wiley-VCH Verlag GmbH & Co. KGaA, 2016, pp. 345-386.
79. J. Kim, S.-N. Kim, H.-G. Jang, G. Seo and W.-S. Ahn, *Appl.Cat. A*, 2013, **453**, 175-180.
80. J. H. Cavka, S. Jakobsen, U. Olsbye, N. Guillou, C. Lamberti, S. Bordiga and K. P. Lillerud, *J. Am. Chem. Soc.*, 2008, **130**, 13850-13851.
81. S. J. Garibay and S. M. Cohen, *Chem. Commun.*, 2010, **46**, 7700-7702.
82. J. M. Roberts, B. M. Fini, A. A. Sarjeant, O. K. Farha, J. T. Hupp and K. A. Scheidt, *J. Am. Chem. Soc.*, 2012, **134**, 3334-3337.
83. W. P. Lustig, S. Mukherjee, N. D. Rudd, A. V. Desai, J. Li and S. K. Ghosh, *Chem. Soc. Rev.*, 2017, **46**, 3242-3285.
84. P. Kumar, A. Deep and K.-H. Kim, *TrAC Trends in Anal. Chem.*, 2015, **73**, 39-53.
85. J.-L. Du, X.-Y. Zhang, C.-P. Li, J.-P. Gao, J.-X. Hou, X. Jing, Y.-J. Mu and L.-J. Li, *Sens. Actuators B*, 2018, **257**, 207-213.
86. C. Jian and T. Xuejiao	 Li and Hongqi, *Curr. Med. Chem.*, 2019, **26**, 1-21.
87. P. Horcajada, C. Serre, G. Maurin, N. A. Ramsahye, F. Balas, M. Vallet-Regí, M. Sebban, F. Taulelle and G. Férey, *J. Am. Chem. Soc.*, 2008, **130**, 6774-6780.
88. S. Tai, W. Zhang, J. Zhang, G. Luo, Y. Jia, M. Deng and Y. Ling, *Microporous and Mesoporous Mater.*, 2016, **220**, 148-154.
89. A. D. Burrows, M. Jurcic, L. L. Keenan, R. A. Lane, M. F. Mahon, M. R. Warren, H. Nowell, M. Paradowski and J. Spencer, *Chem. Commun.*, 2013, **49**, 11260-11262.
90. H. Deng, S. Grunder, K. E. Cordova, C. Valente, H. Furukawa, M. Hmadeh, F. Gándara, A. C. Whalley, Z. Liu, S. Asahina, H. Kazumori, M. O'Keeffe, O. Terasaki, J. F. Stoddart and O. M. Yaghi, *Science*, 2012, **336**, 1018-1023.

91. F. Luo, C. Yan, L. Dang, R. Krishna, W. Zhou, H. Wu, X. Dong, Y. Han, T.-L. Hu, M. O'Keeffe, L. Wang, M. Luo, R.-B. Lin and B. Chen, *J. Am. Chem. Soc.*, 2016, **138**, 5678-5684.
92. A. D. Burrows, C. G. Frost, M. F. Mahon, M. Winsper, C. Richardson, J. P. Attfield and J. A. Rodgers, *Dalton Trans.*, 2008, 6788-6795.
93. T. Devic, O. David, M. Valls, J. Marrot, F. Couty and G. Férey, *J. Am. Chem. Soc.*, 2007, **129**, 12614-12615.
94. A. P. Katsoulidis, D. Antypov, G. F. S. Whitehead, E. J. Carrington, D. J. Adams, N. G. Berry, G. R. Darling, M. S. Dyer and M. J. Rosseinsky, *Nature*, 2019, **565**, 213-217.
95. C. R. Murdock, Z. Lu and D. M. Jenkins, *Inorg. Chem.*, 2013, **52**, 2182-2187.
96. Y.-N. Hou, J. Song, F.-Y. Bai and Y.-H. Xing, *Inorg. Chem.*, 2016, **440**, 69-76.
97. V. Wing-Wah Yam and K. Kam-Wing Lo, *Chem. Soc. Rev.*, 1999, **28**, 323-334.
98. J.-C. Dai, X.-T. Wu, Z.-Y. Fu, C.-P. Cui, S.-M. Hu, W.-X. Du, L.-M. Wu, H.-H. Zhang and R.-Q. Sun, *Inorg. Chem.*, 2002, **41**, 1391-1396.
99. Y.-Q. Lan, S.-L. Li, Y.-M. Fu, Y.-H. Xu, L. Li, Z.-M. Su and Q. Fu, *Dalton Trans.*, 2008, 6796-6807.
100. R. Mas-Ballesté, O. Castillo, P. J. Sanz Miguel, D. Olea, J. Gómez-Herrero and F. Zamora, *Eur. J. Inorg. Chem.*, 2009, **2009**, 2885-2896.
101. X.-C. Yi, M.-X. Huang, Y. Qi and E.-Q. Gao, *Dalton Trans.*, 2014, **43**, 3691-3697.
102. M. Déniz, J. Pasán, B. Rasines, P. Lorenzo-Luis, F. Lahoz, C. Vera-Gonzales, M. Julve and C. Ruiz-Pérez, *Inorg. Chem. Front.,* 2017, **4**, 1384-1392.
103. Y. Zhang, J. Yang, D. Zhao, Z. Liu, D. Li, L. Fan and T. Hu, *CrystEngComm*, 2019, **21**, 6130-6135.
104. J. Bernstein, R. E. Davis, L. Shimoni and N.-L. Chang, Angew. Chem. Int. Ed, 1995, **34**, 1555-1573.
105. D. Fröhlich, S. K. Henninger and C. Janiak, *Dalton Trans.*, 2014, **43**, 15300-15304.
106. P. K. Thallapally, J. Tian, M. Radha Kishan, C. A. Fernandez, S. J. Dalgarno, P. B. McGrail, J. E. Warren and J. L. Atwood, *J. Am. Chem. Soc.*, 2008, **130**, 16842-16843.
107. A. Hazra, D. P. van Heerden, S. Sanyal, P. Lama, C. Esterhuysen and L. J. Barbour, *Chem. Sci.*, 2019, **10**, 10018-10024.
108. C. Triguero, F.-X. Coudert, A. Boutin, A. H. Fuchs and A. V. Neimark, *J. Phys. Chem.*, 2011, **2**, 2033-2037.
109. S.-m. Hyun, J. H. Lee, G. Y. Jung, Y. K. Kim, T. K. Kim, S. Jeoung, S. K. Kwak, D. Moon and H. R. Moon, *Inorg. Chem.*, 2016, **55**, 1920-1925.
110. A. Schneemann, P. Vervoorts, I. Hante, M. Tu, S. Wannapaiboon, C. Sternemann, M. Paulus, D. C. F. Wieland, S. Henke and R. A. Fischer, *Chem. Mater.*, 2018, **30**, 1667-1676.
111. P. Smart, C. A. Mason, J. R. Loader, A. J. H. M. Meijer, A. J. Florence, K. Shankland, A. J. Fletcher, S. P. Thompson, M. Brunelli, A. H. Hill and L. Brammer, *Chem. Eur. J.*, 2013, **19**, 3552-3557.
112. I. J. Vitórica-Yrezábal, G. Mínguez Espallargas, J. Soleimannejad, A. J. Florence, A. J. Fletcher and L. Brammer, *Chem. Sci.*, 2013, **4**, 696-708.
113. I. J. Vitórica-Yrezábal, S. Libri, J. R. Loader, G. Mínguez Espallargas, M. Hippler, A. J. Fletcher, S. P. Thompson, J. E. Warren, D. Musumeci, M. D. Ward and L. Brammer, *Chem.,*2015, **21**, 8799-8811.
114. A. W. Addison, T. N. Rao, J. Reedijk, J. van Rijn and G. C. Verschoor, *Journal of the Chemical Society, Dalton Transactions*, 1984, **7**, 1349-1356.
115. P. Kumar T.K.M and A. Kumar S.K, *Photochem. Photobiol. Sci.*, 2019, **18**, 148-154.
116. G. Sheldrick, *Acta Crystallographica Section A*, 2015, **71**, 3-8.
117. G. Sheldrick, *Acta Crystallographica Section C*, 2015, **71**, 3-8.
118. O. V. Dolomanov, L. J. Bourhis, R. J. Gildea, J. A. K. Howard and H. Puschmann, *J. App. Cryst.*, 2009, **42**, 339-341.

119. S. Henke, A. Schneemann, S. Kapoor, R. Winter and R. A. Fischer, *J. Mater. Chem.*, 2012, **22**, 909-918.
120. A.-P. Jin, Z.-W. Chen, M.-S. Wang and G.-C. Guo, *Dyes and Pigments*, 2019, **163**, 656-659.
121. J.-X. Hou, J.-P. Gao, J. Liu, X. Jing, L.-J. Li and J.-L. Du, *Dyes and Pigments*, 2019, **160**, 159-164.
122. J. Zhang, L. Wojtas, R. W. Larsen, M. Eddaoudi and M. J. Zaworotko, *J. Am. Chem. Soc.*, 2009, **131**, 17040-17041.
123. A. Thirumurugan and C. N. R. Rao, *J. Mater. Chem.*, 2005, **15**, 3852-3858.
124. Z.-J. Zhang, W. Shi, Z. Niu, H.-H. Li, B. Zhao, P. Cheng, D.-Z. Liao and S.-P. Yan, *Chem. Commun.*, 2011, **47**, 6425-6427.
125. A. L. Grzesiak, F. J. Uribe, N. W. Ockwig, O. M. Yaghi and A. J. Matzger, *Angew. Chem. Int. Ed.*, 2006, **45**, 2553-2556.
126. K. K. Tanabe, Z. Wang and S. M. Cohen, *J. Am. Chem. Soc.*, 2008, **130**, 8508-8517.
127. C. A. Allen, J. A. Boissonnault, J. Cirera, R. Gulland, F. Paesani and S. M. Cohen, *Chem. Commun.*, 2013, **49**, 3200-3202.
128. C. A. Allen and S. M. Cohen, *Inorg. Chem.*, 2014, **53**, 7014-7019.
129. L. L. Keenan, H. Amer Hamzah, M. F. Mahon, M. R. Warren and A. D. Burrows, *CrystEngComm*, 2016, **18**, 5710-5717.
130. M.-X. Wu and Y.-W. Yang, *Adv. Mater.*, 2017, **29**, 1606134.
131. S. Rojas, I. Colinet, D. Cunha, T. Hidalgo, F. Salles, C. Serre, N. Guillou and P. Horcajada, *ACS Omega*, 2018, **3**, 2994-3003.
132. J. Gordon, H. Kazemian and S. Rohani, *Mater. Sci. Eng. C*, 2015, **47**, 172-179.
133. L. Zou and H.-C. Zhou, in *Nanostructured Materials for Next-Generation Energy Storage and Conversion: Hydrogen Production, Storage, and Utilization*, eds. Y.-P. Chen, S. Bashir and J. L. Liu, Springer Berlin Heidelberg, 2017, pp. 143-170.
134. E. Barea, C. Montoro and J. A. R. Navarro, *Chem. Soc. Rev.*, 2014, **43**, 5419-5430.
135. P. Gerland, A. E. Raftery, H. Ševčíková, N. Li, D. Gu, T. Spoorenberg, L. Alkema, B. K. Fosdick, J. Chunn, N. Lalic, G. Bay, T. Buettner, G. K. Heilig and J. Wilmoth, *Science*, 2014, **346**, 234-237.
136. W. Zhang, *Proc. Intl. Acad. Eco. Environ. Sci.*, 2018, **8**, 1-27.
137. R. Peshin, *Integrated Pest Management Dissemination and Impact*, Springer Netherlands, 2009.
138. P. Howse, J. Stevens and O. T. Jones, *Insect pheromones and their use in pest management*, Springer Science & Business Media, 2013.
139. P. Karlson and M. Luscher, *Nature*, 1959, **183**, 55.
140. J. Muñoz-Pallares, A. Corma, J. Primo and E. Primo-Yufera, *J. Agric. Food. Chem.*, 2001, **49**, 4801-4807.
141. S. M. Seo, J. M. Lee, H. Y. Lee, J. An, S. J. Choi and W. T. Lim, *J. Porous Mater.*, 2016, **23**, 557-562.
142. A. Tiboni, M. D. A. Coracini, E. R. Lima, P. H. G. Zarbin and A. J. G. Zarbin, *J. Braz. Chem. Soc.*, 2008, **19**, 1634-1640.
143. A. Zada, L. Falach and J. A. Byers, *Chemoecology*, 2009, **19**, 37-45.
144. A. Corma, M. Moliner, M. J. Díaz-Cabañas, P. Serna, B. Femenia, J. Primo and H. García, *New J. Chem.*, 2008, **32**, 1338-1345.
145. B. Zhang, Y. Luo, K. Kanyuck, G. Bauchan, J. Mowery and P. Zavalij, *J. Agric. Food. Chem.*, 2016, **64**, 5164-5170.
146. T. Loiseau, L. Lecroq, C. Volkringer, J. Marrot, G. Férey, M. Haouas, F. Taulelle, S. Bourrelly, P. L. Llewellyn and M. Latroche, *J. Am. Chem. Soc.*, 2006, **128**, 10223-10230.
147. Y. Guan, Z. Teng, L. Mei, J. Zhang, Q. Wang and Y. Luo, *J. Colloid Interface Sci.*, 2019, **533**, 207-215.
148. S. M. Blankenship and J. M. Dole, *Postharvest Biol. Tech.*, 2003, **28**, 1-25.

149. J. Urquhart, *ChemistryWorld*, 2016, *Online*.
150. A. Ghasemi and S. Zahediasl, *Iranian Biomedical Journal*, 2011, **15**, 59-65.
151. B. Xiao, P. S. Wheatley, X. Zhao, A. J. Fletcher, S. Fox, A. G. Rossi, I. L. Megson, S. Bordiga, L. Regli, K. M. Thomas and R. E. Morris, *J. Am. Chem. Soc.*, 2007, **129**, 1203-1209.
152. A. C. McKinlay, B. Xiao, D. S. Wragg, P. S. Wheatley, I. L. Megson and R. E. Morris, *J. Am. Chem. Soc.*, 2008, **130**, 10440-10444.
153. N. J. Hinks, A. C. McKinlay, B. Xiao, P. S. Wheatley and R. E. Morris, *Microporous and Mesoporous Mater.*, 2010, **129**, 330-334.
154. S. R. Miller, E. Alvarez, L. Fradcourt, T. Devic, S. Wuttke, P. S. Wheatley, N. Steunou, C. Bonhomme, C. Gervais, D. Laurencin, R. E. Morris, A. Vimont, M. Daturi, P. Horcajada and C. Serre, *Chem. Commun.*, 2013, **49**, 7773-7775.
155. M. J. Katz, A. J. Howarth, P. Z. Moghadam, J. B. DeCoste, R. Q. Snurr, J. T. Hupp and O. K. Farha, *Dalton Trans.*, 2016, **45**, 4150-4153.
156. M. T. Kapelewski, S. J. Geier, M. R. Hudson, D. Stück, J. A. Mason, J. N. Nelson, D. J. Xiao, Z. Hulvey, E. Gilmour, S. A. FitzGerald, M. Head-Gordon, C. M. Brown and J. R. Long, *J. Am. Chem. Soc.*, 2014, **136**, 12119-12129.
157. V. C. Norman, T. Butterfield, F. Drijfhout, K. Tasman and W. O. H. Hughes, *J. Chem. Ecol.*, 2017, **43**, 225-235.
158. W. O. H. Hughes and D. Goulson, *B. Entomol. Res.*, 2007, **92**, 213-218.
159. J. Montoya-Lerma, C. Giraldo-Echeverri, I. Armbrecht, A. Farji-Brener and Z. Calle, *Int. J. Pest Manage.*, 2012, **58**, 225-247.
160. N. Karimifar, R. Gries, G. Khaskin and G. Gries, *J. Agric. Food. Chem.*, 2011, **59**, 1330-1337.
161. D. G. Cochran, Cockroaches : their biology, distribution and control, *WHO : Institution Repositttory for Information Sharing*, http://www.who.int/iris/handle/10665/65846, 1999. (Accessed 05/01/2020)
162. Y. Feng, R. Bruton, A. Park and A. Zhang, *J. Pest Sci.*, 2018, **91**, 1251-1267.
163. I. W. Keesey, M. Knaden and B. S. Hansson, *J. Chem. Ecol.*, 2015, **41**, 121-128.
164. D. H. Cha, T. Adams, C. T. Werle, B. J. Sampson, J. J. Adamczyk Jr, H. Rogg and P. J. Landolt, *Pest Manage. Sci.*, 2014, **70**, 324-331.
165. S. S. Kaye, A. Dailly, O. M. Yaghi and J. R. Long, *J. Am. Chem. Soc.*, 2007, **129**, 14176-14177.
166. H. Yim, E. Kang and J. Kim, *Bull. Korean Chem. Soc.*, 2010, **31**, 1041-1043.
167. P. D. Beer, P. A. Gale and D. K. Smith, *Supramolecular Chemistry*, Oxford University Press, Oxford, 1999.
168. R. A. Smaldone, R. S. Forgan, H. Furukawa, J. J. Gassensmith, A. M. Z. Slawin, O. M. Yaghi and J. F. Stoddart, Angew. Chem. Int. Ed., 2010, **49**, 8630-8634.
169. T. Loftsson, P. Jarho, M. Másson and T. Järvinen, *Expert Opin. Drug Deliv.*, 2005, **2**, 335-351.
170. R. Arun, K. Ashok and V. V. N. S. S. Sravanthi, *Scientia Pharmaceutica*, 2008, **76**, 567-598.
171. K. J. Hartlieb, A. W. Peters, T. C. Wang, P. Deria, O. K. Farha, J. T. Hupp and J. F. Stoddart, *Chem. Commun.*, 2017, **53**, 7561-7564.
172. T. Rajkumar, D. Kukkar, K.-H. Kim, J. R. Sohn and A. Deep, *J. Ind. Eng. Chem.*, 2019.
173. R. S. Forgan, R. A. Smaldone, J. J. Gassensmith, H. Furukawa, D. B. Cordes, Q. Li, C. E. Wilmer, Y. Y. Botros, R. Q. Snurr, A. M. Z. Slawin and J. F. Stoddart, *J. Am. Chem. Soc.*, 2012, **134**, 406-417.
174. T. Dὺren, *Unpublished Results*.
175. T. G. Glover, G. W. Peterson, B. J. Schindler, D. Britt and O. Yaghi, *Chem. Eng. Sci.*, 2011, **66**, 163-170.
176. S. Gadipelli and Z. Guo, *Chem. Mater.s*, 2014, **26**, 6333-6338.
177. S. J. Yang and C. R. Park, *Adv. Mater.*, 2012, **24**, 4010-4013.

178. M. Dan-Hardi, C. Serre, T. Frot, L. Rozes, G. Maurin, C. Sanchez and G. Férey, *J. Am. Chem. Soc.*, 2009, **131**, 10857-10859.
179. G. Férey, C. Mellot-Draznieks, C. Serre, F. Millange, J. Dutour, S. Surblé and I. Margiolaki, *Science*, 2005, **309**, 2040-2042.
180. T. L. Payne and W. E. Finn, *J. Insect Physiol.*, 1977, **23**, 879-881.
181. T. Zhao, K. Axelsson, P. Krokene and A.-K. Borg-Karlson, *J. Chem. Ecol.*, 2015, **41**, 848-852.
182. S. Cadot, L. Veyre, D. Luneau, D. Farrusseng and E. A. Quadrelli, *J. Mater. Chem.*, 2014, **2**, 17757-17763.
183. W. Wong-Ng, J. A. Kaduk, H. Wu and M. Suchomel, *Powder Diffraction*, 2012, **27**, 256-262.